Structure and Bonding 152
Series Editor: D.M.P. Mingos

Christiane R. Timmel
Jeffrey R. Harmer *Editors*

Structural Information from Spin-Labels and Intrinsic Paramagnetic Centres in the Biosciences

Springer

152
Structure and Bonding

For further volumes:
http://www.springer.com/series/430

Aims and Scope

The series *Structure and Bonding* publishes critical reviews on topics of research concerned with chemical structure and bonding. The scope of the series spans the entire Periodic Table and addresses structure and bonding issues associated with all of the elements. It also focuses attention on new and developing areas of modern structural and theoretical chemistry such as nanostructures, molecular electronics, designed molecular solids, surfaces, metal clusters and supramolecular structures. Physical and spectroscopic techniques used to determine, examine and model structures fall within the purview of *Structure and Bonding* to the extent that the focus is on the scientific results obtained and not on specialist information concerning the techniques themselves. Issues associated with the development of bonding models and generalizations that illuminate the reactivity pathways and rates of chemical processes are also relevant

The individual volumes in the series are thematic. The goal of each volume is to give the reader, whether at a university or in industry, a comprehensive overview of an area where new insights are emerging that are of interest to a larger scientific audience. Thus each review within the volume critically surveys one aspect of that topic and places it within the context of the volume as a whole. The most significant developments of the last 5 to 10 years should be presented using selected examples to illustrate the principles discussed. A description of the physical basis of the experimental techniques that have been used to provide the primary data may also be appropriate, if it has not been covered in detail elsewhere. The coverage need not be exhaustive in data, but should rather be conceptual, concentrating on the new principles being developed that will allow the reader, who is not a specialist in the area covered, to understand the data presented. Discussion of possible future research directions in the area is welcomed.

Review articles for the individual volumes are invited by the volume editors.

In references *Structure and Bonding* is abbreviated *Struct Bond* and is cited as a journal.

Christiane R. Timmel • Jeffrey R. Harmer
Editors

Structural Information from Spin-Labels and Intrinsic Paramagnetic Centres in the Biosciences

With contributions by

P.P. Borbat • A.M. Bowen • J.H. Freed • D. Goldfarb • J.R. Harmer • G. Jeschke • J.P. Klare • O. Schiemann • S.A. Shelke • S.Th. Sigurdsson • H.-J. Steinhoff • C.E. Tait • C.R. Timmel • R. Ward

Springer

Editors
Christiane R. Timmel
Inorganic Chemistry Laboratory
University of Oxford
Oxford
United Kingdom

Jeffrey R. Harmer
Inorganic Chemistry Laboratory
University of Oxford
Oxford
United Kingdom

Centre for Advanced Imaging
University of Queensland
St Lucia
Australia

ISSN 0081-5993 ISSN 1616-8550 (electronic)
ISBN 978-3-642-39124-8 ISBN 978-3-642-39125-5 (eBook)
DOI 10.1007/978-3-642-39125-5
Springer Heidelberg New York Dordrecht London

Library of Congress Control Number: 2014933680

Printed on acid-free paper

Springer is part of Springer Science+Business Media (www.springer.com)

Preface

Contemporary science is ever more reliant on elucidating the structure and function of matter's molecular building blocks, be it in medical or materials research. Much of today's scientific progress hence depends crucially on the ability to measure molecular structure and mechanism with ever-increasing sensitivity and accuracy, with regard to both spatial and temporal resolutions. Electron paramagnetic resonance (EPR) with its wide armoury of powerful techniques has long been established as a versatile and powerful tool in the study of both structure and dynamics of molecular systems. Thanks to the development of site-directed mutagenesis methodologies, the availability of suitable spin labels and the simultaneous technological and methodological developments, the applicability of the technique particularly for the study of biological molecules and their assemblies seems virtually boundless.

Many of the recent advances and applications of EPR spectroscopy relate to the determination of structural constraints on the nanometre scale obtained from systems containing paramagnetic centres, such as cofactors, metals, metal clusters or indeed spin labels. Continuous wave (CW) and pulse EPR techniques exploit the dipolar coupling between these paramagnetic centres in order to determine their inter-spin distance(s). Double electron–electron resonance (DEER) or synonymously pulsed electron double resonance (PELDOR) is the EPR technique most widely applied to the determination of distance constraints between paramagnetic centres in frozen solutions or powders. Double quantum coherence (DQC) EPR yields at least the same distance information as well as having several other virtues, but is not as widespread due to the higher power requirements that are not provided by most pulse spectrometers.

Over recent years the desire to study ever more complex (mainly biological) systems has prompted the further development of both the spectroscopic techniques (including novel or modified pulse sequences) and sophisticated data analysis and interpretation methods. The design and synthesis of new spin labels has been driven by ambitious goals such as the study of protein structure and dynamics in cells. At the same time, the need for higher sensitivity such as what has been achieved at

Ku-band has led to an increased interest in even higher frequency PELDOR at Q- and W-band.

This volume of Structure and Bonding is devoted to a review of the state-of-the-art EPR techniques in the determination of structure and dynamics of biological systems with a particular focus on inter-spin distance measurements, some 13 years after the excellent review of the same subject by L. J. Berliner, S. S. Eaton and G. R. Eaton (Distance Measurements in Biological Systems by EPR, Vol. 19, 2000, Kluwer Academic/Plenum Publishers, New York).

Borbat and Freed commence the series with an extensive review of the theoretical concepts of DQC EPR and DEER in the chapter "Pulse Dipolar Electron Spin Resonance: Distance Measurements". Technical aspects and sensitivity considerations are discussed in detail, as well as a new 5-pulse DEER sequence enabling higher sensitivity and longer-range distance measurements. They show that these three complementary techniques, which they implemented at Ku-band, offer outstanding versatility and very high sensitivity.

Jeschke discusses the data analysis and interpretation of experimental PELDOR data in the chapter "Interpretation of Dipolar EPR Data in Terms of Protein Structure". Strategies for extracting information from the PELDOR trace (i.e. mean inter-spin distance, distance distribution, number of spins and local concentration) are described as well as the measurement conditions required for optimal data collection and analysis. Furthermore, methods to infer backbone–backbone distances from label–label distances are reviewed.

The methods for spin labelling of proteins and nucleic acids are examined in the chapter "Site-Directed Nitroxide Spin Labeling of Biopolymers" by Shelke and Sigurdsson. The three approaches, i.e. site-directed Nitroxide Spin Labeling, spin labelling through biopolymer synthesis and non-covalent labelling, are described in detail for proteins and nucleic acids. The authors also provide a comprehensive overview of available spin labels and their characteristics.

Goldfarb reviews the existing methods of distance determination on systems with paramagnetic metal-based spin labels, with a particular emphasis on Gd^{3+} in the chapter "Metal-Based Spin Labeling for Distance Determination". The advantages and limitations of metal-based spin labels over nitroxide spin labels are presented, and a new approach to spin labelling based on high-spin metal ions such as Mn^{2+} and Gd^{3+} is introduced. It is shown that the use of Gd^{3+} spin labels in high-field measurements may lead to a much increased sensitivity as demonstrated for a series of model systems.

Klare and Steinhoff focus on the use of CW EPR and pulse EPR methods to obtain information on spin label side chain mobility, solvent accessibility, environment polarity and inter-spin distances with particular emphasis on membrane-bound proteins in the chapter "Structural Information from Spin-Labelled Membrane-Bound Proteins". The theoretical background and techniques for determination of these properties are reviewed, and examples showing the use of these techniques for the determination of structure and dynamics of membrane proteins are given.

Ward and Schiemann explore the recent developments and applications in the study of oligonucleotides by CW and pulse dipolar EPR in the chapter "Structural Information from Oligonucleotides". Studies on model DNA and RNA systems aimed at establishing the range, accuracy and robustness of distance determination using PELDOR on these systems are presented, as well as the use of PELDOR to identify structure elements and determine conformational changes.

Bowen at al. describe the practical and theoretical aspects of orientation-selective PELDOR in the chapter "Orientation-Selective DEER Using Rigid Spin Labels, Cofactors, Metals, and Clusters". Experimental approaches to orientation-selective PELDOR at different frequencies, methods for the calculation of orientation-selective PELDOR traces and the interpretation of experimental data in terms of both distance and orientation of pairs of spin labels are discussed in detail. The chapter concludes with a report on recent applications employing nitroxide spin-labelled and metal containing systems.

Oxford, United Kingdom

Christiane R. Timmel
Jeffrey R. Harmer

Contents

Struct Bond (2014) 152: 1–82
DOI: 10.1007/430_2012_82

Published online: 12 April 2013

Pulse Dipolar Electron Spin Resonance: Distance Measurements

Peter P. Borbat and Jack H. Freed

Abstract In recent years electron spin resonance (ESR) has provided the means to obtain structural constraints in the field of structural biology on the nanoscale by measuring distances between paramagnetic species, which usually have been nitroxide spin-labels. These ESR methods enable the measurement of distances over the wide range from ca. 6–10 Å to nearly 90 Å. While cw methods may be used for the shortest distances, it is the pulse methods that enable this wide range, as well as determination of the distributions in distance. In this chapter we first describe the underlying theoretical concepts for understanding the principal pulse methods of double quantum coherence (DQC)-ESR and double-electron–electron-resonance (DEER), which we collectively refer to as Pulse-Dipolar ESR Spectroscopies (PDS). We then provide technical aspects of pulse ESR spectrometers required for high quality PDS studies. This is followed by an extensive description of sensitivity considerations in PDS, based largely upon our highly sensitive 17.3 GHz pulse spectrometer at ACERT. This description also includes a comparison of the effectiveness of the respective PDS pulse methods. In addition, the newer methods of 5-pulse DEER, which enables longer distances to be measured than by standard DEER, and 2D-DQC, which provides a convenient mapping for studying orientational coherence between spin labels and their interspin vector, are described.

Keywords ESR · PDS · DQC · DEER · Dipole-dipole · PELDOR · Spin-label

Contents

P.P. Borbat and J.H. Freed (✉)
Department of Chemistry and Chemical Biology, ACERT National Biomedical Center for Advanced ESR Technology, Cornell University, Ithaca, NY 14853-1301, USA

Abbreviations

cw	Continuous-wave
DEER	Double electron–electron resonance
DQ, DQC	Double-quantum, double-quantum coherence
DQF	Double-quantum filtering
ESEEM	Electron spin-echo envelope modulation
ESR	Electron spin resonance
FID	Free induction decay
hf	Hyperfine
log	Natural logarithm
MEM	Maximum entropy method
MTSSL	Methane-thiosulfonate spin-label
mw	Microwave
PDS	Pulsed dipolar spectroscopy
PELDOR	Pulsed electron–electron double resonance
RPE	Refocused primary echo
SNR	Signal-to-noise ratio
SQ, SQC	Single-quantum, single-quantum coherence
SSPA	Solid-state power amplifier
TWTA	Traveling-wave tube amplifier

1 Introduction

Applications of pulse and continuous-wave (cw) electron spin resonance (ESR) in the field over the last decade [1–15] even surpass the more traditional study of molecular dynamics [16–19]. ESR has provided the means to obtain structural constraints on the nanoscale by measuring distances between paramagnetic species, which usually have been nitroxide spin-labels. Both, cw [8, 9] and pulsed [1–3, 5–7, 10–15, 20] ESR, have been useful in this regard. However, pulsed ESR methods are not limited to just nitroxides; all possible combinations amongst nitroxides, radical cofactors, and transition metal ions have been investigated [10, 21–28]. Taken together, cw and pulsed ESR enable the measurement of distances over the wide range from ca. 6–10 Å to nearly 90 Å, with only the shorter range of ESR-measurable distances readily accessible to cw ESR.

Distance measurement by pulsed double electron–electron resonance (DEER, also referred to as PELDOR) [29–32] was introduced as an alternative for isolating weak electron–electron dipolar couplings from electron-spin-echo decays, which are usually dominated by relaxation and nuclear modulation effects [33, 34]. Since then several other pulsed methods of distance measurements were introduced [15, 35–38] and most notable is double-quantum coherence ESR (DQC ESR or DQC for short) [15, 35]. Applications of the mainstream pulse methods of DEER and DQC to structural problems in biology have been growing rapidly over the past few years [2, 5, 11, 12, 39–42]; consequently, in this chapter the focus is on them. At ACERT, we intensively apply and actively develop all aspects for both methods. Therefore, we refer to them collectively as pulse dipolar ESR spectroscopy (PDS), since the inclusion of the term "dipolar" makes clear their function and removes any ambiguity with respect to classic ELDOR [43–45]. Continuing progress has been made over the last decade in new and improved pulse ESR methods and instrumentation. This includes the development of pulse spectrometers at several working frequencies [46–50]; resonators [51–57]; new pulse sequences [15, 36, 58–61]; methods of data analysis and structure modeling [1, 62–71]; and expanding the application base.

Even though, as we will demonstrate, our pulse spectrometers at ACERT have achieved high sensitivity permitting one to record very high quality data on samples with biomolecular concentrations in the low micromolar range, this is still insufficient to satisfy the ever-growing demand of related biomedical research. At ACERT this includes multiple collaborations and in-house research. The Center spectrometers, having been in continuous operation for several years, have provided measurements on several thousand samples, but the demand for measurements is increasing. This is caused largely by the rapidly growing interest in the distance information that PDS can uniquely provide, but also by the extensive progress made by biotechnology, which has greatly improved such aspects of biochemical engineering as protein expression and purification, enabling the production and spin labeling of mutated protein variants in large numbers. However, it is clear that in order to continue to attend to the needs of this rapidly expanding field, it will be primarily necessary to achieve greater sensitivity and higher throughput than modern state-of-the-art pulse

spectrometers can provide. This motivates new instrumentation developments and improvements to the existing methods. We show in this chapter examples directed to this goal.

There are several earlier reviews outlining the methods for distance measurements by ESR [17, 18, 30, 72–76]; however, we include in this chapter some background material and emphasize the methodology and the latest developments through examples taken from our laboratory.

2 Distance Measurements by ESR

In the following subsections we provide the background for PDS methods in general, starting with the descriptions of DEER (or PELDOR) and DQC for the ideal two-spin system. Then we will comment on additional essential aspects, such as relaxation, multi-spin systems, intermolecular effects, distance range and distributions, data processing, and orientations.

2.1 General Aspects, Electron Spin Dipolar Coupling

The ESR distance measurements described in this chapter are all conducted in low-temperature frozen solutions, typically using nitroxide spin labels. At the heart of the method is measuring the static dipole–dipole coupling between the spins of unpaired electrons localized in the case of nitroxides on the p–π orbitals of the NO groups.

The magnetic moments $\mathbf{m}_{1,2}$ of two electron spins 1 and 2, separated by the distance $r = |\mathbf{r}_{12}|$, interact through space via the electron spin dipole–dipole interaction

$$H_{\mathrm{dd}} = \frac{1}{r^3}\left(\mathbf{m_1}\cdot\mathbf{m}_2 - 3(\mathbf{m}_1\cdot\mathbf{n}_{12})(\mathbf{m}_2\cdot\mathbf{n}_{12})\right) \tag{1}$$

where $\mathbf{n}_{12} \equiv \mathbf{r}_{12}/r$. In a formal description, the electron spin magnetic moment $\mathbf{m}_i$ is given by $\mathbf{m}_i = \gamma_{\mathrm{e}}\hbar\mathbf{S}_i$ with γ_{e} the gyromagnetic ratio of an electron spin and $\mathbf{S}_i$ the electron spin operator for the ith spin. Equation (1) for H_{dd} thus may be expressed (in angular frequency units) as:

$$H_{\mathrm{dd}} \cong a\left(S_{1z}S_{2z} - \frac{1}{4}(S_{1+}S_{2-} + S_{1-}S_{2+})\right) \tag{2}$$

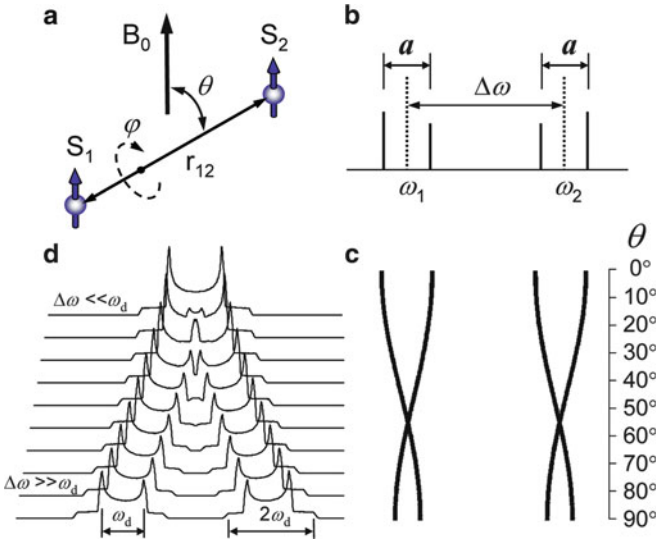

Fig. 1 (**a**) A pair of electron spins $\mathbf{S}_1$ and $\mathbf{S}_2$ coupled via the electron spin dipole–dipole interaction. Vector $\mathbf{r}_{12}$ connecting the spins is directed along the z-axis in the molecular frame of reference. In this molecular frame the direction of the external magnetic field $\mathbf{B}_0$ is determined by Euler angles $\boldsymbol{\eta} = (0, \theta, \varphi)$. (**b**) Dipolar coupling $a = \omega_d(1 - 3\cos^2\theta)$ splits the spectrum of two electron spins resonating at ω_1 and ω_2 into doublets. (**c**) Angular dependence, $a(\theta)$, is shown as a roadmap. (**d**) In isotropic medium the lineshape, resulting from electron dipolar coupling and in the limit of weak coupling case ($\Delta\omega \equiv |\omega_1 - \omega_2| \ll \omega_d$) is the Pake doublet with the prominent splitting of ω_d. As $\Delta\omega$ decreases the lineshape becomes more complicated as the two spectra merge into a single spectrum at $\Delta\omega \cong \omega_d$, and finally in the limit of like spins for sufficiently strong coupling, $\Delta\omega \ll \omega_d$, the spectrum is again a Pake doublet with the splitting $3\omega_d/2$

Here the dependence on $\mathbf{r}_{12}$ of the electron dipolar coupling, a, is given by

$$a(r, \theta) = \omega_d(1 - 3\cos^2\theta) \tag{3}$$

with

$$\omega_d \equiv 2\pi\nu_d = \gamma_e^2\hbar/r^3 \tag{4}$$

We will call ω_d the "dipolar frequency" (ν_d is in Hz). In Eq. (3) the angle θ is between the direction of the external magnetic field $\mathbf{B}_0$ and $\mathbf{r}_{12}$ as shown in Fig. 1a. Equation (2), limited to A (secular) and B (pseudosecular) terms of the "dipolar alphabet," is valid in high magnetic fields, where the non-secular terms C to F (not shown) are unimportant [77]. The term in $S_{1z}S_{2z}$ in Eq. (2) is known as the secular term, and that in $S_{1\pm}S_{2\pm}$ the pseudosecular term.

One usually uses the point dipole approximation in employing Eq. (2), i.e., the electron spins are far enough apart that their distributions (in, e.g., nitroxide p–π orbitals) are unimportant, i.e., $r > 5$ Å for nitroxides. An asymmetry parameter

may be necessary in the case of delocalized spin density, e.g., for closely situated spatially confined tyrosyl radicals, giving rise to a slightly rhombic spectral shape [78]. If in the absence of the dipolar coupling of Eq. (2), the two electron spins have resonance frequencies ω_1 and ω_2, then, the case of unlike spins may be stated as $\omega_d \ll \Delta\omega$, where $\Delta\omega \equiv |\omega_1 - \omega_2|$. In this case, the resonant frequency of each spin is split into a doublet separated by $|a|$, as shown in Fig. 1b arising just from the secular term. The precise value of a thus depends on the angle θ, yielding a range of values of a from $-2\omega_d$ to $+\omega_d$. The dipolar spectrum from the PDS experiment provides this splitting, which in Fig. 1c is plotted for each doublet as a function of the angle θ.

The case of unlike spins requires considering only the secular term in Eq. (2) and dropping the pseudosecular term. In the opposite case of like spins, that is, $\omega_d \gg \Delta\omega$ then the pseudosecular term becomes important and the rhs of Eq. (4) becomes $3\gamma_e^2\hbar/2r^3$. Otherwise the results are equivalent. The intermediate case of $\omega_d \cong \Delta\omega$ is more complex. As $\Delta\omega$ decreases, the two spectra at $\Delta\omega \cong \omega_d$ start to fuse into a single spectrum (cf. Fig. 1d), whose shape is obtained by careful simulation using Eq. (2) including both secular and pseudosecular terms. In the case of nitroxide spin labels, the two nitroxide spins in a given molecule usually have their ω_1 and ω_2 substantially different. This arises from their different orientations with respect to the $\mathbf{B}_0$ field, so their effective hyperfine (hf) and g values (arising from their hf and g tensors) are typically different. In the centimeter range of ESR frequencies (9–17 GHz) and above this means that for nitroxide spins the unlike spin limit is reached for ca. 20 Å.

In a typical case of an isotropic frozen sample, one observes an average over θ, which contains the whole range of splitting, giving rise to a distinct dipolar spectrum, known as a Pake doublet [79], as depicted in Fig. 1d (top). For weak coupling it shows a prominent splitting of ω_d, corresponding to $\theta = 90°$, and another splitting of $2\omega_d$, corresponding to $\theta = 0°$ (Fig. 1d, bottom). As we can see, even when the two electron spins (e.g., of nitroxides) in a given bilabeled molecule resonate at two different frequencies, because of different orientations and/or nuclear magnetic quantum numbers, they still yield a single lineshape (Pake doublet), resulting from their common dipolar interaction. Assuming one knows the correct limit (i.e., of weak or strong coupling), the distance r is then immediately and accurately obtained from a measurement of ω_d. We do not illustrate in the figure the effects of electron exchange J for the following reason. In the case of weak dipolar coupling, J is typically too small and can produce only a small inward or outward shift of the Pake doublet branches, with an overall shape change that is difficult to assign to a finite J. When J becomes large enough to be measured, ω_d is in the range of strong coupling and the whole coupling spectrum becomes complex, especially because ω_d and J are usually distributed.

In cases when ω_d is sufficiently large, it can be determined directly from the static broadening of the nitroxide cw ESR (or FT ESR) spectrum [9], but this is also likely to fall into the regime where pseudo-secular terms are significant requiring careful spectral simulation. As a rule, in cw ESR the dipolar couplings have a small

effect on the spectrum and are masked by much larger broadenings caused by magnetic tensor anisotropy. Smaller couplings ω_d necessitate using pulse ESR methods, as we discuss below. The use of spin echoes in the pulse experiment cancels the effects of hyperfine and g-tensor interactions, but not of the dipolar tensor interaction, which produces a distinct temporal evolution of the spin echo, from which this contribution to the lineshape can be reconstructed. Thus, in all cases, accurate values of distances are produced from the measured dipolar couplings.

2.2 *cw ESR Method and Its Range*

Cw ESR has been most often applied to nitroxides, whose powder spectra are dominated by the (inhomogeneous) broadenings from nitrogen hf and g-tensors, and unresolved proton superhyperfine couplings. One has to extract what usually is a small broadening effect from ω_d to the nitroxide powder spectra, which is usually accomplished by spectral deconvolution [80] or a multiple-parameter fit [9, 81]. When the ω_d is large and the molecule has a rigid structure, fitting cw ESR spectra can provide such useful details of molecular geometry as nitroxide orientations in addition to distances [9, 81].

As the distance increases and dipolar broadening is no longer large, measuring ω_d from cw ESR spectrum broadening may require referencing with the spectra from singly labeled species to approximate background intermolecular dipolar broadening. This presents a complication and is not always an option. Incomplete spin labeling makes the task more complex [82]. Only for distances less than 15 Å, does the dipolar coupling compete with other inhomogeneous spectral broadenings and thus can be reliably inferred from cw ESR spectra. If spectral deconvolution is used, then it should be decided which limit (i.e., of weak or strong coupling) to use. The worst case error, however, is only $(3/2)^{1/3}$, i.e., ~2 Å for $r < 15$ Å, if the incorrect limit is assumed. When one is not sure, taking as the mean $\omega_d \cong (5/4)\gamma_e^2\hbar^2/r^3$ will result in a maximum error in r of ~1 Å.

The case of strong dipolar coupling has been extensively utilized in cw ESR both in establishing proximity and in providing quantitative distances [4, 8, 9, 80, 81, 83–85]. Cw ESR is practical for short distances of about 8 Å up to a maximum of approximately 15–20 Å, with the values for distances under 15 Å being more reliable [86]. Distances in the range of 15–20 Å can be measured, but this usually requires good referencing as well as the spin concentration closer to the millimolar range.

Since pulse techniques have progressed to the state where they give reliable distances over a much wider distance range, with the measurements conducted routinely on just tens of micromolar of protein (or even less at ACERT, see below), the focus has shifted almost entirely to pulse techniques [72–76]. In the case of a broad spectrum, such as is encountered for two Cu^{2+} ions, measuring distances by cw ESR is not feasible unless the ions are very close, but there is no such serious problem for PDS [87]. Ku band DEER and especially DQC ESR, for example, were successful with Cu^{2+}–Cu^{2+} pairs even for distances in the range of 30–50 Å (ACERT, unpublished).

2.3 Pulse Methods

Pulse ESR conducted on solids is based on detecting a spin-echo, wherein the inhomogeneous spectral broadening is canceled out [88]. Spin echo temporal evolution is governed by the weaker effects of spin relaxation, electron–electron spin dipolar and exchange couplings, and (pseudo-secular) electron-nuclear hyperfine and nuclear quadrupole couplings [89–92]. The electron dipolar and exchange couplings can be isolated from the others by means of a suitable pulse sequence. Several pulse sequences were designed to obtain the dipolar coupling: PELDOR or 3-pulse DEER, 4-pulse DEER, single-frequency techniques such as "2+1" [38] and several others [36], methods based on relaxation [37], and DQC [35]. Of these, only 4-pulse DEER and DQC are used often, and the reasons for this will be explained in this chapter. These pulse sequences, to a varying extent, also help to alleviate the problem caused by the presence of single-labeled molecules. Their direct signal is filtered out in DQC, but they do contribute to the background intermolecular dipolar signal, which is best suppressed by working at low concentrations in DQC, but cannot be avoided in single-frequency techniques and DEER. These methods of PDS are routinely used for distances longer than 15 Å [5, 12, 14, 42, 58, 73], and in DQC it works well down to ~10 Å [11] (cf. Sect. 4.2), thereby overlapping significantly with the cw ESR range. However, it is much less affected by inefficient labeling, operates in the low micromolar range, and can readily yield distance distributions!

2.3.1 Theoretical Background

Most known pulse ESR methods conducted on solids are based on detecting the spin echo signal. The significant outcome of a PDS experiment is the modulation, by the electron-spin dipolar coupling, of the spin-echo amplitude as the pulse sequence is stepped out. In this respect, it belongs to the general class of ESEEM experiments [89–92], wherein the pulse sequence is stepped out and a series of spin echoes is acquired in order to obtain the echo modulation, from which weak electron spin interactions with surrounding nuclei or electrons can be inferred. A suitable pulse sequence is applied to the spin system initially in thermal equilibrium, and its associated density matrix evolves under the action of propagators describing the effects of the microwave pulses, interspersed with free evolution periods. Finally, the relevant part of the density matrix associated with the transverse magnetization is selected by using phase cycling to remove the undesired or irrelevant contributions to the spin-echo signal. The density matrix in thermal equilibrium contains only diagonal elements, representing just the populations of the energy levels. The microwave pulses yield off-diagonal density-matrix elements (coherences) with characteristic phases. One can theoretically manipulate these coherences using a series of pulse and free evolution propagators to generate the echo of interest. Stepping out the pulses in their proper sequence produces the time-domain signal

record, whose shape is determined in part or entirely by the electron-spin dipolar coupling. The relevant part of the signal, depending on just the encoded dipolar coupling, is then separated from the rest of the signal and processed into the dipolar spectrum (e.g., Pake doublet). Then the distance information may be inferred, or else it may be used as input into distance reconstruction software. Understanding how this modulation is generated and controlled is thus essential for optimizing and further developing PDS. We give a relatively simple introduction. We will employ the density matrix and spin operator formalisms, which can be applied in different ways depending on the objectives.

The initial density operator in thermal equilibrium, $\boldsymbol{\rho}_0$ for two electron spins $\mathbf{S}_{1,2}$, is described by the static spin-Hamiltonian $\hat{H}_0$ as:

$$\rho_0 = \frac{\exp(-\hat{H}_0/kT)}{Tr[\exp(-\hat{H}_0/kT)]} \propto \hat{S}_{1z} + \hat{S}_{2z}, \tag{5}$$

where the z-axis is defined to coincide with the direction of the external magnetic field, and the subscripts refer to the two interacting spins. First-order expansion of Eq. (5) is appropriate for nitroxide spin labels down to liquid helium temperatures for working frequency up to Ka-band. The time evolution of the spin density operator $\boldsymbol{\rho}$ is governed by the Liouville–von Neumann equation.

$$\frac{d\rho}{dt} = -\frac{\mathrm{i}}{\hbar} H^{\times} \rho(t) - \Gamma(\rho(t) - \rho(0)) \tag{6}$$

Here, $\mathbf{H}^{\times}\boldsymbol{\rho} \equiv [\hat{H},\rho]$ with ρ being the density matrix, $\hbar$ is Plank's constant divided by 2π, $\boldsymbol{\Gamma}$ is the relaxation superoperator, $\mathrm{i}^2 = -1$. In frozen solutions, when dynamic processes are characterized by correlation times τ_c long enough that $\omega_d\tau_c \gg 1$ it is appropriate to introduce relaxation phenomenologically. However, it should be noted that dynamic processes such as caused by a local acyl group and collective dynamics or molecular libration do persist down to liquid helium temperatures and do require careful treatment using Eq. (6). For the purpose of this section we factor out relaxation by dropping the relaxation superoperator (but see Sect. 2.4 where it is discussed). Leaving out the relaxation, the density matrix evolves, under the action of $\hat{H}$ as:

$$\frac{d\rho}{dt} = -\frac{\mathrm{i}}{\hbar}\,[\hat{H}(t),\, \rho(t)] \tag{7}$$

Thus after a period of time Δt for a time-independent $\hat{H}$, the density matrix $\rho(t)$ becomes:

$$\rho(t + \Delta t) = \mathrm{e}^{-(\mathrm{i}\hat{H}\Delta t/\hbar)}\rho(t)\,\mathrm{e}^{\mathrm{i}\hat{H}\Delta t/\hbar} \tag{8a}$$

Or by introducing superoperator notation

$$U\rho(t)\xrightarrow{\hat{H}(\Delta t)}\rho(t+\Delta t) \tag{8b}$$

The superoperator $U(\Delta t) = \exp(-\mathrm{i}H^{\times}\Delta t/\hbar)$ is unitary, implying time-reversal. It can correspond to free-evolution or to pulse excitation. The level of rigor with which Eq. (8a) is treated depends on the particular objective. In general, for an accurate description, Eq. (8b) requires numerical treatment. An example of a numerical implementation to compute the DQC ESR signal carried out in Hilbert space using a series of transformations of Eq. (8a) was described in [93] but is not discussed in this Chapter, thus limiting this subject to a more basic discussion based on the concept of coherences and spin operator techniques.

2.3.2 Coherences

A pulse ESR experiment is essentially based on creation and manipulation of electron-spin (and nuclear-spin) coherences. It is the time evolution of electron-spin coherences under the action of the electron–electron spin dipolar interaction that makes it possible to determine this coupling and then to infer the distance.

We already stated that for a quantum system in thermal equilibrium, only the diagonal density matrix elements are nonzero and they represent the populations of the corresponding energy levels. The absence of off-diagonal elements corresponds to the fundamental assumption of having random phases between any two states of the quantum system at thermal equilibrium. The diagonal elements are automatically independent of the spin phases. In modern parlance, these elements have a coherence order of 0. However, away from equilibrium a correlation between pairs of eigenstates may exist. For example, so-called dipolar order wherein the density matrix is (partially) represented by the operator $2S_{1z}S_{2z}$ connecting the two spins does not require any change in net population of these levels. Off-diagonal density matrix elements such as $S_{\pm}$, $S_{1\pm}S_{2z}$ have distinct phases, corresponding to a coherent superposition of eigenstates and therefore must vanish as the system approaches its equilibrium.

Finite off-diagonal elements of the density matrix with their distinct phases are often referred to as coherences. They can be produced by a coherent perturbation, such as a resonant mw pulse. The action of the pulse on an electron spin yields a coherent superposition between the states involved in the transition, represented by $S_{\pm}$ in the operator expansion of the density matrix, which will persist until the system returns to thermal equilibrium. In magnetic resonance these are single spin ± 1 coherences which are the only coherences that are experimentally detectable. Any density operator ρ can be decomposed into a sum of operator components ρ_p. Each such operator component is associated with a coherence order, p; i.e., under rotation about the z-axis it transforms as $\exp(\mathrm{i}\varphi\hat{F}_z)\rho_p \exp(-\mathrm{i}\varphi\hat{F}_z) = \rho_p \exp(\mathrm{i}p\varphi)$, where $\hat{F}_z = \sum_k S_{kz}$ is the z-component of the total spin angular momentum.

As noted above, single-quantum coherences $S_{1\pm}$ correspond to an observable signal. All other coherences of order one and higher cannot be observed, since average transverse magnetization in such cases is always zero. For example, products such as $2S_{1+}S_{2z}$, $S_{1+}S_{2+}S_{3-}$ have coherence order +1 but they do not correspond to detectable signals. In particular, anti-phase coherence, $2S_{1+}S_{2z}$, involving two spins, with coherence order 1, does not correspond to a detectable signal. Higher order coherence has all spins in a fixed phase relationship with other spins leading to zero net magnetization. For example, a $2S_{1x}S_{2y}$ term describes second order coherence of the two spins, with spins at an angle of 90° in the rotating x,y-plane, pointing either along x and y or $-x$ and $-y$ to the same extent.

Even though anti-phase or multi-quantum coherences cannot be directly observed, they do form and can be detected indirectly. Both in-phase and anti-phase single-quantum coherences (SQC) and double-quantum coherences are very useful in describing the PDS experiment. Multiple-quantum transitions and coherences in general have been treated in detail in numerous studies in the field of NMR (see for example the following [94–97]). Here, we outline the basic concepts and definitions in a way that is appropriate for the PDS experiment.

2.3.3 Single-Quantum Coherences

Let us consider a system of two coupled spins of 1/2. In Fig. 2 we have four allowed single-quantum transitions. These transitions are associated with the corresponding off-diagonal elements of the density matrix for the two spins defined in the product space $|m_1, m_2\rangle$.

As noted above, one can conveniently express the density matrix as the expansion in a complete set of the spin operators, e.g., the density matrix for a single spin $S = 1/2$ is given as a linear combination of the Pauli spin matrices and the unit operator; for many-spin systems one may take the direct product.

Then the coherences can be conveniently expressed by the spin operators corresponding to the elements of the density matrix for two spins. Single quantum coherences are represented by the presence of spin operators $S_{1+}S_{2\alpha}$, $S_{1+}S_{2\beta}$, $S_{1-}S_{2\alpha}$, $S_{1-}S_{2\beta}$ constructed as an outer product in the operator expansion of the density matrix, as well as those obtained by permuting the spins 1 and 2 for a total of eight. Here, $S_{k\alpha} \equiv E_k/2 + S_{kz}$, $S_{k\beta} \equiv E_k/2 - S_{kz}$ and E_k is the 2×2 unit operator for the kth spin. We can rewrite these eight operators, which clearly imply single quantum transitions, which we call the single-quantum coherences (SQC), of which four are "in-phase" coherences, which have the form:

$$S_{1\pm}(S_{2\alpha} + S_{2\beta}) = S_{1\pm}E_2, \ (S_{1\alpha} + S_{1\beta})S_{2\pm} = E_1S_{2\pm} \tag{9}$$

Their existence in the density matrix expansion corresponds to the observable transverse magnetization with all spins having the same phase. The states of the two spins are distinct and not mixed. The other four SQC are the "anti-phase"

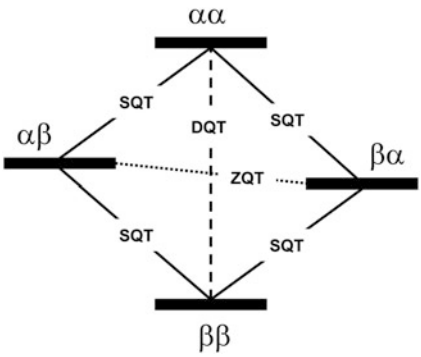

Fig. 2 Energy level diagram for the two-spin system showing single (SQT), double (DQT), and zero (ZQT) quantum transitions. The last two correspond respectively to simultaneous flip or flip-flop of the two spins. If the pulse acts only on one of the spins, DQT and ZQT are forbidden

coherences which cannot be directly detected. These correspond to coherent superposition among the four states of the two spins and they have the form:

$$S_{1\pm}(S_{2\alpha} - S_{2\beta}) = 2S_{1\pm}S_{2z} \tag{10}$$

and the other two obtained by permuting the spins 1 and 2.

The anti-phase SQC can evolve into an observable in-phase SQC and back. The interconversion of these coherences can occur only due to spin coupling, e.g., it is caused by the dipolar part of the spin-Hamiltonian, and the interconversion rate depends on the strength of coupling. This property is used to produce modulation of the detected spin-echo signal. As anti-phase and in-phase coherences evolve, they can be manipulated by applying coherent pulses acting on one or both of the spins, e.g., refocusing them or changing the sense of interconversion. Note that independent of whether a coherence is detectable or not, if its coherence order is ± 1, it can be refocused. This constitutes the basic idea of Pulse Dipolar ESR represented by the different flavors of PDS. This approach permits a relatively simple qualitative description of DEER pulse sequences (cf. Appendix).

We now show with a simple example of two electron spins in the weak coupling regime (cf. Fig. 1) how the evolution of SQC generates dipolar signals. That is in the next subsection we first show how we can derive the expressions for the dipolar signal in DQC and then we discuss DEER.

2.3.4 Double-Quantum Coherence

The double- and zero-quantum coherences (DQC and ZQC, respectively) are associated with the remaining two transitions in Fig. 2. DQC and ZQC correspond to transitions with simultaneous flips or flip-flops of both spins, respectively, and

are located on the anti-diagonal of the density matrix. DQC can be represented by terms in the operator expansion of the density matrix as follows[1] [94, 96]:

$$\begin{aligned} 2\mathrm{DQ}_x &= S_{1-}S_{2-} + S_{1+}S_{2+} = 2S_{1x}S_{2x} - 2S_{1y}S_{2y} \\ 2\mathrm{DQ}_y &= \mathrm{i}(S_{1-}S_{2-} - S_{1+}S_{2+}) = 2S_{1x}S_{2y} + 2S_{1y}S_{2x}. \end{aligned} \tag{11}$$

ZQC looks similar but instead it contains the flip-flop terms $S_{1\pm}S_{2\mp}$. These coherences do not correspond to experimentally detectable observables and can only be detected indirectly in a pulse experiment.

The DQC experiment can be partitioned into four periods: *preparation*, *evolution*, *mixing*, and *detection* [94]. During the "preparation period" the in-phase SQC produced by the first pulse of the sequence evolves into an anti-phase SQC due to the coupling between the spins. Then this coherence is converted by another pulse into DQC, ZQC (and even higher orders of coherence depending on the total number of spins of the system, but we assume only two spins). At this point our focus is on DQC, which then evolves during the "evolution period" (with more pulses being applied during this period, as needed to complete the sequence or enhance performance). Finally, during the "mixing" period these coherences can be converted, e.g., by an appropriate pulse into anti-phase SQC, which then evolves into the observable in-phase SQC that at last is detected as an FID or a spin-echo. The incorporation of the evolution period for DQC into the pulse sequence enables double-quantum filtering. That is, only those coherence pathways that pass through DQC pathways are selected.

We illustrate these principles with examples and tools that are relevant to the pulse schemes currently employed in DQC pulsed ESR experiments, but also will help to explain DEER methods excluding subtle effects, such as phase shifts [98] etc. We assume, for clarity of presentation, that we have an isolated pair of weakly coupled spins of 1/2 and perfect, i.e., intense non-selective mw pulses. For a single pair of spins of 1/2 the highest order of coherence that can be produced is two. In this example we use the spin-Hamiltonian in the frame rotating with the mw field in which it becomes time-independent:

$$H_0 = \omega_1 S_{1z} + \omega_2 S_{2z} + aS_{1z}S_{2z} + b(S_{1+}S_{2-} + S_{1-}S_{2+})/2 \tag{12}$$

Here, $b = -a/2$, with $a = \omega_\mathrm{d}(1 - 3\cos^2\theta)$ as in Eq. (3). [Electron exchange contribution is not included in Eq. (12).] We divide H_0 from Eq. (12) into two parts: H_0' and H_dd. The first part contains resonant offset terms

$$H_0' = \omega_1 S_{1z} + \omega_2 S_{2z} \tag{13}$$

[1] Note the density matrix also contains on the main diagonal ZQ $S_{1z}S_{2z}$ terms (dipolar order), which can be generated by spin manipulation or in equilibrium at low temperatures. They will play no role in the ensuing analysis, unless explicitly mentioned.

Here ω_1 and ω_2 represent, for the spins 1 and 2, their respective resonant frequency offsets from the applied frequency, ω_{mw}, i.e., $\omega_k = \omega_{k0} - \omega_{\mathrm{mw}}$, where ω_{k0} is the Larmor frequency. The second part is the coupling, which is taken in the weak-coupling limit to be:

$$H_{\mathrm{dd}} = aS_{1z}S_{2z} \tag{14}$$

Here the pseudo-secular term [proportional to b in Eq. (12)] is neglected. At this introductory stage, this weak coupling assumption (cf. Fig. 1) is made to simplify the discussion.

Preparation

We describe the preparation of DQC by the use of two or three pulses. These pulse sequences are the standard preparation sequences in NMR [94] and were employed in the DQ ESR experiments by Borbat and Freed [15].

For the 2-pulse preparation sequence (cf. Fig. 3a) the first pulse acts on both spins at equilibrium creating transverse coherence that is proportional to in-phase SQC ($S_{1y} + S_{2y}$). Since S_{1y} and S_{2y} will yield equivalent results (but with subscripts permuted) we need to only follow S_{1y} below. We shall employ, at this introductory stage, the standard Product Operator method [95, 99]. It can be implemented in different flavors, and some are more efficient. Here, we will purposely start with the Cartesian representation, which yields a more lengthy description but is straightforward and transparent. Here the pulses are taken as ideal $\pi/2$ or π pulses and the resonant offset terms in H_0' commute with the dipolar coupling H_{dd}, allowing considering them independently. For example, we find using the Product Operator method that the effect of H_{dd} acting over a time t on S_{1x} and S_{1y} is:

$$\begin{aligned} S_{1x} &\xrightarrow{H_{\mathrm{dd}}t} S_{1x}\cos(at/2) + (2S_{1y}S_{2z})\,\sin(at/2) \\ S_{1y} &\xrightarrow{H_{\mathrm{dd}}t} S_{1y}\cos(at/2) - (2S_{1x}S_{2z})\,\sin(at/2). \end{aligned} \tag{15}$$

One can see from Eq. (15) that the action of a finite spin–spin coupling term a during the time interval t will cause the in-phase SQCs S_{1x}, S_{1y} to evolve as $\cos(at/2)$, whereas anti-phase SQCs $S_{1x}S_{2z}$, $S_{1y}S_{2z}$ evolve as $\sin(at/2)$. That is, there are "coherent oscillations" between these two coherences. When we include the resonance offset terms as well, we find:

$$\begin{aligned} S_{1y} \xrightarrow{H_0' t} &\left(S_{1y}\cos(\omega_1 t) + S_{1x}\sin(\omega_1 t)\right)\cos(at/2) \\ &+ 2\left(S_{1x}S_{2z}\cos(\omega_1 t) - S_{1y}S_{2z}\sin(\omega_1 t)\right)\sin(at/2). \end{aligned} \tag{16}$$

That is, the respective coherences rotate with their angular frequencies in the rotating frame. At the end of the time interval $t = t_p$ the second $\pi/2$-pulse converts the anti-phase coherence into the sum of DQC and ZQC.

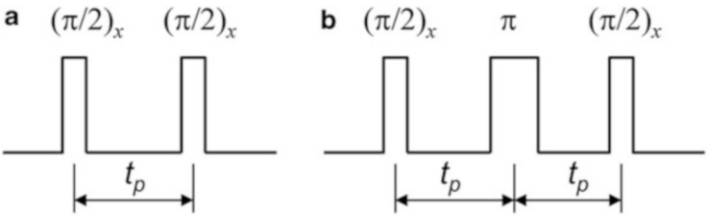

Fig. 3 Preparation of multiple-quantum coherence with two pulses (*left*) or a 3-pulse "sandwich" (*right*). These pulse propagators generate even coherence orders, i.e., 0 and 2 for two spins. If the last pulse is applied along the *y*-axis, odd coherence order will be produced

$$2S_{1x}S_{2z}\cos(\omega_1 t_p)\sin(at_p/2)\xrightarrow{(\pi/2)_x}\cos(\omega_1 t_p)\sin(at_p/2)$$
$$\times[\underbrace{(2S_{1x}S_{2y}+2S_{1y}S_{2x})}_{2DQ_y}/2-\underbrace{(2S_{1y}S_{2x}-2S_{1x}S_{2y})}_{2ZQ_y}/2] \quad (17)$$

In this case the DQC and ZQC will be produced in equal amounts. In the case of $\omega_1 = \omega_2$ the ZQ_y term vanishes[2] when we consider the equivalent expression derived for S_{2y}. In Eq. (17) we do not consider any of the other terms on the rhs, since they will lead to unwanted coherence pathways that must be canceled out by "phase cycling" (cf. below).

With the preparation by the 3-pulse "sandwich," considered next, we can obtain better conditions for generation of DQC. In this sequence, the first $(\pi/2)_x$ pulse again produces SQ coherence $S_{1y} + S_{2y}$. This coherence under the combined action of the spin–spin interaction, and the refocusing π-pulse, evolves into the sums of SQ in-phase $S_{1y} + S_{2y}$ and anti-phase $(S_{1x}S_{2z} + S_{1z}S_{2x})$ coherences:

$$(S_{1y}+S_{2y})\xrightarrow{H_0 t_p}\xrightarrow{(\pi)_x}\xrightarrow{H_0 t_p}(S_{1y}+S_{2y})\cos(at_p)$$
$$+2(S_{1x}S_{2z}+S_{2x}S_{1z})\sin(at_p)\ . \quad (18)$$

Here, the refocusing π-pulse removes any dependence upon the frequency offsets ω_1 and ω_2. In Eq. (18) we see that the in-phase SQC appears as $(S_{1y} + S_{2y})$ $\cos(at_p)$. This will yield a primary echo at $2t_p$, whose intensity is modulated by the dipolar frequency, a. Then the last $(\pi/2)_x$ pulse turns anti-phase SQC into DQC:

$$2(S_{1x}S_{2z}+S_{2x}S_{1z})\sin(at_p)\xrightarrow{(\pi/2)_x}2(S_{1x}S_{2y}+S_{1y}S_{2x})\sin(at_p). \quad (19)$$

Thus all the anti-phase SQC is transformed into DQC when $\sin(at_p) = 1$. For this case, there is no ZQC. Note that if the last pulse in the sequence was applied

[2] This case, however, corresponds to strong coupling when the pseudosecular term cannot be neglected, necessitating replacing of a in Eq. (15) with $3a/2$.

along the y-axis, no DQC would be produced. Thus we see that in the case of nonselective pulses, and the preparation sequence of Fig. 3b, only DQ_y is generated.

Evolution of DQC Due to the Frequency Offsets

During the evolution period the DQC and ZQC evolve due to resonant frequency offsets and are invariant with respect to the dipolar part of the Hamiltonian:

$$\begin{aligned} DQ_{x(y)} &\xrightarrow{H_0 t} DQ_{x(y)}\ \cos(\omega_+ t) \pm DQ_{y(x)}\ \sin(\omega_+ t) \\ ZQ_{x(y)} &\xrightarrow{H_0 t} ZQ_{x(y)}\ \cos(\omega_- t)\ \pm ZQ_{y(x)}\ \sin(\omega_- t)\,, \end{aligned} \tag{20}$$

with $\omega_\pm \equiv \omega_1 \pm \omega_2$. For the case of a typical ESR spectrum where there are wide spectral extents, signals are detected in the form of echoes, and the free-induction decay (FID) is too fast to be detected. To produce the maximum in-phase SQ echo at the final stage, the coherences in Eq. (20) should be refocused. The refocusing can be accomplished by a π-pulse placed at the middle of the DQC (or ZQC) pathway forming the sequence $t_{DQ} - \pi - t_{DQ}$. From Eq. (11) it follows that

$$DQ_y \xrightarrow{\pi_x} -DQ_y, \qquad DQ_x \xrightarrow{\pi_x} DQ_x \tag{21}$$

Let us suppose that the second t_{DQ} interval is changed by an amount δt, then from Eqs. (20) and (21) one finds:

$$DQ_y(2t_1 + \delta t) = DQ_y(0)\ \cos(\omega_+ \delta t) - DQ_x(0)\ \sin(\omega_+ \delta t) \tag{22}$$

Let us assume for simplicity that both spins have identical ESR spectra of the form $g(\omega) = (2\pi\Delta\Omega^2)^{-1}\ \exp(-\omega^2/2\Delta\Omega^2)$ where $\Delta\Omega$ represents the spectral width. Then we can integrate Eq. (22) over the distribution for both spins to obtain the average signal for $DQ_y(2t_1 + \delta t)$. We find:

$$DQ_y(2t_1 + \delta t) = DQ_y(0)\ \exp(-\Delta\Omega^2 \delta t^2) \tag{23}$$

Note the same result holds for ZQC. The reader can see that Eq. (23) describes a virtual echo with maximum at $\delta t = 0$ and half width of $(\log 2)^{1/2}\Delta\Omega^{-1}$.

Mixing and Detection

At the end of the evolution period a $\pi/2$ pulse converts the refocused DQC (cf. previous Section) into SQ anti-phase coherence, which will then evolve into observable in-phase coherence. For the 6-pulse sequence described in Sect. 2.3.5 and Fig. 4, in addition another π pulse and evolution periods are used to evolve (mix) the coherences into detectable in-phase coherence. After the $\pi/2$ pulse we have:

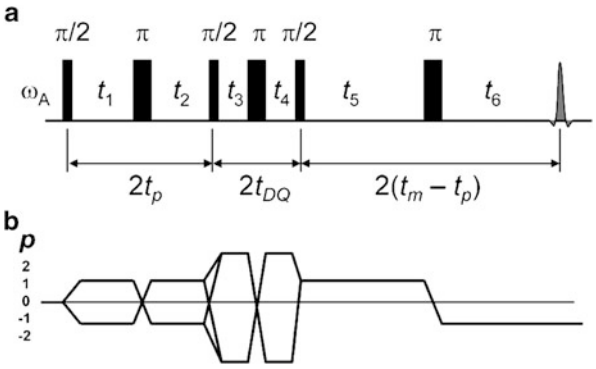

Fig. 4 In this diagram (**a**) shows the 6-pulse DQC sequence. The four desired coherence pathways starting with each spin in (**b**) correspond with the pulses shown in (**a**) in that a transition from one p state to another p state is generated by a pulse; the *horizontal lines* show coherence orders during the evolutions in the absence of a pulse. As for the timing between the various pulses the following is noted. The time interval $t_1 = t_2 = t_p$ is increased in equal steps, Δt_p, over a period of $t_m = t_p + t_5$. The time between the $t_3 = t_4 = t_{\mathrm{DQ}}$ is kept fixed, $t_5 = t_6$ is stepped by $-\Delta t_p$ to maintain a constant evolution time, t_m, which is half the time from the first pulse to the echo, since usually $t_{\mathrm{DQ}} \ll t_m$. The echo amplitude is recorded as a function of the time variable $t_\xi \equiv t_m - 2t_p$ over the range of $\pm t_m$ in steps of $2\Delta t_p$. The evolution time t_ξ starts from the initial time t_m and $t_\xi = 0$ when pulse separations are $t_1 = t_2 = t_5 = t_6$. Phase cycling isolates the dipolar signal, given by the four coherence pathways shown in (**b**) from the other coherence pathways, yielding the DQC signal that is an even function of t_ξ, therefore only one half is usually recorded

$$\begin{aligned}\mathrm{DQ}_y &= \frac{1}{2\mathrm{i}}(S_{1+}S_{2+} - S_{1-}S_{2-})\sin(at_p) \xrightarrow{(\pi/2)_x} \\ &-(S_{1+}S_{2z} + S_{2+}S_{1z} + S_{1-}S_{2z} + S_{2-}S_{1z})\sin(at_p) = 2(S_{1x}S_{2z} + S_{2x}S_{1z})\sin(at_p)\end{aligned} \tag{24}$$

This is essentially the reverse of Eq. (19). The anti-phase coherences evolve during the mixing time back into observable SQ coherences. That is:

$$\begin{aligned}&-\frac{1}{2}(2S_{1+}S_{2z} + 2S_{2+}S_{1z} + 2S_{1-}S_{2z} + 2S_{2-}S_{1z})\sin(at_p) \xrightarrow{H_0 t} \xrightarrow{\pi} \xrightarrow{H_0 t_2} \\ &-\frac{1}{2\mathrm{i}}[S_{1+}\mathrm{e}^{-\mathrm{i}\omega_1\delta t_2} + S_{2+}\mathrm{e}^{-\mathrm{i}\omega_2\delta t_2} - S_{1-}\mathrm{e}^{\mathrm{i}\omega_1\delta t_2} - S_{2-}\mathrm{e}^{\mathrm{i}\omega_2\delta t_2}]\sin(at_p)\sin(at + \delta t_2/2)\end{aligned} \tag{25}$$

where $\delta t_2 \equiv t_2 - t$ ($t \equiv t_m - t_p$, cf. Fig. 4). The π-pulse refocuses the SQC at $t_2 = t$. One of the two counter rotating components in the square brackets of Eq. (25) is sufficient for calculation of the signal. This follows because the observed signal is proportional to the processing magnetization defined as follows:

$$M(t_2) = -\frac{2\,\mathrm{Im}[\mathrm{Tr}(\hat{\rho}(t_2)S_+)]}{\mathrm{Tr}(S_-S_+)}M_0, \tag{26}$$

where M_0 is the static magnetization of the sample and $S \equiv S_1 + S_2$. The signal that is refocused during DQ evolution period is singled out by appropriate phase cycling. The real part of the echo signal becomes:

$$M(t_2) = M_0(\cos(\omega_1\delta t_2) + \cos(\omega_2\delta t_2))\ \sin(at_p)\ \ \sin(a(t+\delta t_2/2))/2\,. \tag{27}$$

The terms in the first set of brackets, after averaging over all resonance offsets, ω_1 and ω_2, produce an echo shape, with the maximum near $\delta t_2 = 0$. The echo envelope is modulated by $\sin(a\delta t_2/2)$. We see that the signal amplitude (at $\delta t_2 = 0$) as a function of preparation and/or mixing times is modulated by $\sin(at_p)\sin(at)$. Fourier transformation of $\cos(a(t_p - t))$, that emerges from the above product of two sin-functions, produces the dipolar spectrum, which in the case of weak dipolar coupling has the shape of and width of 2/3 of the classical Pake doublet [79].

The point of following a particular coherence pathway and "filtering out" the other "unwanted" coherence pathways is to select the one that best provides the desired information, in this case the coupling between the electron spins. As we will show, with a proper pulse phase cycling just the refocused DQC signal is selected. We call this DQ filtering (DQF).

2.3.5 Six-Pulse DQC Sequence

This pulse sequence for distance measurements was introduced in 1996 at Cornell University by Saxena and Freed [100] and was developed into a powerful tool for distance measurements by Borbat and Freed [11, 15]. Although more challenging to implement than DEER, it is superior to DEER in some respects, thereby expanding our capacity to perform distance measurements. It does require, however, more intense microwave pulses and sophisticated phase-cycling.

Its advantages include greater sensitivity, especially for low concentration samples, since (nearly) all the spins are excited; the near absence of orientational effects in its standard 1D versions (with the option of developing them in the 2D version); filtering out single quantum signals and other noise by the double quantum filter; and the ability to obtain good results for distances as short as 10 Å [11, 101]. It is also immune to phase and amplitude drifts that may be troublesome for DEER. We show in Fig. 4 the six pulse sequence used in DQC-ESR. It transforms the initial density matrix under the successive action of six pulses and six subsequent free evolutions.

The 6-pulse sequence of Fig. 4 contains the 3-pulse preparation sequence $(\pi/2)_x - t_p - \pi - t_p - (\pi/2)_x$ which generates DQ coherence that during the evolution is refocused by the $t_{\mathrm{DQ}} - \pi - t_{\mathrm{DQ}}$ sequence, as described in the previous section. The fifth pulse produces anti-phase coherences (cf. Eq. (24)),

which evolve into observable SQ coherences, and the sixth pulse refocuses them (cf. Eq. (25)) to form an echo. This sequence is used with fixed t_m, and t_p is varied. The signal envelope is recorded as a function of $t_\xi \equiv t_m - 2t_p$.

This 6 pulse sequence allows for "zero dead-time" signals, which result from refocusing of first-order coherences in the middle of the data acquisition interval. That is, for Fig. 4 when one steps out t_p in the range $0 \leq t_p \leq t_m$ keeping t_m fixed, this yields a signal vs. t_ξ which ranges from $-t_m \leq t_\xi \leq t_m$. Keeping t_m fixed also has the effect of canceling out the role of phase (or T_2) relaxation on the echo at $t_2 = t_m - t_p$, since the total duration of the pulse sequence is independent of t_p.[3] Note that Fig. 4 shows the four coherence pathways in which both spins participate. It starts and ends with spin 1 and 2. Since if we start with either spin 1 or 2 and independently end with either, then the total number of pathways is $4 \times 4 = 16$.[4] Note that in the DQ coherence state, the spins 1 and 2 are symmetric [cf. Eq. (11)], such that the coherence pathway starting and ending with 1(2) and the coherence transfer pathway starting from 1(2) and ending with 2(1) are possible [35].

Assuming that the matrix elements are known for time-independent pulse propagators $R_k = \exp(-\mathrm{i}(H_0 + H_{1k})\Delta t_k)$, for all pulses, $k = 1, \ldots, 6$, where H_0 is given by Eq. (12) and H_{1k} represents the interaction term of the spin with the kth pulse; a closed form expression for the DQ signal can be written. Such a full expression for the signal in the 6-pulse sequence can be found in [102]. It was obtained by tracking down the density matrix elements along the relevant coherence pathways using the complete dipolar spin-Hamiltonian Eq. (2) instead of the approximate form of Eq. (14), and employing finite pulses. As a result the expression is quite complex. It is suitable for setting up computations, but it does not provide insight into the sequence essentials.

Neglecting dipolar coupling during the pulse allows for writing the explicit form of R_k and consequently for more readily conducting a detailed analysis. Note that in this regard different levels of approximation can be used: (1) weak coupling, ideal pulses; (2) weak coupling, arbitrary pulses; and (3) stronger coupling, arbitrary pulses.

The simplest, Case 1 can be analyzed using a suitable form of the product operator technique [95] and after minor algebraic effort leads to the ideal-case signal where the terms from all 16 pathways add to give:

$$V_{\mathrm{DQ}}(a, t_p) = -R_{\mathrm{DQ}} \sin(at_p) \sin(a(t_m - t_p)) = R_{\mathrm{DQ}}(\cos(at_m) - \cos(at_\xi))/2 \quad (28)$$

R_{DQ} was added to account for relaxation and it can be simply expressed as

$$R_{\mathrm{DQ}} = \exp(-2(t_m/T_{2,\mathrm{SQ}} + t_1/T_{2,\mathrm{DQ}})) \,. \quad (29)$$

[3] Relaxation will however modify the signal if the coupled spins have different relaxation times or relaxation is described by stretched exponentials (cf. Sect. 2.4).

[4] That is two such diagrams should be combined into a graph to give all of 16 contributions.

Here $T_{2,SQ}$ and $T_{2,DQ}$ refer to the T_2 decay constants characteristic of SQC and, DQC, respectively (T_1 processes are neglected in these expressions). However, in general, the two nitroxide electron spins are located in different local environments, hence their respective T_2s may be different, etc. This approach to the treatment of relaxation is a simplified one, but is satisfactory for most distance measurements [35, 101].

The more involved Case 2 requires some modifications to be made to the product operator method to accommodate arbitrary (e.g., selective) pulses, thus algebraically it becomes more involved if accurate amplitude factors are of interest [35]. One may derive a simple expression for DQC-ESR by the product operator method modified for arbitrary pulses [35]. It also works well for DEER. In the weak-coupling limit by using this method for arbitrary pulses one finds that the 6-pulse DQC signal may be written in the following form (or in general as a sum of terms of this form):

$$\begin{aligned} &V_{DQ}(\omega_1,\omega_2,a,t_p) = G(\omega_1)H(\omega_2)F(a,t_p)R_{DQ} \\ &F(a,t_p) = -\sin(at_p)\,\sin(a(t_m-t_p)) = (\cos(at_m)-\cos(at_\xi))/2 \end{aligned} \tag{30}$$

This expression has the same factors $F(a,t)$ and R_{DQ} as in the ideal case, but adds amplitude factors G and H, determining the fraction of spins participating in the signal.[5] In general, there is a sum of terms with different amplitude factors based on the fact that there are four distinct coherence pathways with each of them giving rise to eight terms, accounting for coherence-transfer pathways, as noted above. For like spins, such as a pair of nitroxide spin labels, G and H are nearly equal, being dominated by a product of the resonant offset dependent factors, $S_2(\theta)$, which give the probability, $p(\theta,\omega)$ (or $S_2(\theta)$ for short), for a spin at the resonance offset ω to be flipped by a pulse with $\omega_{1mw} = \gamma_e B_1$ and nominal rotation angle θ . They are expressed as:

$$p(\theta,\omega) = \frac{\omega_{1mw}^2}{\omega^2+\omega_{1mw}^2}\sin^2\left(\frac{\theta_e}{2}\sqrt{1+\omega^2/\omega_{1mw}^2}\right) \tag{31}$$

The dependence of G and H on ω_{1mw} for the case of nitroxides is further discussed in Sect. 3.1. Refocusing of anti-phase and DQ coherences by π-pulses then requires simultaneous flipping of both spins in order to produce the required signal, therefore each of the $G(\omega_k)$ and $H(\omega_k)$ contains the cube of $p(\theta,\omega_k)$, if all three refocusing pulses are equal. They usually are set equal, so we can denote $p(\theta,\omega)$ as $S_2(\pi)$, for π-pulses. G also includes the efficiency to create $S_{k\pm}$ starting

[5] Note that for both DQC and DEER, the expression for the signal contains as a minimum two terms, except for nonoverlapping spectra in DEER, i.e., it contains terms for the signal from spins 1 and 2, and in the general case they are not equal. But we show just one for brevity.

from equilibrium. The effect of the third and fifth $\pi/2$ pulses is much less frequency dependent and usually can be ignored.

In Case 3, when the condition $|\omega_1 - \omega_2| \gg |a|$ no longer holds, the weak-coupling approach should be revised by including the pseudo-secular term, i.e., using Eq. (12), notwithstanding whether the pulses are ideal or not. For nitroxides, this includes distances under ~15 Å for nonselective pulses, corresponding to a large coupling (or to exotic cases of mutual arrangement of the nitroxide moieties such that the magnetic axes substantially coincide, thereby leading to small frequency differences for a significant fraction of pairs).

We outlined [35] a suitable approach for obtaining compact expressions for the signals in this case. The only (weak) assumptions made were that the dipolar interaction during the pulse has only an insignificant effect on the signals and also the DQ filter is "ideal," which implies, as noted above, that the combined effect of preparation and mixing $\pi/2$ pulses is frequency-independent. This is indeed the case for intense pulses ($B_1 \geq 30$ G) and longer distances, ≥12 Å [93]. The agreement between computations based on this approach and rigorous computations [93] was found to be very good, justifying their applicability for most practical purposes. The equation based on the form given by Borbat and Freed [35] used for computing 1D DQC signals [93] is given here. The echo amplitude, V, is a function of $t_\xi \equiv 2t_p - t_m$, and is given by

$$V(t_\xi) = G(\omega_1)H(\omega_2)F(a, t_\xi), \tag{32}$$

with $G(\omega_1)$ and $H(\omega_2)$ taken as $p(\pi,\omega_k)^3$. The time variables are defined in accordance with Fig. 4. The dipolar evolution is contained in $F(a,t_\xi)$ expressed as a product of $f(t_p)\, f(t_m - t_p)$ with $f(t)$ given by:

$$f(t) = (p^2 + q^2 \cos(Wt)) \sin(at) - q \sin(Wt) \cos(at). \tag{33}$$

In Eq. (33), $a = \omega_d(1 - 3\cos^2\theta)$ and $W = (\Delta\omega^2 + b^2)^{1/2}$, where $\Delta\omega = \omega_1 - \omega_2$ and $b = -a/2$ represent the secular, a and pseudosecular, b parts of the dipolar coupling. Also, $q = b/W$ and $p^2 = 1 - q^2$. In the two limiting cases, i.e., when $|\Delta\omega| \gg |a|$ or $|\Delta\omega| \ll |a|$ Eq. (33) reduces to the form of Eq. (30) with $3a/2$ replacing a in the second limit, as expected when pseudo-secular terms are important.

It is evident from Eqs. (32) and (33) that even in the limit of ideal nonselective pulses, the effects of the pseudosecular term do not go away, since the spectral extent is limited, and they could encode orientations, although their overall effect on the 1D signal is small for most practical cases. A rigorous computational analysis [93] has shown that one rarely needs to go to such lengths, and the form given in Eqs. (32) and (33) produces accurate results and in most practical cases Eq. (30) should be adequate (cf. Sect. 2.7). It is in general true about all PDS methods that there is always a trade-off between one's desire to describe a dipolar signal as accurately as possible, and to be able to analyze a broad range of systems, since the experiments inevitably encompass a number of secondary undesired

effects, such as those due to strong dipolar coupling, nonideal or overlapping excitations, complexity in the case of high-spins, relaxation, and ESEEM. It is important to be aware of all these details since this could help one to learn how to reduce them, thereby minimizing the distortions in the dipolar signals.

In computing the DQC signal for a pair of nitroxides, the values of ω_1 and ω_2 depend on the orientation of $\mathbf{r}_{12}$ in the lab frame and the orientations of the nitroxide magnetic tensors in the molecular frame, whose z-axis is taken to coincide with $\mathbf{r}_{12}$. (More on this is in Sect. 5.3.) We shall choose Euler angles $\boldsymbol{\lambda}_i \equiv (\alpha_i, \beta_i, \gamma_i)$, with α_1 set to zero, to represent the transformation from the dipolar frame to the magnetic frame of the ith nitroxide fragment ($i = 1$ or 2), and Euler angles $\boldsymbol{\eta} \equiv (0, \theta, \varphi)$ to represent the transformation from the lab frame to the dipolar frame. Then $\omega_k = \omega_k(\boldsymbol{\lambda}_k, \boldsymbol{\eta})$ for each orientation in $\boldsymbol{\eta}$, determined for each set of nitroxide nuclei magnetic quantum numbers (M_1, M_2). For example $\omega_k(\boldsymbol{\lambda}_k, \boldsymbol{\eta})$ can be calculated based on a commonly used approximation given by Libertini and Griffith, adequate up to Q-band [103]. Then the $G(\omega_1)$ of Eq. (30) will depend upon $\boldsymbol{\lambda}_1$ and $\boldsymbol{\eta}$, while $H(\omega_2)$ depends upon $\boldsymbol{\lambda}_2$ and $\boldsymbol{\eta}$, and $F(a(\mathbf{r}_{12}),t_\xi)$ just depends upon $\boldsymbol{\eta}$ as well as the magnitude $|\mathbf{r}_{12}| \equiv r$. It is then necessary to average the signal over an appropriate distribution in these variables, which we represent by angular brackets as:

$$V(t_\xi) = \Big\langle G(\omega_1(\boldsymbol{\lambda}_1, \boldsymbol{\eta}))H(\omega_2(\boldsymbol{\lambda}_2, \boldsymbol{\eta}))F(r, \boldsymbol{\eta}, t_\xi)\Big\rangle_{r,\ \boldsymbol{\lambda}_1,\ \boldsymbol{\lambda}_1,\ \boldsymbol{\eta}} \tag{34}$$

The relaxation function $R_{\mathrm{DQ}}(\omega_1, \omega_2, \boldsymbol{\lambda}_1, \boldsymbol{\lambda}_2, \boldsymbol{\eta})$, which has been dropped for convenience in Eq. (34) can be placed outside the angular brackets, since for nitroxides, which are the major application of our DQ methods, at the reduced temperatures used, T_2s are not substantially dependent upon $\boldsymbol{\lambda}_1$, $\boldsymbol{\lambda}_2$ nor upon $\boldsymbol{\eta}$. It is easy to see that when there is no correlation between $\boldsymbol{\lambda}_i$ and $\boldsymbol{\eta}$, then Eq. (34) yields the expected simpler form**:**

$$\begin{aligned} V(t_\xi) &= \langle G(\omega_1(\boldsymbol{\lambda}_1, \boldsymbol{\eta}))\rangle_{\boldsymbol{\lambda}_1} \langle H(\omega_2(\boldsymbol{\lambda}_2, \boldsymbol{\eta}))\rangle_{\boldsymbol{\lambda}_2} \langle F(r, \boldsymbol{\eta}, t_\xi)\rangle_{r,\boldsymbol{\eta}} \\ &\equiv G^{\mathrm{AV}} H^{\mathrm{AV}} \langle F(r, \boldsymbol{\eta}, t_\xi)\rangle_{r,\boldsymbol{\eta}}\,. \end{aligned} \tag{35}$$

Thus one can simply integrate over the distribution of orientations and magnitudes of r in the sample. An FT with respect to t_ξ will then yield the familiar Pake doublets.

Another simple limiting case occurs for weak coupling when the pulses can be regarded as nonselective, so that

$$G(\omega_1) \to G^\infty \quad \text{and} \quad H(\omega_2) \to H^\infty \tag{36}$$

independent of ω_1, ω_2, which follows immediately from the $B_1 \to \infty$ limiting forms of Eq. (30). Then Eq. (35) becomes:

$$V(t_\xi) = G^\infty H^\infty \langle F(r, \eta, t_\xi)\rangle_{r,\eta} \tag{37}$$

This ideal case corresponds to all the spins in the sample contributing to the signal, so both G^{∞} and H^{∞} have the asymptotic value of unity. Actual values of G^{AV} and H^{AV} monotonically approach unity as B_1 increases. In this ideal case of an isotropic sample and weak coupling, Eq. (37), after neglecting a small constant term in Eq. (30), takes the form

$$V(t_{\xi}) = \int_0^{\infty} P(r)\, dr \int_0^1 \cos(\omega_{\mathrm{d}} t_{\xi}(1 - 3u^2))\, du \tag{38}$$

where the probability to have separation r, $P(r)$ is given by $4\pi n(r) r^2$ with $n(r)$ being the spin density. $V(t_{\xi})$ in case of $n(r) = \delta(r - r_0)$ can be expressed via Fresnel integrals.

Relaxation factor R_{DQ} is different for all four contributing pathways in the case of unlike spins; faster relaxation pathways could become attenuated. In the limit of one of the two spins relaxing much faster (spin 1) only 4 of 16 terms will survive, that is those involving just spin 2 in the preparation, evolution, and detection periods.

2.3.6 Pulsed ELDOR

The 3-pulse electron–electron double resonance sequence was developed at Novosibirsk in 1981 and later renamed PELDOR (pulsed ELDOR) by its inventors Milov et al. [29]. It is based on modifying the echo produced with a 2-pulse Hahn echo sequence $\pi/2 - \tau - \pi$ at the "observer" frequency, ω_a, by a π-pulse applied at a different frequency, ω_b, as shown in Fig. 5a in the next page.

The position of the π-pulse at the observer frequency is fixed, while the π-pulse at ω_b is applied after a variable delay, t, subsequent to the first observer frequency pulse ($\pi/2$) at the time $t = 0$, as shown in the lower part of Fig. 5a. The spins that give rise to the echo are referred to as "A-spins," and the rest are "B-spins" [34]. Only a fraction of the B-spins are excited by the pump pulse and the A-spins should not be affected by this pulse.

The dipolar signal is obtained by recording the echo amplitude at the observer frequency as a function of variable t. Thus, the 3-pulse sequence is described as:

$$(\pi/2)_a \xrightarrow{H_0(t)} \pi_b \xrightarrow{H_0(\tau - t)} \pi_a \xrightarrow{H_0(\tau)} echo, \tag{39}$$

where subscripts a and b indicate which spin is acted upon by the pulse. Pulses acting on A spins have well-defined phases. They can be used to perform phase-cycling to isolate the spin-echo from the signal offsets of instrumental origin. The magnetic field component of the mw pulse at ω_b is in the frame rotating at ω_a, making rigorous analysis of PELDOR a challenge [104].

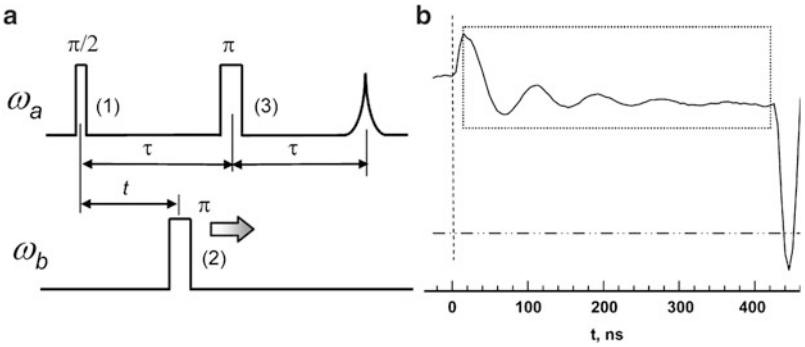

Fig. 5 (**a**) The original 3-pulse form of DEER (PELDOR) [29]. The primary echo is formed by the $\pi/2$ and π pulse sequence at the frequency of A-spins. The pumping pulse at ω_b is applied at a variable time t ranging from 0 to τ to probe the dipolar coupling between A and B spins. The spectral excitations at both frequencies should not overlap, thus the pulses are made selective. (**b**) 3-Pulse DEER for a 16.3 Å rigid biradical [35] in LC phase V, rapidly frozen from the isotropic phase; at −80°C. DEER was set up at 17.4 GHz with a 2 kW mw amplifier working in the linear regime at 10 dB below saturated output level. A low-Q dielectric resonator was used to accommodate the pulses at both DEER frequencies separated by ~100 MHz. The widths of $\pi/2$ and π pulses were 10 and 20 ns. The pumping pulse was positioned at the low-field portion of the nitroxide spectrum. The informative part of the signal trace is enclosed into the *dotted box*. The Bloch–Siegert phase shift of the signal [98] is clearly visible on the lhs and rhs of the box and can be eliminated by taking the magnitude of the signal obtained in quadrature. The *dash-dot line* corresponds to zero amplitude. The "dead-time" is about the width of the pump π-pulse. (**b** adapted from [101].)

A closed-form expression can be written for the primary echo in the presence of dipolar coupling if one ignores this dipolar coupling during the pulse, which would otherwise give rise to "forbidden" coherence pathways [102]. Assuming some simplifying conditions, it suffices to track the evolution of in-phase and anti-phase SQCs for arriving at the simple expression for PELDOR/DEER [105] that is satisfactory for most practical purposes. We have included such a derivation in the Appendix. When the dipolar coupling is large, or pulse excitations at the two frequencies overlap in spectral coverage, the spin dynamics becomes complicated and a closed-form expression cannot be written for the PELDOR pulse sequence, without making additional approximations, because the second pulse propagator is not time-independent in the frame rotating at ω_a introducing, for example a Bloch-Siegert shift [98]. Nevertheless, for this pulse sequence, coupled spin dynamics were analyzed in significant detail by Maryasov after making minor assumptions [104].

In the case of arbitrary pulses, a pulse acting on the anti-phase SQC, $S_{a+}S_{bz}$, may affect either of the two spins. Pulse action on spin A can change coherence order. Selecting the desired coherence pathway is handled by phase-cycling. However, flipping just spin B (i.e., $S_{bz} \rightarrow -S_{bz}$) has no effect on the coherence order of A-spins, but reverses the sense of time-evolution of spin A caused by its dipolar coupling to spin B. Therefore a branching into two signals, different in dipolar evolution ("dipolar pathways") may occur, i.e., spins A associated with spin B that are flipped and those that are not. This resembles the presence of two terms for a given pathway in DQC. These "dipolar pathways" affect most of the PDS pulse

sequences based on selective pulses. Since branching into two pathways can occur after each selective pulse, for an N-pulse sequence there could be as many as 2^{N-1} distinct terms, different in dipolar evolution. One of them corresponds to unperturbed S_{bz}, while the rest may evolve with respect to their specific timing variables that depend on how the evolution periods are prescribed to vary in the pulse sequence. Although these signal pathways may be very different in their dipolar evolution, they cannot be separated by phase-cycling, since they still correspond to the same coherence pathway of A spins. In the DEER technique this would be the case when there is an overlap of the excitations at the two frequencies or more than one pump pulse is applied. [Single-frequency techniques (SQC sequences) also have such features, because anti-phase SQC may or may not change sign after the pulse. It can be shown that such unwanted dipolar pathways do not contribute to the amplitude of the 6-pulse DQC signal, because in-phase SQC will not evolve into anti-phase SQC during the preparation period or else anti-phase SQC produced after the DQC filter will not evolve into observable in-phase SQC during the mixing period, if only one of the spins is flipped by the π-pulse.] For the 3-pulse sequence there are, thus, four terms representing possible dipolar signals. If dipolar coupling is small compared to the B_1s, the sequence can be analyzed with a properly tailored product operator technique. Excitation overlap generates all four pathways. This gives us four terms in PELDOR (cf. Appendix).

$$V(\tau,t) = V_0\langle q_2q_3 + q_2p_3\,\cos(a\tau) + p_2q_3\,\cos(at) + p_2p_3\,\cos a(\tau - t)\rangle_{\omega_a\omega_b} \quad (40)$$

Here we included some amplitude factors giving echo amplitude for a single spin into V_0; p_k is the probability of flipping either S_{az} or S_{bz} by the kth pulse (labeled as given in Fig. 5a), with $q_k = 1 - p_k$ is the probability for them remaining unaffected. When pulse excitations at the two frequencies have only a small overlap, i.e., $\langle p_2p_3\rangle \ll \langle q_2p_2\rangle$, only the first three terms are significant and one arrives at the following form

$$V(\tau,t)/V_0 \cong (1 - p_3)[1 - p_2(1 - \cos(at))] + p_3\,\cos(a\tau) \quad (41)$$

Typically there is only a small effect of pulse 3 on the B-spins, so the fourth term in Eq. (40) is relatively small compared to the others, but it does exist and is a dominant term in "2+1" [38], where excitation overlap is large. Another form of Eq. (41) is

$$V(\tau,t)/V_0 \cong 1 - p_2(1 - \cos(at)) - p_3(1 - \cos(a\tau)) \quad (42)$$

At first glance Eq. (42) appears to contain two similar terms, but they are actually quite different, since the last depends on pseudosecular terms in H_{dd}. However, p_3 is not small compared to p_2 as its main effect is to act on the anti-phase coherence of A spins via S_{az} of the second spin at ω_a. Furthermore, the spin dynamics of A spins is not necessarily in the weak-coupling limit, which could make Eqs. (40) and (41) far more complicated functions of τ than $\cos(a\tau)$ [106], so that Eq. (40) in that case would become unwieldy. To a good approximation one should ignore this entire

nuisance by dropping the second term in Eq. (41) as it dies out for $a\tau \gg 1$, and by including $(1 - p_3)$ into an "initial amplitude," V_0. Note that the latter action is not legitimate for more than two spins when one is interested in spin-counting or "instantaneous diffusion." We do not detail the well-known amplitude factors in V_0 in Eq. (40) (cf. Appendix) that determine spectral excitation of A-spins and the echo amplitude and shape. Since all amplitude factors contained in V_0 of Eq. (41) depend on generally orientationally dependent ω_a and ω_b and are coupled through $a(r,\boldsymbol{\eta})$, the signal in DEER, similar to the DQC case, is expressed as

$$V(t) = V_{12}(t) + V_{21}(t) \tag{43}$$

with each term, after neglecting $p_3 \cos(a\tau)$, having the form:

$$V_{km}(t) = \left\langle G_k(\omega_k(\boldsymbol{\lambda}_k, \boldsymbol{\eta}))[1 - H_m(\omega_m(\boldsymbol{\lambda}_m, \boldsymbol{\eta}))(1 - \cos(\omega(r, \boldsymbol{\eta})t))]\right\rangle_{r,\ \boldsymbol{\lambda}_k,\ \boldsymbol{\lambda}_m,\ \boldsymbol{\eta}} \tag{44}$$

where $G_k, H_m, \omega_{k(m)}(\boldsymbol{\lambda}_{k(m)},\boldsymbol{\eta})$, with k, m (a or b) numbering the spins, have the same meaning as in DQC (cf Sect. 2.3.5). They are expressed differently (cf. Appendix) due to fewer pulses and the nature of the signal, but as in DQC depend mainly on the factors given by Eq. (31). In an ideal case, when there is no correlation between $\boldsymbol{\lambda}_1$ and $\boldsymbol{\lambda}_2$ as well as with $\boldsymbol{\eta}$, $V_{km}(t)$ becomes

$$V_{km}(t) = \langle V_{0k}[1 - p_m(1 - \cos(a(r, \boldsymbol{\eta})t))]\rangle_{r,\ \boldsymbol{\eta}} \tag{45}$$

Finally, for like spins, there is only one term of the form given by Eq. (45) which is the well-known form

$$V(t) = \langle V_0[1 - p(1 - \cos(a(\mathbf{r}, \boldsymbol{\eta})t))]\rangle_{\mathbf{r}} \tag{46}$$

where $a \equiv \omega_d(1 - 3\cos^2\theta)$ [30]. In the isotropic case Eq. (46) becomes

$$V(t) = \int_0^\infty P(r)\, dr \int_0^1 [1 - p(1 - \cos(\omega_d t(1 - 3u^2)))]\, du \tag{47}$$

where $u \equiv \cos\theta$. Equation (47) is quite similar to Eq. (38) for the case of DQC, differing only because $p < 1$, and in Eq. (47) the $V(t)$ is reduced by factors reflecting the fraction of spins irradiated by the selective pulses, ω_{1a} (i.e., the A-spins). As one can notice in Fig. 5b, the signal has a short "dead-time," since the initial part of the signal is distorted in the beginning and this may interfere with measuring a distance shorter than ~25 Å, but it should be less of a problem for longer distances. The implementation is helped by using an independent source for the pump pulse, but a single TWTA with enough power operating in the linear regime (~12 dB backoff from saturation) also does very well (cf. Fig. 5b), if one uses the receiver with full quadrature to account for "dynamic" phase shifts [98].

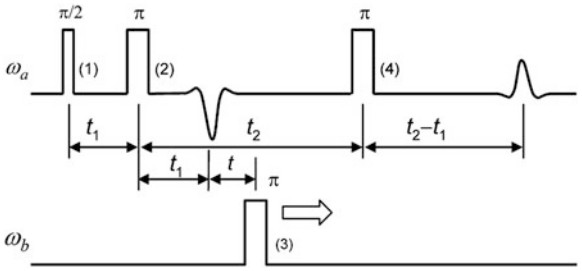

Fig. 6 The 4-pulse form of DEER [107] is a modification of its 3-pulse predecessor. It is based on detecting the refocused primary echo formed by $\pi/2 - t_1 - \pi - (t_1 + t_2) - \pi - t_2 - echo$ pulse sequence at the frequency ω_a of A-spins. The time variable t is referenced to the point where the primary echo from the first two pulses is formed (but is not detected). At $t = 0$ the dipolar phase is zero for all A spins (the precise position of $t = 0$ is limited by the width of the pulses). Shifting the starting point for dipolar evolution away from the second pulse by t_1 makes this pulse sequence dead-time-free with respect to dipolar evolution and eases its technical implementation

2.3.7 Four-Pulse DEER

Four-pulse DEER was introduced in 2000 by the group in the Max-Planck Institute, Mainz [107] to help alleviate issues with the dead-time encountered with setting up 3-pulse PELDOR using a single amplifier that was a limiting factor in accessing a wider range of distances.

This was accomplished by using the pulse sequence based on a refocused primary echo (RPE) $(\pi/2)_a - \tau - \pi_a - t - \pi_b - (2\tau - t) - \pi_a - \tau - echo$ with variable position, t of pump pulse (π_b) in between the second and fourth pulses. The addition of the refocusing pulse modifies the dipolar evolution to shift its initial point to be in the middle of the interval between the two refocusing pulses. Later this sequence was modified as shown in Fig. 6. In this implementation the zero time for the dipolar signal also coincides with the first (primary) echo but one chooses $t_1 \ll t_2$.

This ensures "zero dead-time" since the pump pulse does not need to be close to the detection pulses, thereby permitting easy implementation based on a single high-power mw amplifier, as in a commercial spectrometer. This fact enabled a rapid expansion of this method, known as 4-pulse DEER. Today it is the mainstream technique with several dozen spectrometers in operation worldwide. As a result, the number of studies that use DEER is rapidly increasing.

It should be noted that in the 3-pulse method its "dead-time" is the delay required for the detection pulse 1 (Fig. 5) to create transverse magnetization before the pump pulse flips coupled B-spins (i.e., it is of the order of half the time interval required for the pulses to "pass through each other"). The starting point of the dipolar evolution in the 4-pulse DEER sequence is when the pump pulse is centered on the refocused echo. Therefore, the two sequences are comparable in their capacity

to follow fast dipolar oscillations, due to the main limitation imposed by the width of pulses. However in the single power amplifier Ku-band PELDOR implementation (cf. Sect. 2.3.6) the need to use the linear regime limits the capacity to use a stronger pump pulse and may be not suitable for larger resonators in X-band. Another issue is that pulse interaction often exists in TWT amplifiers depending on the type of TWT and the design of the high-voltage power supply with the effects lasting for several hundred nanoseconds. A dual-amplifier configuration, as we found, is free from such artifacts, but is expensive. In summary, indeed 4-pulse DEER is easier to setup and use than the original PELDOR.

It was shown that the approximate form of 4-pulse DEER signal for two spins has essentially the same form [73] as in 3-pulse PELDOR:

$$V(t_1, t_2, t) = V_0(t_1, t_2)[1 - p(1 - \cos(at))] \tag{48}$$

with the amplitude factors V_0 depend mainly on spectral excitations of observing pulses applied at ω_a, and p is the fraction of spins B flipped by the pump pulse. Equations (42)–(47) from the previous section also apply. These expressions are satisfactory for most practical purposes. As with 3-pulse PELDOR, Eq. (48) is adequate when the pulses at the two frequencies do not overlap. Otherwise, there are eight different dipolar signals, which introduce a moderate level of artifacts (cf. Appendix). It is common to use a ~12 ns pump pulse to maximize the dipolar signal while minimizing unwanted signals. However, a moderate increase in signal amplitude could sometimes be offset in the case of typical T_2s (~1.2–2.5 μs) by the need to discard the latter points of the signal trace and because of nuclear ESEEM effects. The condition of small overlap is substantially satisfied in a typical setup that uses ~32 ns observer and pump π-pulses and a frequency separation of $\geq$70 MHz. It also results in much smaller nuclear ESEEM. This setup is standard at ACERT.

A useful feature of DEER is its flexibility. It can be applied to radicals with nonoverlapping spectra and to very broad spectra. Relaxation effects and ESEEM are mostly factored out. The artifacts due to pulse overlap can be kept small for a broad range of pump pulses. Nevertheless, as we noted, there are a number of effects that should be taken into account, when needed.

To this date DEER has been implemented over a broad frequency range from S-band [108] up to E-band (180 GHz) [48]. It was implemented by us at Ku-band as a very high sensitivity DEER spectrometer that was able to rival our DQC in some cases, as we will show later in this chapter. It has operated for 9 years at ACERT and was used for several studies. PDS, represented by 3- or 4-pulse versions of DEER and 6-pulse DQC, allows one to measure distances from ~10 Å to nearly 90 Å, with DQC having a wider range due to intense B_1s and stronger signals. The main limitation to sensitivity and consequently the long distance range is imposed by phase relaxation, which we discuss next.

2.4 Relaxation

The amplitude of the primary echo V_0 decays during the period 2τ (cf. Fig. 5 for 3-pulse DEER), and during period $2(t_1 + t_2)$ for 4-pulse DEER (cf. Fig. 6), and $2t_m$ for 6-pulse DQC (cf. Fig. 4) due to phase relaxation. Therefore the maximum dipolar evolution time interval, $t_{\max}$ ($=\tau$), available for recording $V(t)$ is ultimately limited by the phase memory time, T_m. In the simplest case, $V(t) = V_0 \exp(-2t/T_m)$. In more general cases several mechanisms contribute to relaxation, some are described by stretched exponentials [109, 110] and some such as instantaneous diffusion [111] are spin concentration dependent. Furthermore, the signal could be the sum of several terms, with each modified by relaxation in its own way. Signal decay due to relaxation is the main factor that limits the maximum distance, $r_{\max}$, that one can measure, over a reasonable period of signal averaging.

Depending on the signal-to-noise ratio (SNR), $t_{\max}$ is ca. (1 to 3)T_m and cannot be extended much further. In DQC (cf. Fig. 4) t_m is essentially taken as $t_{\max}$ and $(t_1 + t_2)$ as $t_{\max}$ in DEER (cf. Fig. 6). The largest measurable distance $r_{\max}$ is proportional to $(t_{\max})^{1/3}$ in order to recover a full dipolar oscillation [32, 35]. Thus only a minor increase in $r_{\max}$ can be made by increasing $t_{\max}$ which would further reduce $V(t_{\mathrm{tmax}})$, and this would necessarily require a large increase in signal averaging to improve SNR. Clearly, significantly improved sensitivity could also be of considerable value here. In the case of relaxation given by a simple exponential, the maximum time $t_{\max}$ that can provide "acceptable" SNR for distance analysis depends on the spectrometer sensitivity, S, as $\log(S)$, where S gives the SNR for a standard sample. An improvement of S by a factor of 5–20 (as we find for DEER and DQC with the ACERT Ku-band spectrometer) extends $t_{\max}$ by a factor of 1.8–3 increasing $r_{\max}$ typically by 20–50% or else dramatically shortening the data averaging time.

For nitroxide-labeled proteins, T_m is largely determined by the dynamics of the nearby protons [110, 112–114] especially those from rotating methyl groups, leading to simple exponential decay as expressed above with T_m in the range of 1–2 μs for buried or partially buried labels. Such relaxation times are characteristic of hydrophobic environments that are encountered in lipid membranes (including fluctuating methylene protons) [115] and the protein interior [112]. At ACERT's Ku band level of sensitivity, this typically limits $t_{\max}$ to about 3–6 μs (in the absence of other relaxation mechanisms that could become dominant at larger $t_{\max}$); thus permitting $r_{\max}$ of ~55–65 Å.

Such short relaxation times could be significantly improved by protein and (when possible) lipid deuteration, with distances as long as 87 Å having been reported [116]. However, even in this case a typical limit is about 60–70 Å, since in such systems the average spin concentrations are often very low (2–20 μM). For water-exposed spin labels in soluble proteins, relaxation times could be considerably longer, ca. 3–4 μs [112] and could be as large as 6–8 μs in a deuterated buffer. Nitroxide probes have T_ms of nearly 100 μs in D_2O/glycerol-d_8 [114]. However, if there are surrounding protons, for example from the protein itself, the relaxation

time becomes much shorter. At longer τ ($\geq$3 μs) relaxation is dominated by the nuclear spin diffusion mechanism, leading to relaxation as $\exp(-m\tau^{\kappa})$ with $\kappa \sim 1.5$–2.5 [110, 117]. We can define the respective phase memory time T_m for such cases by expressing this relaxation term as $\exp[-(2\tau/T_m)^{\kappa}]$. In water, spin-diffusion typically limits T_m to ~4 μs, permitting an $r_{\max}$ of ~50 Å (or ~65 Å with lower accuracy).[6] Using deuterated solvent [35, 58, 59, 109] could extend T_m of spin-labeled proteins to ~6.5 μs and $t_{\max}$ to ca. 8 μs in favorable cases [114], i.e., less than is possible in completely deuterated systems [116, 118, 119], as there still is a bath of protons of the protein that will enable efficient nuclear spin-diffusion.

Another way to deal with such types of nonlinear ($\kappa > 1$) relaxation is to do multiple refocusing of the spin-echo [120]. This can partially suppress this relaxation, since each subsequent refocusing pulse is applied to the spin-echo produced by just the preceding refocusing pulse, so the total decay is a product of the decays between refocused echoes. For example, 6-pulse DQC has two points of refocusing first-order coherence (i.e., π-pulses 2 and 6 in Fig. 4) that help to extend $t_{\max}$ when T_m is dominated by nuclear spin diffusion, so the decay becomes: $\exp[-(2t_p/T_m)^{\kappa} - (2t_5/T_m)^{\kappa}]$ rather than $\exp[-(2t_m/T_m)^{\kappa}]$ (assuming a very short t_{DQ}) [35, 58]. Of course, for $\kappa = 1$ the two expressions are equivalent. This permits a more accurate estimate of $r_{\max}$ to ca. 70 Å.

The longitudinal relaxation time, T_1, determines how frequently the pulse sequence can be repeated (usually no more than at the rate of ~$1.5/T_1$) and consequently the rate at which the data can be averaged. Both T_1 and T_2 are temperature dependent, as is the signal amplitude, which depends on the Boltzmann factor for spins in the static magnetic field. The combined effect of all these factors is such that for proteins in water solution or in membranes the optimal temperature as a rule is in the range of 50–70 K for nitroxide labels. The presence of paramagnetic impurities with short relaxation times shortens both T_1 and T_2. This requires conducting experiments at even lower temperatures. However, it is difficult to use nearby ions to improve sensitivity, as T_2 can quickly become quite short. The distance between two ions [22, 87] or nitroxide to ion [121] can also be measured and the optimal temperature is usually less than 20 K.

2.5 *Distance Ranges*

2.5.1 Long Distances

In the previous section we discussed relaxation as the major limitation in the context of long distance measurements. The other limitations arise due to spectrometer sensitivity and sample properties, such as its morphology and heterogeneity [122]. The ability to measure very long distances is thus limited by the phase memory time,

[6] One could use just a $t_{\max}$ of ~$1.2T_m$ in this case.

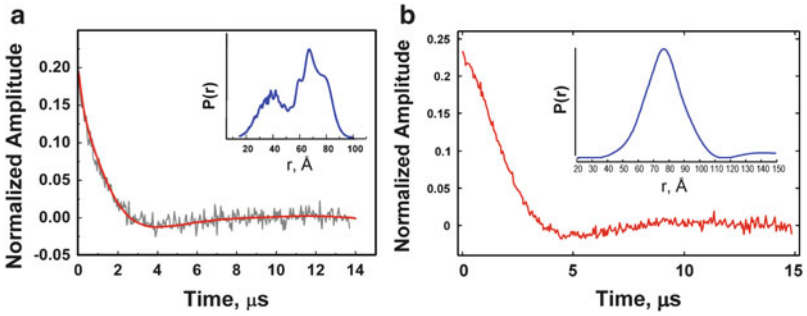

Fig. 7 Time-domain normalized DEER signals after baseline removal and reconstructed distance distributions: (**a**) 70% deuterated α-synuclein Parkinson's A30P mutant spin-labeled at sites 24 and 72 and reconstituted in SDS-d_{25}, (40 μM protein; 3 h of signal averaging); (**b**) 26 b.p. undeuterated TAR-RNA/TAR-cDNA duplex, DNA spin labeled at 3′, 5′. The signal was averaged over an 8 h period. The DNA concentration was 50 μM and D_2O buffer was used. The signal in (**b**) represents a distance of 80 Å with a width of ~30 Å. [The same sample was recorded using a 20 μs "oscillation" time in 3 h with S/N about 50% of that shown. This permits one full period of dipolar frequency corresponding to 101 Å distance. (**a** is adapted from [116]; the sample used in **b** is courtesy of C. P. Scholes.)]

T_m and for proteins, 65–75 Å is about the upper limit with current technology. Also, distances measured in this range are typically not very accurate because of a lower SNR and reduced fractional period of the dipolar oscillation detected. Modified pulse sequences have been shown to bring some level of improvement [58, 59].

Sometimes just buffer or lipid deuteration suffices to measure distances up to 80 Å (Fig. 7b), but in general further improvement would require much greater effort, such as a dramatic increase of the spectrometer sensitivity and/or improvements in sample preparation, e.g., partial or complete protein deuteration (Fig. 7a) [116, 119], which in itself we estimate may extend r_{max} to 100–130 Å and make distances ranging up to 80 Å much more accurate. Since such enrichment also benefits high resolution NMR [123–125], one could hope that this technology may become, in the future, an accepted way to improve the accuracy of distances in the 50–80 Å range, which are currently accessible, and to increase the sensitivity dramatically, bringing it to the micromolar level. This is of particular value for the difficult case of membrane proteins. Alternatively, with a good spin labeling strategy, such long distances can often be avoided, but much more double mutants have to be engineered to recover very long distances by triangulation [1, 5, 63, 71].

2.5.2 Short Distances

While measuring short distances is not limited by sample relaxation, this task has its own challenges. The sensitivity to shorter distances decreases significantly because the dipolar (and J) coupling increases and both components of the Pake doublet can no longer be adequately excited [104] in DEER. Also, account must be taken of the strong dipolar coupling that still exists during these long pulses [102, 104].

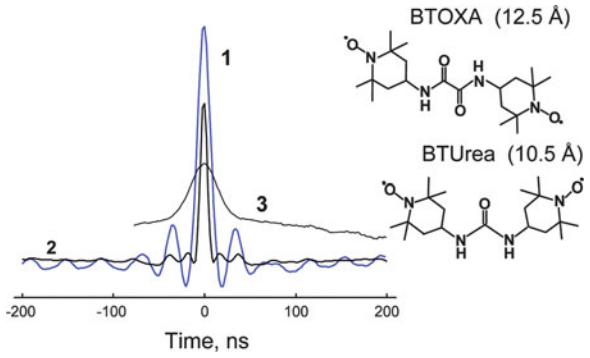

Fig. 8 The challenge of short distances with the example of short biradicals used for DNP. Ku-band (17.3 GHz) DQC (*1*) and DEER (*3*) are compared for a rigid ~12.5 Å nitroxide biradical, BTOXA. Detection $\pi/2$ and π-pulses in 4-pulse DEER were 16 and 32 ns, respectively; the pumping pulse was 18 ns ($B_1 \sim 10$ G). This is found to be insufficient to properly excite the dipolar spectrum. For DQC $\pi/2$ and π pulses of 2 and 4 ns widths were used ($B_1 \sim 45$ G), developing the oscillations very cleanly. The longer pulses of DEER lead to a spread in the refocusing point of different spin packets and the weaker B_1 does not excite the full dipolar spectrum. Both function as a low-pass filter smearing out the high-frequency dipolar oscillations. (*2*) Ku-band (17.3 GHz) DQC signal for an even shorter biradical, BTUrea. In these experiments, $\pi/2$ and π pulses were also 2 and 4 ns. The dipolar spectrum has a characteristic frequency ~50 MHz and spreads up to ~75 MHz. However, it is believed this is in part due to an electron exchange J of 7.8 MHz. (The biradicals is courtesy of R.G. Griffin.)

Below about 18 Å the sensitivity of DEER to short distances reduces significantly and distances shorter than ~15 Å are difficult to measure. The π-pulse excites a spectral extent (in Gauss) of about B_1. It is necessary in DEER to excite both components of the Pake doublet at both pump and detection frequency. DEER normally uses pump π-pulses longer than 20 ns (B_1 of $\leq$9 G) and longer than 32 ns for detection. This imposes a lower limit to DEER of ca. 15–20 Å (cf. Fig. 8). However, π-pulses of 30 ns are typical, since they provide a cleaner implementation of the method, which requires that the pump pulse and observing pulses do not overlap in spectral extent. This tends to limit short distances measurable by DEER to 20 Å. A modification of the 4-pulse DEER sequence for short distance measurement was suggested [60], and may be useful in future applications to biological systems.

DQC uses intense pulses with B_1 of 30 G or greater, hence it can access distances as short as ca. 10 Å [11, 93] (cf. Fig. 8). In this case the pseudosecular part of the dipolar term in the spin-Hamiltonian [i.e., the last term on the right in Eq. (12)] cannot be neglected, but this can be accounted for [35].

Thus, pulse methods could be applied to most practical cases arising in protein distance mapping, i.e., 10–90 Å. The short distance range is more appropriate however for organic biradicals, buried spin labels, or radical cofactors, TOAC, and similar cases, when radicals are substantially immobilized and their geometry is known or can be deduced. This lower range is less relevant for typical nitroxide labels with long tethers, with uncertain geometry.

2.5.3 Optimal (PDS) Range of Distances

In our experience, an optimal range of distances for the purposes of PDS is within 20–50 Å (45 Å for membrane proteins, whose T_ms are 0.8–1.5 μs), even though larger distances can be and have been measured with a longer period of signal averaging, but usually with reduced accuracy. This is based on our extensive experience at ACERT at Ku band, so the upper range would be smaller at X-band (commercial). Distances shorter than 20 Å introduce a relatively larger uncertainty in estimating the C_α–C_α distances. Measurement of distances in the optimal range are fast and accurate in most cases. The labeling sites and distance network should thus be chosen when possible such that they provide optimal conditions for PDS, by increasing the relative number of optimal distances, as needed.

A good example of this effect is the recent study on structural models of the complex between the cytoplasmic domain of erythrocyte band 3 protein and Ankyrin-R repeats 13–24, where PDS data were supplemented by cw ESR for distances shorter than 15 Å [71].

Optimal conditions are not readily available for oligomeric proteins due to multiple labels and their typically large size [5, 65, 122]. For an unknown structure, a preliminary scanning by several trial measurements may be very helpful.

2.6 Distance Distributions and Extracting Distance Information

Several approaches to determine distance distributions of paramagnetic centers in solids were utilized in the early applications of DEER and related methods [29]. Such methods have been improved [66, 67, 69, 70, 126, 127] and Tikhonov regularization is now a major tool for extracting distance distributions from the raw or preprocessed data.

In PDS the "raw" experimental time-domain signal encoding distance information is not an ideal dipolar signal which is the Fourier-transform of the dipolar frequency spectrum. Depending on the method it can contain a constant or decaying background and be modified by some decaying function. Before any attempt to reconstruct the distances is made, the pure dipolar signal should be separated from these. Without going into the details of the forms and origin of these contributions, which we discuss in Sect. 2.8, we express the time-domain PDS signal (both DQC and DEER) in the following general form consistent with the above signal description.

$$V(t) = \left\langle V_{\text{intra}}(t, \boldsymbol{\mu}) V_{\text{inter}}^{(1)}(t, \boldsymbol{\mu}) + V_{\text{inter}}^{(2)} \right\rangle_{\boldsymbol{\mu}}, \tag{49}$$

where V_{intra} is the "dipolar" signal of interest, produced by a pair of spins in the molecule bearing a pair of spins, while the other terms and factors depend on the PDS method to detect the signal and the sample property, for example the contributions to the intramolecular spin-pair signal from the surrounding spins

(vide infra), denoted by the subscript "inter." The averaging in Eq. (49) is conducted over parameters $\boldsymbol{\mu} = (\mu_1, \ldots, \mu_n)$, some of which may be common for contributing terms. For example, they could depend on the distribution of B_1 over the sample, or there could be a local structure, leading to a MOMD[7] case [128]. For DEER a widely accepted approximation is to take $V^{(2)}_{\text{inter}}$ as a constant offset modified by $V^{(1)}_{\text{inter}}$ [105].

These terms can have a different origin in DQC and $V^{(2)}_{\text{inter}}$ could originate from the spins on other molecules and does not factor out in a simple way [1]. DQC filtering helps to make $V^{(2)}_{\text{inter}}$ small and it becomes insignificant at very low concentrations when molecules become essentially isolated. $V^{(1)}_{\text{inter}}$ in DEER could also originate from local aggregation effects that will only modify the signal of the aggregated molecules [129]. In all cases, the task is to extract the "dipolar signal" V_{intra} from $V(t)$. It can be helped by any a priori knowledge about the morphology of the sample. We emphasize that this step is one of the major sources of errors in distance reconstruction.

In most cases, the signal in PDS, used to extract the distance is based on the V_{intra} assumed to be given by the "ideal" signal form given by Eqs. (38) and (47). This level of approximation is often adequate, except for the cases when orientational effects (cf. Sect. 5.3) are significant or aggregation effects cannot be neglected. After extraction of V_{intra}, it is subjected to inverse reconstruction by Tikhonov regularization or related methods. The problem can be represented by a Fredholm integral equation of the first kind

$$V_{\text{intra}}(t) = V_0 \int_0^\infty P(r) K(r,t)\, dr \tag{50}$$

with the kernel $K(r, t)$ for an "ideal" isotropic sample is given by

$$K(r,t) = \int_0^1 \cos(\omega_{\text{d}} t(1 - 3u^2))\, du. \tag{51}$$

The inversion of the signal V_{intra} given by Eq. (50) to obtain $P(r)$, the distance distribution, is in principle achievable by standard numerical methods, such as by singular value decomposition (SVD), but it is an ill-posed problem which requires regularization methods in order to arrive at a stable solution for $P(r)$. In the practical implementation, the data are discrete and available over a limited time interval, and the actual form of the kernel $K(r,t)$ may differ from the ideal form given by Eq. (51), or could be modified to address a specific issue, such as providing corrections to the reduced sensitivity of DEER to short distances.

[7] Microscopic order with macroscopic disorder.

Tikhonov regularization [67, 70] recovers the full distribution in distance, $P(r)$. It is based on seeking an optimum, $P(r)$, which tries to minimize the residual norm of the fit to the data while also trying to maximize the stability of $P(r)$ (i.e., to reduce its oscillations). The relative importance of both is determined by the regularization parameter, λ. The L-curve method for optimizing λ is computationally very efficient and the most reliable to date [70]. In the Tikhonov method the regularization removes the contributions of the small singular values, σ_i in the SVD that are corrupted by the noise by introducing the filter function

$$f_i \equiv \frac{\sigma_i^2}{\sigma_i^2 + \lambda^2}, \tag{52}$$

which filters out those contributions for which $\sigma_i^2 \ll \lambda^2$. Further refinement of the $P(r)$ can be performed by means of the maximum entropy method (MEM) [69], although it is computationally more time consuming.

The latest versions of MEM and Tikhonov regularization permit one to simultaneously fit and remove the effects of $V_{\text{inter}}^{(k)}$ while optimizing the $P(r)$ from raw experimental data[8] [69]. This is important, since any attempt to remove a "prescribed" baseline (assumed to be a linear or a stretched exponential function) in the case of broad distributions usually results in a level of distortion that can render the distribution totally unreasonable. The reconstructed distribution may exhibit, for example, long-distance tails that correspond to distances exceeding the size of the protein.

Experimental artifacts, a multitude of minor effects leading to signal distortions, and residual baseline make the signal recovery somewhat less accurate than what can be achieved with model data generated using the ideal kernel of Eq. (51). The test examples in the literature [69, 70] demonstrate the accuracy of recovery of average distances and distribution widths when the signal is free of artifacts.

The best condition for having the least distorted data is to use a sample with very low concentrations to reduce the baseline practically to a constant in DEER and to a very small (negligible) constant by using DQC. This however requires that one employs a PDS spectrometer with adequate sensitivity. The analysis based on ideal kernel data suggested that the SNR should be not less than 30–50 depending on the reconstruction method [69, 70]. But a low level of distortions is also very important. However, since it is difficult to obtain such high SNR, we commonly find from the literature that distance reconstruction was conducted on data with SNR of ~10 or less or highly distorted in the latter points of the record. This practice is very likely to result in very poor or even unphysical reconstructions.

[8] Available for download through the ACERT web page www.acert.cornell.edu.

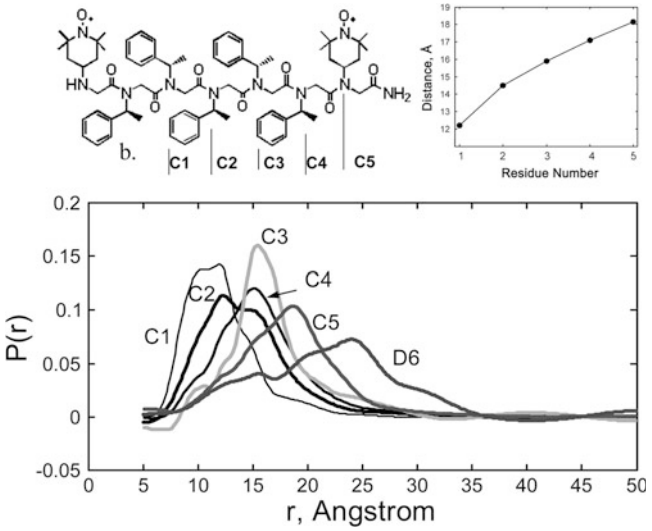

Fig. 9 Distance distributions (*bottom*) obtained from DQC data for double-labeled peptoids C1–C5 (*left top*) as determined by inverse reconstruction by Tikhonov regularization. Distances as a function of inter-residue spacing for C1–C5 (*right top*). Maxima shift from ~12 Å to longer distances (~18 Å) as the residue spacing between labeled side chains increases. Note that D6 (structure not shown) lacks branched structure-inducing side-chains, so it exhibits a wide distance distribution. (Adapted from [11].)

As an example of the viability of distance reconstruction, using short-range distance DQC data, we show in Fig. 9 the reconstruction of distance distributions for peptoids which are synthetic peptide analogs with side-chains attached to nitrogens.

2.7 Orientational Effects in PDS

The signal in DQC or DEER, given by Eqs. (34), (43), and (44), depends on the orientations of the magnetic and dipolar tensors, leading to a dependence of the dipolar spectrum on the exact position of spectral excitation in DQC and of both frequencies in DEER. On one hand, this can confuse the distance measurements, and on the other hand, it provides the opportunity to determine (to some extent) the orientations of spin labels, thus providing additional structural constraints. In cases of strong magnetic anisotropy and broad spectra, such as for Cu^{2+}–Cu^{2+} spin pairs, this orientation selectivity is already available at X-band [87], whereas for nitroxides W-band may be more suitable.

For spin labels with flexible tethers such as MTSSL, orientational effects are usually small and it is difficult to detect them at Ku band, but the effects are more pronounced for cases of more rigid labels such as TOAC and those developed for labeling oligonucleotides [130, 131], or even for MTSSL in some cases [132].

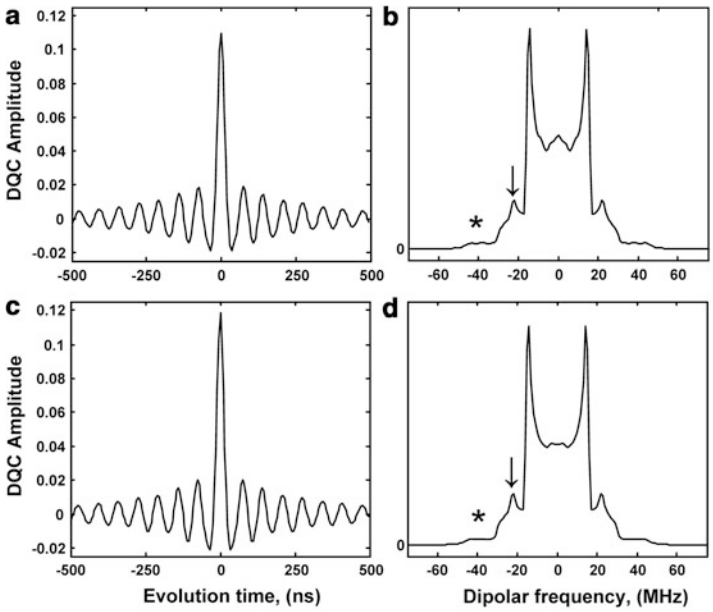

Fig. 10 Time-domain 1D DQC signals and their Fourier transforms for ^{14}N nitroxides with their magnetic tensor axis orientations distributed isotropically in the molecular frame (i.e., referred to as uncorrelated case). (**a**, **b**) A computation based on analytical approximation [cf. Eq. (32)] and (**c**, **d**) that computed rigorously. $B_0 = 6{,}200$ G, $B_1 = 30$ G, and dipolar coupling (ν_d) is 15 MHz (15.1 Å). This figure shows the time-domain data in dipolar and echo times and its FT. A small peak at $3\nu_d/2$ (indicated by *downward arrow*) and a weak shoulder (marked by *asterisk*) extending up to $3\nu_d$ are manifestations of the pseudosecular terms in H_{dd}. The difference between the two cases is quite small, being mostly caused by using simplified amplitude factors in Eq. (32). (Adapted from [93].)

New spin-labels with reduced flexibility [133, 134] may help to achieve stronger orientational effects than what can be achieved with MTSSL.

When a sample containing bilabeled proteins is subjected to a sufficiently strong microwave pulse, as is used in DQC, the nitroxide EPR spectrum is almost uniformly excited by each pulse, and any orientational selection is (largely) suppressed given the excellent Pake doublet predicted for DQC [93] as shown in Fig. 10; that is, it does not modify the echo amplitude (except for the effect of pseudosecular dipolar terms for short distances). Also, in high B_1-fields, the effect of dipolar coupling during the pulses becomes relatively weak so that the spectral rotation of both components of the Pake doublet is essentially the same as in the absence of coupling. In other words, a strong B_1 decouples the spins. Therefore, for not very short distances and in sufficiently strong excitation fields (B_1s), the information on orientations of the magnetic tensors of the spin-label moieties is virtually excluded from the time-domain dipolar evolution of the echo amplitude in DQC. However, as shown by Borbat and Freed [35] and later in [93], orientational information is still retained in the spin-echo evolution, and can be retrieved by

recording the 2D time–domain data as a function of both the spin-echo time (t_{echo}) and the dipolar evolution time (t_{dip}); this is discussed later in this chapter (cf. Sect. 5.3). We remind the reader that the spectral extent that contributes to the DQC signal is less than that given by an individual π-pulse, since there are three such π pulses in the DQC sequence. Therefore not all orientations are equally represented in a real DQC signal.

2.8 Multi-spin Effects

So far, we have been discussing pulse methods for a system of two spins. These methods have also been applied to systems that contain more than two spins, such as oligomeric proteins [5, 65, 122] and small spin clusters [135]. In principle, all electron spins in a sample interact with the spin-pair in spin labeled molecules, giving rise to an intermolecular contribution that modifies the dipolar signal from that of an isolated spin pair or a small cluster [cf. Eq. (49)]. Such contributions are reasonably well understood in the case of DEER, but they are less tractable for single-frequency techniques, such as DQC. In all cases these effects should be accounted for in order to extract the intramolecular signals that encode the information on the relevant distances. Experimentally, intermolecular contributions should be reduced by using samples as dilute as possible consistent with the distance range and the available SNR. Intermolecular contributions on the other hand can be used to estimate spin concentration and homogeneity of the spin distribution in the sample.

2.8.1 Multi-spin and Intermolecular Effects, Clusters, Oligomers, and Spin-Counting

In many cases one has to deal with a protein that may have more than two spin labels, such as an oligomeric protein or a protein binding several spin-labeled substrates. For N spin labels, there could be up to $N(N-1)/2$ distances. For instance, in our work on CheA/CheW complex [5] there were four spins per complex, with six distances possible, limited to four by symmetry, and up to five distances in our study of binding of the receptor by this complex [65]. Therefore, one might expect that except for a few advantageous cases like this, a broad distribution may be the only result, limiting the opportunity to infer detailed information on distances. The study on the CheA/CheW/Receptor complex used modeling to match several broad distance distributions in order to verify rigid-body docking, based on loosely defined constraints [64, 65].

One important application of PDS is spin-counting that could yield aggregation numbers. This currently is based on a well-tested DEER method. Small spin systems based on rigid polyradicals have been studied to correlate the modulation

depth with the number of spins [136] and to estimate nonlinear effects [137] in cases when the pump pulse is not weak enough, as recommended in early work on spin-counting by DEER [105]. Recently a magnetic dilution method was introduced for cases where the aggregate structure is not well defined [129].

In general, the small spin cluster problem is not as simple as it may appear. All A-spins are coupled and in the subsystem of A-spins one has to deal with the multi-spin dipolar Hamiltonian that contains non-commuting pseudosecular terms [138]; therefore the contributions of spins in the cluster to the echo from a particular spin do not factor out, as they do for B-spins or remote spins on other molecules. Thus, a good approach may be in using weak detection pulses minimizing the A-spins in order to limit the task to the first-order in spin number. The contribution from remote A-spins has no such problem and is treated in the same way as for B-spins, since the pseudosecular dipolar term can be neglected. Even in the case of mono-disperse clusters, due to less than ideal spin labeling efficiency, there is a distribution in number of spins per cluster, therefore the term in $\cos(a\tau)$ in Eq. (41) should be explicitly included in computing the signal from the cluster [105]. The case of several spins can become more complicated if the relaxation times of the spins are significantly different due to different local environments [65].

For an N spin system, e.g., for a spin-labeled oligomer of order N, bearing nitroxide spins $k = 1, \ldots, N$, the dipolar signal in DEER can be written as a product according to [105] as:

$$V_{\text{intra}}(t) = V_0 N^{-1} \left\langle \sum_{i=1}^{N} \prod_{k \neq i} \left[1 - p_{ik} u_{ik}(\mathbf{r}_{ik}, t)\right] \right\rangle_{\mathbf{r}_{ik}} \tag{53}$$

Here, $u_{ik}(\mathbf{r}_{ik}, t) \equiv 1 - \cos(a(\mathbf{r}_{ik})t)$ is the dipolar signal detected on spin i when pumping on spin j, p_{ij} is the probability of flipping spin j by the pump pulse; $\mathbf{r}_{ij}$ is the vector connecting spins i and j.

Micro-heterogeneous systems or systems with local order, such as lipid membranes and micelles which have characteristic microscopic order, are usually not amenable to simple analytic solutions, and their signals should be derived based on the appropriate averaging of Eq. (53) for the particular case [135].

The case of a small group of spins (clusters) has been considered in the literature [33, 105, 135]. This case requires numerical treatment based on Eq. (53), typically by the Monte Carlo method, although simplified approaches exist and were used to make crude estimates of the number of spins in a cluster [105]. Actually, an accurate treatment is rarely justified in such cases, since there are too many unknown parameters to fit and the limited data which permit determining one or two parameters at most. In addition one must have a priori knowledge about the system in order to model it properly.

2.8.2 Intermolecular Effects

The spin echo amplitude from an isolated pair of spins in DEER [30, 122, 139] according to Eq. (46) can be written as:

$$V_{\text{intra}}(t) = V_0(1 - p + p\langle\cos(at)\rangle_r) \tag{54}$$

where p is the fraction of B spins flipped by the pump pulse. The angular brackets denote averaging over **r**, which is simplified by assuming no orientation selection [32, 131], which usually holds well for flexible tether MTS spin labels. Note also that $V_{\text{intra}}(t)$ in DEER contains a large contribution from spin pairs not flipped by the pump pulse, $V_0(1 - p)$, cf. Eq. (54).

The amplitude of the DEER time-domain signal, $V(t)$, as noted in Sect. 2.6 can usually be factored into an "intramolecular" contribution, V_{intra} [Eq. (54)], which gives the dipolar interaction in a pair of sufficiently isolated spatially correlated spins (i.e., on the same molecule), and a nonspecific "intermolecular" contribution, V_{inter}, from those spins randomly located within a few hundred angstroms from the pair [139].

$$V(t) = V_{\text{intra}}(t)V_{\text{inter}}(t) \tag{55}$$

V_{inter} is a decaying signal that modifies $V(t)$, resulting in a large decaying background (baseline) signal, and term $V^{(2)}_{\text{inter}}$ could also be present (cf. Eq. (49)), e.g. it can be contributed to from other sources, such as free spin-labels. For a spin i the dipolar signal in DEER due to all surrounding spins can be written as a product according to [105] as:

$$V_{i,\text{inter}}(t) = \left\langle \prod_{j\neq i}^{N-1} [1 - p_{ij}(1 - \cos(a(\mathbf{r}_{ij})t))] \right\rangle \tag{56}$$

where angular brackets denote configurational averaging over all spins in the sample. Relaxation may complicate Eq. (56), but is not included, as is appropriate for most practical cases. Equation (56) can be simplified by Markoff configurational averaging [140] over the spin distribution throughout the sample. Protein solutions can generate an isotropic, but not necessarily uniform spin distribution because of spatial correlations through excluded volume or interaction effects [141]. One finds [129] by using the Markoff method:

$$V_{\text{inter}}(t) = \exp(-k_0 p C_0 t - 9\sqrt{3}k_0 p C_0 \int_0^\infty f(r) r^2\, dr \int_0^1 dx \sin^2(\omega_{\text{d}} t(1 - 3x^2)/2)) \tag{57}$$

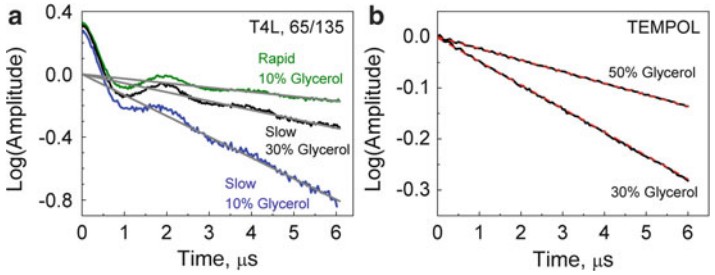

Fig. 11 The effect of the glassing agent and sample freezing method on local concentration. Raw dipolar signals are plotted on semilogarithmic scale for (**a**) 56 μM 65/135 mutant of T4-lysozyme and (**b**) 100 μM TEMPOL (1-oxyl-2,2,6,6-tetramethyl-4-hydroxypiperidine). The samples were prepared using a different percentage of glycerol in D_2O buffer by freeze-punch (slow-freeze) and freeze-quench (rapid-freeze). One can see different slopes, indicating variations in C_{loc}, depending on percentage of glycerol and the freezing method. The slopes for the 10% glycerol rapid-freeze sample, and 30% and 10% glycerol slow-freeze samples correspond to C_{loc} of 122, 248 and 578 μM, respectively. For TEMPOL the slopes correspond to 100 and 200 μM, in 50% and 30% glycerol samples, respectively. Only with 50% glycerol the spin probe distribution in the sample is truly uniform. In the case of T4L, a rapid freeze ensures a nearly uniform distribution even in the presence of just 10% of glycerol. (Adapted from [142].)

where $k_0 = 8\pi^2\gamma_e^2\hbar/9\sqrt{3} \approx 10^{-3}\ \mu\text{M}^{-1}\ \mu\text{s}^{-1}$ and p is the fraction of spins flipped by the pump pulse; C_0 is the average spin concentration over the sample; and $f(r) \equiv 1 - C(r)/C_0$ represents the effect of variable (local) spin concentration, $C(r)$, in heterogeneous samples, and r is the distance from the spin. It is clear from Eq. (57) that the exponent is nonlinear in t, whose character depends on whether the molecules attract or avoid each other [141].

For a uniform spin distribution when $C(r) = C_0$ and $f(r) = 0$, then Eq. (57) reduces to the well-known form $V_{\text{inter}} = \exp(-pk_0C_0t)$. If one approximates $C(r)$ by a constant local concentration, C_{loc}, then

$$V_{\text{inter}} \cong \exp(-pk_0C_{\text{loc}}t) \tag{58}$$

C_{loc} thus can be estimated from the slope k of the baseline (cf. Fig. 11) in the semi-logarithmic plot of $V(t)$, i.e., from

$$k^{-1} = 1.0027\frac{10^3}{pC_{\text{loc}}} \tag{59}$$

where C_{loc} is the molar concentration and p is 0.2–0.35 for typical pump pulses [142]. The dipolar signal from the spin pair of interest [cf. Eq. (54)] is then modified by multiplication by this decaying factor (cf. Figs. 11, 12, 13, 14, and 15 for examples). A similar mechanism works amongst A-spins and is referred to as the

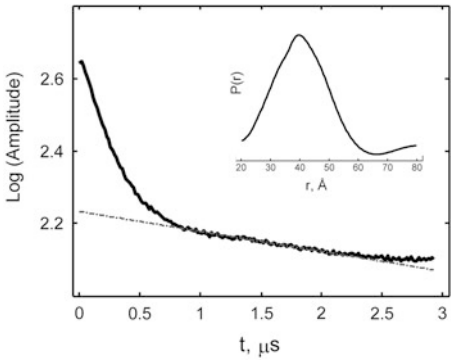

Fig. 12 Time-domain DEER signal for CheW complex with CheA-Δ289 Q545C spin-labeled cysteine mutant. Inset shows broad distance distribution between pairs of nitroxides in this homodimeric protein [5]. CheAΔ289 concentration was 25 μM, signal averaging time was 8 h 20 min due to short T_m. The latter part of the signal deviates from a straight line in the semi-log plot due to the presence of unwanted dipolar signals caused by the overlap of pulse excitation at the two frequencies separated by 65 MHz. DEER was recorded using 20 ns pump pulse in dual amplifier spectrometer configuration, which eliminates the contribution from pulse cross-talk in the TWTA. The signal after subtracting the background has to be truncated or apodized prior to L-curve Tikhonov regularization. This shortens the trace by ~0.5 μs. (Adapted from [122].)

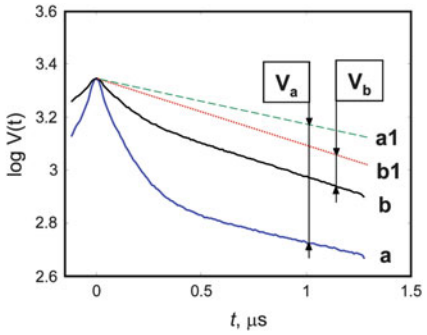

Fig. 13 The DEER data in the case of clusters for spin-labeled alamethicin magnetically diluted (*b*), and without dilution (*a*). (*a1*, *b1*) are *straight line* semi-log fits to the asymptotic parts of (*a*, *b*). (*a*) is typical for a spin cluster; in this case single labeled alamethicin molecules are organized into small clusters with an expected constant number of monomers. The data in (*b*) represent the same spin concentration but magnetically diluted by a factor of 5 with unlabeled peptide, indicating that this signal indeed originates from a spin cluster. The asymptotic DEER amplitudes (V_a, V_b) can be immediately analyzed to yield an estimate of how many peptide molecules, N are in the cluster [105], given that the fraction of peptides in clusters is known. Based on [105] $\log V_a = (N - 1) \log(1 - p)$, where p was 0.2. This yields four peptide molecules per cluster. (Adapted from [122].)

"instantaneous diffusion" mechanism mentioned earlier [34, 111, 117, 138, 143], although it is not a dissipative relaxation mechanism, so it can be partially refocused [95].

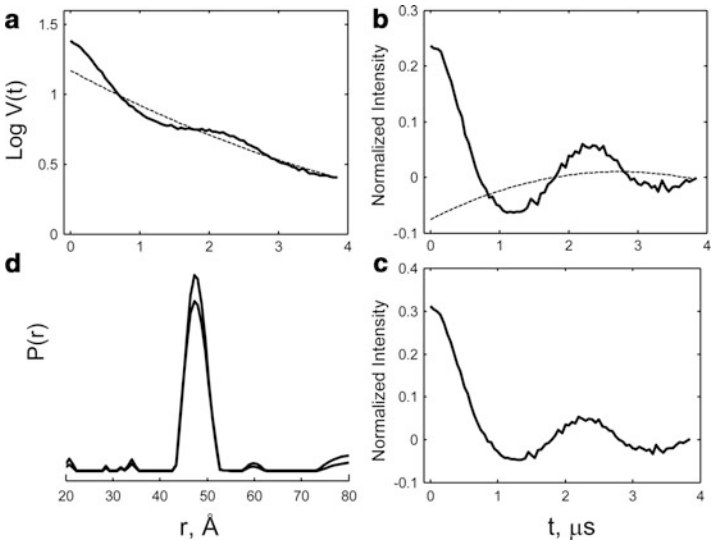

Fig. 14 Data processing of a Ku band time-domain DEER data for monoamine oxidase MAO-B labeled with spin-labeled pargyline substrate and reconstituted in octylglucopyranoside micelles [27]. (**a**) The intermolecular background is removed by first fitting (inappropriately) the data on the 1–4 µs interval to a second degree polynomial (rather than to a *straight line* as relevant for this case) in the semi-log plot, followed by subtracting it out. (**b**) Dipolar signal after removal of background. *Dashed line* shows the correction for the background that was generated in the process of MEM reconstruction [69]. (**c**) Corrected dipolar signal generated by fitting (**a**) to a linear background signal; it is indistinguishable from (**b**), after subtracting from (**b**) the correction, indicating the capability of MEM to adjust the inter-molecular contributions to the dipolar signal, reducing introduced spurious content, without introducing large errors or instability. (**d**) $P(r)$ produced from data from (**b**) (*upper curve*) and (**c**). (Adapted from [122].)

Strictly speaking, Eq. (58) only holds for the primary echo decay in magnetically dilute spin systems. The intermolecular contribution depends on how the multi-pulse sequence manipulates the spins in the surrounding spin bath and all possible dipolar evolution pathways should be considered [38]. In 3-pulse PELDOR the primary echo is the sum of four components that have different time dependencies with respect to the position of the pump pulse (cf. Sect. 2.3.6) [106].

The refocused echo used in 4-pulse DEER is an eight-component signal originating from all dipolar pathways (cf. Appendix). In both cases there is a common intermolecular factor, given by Eq. (58), but the coefficient k may be different from what is given by Eq. (59), if any overlap exists between the excitations at the two frequencies. Even when the overlap is small, it affects the longer time points of the signal and may become comparable to or exceed the dipolar oscillations at these points as illustrated in Fig. 12. This complicates fitting to the baseline. To minimize the distortions of this part of the signal, it is better for the pump pulse to be less than ~32 ns in width for nitroxides and virtually all distance measurements at ACERT were made in this mode.

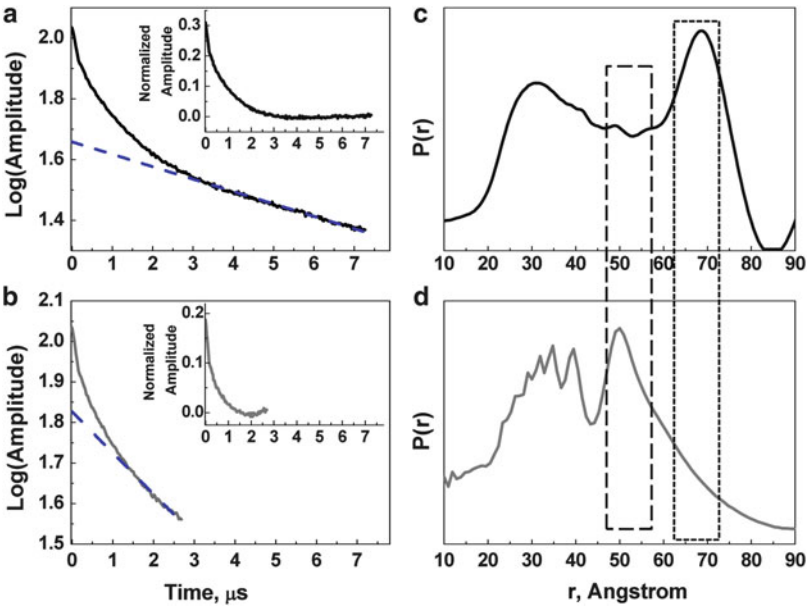

Fig. 15 Distance distribution reconstruction as a function of the evolution time of the dipolar signal. Subplot (**a**) shows the logarithms of raw time-domain DEER data from Parkinson's mutant A30P of α-Synuclein with spin labels introduced at positions 24 and 72 [116], total protein concentration (labeled and unlabeled) was 40 μM in 20 mM SDS-d_{25} solutions. The baseline produced by fitting to log-linear background is plotted as *dashed line*. Subplot (**b**) is otherwise the same as (**a**), but uses the data in (**a**) truncated down to 2.5 μs. The insets in (**a**) and (**b**) show the data after baseline subtraction. The panels (**c**, **d**) show respective $P(r)$s. A better reconstruction is obtained on original 7 μs data. (This lab, unpublished.)

A similar approach can be applied to an isotropic uniform distribution in space with fractal dimensionality, where a closed-form solution can be written [109]. Practical examples of lower dimension are the 2D case of unilamellar lipid membranes or the 1D case of self-avoiding polymer chains.

We note that a generalization of DQC methods to provide multiple-quantum coherence pulses that select the order of coherence is, in principle, possible [35]. Such a methodology would be very useful for spin counting, but it has not yet been developed for practical use in ESR.

For the sophisticated pulse sequence of DQC, there is no rigorous theory yet for the intermolecular dipolar effects in DQC. To first order, it is a linear contribution, which is modified by instantaneous and nuclear spin diffusion effects such as to provide a monotonically decaying nonlinear background, which should be fit to a polynomial or obtained by conducting reference measurements on singly labeled molecules. After correcting for damping as described in [1], MEM with baseline fit [69] can be applied and usually works well.

As either evolution time or concentration increases, higher order coherences will play a further role in reducing the signal. This has been analyzed for a simplified

Many-Spin Hamiltonian by Nevzorov and Freed [138]. Therefore at low concentrations, DQC has the advantages of better sensitivity due to all or nearly all the spins participating and to the weaker effects of the surrounding spins. But in cases of high local concentration (lipid vesicles, protein oligomers, or peptide clusters), DEER is able to produce the same (or sometimes even better) sensitivity than DQC, because of reduced instantaneous diffusion resulting from the weaker DEER pulses.

From the standpoint of PDS the intermolecular term is usually an unwanted complication, requiring that the intramolecular signal of interest be separated from the intermolecular contribution to the signal. Clearly, the best approach is to minimize the latter by sample dilution, whenever it is an option and sensitivity permits, as we continue to point out.

For clusters, controlled magnetic dilution proved useful to detect aggregation [129, 144] and evaluate the size of the clusters and the number of spins [145]. We illustrate in Fig. 13, the practical implementation of the method, with some additional details given in [105].

2.8.3 Data Processing in DQC and DEER

Before the data from a PDS experiment is processed into a distance distribution, it should be separated from the offset and intermolecular contribution, as discussed in Sect. 2.6. As can be seen in the literature, in many (or maybe most) cases the task of extracting the pure intramolecular dipolar signal from the data record is a difficult one, as there is no truly accurate and reliable theory that can describe all the intermolecular contributions. It has been accepted that a benefit of DEER is the multiplicative nature of the background, as it permits one to fit the background to, e.g., a simple (or stretched) exponent and then simply factor it out. However, this is not necessarily true.

In fact, the multiplicative nature of the DEER signal is often not the case and intermolecular and intramolecular signals can be convoluted. Some obvious reasons are: local heterogeneity, excluded volume, and spatial correlation lead to distributions in local concentrations, relaxation times are different, B_1 is not uniform over the sample, fractal distributions are often encountered in anisotropic environment, etc. Nevertheless, our (unpublished) analysis showed that in most of the above cases the assumption of a signal of the form $V_{\text{intra}}V_{\text{inter}}$ does not result in large errors.

But generally speaking, in most cases baseline removal still is a highly empirical procedure, as it can be highly nonlinear. The best solution would be to have it constant or nonexistent, e.g., to use highly dilute samples and when possible, DQC. However, membrane proteins are usually locally too concentrated even for DEER, even though the average (or bulk) spin concentrations are usually much less than 100 μM. So, this recipe would require a level of sensitivity that is beyond the current state of the art. For DQC, one may work with very dilute solutions

(ca. 10 μM) so the small intermolecular background signal is readily removed by means of least squares polynomial fitting in the time-domain of the latter part of the signal with sufficiently decayed oscillations; then this is extrapolated back to the earlier points of the signal and subtracted out. A correction to (quadratic) relaxation decay may be needed for not very small backgrounds [1].

In the case of DEER the removal of (multiplicative) background signal often is performed by fitting the latter part of the signal to a straight line in a log plot under the assumption of an exponent that is linear in time as in Eq. (58). This model often is not the case for the following reasons: fast-relaxing ions, charges on the protein [141], and excluded volume. All these produce a concave baseline on a logarithmic scale, whereas aggregation [cf. Eq. (57)] and fractal dimension [109] lead to the opposite or convex baseline. In these (typical) cases a low-degree polynomial can be used if a reasonable model for V_{inter} cannot accurately reproduce the intermolecular contributions. Referencing using singly labeled protein has proved to be useful for DEER.

When V_{intra} is oscillatory and does not significantly decay, more of the earlier points should be used to determine V_{inter}, sometimes all the way back to $T_d/2$ (T_d is the period of dipolar oscillations). This approach to baseline subtraction could be highly inaccurate; therefore it may be necessary to supplement it by MEM regularization to reduce the error in subtraction (cf. Fig. 14).

In the opposite case of broadly distributed distances the signal makes a gradual transition into the baseline and their separation becomes problematic, especially if the baseline is not expected to be described by a simple exponent, as is typical for membrane proteins reconstituted into liposomes. In the case of broad distributions a very shallow negative oscillation may last for more than one period of dipolar oscillations and cannot be recovered by straightforward log-linear fitting. But it is more successful to use MEM with an integrated baseline fit.

An example of such broad distributions is shown in Fig. 15. The approach is to use as long an evolution time as possible and as low a concentration as possible. This requires very high sensitivity. In Fig. 15 Panels (c) and (d) show the outcome of distance reconstruction, from (a) and (b), respectively, based on L-curve Tikhonov regularization followed by MEM refinement. The long-distance component in (c) (in dashed box) was lost and the peak with a long-distance "tail" (the dot-dashed box) at ~5 nm appears instead from the truncated (b) data set.

As we mentioned above, one way of accounting for the intermolecular background is to use methods of signal reconstruction with simultaneous baseline fitting [69], which separates out the part of the signal governed by the intramolecular kernel. When possible a more dilute sample is recommended, as it reduces background and also helps to make it more linear, ultimately just a constant offset. A related approach for membrane-associated proteins is to modify the sample preparation by using detergents, bicelles, and nanodisks [27, 116, 118, 146], but this may not always be possible or acceptable.

3 Technical Aspects

3.1 Spectrometers

Due to the complexity associated with construction and maintenance of a high-quality (pulse) ESR spectrometer, "home-built" designs have become increasingly uncommon. This could have become a bottleneck for PDS development, confining this method to a few research laboratories, which, over a period of two decades, have developed the adequate technology needed and even state-of-the-art performance in unique designs. PDS gained wide acceptance, however, as a result of the availability of DEER-capable commercial X-band spectrometers (and recently its Q-band extension).

However, several key aspects of PDS continue to be developed using home-built spectrometers, such as ACERT's Ku-band PDS spectrometer and several others [46–50]. The most important feature of our pulse spectrometer is that intense microwave pulses of 1–8 kW are produced, depending on the working frequency, in order to optimize such methods as DQC (and also to satisfy the requirements of 2D-FT ESR). The Ku-band spectrometer used in the PDS work carried out at ACERT is based on a highly successful implementation of X/Ku band 2D-FT ESR [147].

This (upgraded) spectrometer provides accurate pulse widths, with pulses that can be as short as 0.5–0.8 ns, efficient signal capture in up to 1 GHz bandwidth, averaging at the rate of hundreds of kilohertz, generation of accurate phases in quadrature, and complex phase cycling schemes to greatly suppress unwanted signals including DQ filtering. Stability is essential, so the phase drift from all destabilizing factors is less than $\pm 4^\circ$ over a period of several days. The Ku band operation is supported by 2 and 4 kW amplifiers, wherein the latter is capable of providing a $B_1 \sim 45$ G in a 15 μL sample volume, which is highly beneficial for DQC. Importantly, DQC is more immune to pulse distortions typically produced by TWTAs than DEER. However, the 4 kW TWT life span has proved to be shorter than that for 2 kW amplifiers. This is an important consideration, given that the actively used spectrometer operates for nearly 8,000 h per year. Solid-state power amplifiers (SSPA) are commonly used at Q-band and above, with the output power level gradually increasing. But they are not a match to TWTAs and EIKs at least in the foreseeable future. There is also a problem with blanking the output noise of SSPA, the problem is virtually nonexistent for a TWTA.

PELDOR with an independent pumping source (magnetron) has been in use by the Novosibirsk group, who carried out several key studies on PDS methodology and applied it extensively to study aggregation of lipopeptaibols and some biological systems. Magnetrons cannot generate stable pulses shorter than ~30 ns, but this is not a disadvantage for DEER.

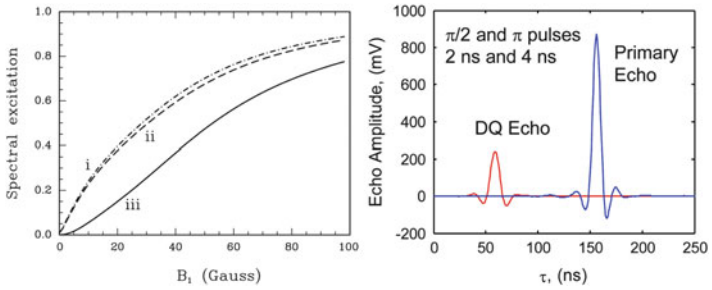

Fig. 16 (*Left*) Amplitude factors in the 6-pulse DQC sequence as a function of B_1 calculated for an uncorrelated pair of ^{14}N nitroxides excited at the center of the ESR spectrum for rectangular pulses. (*i*) G^{AV}, (*ii*) H^{AV}, and (*iii*) their product $M^{\mathrm{AV}} \equiv H^{\mathrm{AV}}G^{\mathrm{AV}}$, which determines the amplitude of the DQC signal for the 6-pulse sequence given by Eq. (35). Note that as $B_1 \to \infty$ one obtains $H_6(\infty) = G_6(\infty) = 1$. These results were calculated for 9.3 GHz. At 17.3 GHz differences from 9.3 GHz are small, so the results are approximately valid at this frequency as well. (Adapted from [35].) (*Right*) A comparison of the primary echo and a "standard" (6-pulse) DQC-filtered echo ("DQ Echo") from 40 μM T4L 8C/44C mutant labeled with MTSSL. $\pi/2$ and π pulses were 2 and 4 ns, respectively, corresponding to B_1 of 45 G. Data were taken at 60 K. The primary echo and DQC echo are plotted to scale. The distance from the first pulse to echo was 0.6 μs in both cases. The DQ echo is ~52% of its theoretical maximum that is 26% of the primary echo

3.1.1 Intense Pulses

Spectral excitation by a sequence of finite pulses[9] depends on the available $\omega_1 = \gamma_e B_1$ and the type of signal, i.e., number of pulses and flip angles. The major factor limiting spectral excitation in DQC arises from the products of "narrow-band" terms in Eq. (30) such as $S_2(\pi)$ [cf. discussion of Eq. (31)]. In Fig. 16 we plot the amplitude factors G^{AV} and H^{AV} of Eq. (35), and their product M^{AV} calculated for an uncorrelated pair of ^{14}N nitroxides at X-band. At Ku-band there is almost no difference. The product of three $S_2(\pi)$ functions arising from the three π pulses in the 6-pulse sequence yields very reasonable values of about 0.5 for the amplitude factors given by G^{AV} or H^{AV} for a B_1 of 30 G, for which the overall amplitude factor, M^{AV}, is about 0.25. It is useful to note that the width of the spectral excitation predicted for a product of N $S_2(\pi)$ terms depends on N as $\sim N^{-1/2}$. For B_1 under 20 G the growth of M^{AV} is faster than linear, and achieving $B_1 \geq 30$ G is essential for producing strong DQC signals.

In the case of short distances (under 15 Å) the distortions of the Pake pattern caused by the pseudo-secular term are less significant at large B_1. For nitroxides whose orientations are correlated, we have shown [93] that by increasing B_1 to ca. 60 G and consequently H to 0.75 would greatly decrease the correlation effects (cf. Sect. 5.3). Further increases in B_1 are not very helpful as the asymptotic value of unity for H is only slowly approached with increasing B_1. The spectral excitation that has been achieved so far at ACERT, based on π-pulses of 4 ns, corresponds to

[9] That is the fraction of spins contributing to the signal of interest.

$B_1 \cong 45$ G, and this is sufficient for producing strong DQC signals even in samples with a small number of spins. With $B_1 \cong 30$ G the amplitude of the DQC signal at $t_\xi = 0$ is about ~0.15 of the primary echo. We show in Fig. 16 that it approaches ~0.26 of the primary echo for $B_1 \cong 45$ G (the theoretical maximum is 0.5). This is somewhat better coverage than expected from Fig. 16 (left), which we attribute to instrumental phase modulation of such short pulses (cf. Sect. 3.1.3).

3.1.2 Phase Cycling

Phase cycling is a powerful method for suppressing unwanted coherence pathways by alternating the phases of the microwave pulses and then combining the detected signals appropriately. It was introduced in NMR and has become widely employed for the selection of desired coherence pathways in numerous types of 1D and 2D experiments [94]. This method was brought into the ESR field [148, 149] in order to select desired signals in 1D and 2D pulsed electron spin-echo experiments.

The general rule for the selection of a particular coherence pathway is based on the fact that if a unitary pulse propagator U acting on the density matrix according to

$$\rho(t) = \mathrm{e}^{\mathrm{i}Ut}\rho(0)\,\mathrm{e}^{-\mathrm{i}Ut} \tag{60}$$

produces a change in the given coherence order p by Δp, then the same pulse propagator, but with the phase shifted by φ, i.e., $U(\varphi)$, will multiply $\rho(t)$ by $\mathrm{e}^{-\mathrm{i}\Delta p\varphi}$. Consequently, a sequence of pulse propagators ($U_1(\varphi_1)$, $U_2(\varphi_2)$, …, $U_N(\varphi_n)$) will multiply the density matrix and hence the signal produced by a particular coherence pathway $\mathbf{p} = (p_1, p_2, \ldots, p_n)$ by:

$$\exp(-\mathrm{i}\sum_k \Delta p_k \phi_k) \tag{61}$$

Stepping the phase φ_k for the kth pulse in increments $2\pi L/N$ ($L = 0,1, \ldots, N-1$) and combining the detected signals having weighting factors $\mathrm{e}^{\mathrm{i}\Delta p_k \varphi_l}$, where the subscript l refers to the L in the incremented phase, selects signals with a change in the coherence order equal to $\Delta p_k \pm Nm$ ($m = 0, 1, \ldots$) [94]. For phase increments of $\pi/2$ one has $N = 4$. Hence a phase cycle that selects $\Delta p_k = \pm 2$ also selects pathways $\Delta p_k = (\pm 6, \pm 10, \ldots)$ and suppresses the others.

For phase increments of π, N is 2. Thus $\Delta p_k = (0, \pm 2, \pm 4, \ldots)$ are selected. We see that $\Delta p_k = 2$ and $\Delta p_k = 0$ are both selected. Therefore a phase cycle based on just the π increment cannot separate DQC from ZQC. The more pathways there are, containing a given Δp_k that can interfere with the desired signal, the more pulse propagators should be included in the phase cycling scheme. It is well known that a series of pulse propagators (which represents unitary transformations) can be replaced by a single propagator representing the cumulative effect of the series. This also applies to a series of pulse propagators interspersed by free evolution

propagators representing the effect of the spin Hamiltonian, Eq. (12). Such a cumulative propagator is referred to as a composite propagator or rotation in NMR [99].

For example, the 2- and 3-pulse sequences for the preparation of DQC (cf. Sect. 2.3.4) can be replaced by a single composite propagator which produces changes in the order of coherence of $\Delta p = 0, \pm 1, \pm 2$. It is the last value that corresponds to DQC. Thus a phase cycle that selects $\Delta p = \pm 2$ is required. The virtue of using the composite propagator is that it is sufficient to consider just its phase shifts in constructing the phase cycling. Then for a given phase shift φ for the composite propagator each pulse in its sequence must be given the identical phase shift, φ.

Consider as an example the 6-pulse DQC sequence. The first three pulses may be considered as a composite propagator that produces DQC. The change in the coherence order Δp is ± 2. We should select all four pathways depicted in Fig. 4 with this change. Using $N = 4$, with the understanding that the phases of the three pulses should be incremented simultaneously, we arrive at a 4-step phase sequence with the phases of these 3 pulses changing as follows $(0, 0, 0)$, $(\pi/2, \pi/2, \pi/2)$, (π, π, π), $(3\pi/2, 3\pi/2, 3\pi/2)$ and each of the four pathways are weighed by factors $(1, -1, 1, -1)$, when they are added in order to combine the signals from the selected pathway(s) constructively. This phase cycle is, in principle, sufficient (for nonselective pulses) because it suppresses all of the pathways that yield SQ or ZQ coherence.

This phase cycle for the 6-pulse sequence is satisfactory if the phases are very accurate, which is hard to achieve in practice. Therefore, it is usually necessary to cycle the phases of the other pulses in order to attain an improved suppression of unwanted signals. Additionally, the phase cycle should be combined with the CYCLOPS (CYClically Ordered Phase Sequence) [150] for suppression of signals at the image frequency. This increases the number of phase steps by a factor of four. The typical phase cycling that we employ for the 6-pulse sequence consists of 64 steps, which combined with CYCLOPS yields 256 steps, although we do find that a nearly comparable level of performance is achieved with only a 64-step phase cycle [35, 63, 151]. With these phase cycles we can suppress unwanted echoes by a factor of 300–3,000 depending on the sharpness of the echoes. The smaller value is more typical for nitroxides.

3.1.3 Composite Pulses

We discussed above some technical aspects of PDS instrumentation hardware that are required for generation of intense mw pulses that benefit DQC (cf. Sects. 3.1 and 3.1.1). It was noted that high-power mw amplifiers, which enable generation of hard pulses, have a shorter life and they are also more expensive. Therefore in order to achieve even better spectral coverage, it would be desirable to utilize a different approach.

Years ago, when we faced the problem of insufficient spectral coverage due to a power-limited source, we showed that the method of Composite Pulses, which is

common in NMR and MRI for a variety of applications, can be applied successfully to the ESR case [152], which requires much shorter pulse widths than NMR (i.e., much shorter than the ESR T_2s, typically in the (sub) microsecond domain). However, the technology available to us at that time was still insufficient to usefully carry out short enough composite pulses, so instead we developed our technology of improving the microwave B_1 field strength at the sample, with much success. However, hardware suitable to effectively accomplish efficient composite pulse generation has become available. Furthermore, widespread use of relatively low-power solid-state power amplifiers (SSPAs) at mm-waves, as well as the desire to utilize smaller more robust TWTAs, provide additional motivation to revisit the theme of composite pulses that has been extensively developed in NMR for more than two decades [153–155]. Broadband (nonselective) spectral excitation, achieved for example by a "hard" RF pulse, formally corresponds to uniform spectral rotation of the spins, by the required rotation angle, θ. This goal can also be achieved by means of a finite shaped pulse. For a well-designed nonselective pulse, the uniformly rotated spectral range, $\pm\omega_0$, usually corresponds to $\omega_0 \geq \omega_1$, with $\omega_1 = \gamma_e B_1$ [154–158]. In our case, we are primarily concerned with rotations by $\pi/2$ and π, where the latter provides the main challenge to broadband excitation.

It is tempting to utilize one of many types of composite rotations, which were developed in NMR [154, 156, 158–163]. Our current need is primarily to provide pulses with broadband excitation for DQC since our best π pulses of 4 ns width are insufficient for uniform excitation (cf. Fig. 25). There are different kinds of uniform rotation that the pulse can provide, namely excitation ($S_z \rightarrow S_\pm$), refocusing ($S_+ \leftrightarrow S_-$), and population inversion ($S_z \leftrightarrow -S_z$) [159]. The rotation of spins by the oscillating mw field can be represented by a density matrix transformation [77, 94, 95, 99]. We have applied such a relevant formalism [35] in our analysis of DQC and SQC sequences. This formalism can also be applied to the general case of shaped pulses generating rotations by Suzuki-Trotter theory [164–166]. It can be shown that phase effects do not contribute a major problem for refocusing, and if Q is adequately lowered to provide sufficient bandwidth to accommodate broadband excitation at the expense of B_1 magnitude, a very uniform population inversion can be achieved.

Another issue concerns pulse sequences based on selective pulses, such as DEER. The demands of PDS applications for structural biology require their further development in order to realize the full potential of ESR. For example, in the study of RNA, which can be large in size, and of large water-soluble proteins and their complexes, long distances ≥60 Å need to be measured. Long relaxation times are necessary to determine such distances, and relaxation processes caused by protons in the system, in particular those of the protein, such as nuclear spin diffusion become important, especially due to their exponent obeying a quadratic to cubic law in time [113, 114]. Suppression of this type of diffusion requires multiple spin refocusing. To increase the upper range of distances, in addition to the DQ-filtered refocused primary echo (DQF-RPE) method [58], we designed a novel 5-pulse sequence for DEER (cf. Sect. 5.1, Fig. 18) intended to provide suppression of nuclear spin diffusion (as in DQF-RPE), but with the advantage of canceling the

effects of relaxation decay in the signal record as in the 3- or 4-pulse DEER sequence. But since this pulse sequence generates a sum of two types of dipolar signals (cf. Sect. 5.1, Figs. 18 and 19), it requires the means to suppress the unwanted signal. A good solution to this would be to employ selective pulse with more uniform spectral excitation. Composite selective pulses have also been successfully developed in ESR for imaging [167], suggesting that this technology could also benefit 5-pulse DEER.

4 Sensitivity Considerations

4.1 Sensitivity in PDS Experiment

The sensitivity of pulse ESR spectroscopy is more difficult to characterize than for cw ESR, wherein strict criteria were established. In pulse ESR, similar criteria are harder to set, because relaxation times, which are the major determinants of the outcome of a pulse experiment, vary over a wide range amongst the systems studied. For this reason, often the single-shot SNR for a standard sample (e.g., gamma-irradiated vitreous silica) can be used [147, 168] to calibrate sensitivity. Due to variations in pulse ESR techniques and samples, the capacity for a meaningful experiment based on considerations of its sensitivity should be decided on a case-by-case basis [47, 147] with all relevant parameters considered.

The sensitivity of PDS techniques, specifically DQC and DEER, has been discussed in [35, 101, 122], where the main criterion for sensitivity was based on the ability to perform a successful experiment (i.e., of reliably measuring a distance) in a reasonable period of time. It was chosen to correspond to a minimum acceptable SNR, nominally taken as a S_{acc} of 10 (S_{acc} is the minimum acceptable SNR), which has to be attained in the time of experiment nominally taken as 8 h of signal averaging. Such an SNR would make it possible to obtain the distance, given a sufficient length of t_{max} (cf. Sect. 2.4), which, conservatively, should be at least one period of the dipolar oscillation, $T_d \equiv 2\pi/\omega_d$. [A relaxed criterion, based on a shorter $t_{max} = T_d/2$, would still enable a less accurate estimate of the distance, depending on the specifics of the signal and given a higher SNR than 10 [122]. This may include a priori knowledge of spin concentration and labeling efficiency or whether the distance is distributed over a narrow or broad range. However, an S_{acc} of 10 is just a bare minimum, and we usually require an SNR of at least 50, but preferably 100–200 to enable reliable distance distribution analysis [69, 70]. [It should be noted that a very high SNR can be undesirable for signal analysis due to the presence of a number of signal distortions that exceed the noise but cannot be adequately accounted for and corrected in the Tikhonov or MEM analysis, thereby leading to instability in the analysis. This is of particular concern regarding the errors introduced in baseline subtraction].

Even though it is possible to estimate sensitivity from first principles [168], we prefer to use an experimental calibration in the spirit of [35], so the following approach has been chosen to give estimates of sensitivity in distance measurements. First of all, a simple and standard experiment, such as a single-shot amplitude measurement of the primary echo, is performed under conditions when relaxation and other complications can be ignored. Then the sensitivity of the single-shot experiment of a more complex pulse sequence is deduced from this, based on the known theory of the method. Within such an approach, it suffices to measure the spin-echo amplitude at a selected point of the nitroxide ESR spectrum with a 2-pulse primary echo sequence, applied at a low repetition rate and with a short inter-pulse spacing. Such an experiment provides the SNR for a single-shot, $S_{1,\mathrm{PE}}$, which we give as per unit of concentration (1 μM) or per the number of spins (1 pmol), whichever is needed. Subsequently, the S_1 for the more complex experiment is estimated by comparison to the S_1 of the primary echo, $S_{1,\mathrm{PE}}$. Due to the limited capacity of simulating the outcome of a complex pulse sequence, such an estimate has limited accuracy, but it should be a reasonable predictor of the actual SNR. Finally, all the other major factors that influence the outcome of the actual experiment, such as relaxation, temperature dependence of the signal, instantaneous diffusion, pulse sequence repetition rate, and noise bandwidth, must be determined and their values used to estimate their effect on the SNR for a given distance and its range of uncertainty.

The calibration of DQC and DEER has been conducted for our pulse ESR spectrometer [5] at the working frequency of 17.35 GHz on a nitroxide sample of 4-hydroxy TEMPO in a vitrified solution of 50% w/v glycerol in H_2O with a 20 μM spin concentration in a 10 μL sample volume at 70 K, at which most PDS measurements are performed. The DEER calibration used a primary echo [169] generated by $\pi/2 - \pi$ pulses (π pulse of 32 ns) separated by 80 ns, with the pulses applied at the low-field edge of the nitroxide spectrum, typical of a DEER pulse setup at centimeter wavelength. The classic analysis of the SNR of a primary echo has been given by Mims [169], and the sensitivity in all PDS is directly related to that of a primary echo. A similar DQC calibration was based on $\pi/2 - \pi$ pulses with a 6 ns π pulse, and the same separation as in DEER, but pulses were applied in the middle of the spectrum. For the two measurements, the ratio of the echo amplitudes (DQC vs. DEER) was ca. 6.5 and the ratio of SNRs of the single-shot signals at the condition of optimal signal acquisition (i.e., given by the integration of the spin echo in the time window defined by the time points corresponding to 0.7 of the echo amplitude) was ca. 3.0, i.e., $S_1 \approx 0.42\ \mu\mathrm{M}^{-1}$ (DEER) and $S_1 \approx 1.25\ \mu\mathrm{M}^{-1}$ (DQC).

Based on these numbers, the estimates of the dipolar signals for the two methods (using the ACERT spectrometer) according to the analyses given in [35, 122] are summarized as follows. For 4-pulse DEER with 16/32/32 ns pulses in the detection sequence and a 32 ns pump pulse, S_1 is $0.084\ \mu\mathrm{M}^{-1}$, and for DQC based on a 3/6/3/6/3/6 ns pulse sequence, S_1 is $0.3\ \mu\mathrm{M}^{-1}$, i.e., it is greater for DQC by a factor of 3.6. It is possible to use a shorter pulse of 12–16 ns in DEER and to increase the signal

by the factor of 1.5, but the resulting distortions and large increase of ESEEM outweigh a small signal increase, generally discouraging this practice. Also the use of 2 and 4 ns pulses in DQC enhances the DQC SNR by a factor of 1.6 (cf. Fig. 16 left). This ratio is supported by our experimental observations (cf. Figs. 10, 16 right). Using the sensitivity analysis of [35] we estimate the SNR of the raw data of the full PDS experiment as

$$\mathrm{SNR} = 2S_1 x^2 C \eta_c K(f, T_1) \left(\frac{f t_{\mathrm{exp}}}{N}\right)^{1/2} \exp\left(-\frac{2t_{\max}}{T_m} - 2kxCG_{\mathrm{d}} t_{\max}\right) \qquad (62)$$

Here, t_{exp} is the duration of the experimental data acquisition; f is the pulse sequence repetition frequency; N is the number of data points in the record; C is the doubly labeled protein concentration (in μM); η_{c} is the ratio of the sample volume ($\leq$15 μL) to that used in the calibration (i.e., 10 μL). The terms in the exponent are consistent with those given in [35], namely the first accounts for the phase relaxation [but we use $\kappa = 1$ in Eq. (62)] and the second for instantaneous diffusion. G_{d} is method-specific [35] and for the pulse sequences defined above it is ca. 0.14 in DEER and ca. 0.52 in DQC. We also include the spin-labeling efficiency, x, which modifies the fraction of both spins that need to be flipped in PDS, showing its strong effect on the outcome of an experiment. Below we assume complete labeling for convenience in the discussion ($x = 1$). $K(f,T_1) = 1 - \exp(-1/fT_1)$ gives the effect of incomplete spin–lattice relaxation for a given relaxation time, T_1 and repetition rate, f (K is 0.72 for the optimal repetition rate, when $fT_1 = 0.79$ and is unity when $fT_1 \ll 1$). The maximum of the *SNR* as a function of f is broad, so selection of f is not critical. Typically f is 0.5–2 kHz for Ku band. As an illustration of the capability of PDS in various regimes, we give the following estimates based on our experience at ACERT at 17.3 GHz.

4.2 Short Distances, Low Concentrations

In the case of short distances, sensitivity is rarely a concern, but it is the capacity of the method to measure this distance, that matters. Assuming a short distance of 20 Å ($T_{\mathrm{d}} = 154$ ns), which is within the DEER capacity and setting $t_{\max} = 0.48\ \mu\mathrm{s} \approx 3T_{\mathrm{d}}$ in order to provide very good resolution of distance; T_m is taken as 1.0 μs, i.e., about the shortest within its typical range; 8 ns steps in t yielding 60 data points are taken as producing the signal record; a pulse repetition frequency f of 1 kHz should be optimal for a spin-labeled protein at 70 K. One finds from Eq. (62) that just $t_{\mathrm{exp}} \cong 4$ min of signal averaging of the DQC signal provides an SNR of 10 for a C of 1 μM. DEER will require nearly 1 h (50 min) for achieving this result. Note that this concentration corresponds to just 10 picomoles of protein in a typical 10 μL Ku-band sample. A high SNR of 100 for DQC could be attained in 6.5 h for the same amount of protein.

4.3 Long Distances

We assume $t_{max} = 4$ μs, which is certainly a challenge using H_2O buffer; a typical T_m for partly buried label [113] of ca. 2 μs, and the steps in t are taken to be 16 ns. Then an SNR of 10 will be reached in 8 h for a C of 3.7 μM for DQC (while for DEER it would be 104 h). By using one period of T_d we find $R_{max} = 59$ Å; for half of the period, R_{max} is 75 Å. Longer distances cannot be estimated reliably with this SNR. An accurate analysis of the distance distribution requires a higher concentration of at least 18 μM in order to provide an SNR of at least 50 [69, 70], under otherwise similar conditions. For t_{max} of 4 μs one should also account for nuclear spin diffusion, which will make this case more difficult, requiring one to increase concentration up to 10–50 μM in practice. Note that standard DQC provides some degree of suppression of spin diffusion [1]. The improvements that can be achieved by deuteration are discussed in the following references [116, 119].

4.4 Distances in the Optimal PDS Range

We consider 50 Å to be an upper limit for the "optimal" PDS distance range [122]; T_d is then 2.4 μs, so a t_{max} of 2.4 μs suffices to provide the distance sufficiently accurate for a structure constraint. However, let us assume the rather challenging case of $T_m = 1.5$ μs; steps in t are taken to be of 32 ns; f is 1 kHz, C is taken as 25 μM; but here we require a good SNR of 50. Such an SNR is achieved in 16 min by DQC. DEER requires nearly 3.5 h for the same result, or else the concentration must be increased (by a factor 2–4). Shorter distances of 20–45 Å are measured faster, or else yield a better SNR or improves distance resolution. This is the case for the ACERT 17 GHz spectrometer. Most published work based on a commercial X-band DEER spectrometer use this range. As a rule t_{max} is around 2–2.5 μs providing good enough resolution in this distance range. Typical data collection time reported is on average 12–24 h per measurement. This may be adequate to characterize a protein in about 2–3 months, unlike the situation at ACERT requiring at least an order of magnitude less time.

4.5 Examples

We conducted Ku-band DEER sensitivity test experiments at ACERT on model systems that include organic biradicals R-I and R-II [35] in perdeuterated *o*-terphenyl glass and spin-labeled T4-Lysozyme, with the results shown in Fig. 17 along with the data on the membrane protein α-Synuclein [116, 118]. These measurements are in good agreement with the estimates given above.

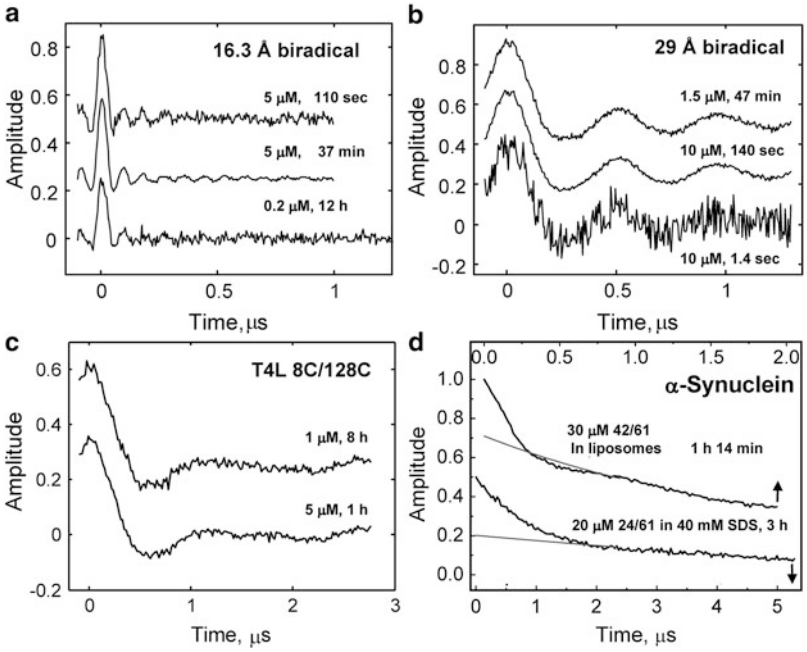

Fig. 17 Sensitivity test of ACERT Ku-band DEER performed on: (**a**, **b**) rigid biradicals (R-I and R-II, [35]) in orthoterphenyl-d_{24} glass prepared in different concentrations and recorded using several signal averaging periods. T_2-relaxation decay can be neglected in this case. Pump pulse was 16 ns, dwell time was 5 ns, pulse repetition rate was 500 Hz for (**a**) and 2 kHz for (**b**); (**c**) T4-Lysozyme double-labeled mutant 8C/128C in D_2O buffer (40 Å interspin distance). The refocused echo decayed by a T_2-mechanism to ~0.35 of its value taken at a short evolution time. (**d**) Liposome and detergent data for wild-type α-Synuclein, labeled at different positions, are plotted with their background fits using different horizontal scales (*top scale*: 42/61 mutant 36 Å distance; *bottom scale*: 24/61 mutant 55 Å distance). The visible slope in the case of detergent (SDS-d_{25} in D_2O buffer) is due to a low content of glycerol, so water freezes out. Repetition rates were 1 kHz for (**c**) and (**d**); pump pulse was 16 ns (in **a**–**c**) and 32 ns (in **d**), temperature was 60 K in all cases. All signals are raw, normalized to unity at zero time and plotted shifted vertically for convenience. Based on these sensitivity calibration data, concentration sensitivity can be estimated for other systems, where relaxation times may be shorter and spin labeling efficiency is less. (Ref. [171] for **a** and **b**; data from [116, 118] for **d**; **c** unpublished.)

Absolute spin sensitivity is closely related to the concentration sensitivity; however, it does increase rapidly with an increase in the working frequency due to the smaller volume of a resonator used at a higher frequency, for example, at Ku band 25–250 picomoles of protein are routinely used in the optimal distance range.

The smaller amounts are better suited for DQC. These amounts can be reduced by about an order of magnitude by using smaller resonators than we currently employ, but by an even greater factor at a higher working frequency [46, 49].

We remind the reader that the previous estimates relate to our 17.3 GHz spectrometer. Lower estimates of sensitivity, in particular absolute sensitivity, would apply to the typical pulse spectrometers that operate at 9 GHz

5 Newer Aspects

5.1 5-Pulse DEER

In order to increase the SNR, and to access longer distances, both DQC and DEER pulse sequences were subsequently tested in the forms of double-quantum filtered RPE (DQF-RPE) [58, 170] and variable time DEER [59], respectively. Both pulse sequences increase SNR by using a variable time. DQF-RPE can be used to measure longer distances due to partial suppression of nuclear spin diffusion by means of multiple refocusing; variable-time DEER improves SNR just because of the variable time. DQF-RPE has finite dead-time and is not immune to ESEEM, which may interfere with the signal when caused by deuterium nuclei. The signals from both pulse sequences are used in conjunction with a suitable recorded reference signal to account for signal decay caused by phase relaxation, however, the referencing is not perfect, since in some cases relaxation does not necessarily factor out and instantaneous diffusion is not the same in the reference signal. In both cases referencing causes a residual background that should be removed in data processing in the manner similar to how it is done in standard DQC or DEER (cf. Sect. 2.6).

It thus was very desirable to construct a constant-time pulse sequence (i.e., using fixed positions of all detection pulses) in order to minimize the impact of relaxation and nuclear ESEEM, to ensure zero dead-time, and to avoid other unwanted effects. A 5-pulse DEER sequence that substantially satisfies these requirements was described by Borbat, Georgieva, and Freed in context of a more general approach [171]. This new pulse sequence is shown in Fig. 18.

The suppression of nuclear spin diffusion by this pulse sequence is essentially based on the same principle that is used in DQF-RPE [58], i.e., by creating a refocusing point in the middle of the detection pulse sequence between the first $\pi/2$ pulse and the echo separated by the time interval $2t_m$, thus minimizing the time interval available for "quadratic" relaxation to develop. The original version of 4-pulse DEER [107] satisfies this criterion; however, it is not optimal with respect to evolving dipolar modulation, which is recorded over one quarter of the time interval between the first pulse and detected echo, i.e., by using only half of the time interval $2t_m$ to evolve dipolar coupling; the rest was wasted. For this reason, this pulse sequence was modified into its current asymmetrical form [59].

In 5-pulse DEER (DEER-5) this task is accomplished by applying an additional pump pulse, which reverses the effect of one of the refocusing pulses, thereby shifting the time-reversal (refocusing) point of the dipolar evolution from the middle of the second interval to the position of the second (for 5′) or the third (for 5) of the detection pulses. However, there is a small problem. This pulse sequence (cf. Appendix) does develop the desired new dipolar pathway, but the original one survives as well, although it is substantially attenuated. Since the same coherence pathway is involved, phase cycling cannot separate them, because it holds for all dipolar signals in a multi-pulse sequence based on selective pulses (cf. Sec. 2.3.6). One immediate solution is to reference this pulse sequence by using

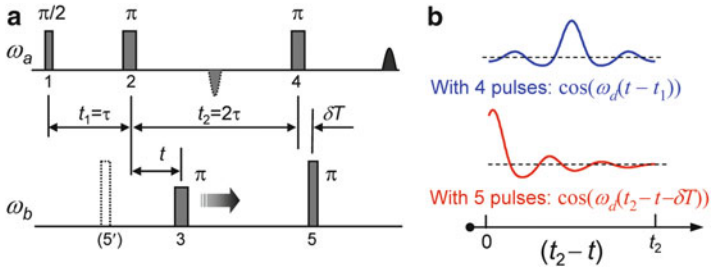

Fig. 18 A 5-pulse DEER pulse sequence uses 3 pulses for signal detection applied at ω_a and the signal is recorded as in the standard 4-pulse DEER by varying the timing of the pump pulse 3, applied at ω_b. Time interval t_2 is set to $2t_1$ to minimize the phase relaxation caused by the nuclear spin diffusion from the surrounding proton bath by refocusing the primary echo exactly in the middle of the interval made by the first $\pi/2$ pulse and the refocused primary echo. In order to utilize all the time from the first pulse to the spin echo for dipolar evolution, an additional pump pulse is applied, with its position fixed. Two essentially equivalent positions (5 or 5′) of the additional π-pulse are possible, that is position 5 following pulse 4 or 5′ before the pulse 2, as shown in the figure. As result, a minor dipolar pathway, which could be formed due to excitation overlap in the 4-pulse sequence (cf. Appendix), becomes the major pathway, while the standard 4-pulse DEER dipolar signal becomes attenuated. On the *right*, these two dipolar signals are shown: the standard (in *blue*) which is symmetrical about the center of the interval (0, t_2) is recorded in the absence of the additional pulse; a new signal (in *red*) appears, starting from time $t = t_2$, in the presence of the fifth pulse at position 5. Using position 5′ instead of 5 will reverse the time changing the signal to cos($\omega_d t$) (cf. Table 1 in Appendix). Shifting pulse 5 (or 5′) as shown by a small amount, $\delta T \sim 100$ ns, results in zero dead-time. The time interval δT is much smaller than t_1 and does not affect the performance. Both cases were tested, the results are shown for preferred position 5, after pulse 4, since for position 5′ a small excursion due to an unwanted primary echo from pulses 5′ and 2 may be visible on the signal

the 4-pulse sequence which generates the signal that should be removed. The subtraction (Fig. 19) is performed as detailed in [171]. Of course, the amplitude of the unwanted signal should be minimized in order to keep the residuals of the unwanted signal pathway at a very low level (Fig. 19) permitting one to use only a small percentage of experimental time to record the reference. This is achieved by making the pulse 5 (or 5′) less selective than the standard pump pulse 3. However, complete suppression has not yet been achieved using this approach and future efforts should be directed toward engineering selective pulses with a more uniform spectral excitation profile.

It should be noted that the subtraction cannot be made perfect because of orientational effects, nonlinear effects caused by intermolecular dipolar coupling, and by nonuniform B_1 over the sample. However, baseline removal in DEER or DQC signals is also never perfect, and orientational correlation effects inevitably result in reconstruction artifacts, which are greater at high concentrations. For not too high concentrations, and in the absence of strong orientational effects, subtraction leaves behind a low level of distortion [171], which does not exceed the typical level of unwanted signals, distortions, and artifacts present in other known pulse sequences. It would be desirable to improve the suppression by another factor of 3.

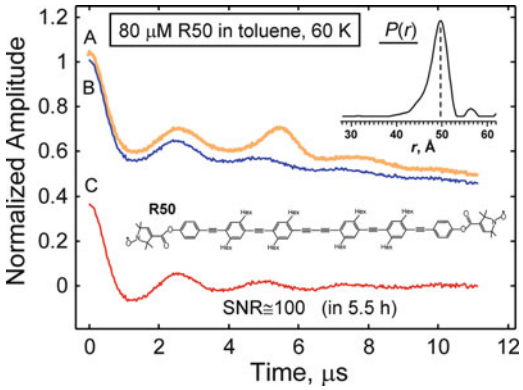

Fig. 19 The raw signal in 5-pulse DEER (*A, top curve*) contains the desired signal, (*B, middle curve*) and the unwanted contribution of the type shown in Fig. 18b top, which is visible as a small hump in the middle. The unwanted signal is partially suppressed by using a stronger fifth pumping pulse in Fig. 18. The residual contribution is removed by subtracting out a 4-pulse DEER reference signal of the type shown in Fig. 18b, recorded in the absence of this pulse [171]. This does not noticeably increase the duration of the experiment, nor does it degrade the SNR. This is because this signal is scaled down by a factor 3–6 in making the subtraction. *C* (*bottom curve*) is *B* after removing homogeneous background. Inset shows the distance distribution produced from *C* by Tikhonov regularization [69, 70]. The data were recorded at 17.3 GHz and 60 K on ~80 μM long biradical [59]. The detection pulse sequence used 32 ns π-pulses and was applied at the high-frequency edge (low field) of the ^{14}N spectrum. Pump pulses (12 ns, pulse 5′ and 29 ns, pulse 3) were applied at 70 MHz lower frequency corresponding to the central peak of the spectrum. (Unpublished data. The biradical is courtesy of Gunnar Jeschke.)

Such improvements could include the following. The size of the sample can be adjusted to achieve more uniform B_1 and better resonators can be employed [56].

Although composite pulses [152] have not yet found routine use in pulse ESR, this could be reconsidered (cf. Sect. 3.1.3), based on current progress with high-speed signal generation in bandwidths wider than 100 MHz, which seems adequate for fine-tuning spectral excitation in 5-pulse DEER, cf. [171].

Intermolecular contributions to the signal do not factor out perfectly, e.g., by dividing the two signals, as they are different in the 4- and 5-pulse DEER sequences [171]. Therefore, high concentrations should be avoided in order to stay practically in the linear regime so that the exponent of the intermolecular contribution should be small, which holds well for spin concentrations less than 100 μM. This however is true for any PDS technique. Strong intermolecular effects are highly undesirable. The removal of such an unwanted signal is more accurate when the intermolecular contribution is in the linear regime (i.e., exponent is $\ll 1$). Finally, in Fig. 20 we show the improvement in the distance range by comparing echo amplitudes, recorded as a function of pulse separation in the standard 4-pulse and 5-pulse DEER sequences. We found the evolution time was expanded by a factor of ~1.94 in this case, whereas only a factor of $2^{1/2} = 1.41$ was expected [58]. The maximum time, t_{max}, was taken

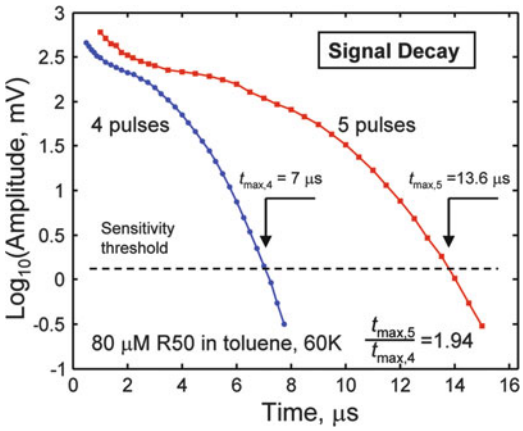

Fig. 20 A comparison of 4- and 5-pulse DEER amplitudes as a function of separation between the two π-pulses of the detection sequence. The 5-pulse DEER signal decays much slower, leading to nearly a factor of 2 increase of the time period, t_m, available for recording a dipolar signal. The data were recorded on ~80 μM of biradical R50 (cf. Fig. 19) at 17.3 GHz and 60 K using the 5-pulse sequence of Fig. 18 and the standard 4-pulse DEER sequence. Since the signal at the sensitivity threshold is only ~0.003 of its value for $t_m < 1$ μs, the presence of slowly relaxing free spin label may offset the measurements, taken at large values of t_m [27]. Therefore, the control DEER experiment was conducted to test the DEER modulation depth, which was found to be the same as for short t_m values where such a contribution is negligible

at the signal level that corresponds to a SNR ~ 10 (in background-subtracted dipolar signal) after ~3 h of data averaging both for the standard 4-pulse DEER and DEER-5.

5.2 *More on Sensitivity: Method Comparison*

So far, the two distance measurement techniques of DEER and DQC detailed above have proven to be very successful. DEER in its 4-pulse form has received wide acceptance due to the availability of commercial spectrometers operating at X-band and permitting easier implementation with a single high-power mw amplifier. However, a Q-band extension has also become commercially available, and it provides significant sensitivity increase [146, 172] compared to the commercial X-band spectrometer.

DQC, for its optimal performance, requires more powerful mw amplifiers than those typically employed in X-band because at this frequency range optimal sample size for maximizing concentration sensitivity could be impractically large, that is ~1–2 ml. At a higher working frequency in Ku- or Ka-band a 1–2 kW amplifier is adequate and the optimal sample sizes can be small (10–80 μL). We employ at Ku-band a 4 kW amplifier for DQC. Ultra-fast MESFET (metal semiconductor field effect transistor) switches allow us to generate pulses as short as 0.8 ns and to achieve B_1s of at least 45 G in a dielectric resonator. This corresponds to 4 ns π-pulses, producing strong signals.

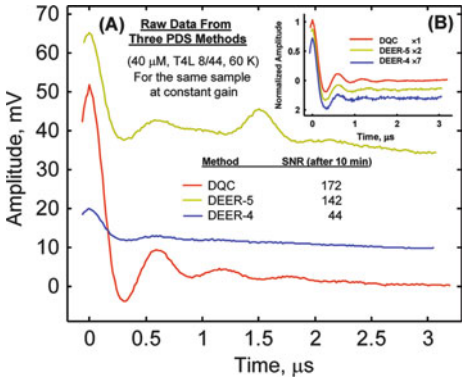

Fig. 21 (*A*) Raw data from 4-pulse DEER (*middle*), 6-pulse DQC (*bottom*), and 5-pulse DEER (*top*), taken on the same sample with the same receiver settings. The measurements were conducted on a 10 μL sample of 40 μM T4L MTSSL-labeled 8/44 cysteine mutant (31 Å avg. distance). The sample was prepared in H_2O buffer containing ~30% (w/v) glycerol. Data were collected at 60 K using Ku-band (17.3 GHz). Both DEER sequences used a 29 ns main pump pulse, and the additional pump pulse in the 5-pulse sequence was 12 ns. DQC used 2 ns π/2 and 4 ns π pulses, corresponding to a B_1 of ~45 G. Signal averaging times were 40 min (4-pulse DEER), 50 min (DQC), and 10 min (5-pulse DEER). The DQC signal is about a factor of 7 greater than the dipolar signal (i.e., the modulated part) in 4-pulse DEER. The ratio of SNRs of DQC to 4-pulse DEER is a factor of ~4.0 due to a wider signal bandwidth used to record the DQC signal. Unprocessed DEER-5 contains an unwanted signal pathway (cf. previous section), (*B*) The same data are shown after removing baselines and unwanted signal in DEER-5. All data were normalized to unity at zero time and distributed vertically for clarity

In Fig. 21 we show a comparison of all three methods using the ACERT Ku band spectrometer, where we already have very high spin sensitivity illustrated for 4-pulse DEER in Fig. 17. At $t_m = 3$ μs, nuclear spin diffusion begins to be important and it dominates the phase relaxation for larger t_m. As one can see, S/N in 5-pulse DEER is already almost on a par with DQC and well above 4-pulse DEER. We cannot detect a useful signal beyond ~5 μs with standard DEER and, for slightly longer t_m, by DQC. (DQC-RPE was not conducted, as it is better suited for longer distances, due to its dead-time) [58]. With the DQC method of PDS, we can achieve a wider distance range and better sensitivity than with 4-pulse DEER for many biological systems. Usually an order-of-magnitude improvement in data averaging time was achieved. However, measurement of long-distances still has limits imposed by the phase relaxation. When it is possible to select solvent-exposed labeling sites, nuclear spin diffusion becomes the dominant mechanism. This can be partly offset by using deuterated solvents, and in some cases (Fig. 7) distances as long as 80 Å can be measured. 5-pulse DEER, that we described above, helps to extend this distance range and/or improve the quality of distance data by suppressing effects of nuclear spin diffusion. It allows a significant extension of the distance range without using deuteration. However, with solvent deuteration we often find substantial improvement [171]. Consequently, a time-consuming and often unfeasible measurement of a 80 Å distance becomes a routine 1-h experiment.

DQC provides the best value in the low concentration range, for not very long distances (~50 Å) as a result of higher sensitivity, and the most accurate dipolar signals. For very long distances (≥60 Å) DEER-5 seems to surpass DQC (at present) but DQC should again provide the higher sensitivity by deuteration of the entire system including the biomolecules. In some cases, deuterated solvent will suffice. For example, for oligonucleotides with highly solvent-exposed spin-labels (cf. Fig. 7b), nuclear spin diffusion is not a dominant relaxation mechanism on the 15–20 μs time-scale used. This is not the case for spin labeled proteins tested in D_2O (T4L and α-Synuclein), where nuclear spin diffusion dominates after ~6 μs.

As is true for DQC, using 5-pulse DEER requires optimizing the spectrometer and resonators in order to maximize the suppression of the unwanted signal, but it is achieved with a smaller, and therefore less expensive and more reliable, high-power mw amplifier, since it uses pulses typical for standard implementation of DEER. Clearly, this pulse sequence adds capability to the two already proven techniques.

5.3 2D-DQC: Orientations

When a sample containing bilabeled proteins is subjected to sufficiently strong microwave pulses, the nitroxide ESR spectrum is almost uniformly excited, so that any dependence of the signal on spectral position (frequency) including orientational effects is largely suppressed. That is, the echo amplitude results from (nearly) all the spins (except for the effect of pseudosecular dipolar terms, important for short distances). Also, as we discussed in Sect. 2.3.5, in high B_1-fields ($\gamma_e B_1 \geq \omega_d$), the effect of the dipolar coupling during the action of the pulses becomes very weak.

Therefore, for not very short distances and in sufficiently strong B_1s, the information on orientations of the magnetic tensors of the spin-label moieties (cf. Fig. 22) is virtually excluded from the time-domain dipolar evolution of the echo amplitude, taken at its maximum. Nevertheless, as we showed [35, 93], it is still retained in the spin-echo signal and can be retrieved by recording the 2D time-domain data as a function of the spin-echo time (t_{echo}) in addition to the dipolar evolution time ($t_{dip} \equiv t_\xi$) and then converting this data into a 2D-FT spectrum. Then by making a "shearing" transformation [128] one achieves two orthogonal dimensions: the nitroxide spectral dimension and the dipolar dimension (i.e., the x and y axes in the "2D" plot). Rigorous computations of 1D and 2D signals have been carried out [93].

In the 2D-DQC experiment the pulse sequence of Fig. 4 is used and pulses are stepped out in the same manner as in 1D-DQC. However, the following is noted. The echo shape is recorded in a window $t_w \sim$ 80–160 ns, centered at a time $2t_m + 2t_{DQ}$ after the first pulse, i.e., at t_6 ($=t_m$) after the sixth pulse. Note that the width of the echo sampling window limits the minimal values of t_6 and t_p by about $t_w/2$ and their maximum values to $(t_m - t_w)/2$. As in the 1D format the dipolar evolution is recorded as a symmetric signal with respect to $t_{dip} \equiv t_\xi$ but over the whole range of $\pm t_m$. In practice t_p starts with a larger t_{p0}, than in the 1D implementation, selected

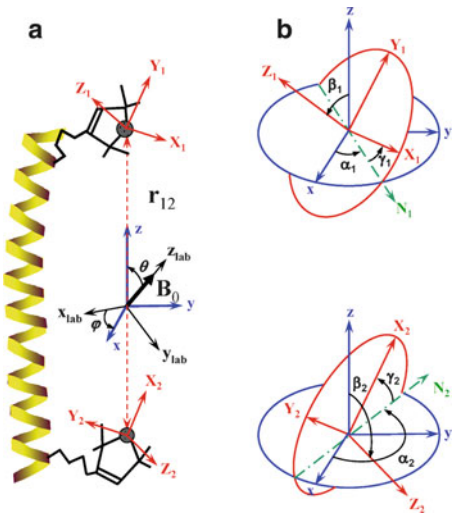

Fig. 22 The set of Euler angles $\boldsymbol{\lambda}_k = (\alpha_k, \beta_k, \gamma_k)$, $(k = 1, 2)$, which define the orientations of the hf and g-tensor tensor principal axes for nitroxides 1 and 2 in the dipolar (molecular) frame of reference. In this frame the z-axis is chosen to coincide with the vector $\mathbf{r}$, connecting the magnetic dipoles of the nitroxides. The orientation of the dipolar frame in the laboratory frame (with z-axis parallel to the external magnetic field $\mathbf{B}_0$) is defined by the Euler angles $\boldsymbol{\eta} = (0, \theta, \varphi)$. Adapted from [93]

such that the last pulse (including the dead-time after the pulse) and the echo window do not overlap.

Therefore, the signal in the 2D DQC experiment is recorded over $\pm\,(t_m - t_{p0})$ with t_{p0} always slightly greater than $t_w/2$. Figure 23 shows an example of a 2D DQC time-domain signal. Note the tilt of spin-echo which is due to the fact that a shift by Δt in the spin echo time t_{echo} corresponds to a shift by $\Delta t/2$ in the position of the dipolar coupling refocusing point. This coupling between t_{echo} and t_{dip} is removed at the signal processing stage by the shearing transformation conducted for convenience in the frequency domain as $f_{\text{echo}} \rightarrow f_{\text{echo}} + f_{\text{dip}}\,(\Delta t_{\text{echo}}/2\Delta t_{\text{dip}})$. This is easier to accomplish on the smoother 2D frequency spectrum with better S/N compared to the oscillatory signal in the time-domain. Also, the 2D signal background is first removed from the time-domain signal by fitting it to a surface, which is extrapolated to small t_{dip}, in a manner similar to 1D DQC before the Fourier Transform.

Figure 24 illustrates the main concept of 2D-FT-DQC. Results for uncorrelated (a) and correlated (b) ^{14}N nitroxide pairs with 2 MHz dipolar coupling (corresponding to ca. 30 Å) are shown in the upper row with a fixed rigid arrangement with $\boldsymbol{\lambda}_{1,2} = (0°, 90°, 0°)$, $(0°, 90°, 0°)$ (cf. Fig. 22 caption) shown in (b). The B_1 was made infinite by using $H_p \propto S_x$ and the pseudosecular term in H_{dd} was set to zero. The 2D FT spectrum may be summed over the range of ESR frequencies to produce a 1D dipolar spectrum (Pake doublet shown) on the right side of the 2D plot. When summed over the range of dipolar frequencies one produces a 1D ESR spectrum at the top of each 2D plot. Note that there is virtually no difference in the 1D dipolar spectra from uncorrelated and correlated cases, as one would expect for the strong pulses, which uniformly excite all orientations. However, this information, hidden in 1D, is developed in the 2D representation, wherein the uncorrelated

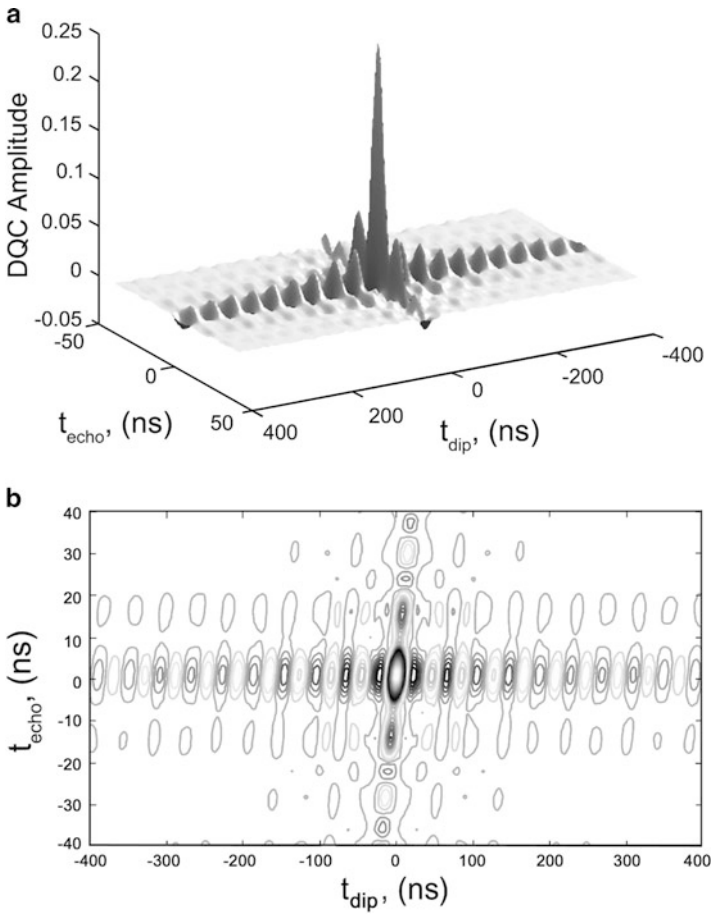

Fig. 23 Time-domain 2D DQC signal is shown as a 3D stack plot (**a**) and contour plot (**b**). The simulation was carried out rigorously for $B_0 = 6{,}200$ G, $B_1 = 60$ G, $\nu_d = 25$ MHz and uncorrelated ^{14}N nitroxides. The tilt of the spin-echo-refocusing line is clearly visible. The reason is due to the fact that the spin-echo envelope is recorded over the time period where only one point corresponds to the dipolar interaction refocusing. A shift by Δt in the spin echo time corresponds to a shift by $\Delta t/2$ in the position of the dipolar coupling refocusing point. (Adapted from [93].)

case shows no variation of the dipolar spectrum along the ESR dimension, whereas in the correlated case there is clearly a distinct pattern of such variations.

Figure 24c–d shows the correlated and the uncorrelated case for $\boldsymbol{\lambda}_{1,2} = (0°, 0°, 0°)$, $(0°, 90°, 0°)$ and $\nu_d = 25$ MHz. The simulation corresponds to a realistic case of a large but finite B_1 of 60 G, which could be produced with our spectrometers if we use a somewhat smaller volume resonator. We observe only small features caused by the pseudosecular terms dipolar coupling. They become more pronounced in the case of stronger correlation effects, for example for β angles both either 0° or 90°. A small distribution in distances washes them out in 1D, leading to

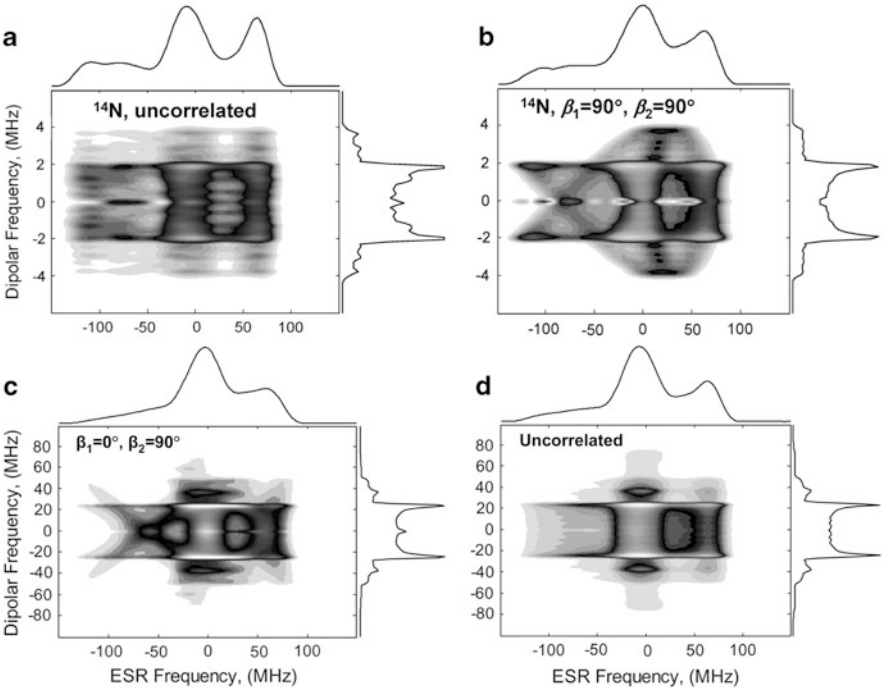

Fig. 24 2D DQC magnitude filled contour plots obtained by 2D FT with respect to t_{dip} and t_{echo}. The magnitude 2D signal is summed along both dimensions and is shown as the 1D ESR absorption spectrum (at the *top*) or Pake doublet (on the *rhs*). *Top row* – uncorrelated (**a**) and correlated (**b**) case. $B_0 = 6{,}200$ G, $\nu_d = 2$ MHz ($r = 29.6$ Å). B_1 was set to infinity (i.e., perfect delta-function pulses), pseudosecular terms were neglected. In (**b**) angles beta were (90°, 90°) corresponding to strong correlations. The other Euler angles were set to zero. Note the similarity of the 1D dipolar spectra obtained by integration along the ESR frequency. They all are classic Pake doublets. But in the 2D representation the differences are striking. For the uncorrelated cases the dipolar spectrum is uniform for different slices along the ESR frequency axis, whereas for the correlated case they show a distinct "fingerprint" of this type of correlation. Since pseudosecular terms are neglected, the results are applicable to long distances, such as the present case. *Bottom row* – Examples of 2D FT magnitude contour plots for another case of orientational correlation: angles beta in (**c**) are (0°, 90°). The other four Euler angles were set to zero. Case (**d**) is the uncorrelated case. Plots (**c**) and (**d**) are very similar in their 1D projection, but still distinct in 2D plots. In both cases $B_0 = 6{,}200$ G, $B_1 = 60$ G, $\nu_d = 25$ MHz (12.7 Å). (Adapted by combining two figures from [93].)

a broadened dipolar spectrum, which gives no clue that there are in fact strong correlations between nitroxide orientations. In the 2D map however this information is clearly seen [93].

Finally, we show an experimental example of 2D DQC conducted on 15 μM solution of rigid biradical [35] in *o*-terphenyl-d_{24} glass. Since B_1 of 45 G is insufficient to provide uniform spectral coverage of the whole nitroxide spectrum, two data collections were made using mw pulse sequences applied at the low-field and high-field part of the spectrum.

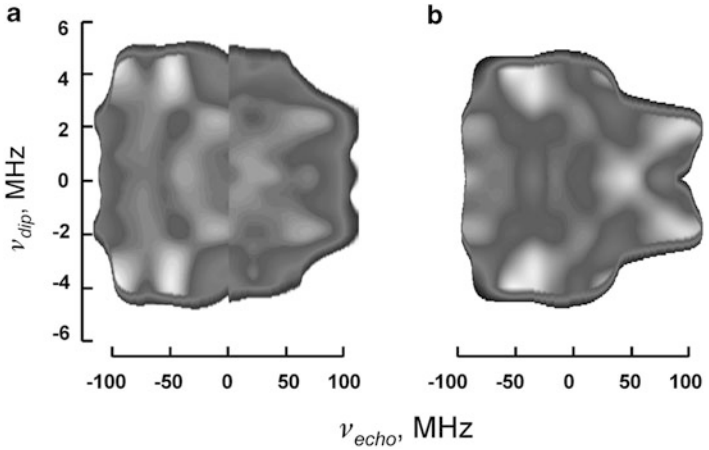

Fig. 25 Experimental (**a**) and calculated (**b**) correlation maps from 17.25 GHz 2D DQC data. 2D correlation map (**a**) is a composite plot made of two correlation plots obtained from 2D data acquired for mw pulses applied at −10 and 20 G field offsets from the center of the ^{14}N nitroxide ESR spectrum. The respective low- and high-field side of these two spectra was used to make a composite plot according to the following procedure. The time-domain signals were first 2D Fourier transformed in the manner used in Fig. 24. Then each resulting contour plot was normalized by dividing it by the 2D spectrum constructed as a product of two 1D spectra, taken as sums along spectral and dipolar frequencies, respectively, as shown in Fig. 24. The low-field and high-field parts of these contour plots were then combined into a single 2D plot (**a**), with the cut-out line set at the field offset of 15 G. The plot in (**b**) was computed using for adequate spectral coverage B_1 of 80 G, $r_{12} = 28.9$ Å, and the set of Euler angles $\boldsymbol{\lambda}_1 = (0°, 75°, 0°)$, $\boldsymbol{\lambda}_2 = (90°, 111°, 0°)$ from molecular modeling [35]. The following experimental conditions were used: Sample temperature was 60 K; $\pi/2$ and π pulse widths were 2 and 4 ns, corresponding to B_1 of 45 G. Pulse repetition frequency was 2 kHz; 2D data sets corresponded to ±4 μs in t_{dip} and ±100 ns in t_{echo} for total of 500 × 200 data points. Data collection time was 9.5 h for the −10 G offset and 19 h for the 20 G offset for very high SNR, although satisfactory data were obtained already in 2 and 4 h, respectively. A 64-step phase cycle [35, 63] was used to get a clean DQC signal. There was no need to suppress ESEEM and a small baseline could simply be ignored for the 15 μM concentration used. (This lab, unpublished.)

For this linear biradical one expects nitroxide moieties to be oriented with their beta angles, $\beta_{1(2)}$ about 90°, the remaining angles are less important. Molecular modeling [35] yielded $r_{12} = 28.9$ Å for the distance measured between the points located at 0.75 of NO bond length to the nitrogens; and for the Euler angles the following values were obtained $\boldsymbol{\lambda}_1 = (0°, 75°, 0°)$, $\boldsymbol{\lambda}_2 = (90°, 111°, 0°)$. In Fig. 25 we compare correlation maps for experimental and calculated data. The maps are built as normalized contour plots. It is clear that the plots are similar, i.e., nitroxides' orientations are of the expected type, but there are some differences that could be addressed after developing a faster computational procedure than is currently available.

In summary, we note that acquiring orientational information necessitates recording several DEER traces [132] whereas 2D DQC can do it in a single pass, if mw pulses can excite the whole spectrum. The advantage of DEER is that it can

be applied to infer orientational information from very broad orientationally well-resolved spectra.

5.4 Multifrequency

High absolute spin sensitivity and potentially improved concentration sensitivity at a higher frequency strongly motivated the development of PDS ESR measurement technology in the mm-wave frequency range. In an important development at St Andrews University, a 1 kW mm-wave amplifier was employed at W-band, providing 12 ns π-pulses in a circular waveguide-based nonresonant induction probe that has a relatively high conversion factor (~0.6 G/W$^{1/2}$) [46], (even shorter π-pulse widths of ~10 ns were achieved at 95 GHz [47] at ACERT with the Fabry–Perot resonator setup developed for aqueous samples). It admits samples as large as at X-band, whereas the high conversion factor and frequency scaling of spin sensitivity as ω^2 (for constant sample volume [147]) have resulted in very high sensitivity comparable to that of our ACERT Ku-band spectrometer [46, 171].

Orientational selectivity is another common argument in favor of the mm-wave range [21]. In the case of rigidly attached spin-labels, determining their orientation provides valuable structural information. The sensitivity to orientations increases at high fields, where the ESR spectrum of nitroxides is dominated by g-tensor anisotropy. In order to infer orientations, the DEER signal is recorded using several field positions of the pump and detection pulses [21, 173, 174]. A modification to the signal acquisition scheme was shown [173] that allowed simultaneous recording at several field points, thereby helping to shorten the duration of the experiment. Given sufficiently broad spectral excitation, 2D-DQC may provide significant improvement in this area, by recording the whole correlation map in a single pass or maybe by using just 2 or 3 field points (cf. Sect. 5.3). High power amplifiers available at W-band [46, 47] and resonators designed to maximize B_1 could make such a plan realistic. However, DQC is not yet an option for these spectrometers, but it seems it is just a matter of time. In Fig. 26 we show a simulated 2D DQC correlation spectrum at Ku- and W-band for ^{14}N nitroxides. The correlation map is richer in detail at W-band. The results for Ka band (35 GHz) look similar to Ku band but are not shown. The uncorrelated case for W-band (not shown) has a similar appearance to the Ku and Ka bands shown in Fig. 24a, d, indicating only the presence of spectral features aligned parallel to the ν_{echo} spectral axis. In all cases, the high-field (low frequency) side of the 2D spectrum is more sensitive to orientations, as expected. Therefore, even with limited B_1 it could be possible to test orientations in this spectral region. At W-band the g_y part of the spectrum is also sensitive and exhibits the effects of pseudosecular terms, which in general are weaker at this frequency due to its wider spectral extent.

It thus seems to be useful to conduct PDS experiments in lower fields, where orientational correlation effects are weaker and more accurate distance reconstruction can be made. This distance information could be combined with orientation-dependent data from the high-field experiment to be used in structure modeling.

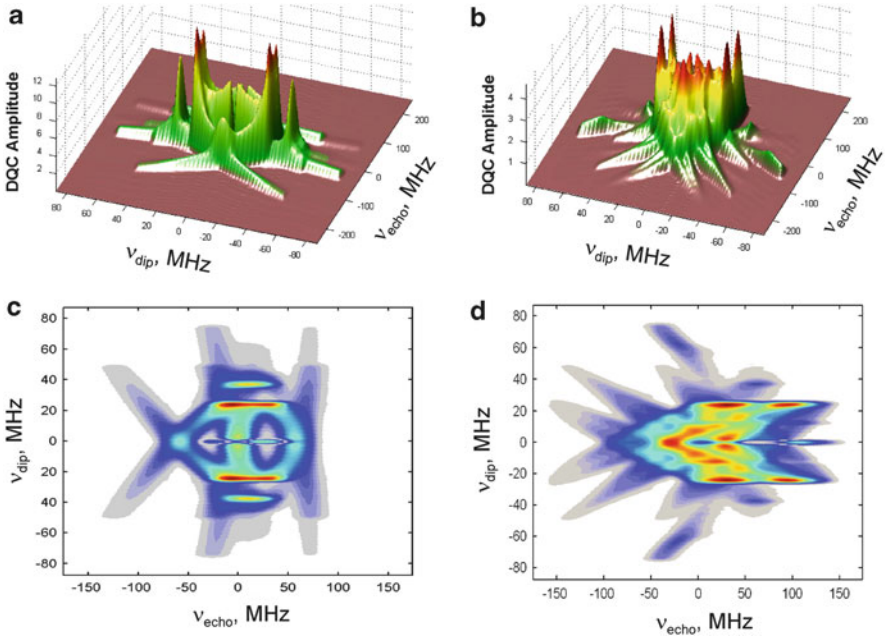

Fig. 26 Frequency dependence of 2D-DQC orientation correlation map. (**a**) 2D spectrum calculated for Ku band and (**b**) for W-band are shown as stack plots. (**c**, **d**) Filled contour plots representation of the above stack plots. The following simulation parameters were used: $B_1 = 60$ G, $\nu_d = 25$ MHz; magnetic tensor frame orientations, $\boldsymbol{\lambda}_1 = (\alpha_1, \beta_1, \gamma_1)$, $\boldsymbol{\lambda}_2 = (\alpha_2, \beta_2, \gamma_2)$ were taken as (0°, 0°, 0°) and (90°, 0°, 0°)

While orientations can be difficult to infer for MTSSL, due to its very substantial side-chain flexibility usually exhibiting multiple rotamers, sometimes spin-labels can become occluded as is the case for MsbA when in the ADP-Vi trapped state the spin-label is buried inside the closed transporter [175]. Recent development of conformationally restricted nitroxide labels [133, 134] may be useful in this regard even for conventional working frequencies. Thus, nitroxides may ultimately fit well into such a multifrequency study. Of course, there are systems that are already orientationally well resolved in the centimeter frequency range but become too broad in W-band and higher, but they may benefit from the slightly higher frequency of Ku or Ka band. For example, DEER was successfully applied at X-band to determine orientational information in a Cu^{2+}–Cu^{2+} biradical and also to a protein–protein complex with $NO^{\bullet}$ and a [2Fe–2S] cluster [87]. In contrast, the Gd^{3+} $-1/2 \leftrightarrow 1/2$ transition becomes very narrow in Ka band and above and carries no significant orientational dependence. These (and some other) properties allow one to use pairs of Gd^{3+} spin labels for distance measurements, free from orientational effects and with spin sensitivity comparable to that generally achieved with nitroxide labels, or else they can be used in combination with nitroxides to even higher sensitivity [121]. Nitroxide labels, however, have the relative advantage of being smaller and least perturbing. They are also easy to attach and use with a

variety of systems and sample types. Another issue with Gd^{3+} labels is that they currently require more expensive operation at 5–10 K and the modulation depth is typically small (ca. 0.01–0.05), thus considerably elevating technical requirements of the pulse spectrometer, which for example become very relaxed for DQC applied to nitroxides or Cu^{2+}. A benefit of Gd^{3+} labels is that their positions are better defined, potentially providing more useful constraints for structure modeling. It is believed [178] that ultimately a higher sensitivity may be achieved than is currently possible with nitroxides using typical X-band DEER spectrometers; naturally one could expect that 5-pulse DEER could benefit distance measurements based on Gadolinium labels, if the challenges with small modulation depth could be overcome. Thus, ongoing development of spectrometers operating at different frequencies, methods, spin-labels, and other aspects continues to make PDS an increasingly more powerful technique for studying biomolecular structure and function.

6 Summary and Perspectives

We have shown that there are currently two pulse ESR methods that are most beneficial for biological pulse dipolar spectroscopy. They are DQC and DEER (PELDOR). In dilute systems DQC is considerably more sensitive in most cases, *shortening the time of the experiment by at least an order of magnitude*. DQC is uniquely applicable to relatively narrow spectra such as nitroxides, which promise the greatest sensitivity improvement, but we also find it (at Ku-band) more sensitive for wide spectra such as for the Cu^{2+}–Cu^{2+} system (unpublished, ACERT), since the concentration sensitivity for this case scales as $(B_1)^{\alpha}$ with α ranging from 1 to 1.5 (cf. Sect. 4.1) [101]. Its double quantum coherence filter suppresses background signals. It has a broader distance range and is substantially free from orientational selection effects in its 1D mode, but reveals them in its 2D mode. DEER on the other hand is very useful for a wide range of systems and uniquely suitable for nonoverlapping spectra. For pairs of spins, it provides very good separation from relaxation effects and is less sensitive to ESEEM. It can be applied to more concentrated spin systems than DQC, thereby extending the concentration range. Also, since it is based on selective pulses and automatically references to the signal at zero time, it helps to study the presence of small spin clusters and in some cases provides an estimate for aggregation numbers.

These two methods actually are quite complex with respect to the underlying spin dynamics; but fortuitously they happen to exhibit minimal artifacts throughout the wide region of dipolar couplings for distances of about 15 Å and greater, so that the ideal kernel (cf. Sect. 2.6) can be used in many cases to reconstruct the distance distributions.

In DEER, unless the pulses are sufficiently selective and the dipolar coupling is small, a more complicated spin dynamics is observed than with the DQC technique. In the latter, pseudosecular terms in dipolar coupling do play a role, but are easy to account for. As we have shown, DQC is typically in the regime of weak coupling,

where its spin dynamics is quite simple. On the other hand in the case of strong correlation effects, a special 2D mode of DQC is a potent technique to yield a correlation map in a single experiment. Furthermore, at low concentrations, where DQC excels, the background is greatly suppressed, aiding its removal, and it can often be ignored altogether in 2D DQC.

Suffice it to say that in all cases, cultivating both DQC and DEER and selecting the most appropriate PDS pulse sequence for the system studied are good strategies.

We conclude that quite remarkable progress has been achieved in pulsed dipolar ESR spectroscopy. This includes continuing progress with instrumentation, pulse sequences, spin-labels, data processing with structure modeling, and system preparation protocols. We see that the number of potential biological applications is growing, and it may be only "the tip of the iceberg."

For more rapidly relaxing spin-labels, such as nitroxides in hydrophobic environments of proteins and in lipid membranes, further spectrometer sensitivity improvement would be highly desirable, especially for proteins from higher organisms, which are difficult or impossible to deuterate. More water-exposed labels would benefit most from solvent deuteration and using new methods such as 5-pulse DEER.

At Ku-band (at ACERT) and higher working frequencies the sensitivity is currently at the low micromolar level of concentration for proteins and nucleotides. This was achieved without compromising the distance range and resolution. Distances can be measured at least to 90 Å, which helps to characterize large objects such as protein complexes and RNA. We anticipate that progress in method development and sensitivity improvement will continue.

Acknowledgments The authors acknowledge Elka R. Georgieva for her help with model systems and figures. This work was supported by NIH grants NIH/NIGMS P41GM103521 and NIH/NCRR P41RR016292.

Appendix

Signals in 3,4,5-Pulse DEER Sequences

Here, we derive the expression given by Eq. (40) for PELDOR/DEER (cf. Fig. 5a), using the spin Hamiltonian given by Eqs. (13) and (14) (which neglects pseudosecular terms), in the absence of pulses. We express H_0 in the frame of reference doubly rotating with frequencies ω_1 and ω_2 of mw pulses applied, respectively, to spins A and B, having their Larmor frequencies at Ω_a and Ω_b (cf. Slichter, p. 279, and assumptions therein [95]). Note that Eqs. (13) and (14) use spins 1 and 2, but for DEER pulse sequences we number spins by the subscripts a and b. In this frame of reference H_0 becomes

$$H_0 = \omega_a S_{az} + \omega_b S_{bz} + a S_{az} S_{bz} \tag{63}$$

In Eq. (63) a is as in Eq. (14), ω_a and ω_b are the Larmor frequency offsets from ω_1 and ω_2 respectively. We further assume the following set of inequalities $a \ll \gamma_e B_{1a(b)} \ll |\omega_1 - \omega_2|$. The first inequality allows us to neglect the dipolar coupling during the pulse, the second ensures that there may be only a small overlap of pulse excitations at the two frequencies, but we will retain related terms that may be produced in the course of calculations of the signal. (The first inequality, as related to A-spins, makes it easier for one to consider pseudosecular terms in conducting a more detailed analysis). Note that for a pair of spins, depending on angle θ, one of or both spins may contribute to the echo. We can assume that the first spin is always an A spin, but the second spin can be either A or B spin. To simplify this matter, we use when needed the subscripts numbering spins as 1 or 2.

The amplitude $V(t)$ of the echo signal that we are interested in computing is given by the trace, $\mathrm{Tr}(S_{a+}\rho(t))/\mathrm{Tr}(S_{a+}S_{a-})$, where $\rho(t)$ is the density matrix measured at time t after the first pulse in the sequence. Therefore in the end we retain in ρ only the terms in S_{a-}. We will follow the evolution of single-quantum in-phase coherences of spin 1, $S_{1a\pm}$ created by the first $\pi/2$ pulse. They evolve due to the dipolar coupling $aS_{1z}S_{2z}$ into anti-phase coherences $S_{1a\pm}S_{2z}$ and vice versa; the process thus interconverts these coherences leading to their modulation by the dipolar frequency $a/2$ as described in Sect. 2.3.1. These coherences under the action of pulses and free evolution periods will turn out as detectable S_{a-} carrying this dipolar modulation.

The pulse sequences for 3-pulse PELDOR and 4-pulse DEER can be expressed in arrow representation respectively as:

$$\begin{aligned} &P_{1a}(\pi/2) \xrightarrow{H_0(t_1-t)} P_{2b}(\pi) \xrightarrow{H_0(t)} P_{3a}(\pi) \xrightarrow{H_0(t_1+t_e)} echo \\ &P_{1a}(\pi/2) \xrightarrow{H_0(t_1)} P_{2a}(\pi) \xrightarrow{H_0(t)} P_{3b}(\pi) \xrightarrow{H_0(t_2-t)} P_{4a}(\pi) \xrightarrow{H_0(t_2-t_1+t_e)} echo, \end{aligned} \tag{64}$$

where $H_0(t)$ denotes free evolution for the duration of t due to H_0 and $P_{ka(b)}$ is the pulse propagator for kth pulse applied nominally at the frequency ω_a or ω_b. The primary echo produced by pulses 1 and 3 in 3-pulse PELDOR corresponds to a coherence pathway, $\mathbf{p} = (+1, -1)$. In 4-pulse DEER based on the refocused echo created by pulses 1, 2, and 4 coherences pass through a $\mathbf{p} = (-1, +1, -1)$ pathway. We describe the action of π-pulses by introducing probability p_{ka} or p_{kb} for the spin at ω_a or ω_b, respectively, to be flipped by the kth pulse. (We may drop the subscript a (or b), when unimportant.) The probability not to be flipped, q_{kc}, is then $1 - p_{kc}$ (where c is a or b). We denote the amount of $S_{1a\pm}$ produced by the first $\pi/2$ pulse as h_{1a}. Note that q, p, and h correspond to standard amplitude factors for the action of selective pulses, for example, as defined in the literature [35]. For a spin at a resonant frequency offset ω from the frequency of the RF pulse, the probabilities p and q to be flipped or not flipped by the pulse with nominal flip angle β is given by

$$p = \sin^2(\beta u/2)/u^2, \quad q = 1 - p \tag{65}$$

Here, $u^2 = 1 + \omega^2/\omega_{\mathrm{mw}}^2$ and $\omega_{\mathrm{mw}} = \gamma_e B_1$.

To manage free evolution, we introduce operators $H_z \equiv \omega_a S_{1z}$ and $\Omega_{12} \equiv aS_{1z}S_{2z}$. Then the free evolution propagator is $\exp[-i(H_z + \Omega_{12})]$. Note that H_z and Ω_{12} commute and we can consider them separately and write for the free evolution of shift operators $S_{1a\pm}$ due to H_z or Ω_{12} the following:

$$\begin{aligned} &S_{1a\pm} \xrightarrow{H_z t} S_{1a\pm}\, \mathrm{e}^{\mp \mathrm{i}\omega_a t} \\ &S_{1a\pm} \xrightarrow{\Omega_{12} t} S_{1a\pm}(\cos(at/2) \mp 2\mathrm{i}S_{2z}\sin(at/2)) \equiv S_{1a\pm}D_{\pm t} \end{aligned} \tag{66}$$

We numbered the spins in Eq. (66). Note that S_z may correspond to spin 2 at ω_a or ω_b, since pseudosecular terms are neglected and the evolution due to weak dipolar coupling is then given by Eq. (15). Since first-order coherences of A-spins pass through the prescribed pathway and all pulses applied during the evolution are nominally π-pulses, we need to consider only the following actions of the pulses:

$$\begin{aligned} &S_{1a\pm} \xrightarrow{P_{kb}} q_{kb}S_{1a\pm}, \qquad S_{1a\pm} \xrightarrow{P_{ka}} p_{ka}S_{1a\mp} \\ &S_{2z} \xrightarrow{P_{kc}} (q_{kc} - p_{kc})S_{2z} \end{aligned} \tag{67}$$

Here, P_k represents the action of pulse k and subscript a or b is added to indicate at what frequency the pulse is applied. Other spin manipulations lead to pathways that do not contribute to the echo of interest. In the following, we drop the subscripts numbering spins. Since pulse excitations at the two frequencies have only small overlap, Eq. (67) is good approximation. We will disregard unessential phase shifts [98] introduced into $S_{a\pm}$ by the pulses applied at ω_b. From Eqs. (66) and (67) we find that D_t has the following properties:

$$D_t \xrightarrow{H_{kc}} q_{kc}D_t + p_{kc}D_t^*, \qquad D_t^* = D_{-t}, \qquad D_{t_1+t_2} = D_{t_1}D_{t_2} \tag{68}$$

We first compute the final density operator ρ_f for 3-pulse PELDOR by tracking the coherence pathway that lead to S_{a-}. We thus start from S_{a+} produced by the first $\pi/2$ pulse. Equations 67 and 68 reduce our task to merely writing all ensuing "dipolar trajectories". By repeatedly applying Eqs. (67) and (68) to S_{a+}, the following sequence of transformations defines the detectable density matrix element in PELDOR:

$$\begin{aligned} &\rho_0 = S_{az} \xrightarrow{P_{1a}} h_{1a}S_{a+} \xrightarrow{H_0(t)} h_{1a}S_{a+}D_t\, \mathrm{e}^{-\mathrm{i}\omega_a t} \\ &\xrightarrow{P_{2b}} h_{1a}q_{2a}S_{a+}(q_2D_t + p_2D_{-t})\, \mathrm{e}^{-\mathrm{i}\omega_a t} \xrightarrow{H_0(\tau - t)} h_{1a}q_{2a}S_{a+}(q_2D_\tau + p_2D_{\tau-2t})\, \mathrm{e}^{-\mathrm{i}\omega_a \tau} \\ &\xrightarrow{P_{3a}} S_{a-}h_{1a}q_{2a}p_{3a}(q_2q_3D_\tau + q_2p_3D_{-\tau} + p_2q_3D_{\tau-2t} + p_2p_3D_{2t-\tau})\, \mathrm{e}^{-\mathrm{i}\omega_a \tau} \\ &\xrightarrow{H_0(\tau+\delta t_\mathrm{e})} S_{a-}h_{1a}q_{2a}p_{3a}(q_2q_3D_0 + q_2p_3D_{-2\tau} + p_2q_3D_{-2t} + p_2p_3D_{2t-2\tau})\, \mathrm{e}^{\mathrm{i}\omega_a \delta t_\mathrm{e}} \end{aligned} \tag{69}$$

Table 1 t-Dependent dipolar pathways in four-pulse sequence

k	B_k	Standard asymmetric 4-pulse DEER ($t_1 \ll t_2$) t_k	"Symmetric" form 4-pulse DEER ($t_2 = 2t_1 \equiv 2\tau$) t_k	Different definition of time variable, t_k ($t \rightarrow t_1 + t$) t_k
(1)	$q_4p_3q_2$	$t - t_1$	$t - \tau$	t
(2)	$q_4p_3p_2$	t	t	$t + t_1$
(3)	$p_4p_3p_2$	$t + t_1 - t_2$	$\tau - t$	$2\ t_1 + t - t_2$
(4)	$p_4p_3q_2$	$t - t_2$	$2\tau - t$	$t + t_1 - t_2$

Coefficients p_k and q_k inside the brackets refer to spin 2, which may be at ω_b or ω_a. The spin echo amplitude, V at time $2\tau + \delta t_e$ is then taken as the trace: $Tr(S_{a+}S_{a-}(2\tau + \delta t_e))/Tr(S_{a+}S_{a-})$. For simplicity, we neglect dipolar evolution during δt_e and after retaining detectable in-phase coherences by substituting D_{2t} with their real parts, $\cos(at)$, we arrive at the expression for the echo signal

$$V(\tau, t, \delta t_e) = \langle h_{1a}q_{2a}p_{3a}[q_2q_3 + q_2p_3\cos(a\tau) + p_2q_3\cos(at) + p_2p_3\cos(a(t-\tau))]\, e^{i\omega_a\delta t_e}\rangle_{a,b} \tag{70}$$

The term in $\exp(i\omega_a\delta\tau_e)$ together with all other frequency-dependent factors (p, q, h) after averaging over $\omega_{a,b}$ produces the spin echo shape, $V(\delta t_e)$ so that Eq. (70) becomes equivalent to Eq. (40). The dipolar modulation in Eq. (70) is represented by the two terms: $\sim q_3[1 - p_2(1 - \cos(at))]$ and $\sim p_3p_2\cos(a(t - \tau))$. The first term is the well-known formula for the PELDOR/DEER signal [30, 73]. The second "back-in-time" signal is relatively small if $\langle p_3p_2\rangle_{a,b} \ll \langle p_2\rangle_{a,b}$. Usually, this is the case for DEER (but in the single-frequency DEER analog, "2 + 1," both signals are comparable [38]). In Eq. (70), there are two more terms that are constant in t: one, which is time independent, corresponds to unaffected spin B; whereas another term in $\cos(a\tau)$ corresponds to the dipolar signal between A spins in the limit of very small a (when pseudosecular term can be neglected). To fully account for their effects more detailed calculations have to be carried out, for example ones based on a modified product operator method as described by Borbat and Freed [35]. Then Eq. (70) becomes at first somewhat unwieldy (e.g., such as an approximate expression given by Raitsimring [106]), but it will simplify practically to Eq. (70) when the "+1" pumping pulse has only a small overlap with the rest of the pulses.

Derivation of the expression analogues to Eq. (70), but for 4-pulse DEER adds one more step to Eq. (69) doubling the number of terms in dipolar signals to a total of eight,

$$V(t) \propto B_a \sum_{k=1}^{8} B_{bk}\cos(at_k) \tag{71}$$

where $B_a = h_{1a}p_{2a}q_{3a}p_{4a}$. Only four terms in Eq. (71) have a dependence on the position t of the pump pulse. Table 1 compiles B_{bk} and respective time variables, t_k defined in different ways for these terms.

The dipolar pathways in the 5-pulse DEER sequence were studied in [171] by employing a similar approach. We can describe them qualitatively using the data from Table 1. Signal (1) is the standard 4-pulse DEER signal whereas signals 2–4 are relatively weak. In the 5-pulse DEER sequence, (2) or (4) are no longer weak, since the extra pulse 5 following pulse 4 makes p_4 greater than p_3, thereby suppressing (1) and developing the 5-pulse dipolar signal (2). Alternatively, the extra pulse may have position $5'$ right before pulse 2 and develops (4) due to increased p_2 and suppresses (1).

References

1. Borbat PP, Mchaourab HS, Freed JH (2002) Protein structure determination using long-distance constraints from double-quantum coherence ESR: study of T4-lysozyme. J Am Chem Soc 124(19):5304–5314
2. Jeschke G, Wegener C, Nietschke M, Jung H, Steinhoff H-J (2004) Interresidual distance determination by four-pulse double electron–electron resonance in an integral membrane protein: the Na+/proline transporter PutP of Escherichia coli. Biophys J 86(4):2551–2557
3. Zhou Z, DeSensi SC, Stein RA, Brandon S, Dixit M, McArdle EJ, Warren EM, Kroh HK, Song L, Cobb CE, Hustedt EJ, Beth AH (2005) Solution structure of the cytoplasmic domain of erythrocyte membrane band 3 determined by site-directed spin labeling. Biochemistry 44 (46):15115–15128
4. McNulty JC, Silapie JL, Carnevali M, Farrar CT, Griffin RG, Formaggio F, Crisma M, Toniolo C, Millhauser GL (2001) Electron spin resonance of TOAC labeled peptides: folding transitions and high frequency spectroscopy. Biopolymers 55(6):479–485
5. Park S-Y, Borbat PP, Gonzalez-Bonet G, Bhatnagar J, Pollard AM, Freed JH, Bilwes AM, Crane BR (2006) Reconstruction of the chemotaxis receptor-kinase assembly. Nat Struct Mol Biol 13(5):400–407
6. Hilger D, Jung H, Padan E, Wegener C, Vogel K-P, Steinhoff H-J, Jeschke G (2005) Assessing oligomerization of membrane proteins by four-pulse DEER: pH-dependent dimerization of NhaA Na+/H + antiporter of E. coli. Biophys J 89(2):1328–1338
7. Milov AD, Erilov DA, Salnikov ES, Tsvetkov YD, Formaggio F, Toniolo C, Raap J (2005) Structure and spatial distribution of the spin-labelled lipopeptide trichogin GA IV in a phospholipid membrane studied by pulsed electron–electron double resonance (PELDOR). Phys Chem Chem Phys 7(8):1794–1799
8. Hubbell WL, Cafiso DS, Altenbach CA (2000) Identifying conformational changes with site-directed spin labeling. Nat Struct Biol 7(9):735–739
9. Hustedt EJ, Smirnov AI, Laub CF, Cobb CE, Beth AH (1997) Molecular distances from dipolar coupled spin-labels: the global analysis of multifrequency continuous wave electron paramagnetic resonance data. Biophys J 72(4):1861–1877
10. Bennati M, Robblee JH, Mugnaini V, Stubbe J, Freed JH, Borbat PP (2005) EPR distance measurements support a model for long-range radical initiation in E. coli ribonucleotide reductase. J Am Chem Soc 127(43):15014–15015
11. Fafarman AT, Borbat PP, Freed JH, Kirshenbaum K (2007) Characterizing the structure and dynamics of folded oligomers: pulsed ESR studies of peptoid helices. Chem Commun (4):377–379

12. Borbat PP, Ramlall TF, Freed JH, Eliezer D (2006) Inter-helix distances in lysophospholipid micelle-bound α-synuclein from pulsed ESR measurements. J Am Chem Soc 128 (31):10004–10005
13. Dzikovski BG, Borbat PP, Freed JH (2004) Spin-labeled gramicidin a: channel formation and dissociation. Biophys J 87(5):3504–3517
14. Banham JE, Timmel CR, Abbott RJM, Lea SM, Jeschke G (2006) The characterization of weak protein-protein interactions: evidence from DEER for the trimerization of a von willebrand factor A domain in solution. Angew Chem Int Ed 45(7):1058–1061
15. Borbat PP, Freed JH (1999) Multiple-quantum ESR and distance measurements. Chem Phys Lett 313(1,2):145–154
16. Borbat PP, da Costa-Filho AJ, Earle KA, Moscicki JK, Freed JH (2001) Electron spin resonance in studies of membranes and proteins. Science 291(5502):266–269
17. Freed JH (2000) New technologies in electron spin resonance. Annu Rev Phys Chem 51:655–689
18. Fanucci GE, Cafiso DS (2006) Recent advances and applications of site-directed spin labeling. Curr Opin Struct Biol 16(5):644–653
19. Columbus L, Hubbell WL (2002) A new spin on protein dynamics. Trends Biochem Sci 27(6):288–295
20. Milov AD, Tsvetkov YD, Formaggio F, Crisma M, Toniolo C, Raap J (2003) Self-assembling and membrane modifying properties of a lipopeptaibol studied by CW-ESR and PELDOR spectroscopies. J Pept Sci 9(11–12):690–700
21. Denysenkov VP, Prisner TF, Stubbe J, Bennati M (2006) High-field pulsed electron–electron double resonance spectroscopy to determine the orientation of the tyrosyl radicals in ribonucleotide reductase. Proc Natl Acad Sci USA 103(36):13386–13390
22. Becker JS, Saxena S (2005) Double quantum coherence electron spin resonance on coupled Cu(II)-Cu(II) electron spins. Chem Phys Lett 414(1–3):248–252
23. Biglino D, Schmidt PP, Reijerse EJ, Lubitz W (2006) PELDOR study on the tyrosyl radicals in the R2 protein of mouse ribonucleotide reductase. Chemphyschem 8(1):58–62
24. Narr E, Godt A, Jeschke G (2002) Selective measurements of a nitroxide-nitroxide separation of 5 nm and a nitroxide-copper separation of 2.5 nm in a terpyridine-based copper(II) complex by pulse EPR spectroscopy. Angew Chem Int Ed 41(20):3907–3910
25. Codd R, Astashkin AV, Pacheco A, Raitsimring AM, Enemark JH (2002) Pulsed ELDOR spectroscopy of the Mo(V)/Fe(III) state of sulfite oxidase prepared by one-electron reduction with Ti(III) citrate. J Biol Inorg Chem 7(3):338–350
26. Elsaesser C, Brecht M, Bittl R (2002) Pulsed electron–electron double resonance on multinuclear metal clusters: assignment of spin projection factors based on the dipolar interaction. J Am Chem Soc 124(42):12606–12611
27. Upadhyay AK, Borbat PP, Wang J, Freed JH, Edmondson DE (2008) Determination of the oligomeric states of human and rat monoamine oxidases in the outer mitochondrial membrane and octyl beta-D-glucopyranoside micelles using pulsed dipolar electron spin resonance spectroscopy. Biochemistry 47(6):1554–1566
28. Astashkin AV, Kodera Y, Kawamori A (1994) Distance between tyrosines Z+ and D+ in plant photosystem II as determined by pulsed EPR. Biochim Biophys Acta 1187(1):89–93
29. Milov AD, Salikhov KM, Shirov MD (1981) Application of the double resonance method to electron spin echo in a study of the spatial distribution of paramagnetic centers in solids. Soviet Phys-Solid State 23:565–569
30. Milov AD, Maryasov AG, Tsvetkov YD (1998) Pulsed electron double resonance (PELDOR) and its applications in free-radicals research. Appl Magn Reson 15(1):107–143
31. Martin RE, Pannier M, Diederich F, Gramlich V Hubrich M, Spiess HW (1998) Determination of end-to-end distances in a series of TEMPO diradicals with a new four-pulse double electron electron resonance experiment. Angew Chem Int Ed 100(32):13428–13432
32. Larsen RG, Singel DJ (1993) Double electron–electron resonance spin-echo modulation: spectroscopic measurement of electron spin pair separations in orientationally disordered solids. J Chem Phys 98(7):5134–5146

33. Raitsimring AM, Salikhov KM (1985) Electron spin echo method as used to analyze the spatial distribution of paramagnetic centers. Bull Magn Reson 7(4):184–217
34. Salikhov KM, Dzyuba SA, Raitsimring A (1981) The theory of electron spin-echo signal decay resulting from dipole-dipole interactions between paramagnetic centers in solids. J Magn Reson 42(2):255–276
35. Borbat PP, Freed JH (2000) Distance measurements in biological systems by EPR. In: Berliner LJ, Eaton GR, Eaton SS (eds) Biological magnetic resonance, vol 19. Academic/Plenum, New York, pp 385–459
36. Jeschke G, Pannier M, Godt A, Spiess HW (2000) Dipolar spectroscopy and spin alignment in electron paramagnetic resonance. Chem Phys Lett 331(2,3,4):243–252
37. Kulik LV, Dzuba SA, Grigoryev IA, Tsvetkov YD (2001) Electron dipole-dipole interaction in ESEEM of nitroxide biradicals. Chem Phys Lett 343(3,4):315–324
38. Kurshev VV, Raitsimring AM, Tsvetkov YD (1989) Selection of dipolar interaction by the "2 +1" pulse train ESE (1969–1992). J Magn Reson 81(3):441–454
39. Schiemann O, Piton N, Mu Y, Stock G, Engels JW, Prisner TF (2004) A PELDOR-based nanometer distance ruler for oligonucleotides. J Am Chem Soc 126(18):5722–5729
40. Steinhoff H-J (2004) Inter- and intra-molecular distances determined by EPR spectroscopy and site-directed spin labeling reveal protein-protein and protein-oligonucleotide interaction. Biol Chem 385(10):913–920
41. Fajer PG (2005) Site directed spin labelling and pulsed dipolar electron paramagnetic resonance (double electron–electron resonance) of force activation in muscle. J Phys Condens Matter 17(18):S1459–S1469
42. Cai Q, Kusnetzow AK, Hubbell WL, Haworth IS, Gacho GPC, Van Eps N, Hideg K, Chambers EJ, Qin PZ (2006) Site-directed spin labeling measurements of nanometer distances in nucleic acids using a sequence-independent nitroxide probe. Nucleic Acids Res 34(17):4722–4730
43. Freed JH (1967) Theory of saturation and double resonance effects in electron spin resonance spectra. 2. Exchange vs dipolar mechanisms. J Phys Chem 71(1):38–51
44. Freed JH (1966) Theory of spin relaxation via quantum-molecular systems – resonance effects. J Chem Phys 45(4):1251–1257
45. Freed JH (1965) Theory of saturation and double-resonance effects in ESR spectra. J Chem Phys 43(7):2312–2332
46. Cruickshank PAS, Bolton DR, Robertson DA, Hunter RI, Wylde RJ, Smith GM (2009) A kilowatt pulsed 94 GHz electron paramagnetic resonance spectrometer with high concentration sensitivity, high instantaneous bandwidth, and low dead time. Rev Sci Instrum 80 (10):103102–103115
47. Hofbauer W, Earle KA, Dunnam CR, Moscicki JK, Freed JH (2004) High-power 95 GHz pulsed electron spin resonance spectrometer. Rev Sci Instrum 75(5):1194–1208
48. Denysenkov VP, Prisner TF, Stubbe J, Bennati M (2005) High-frequency 180 GHz PELDOR. Appl Magn Reson 29(2):375–384
49. Goldfarb D, Lipkin Y, Potapov A, Gorodetsky Y, Epel B, Raitsimring AM, Radoul M, Kaminker I (2008) HYSCORE and DEER with an upgraded 95 GHz pulse EPR spectrometer. J Magn Reson 194(1):8–15
50. Astashkin AV, Enemark JH, Raitsimring A (2006) 26.5-40 GHz K-a-band pulsed EPR spectrometer. Concepts Magn Reson Part B 29(3):125–136
51. Forrer J, Garcia-Rubio I, Schuhmam R, Tschaggelar R, Harmer J (2008) Cryogenic Q-band (35 GHz) probehead featuring large excitation microwave fields for pulse and continuous wave electron paramagnetic resonance spectroscopy: performance and applications. J Magn Reson 190(2):280–291
52. Gromov I, Forrer J, Schweiger A (2006) Probehead operating at 35 GHz for continuous wave and pulse electron paramagnetic resonance applications. Rev Sci Instrum 77(6), Article Number: 064704

53. Simovic B, Studerus P, Gustavsson S, Leturcq R, Ensslin K, Schuhmann R, Forrer J, Schweiger A (2006) Design of Q-band loop-gap resonators at frequencies of 34–36 GHz for single electron spin spectroscopy in semiconductor nanostructures. Rev Sci Instrum 77(6), Article Number: 064702
54. Tschaggelar R, Kasumaj B, Santangelo MG, Forrer J, Leger P, Dube H, Diederich F, Harmer J, Schuhmann R, Garcia-Rubio I, Jeschke G (2009) Cryogenic 35 GHz pulse ENDOR probehead accommodating large sample sizes: performance and applications. J Magn Reson 200(1):81–87
55. Mett RR, Sidabras JW, Golovina IS, Hyde JS (2008) Dielectric microwave resonators in TE (011) cavities for electron paramagnetic resonance spectroscopy. Rev Sci Instrum 79(9), Article Number: 094702
56. Mett RR, Sidabras JW, Hyde JS (2007) Uniform radio frequency fields in loop-gap resonators for EPR spectroscopy. Appl Magn Reson 31(3–4):573–589
57. Tkach I, Sicoli G, Hobartner C, Bennati M (2011) A dual-mode microwave resonator for double electron–electron spin resonance spectroscopy at W-band microwave frequencies. J Magn Reson 209(2):341–346
58. Borbat PP, Davis JH, Butcher SE, Freed JH (2004) Measurement of large distances in biomolecules using double-quantum filtered refocused electron spin-echoes. J Am Chem Soc 126(25):7746–7747
59. Jeschke G, Bender A, Paulsen H, Zimmermann H, Godt A (2004) Sensitivity enhancement in pulse EPR distance measurements. J Magn Reson 169(1):1–12
60. Milikisyants S, Groenen EJJ, Huber M (2008) Observer-selective double electron–electron-spin resonance, a pulse sequence to improve orientation selection. J Magn Reson 192(2): 275–279
61. Milikisyants S, Scarpelli F, Finiguerra MG, Ubbink M, Huber M (2009) A pulsed EPR method to determine distances between paramagnetic centers with strong spectral anisotropy and radicals: the dead-time free RIDME sequence. J Magn Reson 201(1):48–56
62. Hirst SJ, Alexander N, Mchaourab HS, Meiler J (2011) RosettaEPR: an integrated tool for protein structure determination from sparse EPR data. J Struct Biol 173(3):506–514
63. Gaffney BJ, Bradshaw MD, Frausto SD, Wu F, Freed JH, Borbat P (2012) Locating a Lipid at the Portal to the Lipoxygenase Active Site. Biophys J 103(10):2134–2144
64. Bhatnagar J, Freed JH, Crane BR (2007) Rigid body refinement of protein complexes with long-range distance restraints from pulsed dipolar ESR. Two-component signaling systems. Methods Enzymol B 423:117–133
65. Bhatnagar J, Borbat PP, Pollard AM, Bilwes AM, Freed JH, Crane BR (2010) Structure of the ternary complex formed by a chemotaxis receptor signaling domain, the CheA histidine kinase, and the coupling protein CheW As determined by pulsed dipolar ESR spectroscopy. Biochemistry 49(18):3824–3841
66. Jeschke G, Chechik V, Ionita P, Godt A, Zimmermann H, Banham J, Timmel CR, Hilger D, Jung H (2006) DeerAnalysis2006 – a comprehensive software package for analyzing pulsed ELDOR data. Appl Magn Reson 30(3–4):473–498
67. Jeschke G, Panek G, Godt A, Bender A, Paulsen H (2004) Data analysis procedures for pulse ELDOR measurements of broad distance distributions. Appl Magn Reson 26(1–2):223–244
68. Polyhach Y, Bordignon E, Jeschke G (2011) Rotamer libraries of spin labelled cysteines for protein studies. Phys Chem Chem Phys 13(6):2356–2366
69. Chiang Y-W, Borbat PP, Freed JH (2005) Maximum entropy: a complement to Tikhonov regularization for determination of pair distance distributions by pulsed ESR. J Magn Reson 177(2):184–196
70. Chiang Y-W, Borbat PP, Freed JH (2005) The determination of pair distance distributions by pulsed ESR using Tikhonov regularization. J Magn Reson 172(2):279–295
71. Kim S, Brandon S, Zhou Z, Cobb CE, Edwards SJ, Moth CW, Parry CS, Smith JA, Lybrand TP, Hustedt EJ, Beth AH (2011) Determination of structural models of the complex between the

cytoplasmic domain of erythrocyte band 3 and ankyrin-R repeats 13–24. J Biol Chem 286 (23):20746–20757
72. Berliner LJ, Eaton GR, Eaton SS (2000) Distance measurements in biological systems by EPR, vol 19, Biological magnetic resonance. Kluwer, New York
73. Jeschke G (2002) Distance measurements in the nanometer range by pulse EPR. Chemphyschem 3(11):927–932
74. Dzuba SA (2005) Pulsed EPR structural studies in the nanometer range of distances. Russian Chem Rev 74(7):619–637
75. Prisner T, Rohrer M, MacMillan F (2001) Pulsed EPR spectroscopy: biological applications. Annu Rev Phys Chem 52:279–313
76. Borbat PP, Freed JH (2000) In: Berliner LJ, Eaton GR, Eaton SS (eds) Biological magnetic resonance. New York, Kluwer Academic
77. Abragam A (1961) The principles of nuclear magnetism, vol 386. Clarendon, Oxford, pp 442–451
78. Jeschke G, Spiess HW (2006) Distance measurements in solid-state NMR and EPR spectroscopy. In: Dolinsek J, Vilfan M, Zumer S (eds) Novel NMR and EPR techniques. Springer, Berlin, pp 21–63
79. Pake GE (1948) Nuclear resonance absorption in hydrated crystals: fine structure of the proton line. J Chem Phys 16:327–336
80. Rabenstein MD, Shin Y-K (1995) Determination of the distance between two spin labels attached to a macromolecule. Proc Natl Acad Sci USA 92(18):8239–8243
81. Hu KN, Song C, Yu HH, Swager TM, Griffin RG (2008) High-frequency dynamic nuclear polarization using biradicals: a multifrequency EPR lineshape analysis. J Chem Phys 128(5), Article Number: 052302
82. Persson M, Harbridge JR, Hammarstrom P, Mitri R, Martensson L-G, Carlsson U, Eaton GR, Eaton SS (2001) Comparison of electron paramagnetic resonance methods to determine distances between spin labels on human carbonic anhydrase II. Biophys J 80(6):2886–2897
83. Koteiche HA, Mchaourab HS (1999) Folding pattern of the a-crystallin domain in αA-crystallin determined by site-directed spin labeling. J Mol Biol 294(2):561–577
84. Hanson P, Anderson DJ, Martinez G, Millhauser G, Formaggio F, Crisma M, Toniolo C, Vita C (1998) Electron spin resonance and structural analysis of water soluble, alanine-rich peptides incorporating TOAC. Mol Phys 95(5):957–966
85. Xiao W, Poirier MA, Bennett MK, Shin Y-K (2001) The neuronal t-SNARE complex is a parallel four-helix bundle. Nat Struct Biol 8(4):308–311
86. Banham JE, Baker CM, Ceola S, Day IJ, Grant GH, Groenen EJJ, Rodgers CT, Jeschke G, Timmel CR (2008) Distance measurements in the borderline region of applicability of CW EPR and DEER: a model study on a homologous series of spin-labelled peptides. J Magn Reson 191(2):202–218
87. Lovett JE, Bowen AM, Timmel CR, Jones MW, Dilworth JR, Caprotti D, Bell SG, Wong LL, Harmer J (2009) Structural information from orientationally selective DEER spectroscopy. Phys Chem Chem Phys 11(31):6840–6848
88. Hahn EL (1950) Spin echoes. Phys Rev 80(4):580–594
89. Mims WB (1972) Envelope modulation in spin-echo experiments. Phys Rev B-Solid State 5(7):2409–2419
90. Mims WB, Peisach J (1978) Nuclear modulation effect in electron-spin echoes for complexes of Cu2+ and imidazole with N-14 and N-15. J Chem Phys 69(11):4921–4930
91. Schweiger A, Jeschke G (2001) Principles of pulse electron paramagnetic resonance. Oxford University Press, Oxford
92. Dikanov SA, Tsvetkov YD (1992) Electron spin echo envelope modulation (ESEEM) spectroscopy. CRC Press, Boca Raton
93. Misra SK, Borbat PP, Freed JH (2009) Calculation of double-quantum-coherence two-dimensional spectra: distance measurements and orientational correlations. Appl Magn Reson 36(2–4):237–258

94. Ernst RR, Bodenhausen G, Wokaun A (1987) Principles of nuclear magnetic resonance in one and two dimensions. The international series of monographs on chemistry. Clarendon, Oxford
95. Slichter CP (1990) Principles of magnetic resonance, 3rd edn. Springer, Berlin
96. Cavanagh J, Fairbrother WJ, Palmer AG III, Skelton NJ (1996) Protein NMR spectroscopy: principles and practice. Protein NMR spectroscopy: principles and practice. Academic, San Diego
97. Corio PL (1966) Structure of high-resolution NMR spectra. Academic, New York
98. Bowman MK, Maryasov AG (2007) Dynamic phase shifts in nanoscale distance measurements by double electron electron resonance (DEER). J Magn Reson 185 (2):270–282
99. Sorensen OW, Eich GW, Levitt MH, Bodenhausen G, Ernst RR (1983) Product operator-formalism for the description of NMR pulse experiments. Prog Nucl Magn Reson Spectrosc 16:163–192
100. Saxena S, Freed JH (1996) Double quantum two-dimensional Fourier transform electron spin resonance: distance measurements. Chem Phys Lett 251(1):102–110
101. Borbat PP, Freed JH (2007) Pro's and con's of pulse dipolar ESR: DQC and DEER. EPR Newslett 17(2–3):21–33
102. Saxena S, Freed JH (1997) Theory of double quantum two-dimensional electron spin resonance with application to distance measurements. J Chem Phys 107(5):1317–1340
103. Libertini LJ, Griffith OH (1970) Orientation dependence of electron spin resonance spectrum of di tert butyl nitroxide. J Chem Phys 53(4):1359–1367
104. Maryasov AG, Tsvetkov YD (2000) Formation of the pulsed electron–electron double resonance signal in the case of a finite amplitude of microwave fields. Appl Magn Reson 18(4):583–605
105. Milov AD, Ponomarev AB, Tsvetkov YD (1984) Electron–electron double resonance in electron spin echo: model biradical systems and the sensitized photolysis of decalin. Chem Phys Lett 110(1):67–72
106. Raitsimring A (2000) Distance measurements in biological systems by EPR. In: Berliner LJ, Eaton GR, Eaton SS (eds) Biological magnetic resonance, vol 19. Kluwer, New York, pp 385–459
107. Pannier M, Veit S, Godt A, Jeschke G, Spiess HW (2000) Dead-time free measurement of dipole-dipole interactions between electron spins. J Magn Reson 142(2):331–340
108. Weber A, Schiemann O, Bode B, Prisner TF (2002) PELDOR at S- and X-band frequencies and the separation of exchange coupling from dipolar coupling. J Magn Reson 157(2):277–285
109. Milov AD, Tsvetkov YD (1997) Double electron–electron resonance in electron spin echo. Conformations of spin-labeled poly-4-vinylpyridine in glassy solutions. Appl Magn Reson 12(4):495–504
110. Milov AD, Salikhov KM, Tsvetkov YD (1973) Phase relaxation of hydrogen atoms stabilized in an amorphous matrix. Soviet Phys-Solid State 15:802–806
111. Raitsimring AM, Salikhov KM, Umanskii BA, Tsvetkov YD (1974) Instantaneous diffusion in the electron spin echo of paramagnetic centers stabilized in solid matrixes. Fizika Tverdogo Tela (Sankt-Peterburg) 16(3):756–766
112. Lindgren M, Eaton GR, Eaton SS, Jonsson B-H, Hammarstrom P, Svensson M, Carlsson U (1997) Electron spin echo decay as a probe of aminoxyl environment in spin-labeled mutants of human carbonic anhydrase II. J Chem Soc Perkin Trans 2(12):2549–2554
113. Zecevic A, Eaton GR, Eaton SS, Lindgren M (1998) Dephasing of electron spin echoes for nitroxyl radicals in glassy solvents by non-methyl and methyl protons. Mol Phys 95 (6):1255–1263
114. Huber M, Lindgren M, Hammarstrom P, Martensson L-G, Carlsson U, Eaton GR, Eaton SS (2001) Phase memory relaxation times of spin labels in human carbonic anhydrase II: pulsed EPR to determine spin label location. Biophys Chem 94(3):245–256

115. Bartucci R, Erilov DA, Guzzi R, Sportelli L, Dzuba SA, Marsh D (2006) Time-resolved electron spin resonance studies of spin-labelled lipids in membranes. Chem Phys Lipids 141 (1–2):142–157
116. Georgieva ER, Ramlall TF, Borbat PP, Freed JH, Eliezer D (2010) The lipid-binding domain of wild type and mutant alpha-synuclein: compactness and interconversion between the broken and extended helix forms. J Biol Chem 285(36):28261–28274
117. Nevzorov AA, Freed JH (2001) A many-body analysis of the effects of the matrix protons and their diffusional motion on electron spin resonance line shapes and electron spin echoes. J Chem Phys 115(6):2416–2429
118. Georgieva ER, Ramlall TF, Borbat PP, Freed JH, Eliezer D (2008) Membrane-bound alpha-synuclein forms an extended helix: long-distance pulsed ESR measurements using vesicles, bicelles, and rodlike micelles. J Am Chem Soc 130(39):12856–12857
119. Ward R, Bowman A, Sozudogru E, El-Mkami H, Owen-Hughes T, Norman DG (2010) EPR distance measurements in deuterated proteins. J Magn Reson 207(1):164–167
120. Carr HY, Purcell EM (1954) Effects of diffusion on free precession in nuclear magnetic resonance experiments. Phys Rev 94(3):630–638
121. Lueders P, Jeschke G, Yulikov M (2011) Double electron–electron resonance measured between Gd(3+) ions and nitroxide radicals. J Phys Chem Lett 2(6):604–609
122. Borbat PP, Freed JH (2007) Measuring distances by pulsed dipolar ESR spectroscopy: spin-labeled histidine kinases. In: Simon MI, Crane BR, Crane A (eds) Two-component signaling systems, Pt B, vol. 423. Methods in enzymology. Elsevier, San Diego, pp 52–116
123. Venters RA, Farmer BT II, Fierke CA, Spicer LD (1996) Characterizing the use of perdeuteration in NMR studies of large proteins: 13C, 15 N and 1H assignments of human carbonic anhydrase II. J Mol Biol 264(5):1101–1116
124. Horst R, Bertelsen EB, Fiaux J, Wider G, Horwich AL, Wuthrich K (2005) Direct NMR observation of a substrate protein bound to the chaperonin GroEL. Proc Natl Acad Sci USA 102(36):12748–12753
125. Hamel DJ, Dahlquist FW (2005) The contact interface of a 120 kD CheA-CheW complex by methyl TROSY interaction spectroscopy. J Am Chem Soc 127(27):9676–9677
126. Jeschke G, Koch A, Jonas U, Godt A (2002) Direct conversion of EPR dipolar time evolution data to distance distributions. J Magn Reson 155(1):72–82
127. Bowman MK, Maryasov AG, Kim N, DeRose VJ (2004) Visualization of distance distribution from pulsed double electron–electron resonance data. Appl Magn Reson 26(1–2):23–39
128. Lee S, Budil DE, Freed JH (1994) Theory of two-dimensional Fourier transform electron spin resonance for ordered and viscous fluids. J Chem Phys 101(7):5529–5558
129. Bhatnagar J, Sircar R, Borbat PP, Freed JH, Crane BR (2012) Self-association of the histidine kinase CheA as studied by pulsed dipolar ESR spectroscopy. Biophys J 102(9):2192–2201
130. Marko A, Margraf D, Cekan P, Sigurdsson ST, Schiemann O, Prisner TF (2010) Analytical method to determine the orientation of rigid spin labels in DNA. Phys Rev E 81(2), Article Number: 021911
131. Schiemann O, Cekan P, Margraf D, Prisner TF, Sigurdsson ST (2009) Relative orientation of rigid nitroxides by PELDOR: beyond distance measurements in nucleic acids. Angew Chem Int Ed 48(18):3292–3295
132. Endeward B, Butterwick JA, MacKinnon R, Prisner TF (2009) Pulsed electron–electron double-resonance determination of spin-label distances and orientations on the tetrameric potassium ion channel KcsA. J Am Chem Soc 131(42):15246–15250
133. Fawzi NL, Fleissner MR, Anthis NJ, Kalai T, Hideg K, Hubbell WL, Clore GM (2011) A rigid disulfide-linked nitroxide side chain simplifies the quantitative analysis of PRE data. J Biomol NMR 51(1–2):105–114
134. Fleissner MR, Bridges MD, Brooks EK, Cascio D, Kalai T, Hideg K, Hubbell WL (2011) Structure and dynamics of a conformationally constrained nitroxide side chain and applications in EPR spectroscopy. Proc Natl Acad Sci USA 108(39):16241–16246

135. Ruthstein S, Potapov A, Raitsimring AM, Goldfarb D (2005) Double electron electron resonance as a method for characterization of micelles. J Phys Chem B 109(48):22843–22851
136. Bode BE, Margraf D, Plackmeyer J, Durner G, Prisner TF, Schiemann O (2007) Counting the monomers in nanometer-sized oligomers by pulsed electron – electron double resonance. J Am Chem Soc 129(21):6736–6745
137. Jeschke G, Sajid M, Schulte M, Godt A (2009) Three-spin correlations in double electron–electron resonance. Phys Chem Chem Phys 11(31):6580–6591
138. Nevzorov AA, Freed JH (2001) Direct-product formalism for calculating magnetic resonance signals in many-body systems of interacting spins. J Chem Phys 115(6):2401–2415
139. Jeschke G, Polyhach Y (2007) Distance measurements on spin-labelled biomacromolecules by pulsed electron paramagnetic resonance. Phys Chem Chem Phys 9(16):1895–1910
140. Chandrasekhar S (1943) Stochastic problems in physics and astronomy. Rev Mod Phys 15(1):1–89
141. Milov AD, Tsvetkov YD (2000) Charge effect on relative distance distribution of Fremy's radical ions in frozen glassy solution studied by PELDOR. Appl Magn Reson 18(2):217–226
142. Georgieva ER, Roy AS, Grigoryants VM, Borbat PP, Earle KA, Scholes CP, Freed JH (2012) Effect of freezing conditions on distances and their distributions derived from double electron electron resonance (DEER): a study of doubly-spin-labeled T4 lysozyme. J Magn Reson 216:69–77
143. Klauder JR, Anderson PW (1962) Spectral diffusion decay in spin resonance experiments. Phys Rev 125:912–932
144. Dzikovski BG, Borbat PP, Freed JH (2011) Channel and nonchannel forms of spin-labeled gramicidin in membranes and their equilibria. J Phys Chem B 115(1):176–185
145. Milov AD, Maryasov AG, Tsvetkov YD, Raap J (1999) Pulsed ELDOR in spin-labeled polypeptides. Chem Phys Lett 303(1, 2):135–143
146. Zou P, Mchaourab HS (2010) Increased sensitivity and extended range of distance measurements in spin-labeled membrane proteins: Q-band double electron–electron resonance and nanoscale bilayers. Biophys J 98(6):L18–L20
147. Borbat PP, Crepeau RH, Freed JH (1997) Multifrequency two-dimensional Fourier transform ESR: an X/Ku-band spectrometer. J Magn Reson 127(2):155–167
148. Gorcester J, Freed JH (1986) Two-dimensional Fourier transform ESR spectroscopy. J Chem Phys 85(9):5375–5377
149. Fauth JM, Schweiger A, Braunschweiler L, Forrer J, Ernst RR (1986) Elimination of unwanted echoes and reduction of dead time in 3-pulse electron spin-echo spectroscopy. J Magn Reson 66(1):74–85
150. Hoult DI, Richards RE (1975) Critical factors in design of sensitive high-resolution nuclear magnetic-resonance spectrometers. Proc R Soc Lond Ser A-Math Phys Eng Sci 344 (1638):311–340
151. Yang ZY, Liu YP, Borbat P, Zweier JL, Freed JH, Hubbell WL (2012) Pulsed ESR dipolar spectroscopy for distance measurements in immobilized spin labeled proteins in liquid solution. J Am Chem Soc 134(24):9950–9952
152. Crepeau RH, Dulcic A, Gorcester J, Saarinen TR, Freed JH (1989) Composite pulses in time-domain ESR. J Magn Reson 84(1):184–190
153. Levitt MH (1982) Symmetrical composite pulse sequences for NMR population-inversion 1. Compensation of radiofrequency field inhomogeneity. J Magn Reson 48(2):234–264
154. Levitt MH (1986) Composite pulses. Prog Nucl Magn Reson Spectrosc 18:61–122
155. Levitt MH, Freeman R (1979) NMR population-inversion using a composite pulse. J Magn Reson 33(2):473–476
156. Shaka AJ, Pines A (1987) Symmetrical phase-alternating composite pulses. J Magn Reson 71 (3):495–503
157. Zax DB, Goelman G, Vega S (1988) Amplitude-modulated composite pulses. J Magn Reson 80(2):375–382

158. Zax DB, Vega S (1989) Broad-band excitation pulses of arbitrary flip angle. Phys Rev Lett 62(16):1840–1843
159. Baum J, Tycko R, Pines A (1985) Broad-band and adiabatic inversion of a 2-level system by phase-modulated pulses. Phys Rev A 32(6):3435–3447
160. Geen H, Freeman R (1991) Band-selective radiofrequency pulses. J Magn Reson 93(1):93–141
161. Murdoch JB, Lent AH, Kritzer MR (1987) Computer-optimized narrow-band pulses for multislice imaging. J Magn Reson 74(2):226–263
162. Silver MS, Joseph RI, Hoult DI (1985) Selective spin inversion in nuclear magnetic-resonance and coherent optics through an exact solution of the Bloch-Riccati equation. Phys Rev A 31(4):2753–2755
163. Warren WS (1984) Effects of arbitrary laser or NMR pulse shapes on population-inversion and coherence. J Chem Phys 81(12):5437–5448
164. Salikhov KM, Schneider DJ, Saxena S, Freed JH (1996) A theoretical approach to the analysis of arbitrary pulses in magnetic resonance. Chem Phys Lett 262(1, 2):17–26
165. Suzuki M (1985) Decomposition formulas of exponential operators and lie exponentials with some applications to quantum mechanics and statistical physics. J Math Phys 26:601–612
166. Trotter HF (1959) On the product of semi-groups of operators. Proc Am Math Soc 10(4):545–551
167. Devasahayam N, Murugesan R, Matsumoto K, Mitchell JB, Cook JA, Subramanian S, Krishna MC (2004) Tailored sinc pulses for uniform excitation and artifact-free radio frequency time-domain EPR imaging. J Magn Reson 168(1):110–117
168. Rinard GA, Quine RW, Song R, Eaton GR, Eaton SS (1999) Absolute EPR spin echo and noise intensities. J Magn Reson 140(1):69–83
169. Mims WB (1965) Electron echo methods in spin resonance spectrometry. Rev Sci Instrum 36(10):1472–1479
170. Hara H, Tenno T, Shirakawa M (2007) Distance determination in human ubiquitin by pulsed double electron–electron resonance and double quantum coherence ESR methods. J Magn Reson 184(1):78–84
171. Borbat PP, Georgieva ER, Freed JH (2012) Improved sensitivity for long-distance measurements in biomolecules: five-pulse double electron-electron resonance. J Phys Chem Lett. doi: 10.1021/jz301788n
172. Ghimire H, McCarrick RM, Budil DE, Lorigan GA (2009) Significantly improved sensitivity of Q-band PELDOR/DEER experiments relative to X-band is observed in measuring the intercoil distance of a leucine zipper motif peptide (GCN4-LZ). Biochemistry 48(25):5782–5784
173. Kaminker I, Florent M, Epel B, Goldfarb D (2011) Simultaneous acquisition of pulse EPR orientation selective spectra. J Magn Reson 208(1):95–102
174. Reginsson GW, Hunter RI, Cruickshank PAS, Bolton DR, Sigurdsson ST, Smith GM, Schiemann O (2012) W-band PELDOR with 1 kW microwave power: molecular geometry, flexibility and exchange coupling. J Magn Reson 216:175–182
175. Borbat PP, Surendhran K, Bortolus M, Zou P, Freed JH, Mchaourab HS (2007) Conformational motion of the ABC transporter MsbA induced by ATP hydrolysis. PLoS Biol 5(10):2211–2219
176. Yagi H, Banerjee D, Graham B, Huber T, Goldfarb D, Otting G (2011) Gadolinium tagging for high-precision measurements of 6 nm distances in protein assemblies by EPR. J Am Chem Soc 133(27):10418–10421
177. Potapov A, Song Y, Meade TJ, Goldfarb D, Astashkin AV, Raitsimring A (2010) Distance measurements in model bis-Gd(III) complexes with flexible “bridge”. Emulation of biological molecules having flexible structure with Gd(III) labels attached. J Magn Reson 205(1):38–49
178. Song Y, Meade TJ, Astashkin AV, Klein EL, Enemark JH, Raitsimring A (2011) Pulsed dipolar spectroscopy distance measurements in biomacromolecules labeled with Gd(III) markers. J Magn Reson 210(1):59–68

Struct Bond (2014) 152: 83–120
DOI: 10.1007/430_2011_61

Published online: 15 November 2011

Interpretation of Dipolar EPR Data in Terms of Protein Structure

Gunnar Jeschke

Abstract Distances in proteins in the nanometer range can be measured by the combination of site-directed spin labeling and dipolar EPR. The primary data are related to the time evolution of spin label magnetization under the dipole–dipole interaction with other spin labels within the same or within the neighboring protein molecules. The information sought are conclusions on protein structure or structural changes. The link between primary data and these conclusions are distances between backbone atoms in the protein. We discuss which experimental conditions allow for the most precise data analysis in terms of distance distributions and describe techniques for such data analysis. Furthermore, methods are reviewed for prediction of conformational distribution of the spin label, which is required to infer backbone–backbone distances from label–label distances.

Keywords DEER · Distance measurements · Rotamer libraries · Structure determination · Tikhonov regularization

Contents

G. Jeschke (✉)
Laboratory for Physical Chemistry, ETH Zürich, Wolfgang-Pauli-Strasse 10, 8093 Zürich, Switzerland
e-mail: gjeschke@ethz.ch

Abbreviations

DEER	Double electron electron resonance
EPR	Electron paramagnetic resonance
ESEEM	Electron spin echo envelope modulation
IASL	Iodoacetamido-PROXYL spin label
MD	Molecular dynamics
MTSL	Methanethiosulfonato spin label
PDB	Protein data bank

1 Introduction

Dipolar electron paramagnetic resonance (EPR) measurements with DEER (synonymously PELDOR) [1–3], double-quantum [4, 5], or SIFTER [6] experiments are sensitive to spin–spin distances in the range between 1.8 and 5 nm, in favorable cases down to 1.5 and up to 8 nm [7–10]. This range matches the dimension of proteins and moderately sized protein complexes. The measurements do not require regular packing of the molecules as is the case for X-ray crystallography and high-resolution electron microscopy, and they do not require fast tumbling as is the case for high-resolution liquid-state NMR. Packing heterogeneities can be tolerated, which would degrade resolution in solid-state NMR spectra [11]. Samples can be optically opaque and may contain molecules that would quench fluorescence.

These features of dipolar EPR provide much more variability of sample composition than is available with any other technique that provides structural information on proteins. Hence, physiological environments can be mimicked more closely and the response to substrates or other interaction partners can be probed more easily [12, 13]. Furthermore, as a probe technique dipolar EPR avoids crowding of spectra with increasing protein size, so that there is no intrinsic limit to the size of the protein or protein complex under study.

The advantages of dipolar EPR for structural studies on proteins are partially mitigated by the disadvantage that each spin–spin distance to be determined requires a new protein mutant to be generated, expressed, purified, spin labeled, and measured. In any structural study, EPR distance constraints are thus sparse constraints. Accordingly, errors in the individual constraints average only to a limited extent when deriving a model of the structure or of structural change. Structural studies of proteins by dipolar EPR thus require that distance constraints are determined from the primary data with the highest possible precision and that their reliability and precision is known. This causes higher requirements for data analysis than, for instance, with NMR techniques, where a large number of constraints compensate for relatively poor precision – and in a few cases questionable reliability – of individual constraints.

A second disadvantage of dipolar EPR arises in the common case where distances are measured between spin labels rather than native paramagnetic centers. The spin label side group is slightly larger than the side groups of native amino acid residues and needs to be somewhat flexible to fit into the native protein structure. Since the information sought is on structure and structural changes of the protein backbone, it was recognized early that the deviation of spin position from the backbone needs to be accounted for [14]. A later, more detailed study showed that flexibility of the spin label side group must be modeled to interpret label-to-label distances with confidence [15]. Imperfections of such modeling introduce additional uncertainty, which is again problematic because of the sparsity of constraints. Interpretation of dipolar EPR data of spin labels in terms of protein structure thus requires a systematic approach for estimating this uncertainty.

In this chapter, we discuss data processing and modeling techniques that are required to derive conclusions of protein structure or structural changes from primary dipolar EPR data. Since the success of this endeavor crucially depends on data quality, we also consider those decisions in selecting sites for spin labeling and measurement conditions that can have a big impact on suitability of the data for further processing. Most of the discussion relates to the most popular four-pulse DEER experiment [3, 16], but where necessary remarks are made on double-quantum EPR [5]. Discussion of data analysis problems and spin label conformations is kept as general as possible. Where reference to software packages is required, we focus on DeerAnalysis 2011 [17, 18] (http://www.epr.ethz.ch/software/index) and MMM 2010 (http://www.epr.ethz.ch/software/index). All examples are based on simulated data, so that the theoretical result of data analysis is always known.

The chapter is organized as follows. Section 2 considers the information contained in dipolar EPR data starting from general mathematical formulas. Limitations of common assumptions in data analysis are pointed out. Requirements on site selection and measurement conditions are discussed in Sect. 3. In many cases, a label-to-label distance distribution is an important intermediate result. How to obtain such a distance distribution and how to estimate its reliability is the subject of Sect. 4. Finally, Sect. 5 discusses interpretation of the distance distribution or the primary data in terms of backbone structure or structural changes. The chapter concludes with an outlook that addresses open questions and current limitations.

2 Information Content of Dipolar EPR Data

2.1 Theory

Dipolar EPR is usually performed as a constant-time deadtime-free measurement. The data can then be normalized at the time origin $t = 0$ of dipolar evolution and all oscillations and decay of the signal observed at later times are due to electron spin–electron spin couplings. The only exceptions are nuclear modulations, which can be partially averaged (Sect. 3.5), effects from overlapping pump and observer excitation bands, which should be avoided (Sect. 3.7), and signal variation due to imperfections in spectrometer electronics. These electronic imperfections are mostly canceled by a $[(+x)-(-x)]$ phase cycle on the first observer pulse, which also eliminates receiver offset and thus ensures that the signal tends to zero for $t \rightarrow \infty$. The following expressions and all data processing software assume that such a phase cycle is applied. The general form of the normalized dipolar evolution function for a DEER experiment is then given by

$$D(t) = \frac{1}{N} \sum_{o=1}^{N} \left(\prod_{p \neq o} \left(1 - \lambda_p \left(1 - \cos \omega_{op} t\right)\right) \right), \tag{1}$$

where index o runs over all observer spins in the sample and index p runs over all pumped spins (both intra and inter nano-object spins are counted). The subsets of observed and pumped spins may differ if the sample contains paramagnetic species with different EPR spectra. The modulation depth λ_p and spin–spin coupling between the observed and pumped spins ω_{op} depend on orientation of the spin system in the magnetic field. If the coupling between the two electron spins can be described as a coupling between two point dipoles (vide infra), orientation dependence of ω_{op} is fully characterized by the angle θ between the spin–spin vector and the static magnetic field, while the inversion efficiency λ_p of the pump pulse is generally a complicated function of the spin Hamiltonians of the two electron spins, three Euler angles that characterize the relative orientation of the molecular

coordinate frames of these two spins and two polar angles that characterize the direction of the magnetic field in the molecular frame of one of these spins.

Now we assume that the sample consists of M congeneric nano-objects that contain n spins each ($N = nM$). Unless stated otherwise, we consider these nano-objects in the following as spin-labeled protein molecules or protein complexes and n is the number of labels per molecule or complex. We further assume that the sample is sufficiently dilute so that typical distances between spins in different nano-objects are much longer than distances within the same nano-object. We can then separate the right hand side of (1) into a background factor $B(t)$ due to interaction of observer spins with spins in other nano-objects and a form factor $F(t)$ due to interactions within the same object

$$D(t) = B(t)F(t). \tag{2}$$

The term *form factor* is chosen in analogy with the same separation of contributions in scattering techniques. The background factor is analogous to the structure factor in scattering. Here, the term from scattering is not used to avoid confusion. The information on protein structure is contained in the form factor $F(t)$, which is given by

$$F(t) = \frac{1}{n}\sum_{o=1}^{n}\left(\prod_{p\neq o}\left(1-\lambda_p\left(1-\cos\omega_{op}t\right)\right)\right). \tag{3}$$

Although (3) formally looks the same as (1), the two indices now run over only those spins associated with each nano-object, which is clearly far fewer spins. Note that (3) corresponds to only a single orientation of the nano-object with respect to the magnetic field.

In a next step, we assume that the orientation dependence of λ_p can be averaged and that such averaging results in the same value λ for all spin pairs within the nano-object. This requires that all spins have very similar EPR spectra and that orientation selection can be neglected or experimentally averaged (Sect. 3.6). For nitroxide spin labels in proteins at X-band frequencies, this is usually a good approximation. Then it follows from (3) that the dipolar oscillations of the form factor have a modulation depth (see Fig. 1a, b)

$$\Delta = 1-(1-\lambda)^{n-1} \tag{4}$$

with a fraction

$$f_p = \lambda(1-\lambda)^{n-2} \tag{5}$$

corresponding to oscillations with the basic dipolar frequencies ω_{op}. The fraction $\Delta - f_p$ of the form factor oscillates with sum and difference combination frequencies and leads to artifacts if it cannot be separated [19]. For a doubly labeled nano-object

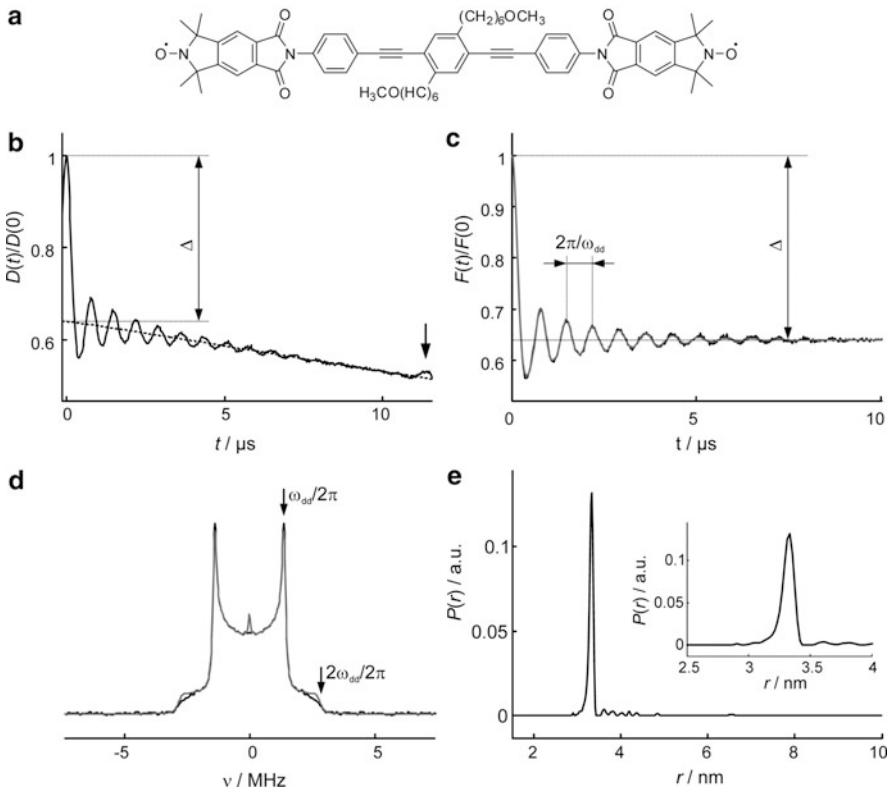

Fig. 1 Analysis of primary DEER data in terms of a distance distribution. (**a**) Model compound. (**b**) Normalized primary DEER data of the model compound (*solid line*) and background function $B(t)$ (*dashed line*). The modulation depth Δ is indicated. The *arrow* marks an end artifact caused by overlap of pump and observer excitation bands. Data were analyzed only for $t \leq 10$ µs. (**c**) Form factor (*black*) obtained by dividing $V(t)$ by $B(t)$ and subsequent normalization at $t = 0$. Modulation depth Δ and period of the dipolar oscillation are indicated. The *gray line* is the simulated form factor corresponding to the distance distribution obtained by Tikhonov regularization. (**d**) Dipolar spectrum (*black*) obtained by subtracting $(1 - \Delta)$ from $F(t)$ and subsequent Fourier transformation. The characteristic frequencies are indicated. The *gray line* is the simulated spectrum corresponding to the distance distribution obtained by Tikhonov regularization. (**e**) Distance distribution obtained by Tikhonov regularization. The *inset* shows the peak at higher resolution

($n = 2$), we have $\Delta = \lambda$ and $f_p = \lambda$ and no such combination frequencies are observed.

The form factor then corresponds to the *isolated pair case*, which is considered in detail below. When the pair contribution for a multispin nano-object can be separated [19], the normalized form factor for this object is the average of the isolated pair form factors. At the expense of signal-to-noise ratio, such separation can be approximated by intentionally decreasing inversion efficiency λ (Sect. 3.3). For a singly-labeled nano-object ($n = 1$), (5) is invalid. We then have $\Delta = 0$,

$F(t) \equiv 1$ and thus $D(t) = B(t)$. This allows for experimental determination of the background function corresponding to a single site.

We now consider the isolated pair case. Now the product in (3) contains only a single factor and the two terms of the sum are equal ($\omega_{12} = \omega_{21} = \omega_{dd}$). The average over all orientations of the nano-object with respect to the magnetic field is given by

$$\langle F(t) \rangle = 1 - \lambda + \lambda \int_0^1 \cos\left[\left(3x^2 - 1\right)\omega_{dd} t\right] \mathrm{d}x, \tag{6}$$

where $x = \cos\theta$ and

$$\omega_{dd} = \frac{\mu_0}{4\pi\hbar} \frac{g_1 g_2 \mu_B^2}{r^3} \tag{7}$$

is the angular dipolar frequency that depends on distance r between the two spins considered as point dipoles. If only one well-defined pair distance within the DEER distance range is present in the sample, ω_{dd} can be directly assigned in a dipolar spectrum (Fig. 1c) or determined from the period of the long-lived oscillation in the form factor (Fig. 1b).

The point-dipole approximation is valid for nitroxide labels at distances above 1.5 nm, but may be questionable for organic radical cofactors in proteins if these feature an extended π electron system. Furthermore, (7) neglects exchange coupling [20], which is permitted for solid nonconducting matrices at distances longer than 1.5 nm unless a fully conjugated pathway of bonds exists between the two labels [21]. For nitroxide spin labels, $g_1 \approx g_2 \approx 2.006$ is a good approximation, corresponding to a dipolar frequency $\omega_{dd}/(2\pi) = 52.23/r^3$ MHz. Since x^2 varies least near $x = 0$, angular frequency ω_{dd}, corresponding to $\theta = 90°$, is the dominating dipolar oscillation frequency.

Equation (6) is valid also for form factors obtained by double-quantum [5] or SIFTER [6] measurements on dilute nano-objects with two electron spins per object. All equations before do not apply in this case since the form factor of multispin systems does not factorize into pair contributions for these single-frequency techniques. For the same reason, background correction is empirical in double-quantum EPR and cannot be based on the theory explained in the following.

For homogeneously distributed nano-objects with a size much smaller than their typical distance, the background function is given by

$$B_{\mathrm{hom}}(t) = \exp\left(-\frac{2\pi\mu_0 g^2 \mu_B^2}{9\sqrt{3}\hbar} N_A c \lambda t\right) \tag{8}$$

where g is a mean g-value of all remote electron spins, N_A is Avogadro's constant, and c the spin concentration in mol L^{-1}. If the distribution of nano-objects is confined, for instance, to two dimensions for a membrane protein in a bilayer, the background factor can often be approximated by a stretched exponential function

$B(t) \approx \exp(-kt^{d/3})$, where k increases with concentration and d is the dimensionality of the confined distribution [22]. Since short distances are necessarily underrepresented in a distribution of objects with long fixed pair distances, apparent background dimensions $d > 3$ may also be observed. For instance, the background function shown as a dashed line in Fig. 1a corresponds to $d = 3.31$ and provides a slightly better fit than the theoretically expected function with $d = 3$. For peptides or membrane proteins in unilamellar vesicles d is also slightly larger than 2 due to this effect as well as curvature and disorder of the bilayer.

To obtain the information on the structure of the nano-object, the primary dipolar evolution data $D(t)$ is preprocessed in the following way:

- Fit of the assumed functional form of $B(t)$ to $D(t)$ for times in the interval $t = t_{\mathrm{bckg}}$ to t_{max} (at most the last point of the time-domain trace), where the form factor has largely or completely decayed
- Computation of the form factor as $\langle F(t)\rangle = D(t)/B(t)$ and computation of the modulation depth $\Delta = 1 - B(0)$
- Computation of a reduced form factor $f(t)$ without the constant contribution as $f(t) = (\langle F(t)\rangle - \Delta)/(1 - \Delta)$

In the example shown in Fig. 1a, $t_{\mathrm{bckg}} = 2.208$ µs gave the best background fit. To avoid contributions from end artifacts (arrow) to the distance distribution, t_{max} was limited to 10 µs. In the following, we discuss the information inherent in this reduced form factor $f(t)$.

2.2 Mean Distance

In general, distance r in (7) is distributed. The dominating frequency $\langle\omega_{dd}\rangle$ of the dipolar evolution function corresponds to a mean distance. Strictly speaking, the averaging is over r^{-3}, however in the usual cases where the standard deviation σ_r is much smaller than the mean distance $\langle r\rangle$, the mean frequency $\langle\omega_{dd}\rangle$ is a good measure for the mean distance.

The width and shape of the distance distribution $P(r)$ hardly influence the initial part of the reduced form factor $f(t)$, as demonstrated in Fig. 2 for three example distance distributions with the same mean distance $\langle r\rangle = 3$ nm. Accordingly, a good estimate of $\langle r\rangle$ can be obtained from the half-life time $t_{1/2}$ when the reduced form factor has decayed to 0.5 (Fig. 2b) (for similar considerations, see [23]). For measurements between two nitroxide spin labels we find $\langle r\rangle \approx 5(t_{1/2}/0.48\ \mu\mathrm{s})^{1/3}$ nm. This formula holds quite well even for much broader distributions (data not shown), but may become imprecise for bimodal distributions.

Such behavior suggests that the mean distance can be inferred from less than half of a dipolar oscillation. In practice, the limit is set by the necessity of background correction, which requires data at $t > t_{\mathrm{bckg}}$ for a reliable fit of $B(t)$. Analysis of simulated test data has shown that a maximum dipolar evolution time of $t_{\mathrm{max}} = 2$ µs is usually sufficient to determine mean distances up to $\langle r\rangle_{\mathrm{max}} = 5$ nm. Note that t_{max} scales with $\langle r\rangle_{\mathrm{max}}^3$. To determine a mean distance of 8 nm with some confidence thus requires dipolar evolution data up to at least 8.2 µs.

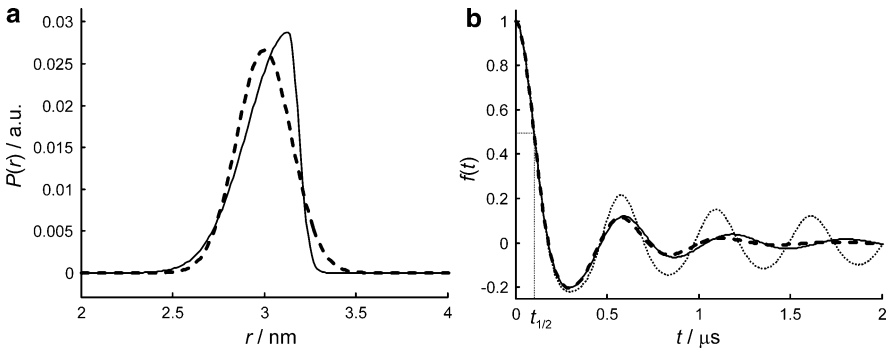

Fig. 2 Model distance distributions and corresponding reduced form factors. (**a**) Gaussian (*dashed line*) and asymmetric (*solid line*) distance distributions with the same mean distance $\langle r \rangle = 3$ nm and standard deviation $\sigma_r = 0.15$ nm. (**b**) Reduced form factors corresponding to the Gaussian (*dashed line*) and asymmetric (*solid line*) distance distributions. The *dotted line* corresponds to a narrow Gaussian distribution with standard deviation $\sigma_r = 0.01$ nm. Time $t_{1/2}$ when the reduced form factor has decayed to half its initial value provides an estimate of the mean distance that is rather insensitive to width and shape of the distance distribution

Longer distances (for instance, up to 6 nm for $t_{max} = 2$ µs) still lead to a dipolar evolution function $D(t)$ that cannot be fitted exclusively by a background function $B(t)$. In this situation, it is possible to state that spin pairs with long distances must exist in the nano-object, although the distance cannot be specified. Note, however, that in the presence of shorter distances, such long distances may be *completely* suppressed by background correction. This is because the wing of the distribution at shorter distances and the background function together can simulate such a contribution.

2.3 Width of the Distance Distribution

As is also apparent from Fig. 2, a difference in the width (standard deviation σ_r) of the distance distribution as large as 5% of the mean distance is hardly visible before the second zero crossing of the reduced form factor. Indeed, reliable determination of σ_r at $t_{max} = 2$ µs is possible only up to mean distances of 4 nm. This limit corresponds to about 1.5 oscillations. Determination of the width is also less robust than determination of the mean distance with respect to noise and uncertainties in background correction [17].

2.4 Shape of the Distance Distribution

Interpretation of the shape of a distance distribution, for instance, of asymmetries or shoulders, requires low-noise data with long maximum dipolar evolution time t_{max},

as is apparent from Fig. 2. Even after 1.5 oscillations, the effect of asymmetry is barely visible if mean distance and width are the same. As a rule of thumb, interpretation of the shape at $t_{max} = 2$ µs is possible up to mean distances of 3 nm, corresponding to the situation shown in Fig. 2.

Bimodality of a distance distribution may be recognizable already at shorter maximum dipolar evolution times. This is shown in Fig. 3 for an example distance distribution with a mean distance of 5.24 nm and a standard deviation of 0.23 nm. The simulated reduced form factor was limited to 6 µs, rescaled to inversion efficiency $\lambda = 0.4$, and multiplied with a background function corresponding to a spin label concentration of roughly 200 µM. Pseudo-random numbers were added to simulate 0.5% noise with respect to maximum amplitude at $t = 0$ at a time increment $\Delta t = 8$ ns. The data were then reanalyzed using standalone versions of subroutines of DeerAnalysis 2011 [17, 18] (http://www.epr.ethz.ch/software/index). The occurrence of two components of the distance distribution as well as their approximate relative contributions is reproducibly detected from simulated data with different pseudo-random noise.

2.5 Number of Spins

The number of spins n per nano-object is obtained by measuring the total modulation depth Δ and inverting (4). This requires that the inversion efficiency λ of the pump pulse is known. The inversion efficiency in turn can be determined by measuring the modulation depth for genuine biradicals, triradicals, and possibly

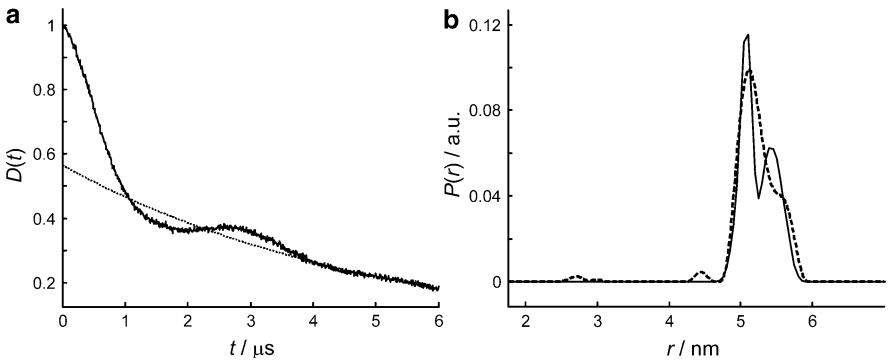

Fig. 3 Reproducibility of the shape of a model distance distribution (simulation). The original distance distribution stems from a rotamer simulation (Sect. 5.3) of site pair 249/318 in a monomer of carnitine transporter CaiT (PDB code 2WSX). (**a**) Simulated dipolar evolution function (noisy trace) with signal-to-noise ratio of 200 at $t = 0$ and time increment $\Delta t = 8$ ns. The *dotted line* is an exponential background fit with the optimum background fit range determined by the algorithm used in DeerAnalysis 2011 [17, 18] (http://www.epr.ethz.ch/software/index). (**b**) Original distance distribution (*solid line*) and distance distribution obtained by Tikhonov regularization of the simulated time-limited noisy data (*dashed line*)

tetraradicals [24, 25]. Such calibration is valid only for a given spectrometer and probehead and for a given length of the pump pulse. A calibration error may arise from different spectral lineshapes of the model compounds and spin-labeled proteins. Differences in relaxation behavior of the multiple labels can also limit the precision of this technique [25]. Due to the functional dependence of (4), the difference in modulation depth by adding another spin decreases with increasing number of spins. Thus, it may only be possible to derive a lower limit for the number of spins if this number is larger than four or five.

The number of spins can also be determined by analyzing the dependence of total modulation depth on pump pulse flip angle [19]. This technique does not require calibration, but may only be able to distinguish the cases of two and three coupled spins.

2.6 Local Concentration

The concentration of nano-objects can be determined from the background function $B(t)$ via (8) if the background function is an exponential. As in the case of spin counting (Sect. 2.5), calibration is required since pump inversion efficiency λ depends on spectrometer, probehead, and length of the pump pulse. The calibration is best done with a homogeneous solution of the same spin label in a similar environment to avoid errors due to different spectral lineshape in the range excited by the pump pulse.

Note, however, that micelle-forming detergents should not be used in such calibration measurements since the spin label would preferentially partition into the micelles. In general, the concentration c in (8) is a local concentration that is sensitive roughly to a range of 40 nm around the spin label. If a sample is heterogeneous with domain sizes on the order of 20 nm or larger, local concentration may deviate significantly from bulk concentration of the label.

3 Measurement Conditions for Optimum Data Analysis

3.1 Maximum Dipolar Evolution Time and Signal-to-Noise Ratio

A maximum dipolar evolution time $t_{max} = 2$ µs is sufficient for elucidating the shape of a distance distribution up to $r_{max,shape} = 3$ nm, for determining its width up to $r_{max,width} = 4$ nm, for measuring a mean distance up to $r_{max,mean} = 5$ nm, and for recognizing the presence of a longer distance in a nano-object in the absence of shorter distances up to $r_{max,detect} = 6$ nm. Depending on the biological question to be answered, it may be sufficient to determine only the mean distance, or mean distance and width. Furthermore, in many cases a hypothesis on the expected mean

distance r_{exp} can be derived from a model for the structure under investigation, preferably by including the label (Sects. 3.7 and 5.3). The required maximum dipolar evolution time can then be computed by

$$t_{\mathrm{max}} = 2\,\mu\mathrm{s} \cdot \left(\frac{r_{\mathrm{exp}}}{r_{\mathrm{max},i}}\right)^3, \tag{9}$$

where $r_{\mathrm{max},i}$ is one of the values $r_{\mathrm{max,shape}}$, $r_{\mathrm{max,width}}$, $r_{\mathrm{max,mean}}$, and $r_{\mathrm{max,detect}}$ defined above. Which of these values needs to be inserted depends on the problem at hand, i.e., on the precision of the information that is required to solve the problem. If no model of the structure is known beforehand, r_{exp} can be obtained from a preliminary measurement with the longest t_{max} that is attainable at reasonable signal-to-noise ratio. In a second measurement with high signal-to-noise ratio, t_{max} can then be adjusted appropriately.

The value predicted by (9) is not necessarily the optimum value. For a given total measurement time, the signal-to-noise ratio decreases roughly exponentially with t_{max} due to relaxational loss of observer echo amplitude. For a four-pulse DEER experiment with interpulse delays τ_1 and τ_2, we need to choose $\tau_2 > t_{\mathrm{max}}$ (since the experimental time trace cannot extend to times longer than τ_2). If the time increment Δt is kept fixed, the number of acquisitions for a given total measurement time is inversely proportional to t_{max} since the number of data points increases linearly with t_{max}. This leads to a square root loss in signal-to-noise ratio S. Assuming that the observer echo decays exponentially with phase memory time T_{m}, we find

$$S \propto \sqrt{\frac{\Delta t}{t_{\mathrm{max}}}} \exp\left(-\frac{2(\tau_1+\tau_2)}{T_{\mathrm{m}}}\right). \tag{10}$$

We now turn to the trade-off between acquiring data with high signal-to-noise ratio but short t_{max} and acquiring data with long t_{max} but poor signal-to-noise ratio. The relation between t_{max} and signal-to-noise ratio arises from scaling of observer echo intensity with approximately $\exp(-2t_{\mathrm{max}}/T_{\mathrm{m}})$. Typically, the values of t_{max} predicted by (9) are longer than T_{m} or at least of the same order. Therefore, any possibility of prolonging T_{m} should be utilized. Deuteration of the matrix [16, 26], for instance, of the cryoprotectant glycerol, of glycerol and water, or even of the protein [27], is a successful strategy. Due to the contribution of instantaneous diffusion to T_{m} too large a sample concentration is also detrimental, so that an optimum concentration exists (Sect. 3.2).

Even after T_{m} optimization, the value of t_{max} predicted by (9) and the corresponding minimal value of τ_2 may lead to an unacceptable signal-to-noise ratio within the available measurement time. As a rule of thumb, for a dipolar evolution trace with 250 data points a signal-to-noise ratio of 50 computed from the signal amplitude at the time origin ($t = 0$) and the noise level observed in the

residual between the experimental and simulated form factor is required for reliable data analysis. This number scales inversely with the square root of the number of data points. If such a signal-to-noise ratio cannot be achieved, t_{max} needs to be shortened and the limitations in available information have to be accepted.

Less often the value of t_{max} predicted by (9) leads to much better signal-to-noise ratio than required at a total measurement time that is comparable to the time required for sample preparation and experiment setup. In this case, t_{max} should be prolonged to provide a signal-to-noise ratio between 100 and 200 at $t = 0$ within a measurement time of one to two hours. Such prolongation of t_{max} improves the reliability of the background correction and thus reduces long-distance artifacts in the distance distribution.

These considerations and the existence of an optimum choice of t_{max} for a given sensitivity and given distance distribution are illustrated in Fig. 4 by simulations for a model distance distribution corresponding to labeling sites 249 and 472 in monomers of the carnitine transporter CaiT (PDB identifier 2WSX). The model distance distribution was computed by the rotamer library approach, assuming methanethiosulfonate (MTSL) spin labels (Sect. 5.3). We assumed $T_m = 1.5$ µs, a signal-to-noise ratio of 200 at $t = 0$ for $t_{max} = 1$ µs, and a fixed time increment $\Delta t = 8$ ns. For each value of t_{max} to be studied, 250 dipolar evolution functions with different pseudo-random white noise were generated and reanalyzed as described in Sect. 2.4. The average root mean square deviation between the original distance distribution and the distance distribution obtained by Tikhonov regularization with an optimal regularization parameter of 10 was computed at $t_{max} = 1$, 1.25, 1.5, 1.75, 2, 2.25, and 2.5 µs. The optimum was observed at $t_{max} = 1.75$ µs (inset of Fig. 4d). Likewise, the mean distance and width and their standard deviations were computed for the 250 trials at each t_{max}. They are displayed in Fig. 4a, b, respectively. Figure 4d shows the original distance distribution (solid line) together with the distributions obtained at the shortest (dashed), optimum (dash-dotted), and longest (dotted) value of t_{max}. The corresponding dipolar evolution functions together with optimal background fit are displayed in Fig. 4c.

For too short t_{max} (1.00 µs), deviations of the distance distribution from the original distribution arise from errors in background correction (peak marked with an ampersand in Fig. 4d). For too long t_{max} (2.00, 2.25, 2.50 µs), deviations arise from noise-related artifacts (peaks marked with asterisks in Fig. 4d). Both types of artifacts cause a larger apparent width of the distribution (Fig. 4b) and larger uncertainties of the mean distance and width (Fig. 4a, b).

3.2 Sample Concentration

In the absence of instantaneous diffusion signal amplitude is proportional to spin concentration c'. Instantaneous diffusion causes signal decay for time $2(\tau_1 + \tau_2)$

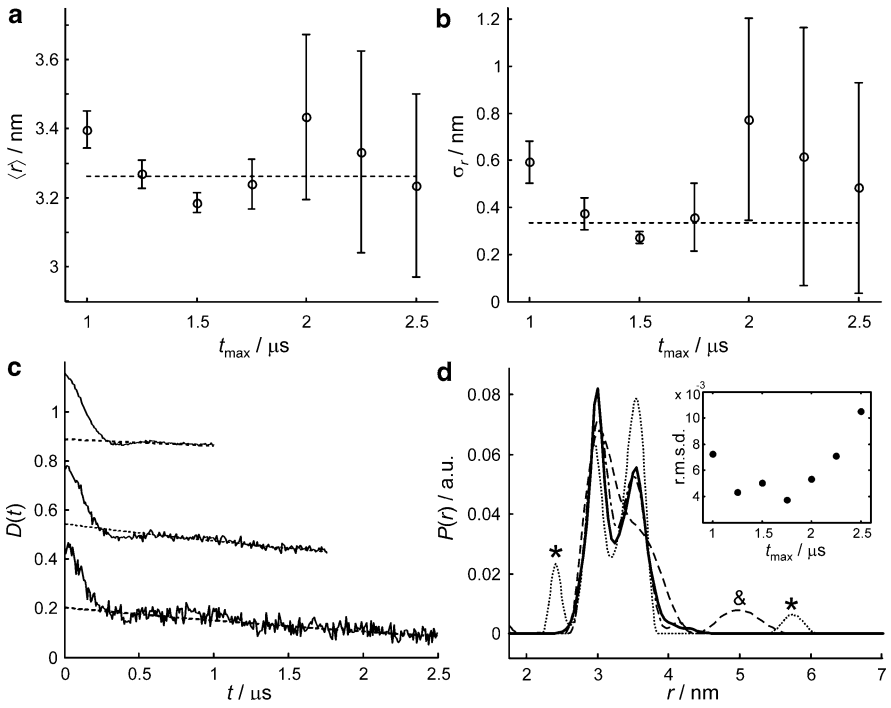

Fig. 4 Dependence of data quality on maximum dipolar evolution time t_{max} (simulation). The original distance distribution stems from a rotamer simulation (Sect. 5.3) of site pair 249/472 in a monomer of the carnitine transporter CaiT (PDB code 2WSX). (**a**) Mean distances $\langle r \rangle$ determined at different t_{max} with 95% confidence intervals (two times standard deviation). The *dashed horizontal line* denotes the correct mean distance. (**b**) Widths σ_r of the distance distributions with 95% confidence intervals. The *dashed horizontal line* denotes the correct width. (**c**) Dipolar evolution functions $D(t)$ for three selected values of t_{max}. The *dotted lines* are optimum background fits. Note the underestimate of background decay rate for the shortest trace (*top*). (**d**) Distance distributions: *Solid line* – original distribution, *dotted line* – $t_{max} = 1$ µs, *dash-dotted line* – optimum $t_{max} = 1.75$ µs, *dashed line* – $t_{max} = 2.5$ µs. *Asterisks* denote noise-related artifacts, the *ampersand* a background correction artifact. The *inset* shows the dependence on t_{max} of the root mean square deviation between the original distribution and the distribution computed by Tikhonov regularization

with a rate that is proportional to concentration. We have previously derived an expression for the concentration that maximizes signal-to-noise ratio at $t = 0$ assuming $2(\tau_1 + \tau_2) \approx 2\ t_{max}$ [7]. The effective signal-to-noise ratio for the whole trace is also affected by the dampening of the form factor by the background function. Thus, the proper figure of merit is

$$m = c' \exp(-2\lambda_{obs} k c' t_{max}) \int_0^{t_{max}} \exp(-\lambda_{pump} k c' t)\, \mathrm{d}t, \tag{11}$$

where the integral is proportional to the average signal-to-noise ratio over the whole dipolar evolution function, λ_{obs} and λ_{pump} are inversion efficiencies of the observer and pump π pulse, respectively, and

$$k = -\frac{\pi}{9\sqrt{3}} \times \frac{\mu_0 g^2 \mu_B^2}{\hbar} N_A. \tag{12}$$

Introducing the concentration $c = c'/(nf)$ of nano-objects with f being the mean labeling efficiency and n the number of spins, this figure of merit is maximized at

$$c_{opt} = \frac{\ln\left[\left(2\lambda_{obs} + \lambda_{pump}\right)/(2\lambda_{obs})\right]}{nfk\lambda_{pump} t_{max}}. \tag{13}$$

Assuming standard conditions at X-band with $\lambda_{obs} = 1/4$ and $\lambda_{pump} = 1/2$ roughly corresponding to a 32 ns observer π pulse and a 12 ns pump π pulse and further assuming doubly labeled protein molecules or protein complexes, we find

$$c_{opt,\,std} = \frac{\ln 2}{fkt_{max}} = \frac{1.38\mu s}{ft_{max}} \cdot \text{mmol} \cdot \text{L}^{-1}. \tag{14}$$

For reliable determination of mean distance and width of the distribution at a distance of about 5 nm, we have $t_{max} = 3.9$ µs according to (9). Hence, a concentration of doubly labeled protein of about 350 µmol L^{-1} would provide optimum signal amplitude at a labeling efficiency of 100%. Note that this value is larger than suggested by Fig. 7 in [7], as our estimates for the necessary t_{max} were significantly reduced on the basis of new simulations. At a distance of 8 nm, $t_{max} = 16$ µs needs to be achieved at an optimum concentration of 86 µmol L^{-1} of doubly labeled protein to determine mean distance and width.

Note that this concentration is a local concentration. For membrane proteins in liposomes, such values can be reached at much smaller bulk concentrations. For many proteins, such concentrations may also not be achievable, either for lack of material or because the protein tends to aggregate or precipitate at high concentrations. Last but not least it may be beneficial to work at lower concentrations to aid separation of form factor and background factor.

3.3 Length and Flip Angle of the DEER Pump Pulse

At given signal-to-noise ratio of the observer echo, the signal-to-noise ratio of the form factor increases with inversion efficiency λ of the pump pulse. Inversion efficiency is maximum at flip angle π and increases with decreasing pump pulse length due to an increase in excitation bandwidth and thus in the fraction of pumped spins. The requirement to avoid overlap of pump and observer excitation bands

(Sect. 3.7) puts a lower limit to the pulse lengths. Popular choices at X-band frequencies are a 12 ns pump pulse length with either all observer pulses having a length of 32 ns or observer π/2 and π pulses having lengths of 16 and 32 ns. The two choices with equal and different observer pulse lengths lead to almost indistinguishable results.

The use of a shorter pump pulse improves data quality more strongly than the use of shorter observer pulses in the presence of significant phase noise. This is because phase noise is proportional to the total signal, so that increasing signal amplitude by increasing observer pulse bandwidth does not suppress phase noise. In contrast, increasing the modulation depth Δ does diminish phase noise in the form factor, as form factor computation scales noise of the primary data by a factor $1/\Delta$. However, when optimizing for the measurement of short distances [28] equal lengths of all pulses of 24 ns are preferable. At higher frequencies, the lower limit of pump and observer pulse lengths is often set by the maximum available power and the required flip angles.

In multispin systems, large inversion efficiencies λ introduce sum and difference frequencies of the basic dipolar frequencies into the form factor [19], which then cause artifacts in the distance distribution. Currently, a separation technique exists only for three-spin systems [19]. For more spins, the multispin contributions can be decreased by the intentional reduction of the pump pulse flip angle. According to (5), the wanted pair contribution for an n-spin system is maximized at $\lambda f = 1/(n-1)$, where f is the labeling efficiency. The ratio of the pair contribution to the three-spin contribution (the latter one being the leading term of the artifact contributions) is $(1-\lambda f)/(\lambda f)$. For an octamer with labeling efficiency of 100%, the pair contribution is maximized at $\lambda = 1/7$, corresponding to a flip angle of about $2\pi/7$ for a 12 ns pump pulse at X-band frequencies. This results in a ratio of $n - 2 = 6$ between the wanted and the leading artifact contribution, which may be acceptable, depending on the question to be answered. If a high-quality distance distribution is required or the effective number nf of spins per nano-object is smaller, it may be necessary to work with smaller flip angles than are required to maximize the pair contribution.

If a preliminary model for the structure is available, MMM 2010 (http://www.epr.ethz.ch/software/index) can simulate multispin effects on the form factor up to $n = 5$ based on rotamer simulations of spin label conformations (Sect. 5.3). The simulated form factor can be saved and reanalyzed with DeerAnalysis 2011 [17, 18] (http://www.epr.ethz.ch/software/index) to reveal where multispin artifacts are likely to occur in the distance distribution.

3.4 Total Measurement Time

Sample preparation starting from a fully labeled protein and setup of a dipolar EPR experiment can hardly be achieved in less than half an hour. Preparation of the labeled protein, including mutations, expression, purification, and labeling requires several days if not weeks. For these reasons, it does not make much sense to

decrease measurement times to less than 1–2 h per sample. In the few cases where a very good signal-to-noise ratio can be achieved in shorter times, it is advisable to increase t_{max}, as this leads to more reliable background fits and a more reliable shape of the distance distribution.

Standard measurement times currently rather correspond to two samples per 24 h, i.e., net measurement times of about 11 h. For very weak or very fast relaxing samples, an increase to 48 or 60 h per sample may be advisable, depending on the importance of the question and on possibilities to improve the situation by a different choice of labeling sites (Sect. 3.8). Beyond such measurement times, significant improvements of data quality can hardly be achieved. Data quality is then limited by spectrometer stability and electronic artifacts that are not fully eliminated by phase cycling.

3.5 Nuclear Modulation Averaging

All dipolar EPR experiments introduce a small artifact contribution from electron spin echo envelope modulation into the form factor. In single-frequency experiments, such as double-quantum EPR [4, 5] or SIFTER [6], this is unavoidable since nuclear modulations cannot be eliminated by phase cycling. In DEER, the nuclear modulations arise from the small residual overlap of pump and observer excitation bands, which is more severe for the forbidden electron-nuclear transitions, which induce the electron spin echo envelope modulation (ESEEM) effects, than for the allowed transitions that create most of the observer echo.

The phase of nuclear modulations depends on interpulse delays that do not influence the phase of the dipolar modulation. This creates the opportunity to average nuclear modulations by variation of such interpulse delays [16]. In four-pulse DEER interpulse delay τ_1 between the first two observer pulses is varied over one full period of the nuclear modulation that is to be suppressed. For protons at X-band, the period of the dominating matrix line varies between about 64 and 80 ns, depending on the magnetic field. Hence, 8–10 steps of nuclear modulation averaging with an increment of 8 ns are appropriate. The ratio between proton and deuterium Zeeman frequencies is about 6.5; therefore, the same number of steps with an increment of 52 ns can be used. A slight reduction of the signal-to-noise ratio arises from additional relaxation by prolonging τ_1 more than necessary without such averaging.

In double-quantum EPR nuclear modulation averaging by appropriate adjustment of the echo integration window was also suggested [29]. This technique has the disadvantage of more strongly diminishing signal-to-noise ratio by not using the optimal width of the integration gate, which should match the width of the observer echo.

Neither modulation averaging technique completely eliminates nuclear modulations. At X-band frequencies, proton modulations correspond to a distance of about 1.5 nm, outside the sensitive range of DEER. In contrast, deuterium

modulations correspond to a distance of about 2.8 nm and may be easily mistaken for dipolar modulations. At Q-band frequencies, deuterium modulations shift to about 1.8 nm and are weaker by an order of magnitude, as modulation depths of weakly coupled nuclei scale inversely with the square of the magnetic field.

3.6 Avoiding Orientation Selection

Orientation selection in DEER is a source of additional information on molecular geometry [30–32]. However, in many cases this information cannot be obtained with reasonable effort or cannot easily be interpreted since label orientation may not be closely related to protein backbone orientation. Since orientation selection leads to orientation dependence of pump inversion efficiency λ, a general derivation of (6) from (3) is no longer possible. Hence, the distance distribution cannot be computed without fully analyzing orientation selection.

For nitroxide spin labels in proteins significant orientation selection at X-band frequencies is a rare phenomenon and occurs only if both labeling sites are tight. In many cases, such a choice of labeling sites can and should be avoided (Sect. 3.8). The situation is different for nucleic acids, where rigid spin labels can be incorporated without affecting backbone conformation [8], and where such rigid labels provide higher precision due to reduced uncertainty of spin label conformation. In such cases or after accidental choice of two tight sites in proteins orientation selection can be reduced by averaging dipolar evolution functions over a range of magnetic fields [33]. Such averaging should be applied only when necessary since it entails some loss in signal-to-noise ratio and causes deviation of the background factor from (8). Note also that orientation averaging by a field sweep is not complete [34].

At high fields and low microwave powers orientation selection may be strong even in the presence of substantial conformational freedom of the labels [32]. The use of high-field DEER measurements with excitation bandwidths much smaller than the total width of the nitroxide spectrum is not advisable if the main information sought is the distance distribution.

3.7 Avoiding Overlap of Pump and Observer Excitation Bands

Overlap of pump and observer excitation bands leads to a contribution to the dipolar evolution function that is analogous to the dipolar modulation observed in the "2+1" pulse train [35]. This is apparent as a deviation of $D(t)$ from the expected behavior at long times near $t_{\max}$, where the signal starts to rise with respect to the background fit, as follows from (8) of [35] by realizing that the "2+1" signal contains a component of dipolar modulation as a function of $\tau - t$. Depending on severity of the excitation band overlap and on the mean distance and width of the distance distribution, this additional component can significantly distort the dipolar

evolution function in a broad time interval. Even if the effect is weak, it may lead to a deviation of the long-time decay of $D(t)$ from $B(t)$ and thus to erroneous background fitting.

Under standard conditions (65 MHz frequency difference between observer pulses with 32 ns length and a pump pulse with 12 ns length at X-band frequencies), overlap is insignificant. When deviating from such conditions, one should test for distortions near t_{max} by measuring a model system with narrow distance distribution. It is strongly advisable to avoid the overlap effect by increasing the pump-observer frequency difference or by prolonging pulses. The stop-gap solution of reducing t_{max} (i.e., by discarding points from the end of the recorded time trace) at given τ_2 corresponds to a loss in signal-to-noise ratio and still leads to an increased uncertainty of the background fit.

3.8 Choice of Labeling Sites

Interpretation of dipolar evolution data in terms of structure or structural changes is most reliable and precise when mean spin–spin distances are in the range between 2.2 and 4 nm and the conformational distribution of the spin label is moderately broad. At shorter distances, part of the distance distribution may be suppressed since short distances correspond to dipole–dipole couplings larger than the excitation bandwidth that cannot be detected [28, 36, 37]. At longer distances, the required length of the pulse sequence (set by t_{max}) may be incompatible with the required signal-to-noise ratio. A very narrow conformational distribution increases orientation selection artifacts (Sect. 3.6) and may lead to large uncertainties in deriving backbone–backbone distances from spin–spin distances (Sect. 5.1). A very broad conformational distribution also increases uncertainty of backbone–backbone distances. If several distance constraints are combined in structural modeling, they should be linearly independent, a problem that has been considered in [38].

These requirements suggest that spin–spin distances and conformational distribution of the spin labels should be predicted for the whole protein or protein complex to select preferable labeling sites. This is possible if a model for the expected structure exists. Advantageous pairs of spin label sites can then be selected from in silico spin-labeling site scans [39] as implemented in MMM 2010 (http://www.epr.ethz.ch/software/index).

4 Data Analysis in Terms of a Distance Distribution

4.1 Tikhonov Regularization or Model-Based Fitting?

Proteins are designed as semiflexible peptides to ensure a balance between well-defined structure and easy access to structural transitions that are required for their function. How this balance is struck depends on the particular type of function, so that both very rigid and largely disordered proteins occur. Dipolar EPR tends to be most useful for moderately to strongly flexible proteins, where higher-resolution techniques such as crystallography or NMR fail or can characterize only the well-ordered part of the structure.

Consequently, not only the mean structure but also the extent of structural disorder may need to be elucidated to understand protein function. This requires that not only mean distances, but also distance distributions need to be measured. It was recognized early on [40] and later demonstrated conclusively [41] that distance distributions can be extracted from dipolar evolution data. The problem is ill-posed, i.e., small deviations of the input data from the ideal expressions can cause large errors in the output. The mathematically most formalized and best understood algorithm for solving such ill-posed problems is Tikhonov regularization [17, 23, 42], which stabilizes the solution by imposing a smoothness criterion on the output data. The relative contributions to the error function by the mean square deviation between simulated and experimental form factor and by the roughness of the distance distribution is set by the regularization parameter (Sect. 4.4).

Tikhonov regularization minimizes this error function by direct matrix computations. Since no fitting is involved, the algorithm provides the distance distribution corresponding to the global minimum of the error function. The solution can further be stabilized by imposing non-negativity on the distance distribution, $P(r) \geq 0$ [43], which is justified in our case since any probability distribution must be non-negative. The non-negativity constraint also removes the most common type of orientation selection artifacts (Sect. 3.6), which is caused by missing contributions from spin pairs with a spin–spin vector parallel or nearly parallel to the external magnetic field.

Alternatively, the solution of an ill-posed problem can be stabilized by fitting a model for the distance distribution to the experimental data by varying a small number of parameters. This approach is very attractive in materials science applications [33, 34, 44–46] where variation of the model parameters on variation of the studied material is the basis for understanding the problem. For biomacromolecules with flexible spin labels such an approach may not appear obvious since conformational distribution of the label (Sect. 5.1) cannot be easily modeled with a small number of parameters. If this distribution is predicted by the rotamer library approach (Sect. 5.3), models for backbone structure can be directly fitted to the dipolar evolution function [47, 48]. This avoids the uncertainty of solving an ill-posed problem and partially removes the uncertainty of background correction since background fitting can be integrated in global fitting of the model. To keep

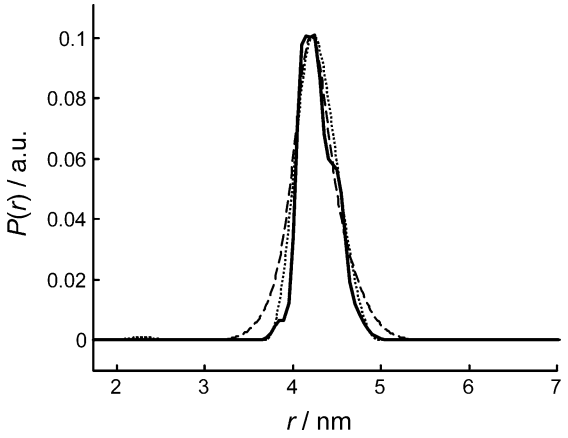

Fig. 5 Comparison of Tikhonov regularization and multi-Gaussian fitting for a model distance distribution corresponding to site pair 374/433 in monomers of carnitine transporter CaiT (PDB 2WSX, simulation based on a rotamer library). Shown are the original distance distribution (*solid line*), the result of Tikhonov regularization with a regularization parameter of 100 (*dotted line*), and the result of multi-Gaussian fitting (*dashed line*). The corresponding simulated dipolar evolution function is shown in Fig. 6a

the number of parameters manageable, the backbone model must be strongly simplified. In the case of a sodium/proton antiporter dimer, the monomers were treated as rigid bodies and only their relative arrangement was fitted [47]. Later, it turned out that one domain in the monomer structure was influenced by crystal packing effects [49].

Finally, it is possible to obtain distance distributions from a model-based approach by expressing them as a sum of Gaussian functions [44]. The most sophisticated program for such multi-Gaussian fits, DEfit by Sen and Fajer (http://ilkersen.net/), automatically adapts the number of required Gaussians by statistical criteria. Still, at least in our hands, this approach is less efficient than Tikhonov regularization in reproducing the shape of a distance distribution (Fig. 5). This is probably due to a principal difficulty of reproducing asymmetric distributions with a small number of Gaussians. Part of the problem may also arise from the use of background subtraction rather than background deconvolution in DEFit.

4.2 Determining Time Zero of Dipolar Evolution Data

Due to the finite length and nonrectangular shape of the microwave pulses, the interpulse delay corresponding to $t = 0$ is not trivial to predict. In fact, $t = 0$ may not even correspond to the time of a data point in the digitized dipolar evolution function with a time increment of $\Delta t = 8$ ns. For short distances, this may cause systematic errors in distance determination. To avoid this problem, DeerAnalysis

2011 [17, 18] (http://www.epr.ethz.ch/software/index) allows for adjusting zero time on a 1 ns raster by data interpolation, which is sufficiently precise for the shortest distances that can be measured by DEER. Automatic adjustment is based on minimization of the first moment of the dipolar evolution function in the vicinity of the global maximum. This is more robust with respect to noise than just taking the global maximum of the dipolar time evolution function as $t = 0$.

Nevertheless, the zero time determined from noisy dipolar evolution functions may have some error. It is advantageous to determine zero time for a given spectrometer and probe head and for given pulse sequence settings (pulse lengths and fixed interpulse delay τ_1) on a high signal-to-noise trace of a model compound with a short distance. This value should then be manually set and used in the analysis of measurements on samples with lower signal-to-noise ratio.

4.3 Optimizing the Background Correction

Background correction involves three uncertainties [18]:

- The optimum starting time of the background fit range is unknown
- The correct dimensionality d of the background function $\exp(-kt^{d/3})$ is unknown
- As nano-objects cannot overlap, short spin–spin distances are underrepresented compared to a homogeneous or confined distribution, so that theoretical background functions are not adhered to at short times

Measurements on singly-labeled samples of the same protein or protein complex are by far the most reliable way of reducing these uncertainties if such samples are accessible. DeerAnalysis 2011 [17, 18] (http://www.epr.ethz.ch/software/index) allows for modeling an experimental background function by a polynomial and using it for background correction of double mutants. For best precision, experimental background functions are needed for all labeling sites. This may be too much effort unless very precise distance distributions are required, but at least one or two singly-labeled proteins should be measured for any protein studied by dipolar EPR to obtain some understanding of possible deviations of the background function from theoretical functions. Such measurements also test for protein aggregation or oligomerization.

The data of singly-labeled proteins should then be used to establish dimensionality d and the short time limit $t_{\mathrm{bckg,min}}$ after which a stretched exponential $\exp(-kt^{d/3})$ is a good fit to the dipolar evolution function (i.e., a fit to the time trace over the interval $t_{\mathrm{bckg,min}}$ to t_{max}). If for a sample of a doubly labeled protein a background fit with $t_{\mathrm{bckg}} \geq t_{\mathrm{bckg,min}}$ and dimensionality d as a fit parameter results in the same dimensionality d as the fit for the singly-labeled protein, the background fit is usually reliable.

If no such starting time t_{bckg} for the background fit can be established, d should be fixed to the value observed on the singly-labeled protein and the automatic determination of time t_{bckg} in DeerAnalysis 2011 [17, 18] (http://www.epr.ethz.ch/software/index)

should be used. The algorithm minimizes contributions of the distance distribution at the upper end of the distance range, which is sensible unless the protein aggregates or t_{max} is too short. Simultaneous fitting of d and t_{bckg} is unstable and should be avoided. Note also that values $d \neq 3$ for soluble proteins or membrane proteins in detergent micelles indicate problems. In some cases, $d > 3$ compensates for the suppression of short interobject distances by excluded volume [50].

For proteins that are stable only as oligomers, it is impossible to generate singly-labeled samples. In this situation, it is advantageous to select at least one labeling site for which all distances within the oligomer are so short that a proper separation of form factor and background function $B(t)$ can be achieved in the primary data. Depending on the achievable t_{max} that may require distances shorter than 2.5–3 nm. The background $B(t)$ determined for this sample can then be used in data analysis for the other samples.

4.4 Best Choice of the Regularization Parameter

Tikhonov regularization minimizes an error function

$$G_\alpha = \|KP(r) - f(t)\|^2 + \alpha \left\| \frac{d^2}{dr^2} P(r) \right\|^2 = \rho + \alpha\eta, \tag{15}$$

where the roughness η (square norm of the second derivative of the distance distribution) is weighted by regularization parameter α with respect to the square deviation ρ between the simulated reduced form factor $KP(r)$ and the experimental reduced form factor $f(t)$. The kernel K relates the distance distribution $P(r)$ to the reduced form factor. At very small regularization parameters α, the distance distribution $P(r)$ is undersmoothed and consists of a series of narrow peaks that partially simulate the noise in $f(t)$. At very large α, $P(r)$ is oversmoothed and thus broader than the true distance distribution, so that the simulated reduced form factor $KP(t)$ is overdamped compared to $f(t)$.

With reasonable signal-to-noise ratio, a sufficiently large value of t_{max}, and appropriate background correction, the optimum value of the regularization parameter α can be guessed from the L curve [42, 51], which is a parametric plot of log η vs. log ρ for a range of α values. This plot has an almost vertical branch in the regime of undersmoothing, where roughness ρ decreases strongly with increasing α and an almost horizontal branch in the regime of oversmoothing where the square deviation of $KP(r)$ from $f(t)$ increases strongly with increasing α. The two branches intersect in the corner of the L and the point closest to this corner corresponds to the optimal regularization parameter.

Strictly speaking, the optimum regularization parameter can be derived from an L curve only for a distance distribution with an approximately Gaussian shape. If the distance distribution contains both narrow and broad features, the narrow

features tend to be slightly oversmoothed in the corner of the L. In this case, the root mean square deviation between the true distance distribution and the result of Tikhonov regularization may be minimal at a smaller regularization parameter.

Use of the L curve, under- and oversmoothing, and the possible deviation of the optimum regularization parameter from the corner of the L curve are illustrated in Fig. 6 for a model distance distribution corresponding to site pair 374/433 in the monomers of carnitine transporter CaiT (PDB 2WSX). The simulated dipolar evolution function with a signal-to-noise ratio of 200 at $t = 0$ is shown in Fig. 6a. The original distance distribution (solid line) and the best-fitting result of Tikhonov regularization (dotted line), corresponding to $\alpha = 1$ (full black circle in Fig. 6b), are displayed in the inset. Comparison with Fig. 5 reveals that the regularization

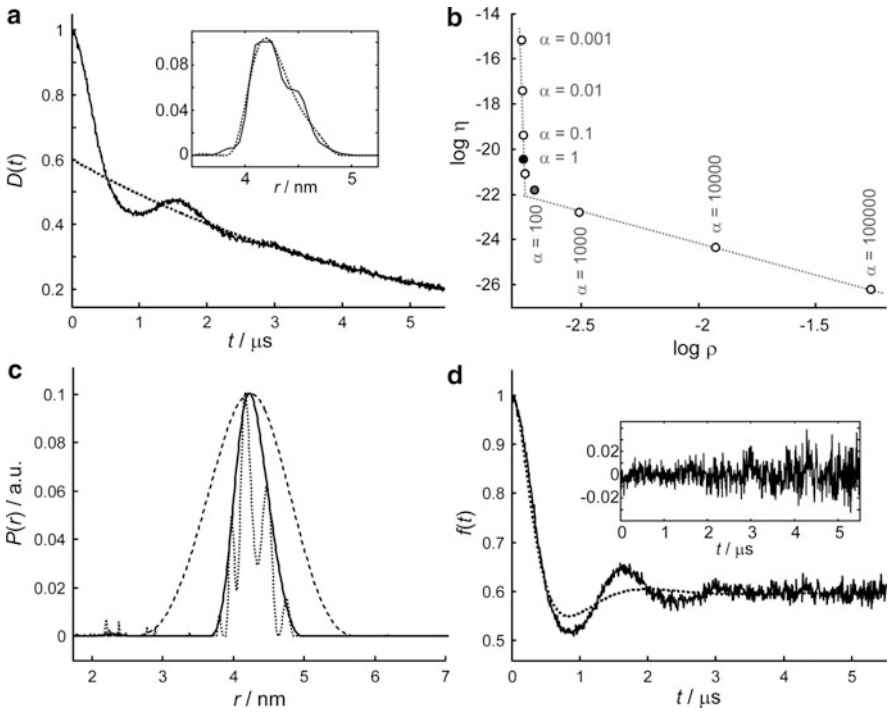

Fig. 6 Tikhonov regularization for a model distance distribution corresponding to site pair 374/433 in the carnitine transporter CaiT. (**a**) Simulated dipolar evolution function (*solid line*) and optimized background fit (*dotted line*). The *inset* shows the original distance distribution (*solid line*) and the best result of Tikhonov regularization obtained with regularization parameter $\alpha = 1$. (**b**) L curve. The corner is situated near $\alpha = 100$ (*full gray circle*). The true optimal regularization parameter $\alpha = 1$ is marked by a *full black circle*. (**c**) Effects of under- and oversmoothing. The distance distributions are results for $\alpha = 0.001$ (*dotted line*, undersmoothing), $\alpha = 100$ (*solid line*, L curve corner), and $\alpha = 100{,}000$ (*dashed line*, oversmoothing). (**d**) Effects of oversmoothing in form factor simulations $KP(r)$. The pseudo-experimental form factor (*solid line*) is not well fitted by the simulation $KP(r)$ for $\alpha = 100{,}000$ (*dotted line*). The *inset* shows the residual $KP(r) - f(t)$ for $\alpha = 100$, which deviates from white noise by perceptible slow oscillations

parameter $\alpha = 100$ (full gray circle in Fig. 6b), corresponding to the corner of the L curve, leads to slight oversmoothing. Even at $\alpha = 1$ the shoulder in the original distance distribution is lost. The shoulder is visible at $\alpha = 0.1$, but only at the expense of an unnatural sharpening of the main peak (data not shown). The slight oversmoothing at $\alpha = 100$ can also be seen in the residual $KP(t) - f(t)$ of the form factor plotted in the inset of Fig. 6d, which deviates from white noise and contains perceptible, though weak oscillations.

4.5 Estimating Precision and Reliability of a Distance Distribution

In an ill-posed problem, errors of the output data are not a linear function of noise in the input data. Furthermore, errors in the distance distribution arise not only from noise, but also from other sources, mainly from uncertainties in the background decay rate and in the exact functional form of the background factor $B(t)$. Since no general mathematical theory is available for predicting output error from input error in such a problem, precision and reliability of the result can only be estimated by numerical simulations.

The validation tool of DeerAnalysis 2011 [17, 18] (http://www.epr.ethz.ch/software/index) generates error estimates by a Monte Carlo algorithm for testing the influence of noise and by systematic scans of background correction parameters. The noise test is based on increasing the noise level by a user-supplied factor by adding pseudo-random numbers to the data. A number of Monte Carlo trials with noise-enhanced input data are performed and the variation of the distance distribution is examined.

With respect to background uncertainty, the starting time t_{bckg} of the background fit range or the background dimension d can be varied in user-defined ranges with a user-defined number of trials (increments). Any combination of noise test, test for variation of t_{bckg} and test for variation of background dimension d is possible. Computational times can be long in such combined tests, as the total number of trials is the product of the numbers of trials of all individual tests.

In older versions of DeerAnalysis, background tests were performed by direct variation of the decay rate k (density of spins) and modulation depth Δ. For backward compatibility, this option still exists. We now discourage background tests by such direct variation since in a two-dimensional grid (k_i, Δ_j) many parameter combinations correspond to very poor background fits, which leads to an overestimation of errors.

For illustration we have performed model computation for the site pair 249/318 in a monomer of carnitine transporter CaiT (PDB code 2WSX), for which data analysis with sufficient t_{max} and good signal-to-noise ratio is shown in Fig. 3. We now assume that data could only be acquired for $t_{\mathrm{max}} = 3.5$ μs with a signal-to-noise ratio of about 67 at $t = 0$ (Fig. 7a). Such data quality is rather typical for dipolar EPR

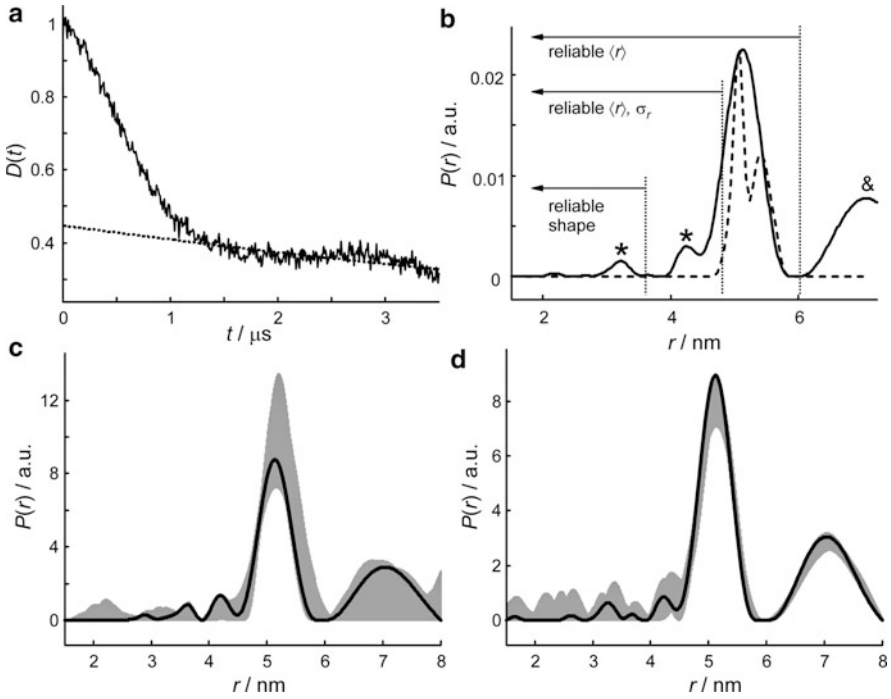

Fig. 7 Validation of a distance distribution derived from a simulated data set with insufficient t_{max} and moderate signal-to-noise ratio (site pair 249/318 in CaiT). (**a**) Simulated dipolar evolution function with $t_{max} = 3.5$ µs and signal-to-noise ratio of 67 at $t = 0$. The *dotted line* is the optimal background fit. (**b**) Distance distribution obtained by Tikhonov regularization with the optimal regularization parameter $\alpha = 100$ suggested by the L curve (*solid line*) and original distance distribution used in simulating the data (*dashed line*). Indicated are also distance ranges where a reliable shape of the distribution, reliable mean distance $\langle r \rangle$ and width σ_r, or only a reliable mean distance $\langle r \rangle$ can be expected (*dotted vertical lines* and *horizontal arrows*). (**c**) Validation by testing the influence of noise and starting time t_{bckg} for the background fit (see text). Shown are the best guess (*solid line*) and the confidence interval (*gray area*) of the distance distribution. (**d**) Validation by testing only the influence of noise

measurements at X-band frequencies. According to the L curve (not shown), the optimum regularization parameter is $\alpha = 100$. The distance distribution corresponding to this regularization parameter and to optimized t_{bckg} is shown in Fig. 7b. Compared to the original distribution, the result of Tikhonov regularization is artificially broadened, so that the splitting into a bimodal distribution is lost. Furthermore, a peak at the upper limit of the distance distributions (&) indicates problems in background correction. Note also the uncertainty of the long-distance edge of the distribution. Finally, minor peaks appear at shorter distances than are present in the original distribution, which are due to noise (asterisks).

The limits for determining the shape and width of the distribution or only the mean distance are indicated in Fig. 7b. DeerAnalysis 2011 [17, 18] (http://www.epr.ethz.ch/software/index) displays these limits by color coding of the plot

background. These limits suggest that only the mean distance $\langle r \rangle$ is reliable and that the peak at a distance longer than 6 nm has no meaning. Validation with 11 noise trials at a noise level enhanced by a factor of 1.5 as well as 21 background start trials in the range between $t_{\mathrm{bckg}} = 600$–$2{,}100$ ns (Fig. 7c) confirms these suggestions and reveals that the small peaks at distances shorter than 4.5 nm can be explained by noise. The lower limit for the test of t_{bckg} corresponds to the decay of $f(t)$ to more than half of the total modulation depth Δ and the upper limit to about 60% of the cutoff time. Validation with respect to only noise is shown in Fig. 7d. Thus, neglecting background uncertainty the peak at about 7 nm would falsely appear to be a true feature of the data.

5 Relating Spin–Spin Distances to the Protein Backbone

5.1 Conformational Distribution of Spin Labels

Generally applicable spin labels for proteins require some side group flexibility so that they can adapt to the available space at the labeling site. Completely rigid labels may force unnatural repacking of neighboring side groups and backbone deformation or may even prevent proper folding when attached in an unfolded state or may not react with the folded protein. For these reasons and the necessity for a few side group atoms to construct a selectively reactive group, the most common spin labels MTSL (PDB residue identifier R1) and iodoacetamido-PROXYL spin label (IASL) contain five and six rotatable side chain bonds, respectively. The number of bonds corresponds to the number of variable dihedral angles χ_i. In general, each of these angles can assume a multimodal distribution that typically peaks around two or three canonical values (see Fig. 8a, b).

As a consequence, the spin label side chain can exist in about 100–200 canonical conformations, called rotamers, with some additional librational flexibility around these conformations. This leads to a spatial distribution of the electron spin, the spin being located approximately at the midpoint of the N–O bond of the nitroxide moiety. The situation is further complicated by two phenomena. First, the individual rotamers have different internal energies $\varepsilon_{j,\mathrm{int}}$ and thus different populations in the conformational ensemble. It is difficult to predict these relative energies with high precision. Second, the individual rotamers interact differently with their surroundings in the protein, leading to different external interaction energies $\varepsilon_{j,\mathrm{ext}}$, which are also difficult to predict with high precision. The spatial distribution of the electron spin with respect to a local frame at the labeling site is determined by the rotamer populations

$$p_j = \exp\left(-\frac{\varepsilon_{j,\mathrm{int}} + \varepsilon_{j,\mathrm{ext}}}{k_{\mathrm{B}}T}\right) \tag{16}$$

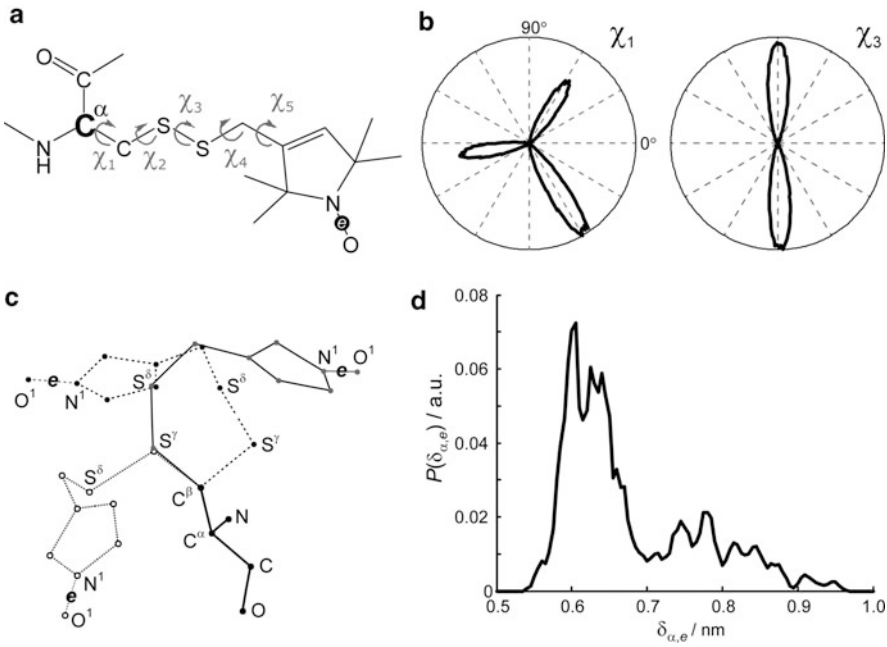

Fig. 8 Conformational distribution of MTSL. (**a**) Different values of the dihedral angles χ_1–χ_5 lead to a distribution of the distance between the C^α backbone atom and the unpaired electron e, which is situated approximately in the midpoint of the N–O bond. (**b**) Polar histograms of the distribution of dihedral angles χ_1 and χ_3 in a CHARMM molecular dynamics simulation at 175 K with heating cycles to 600 K to overcome rotational barriers. (**c**) Visualization of three selected rotamers of MTSL. The methyl groups of the nitroxide rings are omitted for clarity. (**d**) Distribution of the C^α – electron spin distance $\delta_{\alpha,e}$ of all rotamers in the absence of any interaction with the protein

where k_B is the Boltzmann constant and T the temperature. Dipolar EPR is performed at low temperatures (typically at 50 K). However, samples are shock-frozen and the conformational ensemble cannot equilibrate in the solid state. Hence, the conformational ensemble in the frozen sample corresponds to the glass transition temperature T_g of the matrix [52], as was quantitatively confirmed on model compounds [34]. For both membrane proteins and soluble proteins, T in (16) can be approximated by 175 K, which corresponds to the glass transition of water confined in lipid bilayers [53] as well as of the solvation shell of proteins in aqueous solution [54].

For a rotamer library (Sect. 5.3) of MTSL at $T = 175$ K, the distance $\delta_{e,\alpha}$ between the C^α atom of the labeled residue and the electron spin varies approximately between 0.55 and 0.95 nm (Fig. 8d), with a mean distance of $\langle\delta_{e,\alpha}\rangle = 0.68$ nm. Depending on relative orientation of the two labeled residues and the number of populated rotamers, the measured spin–spin distances can be larger or smaller than the C^α–C^α distance by up to $2 \times \max(\delta_{e,\alpha}) = 1.9$ nm, with the largest deviation if at both sites only the rotamer with the largest electron spin–C^α distance is populated.

The maximum possible deviation of the mean spin–spin distance from the C^{α}–C^{α} distance reduces to approximately $2\langle\delta_{e,\alpha}\rangle = 1.36$ nm if a large number of rotamers are populated.

To relate the spin–spin distance to the backbone structure, the relative orientation of the spin-labeled residues (three Euler angles) and the orientation of the spin–spin vector with respect to one of the local frames (two polar angles) must be known. Thus, quantitative analysis of spin–spin distance distributions requires that a structural model is fitted to the data. Qualitative analysis also requires some kind of a structural model, which is then found to be consistent or inconsistent with dipolar EPR information. We thus need a general method for predicting the conformational distribution of the spin label from a given structural model.

5.2 Molecular Dynamics Approaches

The standard approach for computing interaction energies and conformational distributions for proteins is based on molecular force fields. Molecular dynamics (MD) simulations can provide trajectories of the N–O bond midpoint coordinate of the label at a given site. From trajectories for both sites of a label pair, distance distributions can be computed.

This simple concept is fraught with some difficulties. First, molecular force fields are not usually parameterized for spin labels. This problem can be solved by deriving force-field parameters by analogy, for instance using a carbonyl (C = O) group as a substitute for the N–O group. For MTSL, a high-quality parameterization is available for the CHARMM force field [55].

Second, rotational barriers for some dihedral angles, in particular χ_3 in MTSL, are too high to observe a sufficient number of transitions in trajectories of affordable length computed at the temperature where the conformational distribution is required. This problem was solved by performing the computations at elevated temperature [56] or by combining Monte Carlo conformational searches with short MD simulations in the vicinity of some low-energy conformers [15]. Although neither of these approaches provides the true thermodynamic ensemble at the target temperature, results of both approaches were found to be in reasonable to good agreement with experimental results. The latter approach appears to be able to predict mean distances with an uncertainty of 0.3 nm.

At much increased computational expense, the true thermodynamic ensemble could be obtained by replica-exchange molecular dynamics [57]. Given the fact that dihedral angle distributions for native amino acid residue side groups even in high-level unsteered MD simulations are in only mediocre agreement with experimental NMR data [58], it is doubtful whether such additional computational effort would be worthwhile. The good agreement seen with the simpler approaches rather suggests that rough prediction of the conformational ensemble is sufficient to match the precision of the dipolar EPR measurements.

Even the simpler MD approaches require several hours of computation time per labeling site. Although this compares well to the time required to produce a spin-labeled protein and measure the distance, it precludes systematic computational site scans for selecting favorable labeling positions. Furthermore, these MD approaches are too slow for fitting structures or structural transitions, tasks where the conformational distribution of spin labels may have to be predicted for a large number of intermediate structural models.

5.3 Rotamer Library Approach

Preferred rotamers of native side chains are predicted routinely and with good success on the basis of rotamer libraries [59]. Such rotamer libraries contain the relative coordinates of the side chain atoms with respect to a frame defined by the backbone atoms for a set of rotamers. Furthermore, they contain information on relative preferences for these rotamers corresponding to the $\varepsilon_{\mathrm{int},j}$. This information is compiled from the set of known protein structures in the protein data bank (PDB). To account for the side chain surroundings, a strongly simplified force field consisting only of pairwise Lennard-Jones potentials for nonhydrogen atoms is used. This simplification is based on the principle that molecular packing is dominated by repulsion of atoms and modified by the attractive van-der-Waals interaction.

For spin label side groups, quantitative information on $\varepsilon_{\mathrm{int},j}$ cannot be derived from known crystal structures with labels attached since the number of such structures is still too small. Our first- [47] and second-generation [48] rotamer libraries ignored this energy term. In our third-generation rotamer libraries [49], information on $\varepsilon_{\mathrm{int},j}$ is derived from 100 ns long CHARMM 27 MD trajectories at the target temperature. Rotational energy barriers are overcome by intervening heating cycles at 600 K and subsequent equilibration at the target temperature. Computation of $\varepsilon_{\mathrm{ext},j}$ assumes a rigid protein environment. To simulate some flexibility, atom–atom distances in computation of the CHARMM 27 Lennard-Jones potential are scaled by a forgive factor. This means that label-protein clashes are tolerated to a certain extent to account for the fact that in reality the protein is not rigid and will slightly adapt to the presence of the label. Such scaling is also used in rotamer library predictions of native side chain conformation. Such rotamer libraries for MTSL and IASL were tested by comparison of distance distributions predicted for label pairs in known structures with those obtained by DEER measurements. Generally good agreement was found [49]. Note, however, that in some cases rotamer library predictions may significantly deviate from true label conformations. This is more likely for tight sites [39, 49], where slight deviations in backbone conformation between the native and spin-labeled protein and repacking of neighboring side groups can strongly influence available space. In particular, like any other hydrophobic side group spin labels have a preference for fitting snugly into a hydrophobic cavity and protein structure may locally adapt to create such a

cavity. A case has been reported [60] where the crystal structure shows the label in such a cavity, while rotamer library analysis on the wild-type structure predicts a multitude of label conformations. In this case, DEER data indicate that in frozen solution the same cavity is occupied as in the crystal structure. We encountered a similar case when comparing data from a combined crystal structure, NMR, and EPR study [61] with predictions of the rotamer library approach. Although in this case the difference in predicted mean distances is only 0.16 nm, the general scenario appears to be the same. This indicates that the current rotamer library approach, which was parameterized and tested on membrane proteins, underestimates the hydrophobic interaction of the MTSL with soluble proteins.

Computation of the conformational ensemble with the rotamer library approach takes about 1–2 min per site, so that computational site scans [39] can be performed in a few hours even for large proteins and protein complexes. The approach is available via MMM 2010 (http://www.epr.ethz.ch/software/index), which can also replace nonstandard residues such as selenomethionine or selenocysteine in crystal structures by their standard analogs methionine and cysteine. Such replacement is required as proteins expressed for EPR experiments do not feature these amino acids that are introduced solely for phasing X-ray data. Furthermore, MMM 2010 can reconstruct side groups missing in a structure if SCWRL4 [59] is installed. Without such reconstruction, the predicted conformational ensembles of spin labels are too broad. Likewise, predicted distributions may be too broad if parts of the peptide chain are missing in the structure.

Probably the most serious approximation in the rotamer library approach is the assumption of fixed conformations of native amino acid side groups in the vicinity of the spin label. In reality, conformations of neighboring side groups might adapt to the presence of the spin label, and there may even be a conformational distribution of neighboring side groups in glassy frozen protein preparations. To test for the influence of such side group repacking, we have performed model computations (Fig. 9).

For these tests, rotamer distributions of MTSL were computed for the X-ray structure with PDB identifier 2WSX of the carnitine transporter CaiT (solid lines in Fig. 9) and for two modified structures with side groups repacked by the SCWRL4 program [59]. In the first modified structure amino acid residues at the labeling sites were replaced by glycine to mimic a situation where neighboring side groups have most freedom to assume their own preferential conformations (scenario: minimum space for the label). In the second modified structure amino acid residues at the labeling sites were replaced by the most bulky native residue tryptophan to mimic a situation where neighboring side groups are forced to free a lot of space at the labeling site (scenario: maximum space for the label).

Part of the change in distance distributions between the unmodified structure and the modified structures is the same for the minimum and maximum space scenarios, as is demonstrated for two typical label pairs, double mutants C249R1/V318R1 (Fig. 9a) and I374R1/S433R1 (Fig. 9b). This part of the change comes from differences between experimental side group conformations in the X-ray structure and side group conformations predicted by SCWRL4. For double mutant C249R1/V318R1, it can be traced back to a different conformation of the side group of a single residue,

L251 (see inset in Fig. 9a), which in turn influences the conformational distribution of the label at site C249R1. This leads to an increase in the mean distance by 0.04 nm.

For double mutant I374R1/S433R1, the short-distance wing of the distance distribution is partially suppressed after SCWRL4 repacking due to a slightly different conformation of the side group of residue Y113 (r.ms.d. of 1.9 Å between the two conformations, see inset in Fig. 9b), which in turn influences the rotamer distribution of the spin label at site I374R. This leads to an increase in the mean distance by 0.1 nm.

For double mutant C249R1/V318R1 (Fig. 9a), differences between the minimum and maximum space scenarios are minor. In other words, the replacement of C249 and V318 by either glycine or tryptophan does not influence the packing of other side groups in the vicinity of the spin label sites (as predicted by SCWRL4) to a significant extent. In contrast, for double mutant I374R1/S433R1 (Fig. 9b) replacement of the side chain at site S433 by tryptophan causes a significant change in the distance distribution, while replacement by glycine at both sites 374 and 433 as well as replacement by tryptophan at site I374 do not. The change can be traced back to a repacking of the side group of residue Q330 (r.ms.d. of 2.4 Å between the two conformations). It leads to a decrease in the mean distance by 0.04 nm compared to SCWRL4 repacking without previous mutation S433W.

In general, uncertainties in orientations of neighboring side groups have a larger influence for spin labels at tight sites than for those at loose sites, in line with the

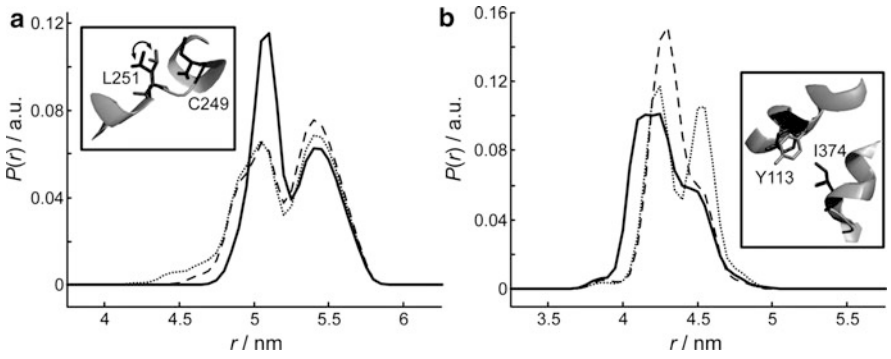

Fig. 9 Influence of side group repacking on spin–spin distance distributions computed with the rotamer library approach of MMM 2010 (http://www.epr.ethz.ch/software/index) (model computations on CaiT). *Solid lines* – all neighboring side chains as in the crystal structure 2WSX; *dotted lines* – side groups at labeling sites removed (mutation to glycine) and other side groups repacked with SCWRL4 before in silico spin labeling; *dashed lines* – side groups at labeling sites mutated to tryptophan and other side groups repacked with SCWRL4 before in silico spin labeling. Distance distributions are normalized to their integral. (**a**) Double mutant C249R1/V318R1, where R1 is MTSL. The *inset* visualizes the conformational difference at residue L251 that causes the change in distance distribution on SCWRL4 repacking. (**b**) Double mutant I374R1/S433R1. The *inset* visualizes the conformational difference at residue Y113 that causes the change in distance distribution on SCWRL4 repacking

results shown in Fig. 9. The broader distance distribution in Fig. 9a is less affected by repacking than the narrower distribution in Fig. 9b. Even more dramatic effects can be seen if only a few rotamers are populated at both sites (data not shown). Hence, contrary to what one might expect, tight labeling sites that lead to narrow distance distributions can introduce more, not less uncertainty about backbone-to-backbone distances. This is because the few populated rotamers are more difficult to predict than a moderately broad conformational distribution [49]. Such sites are thus better avoided in spin labeling, even if they lead to reasonable labeling efficiencies and properly folded, active proteins.

These examples indicate that with the current rotamer library approach uncertainty of the mean distance due to uncertainty in conformations of neighboring side groups is typically less than 0.2 nm. They also show that the *shape* of the distance distribution can change significantly due to rather minor changes in conformation of a single neighboring side chain (see inset in Fig. 9b). Thus, changes of this magnitude should not be interpreted as conclusive evidence for a change in backbone conformation.

5.4 *Testing Model Hypotheses by Experimental Dipolar EPR Data*

When a structural model is directly fitted to dipolar EPR constraints (Sect. 4.1) uncertainty can be estimated by statistical tests. In such tests, artificial noise is added to the dipolar evolution function and parts of the constraints are systematically neglected. The variation of the structural model due to noise and different combinations of constraints is a measure for uncertainty of the model. To date special modeling procedures have been developed for elucidating the structure of a protein dimer from known structures of the monomers [47, 62] and for elucidating the shape of a nonideal helix [48]. No general modeling procedure is available yet.

In many cases, development of a special modeling procedure is not required to answer the underlying biological problem. In some of these cases, outright modeling would require many more distance constraints than are necessary to show whether an experiment is consistent with a given hypothesis on protein function. Such problems can often be posed in terms of the direction and amplitude of relative backbone motions in a pair of sites. The test of a hypothesis on such relative motion boils down to the question whether observed label-to-label distance distributions are consistent with expected backbone-to-backbone distances. The same question needs to be answered to decide whether the structure of a protein in a physiologically more relevant environment is the same as in a crystal.

A related question is the one whether a certain part of a protein structure is well defined or partially disordered. This question can be rephrased as follows: is the width of experimental label-to-label distance distributions consistent with the hypothesis that the C^{α}–C^{α} distance of the labeled sites is fixed?

Although in such cases only a qualitative or semiquantitative answer is required to gain understanding, even such an answer has some uncertainty. This uncertainty derives from three sources. First, the width and shape of the label-to-label distance distribution may not be well defined, depending on the maximum dipolar evolution time t_{max} and the signal-to-noise ratio, as was explained in detail in Sects. 3.1 and 4. Second, the conformational distribution of the spin label side group is known with only limited precision, as was shown in Sect. 5.3. Any conclusion regarding the C^{α}–C^{α} distance and its distribution width is thus fraught with a certain error. Third, a difference between the expected mean distance $\langle r \rangle$ and the width of the distance distribution σ_r and the experimentally determined values may not exclusively be caused by a change in the C^{α}–C^{α} distance, but also by reorientation of the (anisotropic) conformational distribution of the spin label. In other words, a relative rotation of two domains can lead to a significant increase or decrease of the label-to-label distance, even if the C^{α}–C^{α} distance barely changes. While the third source of uncertainty can only be tested by a general modeling approach, the first two sources can be eliminated by proper experimentation and data analysis (first source) and consideration of all possible pairs of rotamers (second source). Consideration of all rotamers is a feature of MMM 2010 (http://www.epr.ethz.ch/software/index), which is demonstrated by a model computation (Fig. 10).

This model computation concerns the question whether dipolar EPR measurements on 5-enolpyruvylshikimate 3-phosphate (EPSP) synthase would be able to detect and quantify the domain movement that occurs on substrate binding [63]. The open apo form (PDB 2GG4) and closed substrate-bound form (PDB 2GG6) are visualized in Fig. 9a by light gray and dark gray ribbon plots, respectively. Labeling by MTSL was simulated with a rotamer library approach (Sect. 5.3) for sites S146 and D373 in

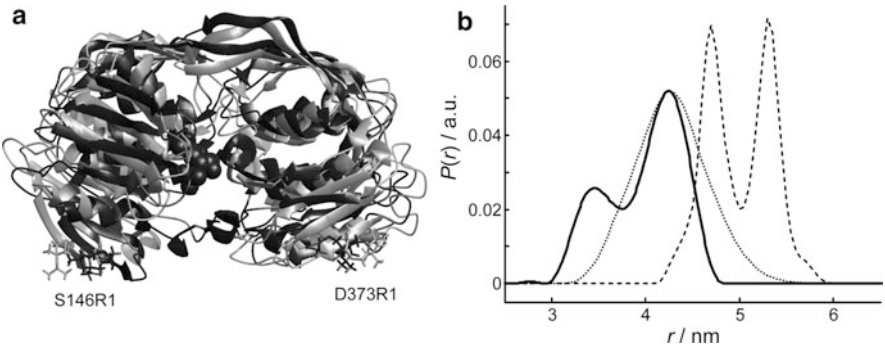

Fig. 10 Test of a domain-movement hypothesis (simulation). The model system is 5-enolpyruvylshikimate 3-phosphate (EPSP) synthase. (**a**) Ribbon plots of apo (*light gray*, PDB 2GG4) and substrate-bound (*dark gray*, PDB 2GG6) forms of EPSP synthase. The substrate is shown as a space-filling model. Labeling sites S146 and D373 are visualized by stick plots of the leading rotamer of MTSL. (**b**) Label-to-label distance distributions. *Solid line* – mock experimental distance distribution for the substrate-bound form (see text). *Dashed line* – simulated distance distribution for the apo form. *Dotted line* – Tweaked distance distribution for the apo form by selecting those rotamer pairs that best fit the mock experimental distribution

both structures. These sites are located in different domains and the C^{α}–C^{α} distances of 4.72 nm (apo form) and 3.58 nm (substrate-bound form) are within the range that is accessible by dipolar EPR measurements. We prepared mock experimental data by computing the dipolar evolution function for the substrate-bound form from the simulated distance distribution, assuming a signal-to-noise ratio of 100 at $t = 0$ for $t_{max} = 3$ μs, a modulation depth of 0.4, and a protein concentration of about 100 μM. These data were reanalyzed with DeerAnalysis 2011 [17, 18] (http://www.epr.ethz.ch/software/index).

The mock experimental distance distribution, obtained by Tikhonov regularization with an optimum regularization parameter of $\alpha = 100$ (L curve criterion), is shown in Fig. 10b as a solid line. This distribution has a mean distance $\langle r \rangle = 3.99$ nm and a width $\sigma_r = 0.41$ nm. The values for the original simulated distance distribution are $\langle r \rangle = 4.00$ nm and $\sigma_r = 0.40$ nm. The simulated distance distribution for the apo form (dashed line in Fig. 10b) is clearly shifted to longer distances. The characteristic parameters are $\langle r \rangle = 5.00$ nm and $\sigma_r = 0.35$ nm. Disregarding the possible influence of relative reorientation of the domains and uncertainties in the rotamer distributions, this suggests a movement of the C^{α} atoms of residues S146 and D373 toward each other by 1.01 nm on substrate binding, which compares to a movement of 1.14 nm towards each other in the crystal structures.

We now consider whether this domain movement can be detected independently of the precision of the rotamer library approach and, if so, which is the lower bound for the domain movement that we can derive from the mock experimental data. For this we consider all possible pairs of spin label rotamers at sites S146R1 and D373R1 in the apo form, irrespective of the computed populations of the rotamers. Populations are reassigned so as to best fit the mock experimental distance distribution. Such reassignment of populations corresponds to asking the question whether any tweaked conformational distribution of the spin labels in the apo structure can fit the mock experimental distance distribution of the substrate-bound structure. This type of test is available in MMM 2010 via the "Any rotamers?" button in the DEER window.

As is apparent in Fig. 10, the tweaked distribution (dotted line) does not fit the mock experimental distribution (solid line). In particular, the minor peak at about 3.4 nm cannot be explained by any combination of spin label rotamers when assuming that the backbone structure is the one of the apo form. Furthermore, there is a contribution in the tweaked distribution at distances longer than 4.8 nm that cannot be suppressed and is not matched by the mock experimental distribution. Hence, the hypothesis that the mock experimental data are consistent with the backbone structure of the apo form has to be rejected.

More quantitatively, the tweaked distribution is characterized by $\langle r \rangle = 4.28$ nm and $\sigma_r = 0.39$ nm. This suggests a movement of the C^{α} atoms of residues S146 and D373 toward each other by at least 0.72 nm, disregarding reorientation effects. In any case, substantial closing of the gap between the domains is required to explain the mock experimental data.

Note that this example was chosen to illustrate a critical case, where only one constraint is available. Furthermore, the selected sites are not optimal. A better strategy to characterize this movement would be based on a spin labeling site scan of the apo structure and selection of several interdomain pairs in the distance range $\langle r \rangle = 2.5 \ldots 3.5$ nm.

6 Conclusion and Outlook

Under typical conditions, with data quality as illustrated in Fig. 4, mean label-to-label distances in proteins can be determined within approximately ± 0.2 nm in the range from 1.8 to 5 nm. Extension of this range toward longer distances or improvement of precision requires maintaining a signal-to-noise ratio of approximately 100 at $t = 0$ for data with $t_{\max} > 3$ µs. This is mainly an issue of increasing spectrometer sensitivity and improving sample preparation.

Uncertainties in predicting the label-to-label distance distribution from a known structural model of the protein backbone also amount to approximately ± 0.2 nm for the mean label-to-label distance. It follows that with current data analysis and modeling techniques, conclusions on protein structure derived from a single doubly labeled protein have a precision of about ± 0.3 nm (sum of variances). When using about ten site pairs, errors partially average and a precision of about ± 0.1 nm might be expected. This number compares favorably with the resolution of X-ray structures of many proteins, in particular membrane proteins, and with the structural distribution in NMR ensembles.

Improvements in predicting the label-to-label distance distribution will require a next generation rotamer library approach with internal rotamer energies $\varepsilon_{\mathrm{int},j}$ based on experimental data and an algorithm for computation of external interaction energies $\varepsilon_{\mathrm{ext},j}$ that allows for repacking of native amino acid side chains in the vicinity of the spin label. Given the approximations that will still be required, it may be unrealistic to expect a combined precision for measurement and prediction of spin label conformational distribution better than ± 0.2 nm for a single site pair. The lower limit for structural changes that can be discussed on the basis of five to ten site pairs may then be around 0.3 nm.

With respect to detection of backbone disorder, label-to-label distance distributions typically have widths between 0.2 and 0.5 nm for a rigid, well-defined backbone structure. It follows that variability of backbone structure up to about ± 0.5 nm may be masked by conformational variability of the labels. Computation of tweaked distance distributions with reassigned rotamer populations (Fig. 10) may reveal whether the width of an experimental distance distribution can be explained without assuming backbone disorder. Problems of this type would benefit tremendously from reduced uncertainty in predicting the spin label conformational distribution.

As far as quantitative information on structure and structural changes is concerned, the single most limiting factor is currently the absence of a general

modeling procedure that makes best use of sparse long-range distance constraints of the type provided by dipolar EPR spectroscopy. Encouraging first steps along this line have been taken by using the EPR constraints to improve ab initio Rosetta modeling of protein structures [64–66]. An alternative approach amenable to larger proteins could be based on the result that about ten distance constraints are sufficient to model a structural transition by flexible fitting with an elastic network model [38]. Implementation of the latter approach into MMM and experimental tests are now underway in our laboratory.

Acknowledgments The author thanks Yevhen Polyhach and Enrica Bordignon for helpful advice and SNF (grant 200020_132255/1) for financial support.

References

1. Milov AD, Salikhov KM, Shchirov MD (1981) Sov Phys Solid State (USA) 23:565
2. Milov AD, Ponomarev AB, Tsvetkov YD (1984) Chem Phys Lett 110:67
3. Pannier M, Veit S, Godt A, Jeschke G, Spiess HW (2000) J Magn Reson 142:331
4. Saxena S, Freed JH (1996) Chem Phys Lett 251:102
5. Borbat PP, Freed JH (1999) Chem Phys Lett 313:145
6. Jeschke G, Pannier M, Godt A, Spiess HW (2000) Chem Phys Lett 331:243
7. Jeschke G, Polyhach Y (2007) Phys Chem Chem Phys 9:1895
8. Schiemann O, Prisner TF (2007) Q Rev Biophys 40:1
9. Tsvetkov YD, Milov AD, Maryasov AG (2008) Uspekhi Khimii 77:515
10. Tsvetkov YD, Grishin YA (2009) Instrum Exp Tech 52:615
11. Igumenova TI, McDermott AE, Zilm KW, Martin RW, Paulson EK, Wand AJ (2004) J Am Chem Soc 126:6720
12. Hubbell WL, Cafiso DS, Altenbach C (2000) Nat Struct Biol 7:735
13. Klare JP, Steinhoff HJ (2009) Photosynth Res 102:377
14. Borbat PP, Mchaourab HS, Freed JH (2002) J Am Chem Soc 124:5304
15. Sale K, Song LK, Liu YS, Perozo E, Fajer P (2005) J Am Chem Soc 127:9334
16. Jeschke G, Bender A, Paulsen H, Zimmermann H, Godt A (2004) J Magn Reson 169:1
17. Jeschke G, Panek G, Godt A, Bender A, Paulsen H (2004) Appl Magn Reson 26:223
18. Jeschke G, Chechik V, Ionita P, Godt A, Zimmermann H, Banham J, Timmel CR, Hilger D, Jung H (2006) Appl Magn Reson 30:473
19. Jeschke G, Sajid M, Schulte M, Godt A (2009) Phys Chem Chem Phys 11:6580
20. Weber A, Schiemann O, Bode B, Prisner TF (2002) J Magn Reson 157:277
21. Jeschke G (2002) Macromol Rapid Commun 23:227
22. Milov AD, Tsvetkov YD (1997) Appl Magn Reson 12:495
23. Bowman MK, Maryasov AG, Kim N, DeRose VJ (2004) Appl Magn Reson 26:23
24. Hilger D, Jung H, Padan E, Wegener C, Vogel KP, Steinhoff HJ, Jeschke G (2005) Biophys J 89:1328
25. Bode BE, Margraf D, Plackmeyer J, Durner G, Prisner TF, Schiemann O (2007) J Am Chem Soc 129:6736
26. Borbat PP, Davis JH, Butcher SE, Freed JH (2004) J Am Chem Soc 126:7746
27. Ward R, Bowman A, Sozudogru E, El-Mkami H, Owen-Hughes T, Norman DG (2010) J Magn Reson 207:164
28. Banham JE, Baker CM, Ceola S, Day IJ, Grant GH, Groenen EJ, Rodgers CT, Jeschke G, Timmel CR (2008) J Magn Reson 191:202
29. Bonora M, Becker J, Saxena S (2004) J Magn Reson 170:278

30. Larsen RG, Singel DJ (1993) J Chem Phys 98:5134
31. Denysenkov VP, Prisner TF, Stubbe J, Bennati M (2006) Proc Natl Acad Sci USA 103:13386
32. Polyhach Y, Godt A, Bauer C, Jeschke G (2007) J Magn Reson 185:118
33. Godt A, Schulte M, Zimmermann H, Jeschke G (2006) Angew Chem Int Ed 45:7560
34. Jeschke G, Sajid M, Schulte M, Ramezanian N, Volkov A, Zimmermann H, Godt A (2010) J Am Chem Soc 132:10107
35. Kurshev VV, Raitsimring AM, Tsvetkov YD (1989) J Magn Reson 81:441
36. Maryasov AG, Tsvetkov YD (2000) Appl Magn Reson 18:583
37. Milov AD, Naumov BD, Tsvetkov YD (2004) Appl Magn Reson 26:587
38. Zheng W, Brooks BR (2006) Biophys J 90:4327
39. Polyhach Y, Jeschke G (2010) Spectrosc Int J 24:651
40. Shokhirev NV, Raitsimring AM, Rapatsky LA (1986) Chem Phys 105:117
41. Jeschke G, Koch A, Jonas U, Godt A (2002) J Magn Reson 155:72
42. Chiang YW, Borbat PP, Freed JH (2005) J Magn Reson 172:279
43. Weese J (1992) Comput Phys Commun 69:99
44. Pannier M, Schadler V, Schops M, Wiesner U, Jeschke G, Spiess HW (2000) Macromolecules 33:7812
45. Jeschke G, Godt A (2004) ChemPhysChem 4:1328
46. Ionita P, Volkov A, Jeschke G, Chechik V (2008) Anal Chem 80:95
47. Hilger D, Polyhach Y, Padan E, Jung H, Jeschke G (2007) Biophys J 93:3675
48. Hilger D, Polyhach Y, Jung H, Jeschke G (2009) Biophys J 96:217
49. Polyhach Y, Bordignon E, Jeschke G (2011) Phys Chem Chem Phys 13:2356
50. Junk MJ, Spiess HW, Hinderberger D (2010) Angew Chem Int Ed Engl 49:8755
51. Hansen PC (1992) SIAM Rev 34:56
52. Lovett JE, Hoffmann M, Cnossen A, Shutter AT, Hogben HJ, Warren JE, Pascu SI, Kay CW, Timmel CR, Anderson HL (2009) J Am Chem Soc 131:13852
53. Castellano C, Generosi J, Congiu A, Cantelli R (2006) Appl Phys Lett 89:233905
54. Doster W (2009) Biochim Biophys Acta 1804:3
55. Sezer D, Freed JH, Roux B (2008) J Phys Chem B 112:5755
56. Borovykh IV, Ceola S, Gajula P, Gast P, Steinhoff HJ, Huber M (2006) J Magn Reson 180:178
57. Earl DJ, Deem MW (2005) Phys Chem Chem Phys 7:3910
58. Allison JR, van Gunsteren WF (2009) ChemPhysChem 10:3213
59. Krivov GG, Shapovalov MV, Dunbrack RL Jr (2009) Proteins 77:778
60. Lillington JED, Lovett JE, Johnson S, Roversi P, Timmel CR, Lea SM (2011) J Mol Biol 405:427
61. Gruene T, Cho MK, Karyagina I, Kim HY, Grosse C (2011) J Biomol NMR 49:111
62. Bhatnagar J, Borbat PP, Pollard AM, Bilwes AM, Freed JH, Crane BR (2010) Biochemistry 49:3824
63. Funke T, Han H, Healy-Fried ML, Fischer M, Schonbrunn E (2006) Proc Natl Acad Sci USA 103:13010
64. Alexander N, Bortolus M, Al-Mestarihi A, Mchaourab H, Meiler J (2008) Structure 16:181
65. Hirst SJ, Alexander N, Mchaourab HS, Meiler J (2011) J Struct Biol 173:506
66. Kazmier K, Alexander NS, Meiler J, Mchaourab HS (2011) J Struct Biol 173:549

Struct Bond (2014) 152: 121–162
DOI: 10.1007/430_2011_62

Published online: 25 April 2012

Site-Directed Nitroxide Spin Labeling of Biopolymers

Sandip A. Shelke and Snorri Th. Sigurdsson

Abstract The application of electron paramagnetic resonance (EPR) spectroscopy to the study of biopolymer structure and dynamics has seen rapid growth in the last decade. In addition to advances in instrumentation – in particular, the development of high-field spectrometers and pulsed-EPR methods – spin-labeling techniques have evolved. Nitroxide spin labels can now routinely be incorporated at selected sites to interrogate how structure and dynamics at specific locations relate to biopolymer function. Furthermore, spin labels with improved properties have emerged, in particular, rigid labels that yield more accurate distance measurements, give information about orientation, and faithfully report site-specific dynamics. This review recounts how the three main approaches for site-directed spin labeling of biopolymers, namely, postsynthetic labeling, labeling during biopolymer synthesis, and noncovalent labeling, have been used to label proteins as well as nucleic acids.

Keywords Aminoxyl radical · Electron paramagnetic resonance · Electron spin resonance · Noncovalent spin labeling · Nucleic acids · Proteins

Contents

S.A. Shelke and S.T. Sigurdsson (✉)
Science Institute, University of Iceland, Dunhaga 3, 107 Reykjavik, Iceland
e-mail: snorrisi@hi.is

Abbreviations

2AP	2-Aminopurine
4-SU	4-Thiouridine
ADP	Adenosine diphosphate
AMP	Adenosine monophosphate
Arg	Arginine
ATP	Adenosine triphosphate
BSA	Bovine serum albumin
CoA	Coenzyme A
CW	Continuous wave
Cys-tRNA	Cysteine tRNA
dA	Deoxyadenosine
DEER	Double electron–electron resonance
DNA	Deoxyribonucleic acid
DQC	Double-quantum coherence
EPR	Electron paramagnetic resonance
Fmoc	9-Fluorenylmethyloxycarbonyl
Glu-tRNA	Glutamyl tRNA
GMPS	Guanosine monophosphorothioate
HPLC	High-performance liquid chromatography
mRNA	Messenger ribonucleic acid
MTS	1-Oxyl-2,2,5,5-tetramethylpyrrolinyl-3-methyl)-methanethiosulfonate
NAD^+	Nicotinamide adenine dinucleotide
NC-SDSL	Noncovalent and site-directed spin labeling
NMR	Nuclear magnetic resonance
PELDOR	Pulsed electron–electron double resonance
Phe-tRNA	Phenylalanine tRNA
POAC	2,2,5,5-Tetramethylpyrrolidine-*N*-oxyl-3-amino-4-carboxylic acid
RNA	Ribonucleic acid
SDSL	Site-directed spin labeling
Ser	Serine
SPPS	Solid-phase peptide synthesis
TAR RNA	*Trans*-activation responsive RNA
TEMPO	2,2,6,6-Tetramethylpiperidine-1-oxyl

TOAC	2,2,6,6-Tetramethylpiperidine-1-oxyl-4-amino-4-carboxylic acid
TPA	2,2,5,5-Tetramethyl-pyrrolin-1-yloxy-3-acetylene
tRNA	Transfer ribonucleic acid
Tyr	Tyrosine
UDP	Uridine diphosphate

1 Introduction

The function of biopolymers is intertwined with their structure and conformational dynamics. Electron paramagnetic resonance (EPR) spectroscopy is a valuable magnetic resonance technique for extracting information about both structure and dynamics of biopolymers, as described in detail in other chapters of this volume. In short, mobility of paramagnetic groups at specific sites can be directly ascertained from the shape of continuous-wave-(CW) EPR spectra, while dipolar interactions between unpaired electrons using either CW- or pulsed-EPR techniques, such as pulsed electron–electron double resonance (PELDOR) – also known as double electron–electron resonance (DEER), yield structural information [1–6]. Structural insights can also be obtained indirectly from changes in the collective dynamics of several sites upon ligand binding [7, 8]. EPR is also valuable for determining site-specific solvent accessibility and the polarity of its surrounding environment [9–11]. EPR studies can be carried out under biologically relevant conditions and are especially useful for large biopolymers that are difficult to study by NMR spectroscopy or X-ray crystallography, such as membrane-bound proteins.

EPR studies of biopolymers require the presence of paramagnetic centers. A few biopolymers contain intrinsic paramagnetic metal ions that are useful spin labels [12]. There are also instances where the biopolymer may contain a metal-ion binding site, which normally hosts a diamagnetic metal ion that can be replaced with a paramagnetic ion. For example, Mg^{2+} is frequently replaced with Mn^{2+} (see chapter by Goldfarb) [4, 13]. However, most biopolymers are diamagnetic and, therefore, require incorporation of an unpaired electron, usually referred to as a spin label [14–20]. Moreover, the EPR reporter groups need to be directed to chosen sites, i.e., the spin labels need to be incorporated at specific sites.

The spin labels have to be stable enough to enable incorporation into the biopolymer and allow EPR measurements under biologically relevant conditions. The most commonly used spin labels are aminoxyl radicals, commonly referred to as nitroxides, that are not in conjugation with π-bonds. The carbon atoms adjacent to the nitroxide contain methyl groups that contribute to the persistence of the otherwise rather unstable radical by steric and inductive effects [21–23]. The structure of a typical nitroxide (**1**) is shown in Fig. 1, along with its X-band CW-EPR spectrum. The EPR spectrum shows three lines due to the hyperfine coupling of the electron with the nitrogen atom.

There are two important factors to consider when selecting a nitroxide spin label for a biopolymer: the structure of the linker and the method for attachment of the

Fig. 1 Structure of 2,2,6,6-tetramethylpiperidine-1-oxyl (TEMPO) radical (**1**) and its X-band CW-EPR spectrum

label. The properties of the linker will affect the spectrum of the nitroxide spin label. For example, if the nitroxide is linked to the polymer with a long and flexible linker, the dynamics of the probe, as manifested in the EPR spectrum, will reflect motion of the linker rather than the biopolymer. Distance measurements between two such labels will also not be accurate since the ensemble of linker conformations will yield a distribution of distances. In contrast, if the linker does not have any intrinsic mobility, then the nitroxide will report the motion of the site to which it is attached and yield accurate distances between two such labels in the biopolymer.

The chemistry of conjugation is another key aspect of biopolymer spin labeling. There are three main strategies for incorporation of a spin label or other reporter groups into specific sites, referred to as site-specific or site-directed spin labeling (SDSL) (Scheme 1). The first approach is postsynthetic labeling, which refers to labeling after synthesis of the biopolymer (Scheme 1a). Here, the biopolymer contains a uniquely reactive group that can be selectively targeted with a spin-labeling reagent. This is the most common approach for proteins, utilizing the reactivity of sulfhydryl groups of cysteine. Disadvantages include possible side reactions of the spin-labeling reagent with other reactive functional groups of the biopolymer and incomplete labeling.

The second approach is incorporation of the label during synthesis of the biopolymer, which is usually the method of choice for spin labeling of nucleic acids (Scheme 1b). This approach is advantageous for incorporation of structurally complex labels, such as rigid spin labels, and ensures site-specific labeling. However, this approach is often more laborious than the aforementioned postsynthetic spin-labeling strategy due to the synthetic effort required for preparation of the spin-labeled building blocks. Furthermore, if the biopolymer is synthesized chemically, the reaction conditions must be compatible with the label, i.e., the nitroxides should not participate in reactions during the polymer synthesis.

The third method is noncovalent labeling, in which the biopolymer binds a ligand, for example, at the active site of an enzyme or a cofactor binding site through noncovalent interactions, such as hydrogen bonding, ionic-, hydrophobic-, and π-stacking interactions (Scheme 1c). The spin label is conjugated to the ligand such that the label will not interfere with binding to the receptor site on the biopolymer. Since the label is not firmly attached to the biopolymer with a covalent bond, the affinity needs to be high enough to get complete labeling. Spin-label binding through such ligand–receptor interactions can be readily monitored by EPR spectroscopy since the free and bound ligands have very different rotational

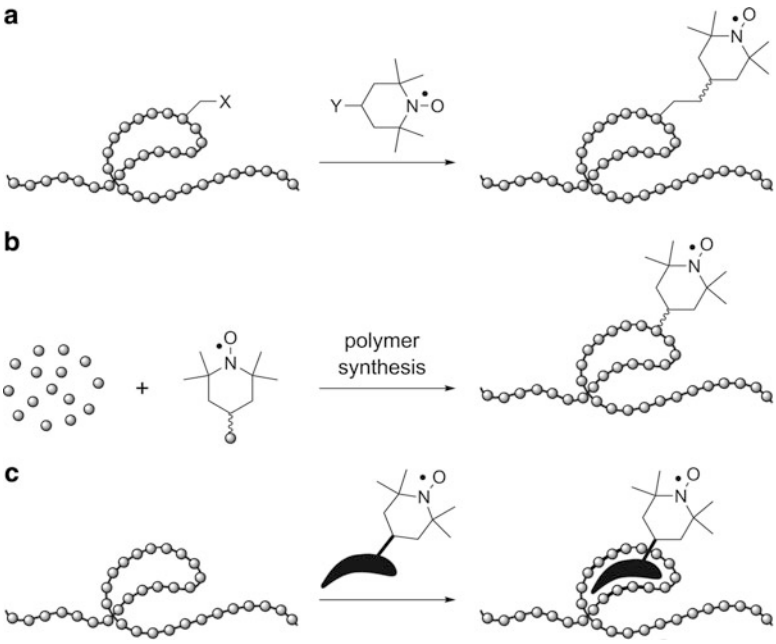

Scheme 1 A cartoon representation of the three main strategies for site-directed conjugation of reporter groups to biopolymers. (**a**) Postsynthetic labeling. *X* and *Y* indicate functional groups that react to form covalent bond(s) between the polymer and the spin label. (**b**) Labeling during polymer synthesis. (**c**) Noncovalent and site-directed spin labeling. TEMPO is used as a representative nitroxide spin label

correlation times [24–26]. Potential disadvantages of noncovalent labeling include the limited number of naturally occurring binding sites and competition between binding sites. Another restriction is that ligand-binding sites cannot be readily moved around in proteins while maintaining form and function.

After the biopolymer spin labeling, the incorporation of the label needs to be verified. EPR spectroscopy can both confirm that the spin label has been incorporated and be used to quantify the extent of labeling. For nucleic acids, enzymatic digestions of labeled material, followed by an HPLC analysis of the digest in comparison to authentic samples, have traditionally been used to verify incorporation of labeled nucleosides [27, 28]. In recent years, mass spectrometry has increasingly been used to verify the spin labeling.

The most important criterion for spin labels and other reporter groups is that they do not perturb the structure and/or function of the biopolymer. This can be readily verified after spin labeling when the biopolymer has a function that is easy to monitor. For example, if the catalytic activity of an enzyme [29, 30] or a nucleic acid [31–33] is similar before and after incorporation of the spin label(s), it is a good indication that the spin labeling is not perturbing the structure of the enzyme. In addition, the thermodynamics of folding can be used to gain insight into possible structural perturbations by the probe. For example, thermal denaturation of nucleic

acid helices can readily ascertain if the spin label affects the duplex helix. If there are only minor changes in the melting temperature, it is unlikely that the label has significantly affected the duplex structure.

The aim of this review is to give a fairly complete, albeit not a fully comprehensive, overview of the spin-labeling methods that have been applied to proteins and nucleic acids. After a short historical perspective, a detailed overview is given of both the labeling sites and the structures of the labels. The protein labeling is described in the context of the labeling strategy used, whereas the nucleic acid spin labeling is categorized according to labeling sites.

2 Protein Spin Labeling

Although short peptides can be readily synthesized by automated chemical synthesis, the chemical synthesis of longer chains, such as found in most proteins, remains challenging. Therefore, postsynthetic labeling has been the method of choice to spin-label proteins. However, because of the multitude of functional groups present on the side chains, the challenge has been to selectively modify the desired amino acid(s). Most of the labeling reagents react with more than one type of side chain, but selectivity has often been achieved by changing the reaction conditions used for labeling. For example, the amino group of lysine is nucleophilic and reactive toward most of the known electrophilic spin labels, but when the reactions are carried out at neutral pH, the amino group is protonated and, thus, nonnucleophilic [34]. Some reagents are specific for a certain side chain, the best example being cysteine spin labeling through formation of disulfides. In fact, most spin-labeling reactions of proteins today rely on cysteine labeling.

2.1 The Early Days of Protein Spin Labeling

The concept of biopolymer spin labeling was introduced by McConnell in 1965 [35, 36]. He chose nitroxide radicals as the reporter groups, due to their stability and relative ease of synthetic manipulation as well as the simplicity of their EPR spectra. Initially, McConnell and his colleagues prepared the nitroxide-containing isocyanate **2** (Fig. 2) for labeling poly-L-lysine and bovine serum albumin (BSA) [36]. They subsequently used EPR spectroscopy to study pH-dependent structural transitions of the labeled polymers, such as the random coil to helix transition of poly-L-lysine. The isocyanate spin-labeling reagent **2** was found to be unstable in aqueous solutions; hence, the more stable maleimide **3** was subsequently introduced by the same group [37]. The maleimide spin-labeling reagent was used to spin label a number of proteins, including poly-L-lysine, BSA, and α-chymotrypsin [37]. The maleimide reacted preferentially with the sulfhydryl group of cysteine, but there was evidence for reaction at other amino acids, presumably lysines [37].

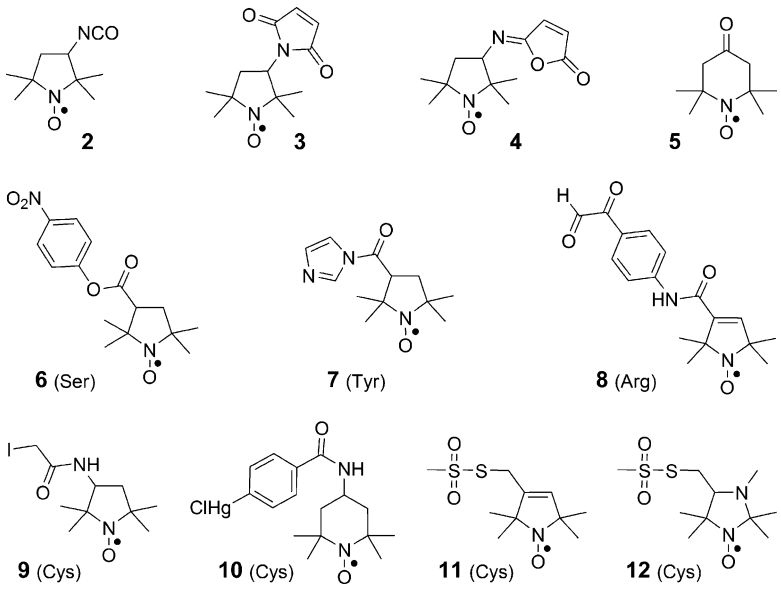

Fig. 2 Spin-labeling reagents for postsynthetic labeling of proteins. *Three-letter abbreviations* indicate amino acids that can be preferentially targeted with the reagent

Another variant of the maleimide-labeling reagent is the isomaleimide **4**, which was found to be eight times more efficient for lysine-labeling than maleimide [38]. It was also found that **3** and **4** report different mobility when attached to similar sites. During the same period, Wagner and Jung Hsu reported spin labeling of poly-L-lysine using reductive alkylation of the amino groups of lysine with spin-labeled ketone **5** in the presence of sodium borohydride. An advantage of this method was its specificity for labeling amino groups and the high water solubility of **5** [39].

Berliner and McConnell reported the nitroxide radical nitrophenyl ester **6** (Fig. 2), a substrate for α-chymotrypsin, which formed a spin-labeled acyl enzyme intermediate with serine that was stable at low pH [40]. This was the first time that an active site of an enzyme was spin-labeled and enabled investigation of the nature of the binding site and the catalytic mechanism of the enzyme.

A major focus during the early days of protein spin labeling was to develop reagents that could target different amino acids in a protein. For example, spin label **7** was reported for acylation of the hydroxyl group of tyrosine [41] and has been used to study nucleosome core particles by EPR [42, 43]. A few spin-labeling reagents have also been reported for arginine, such as the 1,2-dicarbonyl compound **8** [44]; however, the detailed structural characterization of the resulting arginine-spin-label conjugates has not been reported.

McConnell's group has also employed maleimide **3** and alkylating reagents, such as iodoacetamide derivative **9**, for the labeling of cysteines in proteins [34, 45]. Neither of these reagents was completely specific for cysteine since they also react with histidines, methionines, and lysine. However, the extent and selectivity of

labeling largely depends on the pH of the reaction solution. For example, histidines react under slightly acidic conditions (pH 5–6), cysteines under slightly basic conditions, and lysines under alkaline conditions (pH $>$ 8), whereas methionine reacts in this whole pH range [34]. Thus, methionine can be selectively spin-labeled in the presence of amino groups under acidic conditions. Selectivity can also be achieved by carefully monitoring the reaction time. For example, cysteines react completely within a few hours, while others may take days. A nitroxide derivative of *p*-chloromercuribenzoate **10** and its pyrrolidine analogue has also been reported as a specific reagent for cysteine [46, 47], but has not been used extensively due to size of the linker and its decomposition upon exposure to light.

The aforementioned spin-labeling reagents are selective rather than specific toward a selected amino acid. Therefore, it was a major breakthrough when Berliner and coworkers reported the reactive and thiol-specific spin label 1-oxyl-(2,2,5,5-tetramethylpyrrolinyl-3-methyl)-methanethiosulfonate (MTS) (**11**), which forms a mixed disulfide with cysteine [29]. In addition to the high specificity of this reagent toward thiol, the reversibility of disulfide bond formation can be readily used to verify the labeling stoichiometry upon release of the label by incubation with a mild reducing agent. Furthermore, the side chain is relatively small and found to be well tolerated in proteins. A similar spin label (**12**) was later reported by Smirnov and coworkers, where the nitroxide-bearing ring contained a nitrogen atom, which made the label sensitive to changes in pH and polarity [48]. Thus, the thiosulfonate spin labels have contributed to cysteine becoming the most useful amino acid for spin labeling. The only remaining obstacle at this point for obtaining a general procedure for site-specific spin labeling of proteins was to obtain proteins with cysteine amino acid(s) in chosen location(s).

2.2 Site-Directed Spin Labeling of Proteins

Hubbell and coworkers combined site-directed mutagenesis, a molecular biology technique for introducing point mutations into proteins [49], with the cysteine-specific spin label (**11**) to provide a general solution for protein spin labeling, termed SDSL [9, 50, 51]. First, any cysteines native to the protein are changed to nonreactive and structurally similar amino acids like serine or alanine. If these mutations do not affect the activity of the protein, chosen amino acid(s) are replaced with cysteine(s) that are subsequently spin-labeled and the activity of the spin-labeled protein is verified. This method ensures that only selected amino acids are spin-labeled.

The inherent conformational flexibility of the nitroxide-bearing side chain **R1** (Scheme 2), formed by the reaction of the cysteine sulfhydryl with **11** (Fig. 2), has the advantage of minimizing possible interference of the label with the protein folding into the native structure. Moreover, changes in the mobility of the flexible

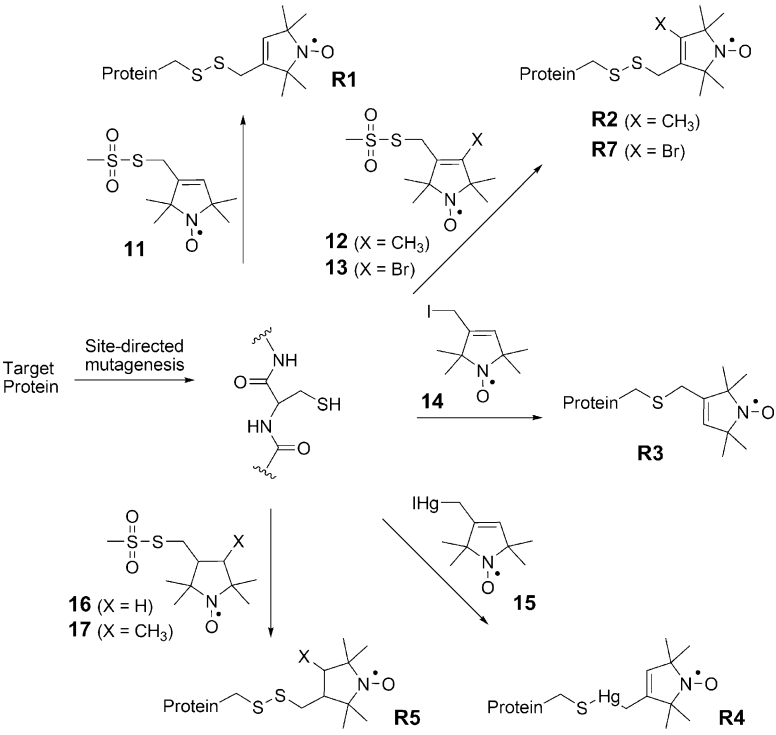

Scheme 2 Site-directed spin labeling of proteins, including structures of several spin-labeled side chains

linker of **R1** can yield structural information by EPR, for example, to distinguish between amino acids at the surface of the protein and those that are involved in tertiary interactions or even buried in the interior of the protein [52]. Disadvantages of such a flexible side chain include less sensitivity of the label to motions of the protein backbone being probed by EPR and inaccurate distance measurements between two such labels.

Structure–function studies of different side chains in T4 lysozyme unexpectedly revealed that the shorter label **R3** (Scheme 2) was more mobile than **R1** [53]. This was interpreted to be due to attractive interactions between the disulfide and the protein backbone, rather than restricted rotation around the disulfide bond, which explained the conformational heterogeneity found in some **R1**-containing proteins [54, 55]. The side chains **R4** and **R5** (Scheme 2) showed relatively higher mobility than **R1**, in spite of having approximately same length and equal molecular volume, which made them more suitable for probing tertiary interactions through dynamics [53]. In contrast, substituents in the 4-position of the nitroxide-containing ring, such as methyl (**R2**) and bromo (**R7**) resulted in reduced mobility of the side chain. Therefore, **R2** and **R7** are better probes of the protein backbone flexibility than **R1**.

2.3 Protein Labeling Through Protein/Peptide Synthesis

As mentioned above, a potential drawback of the SDSL approach is the necessity to remove native cysteines that may be necessary for folding or function of the protein being studied. Incorporation of the spin-labeled amino acid at specific sites during the polymer synthesis circumvents that potential complication. The polymerization can be carried out using ribosomal synthesis of proteins or by using the methods of organic synthesis.

2.3.1 Spin Labeling by Ribosomal Synthesis of Proteins

Proteins can be prepared in cell-free expression systems using an extract containing the components for translation, ribosomes, tRNAs, mRNA template, etc. Schultz and coworkers have pioneered the use of this approach for the preparation of proteins containing unnatural amino acids at specific sites [56, 57]. Incorporation of the unnatural amino acids is enabled by the use of an amber suppressor tRNA that has been chemically charged with the amino acid of choice, in conjunction with an mRNA that contains the amber nonsense codon. This method has been used for the incorporation of the spin-labeled amino acid **18** into T4 lysozyme (Scheme 3), which also showed limitations of this approach: low expression efficiency, only two

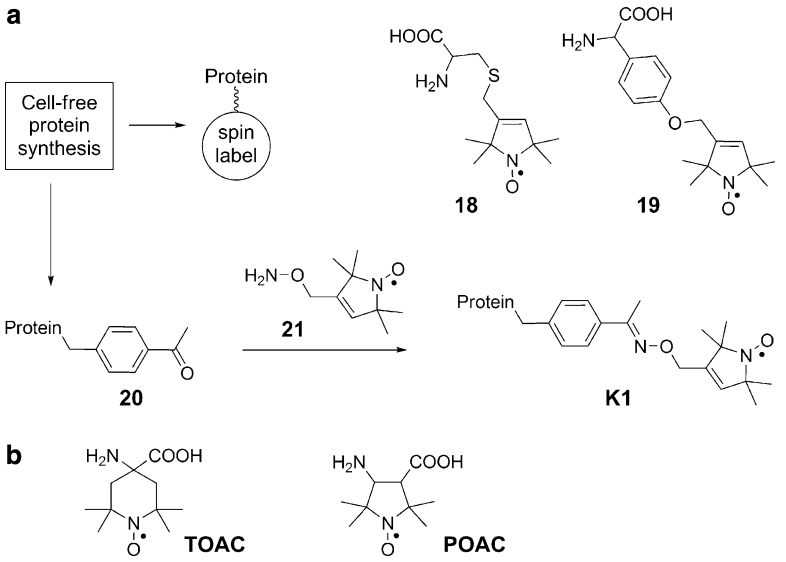

Scheme 3 Incorporation of spin labels into proteins and peptides during polymer synthesis. (**a**) Spin labeling based on cell-free ribosomal protein synthesis, along with the spin-labeled amino acids **18** and **19**, as well as side chain **K1**. (**b**) Structures of the spin labels 2,2,6,6-tetramethyl-piperidine-1-oxyl-4-amino-4-carboxylic acid (**TOAC**) and 2,2,5,5-tetramethylpyrrolidine-*N*-oxyl-3-amino-4-carboxylic acid (**POAC**)

out of six chosen positions could be spin-labeled and only one out of three spin-labeled amino acids was incorporated [58]. Voss and coworkers also used this approach to incorporate spin-labeled amino acids **18** and **19** (Scheme 3) in oocytes, using the luciferase reporter gene [59]. However, the incorporation efficiencies were only 1% for the spin-labeled amino acids, compared to 9% for phenylalanine. A ketone-containing amino acid has also been incorporated into proteins [60] by in vitro translation and subsequently reacted with a hydroxylamine-functionalized nitroxide (**21**) to yield an oxime-modified amino acid (Scheme 3) [61]. However, the spin-labeled side chain (**K1**) is more mobile than **R1** (Scheme 2) and gives a wide distribution of distances when used in distance measurements by PELDOR or DEER [61]. The latter approach, although described in this section, is another variant of the SDSL, where an amino acid (cysteine or the keto-modified amino acid) is postsynthetically converted into a spin-labeled amino acid.

Although preparation of spin-labeled proteins by incorporation of an unnatural amino acid through translation is a valuable approach, the technology is not readily available and there are limitations to what amino acids can be incorporated. The same is true for postsynthetic labeling. For example, all the spin-labeled amino acids that have been incorporated into proteins either through ribosomal protein synthesis or postsynthetic spin labeling contain a nitroxide that is attached through a flexible tether. For incorporation of conformationally restricted (rigid) amino acids into peptides/proteins, peptide synthesis remains the method of choice, which enables incorporation of unnatural amino acids irrespective of their structures.

2.3.2 Spin Labeling Through Solid-Phase Peptide Synthesis

In solid-phase peptide synthesis (SPPS) [62], also termed the Merrifield synthesis [63], amino acids are stitched together in a stepwise fashion using organic chemistry. The main advantage of SPPS is that it is possible to incorporate nonnative amino acids with the desired structures at any position in the sequence. Initially, incorporation of spin-labeled amino acids into peptides was limited to the terminal positions, due to the instability of nitroxide group in trifluoroacetic acid, used in the deprotection step in the peptide synthesis cycle. [64–66]. To avoid the repeated acid exposure, Nakaie incorporated the spin-labeled amino acid 2,2,6,6-tetramethylpiperidine-1-oxyl-4-amino-4-carboxylic acid (**TOAC**) [67] (Scheme 3b) at an internal site of an octapeptide using Fmoc N^{α}-protection strategy [68]. Upon cleavage of the peptide from the resin, the nitroxide was reduced to the corresponding hydroxyl amine, but could be readily recovered upon exposure to air under basic conditions.

Although only relatively short spin-labeled peptides can be prepared by SPPS [69], it is possible to link such peptides to larger peptides or protein, using classical fragment condensation through disulfide formation or native chemical ligation [70]. In the latter approach, a C-terminal thioester is coupled with a protein or a peptide containing an N-terminal cysteine amino acid. After thiotransesterification, a peptide bond is formed through an intramolecular reaction between the alpha-amino group of the cysteine with the thioester. Polypeptides as long as 304

amino acids have been prepared by a combination of solid-phase synthesis and chemical ligation [71].

The aforementioned spin-labeled amino acid **TOAC** (Scheme 3b) has the advantage of being achiral, which avoids isolation of enantiomerically pure amino acids. Another advantage of **TOAC** is that it has limited flexibility; the only movement of the label independent of the protein backbone is conformational motion in the nitroxide-bearing ring. As a result, more detailed information about dynamics of the peptide backbone can be extracted from the EPR spectra. Moreover, distance measurements between two **TOAC** nitroxides are more accurate than for spin labels linked to the protein with flexible tethers. Therefore, it is not surprising that **TOAC** has been used in several structural studies, in particular, to study conformations of short helical peptides [72–80]. However, there are indications based on EPR studies that helical conformations of **TOAC**-labeled peptides differ from the common helical structures found in proteins [81]. Another drawback of **TOAC** is that the coupling yields during peptide synthesis is not very good; the alpha position in **TOAC** has two substituents, which makes the amino group less accessible for coupling due to steric hindrance. To remedy that situation, the rigid and spin-labeled β-amino acid 2,2,5,5-tetramethylpyrrolidine-*N*-oxyl-3-amino-4-carboxylic acid (**POAC**) has been prepared [82]. **POAC** has better coupling yields than **TOAC**, but has the drawback that its stereoisomers need to be separated before peptide synthesis.

Several other spin-labeled amino acids have been reported. In particular, Hideg and coworkers have prepared a number of spin-labeled amino acids that vary in nitroxide structure as well as the polarity and conformational mobility of the side chain [83–87]. However, most of these spin-labeled amino acids have not been incorporated into peptides.

2.4 Noncovalent and Site-Directed Spin Labeling of Proteins

Stryer and Griffith reported the first example of noncovalent and site-directed spin labeling (NC-SDSL) of proteins, using a spin-labeled hapten (**22**) to probe interactions with an antibody that had been raised against a 2,4-dinitrophenyl moiety [88]. Several spin-labeled ligands, or spin probes, have subsequently been prepared to study proteins. In general, the probes are cofactors to which a nitroxide spin label has been attached.

Trommer and coworkers prepared spin-labeled NAD^+ derivatives, where the nitroxide was attached to the 6- (**23**) [89, 90] or the 8-position (**24**) of the base [91] (Fig. 3). Both derivatives have also been prepared with a perdeuterated nitroxide [92] to avoid the inhomogeneous line broadening that originates from the protons on the piperidine ring. Furthermore, photoaffinity derivatives of **23** and **24** have also been prepared [93]. The noncovalent complexes of NAD^+ derivatives **23** and **24** with several enzymes have been studied by EPR, including lactate dehydrogenase [90, 94, 95], glyceraldehyde-3-phosphate dehydrogenase [96–98], alcohol dehydrogenase [99], and liver glutamate dehydrogenase [24] (Fig. 3).

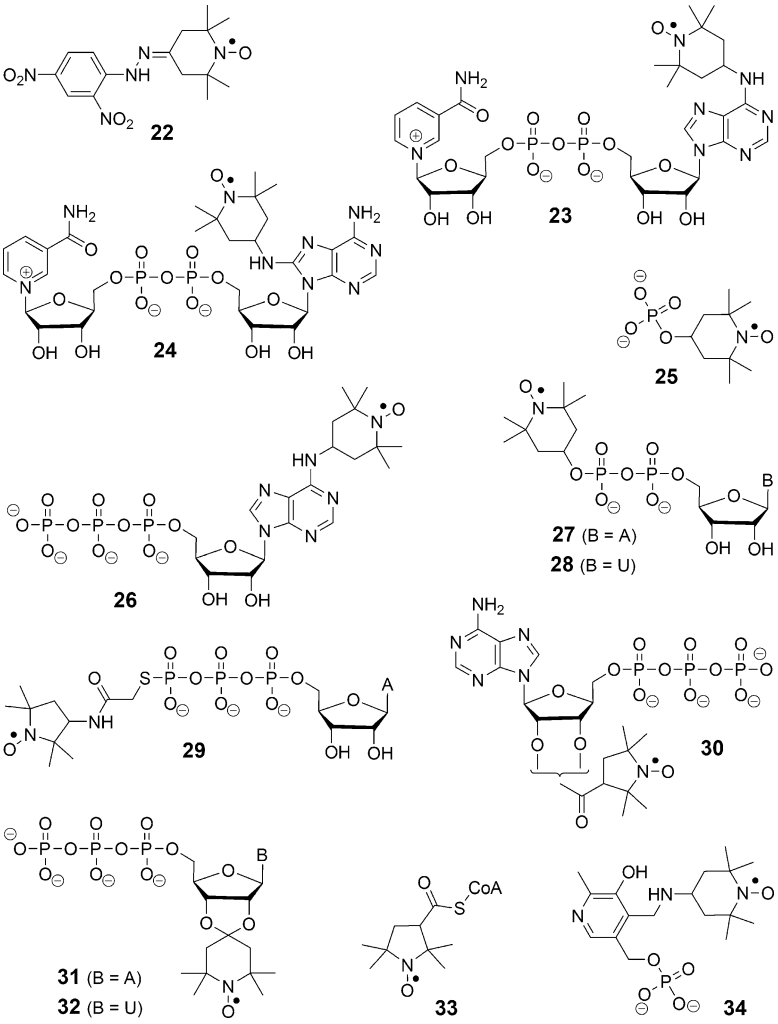

Fig. 3 Spin-labeled ligands for noncovalent spin labeling

Many enzymes bind phosphates, and several such spin-labeled derivatives have been prepared. One of the first examples, and the simplest derivative, was the spin-labeled monophosphate **25**, which was used to study binding of inorganic phosphate to ribonuclease [100]. Most of the other phosphate-derived labels for noncovalent labeling of proteins are nucleotides. Nitroxides have been incorporated into all three moieties of nucleotides: the base, the phosphate, and the sugar. The N-6-labeled ATP (**26**), along with analogous derivatives of AMP and ADP, was prepared for a study of glutamine adenylyltransferase [101]. The terminal phosphates can also be readily spin-labeled. The phosphate-labeled ADP (**27**) was

prepared as an analogue of NAD, for studies of alcohol dehydrogenase [99, 102, 103] and used later to study conformational changes in myosin [25], while spin-labeled UDP (**28**) was used as a competitive inhibitor of galactosyltransferase [104]. Reactions of a phosphorothioate with the spin-labeling reagent **41** (Fig. 5) have also been used to prepare nucleotides containing a nitroxide on the terminal phosphate, including AMP, ADP, and ATP (**29**), the last of which was used to study phosphoribulokinase [105].

Incorporation of a single spin label into ATP through an ester linkage to either the 2′- or the 3′-OH of the nucleotide sugar yields a mixture of the 2′- and 3′-esters (**30**) due to a facile intramolecular transesterification [106–108]. For preparation of the 2′-labeled nucleotide, the 3′-deoxynucleotide must be used and the 2′-deoxy-nucleotide if the 3′-labeled nucleoside is to be prepared [107]. Adenosine phosphatase [106, 108] and myosin [107] have been studied with **30,** and its azido-containing photoaffinity labels have also been prepared for the study of adenosine triphosphatase [109] and a calcium pump protein [110]. The spin-labeled trinucleotides of ATP and UTP, **31** [111] and **32** [112], respectively, contain a spin label that bridges the 2′- and 3′-hydroxyl groups on the sugar; the latter has been used to study myosin and actomyosin [112]. An advantage of the spiroketal derivatives **31** and **32** over the other nucleotide derivatives is that the spin label is conformationally restricted and, therefore, a more accurate reporter of both dynamics and structure.

Spin-labeled acetyl CoA [113] has been prepared as a thioester (**33**) and used to study citrate synthase [113], 3-hydroxy-3-methylglutaryl-CoA synthase [114], and 3-hydroxy-3-methylglutaryl-CoA lyase [115]. Several spin-labeled derivatives of vitamin B6, such as **34**, have been used to study the active site of aspartate aminotransferase [116].

Aromatic sulfonamides are known noncovalent inhibitors of carbonic anhydrases [117]. Several spin-labeled analogues have been reported that contain different linkers between the nitroxide and the sulfonamide functionalities (**35**–**38**) (Fig. 4) and used for studying the topography of the active sites of bovine erythrocyte carbonic anhydrase B [118], human erythrocyte carbonic anhydrases B and C [119, 120], and other mammalian erythrocyte carbonic anhydrases [121].

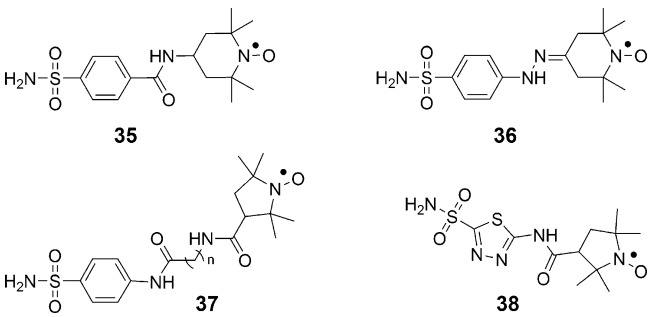

Fig. 4 Spin-labeled aromatic sulfonamides

3 Nucleic Acid Spin Labeling

Although chemistry of oligonucleotide synthesis was being developed as early as in the 1950s, it was not until the 1980s that automated synthesis on a solid support using commercially available reagents became routine. This development made a large impact on nucleic acid labeling since labeled nucleotides could be incorporated at specific sites in oligonucleotides using automated chemical synthesis. This is in contrast to proteins, where limitations in synthesis of long polypeptides have prevented routine labeling of proteins through peptide/protein synthesis. Thus, postsynthetic labeling of proteins is the most popular approach, whereas labeled oligonucleotides are usually prepared by direct synthesis.

Below is an overview of spin-labeled nucleic acids, which starts with a description of the early work. This is followed by site-directed labeling of nucleic acids, which is divided into sections based on the site of modification, i.e., whether the label is connected to the base, sugar, or phosphate. Toward the end, a new noncovalent approach for SDSL of nucleic acids is described.

3.1 The Early Days of Nucleic Acid Spin Labeling

The first application of spin labeling, in combination with EPR spectroscopy, for the study of nucleic acids was reported by Ohnishi and McConnell, who used the relatively unstable chlorpromazine radical cation as a spin-labeled DNA intercalator [35]. Subsequently, Yamane and Smith reported the use of alkylating reagents **39** [122], **40** [123], and **41** [45] (Fig. 5a) to spin-label DNA and RNA [124]. Nitroxide **41** was found to be the most reactive and preferentially targeted purines, presumably through N7 alkylation. Similarly, Bobst used nitroxide-containing iodoacetamide **43** [125] for spin-labeling homopolynucleotides (rA), (rU), and (rG) and studied conformational transitions of poly(rA) by EPR spectroscopy [126]. Iodoacetamide **9** (Fig. 2) has also been used for spin-labeling homopolynucleotides [127]. However, all these reagents suffer from the lack of nucleotide-and-sequence selectivity.

Known nucleic acid cross-linking agents have also been utilized for the delivery of nitroxides to nucleic acids. Spin-labeled derivatives of DNA–DNA cross-linking agents have increased efficiency of alkylation and, in some cases, target-specific 2–6-nucleotide-long sequences. Examples include the hydrazine mustard spin label **44** (Fig. 5b), which was used to target guanines in single- and double-stranded DNA [128], and nitroxide derivatives of psoralen (**45** and **46**) that form a photoadduct with double-stranded DNA through sequence- and site-specific cross-linking [129]. Similarly, Lippard and Dunham reported sequence-specific spin labeling of DNA using the *cis*-platin derivative **47** [130]. The solution structure of a **47**-labeled duplex was solved by NMR spectroscopy, utilizing the paramagnetic spin label to provide additional structural restrains at the site of cross-linking [131].

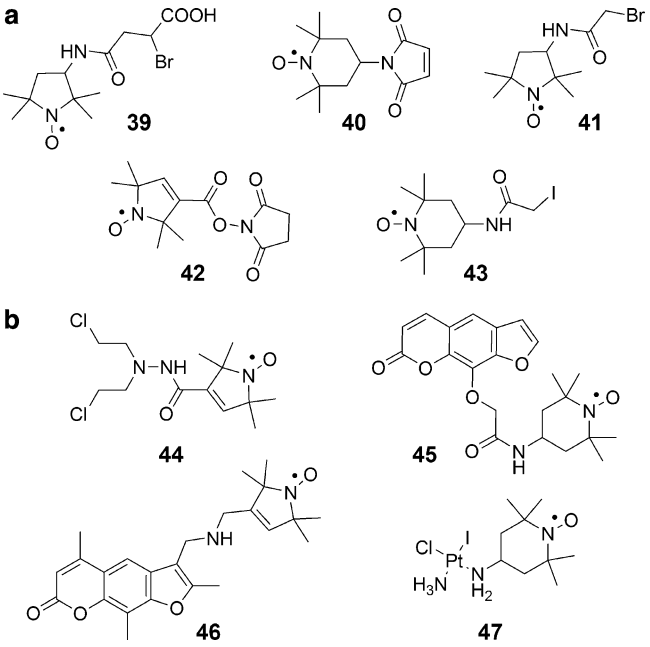

Fig. 5 Nitroxide spin-labeling reagents. (**a**) Alkylating agents. (**b**) Bifunctional alkylating agents

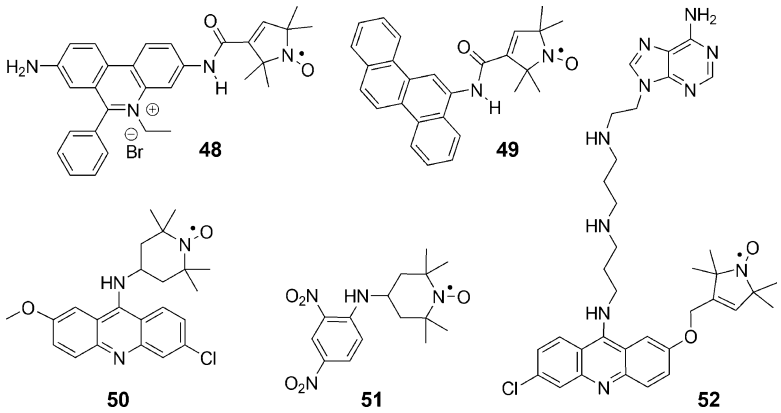

Fig. 6 Spin-labeled nucleic acid intercalators

Nitroxide-containing intercalators have been used for noncovalent spin labeling of nucleic acids (Fig. 6). Hong and Piette used spin-labeled ethidium bromide (**48**) and nitroxide derivatives of polyaromatic carcinogens, such as **49** to bind to duplex DNA [132]. Temperature-dependent EPR studies of these complexes gave insights into dissociation of the DNA–carcinogen complexes. Other examples include the spin-labeled acridine analogue **50** [133] and the nitrobenzene derivative **51** [134].

Although these spin-labeled intercalators bind well to DNA duplexes, they lack site selectivity. Lhomme and coworkers have linked a spin-labeled intercalator to adenine (**52**), which can bind to an abasic site in duplex DNAs [135, 136]. The adenine was found to direct the intercalator into the vicinity of the abasic site.

In contrast to DNA, some RNAs contain unique reactive groups that can be utilized for SDSL. In fact, the first example of SDSL of nucleic acids was that of transfer RNA (tRNA), where *N*-hydroxysuccinimide ester **42** (Fig. 5a) was used to label the α-amino group of valine on a valine-charged tRNA from *Escherichia coli* [137]. Similar labeling strategies have also been reported on *E. coli* Phe-tRNA [138] and yeast Cys-tRNA, the latter by selective labeling of free sulfhydryl group of cysteine with iodoacetamide **9** (Fig. 2) [139].

Thio-modified bases are found in several tRNAs and can be selectively alkylated. Hara et al. reported the site-specific labeling of tRNAs from *E. coli* by selectively reacting bromoacetamide spin label **41** (Fig. 5a) with 4-thiouridine (4-SU, **53**) (Scheme 4a), while retaining their biological activity [140]. This reaction can be conveniently monitored by the disappearance of the absorbance of 4-SU at 330 nm. Nitroxide **43** (Fig. 5a) has also been used to spin-label 2-thiocytidine after its enzymatic incorporation into tRNA using tRNA nucleotidyl transferase, to yield spin-labeled nucleotide **55** [141]. The rare base 2-thio-5-(*N*-methylaminomethyl)-uridine of the anticodon of *E. coli* Glu-tRNA has also been spin-labeled by acylation with a mixed anhydride spin-labeling reagent to yield

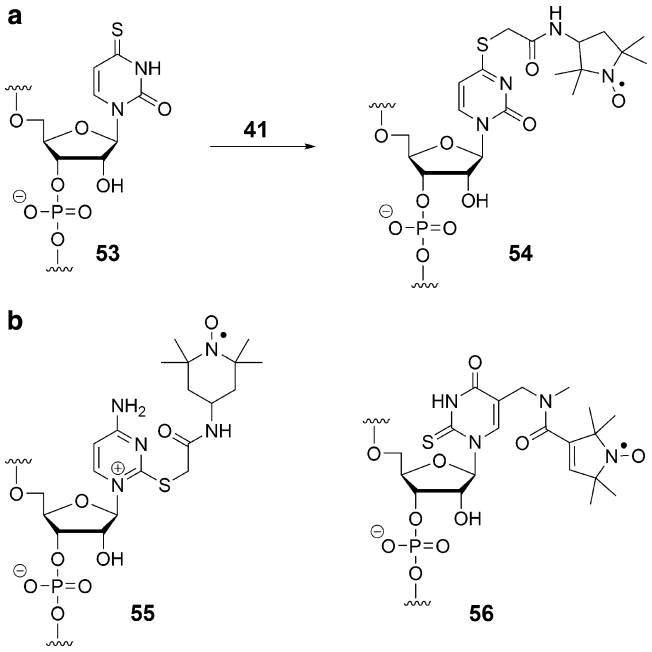

Scheme 4 Site-directed spin labeling of RNA containing thio-modified bases. (**a**) Spin labeling of 4-SU. (**b**) Spin-labeled 2-thiocytidine (**55**) and 2-thio-5-(*N*-methylaminomethyl)-uridine (**56**)

nucleotide **56**, through a reaction of the amine rather than the sulfur atom (Scheme 4b) [142, 143].

3.2 Site-Directed Spin Labeling of Nucleobases

Nucleobase spin labeling is the most frequent approach for incorporation of labels into nucleic acids. Attachment of reporter groups on the base enables placement of the label into one of the grooves, usually the major groove, which does not perturb the nucleic acid helix. The C5-position of pyrimidines has been most frequently modified, while spin labels have been incorporated at C2 and C7, the latter using 7-deaza nucleosides. The exocyclic amino groups of cytosine (N4), guanine (N2), and adenine (N6) have also been used for labeling. Below is a description of the base spin labeling, from pyrimidines to purines, with a separate section about amino group labeling for both pyrimidines and purines.

3.2.1 Pyrimidines

The C5-Position of Pyrimidines

Incorporation of spin labels into the 5-position of pyrimidines (Fig. 7) is perhaps the most popular method for nucleic acid modification. The main reason is that there are relatively straightforward methods available for conjugation to C5, such as halogenation and subsequent carbon–carbon bond formation between the base and the label through a transition-metal-catalyzed coupling. Before chemical synthesis of spin-labeled oligonucleotides became routine, Bobst and coworkers incorporated C5-labeled nucleobases into nucleic acids by enzymatic methods using several different C5-labeled pyrimidine triphosphate analogues (**57**–**60**) [144–149]. However, most of these studies incorporated multiple spin labels into each strand since the incorporation is difficult to control using the enzymes. For site-specific spin labeling using the enzymatic approach, a single dA had to be incorporated into the template for the polymerase [150]. Bobst and coworkers later used the phosphotriester method for chemical incorporation of spin labels into oligonucleotides [151, 152]. Spin-labeled nucleotides **57**–**60** differ with respect to tether length, nitroxide ring size, and attachment to the C5-position of pyrimidine bases and have been used for studying nucleic acid local conformations [153] and structural dynamics [154–157].

In 1988, Hopkins and coworkers reported the first chemical synthesis of oligonucleotides containing nitroxide spin labels at specific sites, using phosphoramidite chemistry [158]. The spin-labeled 2′-deoxyuridine **61** (Fig. 7a) was prepared by coupling 2,2,5,5-tetramethyl-pyrrolin-1-yloxy-3-acetylene (TPA) to the nucleoside via a palladium-catalyzed Sonogashira cross-coupling reaction. Similarly, cytidine analogue **63** was synthesized and incorporated into DNA [159]. These labels had vastly improved spectroscopic properties compared to the

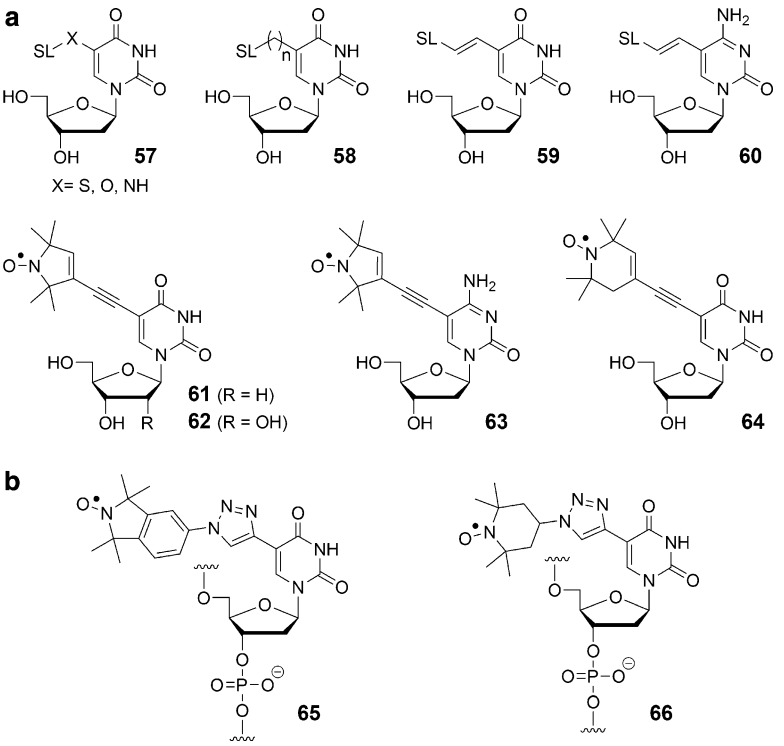

Fig. 7 Pyrimidine nucleosides spin-labeled at the C5-position. (**a**) Nucleosides that contain flexible (**57–60**) and semiflexible (**61–64**) spin labels. (**b**) Triazole-linked spin labels prepared by "click" chemistry. *SL* represents nitroxide spin label

previously published labels, due to the restricted motion of the label relative to the nucleic acid; only rotation around the single bonds flanking the acetylene was possible. Furthermore, even rotation around these bonds was restricted by the surrounding nucleotides when the nucleotide was placed in a B-DNA duplex; extending the tether of **61** by one single and one triple bond increased the motion of the probe considerably [160]. The limited motion of the nitroxide **61** enabled it to report the motion of the DNA to which it was attached [161] and was used to distinguish between different structural contexts of the probe [162]. Later, Schiemann et al. incorporated spin labels **61** and **62** into oligonucleotides by an on-column-coupling method during the solid-phase synthesis of DNA [163] and RNA [164], respectively. Spin labels **61** and **62** have been used for PELDOR-based distance measurements on nucleic acids in several different studies [163–166].

Spin-labeled nucleoside **64**, prepared by Gannett and coworkers, also contains a nitroxide that has limited motions relative to the base to which it is attached [167]. Moreover, since the single bonds flanking the triple bond are on the same axis as the N–O bond, any rotation will result in minimal displacement of the nitroxide relative to the base and thereby allowing accurate distance measurements by EPR. Nucleoside **64**

has been incorporated into oligonucleotides and used to probe structural changes during DNA triplex formation by CW-EPR [168, 169] and to study G-quadruplex conformations in human telomeric DNA using PELDOR [170].

In addition to incorporation of C5-labeled pyrimidines during oligonucleotide synthesis, postsynthetic labeling has also been used for this purpose. Our group recently reported spin labeling using the Cu(I)-catalyzed Huisgen–Meldal–Sharpless (3 + 2) cycloaddition reaction (click reaction) [171]. An oligonucleotide containing 5-ethynyl-2′-deoxyuridine, which had been incorporated into the oligomer by solid-phase synthesis employing a commercially available phosphoramidite, was reacted with a spin-labeled aromatic azide. This reaction was carried out before deprotection of the oligomer and cleavage from the resin, resulting in nearly quantitative conversion to the triazole product **65** (Fig. 7b), which has been used to detect local structural lesions in duplex DNA, such as abasic sites and mismatches [171]. Steinhoff and coworkers subsequently reported a similar SDSL approach using a click reaction after deprotection of the oligomer. The resulting spin-labeled nucleoside (**66**) was used for distance measurements in DNA by CW- and pulsed-EPR spectroscopy [172].

4-Thiouracil

As described above, 4-SU present in tRNA has been spin-labeled by reaction with nitroxide-containing alkylating agents (Fig. 8). The commercial availability of the 4-SU phosphoramidite building block has enabled the chemical synthesis of RNA oligomers containing 4-SU and subsequent spin labeling to yield nucleotide **54** (Scheme 4a) for both NMR studies of RNA-protein complexes [173, 174] and long-range distance measurements by double-quantum coherence (DQC) EPR spectroscopy [175].

Qin and coworkers have also spin-labeled 4-SU in RNA by reaction with the thiol-specific spin-labeling reagent **11** (Fig. 2) to yield **67** [176]. Spin-labeled nucleosides **68** and **69** (Fig. 8) were also incorporated into RNA, and the nitroxides were shown to have restricted internal motion, relative to the nitroxide of **67**, which facilitated the study of both dynamics and structural contexts of the bases to which they were

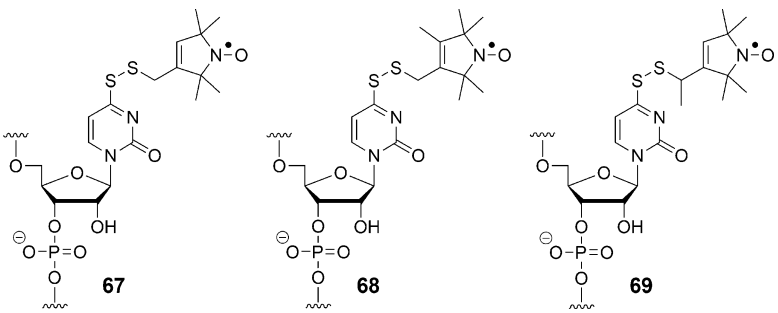

Fig. 8 Attachment of spin labels to 4-SU through alkylation or disulfide bond formation

attached [176–178]. The tetracycline riboswitch containing spin-labeled nucleotide **67** has been prepared and used for EPR studies of dynamics and conformational changes of the aptamer upon ligand binding [179]. It should be noted that spin labeling of 2- and 4-SU changes the base-pairing properties of the base and may, therefore, be structurally perturbing when the base is involved in hydrogen bonding.

3.2.2 Exocyclic Amino Groups of Pyrimidines and Purines

All the exocyclic amino groups of the naturally occurring bases have been modified with a spin label, through chemical synthesis or postsynthetic modification (Fig. 9).

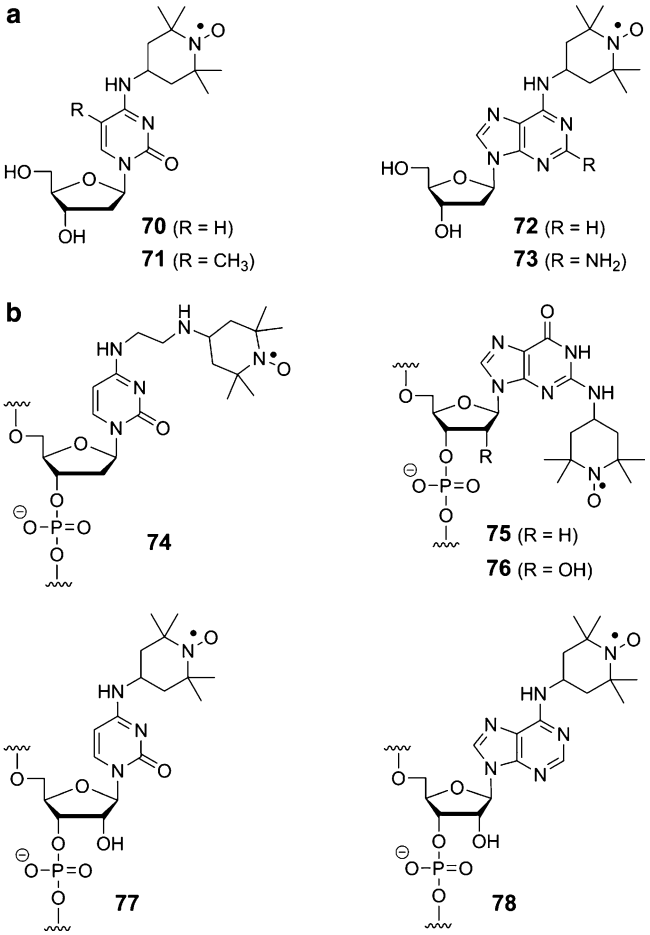

Fig. 9 Spin labeling of the exocyclic amino groups of pyrimidines and purines. (**a**) Spin labels incorporated by the phosphoramidite method. (**b**) Spin labels incorporated postsynthetically via the convertible nucleoside approach

A single alkylation of an amino group still allows for hydrogen bonding to a complementary base through the remaining proton. Bannwarth and Schmidt reported the synthesis of N4-TEMPO-modified 2′-deoxycytidine spin label (**70**) [180]. This synthesis was later improved by Giordano and coworkers who also prepared **71**–**73** and incorporated them into oligonucleotides [181]. The motions of a spin label connected to an exocyclic amino group are sensitive to the microenvironment of the amino group, in particular, hydrogen bonding. This was demonstrated by the use of spin label **70** for detection of mismatches in duplex DNA by CW-EPR spectroscopy, where **70** was able to report on the identity of its base-pairing partner in duplex DNA [182].

Verdine and coworkers developed the postsynthetic "convertible nucleoside approach," which enables preparation of N-substituted exocyclic amino groups of the bases [183]. In this method, a nucleoside that contains a leaving group on the base that can be displaced by amines is incorporated into the oligomer using commercially available phosphoramidites. After the oligomer synthesis, the resin is incubated with the amine, which displaces the leaving group of the convertible nucleoside, deprotects the oligomer, and cleaves it from the resin. Budil et al. incorporated the flexible spin-labeled nucleotide **74** into DNA by using this strategy and studied its dynamics by high-field EPR spectroscopy [184]. The label could also be placed in the propinquity to the active site of an endonuclease–DNA complex [185]. Similarly, Saito and coworkers spin-labeled the exocyclic group of guanine (**75**) by postsynthetic modification of 2-fluorohypoxanthine with 4-amino TEMPO and used it to probe both DNA duplex and quadruplex formation [186]. Spin label **75** has also been used for studying the A to B conformational equilibria of DNA duplexes [187] and the influence of lesions on nucleic acid structure by pulsed-EPR spectroscopy [188].

Recently, Hobartner and coworkers used the convertible nucleoside approach to spin label the naturally occurring RNA nucleotides by reaction of 4-chlorophenyl- or fluoride-modified nucleotides with 4-amino TEMPO to yield RNAs containing **76**–**78** in good yields [189]. These spin-labeled nucleotides were shown to yield accurate intermediate range distance measurements in RNA duplexes and quadruplexes by PELDOR and were used to detect alternative RNA secondary structures.

3.2.3 Purines

Purines have not been as extensively labeled as pyrimidines. In addition to the aforementioned conjugation of spin labels to the exocyclic amino group of purines (**72**, **73**, **75**, **76**, **78**, Fig. 9), purines have also been spin-labeled through carbon–carbon bond formation. The nonnatural nucleoside 7-vinyl-7-deaza-2′-deoxyguanosine was introduced into a short DNA oligonucleotide by solid-phase synthesis, and a subsequent high-yielding Diels–Alder (4 + 2) cycloaddition reaction with a nitroxide-functionalized maleimide afforded an oligomer that contained spin-labeled nucleotide **79** (Fig. 10) [190]. However, the effects of the modified nucleoside on the structure of nucleic acids have not been investigated.

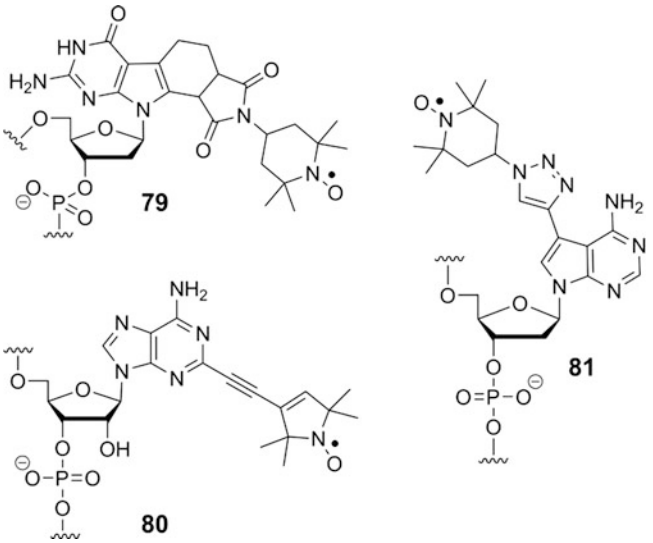

Fig. 10 Spin-labeled purine nucleosides

The spin-labeled adenosine **80** was incorporated into RNA through an on-column Sonogashira cross-coupling reaction, during the chemical synthesis of the oligonucleotides, between an alkyne-derived spin label and 2-iodo adenine [164]. Recently, DNA oligomers containing the spin-labeled 7-deazaadenosine analogue **81** were prepared by a postsynthetic "click reaction," and the label evaluated as a probe for distance measurements by PELDOR [172].

3.2.4 Rigid Spin Labels for Nucleic Acids

Most spin labels have motion independent of the biopolymer to which they are attached. This motion originates in conformational flexibility of the tether that is used to attach the nitroxide to the biopolymer, including the ring in which the nitroxide is located. The result of such flexibility is that distance measurements by EPR are not as accurate, and for the study of dynamics, it can be difficult to disentangle the motion of the probe from that of the biopolymer itself. Therefore, spin labels that have restricted motion, like **TOAC** (Scheme 3b) as well as nitroxide **61** (Fig. 7) have been designed. However, neither of those probes are completely rigid due to rotation around single bonds and are more appropriately termed semiflexible or semirigid.

The first truly rigid spin label, a C-nucleoside named **Q** (Fig. 11), was prepared by Hopkins and coworkers [191, 192]. In **Q**, the nitroxide ring is fused to the ring system of a nucleoside base, which circumvents motion of the nitroxide independent of the base. This nonnatural nucleobase forms a base pair with 2-aminopurine (**2AP**) in duplex DNA [192]. The rigid spin label **Q** has been used for studying sequence-dependent dynamics of DNA [193–195].

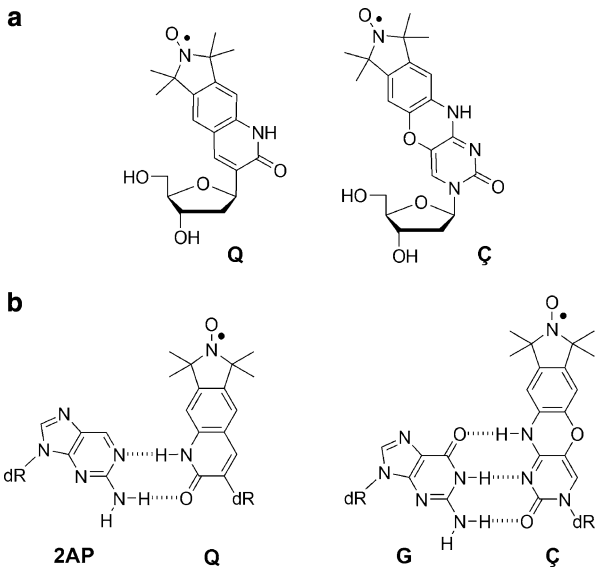

Fig. 11 Nucleosides containing a rigid spin label. (**a**) Structures of the rigid spin labels **Q** and **Ç**. (**b**) Base-pairing schemes of **Q** and **Ç**

Due to the synthetic challenges in preparation of **Q** and its requirement to base pair to **2AP**, our group prepared the rigid spin label **Ç** ("C-spin") (Fig. 11) [196]. In this phenoxazine-derived nucleoside, a nitroxide-bearing isoindol ring is fused to cytidine and forms a stable and structurally nonperturbing base pair with guanine, as seen in a recent crystal structure of **Ç**-labeled DNA duplex [197]. In addition to accurate distance measurements, the rigidity of **Ç** has enabled the determination of angular orientation in nucleic acids by PELDOR [198, 199] and given insights into internal motions of DNA duplexes [200]. The rigid spin label **Ç** has also been used for studying dynamics and conformations of DNA hairpin loops [201]. An added advantage of **Ç** is that the nitroxide can be reduced with a mild-reducing agent to yield a fluorescent probe, which was used to detect and identify specific mismatches in duplex DNA [202, 203] and to study the folding of the cocaine aptamer by fluorescence and EPR spectroscopies [204].

3.3 Site-Directed Spin Labeling of the Sugar-Phosphate Backbone

3.3.1 The Sugar

From a synthetic standpoint, there are not many straightforward methods to label the sugars of nucleosides/nucleotides in internal positions of DNA or RNA. In fact, all known sugar spin-labeling methods rely on modification of the 2′-position.

The most widely used method is the high-yielding postsynthetic modification of 2′-amino-modified oligonucleotides with a spin-labeled aliphatic isocyanate [205, 206], both of which are commercially available and have been used for labeling both DNA [207] and RNA [32, 33, 205, 206, 208]. This method utilizes the fact that the 2′-amino groups are more reactive than the amino groups of the bases. The resulting 2′-uredo spin label (**82**) (Fig. 12a) has been used for studying dynamics of the TAR RNA by EPR upon binding of small molecules [7], metal ions [8, 209], and peptides [8, 210]. Spin label **82** has also been used to study changes in site-specific dynamics of the hammerhead ribozyme upon metal-ion-induced folding [31, 32] and for distance measurements by PELDOR [33, 207, 208]. The 2′-amino group has also been conjugated to a spin label through an amide linkage (**83**), but unlike the 2′-uredo label, the short amide linkage was found to have destabilizing effects on duplex RNA [211].

"Click" chemistry has been used for postsynthetic modification of sugars in DNA, through incorporation of 2′-O-propargyl-modified uridine and a subsequent spin-labeling reaction with a nitroxide-containing azide to yield spin-labeled nucleotide **84** (Fig. 12a) [212]. However, a rather wide distribution of distances was obtained when using PELDOR to measure distances between two such labels in DNA, indicating considerable flexibility of the linker.

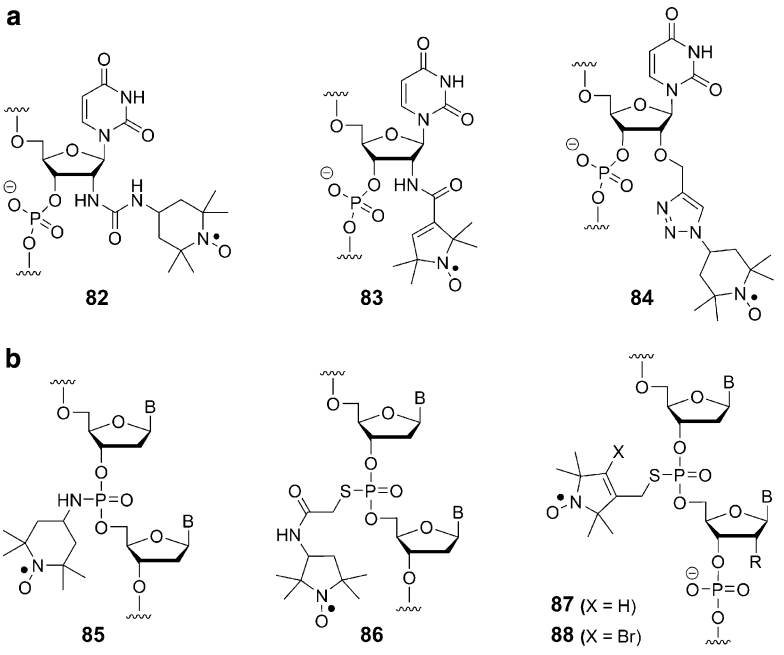

Fig. 12 Spin labeling of the sugar-phosphate backbone. (**a**) Spin-labeled 2′-sugar modifications (**b**) Spin-labeled phosphodiesters. *R* stands for OH or H, and *B* represents a nucleobase

3.3.2 The Phosphodiester

Spin labels have been linked to the phosphorous atom of the nucleic acid sugar-phosphate backbone through replacement of one of the nonbridging oxygens with the label. In contrast to sugar or base labeling, the phosphodiester labeling can be performed at any place in the sequence without having to prepare a specifically labeled nucleoside/nucleotide. Another advantage is that since the phosphodiesters are placed at the edge of nucleic acid helices, the labels are less likely to interfere with duplex formation than those connected to a sugar or a base. However, the phosphodiester group, which contains a negative charge at neutral or basic pH, becomes neutral upon spin labeling and can affect electrostatic interactions both within the nucleic acid as well as with other molecules. Another potential complication is that the two nonbridging oxygen atoms are diastereotopic, resulting in a mixture of the R_P and S_P diastereomers upon labeling. Furthermore, a 2′-OH group cannot be present at the site of spin labeling due to intramolecular transesterification that can lead to strand cleavage or loss of labeling. Therefore, the ribonucleotide at the site of modification is usually replaced with either a 2′-deoxy- or a 2′-O-methyl nucleotide when the phosphate is labeled in RNA [213].

DNA synthesis using the H-phosphonate chemistry can be used to prepare phosphoramidates, where one of the nonbridging oxygens is replaced with an amine [214]. In this method, a hydrogen-phosphonate internucleotide linkage is introduced at the desired site during the oligomer synthesis and oxidized in the presence of an amine to yield a phosphoramidate. Makino and coworkers applied this method, using 4-amino TEMPO during the oxidation step, which afforded the spin-labeled nucleotide **85** in good yield (Fig. 12b) [215, 216].

One of the nonbridging oxygens of specific nucleotides can be conveniently replaced with sulfur by using a sulfurizing reagent instead of an oxidizing agent at that step during the oligonucleotide synthesis [217]. The high reactivity of such phosphorothioates in DNA has been utilized for spin labeling through specific alkylation with reagents such as **9** or **41** (Figs. 2 and 5) to yield the spin-labeled nucleotide **86** [218, 219]. Qin and coworkers used a similar strategy to spin-label RNA by reacting the thiol-reactive, spin-labeling reagent **14** (Scheme 2) under mild conditions [220, 221]. The resulting spin label (**87**) has been used for studying metal-ion-dependent tetraloop–receptor interactions in RNA [220], nucleic acid dynamics [222], and for distance measurements in nucleic acids using pulsed-EPR techniques [221, 223, 224]. 4-Bromo substituted (**88**) analogue of **87** (Fig. 12b) has also been used to study nanosecond timescale motions of the substrate-recognition RNA element in the group I intron ribozyme by CW-EPR spectroscopy [225]. The spin-labeled diastereomers have also been separated by HPLC [226] and used individually for studying stereospecific dynamics in DNA [227].

3.3.3 The 3′- and the 5′-End

Spin labels have been incorporated into both the 3′- and the 5′-end of oligonucleotides. The main advantages of end labeling are the ease of labeling and

minimal interference with the nucleic acid structure. Depending on the application, a potential drawback is that the labels have relatively unrestricted motion and are, therefore, rather flexible.

The 3′-sugar of RNA has a unique functional group, a *cis*-geminal diol, which can be oxidized to a dialdehyde using periodate. Caron and Dugas utilized this chemical transformation for spin labeling the 3′-end of tRNA; after periodate oxidation, a reductive amination in the presence of 4-amino TEMPO and sodium borohydride afforded morpholino spin-labeled tRNA (**89**, Fig. 13a) [228]. Reductive amination with sodium cyanoborohydride yielded spin label **90**, which has more motional freedom than **89** [229]. Such spin labels have been used for studying conformations of 3′-terminus in tRNA [229, 230]. Although this labeling strategy has only been applied to RNA, it should also be applicable to chemically synthesized DNA containing a 3′-ribonucleotide.

Terminal phosphates are more nucleophilic than the phosphodiesters and can be postsynthetically spin-labeled. For example, Dzuba and coworkers prepared spin-labeled phosphoramidates of both the 3′- (**91**) and the 5′-end (**92**) of DNA oligonucleotides to study conformational changes induced by damaged and non-nucleotide residues at the center of single- and double-stranded oligonucleotides by PELDOR [231]. Terminal phosphorothioates are even more reactive than terminal phosphates, resulting in greater selectivity and milder reaction conditions. For example, Shin and coworkers incorporated a 5′-guanosine monophosphorothioate (GMPS) into the 5′-end of RNA during in vitro transcription from a DNA template using T7 RNA polymerase, which yielded **93** after reaction with the thiol-specific

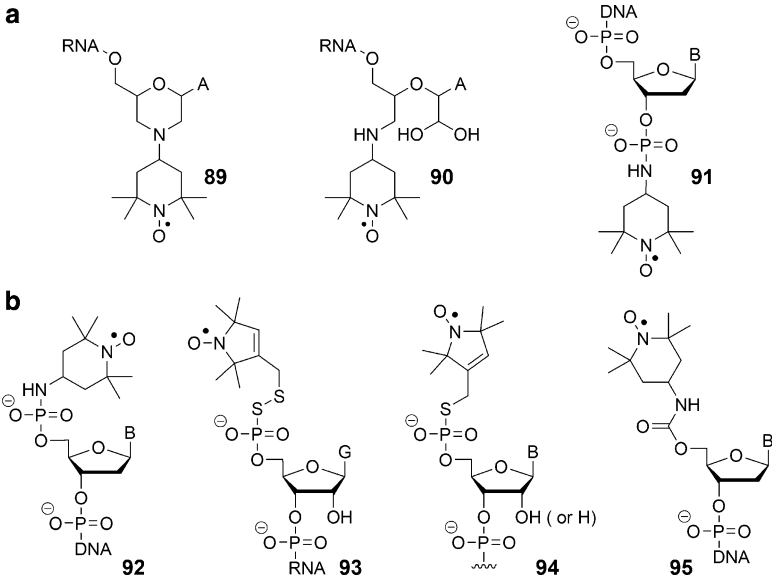

Fig. 13 Nucleic acid end labeling. (**a**) Spin labels at the 3′-end. (**b**) Spin labels at the 5′-end. *B* represents a nucleobase

spin-labeling reagent **11** (Fig. 2) [232]. More recently, Qin and coworkers reported a general approach to transfer a phosphorothioate to the 5′-end of either DNA or RNA using T4 polynucleotide kinase [233]. Subsequent reaction of the phosphorothioates with spin label **14** (Scheme 2) yielded nucleotide **94**, used to detect nucleic acid hybridization and metal-ion-induced folding of tRNA.

Spin-labeled amines can be attached to the 5′-end of DNA oligonucleotides by modifying the 5′-hydroxyl group immediately after the synthesis of the oligonucleotide, while still attached to the column, by a sequential reaction with *N*,*N*′-carbonyldiimidazole and an amine [234]. This protocol has been used to spin label the 5′-end of DNA to yield carbamate-linked TEMPO labels, such as **95** (Fig. 13b) [235].

3.4 Noncovalent and Site-Directed Spin Labeling of Nucleic Acids

In contrast to proteins, nucleic acids usually do not contain well-defined and tight-binding pockets to which organic ligands can bind. A notable exception is the recently discovered riboswitches that bind specific small organic molecules and thereby regulate their cellular concentrations [236, 237]. Binding of small molecules to nucleic acids generally takes place in helical regions, either by intercalation or groove binding [238]. As mentioned above, intercalators have very limited sequence selectivity and cannot be used for SDSL. Nearly all DNA groove binders are polyaromatic compounds that bind in the minor groove and usually at AT-rich sequences, where the minor groove is narrower. The reasons that minor-groove binders have not been used for spin labeling might be that they can have different orientations in the groove and because it is sometimes possible to bind more than one ligand at the same site [239, 240]. Moreover, most minor-groove ligands have limited sequence selectivity [241], although Dervan and coworkers have prepared longer polyamides that have high sequence selectivity [241]. Therefore, there are not many examples of NC-SDSL of nucleic acids.

We have recently described a general strategy for NC-SDSL of DNA by using an abasic site in duplex regions as a receptor for a spin-labeled base that binds in the abasic site through hydrogen bonding and π stacking (Scheme 5) [26]. We chose the base of **Ç** (**ç**) (Fig. 11) for incorporation at the abasic site, where it should form three hydrogen bonds with a guanine base on the opposing strand. Only minor binding could be observed at 25°C (ca 5%), but as the temperature was lowered, binding increased. At −30°C, the ligand was fully bound. Control experiments showed that the label bound specifically at the abasic site.

Since stable abasic sites can be readily incorporated into nucleic acids by chemical synthesis using commercially available phosphoramidites, samples for EPR studies with **ç** can be readily prepared by mixing the abasic site-containing nucleic acid with the spin-label ligand. In spite of the low temperature that is

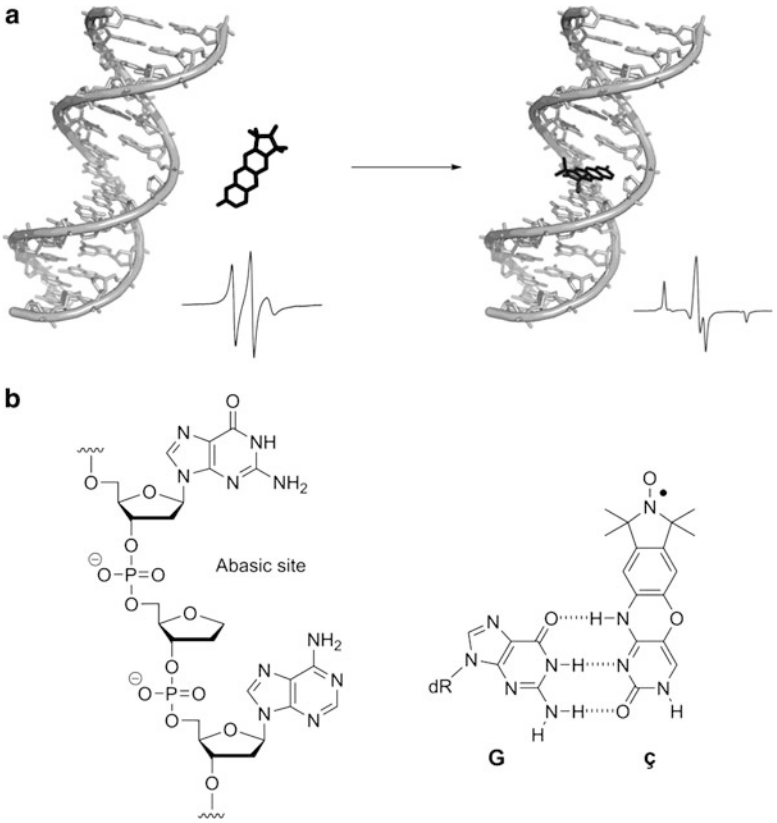

Scheme 5 Noncovalent and site-directed spin labeling (NC-SDSL) of nucleic acids. (**a**) Schematic depiction of the noncovalent spin-labeling strategy that utilizes abasic sites, showing a DNA duplex (*gray*) containing an abasic site, the spin label **ç** (*black*), and the EPR spectra of the unbound (*left*) and the bound (*right*) spin label. (**b**) Structure of an abasic site and the base-pairing scheme between **ç** and guanine

required for full binding, this approach should prove to be useful for distance measurements in nucleic acids using PELDOR, because they are conducted in frozen solutions.

4 Conclusions and Future Prospects

Since the pioneering work of McConnell and coworkers in the early 1960s, substantial advances in biopolymer spin labeling have taken place. Spin labels with limited selectivity have been replaced with ones that target specific atoms of specific residues in biopolymers. Moreover, labels with improved spectroscopic properties have emerged. For example, the rigid spin label **Ç** for nucleic acids has

enabled determination of orientations in addition to distance measurements [198] and provided an opportunity to access internal dynamics of DNA duplexes [200].

The three strategies of spin labeling are all likely to continue to contribute to EPR spectroscopic studies of biopolymers. Each approach has advantages as well as disadvantages, and they should be viewed as complementary to each other. Spin labeling during chemical synthesis of the polymer requires synthetic expertise and can be labor intensive, but enables incorporation of tailor-made labels. Postsynthetic labeling usually utilizes readily available materials and relatively simple protocols. However, the labels have some flexibility, which affects determination of accurate distances and dynamics of the residue to which they are attached. Noncovalent and site-directed labeling is the simplest labeling method as the sample is prepared by mixing the spin label and the biopolymer. Drawbacks include a limited availability of binding sites and ligands that bind selectively.

Further progress in biopolymer spin labeling is expected in the years to come, which will give EPR spectroscopy more impact in the area of structural biology. In addition to expanding the chemistry of labeling to specific sites and the development of labels with improved spectroscopic properties, the field will be advanced by enhanced availability of labeled biopolymers. Therefore, it is likely that noncovalent labeling will become more prevalent, in particular, for distance measurements by PELDOR, since the low temperature at which those experiments are carried out at does not require high-affinity spin labels.

References

1. Hustedt EJ, Beth AH (1999) Nitroxide spin-spin interactions: applications to protein structure and dynamics. Annu Rev Biophys Biomol Struct 28:129–153
2. Prisner T, Rohrer M, MacMillan F (2001) Pulsed EPR spectroscopy: biological applications. Annu Rev Phys Chem 52:279–313
3. Schiemann O, Prisner TF (2007) Long-range distance determinations in biomacromolecules by EPR spectroscopy. Q Rev Biophys 40(1):1–53. doi:10.1017/s003358350700460x
4. Hunsicker-Wang L, Vogt M, DeRose VJ (2009) EPR methods to study specific metal-ion binding sites in RNA. Methods Enzymol 468:335–367. doi:10.1016/s0076-6879(09)68016-2
5. Schiemann O (2009) Mapping global folds of oligonucleotides by pulsed electron–electron double resonance. Methods Enzymol 469:329–351. doi:10.1016/s0076-6879(09)69016-9
6. Schiemann O, Reginsson GW (2011) Studying bimolecular complexes with pulsed electron–electron double resonance spectroscopy. Biochem Soc Trans 39:128–139. doi:10.1042/Bst0390128
7. Edwards TE, Sigurdsson ST (2002) Electron paramagnetic resonance dynamic signatures of TAR RNA-small molecule complexes provide insight into RNA structure and recognition. Biochemistry-US 41(50):14843–14847. doi:bi026299a [pii]
8. Edwards TE, Okonogi TM, Sigurdsson ST (2002) Investigation of RNA-protein and RNA-metal ion interactions by electron paramagnetic resonance spectroscopy. The HIV TAR-Tat motif. Chem Biol 9(6):699–706. doi:S1074552102001503 [pii]
9. Altenbach C, Marti T, Khorana HG, Hubbell WL (1990) Transmembrane protein structure: spin labeling of bacteriorhodopsin mutants. Science 248(4959):1088–1092
10. Altenbach C, Greenhalgh DA, Khorana HG, Hubbell WL (1994) A collision gradient method to determine the immersion depth of nitroxides in lipid bilayers: application to spin-labeled mutants of bacteriorhodopsin. Proc Natl Acad Sci USA 91(5):1667–1671

11. Lin Y, Nielsen R, Murray D, Hubbell WL, Mailer C, Robinson BH, Gelb MH (1998) Docking phospholipase A2 on membranes using electrostatic potential-modulated spin relaxation magnetic resonance. Science 279(5358):1925–1929
12. Ubbink M, Worrall J, Canters G, Groenen E, Huber M (2002) Paramagnetic resonance of biological metal centers. Annu Rev Biophys Biomol Struct 31:393–422. doi:091701.171000 [pii] 10.1146/annurev.biophys.31.091701.171000
13. Kisseleva N, Kraut S, Jaschke A, Schiemann O (2007) Characterizing multiple metal ion binding sites within a ribozyme by cadmium-induced EPR silencing. HFSP J 1(2):127–136. doi:10.2976/1.2756332
14. McConnell HM, McFarland BG (1970) Physics and chemistry of spin labels. Q Rev Biophys 3(1):91–136
15. Dugas H (1977) Spin-labeled nucleic-acids. Acc Chem Res 10(2):47–54
16. Berliner LJ (1983) The spin-label approach to labeling membrane-protein sulfhydryl-groups. Ann NY Acad Sci 414:153–161
17. Sowa GZ, Qin PZ (2008) Site-directed spin labeling studies on nucleic acid structure and dynamics. Prog Nucleic Acid Res Mol Biol 82:147–197. doi:Doi 10.1016/S0079-6603(08)00005-6
18. Smirnova TI, Voinov MA, Smirnov AI (2009) Spin probes and spin labels. Encyclopedia of analytical chemistry. Wiley
19. Zhang X, Cekan P, Sigurdsson ST, Qin PZ (2009) Studying RNA using site-directed spin-labeling and continuous-wave electron paramagnetic resonance spectroscopy. Methods Enzymol 469:303–328. doi:S0076-6879(09)69015-7 [pii] 10.1016/S0076-6879(09)69015-7
20. Sigurdsson ST (2011) Nitroxides and nucleic acids: chemistry and electron paramagnetic resonance (EPR) spectroscopy. Pure Appl Chem 83(3):677–686. doi:10.1351/Pac-Con-10-09-28
21. Kinoshita Y, Yamada KI, Yamasaki T, Sadasue H, Sakai K, Utsumi H (2009) Development of novel nitroxyl radicals for controlling reactivity with ascorbic acid. Free Radic Res 43(6):565–571. doi:10.1080/10715760902914575
22. Sakai K, Yamada K, Yamasaki T, Kinoshita Y, Mito F, Utsumi H (2010) Effective 2,6-substitution of piperidine nitroxyl radical by carbonyl compound. Tetrahedron 66(13):2311–2315. doi:10.1016/j.tet.2010.02.004
23. Yamasaki T, Mito F, Ito Y, Pandian S, Kinoshita Y, Nakano K, Murugesan R, Sakai K, Utsumi H, Yamada K (2011) Structure-reactivity relationship of piperidine nitroxide: electrochemical, ESR and computational studies. J Org Chem 76(2):435–440. doi:10.1021/Jo101961m
24. Zantema A, Trommer WE, Wenzel H, Robillard GT (1977) Binding studies of a spin-labelled oxidized coenzyme to bovine-liver glutamate dehydrogenase. Eur J Biochem 72(1):175–184
25. Naber N, Malnasi-Csizmadia A, Purcell TJ, Cooke R, Pate E (2010) Combining EPR with fluorescence spectroscopy to monitor conformational changes at the myosin nucleotide pocket. J Mol Biol 396(4):937–948. doi:10.1016/j.jmb.2009.12.035
26. Shelke SA, Sigurdsson ST (2010) Noncovalent and site-directed spin labeling of nucleic acids. Angew Chem Int Ed Engl 49(43):7984–7986. doi:10.1002/anie.201002637
27. Connolly BA (1991) In: Eckstein F (ed) Oligonucleotides and analogues. IRL Press, New York, pp 155–183
28. Farand J, Gosselin F (2009) De novo sequence determination of modified oligonucleotides. Anal Chem 81(10):3723–3730. doi:10.1021/ac802452p
29. Berliner LJ, Grunwald J, Hankovszky HO, Hideg K (1982) A novel reversible thiol-specific spin label: papain active site labeling and inhibition. Anal Biochem 119(2):450–455. doi:0003-2697(82)90612-1 [pii]
30. Horvath LI, Dux L, Hankovszky HO, Hideg K, Marsh D (1990) Saturation transfer electron-spin-resonance of Ca2+-ATPase covalently spin-labeled with beta-substituted vinyl ketone-nitroxide and maleimide-nitroxide derivatives - effects of segmental motion and labeling levels. Biophys J 58(1):231–241
31. Edwards TE, Sigurdsson ST (2005) EPR spectroscopic analysis of U7 hammerhead ribozyme dynamics during metal ion induced folding. Biochemistry-US 44(38):12870–12878. doi:10.1021/bi050549g

32. Kim NK, Murali A, DeRose VJ (2005) Separate metal requirements for loop interactions and catalysis in the extended hammerhead ribozyme. J Am Chem Soc 127(41):14134–14135. doi:10.1021/ja0541027
33. Kim NK, Bowman MK, DeRose VJ (2010) Precise mapping of RNA tertiary structure via nanometer distance measurements with double electron–electron resonance spectroscopy. J Am Chem Soc 132(26):8882–8884. doi:10.1021/ja101317g
34. Kosen PA (1989) Spin labeling of proteins. Methods Enzymol 177:86–121
35. Ohnishi SI, McConnell HM (1965) Interaction of the radical ion of chlorpromazine with deoxyribonucleic acid. J Am Chem Soc 87:2293
36. Stone TJ, Buckman T, Nordio PL, McConnell HM (1965) Spin-labeled biomolecules. Proc Natl Acad Sci USA 54(4):1010–1017
37. Griffith OH, McConnell HM (1966) A nitroxide-maleimide spin label. Proc Natl Acad Sci USA 55(1):8–11
38. Barratt MD, Davies AP, Evans MTA (1971) Maleimide and isomaleimide pyrrolidine-nitroxide spin labels. Eur J Biochem 24(2):280–283
39. Wagner TE, Hsu CJ (1970) Paramagnetic labeling studies.1. A new method for labeling proteins with a stable paramagnetic nitroxide radical. Anal Biochem 36(1):1–5
40. Berliner LJ, McConnell HM (1966) A spin-labeled substrate for alpha-chymotrypsin. Proc Natl Acad Sci USA 55(4):708–712
41. Adackaparayil M, Smith JH (1977) Preparation and reactivity of a new spin label reagent. J Org Chem 42(9):1655–1656
42. Chan DCF, Piette LH (1980) Electron-spin-resonance spin label studies of the nucleosome core particle and histone core. Biochim Biophys Acta 623(1):32–45
43. Chan DCF, Piette LH (1982) Effect of tyrosyl modifications on nucleosome reconstitution - a spin-labeling study. Biochemistry-US 21(12):3028–3035
44. Hankovszky OH, Hideg K, von Goldammer E, Matuszak E, Kolkenbrock H, Tschesche H, Wenzel HR (1987) New nitroxide reagents for the selective spin-labeling at the guanidino moiety of arginine residues in peptides and proteins. Biochim Biophys Acta 916(1):152–155
45. Ogawa S, McConnell HM (1967) Spin-label study of hemoglobin conformations in solution. Proc Natl Acad Sci USA 58(1):19–26
46. Boeyens JC, McConnell HM (1966) Spin-labeled hemoglobin. Proc Natl Acad Sci USA 56 (1):22–25
47. Jallon JM, Di Franco A, Leterrier F, Piette L (1977) Spin-labeling studies of beef-liver glutamate dehydrogenase. Biochem Biophys Res Commun 74(3):1186–1191
48. Smirnov AI, Ruuge A, Reznikov VA, Voinov MA, Grigor'ev IA (2004) Site-directed electrostatic measurements with a thiol-specific ph-sensitive nitroxide: differentiating local pK and polarity effects by high-field EPR. J Am Chem Soc 126(29):8872–8873. doi:10.1021/ja048801f
49. Carter P (1986) Site-directed mutagenesis. Biochem J 237(1):1–7
50. Altenbach C, Flitsch SL, Khorana HG, Hubbell WL (1989) Structural studies on transmembrane proteins. 2. Spin labeling of bacteriorhodopsin mutants at unique cysteines. Biochemistry-US 28(19):7806–7812
51. Todd AP, Cong J, Levinthal F, Levinthal C, Hubbell WL (1989) Site-directed mutagenesis of colicin E1 provides specific attachment sites for spin labels whose spectra are sensitive to local conformation. Proteins 6(3):294–305. doi:10.1002/prot.340060312
52. McHaourab HS, Lietzow MA, Hideg K, Hubbell WL (1996) Motion of spin-labeled side chains in T4 lysozyme. Correlation with protein structure and dynamics. Biochemistry-US 35(24):7692–7704. doi:10.1021/bi960482k bi960482k [pii]
53. McHaourab HS, Kalai T, Hideg K, Hubbell WL (1999) Motion of spin-labeled side chains in T4 lysozyme: effect of side chain structure. Biochemistry-US 38(10):2947–2955. doi:10.1021/bi9826310 bi9826310 [pii]
54. Fleissner MR, Cascio D, Hubbell WL (2009) Structural origin of weakly ordered nitroxide motion in spin-labeled proteins. Protein Sci 18(5):893–908. doi:10.1002/pro.96

55. Kroncke BM, Horanyi PS, Columbus L (2010) Structural origins of nitroxide side chain dynamics on membrane protein alpha-helical sites. Biochemistry-US 49(47):10045–10060. doi:10.1021/Bi101148w
56. Bain JD, Glabe CG, Dix TA, Chamberlin AR, Diala ES (1989) Biosynthetic site-specific incorporation of a non-natural amino-acid into a polypeptide. J Am Chem Soc 111(20):8013–8014
57. Noren CJ, Anthonycahill SJ, Griffith MC, Schultz PG (1989) A general-method for site-specific incorporation of unnatural amino-acids into proteins. Science 244(4901):182–188
58. Cornish VW, Benson DR, Altenbach CA, Hideg K, Hubbell WL, Schultz PG (1994) Site-specific incorporation of biophysical probes into proteins. Proc Natl Acad Sci USA 91(8):2910–2914
59. Shafer AM, Kalai T, Bin Liu SQ, Hideg K, Voss JC (2004) Site-specific insertion of spin-labeled L-amino acids in *Xenopus oocytes*. Biochemistry-US 43(26):8470–8482. doi:10.1021/bi035542i
60. Wang L, Zhang ZW, Brock A, Schultz PG (2003) Addition of the keto functional group to the genetic code of *Escherichia coli*. Proc Natl Acad Sci USA 100(1):56–61
61. Fleissner MR, Brustad EM, Kalai T, Altenbach C, Cascio D, Peters FB, Hideg K, Peuker S, Schultz PG, Hubbell WL (2009) Site-directed spin labeling of a genetically encoded unnatural amino acid. Proc Natl Acad Sci USA 106(51):21637–21642. doi:0912009106 [pii] 10.1073/pnas.0912009106
62. Kent SB (1988) Chemical synthesis of peptides and proteins. Annu Rev Biochem 57:957–989. doi:10.1146/annurev.bi.57.070188.004521
63. Merrifield RB (1963) Solid phase peptide synthesis. 1. Synthesis of a tetrapeptide. J Am Chem Soc 85(14):2149–2154
64. Weinkam RJ, Jorgense Ec (1971) Angiotensin-II analogs. 8. Use of free radical containing peptides to indicate conformation of carboxyl terminal region of angiotensin-II. J Am Chem Soc 93(25):7033–7038
65. Nakaie CR, Goissis G, Schreier S, Paiva ACM (1981) pH-dependence of electron-paramagnetic-res spectra of nitroxides containing ionizable groups. Braz J Med Biol Res 14(2–3):173–180
66. Nakaie CR, Schreier S, Paiva ACM (1983) Synthesis and properties of spin-labeled angiotensin derivatives. Biochim Biophys Acta 742(1):63–71
67. Rassat A, Rey P (1967) Nitroxides. 23. Preparation of amino acid free radicals and their complex salts. Bull Soc Chim Fr 3:815–818
68. Marchetto R, Schreier S, Nakaie CR (1993) A novel spin-labeled amino-acid derivative for use in peptide-synthesis - (9-fluorenylmethyloxycarbonyl)-2,2,6,6-tetramethylpiperidine-N-oxyl-4-amino-4-carboxylic acid. J Am Chem Soc 115(23):11042–11043
69. Becker CFW, Lausecker K, Balog M, Kalai T, Hideg K, Steinhoff HJ, Engelhard M (2005) Incorporation of spin-labelled amino acids into proteins. Magn Reson Chem 43:S34–S39. doi:Doi 10.1002/Mrc.1688
70. Dawson PE, Muir TW, Clark-Lewis I, Kent SB (1994) Synthesis of proteins by native chemical ligation. Science 266(5186):776–779
71. Kumar KSA, Bavikar SN, Spasser L, Moyal T, Ohayon S, Brik A (2011) Total synthesis of a 304-residue, K48-linked tetraubiquitin peptide. Angew Chem Int Ed Engl 50:6137–6141. doi:10.1002/anie.201101920
72. Smythe ML, Nakaie CR, Marshall GR (1995) Alpha-helical versus 3(10)-helical conformation of alanine-based peptides in aqueous-solution - an electron-spin-resonance investigation. J Am Chem Soc 117(42):10555–10562
73. Toniolo C, Valente E, Formaggio F, Crisma M, Pilloni G, Corvaja C, Toffoletti A, Martinez GV, Hanson MP, Millhauser GL et al (1995) Synthesis and conformational studies of peptides containing TOAC, a spin-labelled C alpha, alpha-disubstituted glycine. J Pept Sci 1(1):45–57. doi:10.1002/psc.310010107
74. Hanson P, Millhauser G, Formaggio F, Crisma M, Toniolo C (1996) ESR characterization of hexameric, helical peptides using double TOAC spin labeling. J Am Chem Soc 118(32): 7618–7625

75. Hanson P, Martinez G, Millhauser G, Formaggio F, Crisma M, Toniolo C, Vita C (1996) Distinguishing helix conformations in alanine-rich peptides using the unnatural amino acid TOAC and electron spin resonance. J Am Chem Soc 118(1):271–272
76. Anderson DJ, Hanson P, McNulty J, Millhauser G, Monaco V, Formaggio F, Crisma M, Toniolo C (1999) Solution structures of TOAC-labeled trichogin GA IV peptides from allowed (g approximate to 2) and half-field electron spin resonance. J Am Chem Soc 121 (29):6919–6927
77. Bui TTT, Formaggio F, Crisma M, Monaco V, Toniolo C, Hussain R, Siligardi G (2000) TOAC: a useful C-alpha-tetrasubstituted alpha-amino acid for peptide conformational analysis by CD spectroscopy in the visible region. Part I. J Chem Soc Perk Trans 2(5):1043–1046
78. McNulty JC, Silapie JL, Carnevali M, Farrar CT, Griffin RG, Formaggio F, Crisma M, Toniolo C, Millhauser GL (2000) Electron spin resonance of TOAC labeled peptides: folding transitions and high frequency spectroscopy. Biopolymers 55(6):479–485. doi:10.1002/1097-0282(2000) 55:6<479::AID-BIP1023>3.0.CO;2-F [pii] 10.1002/1097-0282(2000) 55:6<479::AID-BIP1023>3.0.CO;2-F
79. Martin L, Ivancich A, Vita C, Formaggio F, Toniolo C (2001) Solid-phase synthesis of peptides containing the spin-labeled 2,2,6,6-tetramethylpiperidine-1-oxyl-4-amino-4-carboxylic acid (TOAC). J Pept Res 58(5):424–432
80. Van Eps N, Anderson LL, Kisselev OG, Baranski TJ, Hubbell WL, Marshall GR (2010) Electron paramagnetic resonance studies of functionally active, nitroxide spin-labeled peptide analogues of the C-terminus of a G-protein alpha subunit. Biochemistry-US 49(32): 6877–6886. doi:Doi 10.1021/Bi100846c
81. Elsaber C, Monien B, Haehnel W, Bittl R (2005) Orientation of spin labels in de novo peptides. Magn Reson Chem 43:S26–S33. doi:10.1002/mrc.1692
82. Tominaga M, Barbosa SR, Poletti EF, Zukerman-Schpector J, Marchetto R, Schreier S, Paiva AC, Nakaie CR (2001) Fmoc-POAC: [(9-fluorenylmethyloxycarbonyl)-2,2,5,5-tetramethylpyrrolidine-N-oxyl-3-am ino-4-carboxylic acid]: a novel protected spin labeled beta-amino acid for peptide and protein chemistry. Chem Pharm Bull (Tokyo) 49(8):1027–1029
83. Odonnell MJ, Bennett WD, Wu SD (1989) The stereoselective synthesis of alpha-amino-acids by phase-transfer catalysis. J Am Chem Soc 111(6):2353–2355
84. Balog M, Kalai T, Jeko J, Berente Z, Steinhoff HJ, Engelhard M, Hideg K (2003) Synthesis of new conformationally rigid paramagnetic alpha-amino acids. Tetrahedron Lett 44(51): 9213–9217. doi:10.1016/j.tetlet.2003.10.020
85. Balog MR, Kalai TK, Jeko J, Steinhoff HJ, Engelhard M, Hideg K (2004) Synthesis of new 2,2,5,5-tetramethyl-2,5-dihydro-1H-pyrrol-1-yloxyl radicals and 2-substituted-2,5,5-trimethylpyrrolidin-1-yloxyl radicals based alpha-amino acids. Synlett (14):2591–2593. doi:10.1055/s-2004-834806
86. Wright K, Sarciaux M, de Castries A, Wakselman M, Mazaleyrat JP, Toffoletti A, Corvaja C, Crisma M, Peggion C, Formaggio F, Toniolo C (2007) Synthesis of enantiomerically pure cis- and trans-4-amino-l-oxyl-2,2,6,6-tetramethylpiperidine-3-carboxylic acid: a spin-labelled, cyclic, chiral beta-amino acid, and 3D-Structural analysis of a doubly spin-labelled beta-hexapeptide. Eur J Org Chem (19):3133–3144. doi: 10.1002/ejoc.200700153
87. Kalai T, Schindler J, Balog M, Fogassy E, Hideg K (2008) Synthesis and resolution of new paramagnetic alpha-amino acids. Tetrahedron 64(6):1094–1100. doi:10.1016/j.tet.2007.11.020
88. Stryer L, Griffith OH (1965) A spin-labeled hapten. Proc Natl Acad Sci USA 54(6): 1785–1791
89. Trommer WE, Wenzel H, Pfleider G (1974) Note on synthesis and biochemical properties of a spin-labeled nicotinamide adenine-dinucleotide. Liebigs Ann Chem (8):1357–1359
90. Wenzel HR, Pfleiderer G, Trommer WE, Paschenda K, Redhardt A (1976) Synthesis of spin-label derivatives of nad and its structural components and their binding to lactate-dehydrogenase. Biochim Biophys Acta 452(2):292–301

91. Wenzel HR, Trommer WE (1977) 8-Spin-label nicotinamide adenine-dinucleotide, synthesis and properties of a new spin-labeled coenzyme. FEBS Lett 78(2):184–188
92. Gloggler KG, Balasubramanian K, Beth A, Fritzsche TM, Park JH, Pearson DE, Venkataramu SD, Trommer WE (1982) The synthesis of deuterium-substituted, spin-labeled analogs of AMP and NAD+ and their use in electron-spin-resonance studies of lactate-dehydrogenase. Biochim Biophys Acta 701(2):224–228
93. Wolf A, Fritzsche TM, Rudy B, Trommer WE (1987) Synthesis of spin-labeled photoaffinity derivatives of NAD+ and their interaction with lactate-dehydrogenase. FEBS Lett 212(2): 203–207
94. Trommer WE, Huth H, Wenzel HR (1979) Nature of the substrate-inhibition in lactate-dehydrogenases as studied by a spin-labeled derivative of NAD. Biochim Biophys Acta 567(1):49–59
95. Trommer WE, Gloggler K (1979) Solution conformation of lactate-dehydrogenase as studied by saturation transfer ESR spectroscopy. Biochim Biophys Acta 571(2):186–194
96. Deparade MP, Gloggler K, Trommer WE (1981) Isolation and properties of glyceraldehyde-3-phosphate dehydrogenase from a sturgeon from the Caspian Sea and its interaction with spin-labeled NAD+ derivatives. Biochim Biophys Acta 659(2):422–433
97. Beth AH, Robinson BH, Cobb CE, Dalton LR, Trommer WE, Birktoft JJ, Park JH (1984) Interactions and spatial arrangement of spin-labeled NAD+ bound to glyceraldehyde-3-phosphate dehydrogenase - comparison of electron-paramagnetic-res and X-ray modeling data. J Biol Chem 259(15):9717–9728
98. Hustedt EJ, Smirnov AI, Laub CF, Cobb CE, Beth AH (1997) Molecular distances from dipolar coupled spin-labels: the global analysis of multifrequency continuous wave electron paramagnetic resonance data. Biophys J 72(4):1861–1877. doi:S0006-3495(97)78832-5 [pii] 10.1016/S0006-3495(97)78832-5
99. Mildvan AS, Weiner H (1969) Interaction of a spin-labeled analogue of nicotinamide adenine dinucleotide with alcohol dehydrogenase. 3. Thermodynamic, kinetic, and structural properties of ternary complexes as determined by nuclear magnetic resonance. J Biol Chem 244(9):2465–2475
100. Roberts GC, Hannah J, Jardetzky O (1969) Noncovalent binding of a spin-labeled inhibitor to ribonuclease. Science 165(892):504–506
101. Ubom GA, Hunt JB, Timmons RB (1989) Spin-labeled analogues of ATP, ADP and AMP: substitutes for normal nucleotides in biochemical systems. Biochim Biophys Acta 997(1–2):1–8. doi:0167-4838(89)90128-3 [pii]
102. Weiner H (1969) Interaction of a spin-labeled analog of nicotinamide-adenine dinucleotide with alcohol dehydrogenase. I. Synthesis, kinetics, and electron paramagnetic resonance studies. Biochemistry-US 8(2):526–533
103. Mildvan AS, Weiner H (1969) Interaction of a spin-labeled analog of nicotinamide-adenine dinucleotide with alcohol dehydrogenase II. Proton relaxation rate and electron paramagnetic resonance studies of binary and ternary complexes. Biochemistry-US 8(2):552–562
104. Berliner LJ, Wong SS (1975) Manganese(II) and spin-labeled uridine 5'-diphosphate binding to bovine galactosyltransferase. Biochemistry-US 14(22):4977–4982
105. Koteiche HA, Narasimhan C, Runquist JA, Miziorko HM (1995) Utility of a novel spin-labeled nucleotide in investigation of the substrate and effector sites of phosphoribulokinase. Biochemistry-US 34(46):15068–15074
106. Streckenbach B, Schwarz D, Repke KRH (1980) Analysis of phosphoryl transfer mechanism and catalytic center geometries of transport ATPase by means of spin-labeled ATP. Biochim Biophys Acta 601(1):34–46
107. Crowder MS, Cooke R (1987) Orientation of spin-labeled nucleotides bound to myosin in glycerinated muscle-fibers. Biophys J 51(2):323–333
108. Oliveira CRG, Coan C, Verjovskialmeida S (1988) Interaction of spin-labeled nucleotides with sarcoplasmic-reticulum adenosine-triphosphatase. Biochemistry-US 27(16):5923–5927

109. Vogel-Claude P, Schafer G, Trommer WE (1988) Synthesis of a photoaffinity-spin-labeled derivative of ATP and its first application to F1-ATPase. FEBS Lett 227(2):107–109. doi:0014-5793(88)80878-0 [pii]
110. Jakobs P, Sauer HE, McIntyre JO, Fleischer S, Trommer WE (1989) Synthesis of spin-labeled 2-azido-ATP: evidence for distinct nucleotide-binding sites in calcium pump protein from sarcoplasmic reticulum. FEBS Lett 254(1–2):8–12. doi:0014-5793(89)80998-6 [pii]
111. Alessi DR, Corrie JET, Feeney J, Trayer IP, Trentham DR (1991) Conformationally restricted spin labeled nucleotides - a model study of the synthesis and properties of the 2',3'-O-spiro ketal of uridine and 4-oxo-2,2,6,6-tetramethyl-1-piperidyloxy. J Chem Soc Perk T 1 (9):2243–2247
112. Alessi DR, Corrie JET, Fajer PG, Ferenczi MA, Thomas DD, Trayer IP, Trentham DR (1992) synthesis and properties of a conformationally restricted spin-labeled analog of ATP and its interaction with myosin and skeletal-muscle. Biochemistry-US 31(34):8043–8054
113. Weidman SW, Drysdale GR, Mildvan AS (1973) Interaction of a spin-labeled analog of acetyl coenzyme a with citrate synthase - paramagnetic-resonance and proton relaxation rate studies of binary and ternary complexes. Biochemistry-US 12(10):1874–1883
114. Misra I, Narasimhan C, Miziorko HM (1993) Avian 3-hydroxy-3-methylglutaryl-CoA synthase - characterization of a recombinant cholesterogenic isozyme and demonstration of the requirement for a sulfhydryl functionality in formation of the acetyl-enzyme reaction intermediate. J Biol Chem 268(16):12129–12135
115. Narasimhan C, Roberts JR, Miziorko HM (1995) *Pseudomonas mevalonii* 3-hydroxy-3-methylglutaryl-CoA lyase - testing the function of the active-site cysteine by site-directed mutagenesis. Biochemistry-US 34(31):9930–9935
116. Misharin AY, Polyanovsky OL, Timofeev VP (1979) Spin-labeled vitamin B6 derivatives: synthesis and interaction with aspartate aminotransferase. Methods Enzymol 62:495–510
117. Tripp BC, Smith K, Ferry JG (2001) Carbonic anhydrase: new insights for an ancient enzyme. J Biol Chem 276(52):48615–48618. doi:10.1074/jbc.R100045200 R100045200 [pii]
118. Chignell CF, Starkweather DK, Erlich RH (1972) The interaction of some spin-labeled sulfonamides with bovine erythrocyte carbonic anhydrase B. Biochim Biophys Acta 271(1):6–15
119. Mushak P, Coleman JE (1972) Electron spin resonance studies of spin-labeled carbonic anhydrase. J Biol Chem 247(2):373–380
120. Erlich RH, Starkweather DK, Chignell CF (1973) A spin label study of human erythrocyte carbonic anhydrases B and C. Mol Pharmacol 9(1):61–73
121. Wee VT, Feldmann RJ, Tanis RJ, Chignell CF (1976) A comparative study of mammalian erythrocyte carbonic anhydrases employing spin-labeled analogues of inhibitory sulfonamides. Mol Pharmacol 12(5):832–843
122. Smith IC (1968) A study of the conformational properties of bovine pancreatic ribonuclease A by electron paramagnetic resonance. Biochemistry-US 7(2):745–757
123. Ohnishi S, Boeyens JC, McConnell HM (1966) Spin-labeled hemoglobin crystals. Proc Natl Acad Sci USA 56(3):809–813
124. Smith IC, Yamane T (1967) Spin-labeled nucleic acids. Proc Natl Acad Sci USA 58(3): 884–887
125. McConnell HM, Hamilton CL (1968) Spin-labeled hemoglobin derivatives in solution and in single crystals. Proc Natl Acad Sci USA 60(3):776–781
126. Bobst AM (1972) Studies on spin-labeled polyriboadenylic acid. Biopolymers 11(7): 1421–1433. doi:10.1002/bip. 1972.360110710
127. Caspary WJ, Greene JJ, Stempel LM, Ts'o PO (1976) Spin labeled nucleic acids. Nucleic Acids Res 3(4):847–861
128. Raikova E, Ivanov I, Kaffalieva D, Demirov G, Raikov Z (1982) Spin-labelling of DNA with hydrazine mustard spin label (HMSL). Int J Biochem 14(1):41–46
129. Spielmann HP, Chi DY, Hunt NG, Klein MP, Hearst JE (1995) Spin-labeled psoralen probes for the study of DNA dynamics. Biochemistry-US 34(45):14801–14814

130. Dunham SU, Lippard SJ (1995) Long-range distance constraints in platinated nucleotides - structure determination of the 5'-orientational isomer of Cis-[Pt(NH3)(4-aminotempo)(D(GpG))](+) from combined paramagnetic and diamagnetic nmr constraints with molecular modeling. J Am Chem Soc 117(43):10702–10712
131. Dunham SU, Dunham SU, Turner CJ, Lippard SJ (1998) Solution structure of a DNA duplex containing a nitroxide spin-labeled platinum d(GpG) intrastrand cross-link refined with NMR-derived long-range electron-proton distance restraints. J Am Chem Soc 120(22): 5395–5406
132. Hong SJ, Piette LH (1976) Electron-spin resonance spin-label studies of intercalation of ethidium-bromide and aromatic amine carcinogens in DNA. Cancer Res 36(3):1159–1171
133. Sinha BK, Chignell CF (1975) Acridine spin labels as probes for nucleic-acids. Life Sci 17(12):1829–1836
134. Hong SJ, Piette LH (1978) Electron-spin resonance spin label studies of intercalation of nitrobenzene in DNA. Arch Biochem Biophys 185(2):307–315
135. Belmont P, Chapelle C, Demeunynck M, Michon J, Michon P, Lhomme J (1998) Introduction of a nitroxide group on position 2 of 9-phenoxyacridine: easy access to spin labelled DNA-binding conjugates. Bioorg Med Chem Lett 8(6):669–674. doi:S0960894X98000894 [pii]
136. Thomas F, Michon J, Lhomme J (1999) Interaction of a spin-labeled adenine-acridine conjugate with a DNA duplex containing an abasic site model. Biochemistry-US 38(6): 1930–1937
137. Hoffman BM, Schofield P, Rich A (1969) Spin-labeled transfer RNA. Proc Natl Acad Sci USA 62(4):1195–1202
138. Schofield P, Hoffman BM, Rich A (1970) Spin-labeling studies of aminoacyl transfer ribonucleic acid. Biochemistry-US 9(12):2525–2533
139. Kabat D, Hoffman B, Rich A (1970) Synthesis and Characterization of a Spin-Labeled Aminoacyl Transfer Ribonucleic Acid. Biopolymers 9(1):95–101
140. Hara H, Horiuchi T, Saneyosh M, Nishimur S (1970) 4-Thiouridine-specific spin-labeling of *E Coli* transfer RNA. Biochem Biophys Res Commun 38(2):305–311
141. Sprinzl M, Kramer E, Stehlik D (1974) Structure of phenylalanine transfer-RNA from yeast - spin-label studies. Eur J Biochem 49(3):595–605
142. Cedergre RJ, Beauchem N, Toupin J (1973) Incorporation of Acyl groups into anticodon of *Escherichia coli* glutamic-acid transfer ribonucleic-acid. Biochemistry-US 12(23):4566–4570
143. Mcintosh AR, Caron M, Dugas H (1973) Specific spin labeling of anticodon of *Escherichia coli* transfer-RNA Glu. Biochem Biophys Res Commun 55(4):1356–1363
144. Warwick PE, Hakam A, Bobst EV, Bobst AM (1980) Reactivity of reverse-transcriptase toward (S4u, U)N co-polymers and spin-labeled nucleic-acid lattices. Proc Natl Acad Sci USA 77(8):4574–4577
145. Toppin CR, Thomas IE, Bobst EV, Bobst AM (1983) Synthesis of spin labeled deoxynucleotide analogs and their incorporation with terminal deoxynucleotidyl transferase into DNA. Int J Biol Macromol 5(1):33–36
146. Kao SC, Polnaszek CF, Toppin CR, Bobst AM (1983) Internal motions in ribonucleic-acid duplexes as determined by electron-spin resonance with site-specifically spin-labeled uridines. Biochemistry-US 22(24):5563–5568
147. Bobst AM, Kao SC, Toppin RC, Ireland JC, Thomas IE (1984) Dipsticking the major groove of DNA with enzymatically incorporated spin-labeled deoxyuridines by electron-spin resonance spectroscopy. J Mol Biol 173(1):63–74
148. Pauly GT, Thomas IE, Bobst AM (1987) Base dynamics of nitroxide-labeled thymidine analogs incorporated into (Da-Dt)N by DNA-polymerase-I from *Escherichia coli*. Biochemistry-US 26(23):7304–7310
149. Strobel OK, Keyes RS, Bobst AM (1990) Base dynamics of local Z-DNA conformations as detected by electron-paramagnetic resonance with spin-labeled deoxycytidine analogs. Biochemistry-US 29(37):8522–8528

150. Bobst AM, Pauly GT, Keyes RS, Bobst EV (1988) Enzymatic sequence-specific spin labeling of a DNA fragment containing the recognition sequence of EcoRI endonuclease. FEBS Lett 228(1):33–36
151. Duh JL, Bobst AM (1991) Sequence-specific spin labeling of oligothymidylates by phosphotriester chemistry. Helv Chim Acta 74(4):739–747
152. Strobel OK, Kryak DD, Bobst EV, Bobst AM (1991) Preparation and characterization of spin-labeled oligonucleotides for DNA hybridization. Bioconjugate Chem 2(2):89–95
153. Strobel OK, Keyes RS, Bobst AM (1990) An electron-paramagnetic resonance probe to detect local Z-DNA conformations. Biochem Biophys Res Commun 166(3):1435–1440
154. Kao SC, Bobst AM (1985) Local base dynamics and local structural features in RNA and DNA duplexes. Biochemistry-US 24(20):5465–5469
155. Keyes RS, Bobst AM (1995) Detection of Internal and overall dynamics of a 2-atom-tethered spin-labeled DNA. Biochemistry-US 34(28):9265–9276
156. Keyes RS, Bobst EV, Cao YY, Bobst AM (1997) Overall and internal dynamics of DNA as monitored by five-atom-tethered spin labels. Biophys J 72(1):282–290
157. Liang ZC, Freed JH, Keyes RS, Bobst AM (2000) An electron spin resonance study of DNA dynamics using the slowly relaxing local structure model. J Phys Chem B 104(22): 5372–5381. doi:Doi 10.1021/Jp994219f
158. Spaltenstein A, Robinson BH, Hopkins PB (1988) A rigid and nonperturbing probe for duplex DNA motion. J Am Chem Soc 110(4):1299–1301
159. Fischhaber PL, Reese AW, Nguyen T, Kirchner JJ, Hustedt EJ, Robinson BH, Hopkins PB (1997) Synthesis of duplex DNA containing a spin labeled analog of 2'-deoxycytidine. Nucleos Nucleot 16(4):365–377
160. Kirchner JJ, Hustedt EJ, Robinson BH, Hopkins PB (1990) DNA dynamics from a spin probe - dependence of probe motion on tether length. Tetrahedron Lett 31(5):593–596
161. Spaltenstein A, Robinson BH, Hopkins PB (1989) Sequence-dependent and structure-dependent DNA-base dynamics - synthesis, structure, and dynamics of site and sequence specifically spin-labeled DNA. Biochemistry-US 28(24):9484–9495
162. Spaltenstein A, Robinson BH, Hopkins PB (1989) DNA structural data from a dynamics probe - the dynamic signatures of single-stranded, hairpin-looped, and duplex forms of DNA are distinguishable. J Am Chem Soc 111(6):2303–2305
163. Schiemann O, Piton N, Mu YG, Stock G, Engels JW, Prisner TF (2004) A PELDOR-based nanometer distance ruler for oligonucleotides. J Am Chem Soc 126(18):5722–5729. doi:Doi 10.1021/Ja0393877
164. Piton N, Mu YG, Stock G, Prisner TF, Schiemann O, Engels JW (2007) Base-specific spin-labeling of RNA for structure determination. Nucleic Acids Res 35(9):3128–3143. doi:Doi 10.1093/Nar/Gkm169
165. Schiemann O, Piton N, Plackmeyer J, Bode BE, Prisner TF, Engels JW (2007) Spin labeling of oligonucleotides with the nitroxide TPA and use of PELDOR, a pulse EPR method, to measure intramolecular distances. Nat Protoc 2(4):904–923. doi:nprot.2007.97 [pii] 10.1038/nprot.2007.97
166. Krstic I, Frolow O, Sezer D, Endeward B, Weigand JE, Suess B, Engels JW, Prisner TF (2010) PELDOR spectroscopy reveals preorganization of the neomycin-responsive riboswitch tertiary structure. J Am Chem Soc 132(5):1454–1455. doi:10.1021/Ja9077914
167. Gannett PM, Darian E, Powell JH, Johnson EM (2001) A short procedure for synthesis of 4-ethynyl-2,2,6,6-tetramethyl-3,4-dehydro-piperidine-1-oxyl nitroxide. Synth Commun 31(14):2137–2141
168. Gannett PM, Darian E, Powell J, Johnson EM II, Mundoma C, Greenbaum NL, Ramsey CM, Dalal NS, Budil DE (2002) Probing triplex formation by EPR spectroscopy using a newly synthesized spin label for oligonucleotides. Nucleic Acids Res 30(23):5328–5337
169. Gannett PM, Powell JH, Johnson EM, Darian E, Dalal NS, Norton ML, Budil DE (2002) Solid-phase DNA binding detection by EPR spectroscopy. Tetrahedron Lett 43(11): 1931–1933. doi:Pii S0040-4039(02)00161-2

170. Singh V, Azarkh M, Exner TE, Hartig JS, Drescher M (2009) Human telomeric quadruplex conformations studied by pulsed EPR. Angew Chem Int Ed Engl 48(51):9728–9730. doi:10.1002/anie.200902146
171. Jakobsen U, Shelke SA, Vogel S, Sigurdsson ST (2010) Site-directed spin-labeling of nucleic acids by click chemistry: detection of abasic sites in duplex DNA by EPR spectroscopy. J Am Chem Soc 132(30):10424–10428. doi:10.1021/ja102797k
172. Ding P, Wunnicke D, Steinhoff HJ, Seela F (2010) Site-directed spin-labeling of DNA by the azide-alkyne 'click' reaction: nanometer distance measurements on 7-deaza-2'-deoxyadenosine and 2'-deoxyuridine nitroxide conjugates spatially separated or linked to a 'dA-dT' base pair. Chem Eur J 16(48):14385–14396. doi:10.1002/chem.201001572
173. Ramos A, Varani G (1998) A new method to detect long-range protein-RNA contacts: NMR detection of electron-proton relaxation induced by nitroxide spin-labeled RNA. J Am Chem Soc 120(42):10992–10993
174. Leulliot N, Quevillon-Cheruel S, Graille M, van Tilbeurgh H, Leeper TC, Godin KS, Edwards TE, Sigurdsson STL, Rozenkrants N, Nagel RJ, Ares M, Varani G (2004) A new alpha-helical extension promotes RNA binding by the dsRBD of Rnt1p RNAse III. EMBO J 23(13):2468–2477. doi:10.1038/sj.emboj.7600260
175. Borbat PP, Davis JH, Butcher SE, Freed JH (2004) Measurement of large distances in biomolecules using double-quantum filtered refocused electron spin-echoes. J Am Chem Soc 126(25):7746–7747. doi:10.1021/Ja049372o
176. Qin PZ, Hideg K, Feigon J, Hubbell WL (2003) Monitoring RNA base structure and dynamics using site-directed spin labeling. Biochemistry-US 42(22):6772–6783. doi:10.1021/Bi027222p
177. Qin PZ, Feigon J, Hubbell WL (2005) Site-directed spin labeling studies reveal solution conformational changes in a GAAA tetraloop receptor upon Mg2+−dependent docking of a GAAA tetraloop. J Mol Biol 351(1):1–8. doi:10.1016/j.jmb.2005.06.007
178. Qin PZ, Iseri J, Oki A (2006) A model system for investigating lineshape/structure correlations in RNA site-directed spin labeling. Biochem Biophys Res Commun 343(1): 117–124. doi:10.1016/j.bbrc.2006.02.138
179. Wunnicke D, Strohbach D, Weigand JE, Appel B, Feresin E, Suess B, Muller S, Steinhoff HJ (2011) Ligand-induced conformational capture of a synthetic tetracycline riboswitch revealed by pulse EPR. RNA 17(1):182–188. doi:Doi 10.1261/Rna.2222811
180. Bannwarth W, Schmidt D (1994) Oligonucleotides containing spin-labeled 2'-deoxycytidine and 5-methyl-2'-deoxycytidine as probes for structural motifs of DNA. Bioorg Med Chem Lett 4(8):977–980
181. Giordano C, Fratini F, Attanasio D, Cellai L (2001) Preparation of spin-labeled 2-amino-dA, dA, dC and 5-methyl-dC phosphoramidites for the automatic synthesis of EPR active oligonucleotides. Synthesis-Stuttgart (4):565–572
182. Cekan P, Sigurdsson ST (2009) Identification of single-base mismatches in duplex DNA by EPR spectroscopy. J Am Chem Soc 131(50):18054–18056. doi:10.1021/ja905623k
183. Macmillan AM, Verdine GL (1990) Synthesis of functionally tethered oligodeoxynucleotides by the convertible nucleoside approach. J Org Chem 55(24):5931–5933
184. Budil DE, Kolaczkowski SV, Perry A, Varaprasad C, Johnson F, Strauss PR (2000) Dynamics and ordering in a spin-labeled oligonucleotide observed by 220 GHz electron paramagnetic resonance. Biophys J 78(1):430–438
185. Kolaczkowski SV, Perry A, Mckenzie A, Johnson F, Budil DE, Strauss PR (2001) A spin-labeled abasic DNA substrate for AP endonuclease. Biochem Biophys Res Commun 288(3):722–726
186. Okamoto A, Inasaki T, Saito I (2004) Nitroxide-labeled guanine as an ESR spin probe for structural study of DNA. Bioorg Med Chem Lett 14(13):3415–3418. doi:10.1016/j.bmcl.2004.04.076

187. Sicoli G, Mathis G, Delalande O, Boulard Y, Gasparutto D, Gambarelli S (2008) Double electron–electron resonance (DEER): a convenient method to probe DNA conformational changes. Angew Chem Int Ed Engl 47(4):735–737. doi:10.1002/anie.200704133
188. Sicoli G, Mathis G, Aci-Seche S, Saint-Pierre C, Boulard Y, Gasparutto D, Gambarelli S (2009) Lesion-induced DNA weak structural changes detected by pulsed EPR spectroscopy combined with site-directed spin labelling. Nucleic Acids Res 37(10):3165–3176. doi:10.1093/Nar/Gkp165
189. Sicoli G, Wachowius F, Bennati M, Hobartner C (2010) Probing secondary structures of spin-labeled RNA by pulsed EPR spectroscopy. Angew Chem Int Ed Engl 49(36):6443–6447. doi:10.1002/anie.201000713
190. Okamoto A, Taiji T, Tainaka K, Saito I (2002) Oligonucleotides containing 7-vinyl-7-deazaguanine as a facile strategy for expanding the functional diversity of DNA. Bioorg Med Chem Lett 12(15):1895–1896. doi:S0960894X02003347 [pii]
191. Miller TR, Hopkins PB (1994) Toward the synthesis of a 2nd-generation nitroxide spin-probe for DNA dynamics studies. Bioorg Med Chem Lett 4(8):981–986
192. Miller TR, Alley SC, Reese AW, Solomon MS, Mccallister WV, Mailer C, Robinson BH, Hopkins PB (1995) A probe for sequence-dependent nucleic-acid dynamics. J Am Chem Soc 117(36):9377–9378
193. Okonogi T, Reese AW, Alley SC, Hopkins PB, Robinson BH (1999) Flexibility of duplex DNA on the submicrosecond timescale. Biophys J 77(6):3256–3276
194. Okonogi TM, Alley SC, Reese AW, Hopkins PB, Robinson BH (2000) Sequence-dependent dynamics in duplex DNA. Biophys J 78(5):2560–2571
195. Okonogi TM, Alley SC, Reese AW, Hopkins PB, Robinson BH (2002) Sequence-dependent dynamics of duplex DNA: the applicability of a dinucleotide model. Biophys J 83(6): 3446–3459. doi:S0006-3495(02)75344-7 [pii] 10.1016/S0006-3495(02)75344-7
196. Barhate N, Cekan P, Massey AP, Sigurdsson ST (2007) A nucleoside that contains a rigid nitroxide spin label: a fluorophore in disguise. Angew Chem Int Ed Engl 46(15):2655–2658. doi:10.1002/anie.200603993
197. Edwards TE, Cekan P, Reginsson GW, Shelke SA, Ferre-D'Amare AR, Schiemann O, Sigurdsson ST (2011) Crystal structure of a DNA containing the planar, phenoxazine-derived bi-functional spectroscopic probe C. Nucleic Acids Res. doi:gkr015 [pii] 10.1093/nar/gkr015
198. Schiemann O, Cekan P, Margraf D, Prisner TF, Sigurdsson ST (2009) Relative orientation of rigid nitroxides by PELDOR: beyond distance measurements in nucleic acids. Angew Chem Int Ed Engl 48(18):3292–3295. doi:10.1002/anie.200805152
199. Marko A, Margraf D, Cekan P, Sigurdsson ST, Schiemann O, Prisner TF (2010) Analytical method to determine the orientation of rigid spin labels in DNA. Phys Rev E 81(2):21911–21919 doi:10.1103/Physreve.81.021911
200. Marko A, Denysenkov V, Margraf D, Cekan P, Schiemann O, Sigurdsson ST, Prisner TF (2011) Conformational flexibility of DNA. J Am Chem Soc 133(34):13375–13379
201. Cekan P, Smith AL, Barhate N, Robinson BH, Sigurdsson ST (2008) Rigid spin-labeled nucleoside C: a nonperturbing EPR probe of nucleic acid conformation. Nucleic Acids Res 36(18):5946–5954. doi:gkn562 [pii] 10.1093/nar/gkn562
202. Cekan P, Sigurdsson ST (2008) Single base interrogation by a fluorescent nucleotide: each of the four DNA bases identified by fluorescence spectroscopy. Chem Commun (Camb) 29:3393–3395. doi:10.1039/b801833b
203. Gardarsson H, Sigurdsson ST (2010) Large flanking sequence effects in single nucleotide mismatch detection using fluorescent nucleoside C-f. Bioorg Med Chem 18(16):6121–6126. doi:10.1016/j.bmc.2010.06.060
204. Cekan P, Jonsson EO, Sigurdsson ST (2009) Folding of the cocaine aptamer studied by EPR and fluorescence spectroscopies using the bifunctional spectroscopic probe C. Nucleic Acids Res 37(12):3990–3995. doi:gkp277 [pii] 10.1093/nar/gkp277

205. Edwards TE, Okonogi TM, Robinson BH, Sigurdsson ST (2001) Site-specific incorporation of nitroxide spin-labels into internal sites of the TAR RNA; structure-dependent dynamics of RNA by EPR spectroscopy. J Am Chem Soc 123(7):1527–1528
206. Edwards TE, Sigurdsson ST (2007) Site-specific incorporation of nitroxide spin-labels into 2'-positions of nucleic acids. Nat Protoc 2(8):1954–1962. doi:nprot.2007.273 [pii] 10.1038/nprot.2007.273
207. Ward R, Keeble DJ, El-Mkami H, Norman DG (2007) Distance determination in heterogeneous DNA model systems by pulsed EPR. Chembiochem 8(16):1957–1964. doi:10.1002/cbic.200700245
208. Schiemann O, Weber A, Edwards TE, Prisner TF, Sigurdsson ST (2003) Nanometer distance measurements on RNA using PELDOR. J Am Chem Soc 125(12):3434–3435. doi:10.1021/ja0274610
209. Edwards TE, Sigurdsson ST (2003) EPR spectroscopic analysis of TAR RNA-metal ion interactions. Biochem Biophys Res Commun 303(2):721–725. doi:S0006291X0300411X [pii]
210. Edwards TE, Robinson BH, Sigurdsson ST (2005) Identification of amino acids that promote specific and rigid TAR RNA-tat protein complex formation. Chem Biol 12(3):329–337. doi:S1074-5521(05)00033-5 [pii] 10.1016/j.chembiol.2005.01.012
211. Kim NK, Murali A, DeRose VJ (2004) A distance ruler for RNA using EPR and site-directed spin labeling. Chem Biol 11(7):939–948. doi:10.1016/j.chembiol.2004.04.013 S1074552104001619 [pii]
212. Flaender M, Sicoli G, Fontecave T, Mathis G, Saint-Pierre C, Boulard Y, Gambarelli S, Gasparutto D (2008) Site-specific insertion of nitroxide-spin labels into DNA probes by click chemistry for structural analyses by ELDOR spectroscopy. Nucleic Acids Symp Ser (Oxf) (52):147–148. doi:nrn075 [pii] 10.1093/nass/nrn075
213. Gish G, Eckstein F (1988) DNA and RNA sequence determination based on phosphorothioate chemistry. Science 240(4858):1520–1522
214. Atherton FR, Openshaw HT, Todd AR (1945) Studies on phosphorylation .2. the reaction of dialkyl phosphites with polyhalogen compounds in presence of bases - a new method for the phosphorylation of amines. J Chem Soc 660–663
215. Makino K, Murakami A, Nagahara S, Nakatsuji Y, Takeuchi T (1989) A study on spin-labeled oligonucleotide synthesis and its electron-spin resonance behavior in solution. Free Radical Res Commun 6(5):311–316
216. Nagahara S, Murakami A, Makino K (1992) Spin-labeled oligonucleotides site specifically labeled at the internucleotide linkage - separation of stereoisomeric probes and EPR spectroscopical detection of hybrid formation in solution. Nucleos Nucleot 11(2–4):889–901
217. Burgers PMJ, Eckstein F (1979) Diastereomers of 5'-O-adenosyl 3'-O-uridyl phosphorothioate - chemical synthesis and enzymatic properties. Biochemistry-US 18(4):592–596
218. Fidanza JA, Mclaughlin LW (1989) Introduction of reporter groups at specific sites in DNA containing phosphorothioate diesters. J Am Chem Soc 111(25):9117–9119
219. Fidanza JA, Ozaki H, Mclaughlin LW (1992) Site-specific labeling of DNA-sequences containing phosphorothioate diesters. J Am Chem Soc 114(14):5509–5517
220. Qin PZ, Butcher SE, Feigon J, Hubbell WL (2001) Quantitative analysis of the isolated GAAA tetraloop/receptor interaction in solution: a site-directed spin labeling study. Biochemistry-US 40(23):6929–6936. doi:Doi 10.1021/Bi010294g
221. Qin PZ, Haworth IS, Cai Q, Kusnetzow AK, Grant GP, Price EA, Sowa GZ, Popova A, Herreros B, He H (2007) Measuring nanometer distances in nucleic acids using a sequence-independent nitroxide probe. Nat Protoc 2(10):2354–2365. doi:nprot.2007.308 [pii] 10.1038/nprot.2007.308
222. Popova AM, Kalai T, Hideg K, Qin PZ (2009) Site-specific DNA structural and dynamic features revealed by nucleotide-independent nitroxide probes. Biochemistry-US 48(36):8540–8550. doi:Doi 10.1021/Bi900860w

223. Cai Q, Kusnetzow AK, Hubbell WL, Haworth IS, Gacho GPC, Van Eps N, Hideg K, Chambers EJ, Qin PZ (2006) Site-directed spin labeling measurements of nanometer distances in nucleic acids using a sequence-independent nitroxide probe. Nucleic Acids Res 34(17):4722–4730. doi:Doi 10.1093/Nar/Gkl546
224. Cai Q, Kusnetzow AK, Hideg K, Price EA, Haworth IS, Qin PZ (2007) Nanometer distance measurements in RNA using site-directed spin labeling. Biophys J 93(6):2110–2117. doi: S0006-3495(07)71465-0 [pii] 10.1529/biophysj.107.109439
225. Grant GPG, Boyd N, Herschlag D, Qin PZ (2009) Motions of the substrate recognition duplex in a group I intron assessed by site-directed spin labeling. J Am Chem Soc 131(9):3136–3137. doi:10.1021/Ja808217s
226. Grant GPG, Popova A, Qin PZ (2008) Diastereomer characterizations of nitroxide-labeled nucleic acids. Biochem Biophys Res Commun 371(3):451–455. doi:10.1016/j.bbrc.2008.04.088
227. Popova AM, Qin PZ (2010) A nucleotide-independent nitroxide probe reports on site-specific stereomeric environment in DNA. Biophys J 99(7):2180–2189. doi:10.1016/j.bpj.2010.08.005
228. Caron M, Dugas H (1976) Specific spin-labeling of transfer ribonucleic acid molecules. Nucleic Acids Res 3(1):19–34
229. Pscheidt RH, Wells BD (1986) Different conformations of the 3' termini of initiator and elongator transfer-ribonucleic-acids - an electron-paramagnetic-res study. J Biol Chem 261(16):7253–7256
230. Luoma GA, Herring FG, Marshall AG (1982) Flexibility of end-labeled polymers from electron-spin resonance line-shape analysis - 3' terminus of transfer ribonucleic-acid and 5S ribonucleic-acid. Biochemistry-US 21(25):6591–6598
231. Kuznetsov NA, Milov AD, Koval VV, Samoilova RI, Grishin YA, Knorre DG, Tsvetkov YD, Fedorova OS, Dzuba SA (2009) PELDOR study of conformations of double-spin-labeled single- and double-stranded DNA with non-nucleotide inserts. Phys Chem Chem Phys 11(31):6826–6832. doi:10.1039/b904873a
232. Macosko JC, Pio MS, Tinoco I Jr, Shin YK (1999) A novel 5 displacement spin-labeling technique for electron paramagnetic resonance spectroscopy of RNA. RNA 5(9):1158–1166
233. Grant GP, Qin PZ (2007) A facile method for attaching nitroxide spin labels at the 5' terminus of nucleic acids. Nucleic Acids Res 35(10):e77. doi:gkm240 [pii] 10.1093/nar/gkm240
234. Wachter L, Jablonski JA, Ramachandran KL (1986) A simple and efficient procedure for the synthesis of 5'-aminoalkyl oligodeoxynucleotides. Nucleic Acids Res 14(20):7985–7994
235. Murakami A, Mukae M, Nagahara S, Konishi Y, Ide H, Makino K (1993) Oligonucleotides site-specifically spin-labeled at 5'-terminal or internucleotide linkage and their use in gene analyses. Free Radic Res Commun 19(Suppl 1):S117–S128
236. Winkler WC, Breaker RR (2003) Genetic control by metabolite-binding riboswitches. Chembiochem 4(10):1024–1032. doi:10.1002/cbic.200300685
237. Blount KF, Breaker RR (2006) Riboswitches as antibacterial drug targets. Nat Biotechnol 24(12):1558–1564. doi:10.1038/Nbt1268
238. Demeunynck M, Bailly C, Wilson WD (eds) (2004) Small molecule DNA and RNA binders: from synthesis to nucleic acid complexes, vol 1 and 2. Wiley-VCH Verlag GmbH & Co. KGaA, Weinheim
239. Pelton JG, Wemmer DE (1989) Structural Characterization of a 2–1 Distamycin A.D (Cgcaaattggc) Complex by Two-Dimensional NMR. Proc Natl Acad Sci USA 86(15):5723–5727
240. Chen X, Ramakrishnan B, Rao ST, Sundaralingam M (1994) Binding of 2 distamycin-a molecules in the minor-groove of an alternating B-DNA duplex. Nat Struct Biol 1(3):169–175
241. Dervan PB (2001) Molecular recognition of DNA by small molecules. Bioorg Med Chem 9(9):2215–2235

Struct Bond (2014) 152: 163–204
DOI: 10.1007/430_2011_63

Published online: 25 April 2012

Metal-Based Spin Labeling for Distance Determination

Daniella Goldfarb

Abstract Long-range (nm scale) distance measurements between specific sites in biological macromolecules offer important insights into their structure and interactions. In the last decade, such distance measurements by pulse electron paramagnetic resonance (EPR) techniques have proven highly efficient on nitroxide-labeled proteins and nucleic acids. In this chapter, we introduce the idea of using spin labels that are based on paramagnetic metal ions. We review distance measurements carried out on pairs of $S = 1/2$ metal ions in model complexes and in intrinsic binding sites in biomacromolecules. We discuss their potential as general purpose spin labels for distance measurements based on their spectroscopic properties. Then, we present a new approach to spin labeling that is based on half-integer high-spin metal ions, mainly Gd^{3+}, coordinated to chelating tags that are covalently attached to the molecules at specific sites. This approach is particularly suitable for high-field measurements and is attractive because of the high absolute sensitivity it offers.

Keywords Distance measurements · EPR · ESRPELDOR · DEER · Gd^{3+} chelates · High field · Paramagnetic metal ions · Spin labels

Contents

D. Goldfarb (✉)
Department of Chemical Physics, Weizmann Institute of Science, Rehovot 76100, Israel
e-mail: Daniella.goldfarb@weizmann.ac.il

Abbreviations

3MDPA	3-Mercapto-dipicolinic acid
4MMDPA	4-Mercaptomethyl-dipicolinic acid
CoA	Coenzyme A
CW	Continuous wave
DEER	Double electron–electron resonance
DNA	Deoxyribose nucleic acid
DOTA	1,4,7,10-Tetraazacyclododecane-1,4,7,10-tetraacetic acid
DQC	Double-quantum coherence
EDTA	Ethylenediaminetetraacetic acid
ENDOR	Electron-nuclear double resonance
EPR	Electron paramagnetic resonance
ESEEM	Electron spin echo envelope modulation
FT	Fourier transform
HE	Hydroxyethylidene
HFHS	Half-filled high-spin
Lf	Lactoferrin
NMR	Nuclear magnetic resonance
PELDOR	Pulse electron–electron double resonance
PFOR	Pyruvate ferredoxin oxidoreductase
PuR	Palustrisredoxin reductase
Pux-B	Palustrisredoxin
RIDME	Relaxation-induced dipolar modulation enhancement
RNA	Ribose nucleic acid
SDSL	Site-directed spin labeling
Tf	Transferrin
TPP	Thiamine pyrophosphate
ZFS	Zero-field splitting

1 Introduction

The most widely used spin labels and spin probes are based on the nitroxyl radical (N–O) that is usually incorporated into a heterocyclic ring (e.g., pyrrolidine), and the unpaired electron is predominantly localized in the N–O bond. Such a group can

be attached covalently to a molecule of interest at a specific site (spin label) or introduced as an individual molecule (spin probe) designed to explore a particular region of interest in the system under investigation. These stable radicals, generally referred to as nitroxides, were first introduced by McConnell in the 1960s [1]. All nitroxides share common spectroscopic features which establish their prominence for the study of molecular and material systems. The EPR spectrum of nitroxides is very sensitive to molecular motions in the nano- to millisecond range, and the ^{14}N hyperfine coupling and the g-factor are sensitive to the polarity of the environment. Moreover, the EPR spectrum can reveal dipolar interactions between nitroxides with distances in the range of 0.7–2.0 nm [2]. This range can be extended to 8.0 nm by applying pulse EPR methods [3–6].

One way to attach nitroxide spin labels to proteins is by conjugation through the thiol group of cysteine residues. These can be native or introduced using site-directed mutagenesis [7]. This approach to spin labeling of proteins is referred to as site-directed spin labeling (SDSL). Although highly convenient, SDSL fails when the protein contains a large number of cysteines or cysteines that are important for function. Recently, the incorporation of a nitroxide bearing unnatural amino acid has been reported [8]. This new method is particularly appropriate for overcoming the above-mentioned problems. Methods have also been devised for labeling nucleic acids [9]. Nitroxide spin labels and those based on other organic molecules have been extensively reviewed in the chapter by Sigurdsson.

The spin-bearing moiety in spin labels can also be a paramagnetic metal ion. There are many metalloproteins that have paramagnetic metal ions or clusters that are essential to their activity. These can be used as intrinsic spin labels, and indeed, EPR spectroscopic techniques are among the best suited for studies of paramagnetic metalloenzymes. In the case of metalloenzymes with diamagnetic metal ions, paramagnetic metal ions are used as substitutes for the diamagnetic ions, provided they possess the right properties (e.g., size, charge), can be directed to the same location and retain the activity of the enzyme. Paramagnetic metal ions such as Cu^{2+}, VO^{2+}, and Mn^{2+} are very convenient EPR probes, they are stable, and their EPR spectral characteristics are well known and understood. These have been commonly used as spin probes for diamagnetic metal ion sites in EPR investigations. For example, a popular substitution in biological systems is of Mn^{2+} for Mg^{2+} in both proteins [10] and nucleic acids [11]. This approach is highly valuable and well established; however, it is not a general purpose spin labeling approach and is specific to biomolecules that have metal ion binding sites. A more general approach is engineering metal-binding sites into proteins [12].

An isolated paramagnetic center can provide structural information within a radius of less than ca. 1 nm by measurement of the hyperfine interactions with nearby magnetic nuclei. Longer range structural information is derived from electron–electron spin interactions, and this, naturally, requires at least two separate paramagnetic centers. Accordingly, paramagnetic metal substitution cannot be simply extended for long-distance measurements by introducing a second paramagnetic metal ion because such a second specific binding site is usually not available. It can be applied to specific cases when the interaction between two biomolecules,

both with a metal active site, is of interest. Otherwise such a site should be engineered or introduced as a spin label.

In this chapter, we describe a new approach to general purpose spin labeling that is based on metal ions, mainly Gd^{3+}, with emphasis on the application to long-range distance measurements. We refer to these as metal spin labels as opposed to metal ion substitutions. In the context of paramagnetic metal ions and spin labeling, several schemes of spin pairs for distance determination can be envisioned: (1) two metal spin labels, (2) a metal spin label and a nitroxide spin label, (3) an intrinsic paramagnetic metal center and a nitroxide or a metal spin label (4), and a substituting paramagnetic ion and a nitroxide or a metal spin label (5).

There are several methods for determining the dipolar interaction between two electron spins [13]. Briefly, these are based on (1) analysis of line broadening of the continuous wave (CW) EPR spectrum caused by the dipolar coupling, suitable for distances below ca. 2 nm (a comparative study of such analyses has been recently published [14]); (2) relaxation measurements examining the enhancement of the relaxation rate of a slow relaxing spin by the presence of a fast relaxing spin (this method extends to distances up to 2.7 nm [15]); and (3) pulse EPR methods such as DEER (double electron–electron resonance), termed also PELDOR (pulse electron–electron double resonance), DQC (double-quantum coherence), and RIDME (relaxation-induced dipolar modulation enhancement), which can routinely access distances in the range of 1.8–5 nm and under favorable conditions can be extended to 8 nm. [4].

This chapter concentrates primarily on applications and methods pertaining to long-range distance measurements using pulse EPR techniques because these represent the most recent developments in the field and have attracted considerable attention in terms of applications to biological systems.

1.1 Why Do We Need Alternatives to Nitroxide Spin Labels?

Currently, the challenge is to extend the accessible distance range to longer distances and to increase the sensitivity of the measurements. In addition, there is a need to access distances below 2 nm, particularly within the "gray" range of 1.5–2.0 nm that is between the applicability of CW EPR and DEER for nitroxides. Short-range distance measurements by pulse methods at X-band are limited by the spectral width of the nitroxide spectrum. The amount of sample required for X-band (~9.5 GHz, ~0.35 mT) DEER measurements is 30–80 μl of at least 0.1 mM solutions of doubly labeled proteins, and the measurement time is about 12–24 h at 50 K. This is a relatively large sample quantity that can be difficult to obtain for some proteins or nucleic acids, limiting the applicability of the method. Extension to longer distances beyond 5 nm is immediately associated with low concentration needed for a reliable removal of interferences from interpair dipolar interactions. Therefore, measurements of long distances require an increase in sensitivity.

One way to reduce the amount of sample (paramagnetic centers) needed is to carry out the measurements at higher frequencies [16, 17]. The sensitivity of early W-band (95 GHz, 3.5 T) DEER measurements on a nitroxide biradical model compound carried out on a commercial spectrometer was severely compromised by the limited microwave (mw) power available [18]. Recent measurements on homebuilt spectrometers, however, showed that the sensitivity could be augmented dramatically by increasing the microwave (mw) power, allowing DEER measurements of as little as 2–3 μl of 100 μM solutions [19] or ~200 μl of 1 μM solutions [20]. This corresponds to an order of magnitude improvement in sensitivity in terms of the amount of sample needed compared with X-band measurements. Sensitivity improvement has been recently reported for Q-band (~34 GHz, ~1.2 T) measurements [21] or by using perdeuterated proteins [22], which exhibit a considerably longer-phase memory time as compared to natural abundance proteins.

The difficulties of high-field distance measurements using nitroxide spin labels lie in the data analysis required for the extraction of the distance distribution. At high fields, the nitroxide g-anisotropy becomes resolved and the spectral width increases. Because the microwave pulses excite only a fraction of the EPR spectrum only a subset of molecules with selected orientations with respect to the magnetic field contributes to the DEER trace. This is referred to as orientation selection [23, 24], and it has to be taken into account explicitly in the extraction of distance distributions from DEER data [25–30]. This requires a series of measurements at several magnetic field positions along the EPR powder pattern and a rather complex data analysis. A more detailed description of DEER analysis under orientation selection conditions is given in the chapter by Timmel and Freed. While the above motivations for searching for alternatives to nitroxide spin labels are spectroscopic in nature, there may also be chemically related reasons. There are conditions under which nitroxide radicals are not stable such as in highly acidic solutions or in a reducing environment.

The above-mentioned limitations call for alternative spin labels that provide high sensitivity, particularly at high fields, and are free from orientation selection effects. Such new spin labels could be based on a metal ion as the spin-bearing unit. Next, we discuss the use of metal spin labels or metal substitution for distance measurements according to the spin of the metal ion, which determines the characteristics of its EPR spectrum. The EPR spectrum, in turn, is one of the important physical factors that affect the performance of particular spin labels in distance measurements, and therefore, we shall start with its description. We begin with $S = 1/2$ metal ions where the g- and hyperfine anisotropies are the dominant interactions, similar to nitroxides, just with larger anisotropies, and then proceed to half-integer high-spin systems ($S = 5/2$, $S = 7/2$) with half-filled valence orbitals. In these ions, the g-factor is isotropic, and the anisotropic term in the spin Hamiltonian is the zero-field splitting. We refer to these as HFHS (half-filled high-spin) systems.

2 Paramagnetic Metal Ion Probes with $S = 1/2$

2.1 The EPR Spectrum

The EPR spectrum of $S = 1/2$ paramagnetic metal ions, such as Cu^{2+} and VO^{2+}, is determined by the following spin Hamiltonian that is governed by the g- and the center metal hyperfine (A) anisotropic interactions:

$$\mathcal{H} = \beta_e \vec{B} \cdot \boldsymbol{g} \cdot \hat{S} + \hbar \, \hat{S} \cdot \boldsymbol{A} \cdot \hat{I}. \tag{1}$$

In (1), $\vec{B}$ is the external magnetic field, $\hat{S}, \hat{I}$ are the electron and nuclear spin operators, respectively, and **g** and **A** are the g- and A-tensors. Both the g- and the A-anisotropies are usually substantial and already well resolved at X-band frequencies (~9.5 GHz). For the sake of simplicity, we shall focus on Cu^{2+} EPR characteristics because distance measurements carried out between two $S = 1/2$ metal centers have been conducted mainly on Cu^{2+} pairs. This is general enough as other common $S = 1/2$ metal ions, such as VO^{2+}, behave similarly. Furthermore, we shall only consider axially symmetric **g**- and **A**-tensors, as is often found for Cu^{2+}. To first order the resonance magnetic field, B_{res} is given by

$$B_{res} = \frac{\hbar}{\beta_e g_{eff}} [\omega_0 - A_{eff} M_I], \tag{2}$$

where

$$g_{eff} = [g_\perp^2 \sin^2\beta + g_\parallel^2 \cos^2\beta]^{1/2}, \tag{3}$$

$$A_{eff} = \frac{1}{g_{eff}} [(A_\parallel^2 g_\parallel^2 - A_\perp^2 g_\perp^2)\cos^2\beta + A_\perp^2 g_\perp^2]^{1/2}, \tag{4}$$

ω_0 is the spectrometer frequency, M_I is the spin quantum number for the projection of the $\hat{I}_z$ spin operator, g_{eff} and A_{eff} are the orientation-dependent g-factor and hyperfine coupling, respectively, given in (3) and (4), and β is the angle between the external magnetic field vector $\mathbf{B}_0$, with respect to the direction of $g_\parallel$ and $A_\parallel$. Here, the principal axes systems of **g** and **A** are taken as coinciding.

Figure 1a shows a typical calculated CW EPR spectrum of Cu^{2+} in an orientationally disordered system such as a polycrystalline sample or a frozen solution (obtained using Easyspin [31]). It also displays the individual powder patterns for each of the four M_I values arising from the $I = 3/2$ of $^{63,65}Cu$. The EPR powder pattern is obtained by summing the individual powder patterns.

In typical pulse EPR experiments, the minimum π pulse length is usually 12 ns. The bandwidth of such a pulse is approximately 160 MHz (6 mT), and therefore,

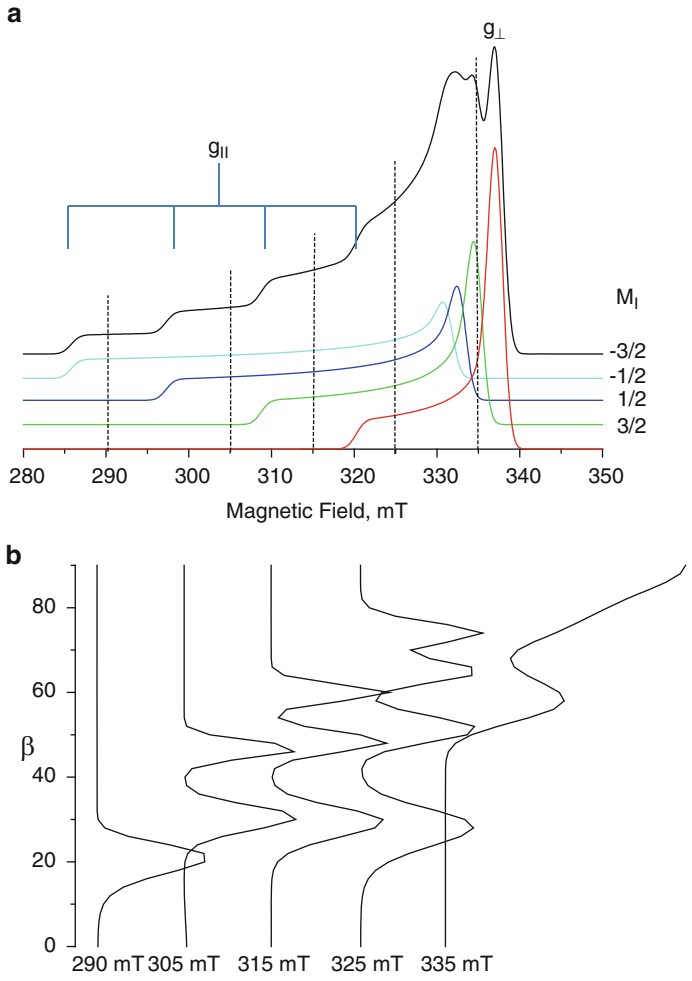

Fig. 1 (**a**) A calculated solid state X-band EPR spectrum of $^{63}Cu^{2+}$ with $g_\perp = 2.03$, $g_\parallel = 2.24$, $A_\perp = 50$ MHz, and $A_\parallel = 350$ MHz. The individual powder patterns for each M_I value are shown as well. (**b**) The selected β (in degrees) orientations for four different magnetic fields for an excitation bandwidth of 100 MHz. These fields are indicated in (**a**) by *dotted lines*. The simulations were done with Easyspin

only a part of the Cu^{2+} spins will be affected by the pulse, depending on the field at which the experiment is carried out and the **g**- and **A**-strain that represent the distribution of **A** and **g**. Figure 1b presents the set of orientations β excited by the mw pulse for several magnetic field positions within the EPR powder pattern. It shows that as $g_\perp$ is approached, the range of the selected β orientations becomes larger due to the overlap of the different M_I powder patterns.

2.2 DEER Between Two S = 1/2 Metal Centers

The spin Hamiltonian that describes the electron Zeeman interactions and dipolar interaction between the two $S = 1/2$ spins (radicals or metal ions/clusters), A and B, is

$$\mathcal{H} = \omega_A \hat{S}_z^A + \omega_B \hat{S}_z^B + \mathcal{H}_{dip}, \tag{5}$$

$$\mathcal{H}_{dip} = \omega_{dd} \left[\hat{S}_z^A \hat{S}_z^B + \frac{1}{4} \left(\hat{S}_+^A \hat{S}_-^B + \hat{S}_-^A \hat{S}_+^B \right) \right], \tag{6}$$

$$\omega_{dd} = \frac{\mu_0 \beta_e^2 g_A g_B}{4\pi\hbar r^3} (3\cos^2\theta - 1) = \omega_{dd}^0 (3\cos^2\theta - 1), \tag{7}$$

where ω_A and ω_B represent the resonant frequencies of spins A and B, respectively. These will be a function of **g** and **A**. Equation (6) describes the dipolar Hamiltonian $\mathcal{H}_{dip}$. ω_{dd} corresponds to the dipolar coupling between spins A and B, which are separated by distance r, and θ is the angle between vector **r** and the external magnetic field. In (5), the exchange interaction was neglected, which is valid for nonconjugated systems and when $r > 1$ nm [32]. The second term in $\mathcal{H}_{dip}$ (6) represents the pseudosecular terms that are ignored when $\omega_{dd} \ll |\omega_A - \omega_B|$. This has been shown to be valid also for typical Cu^{2+} centers where the g-anisotropy is not very large [27].

Currently, the dipolar interaction is usually measured by the constant time four-pulse DEER sequence (Fig. 2a) [34], which is an improvement over the initially used three-pulse DEER sequence [3]. In this experiment, the A spins are the observer spins, whereas the B spins are the pumped spins. The time dependence of the echo intensity, $V(t)$, is [35]

$$V(t) = V_{intra}(t) V_{inter}(t), \tag{8}$$

where $V_{intra}(t)$ describes the contribution of the dipolar interaction between two labels on the same molecule or molecular assembly, whereas $V_{inter}(t)$ corresponds to contributions from dipolar interactions between spin labels on different molecules. The latter just contributes to a background decay that is usually removed during data analysis and is given by

$$V_{inter}(t) = V_0 \exp(-bC\lambda t), \tag{9}$$

where $b = 9\sqrt{3\hbar}/(2\pi\mu_0 g_A g_B \beta_e^2)$, C is the spin concentration, and V_0 is the echo intensity at $t = 0$.

The part of interest is $V_{intra}(t)$, which in an orientationally disordered system, such as a polycrystalline sample or a frozen solution is [24, 35]

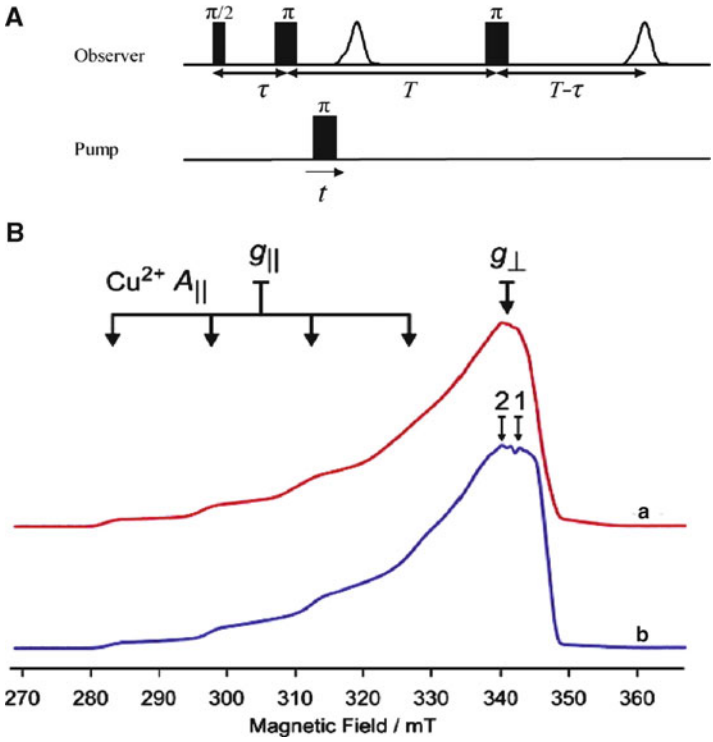

Fig. 2 (**A**) The four-pulse DEER sequence. (**B**) X-band echo-detected EPR spectra of (*a*) Cu_2Tf and (*b*) Cu_2Lf recorded at 10 K. The *arrows* indicate the positions of pumping (*1*) and detection (*2*) in the DEER experiments shown in Fig. 3. (*a*) and (*b*) were adapted with permission from [33]. Copyright 2007 American Chemical Society

$$V_{\text{intra}}(t) = \left(1 - \int_0^{\infty} P(r) \int_0^{\pi/2} P(\theta)[1 - \cos(\omega_{\text{dd}} t)]\mathrm{d}r\mathrm{d}\theta\right), \tag{10}$$

where $P(r)$ is the intrapair distance distribution and $P(\theta)$ is the distribution function of the angle θ given by

$$P(\theta) = \lambda(\theta)\sin\theta. \tag{11}$$

$\lambda(\theta)$ is the probability of flipping spin B and is often referred to as the modulation depth parameter. In an orientationally disordered system when there is no correlation between the orientations of the two spins, λ is independent of θ. In this case

$$V_{\text{intra}}(t) = 1 - \lambda \int_0^{\infty} P(r) \int_0^{\pi/2} [1 - \cos(\omega_{\text{dd}} t)\mathrm{d}r \sin\theta \,\mathrm{d}\theta, \tag{12}$$

where λ depends on the pump pulse duration and the EPR lineshape, $g(\Delta\omega)$, according to [36]

$$\lambda = \int_0^\infty \frac{\omega_1^2}{\Omega^2} \sin^2\left[\frac{\Omega}{2} t_p\right] g(\Delta\omega) \mathrm{d}(\Delta\omega), \tag{13}$$

$$\Omega^2 = \omega_1^2 + \Delta\omega^2, \tag{14}$$

where ω_1 is the amplitude of the mw irradiation field, $\Delta\omega$ is the off-resonance frequency relative to the pump-pulse frequency, and t_p is the pump-pulse duration.

The modulation depth λ can be determined from (13) or from (9) using a series of solutions with varying concentrations of the radicals or ions. Alternatively, in frozen solutions at long enough t values, the modulations in the DEER trace are damped, and $V_{intra}(t)$ reaches an asymptotic value of $(1 - \lambda)$ from which λ can be readily obtained. λ determined this way is referred to as λ_{exp}, and it can be smaller than the λ value obtained by the other two methods. This occurs when there are spin pairs in the samples that exhibit distances that are too short to be accessed by the DEER experiment. When the bandwidth of the observer and pump pulses does not exceed ω_{dd}, then λ becomes also a function of ω_{dd} according to [26, 37]

$$\lambda(\omega_{dd}) = \lambda(\theta)[\exp(-4\omega_{dd}^2 t_p^2) \exp(-4\omega_{dd}^2 t_o^2)], \tag{15}$$

where t_o is the observer pulse duration. For metal ions with large g- or A-anisotropies, the EPR spectral width becomes considerably larger than that of nitroxides, and therefore, λ is usually much smaller. When there is correlation between the orientations of the g-tensors of the two metal ions, $\lambda(\theta)$ will depend on this relative orientation and on the orientation of the vector connecting the two spins, **r**, with respect to one of the g-tensors [17, 24]. An extensive discussion on DEER under orientation-selective conditions is given in the chapter by Timmel and Freed.

So far, the electron spin was considered to be localized on a single atom. However, in many metal ion complexes, the spin can be also delocalized on the ligands. In this case

$$\omega_{dd} = \frac{\mu_0 \beta_e^2 g_A g_B}{4\pi\hbar} \sum_{n,m} \frac{(3\cos^2\theta_{nm} - 1)}{r_{nm}^3} \rho_n \rho_m, \tag{16}$$

where n and m are spin-bearing atoms in A and B with spin densities of ρ_n and ρ_m, respectively, and θ_{nm} and r_{nm} are the corresponding orientations and distances with respect to B_0 [26, 27, 38]. Accordingly, the derivation of the distance from the measured ω_{dd} is not as straightforward as in the spin-localized case.

2.3 DQC and RIDME

Another method for measuring long-range distances is the double-quantum coherence (DQC) technique [39, 40]. This method is based on the generation of double-quantum coherences and is discussed in detail in the chapter by Timmel and Freed. The six-pulse sequence is the most effective one and yields a time evolution similar to that observed with DEER, showing modulation at frequency ω_{dd}. For two $S = 1/2$ spins, the echo intensity is given by [4]

$$V(t_\xi) = 0.5V_0[\cos(\omega_{dd}t_m) - \cos(\omega_{dd}t_\xi)], \tag{17}$$

where t_m is a fixed time and t_ξ is the variable time. For disordered systems, the first term becomes zero for large enough $\omega_{dd}t_m$ values. The virtue of this technique is that it is a single frequency technique, namely, all spin are regarded as A spins. It is important that the pulses are short and intense in order to create DQCs over the whole spectral distribution of the spins. In addition, it requires extensive phase cycling to select the desired DQC coherence pathway and remove unwanted echoes generated by the six pulses in the sequence. It also suffers from interferences from nuclear modulation frequencies when these are present. In systems with a narrow spectral width, DQC should be advantageous over DEER. However, for $S = 1/2$ metal centers with large g-anisotropy, the advantages are not obvious.

Under some favorable conditions, the distance between two spins can be measured by the simple stimulated echo sequence ($\pi/2 - \tau - \pi/2 - T - \pi/2 - \tau -$ echo), where T is kept fixed and rather long and the echo intensity is measured as a function of τ. This method is referred to as RIDME (relaxation-induced dipolar modulation enhancement) [41], and in contrast to DEER where the flips of spin B are induced by the pump pulse, in RIDME, the B spin flips are induced by the electron spin lattice relaxation that takes place during the time T at a rate of $1/T_1$. When $T_1 \gg \tau$ and ${T_1}^2{\omega_{dd}}^2 \gg 1$, the echo intensity is given by [41]

$$V(2\tau + T) = 0.5\left(1 + e^{-T/T_1}\right) + 0.5\left(1 - e^{-T/T_1}\right)\cos\omega_{dd}\tau. \tag{18}$$

In (18), the decay due to phase memory time has not been taken into account. Because the modulations are induced by a stochastic T_1 process, it covers all spins, and orientation selection effects are induced only by the observer pulses and therefore are expected to be smaller than in DEER. A major drawback of this experiment is interferences from nuclear modulations, which can be reduced if the experiment is performed at high fields [42]. Recently, a dead-time-free variation of the RIDME sequence has been proposed [43]. RIDME is most efficient when T is on the order of T_1 of the B spins. Therefore, one may have to search for the optimum temperature at which to perform the measurements, and this is somewhat inconvenient.

2.4 Long-Range Distance Measurements Between S = 1/2 Metal Centers

So far, most of the applications of DEER or DQC to determine distances between metal centers concerned intrinsic sites, mostly containing Cu^{2+} ions. We shall review them here briefly because they are relevant for understanding the potential of $S = 1/2$ metal ions as general purpose spin labels, which is rather limited due to low sensitivity because of their broad spectrum.

The effect of orientation selection on DEER of a Cu^{2+}–Cu^{2+} pair was clearly demonstrated on a rigid bis Cu-porphyrin model (3-phenyl diporphyrin dicopper) complex [27]. It was noted that if the pump and observer pulses are set to the $g_{\perp}$ region, then an approximate Pake doublet with distinct ω_{dd} features for $\theta = 90^0$ becomes clear, thereby providing a straightforward determination of the Cu–Cu distance. In this particular case, an additional complication was that only 85% of the spin is located on the Cu^{2+} and the rest is distributed among the porphyrin nitrogens. This was taken into account in the simulations of the DEER traces (see (16)), which were based on a set of conformations obtained from the accessible porphyrin/phenyl and phenyl/phenyl dihedral angles. A very good agreement between the calculated and experimental DEER traces was obtained.

One of the earliest reports of a DEER application to metal ion pairs in biomolecules involved covalently linked dimers of the electron transfer protein azurin [44], which has a type I copper site. Two azurin dimers were prepared, and their crystal structures were determined. In one of the dimers, the Cu^{2+} – Cu^{2+} distance was 1.42 nm, and no modulations could be observed due to limitations in pulse length – this distance is usually outside the range of DEER applicability. In the other dimer, the distance was 2.59 nm and $\omega_{dd}^0 = 3.0$MHz was expected. Only one DEER trace with the pump and observer pulses set to the $g_{\perp}$ region was reported, and data were collected only up to $t = 500$ ns, yet modulations at 2.7 MHz were clear. In this particular Cu center, there is a significant delocalization of the spin on the thiolate ligand [45], but the effect of this on the measured distance has not been discussed.

Cu^{2+}–Cu^{2+} distances of ~4 nm were measured in 0.4 mM transferrin (Tf) and lactoferrin (Lf) solutions [33]. Each one of these proteins contains two Fe^{3+}-binding sites. The Fe^{3+} ions were replaced with Cu^{2+} ions, which have more convenient EPR spectroscopic properties for distance measurements. This is an example of a metal substitution probe. Four-pulse DEER was applied, and the pump and observer pulses were set at the $g_{\perp}$ region, as indicated in Fig. 2b. The dipolar evolution time was measured up to 3 μs, and clear modulations were observed for both samples as shown in Fig. 3. Fourier transform (FT) of the data after background removal yielded Pake doublets showing that orientation selection can be neglected when the pulses are set to the $g_{\perp}$ region. In both samples, the width of the derived distance distribution was rather narrow, ~0.3 nm. The distances found were 0.1–0.2 nm shorter than the Fe–Fe distances in the crystal structure.

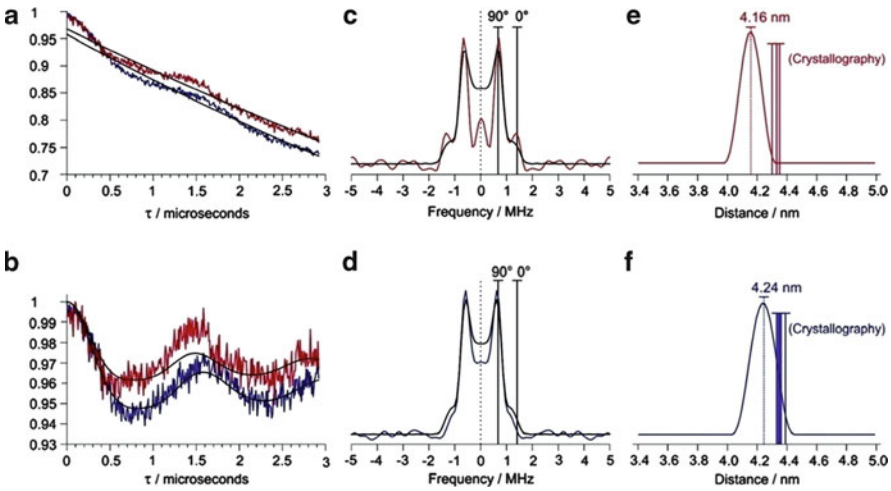

Fig. 3 (**a**) Four-pulse DEER traces of Cu_2Tf (*red*) and Cu_2Lf (*blue*) at 10 K with the corresponding fitted background decay, recorded close to $g_\perp$ at 341 mT (see Fig. 2) with $\nu_{observe} = 9.845$ GHz and $\nu_{pump} = 9.775$ GHz. (**b**) The time traces after background removal and fits (*black*) with the distance distribution shown in (**e**, **f**). (**c**, **d**) FT of the data shown in (**b**) Cu_2Tf (*red*) and simulation (*black*) and (**d**) Cu_2Lf (*blue*) and simulation (*black*). The distance distributions of (**e**) Cu_2Tf and (**f**) Cu_2Lf also show the intermetal distances derived from X-ray structures. Adapted with permission from [33]. Copyright 2007 American Chemical Society

A polyproline-based peptide containing two Cu^{2+}-binding motives has also been subjected to DEER measurements [25]. Here, the pump and observer frequencies, with a difference $\Delta\nu = 100$ MHz, were placed in four different positions in the EPR powder spectrum. The DEER traces, collected up to $t = 1.27$ μs, reveal a weak dipolar modulation, and all traces were practically the same, showing that there was no orientation selection due to the high flexibility of the peptide. FT gave a dipolar frequency of 3.9 MHz, which corresponds to a distance of 2.2 nm. More recently, similar measurements on a polyalanine-based peptide with two Cu^{2+} sites were carried out; again, due to the flexibility of the peptide, the orientation selection was very mild. DQC was also used to determine the distance between the two Cu^{2+} ions bound to a peptide [46]. From the FT of the DQC data, ω_{dd}^0 has been determined, and the distance was derived from it. The problem in this DQC measurement is the significant interference from ^{14}N nuclear modulation signals.

Another early application of DEER to paramagnetic metal sites was the measurement of the distance between two metal clusters in hydrogenase [38]. In the oxidized state, hydrogenase consists of two paramagnetic centers: a [NiFe] center, which has an effective $S = 1/2$ with most of the spin density on the Ni, and a $[3Fe–4S]^+$ iron–sulfur center, also with an effective $S = 1/2$. This system has two complications: the first originates from the large g-anisotropy of the [NiFe] center that results in a high degree of orientation selection, and the second is the spin delocalization over the different Fe in the $[3Fe–4S]^+$ cluster making the point dipole approximation inappropriate. Accordingly, the interpretation of the DEER data should include the explicit interaction with each of the Fe atoms. In this case, the dipolar frequency is approximated by [38, 47]

$$\omega_{\mathrm{dd}} = \frac{\mu_0 \beta_e^2 g_{\mathrm{Ni}} g_{\mathrm{FeS}}}{4\pi\hbar} \sum_{i=1}^{3} K_i \frac{3\cos^2\theta_i - 1}{r_{i,\mathrm{Ni}}^3}. \tag{19}$$

In (19), the index i corresponds to a particular Fe in the cluster, $r_{i,\mathrm{Ni}}$ is the distance between the Ni ion in the [NiFe] cluster and that particular Fe, θ_i is the angle between the external magnetic field direction and the $r_{i,\mathrm{Ni}}$ vector, K_i is the spin projection factor of the individual ion, and g_{FeS} and g_{Ni} correspond to the g-factors of the two centers.

The DEER measurements were carried out by setting the pump-pulse frequency on the relatively narrow powder pattern of the $[3Fe–4S]^+$ cluster, and the observer pulse frequency was set to the signal of the [NiFe] cluster within the limited frequency range allowed by the spectrometer hardware. Another difficulty of this system was the rather short phase memory times of the [NiFe] and $[3Fe–4S]^+$ clusters, 360 and 800 ns, respectively, which restricts the measurements to rather short distances. Nevertheless, the authors obtained high-quality DEER data, with a clear modulation frequency of 8.5 MHz. In this particular application, the crystal structure was solved, and the known $r_{i,\mathrm{Ni}}$ distances were used to determine the K_i values, namely, the DEER experiment gave insight into the electronic structure of the $[3Fe–4S]^+$ cluster [47].

This rather small number of pulse EPR applications to long-range distance measurements between metal ions or clusters reflects the fact that such applications are still not routine. The difficulties arise from relatively short phase memory times that limit the dipolar evolution time and consequently the distance that can be accessed. Moreover, the large width of the EPR spectra and consequently also the low value of λ lower the sensitivity of DEER as concentrations of 0.4 mM (or higher) are often needed. Therefore, the common $S = 1/2$ metal ions are not very attractive as general purpose spin labels for biomolecules as compared to nitroxides. This situation is worsened at higher fields because of broadening of the spectrum due to the g-anisotropy. They are of course attractive for metal-ion-site-specific studies.

2.5 *Metal Center ($S = 1/2$)-Nitroxide Label Distance Measurements*

Although $S = 1/2$ metal ions have not been used so far as directly observed, general purpose spin labels, they were introduced into proteins through specifically engineered metal-binding sites. The purpose of this site-specific metal ion labeling was to measure the distance between the metal ion and a nitroxide spin label introduced via SDSL for obtaining tertiary structure information like helix packing [48]. The engineered binding site included mutations to histidines that are known to be excellent ligands for Cu^{2+}. The distance was determined at room temperature by measuring the broadening of the nitroxide spectrum due to the fast relaxing

Cu^{2+} [49], and distances in the range of 1.1–1.8 nm were reported. This labeling approach can now be used for distance measurements using pulse EPR methods accessing longer distances. Distance measurements between a nitroxide spin label and a functional diamagnetic ion may also be obtained if the ion can be substituted by a paramagnetic metal ion. Here, the aim is to locate a metal-binding site in the protein or a protein/nucleic acid complex. Alternatively, one could probe the interaction between biomolecules: one labeled with a metal spin label or an intrinsic metal site, and the other labeled with a nitroxide.

Paramagnetic metal ion – nitroxide distance measurements by DEER have been carried out so far mainly on model compounds, demonstrating the feasibility of such measurements and setting the stage for real applications. A rigid model compound containing one Cu^{2+} and two nitroxides was subjected to DEER measurements at X-band, and both the Cu – nitroxide and the nitroxide – nitroxide distances could be determined by a proper selection of the position of the pulses [50]. Here, the largest modulation depth was obtained by setting the pump pulse to the maximum of the nitroxide spectrum and observing the Cu^{2+} signal. Such a setup is also more efficient in terms of S/N because the signal averaging rate is determined by the T_1 of the observer spins, and the Cu^{2+} ion has a shorter T_1. On the other hand, it also has a shorter phase memory time, T_M, which limits the maximum dipolar evolution time. Also here, placing the observer pulse at the $g_\perp$ feature of the Cu^{2+} spectrum reduced the orientation selection significantly. In more recent measurements of a Cu^{2+} ion and a single nitroxide in a rigid model system, the orientation selectivity was taken into account explicitly and the exchange interaction between the Cu^{2+} ion and the nitroxide was determined as well [26, 51].

A nice application of a DEER distance measurement between a paramagnetic metal center in one protein and a nitroxide spin label in a second protein has been recently reported [27]. Specifically, the complex between two proteins in the electron transport chain for heme-dependent cytochrome P450 enzymes was investigated in order to determine how palustrisredoxin reductase (PuR) and palustrisredoxin (Pux-B) bind. Distance measurements were carried out between a reduced (Fe^{3+}/Fe^{2+}) form of the [2Fe–2S] cluster in Pux-B, which has a $S = 1/2$ ground state with a considerable g-anisotropy, and PuR labeled with a nitroxide. Here, the orientation selection was extensive, and a set of 5 DEER traces were analyzed to yield the distance and orientation with respect to the g-tensor of the [2Fe–2S] center.

Distance measurements between an intrinsic radical intermediate and a metal cluster have also been reported. We note such earlier applications, using the three-pulse DEER sequence, to photosystem II. In one application, the distance between the redox active tyrosine residue radical, Y_D, and the Mn cluster in the S2 ($S = 1/2$) and S3 states was determined (2.7 and 3.0 nm) [52]. In another study, the distance between the quinone radical, Q_A^-, and the low-spin heme in cytochrome b_{559}^+ was determined (~4 nm) [53]. A more recent example concerns pyruvate ferredoxin oxidoreductase (PFOR). This is a thiamine pyrophosphate (TPP)-dependent enzyme that catalyzes the anaerobic oxidation of pyruvate (with coenzyme A (CoA)) to acetyl-CoA, CO_2, and two electrons that are transferred to ferredoxin [54].

Here, an intermediate state that contains the hydroxyethylidene-TPP (HE-TPP) radical and a [4Fe-4 S]$^{1+}$ cluster with $S = 1/2$ was trapped and studied by DEER spectroscopy. Again, the metal cluster was observed, and the pump pulse was set to the HE-TPP organic radical intermediate. A modulation frequency of 1.48 MHz was observed, and to further translate it into a distance, the spin distribution in both paramagnetic centers had to be considered, complicating the analysis. To ensure that the DEER measurements were free of orientation selection, RIDME measurements were carried out as well. In this experiment, the refocused stimulated ESE signal of the HE-TPP radical was observed, while the longitudinal relaxation of the [4Fe–4S]$^{1+}$ center served the purpose of modifying the local magnetic field for the organic radical spin (instead of pumping at a different microwave frequency). Since the [4Fe–4S]$^{1+}$ center at any orientation is subject to longitudinal relaxation, it does not introduce orientation selectivity. RIDME was also used to determine the distance between paramagnetic flavin mononucleotide and a heme, in human inducible NO synthase [54].

3 Half-Integer High-Spin Metal Ions ($S = 5/2, 7/2$)

3.1 Gd^{3+} and Mn^{+2}

One of the major requirements of a good spin label is that it can be directed to specific sites of interest without interfering with the systems' properties. Unlike nitroxide spin labels that are covalently linked to the molecules of interest, metal ions attachment is through coordination to ligands. Accordingly, the binding constant must be high, and competition with natural binding sites in the molecules should be avoided. One approach that is applicable to proteins is to engineer a binding site by the introduction of metal-binding amino acids as described earlier [55]. This has been demonstrated for Mn^{2+} [12]. Another simpler, more effective, and general approach would be to covalently attach to the biomolecule a chelator, referred to as a tag, that will bind the metal with high efficiency. Such a lanthanide tag has been reported for the purpose of distance measurements to a nitroxide via relaxation effects [56]. The tag should exert a minimum perturbation on the biomolecule and should be rigid to avoid large distance distributions that are a consequence of the motion of the tag tether rather than that of the labeled molecule.

The attachment of paramagnetic lanthanide tags to biomolecules is rather well developed and extensively used in NMR studies of biomolecules. Paramagnetic lanthanides exert large effects in protein NMR spectra, including changes in chemical shifts ("pseudocontact shifts") and the disappearance of NMR signals due to pronounced relaxation enhancements in the vicinity of the metal ion. The effects act over large distances (>4 nm) and can be accurately described mathematically, and therefore, they are most useful for 3-D structure analysis of biomolecules in solution [57]. Accordingly, efforts to tag (label) proteins, DNA, and RNA molecules site specifically with single lanthanide ions have recently

emerged [58]. Pseudocontact shifts easily average to zero if the tag is tethered to the biomolecule via a flexible linker; therefore, rigid tags with high lanthanide affinity are desired. These requirements are concomitant with the requirements for EPR distance measurements mentioned above. While most of the lanthanides have very fast relaxation times and are therefore inappropriate as EPR spin labels, Gd^{3+} stands out due to its considerably longer relaxation time [57]. Tags capable of binding lanthanide ions for NMR can also be used as Gd^{3+} spin labels. Unlike Mn^{2+}, Gd^{3+} is not a naturally occurring metal ion in biology and therefore is unlikely to have natural binding sites in molecules that can compete with the engineered tag. Another advantage of Gd^{3+} is that the unpaired electrons are in the inner f orbitals and their interaction with the ligands is mostly ionic in nature, and therefore, the unpaired electrons do not reside on the ligands. Finally, Gd^{3+} complexes are quite robust chemically.

To date, all protein tags for NMR rely on either N- or C-terminal fusions of proteins with lanthanide-binding peptides or on synthetic tags that are attached via disulfide bonds to single cysteine thiol groups, just like nitroxide attachments [57–59]. Although extensively used, the conjugation of a lanthanide ion via a cysteine thiol bond can encounter the same difficulties as mentioned earlier for nitroxides in Sect. 1. An EDTA-derivatized nucleic acid has been developed for binding paramagnetic ions to DNA [60]. Figure 4 shows some Gd^{3+} tags.

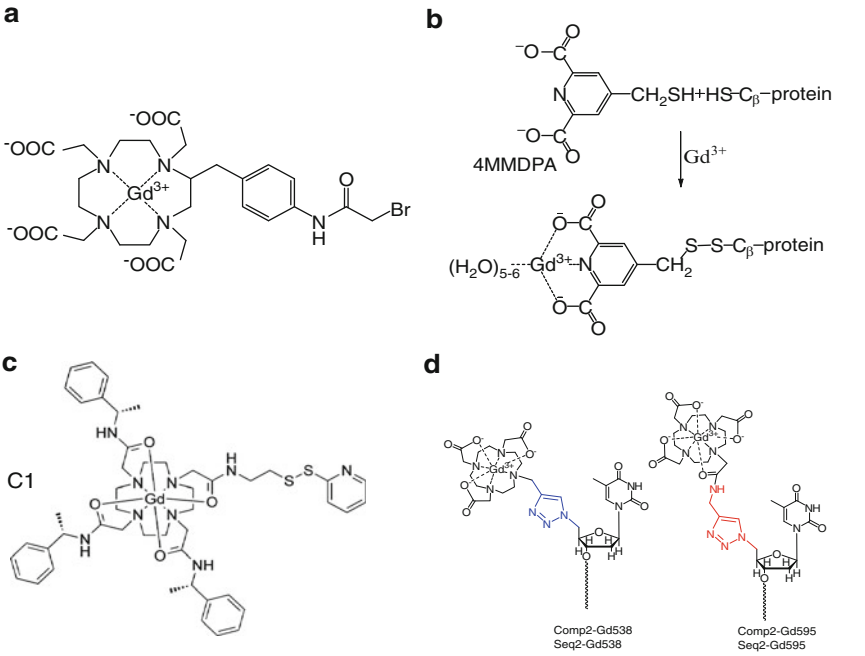

Fig. 4 Gd^{3+} tags for labeling biomolecules

3.2 The EPR Spectrum of Gd^{3+}

A key to understanding the utility of a spin label for distance determination is its EPR spectrum. Here lies the major difference between the nitroxide or any other $S = 1/2$ paramagnetic center, including metal ions, and half-integer high-spin systems with half-filled valence orbitals, (HFHS) such as Gd^{3+} that has 7 unpaired electrons in its *f* orbitals. Two isotopes of Gd, ^{155}Gd and ^{157}Gd, have a nuclear spin of 3/2, but their natural abundance is only ~15% each, and their gyromagnetic moment is very low. Therefore, the EPR spectrum does not show any hyperfine couplings. The EPR spectrum of a single Gd^{3+} ion is determined by the following spin Hamiltonian:

$$\mathcal{H} = g\beta_e \vec{B}_0 \hat{S}_z + \hbar \hat{S} \cdot \boldsymbol{D} \cdot \hat{S} \tag{20}$$

In (20), the first term corresponds to the isotropic electron spin Zeeman interaction ($g = 2$). The second term is the zero-field splitting (ZFS) term with principal components D_{xx}, D_{yy}, and D_{zz} (given in frequency units), where conventionally $|D_{xx}| < |D_{yy}| < |D_{zz}|$. **D** is often traceless and characterized by two values, $D = 3/2\, D_{zz}$ and $E = (D_{xx} - D_{yy})/2$. For simplicity, we shall assume axial symmetry, $E = 0$. In this case, the first-order transition frequencies are given by

$$\omega_{M_s \to M_s+1} = \frac{1}{\hbar} g\beta_e B_0 + \frac{2M_s - 1}{2}[D(3\cos^2\alpha - 1)], \tag{21}$$

where M_S is the projection of the $\hat{S}_z$ operator, and α is the angle between B_0 and the direction of D_{zz}. To first order, there is no dependence of the central transition, $|-1/2> \to |1/2>$, on the ZFS parameters. However, there is a contribution to second order (valid when $\frac{1}{\hbar} g\beta B_0 \gg D,$), given by [61]

$$\omega^{(2)}_{-1/2 \to 1/2} = \frac{\hbar D^2}{16 g\beta_e B_0}(4S(S+1) - 3)[-2(\sin^2 2\alpha) + (\sin^4\alpha)]. \tag{22}$$

Equation (22) shows that as long as $\hbar D^2/16 g\beta_e B_0 \ll 1$, the central transition in Gd^{3+} remains narrow and practically unaffected by the ZFS. Accordingly, at sufficiently large fields, the spectrum of an orientationally disordered sample is composed of a narrow central transition, with an isotropic character, superimposed on a broad background due to the other transitions. The width of the latter is determined by (21).

The allowed EPR transition probabilities (to first order) are given by

$$\mathrm{TP}_{M_s \to M_s+1} = [S(S+1) - M_s(M_s+1)]. \tag{23}$$

This yields for the central transition a transition probability of 16 for $S = 7/2$, whereas for $S = 1/2$, the transition probability is unity.

A large distribution of D and E was found in many of the Gd^{3+} complexes in frozen solutions, thus smearing the powder pattern singularities and reducing effects of orientation selection in pulse EPR experiments [62]. In Fig. 5, we compare 10-K-calculated X-, Q-, and W-band Gd^{3+} EPR spectra with D and E values and distributions typical for a Gd^{3+} aquo complex in frozen solution. The central transition narrows considerably as the frequency increases, whereas the other individual transitions retain their width, but their relative intensities change due to the different thermal polarizations. For comparison, nitroxide spectra, separated into the individual M_I components, are shown in Fig. 5 as well. Here, unlike Gd^{3+}, the spectrum broadens as the spectrometer frequency increases. The behavior of Mn^{2+} is similar to that of Gd^{3+} except for the presence of an isotropic ^{55}Mn hyperfine interaction that introduce splitting into six lines. In frozen solutions, this hyperfine coupling is resolved only in the central transition. Considering the narrower linewidth of the central transition and its high transition probability, it is clear that high-field measurements offer a considerable sensitivity increase for Gd^{3+} and Mn^{2+} [63]. High-spin Fe^{3+} is also an HFHS ion, but unlike Gd^{3+} and Mn^{2+}, it usually has a very large ZFS, and therefore, it is not appropriate as a spin label. As shown in Figs. 5 and 6, the solid state EPR spectrum of HFHS is not only field dependent but also temperature dependent, particularly at high fields where thermal polarization becomes substantial. As the temperature decreases, the lower energy levels become more populated at the expense of the higher energy levels and this changes the relative intensities of the various transitions in the EPR spectrum. In Fig. 6, we compare the temperature dependence of the population difference of the

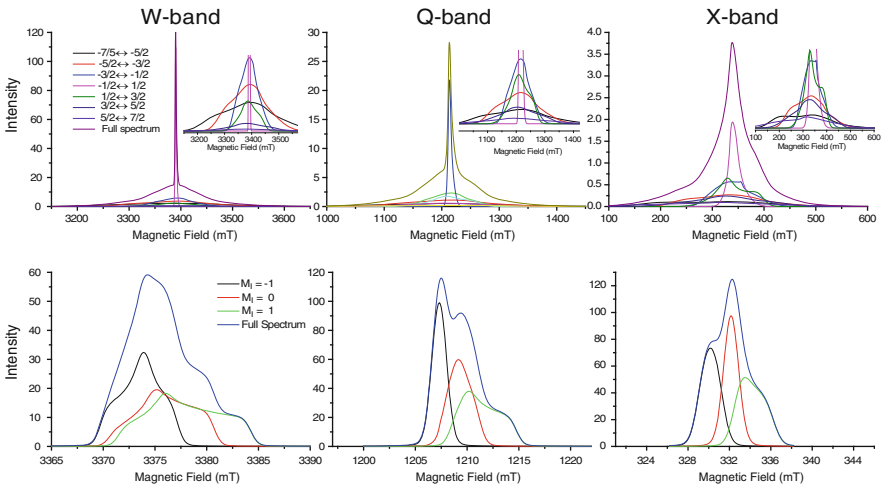

Fig. 5 *Top row* shows calculated W-, Q-, and X-band EPR spectra of Gd^{3+} at 10 K. The individual transitions are shown as well and blown up in the inserts. The parameters used to calculate the spectra are $D = 850$ MHz, $E = 270$ MHz, and distribution of 700 and 130 MHz, respectively. The *bottom row* depicts calculated nitroxide spectra for these three frequencies, also showing the individual M_I spectra. All spectra were calculated using Easyspin [31]

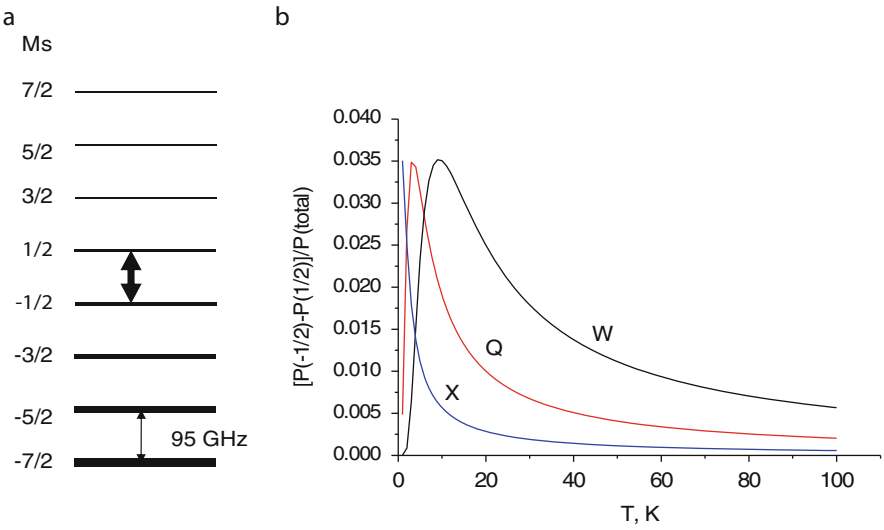

Fig. 6 (**a**) The energy level diagram of Gd^{3+} at W-band and a low temperature. The thickness of the lines represents the population of the levels. The central transition is noted by an *arrow*. (**b**) The Boltzmann population difference of the central transition as a function of temperature for X- (9.5 GHz), Q- (34 GHz), and W-band (95 GHz)

central transition of Gd^{3+} at X-, Q-, and W-band. These plots show that a maximum intensity of the central transition is reached at ~10 K at W-band; at ~3 K at Q-band and at X-band, it is close to zero.

3.3 Gd^{3+} – Gd^{3+} Distance Measurements

Given the spectroscopic properties mentioned above, Gd^{3+} offers a number of critical advantages as the spin-carrying moiety in spin labels for high-field EPR applications. Its spin is closely localized on the Gd^{3+} atom, and D is relatively small in most complexes ($D < 40$ mT) [62]. Consequently, the width of the subspectrum of the central transition is narrow for spectrometer frequencies $\nu_0 > 30$ GHz, resulting in very high sensitivity. The large transition probability of the Gd^{3+} ion (see (23)) leads to about a fourfold larger effective amplitude of the irradiating microwave field ω_1 for the central transition of Gd^{3+} as compared to the nitroxide spin. This allows short π pump pulses to be applied also in spectrometers with limited mw power. The spin–lattice relaxation time of Gd^{3+} is short compared to those of nitroxides, allowing rapid signal averaging at cryogenic temperatures (~10 K). Most importantly, the central transition, as well as the other transitions, can be considered as effectively isotropic with respect to the ligand orientation because the large ZFS distribution (in amplitude and orientation) [62] abolishes the

orientation selection. Finally, the broad spectrum of the "other" transitions, which spans thousands of Gausses, opens up the possibility for extending the short-distance limit of DEER as large $\Delta\nu$-values (the pump-observ) pulse frequency separation can be accessed. In this case, the exchange interaction, J, will have to be considered as well. It is also possible that the dipolar splitting will be resolved in the narrow central transition. Before going into the specifics of DEER of HFHS systems, we review the long-range distance measurements carried out so far on Gd^{3+}–Gd^{3+} pairs.

3.3.1 Model Systems

The feasibility of distance measurements between two Gd^{3+} ions was first demonstrated using the simple rigid bis-Gd^{3+} complex shown in Fig. 7a [64]. The DEER measurements were performed at Ka- (33.78 and 29.6 GHz) and W- (94.9 GHz) bands, and the corresponding echo-detected (ED) EPR spectra are shown in Fig. 7b, c. The width of the W-band central transition is about 0.4 of the Ka-band width, as expected (see (22)). The four-pulse, time-domain DEER traces, shown in Fig. 8a, exhibit a steep initial decay followed by shallow but clear modulations. Such a time-domain trace is characteristic of a short distance with some distribution. The distance was derived from (10), using DeerAnalysis2006 [37], neglecting the exchange interaction and ZFS effects on ω_{dd}. The distance distributions obtained, shown in Fig. 8b, yield a maximum at 2.0–2.05 nm as compared to

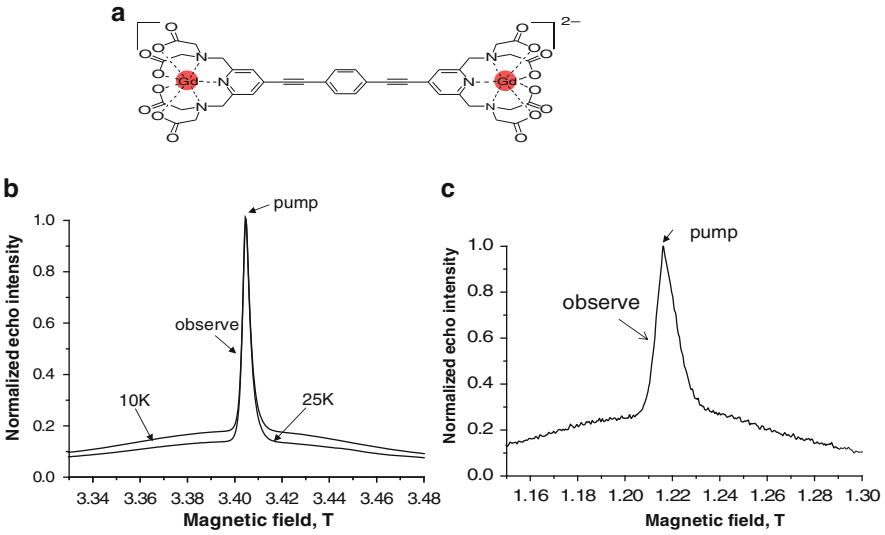

Fig. 7 (**a**) The structure of the bis-Gd^{3+} complex. (**b** and **c**) ED-EPR spectra of the bis-Gd^{3+} complex recorded at (**b**) W-band (0.2 mM, 10 and 27 K) and (**c**) Ka-band (~1.5 mM, 13K). The positions of the pump and observer pulses for the DEER traces shown in Fig. 8 are indicated

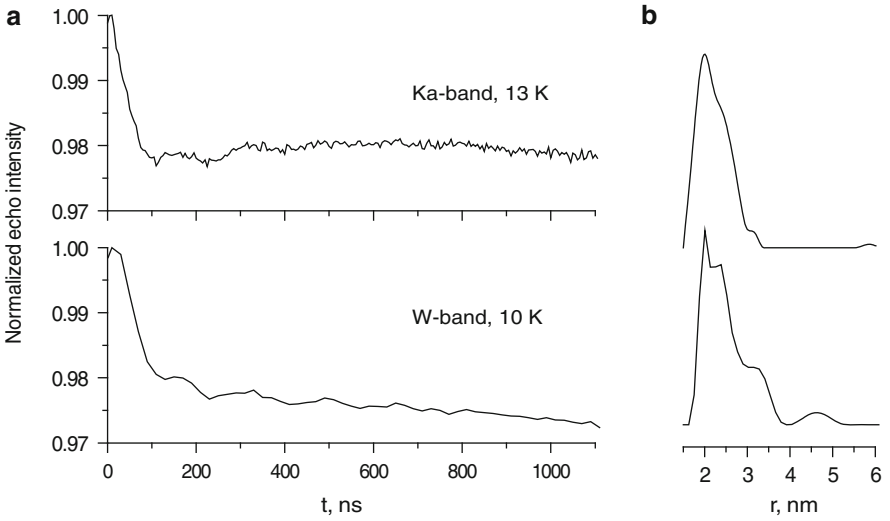

Fig. 8 (**a**) The four-pulse DEER traces of the bis-Gd^{3+} complex shown in Fig. 7 recorded at (*top*) Ka-band, 13 K, data shown are after removal of the background (t_o = 15/25/25 ns, t_p = 12 ns, $\Delta\nu$ = 160 MHz), (*bottom*) W-band, 10 K (t_o = 20/40/40 ns, t_p = 16 ns, $\Delta\nu$ = 83 MHz). (**b**) The corresponding distance distributions

2.12 nm determined later from the crystal structure [65]. This good agreement shows that (10) holds also for this high-spin system and that DEER data can be analyzed accordingly. This will be further discussed in Sect. 3.4. The modulation depth is low, a few%, as is expected considering the bandwidth of the pump pulse with respect to the total width of the spectrum. The shallow modulation depth is compensated by the very intense EPR signal. In addition to the peak at 2 nm (Fig. 8b), the distance distributions show shoulders at higher distances, which were attributed primarily to artifacts due to some uncertainty in the background removal.

Following this first demonstration of distance measurements between two Gd^{3+} ions in a rigid molecule, a bis-Gd^{3+} complex with a flexible "bridge," C2-Gd-595, was investigated (see Fig. 9a) [67]. This flexible molecule was taken as a model for a highly flexible protein, and a simple evaluation of the conformations of C2-Gd-595 showed that distances in the range of 0.5–2.6 nm are expected. The Ka-band DEER data are shown in Fig. 9b. Here, again, the modulation depth is very low, and no modulations past the first period are observed. The damping of the modulation is attributed, at least partially, to the broad distance distribution. The lower than expected modulation depth is due to the presence of spin pairs with short distances that are outside the bandwidth of the pulses. Measurements were also carried out at W-band (data not shown), with a pump pulse longer than that used at Ka-band, 12 vs 25 ns. Therefore, while the Ka-band data revealed distances down to ~1.3 nm, at W-band, the cut off was at 1.9 nm (Fig. 9c). Recent measurements (Raitsimring, unpublished results) carried out at Ka-band,

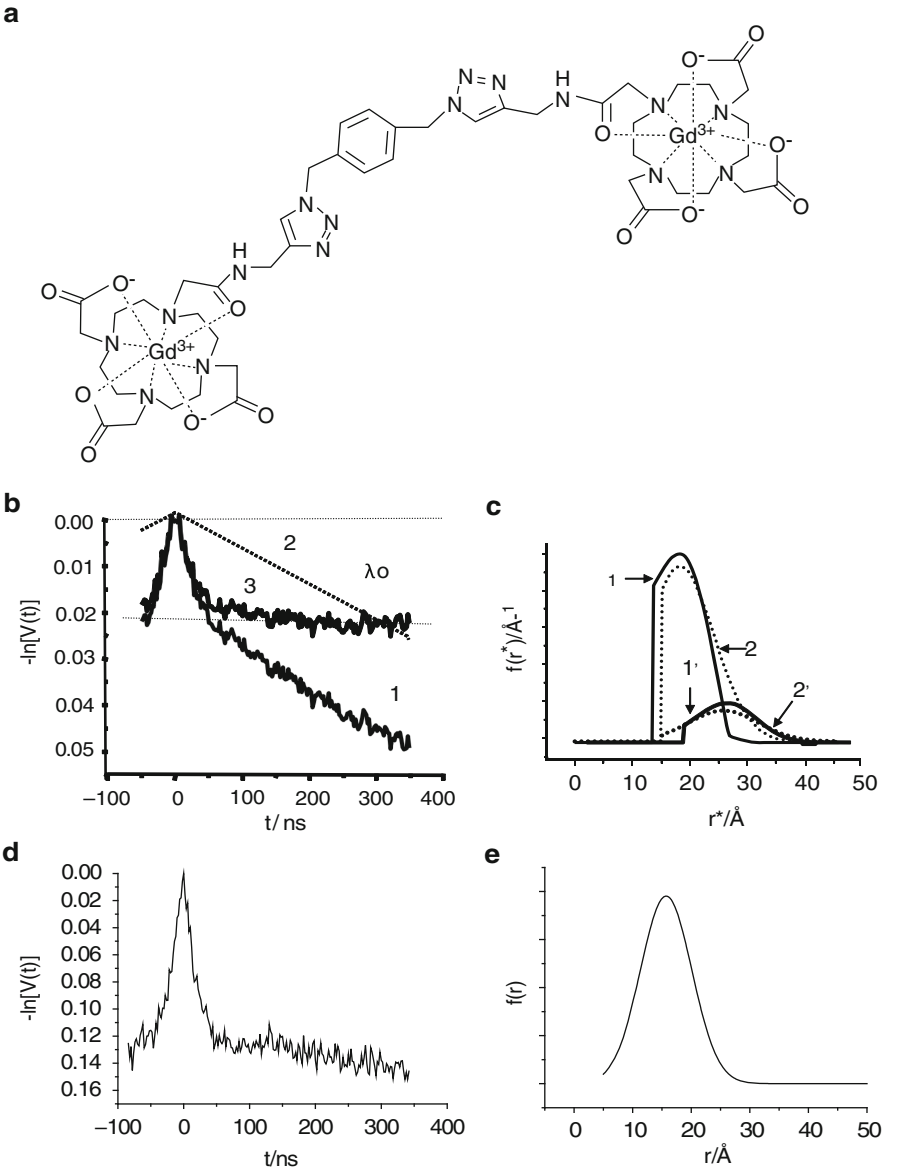

Fig. 9 (**a**) C2-Gd595. (**b**) Ka-band (29.9 GHz) DEER traces of C2-Gd595 (0.5 mM) obtained with a pumping pulse applied to the maximum for the $-½\leftrightarrow½$ transition: trace 1 data after subtraction of a trace obtained with t_p applied -70 G from the maximum $-½\leftrightarrow½$ peak to remove contributions from other transitions, trace 3 after removal of the background (trace 2). Pulse durations: $t_p = 12$ ns, $t_o = 30$ ns for π-pulse, $\Delta\nu = 200$ MHz. Repetition rate = 1 kHz, total accumulation time = 2 h, $T = 15$K. The height between the two horizontal *dotted lines* denotes the modulation depth λ_o. (**c**) *Solid lines*, distance distributions derived from Ka-band DEER data (1, 2) shown in (**b**) and W-band DEER data(not shown) (1' 2'). The *dashed line* was obtained using

with significantly shorter pulses (8 and 10 ns for the pump and observer pulses) and a considerably larger $\Delta\nu$, were able to cover the full range of dipolar interactions (Fig. 9d, e), confirming the loss of modulation depth due to the presence of spin pairs with distances that are too short to be accessed by the pulses. Note that here the modulation depth increased to 11–12%, which is close to the expected value.

3.3.2 Proteins and Peptides

The Gd^{3+}–Gd^{3+} distance measurements on models were followed by measurements on biomolecules. Proteins and peptides were labeled according to the scheme shown in Fig. 4b where the attachment is via cysteine residues through the formation of an S–S bond [66, 68], just as is routinely done for nitroxide labeling. Two different dipicolinic acid derivatives were tested as tags, 4MMDPA (4-mercaptomethyl-dipicolinic acid) and 3MDPA (3-mercapto-dipicolinic acid). They differ by the length of the tethers (one CH_2 group) and the position of the SH group. To evaluate the performance of such Gd^{3+} tags for distance measurements, DEER measurements were carried out on two proteins, p75ICD and τ_C14, each labeled with two nitroxides or two Gd^{3+} spin labels at the same sites [68]. The two types of labels were compared at W-band, and the nitroxide-labeled proteins were further investigated with X-band DEER measurements. Both proteins have known NMR structures [69, 70]. In p75ICD, the orientations of the two nitroxides were found to be uncorrelated, and the same distance, 2.5 nm (maximum of the distance distribution), was obtained from the X- and W-band measurements. The measured Gd^{3+}–Gd^{3+} distance was 2.9 nm for both 4MMDPA and 3MDPA. In contrast to p75CD, in τ_C14, the orientations of the nitroxides are correlated, and the W-band measurements exhibited strong orientation selection as shown in Fig. 10. These data show that with π mw pulses of 25 ns, the S/N that can be obtained in W-band DEER of nitroxides is rather good, except at the g_{zz} region. This strong orientation selection prevented a straightforward extraction of the distance distribution. The X-band measurements gave a nitroxide–nitroxide distance of 2.5 nm (maximum of the distance distribution). W-band DEER data for τ_C14 labeled with 4MMDPA and 3MDPA are shown in Fig. 11. The Gd^{3+}–Gd^{3+} distance distributions showed maximum at 3.4 nm for both Gd^{3+} tags. Also here, the modulation depth was found to be significantly lower than expected and attributed mainly to the presence of free Gd^{3+}.

Fig. 9 (continued) the step function approximation for deriving the distance distribution and the *dashed lines* by DeerAnalysis, Gaussian fit option. (**b**) and (**c**) are reproduced from [66] with permission, Copyright © 2010, Elsevier. (**d**) Ka-DEER data obtained with $t_p = 8$ ns, $t_o = 10$ ns for the detection π-pulses, and $\Delta\nu = 800$ MHz. (**e**) The distance distribution derived from (**d**)

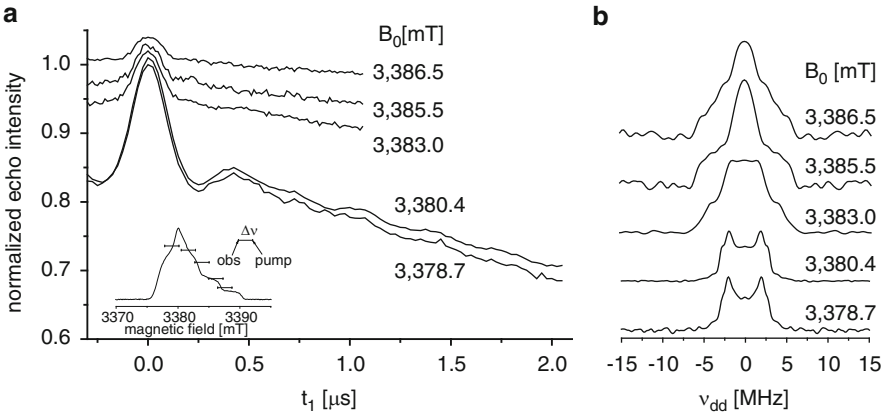

Fig. 10 W-band DEER results (40 K) of doubly nitroxide-labeled τ_C14 (~60 μM). (**a**) DEER raw data measured at 40 K at different magnetic fields. The *inset* shows the ED-EPR spectrum of this sample at 40 K, indicating the positions of the pump and observer pulses. Experimental conditions for microwave observer and pump pulses: t_o = 30/60/60 ns, t_p = 25 ns, $\Delta\nu$ = 65 MHz. The measurement time was 0.5 h with the field set at the maximum EPR signal, and 13 h for the highest field position. (**b**) Fourier transform of the time-domain DEER data obtained after subtraction of the background. Adapted with permission from [68]. Copyright 2010 American Chemical Society

To rationalize the distance distributions measured with the three types of spin labels and the difference between the Gd^{3+}–Gd^{3+} and nitroxide–nitroxide distances, the distance distributions between the spin labels were calculated [68]. This was achieved by computationally attaching to the cysteine residues in model 1 of the NMR structures (PDB codes 1NGR for p75ICD and 2AYA for τ_C14), molecular models of the spin labels with optimal bond lengths and bond angles, and randomly sampling rotamer configurations of the spin label tethers. The results of the simulations for the Gd^{3+} tags, shown in Fig. 12, are in good agreement with the experimental distance distributions both in terms of the positions of the maxima and their widths. The maximum of the distance distribution of Gd^{3+}–Gd^{3+} ions in the samples tagged with 3MDPA is predicted to be at a distance shorter by 0.2 nm than for the samples tagged with 4MMDPA for both proteins. This small difference has not been resolved experimentally. The maximum of the Gd^{3+}–Gd^{3+} distance distribution is predicted to be at 3.3 nm for τ_C14, which is close to the measured value of 3.4 nm. For p75ICD, the maximum of the calculated Gd^{3+}–Gd^{3+} distance distribution is at 3.2 nm. This distance reduces to 2.9 nm when one of the Gd^{3+} ions is assumed to be immobilized by coordination to Asp397, leading to better agreement with the experimental values. The coordination of Asp397 to the Gd^{3+} ion was supported by ENDOR (electron-nuclear double resonance) and NMR results. The simulations show distance distributions with a width at half-height of about 0.8 nm, in close agreement with the experimental results [68]. In the case of the nitroxide-labeled proteins, the maximum of the calculated distance distribution (2.9 nm) was longer than the experimental value (2.5 nm) for both proteins.

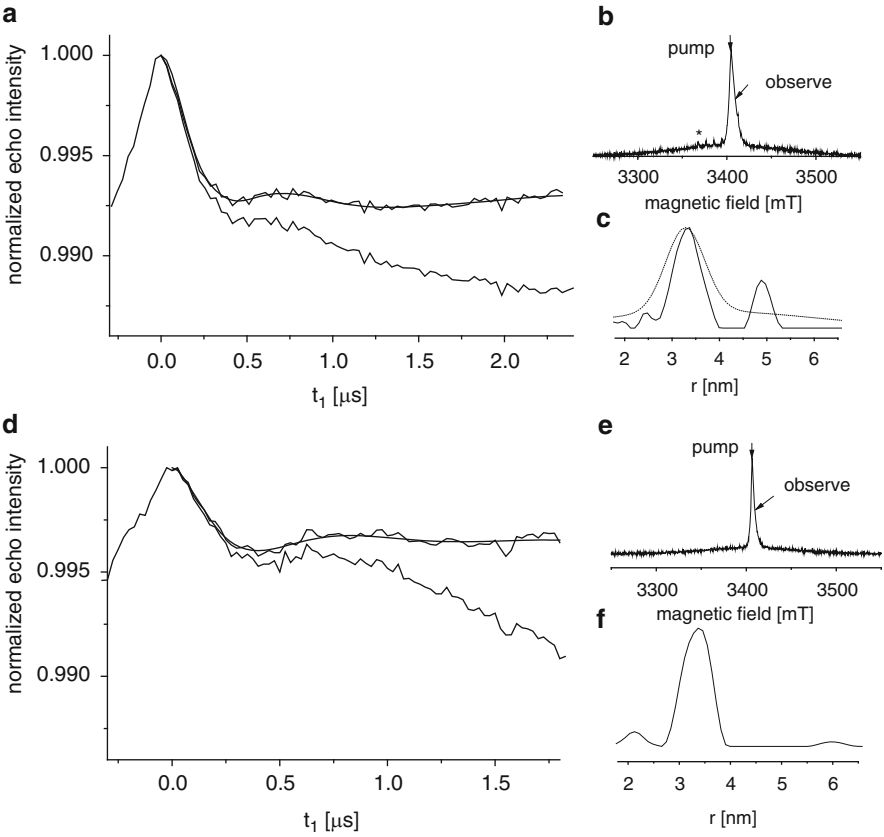

Fig. 11 W-band DEER results (25 K) for τ_C14 doubly labeled with Gd^{3+}-4MMDPA and Gd^{3+}-3MDPA (~100 μM). (**a**) Raw DEER time-domain data of τ_C14 tagged with 4MMDPA-Gd^{3+}, DEER trace after subtraction of the background decay, and the corresponding superimposed calculated trace obtained with the distance distribution shown in (**c**). The experimental conditions were t_p = 12.5 ns, t_o =12.5/25/25 ns, $\Delta\nu$ = 78 MHz. (**b**) Echo-detected EPR spectrum of τ_C14 tagged with 4MMDPA-Gd^{3+} recorded with the two-pulse echo sequence. *Arrows mark* the positions of the pump and observer pulses. (**c**) Gd^{3+}–Gd^{3+} distance distribution. The *dashed curve* was obtained by a Gaussian fit. The calculated DEER trace in (**a**) was obtained with the Gaussian fit; the same quality fit was obtained with the Tikhonov regularization (*solid line* in **c**). (**d**–**f**) Same as (**a**–**c**) except that τ_C14 was tagged with 3MDPA-Gd^{3+}. Here, fit with only Tikhonov regularization is shown. Adapted with permission from [68]. Copyright 2010 American Chemical Society

The above example showed that spin labeling with Gd^{3+} is a feasible and attractive approach for distance measurements at high fields. The sample requirements are 2–3 μl of a 50–100-μM-labeled protein in a D_2O/glycerol-d_8 solution. The latter is needed for obtaining a phase memory time that is as long as possible. This protein quantity is smaller by an order of magnitude than that needed for DEER measurements on nitroxide-labeled proteins at X-band.

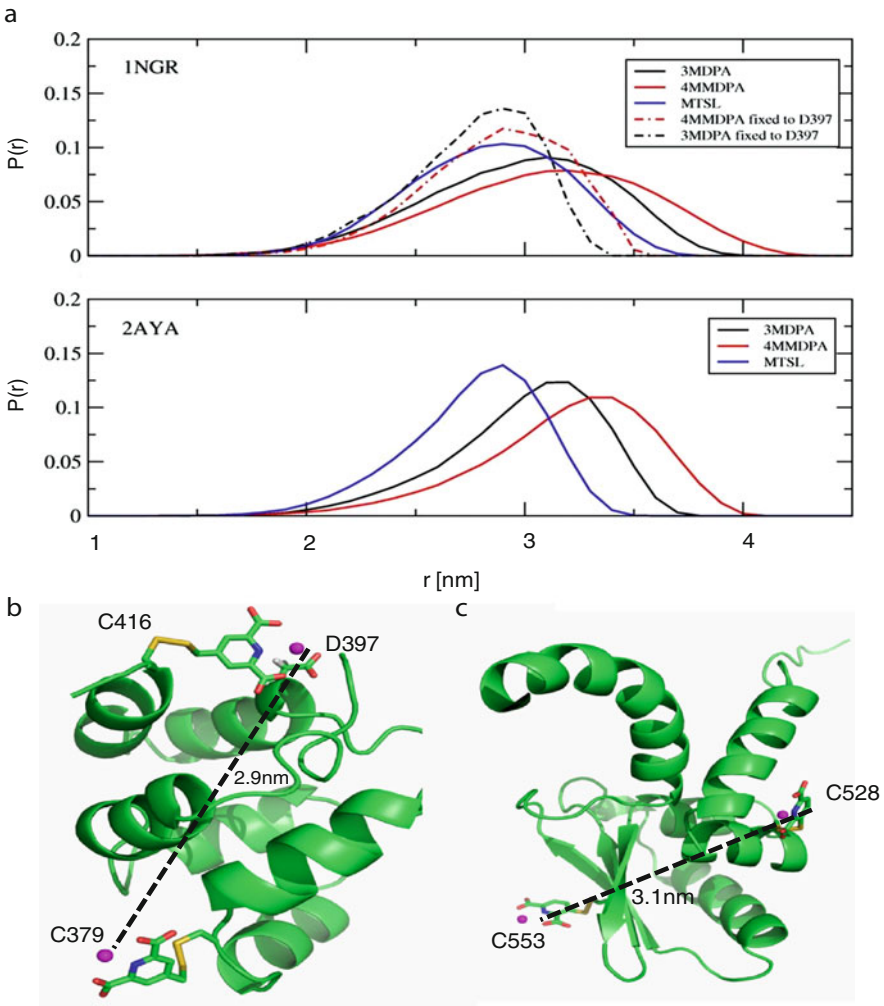

Fig. 12 Distributions of Gd^{3+}–Gd^{3+} and nitrogen–nitrogen distances in p75ICD (PDB code 1NGR) and τ_C14 (PDB code 2AYA). Distances were calculated by randomly generating rotamers of the bonds connecting the paramagnetic centers with the C^{α} atom of the tagged cysteine residues, excluding conformations that clash with protein atoms in the NMR structures. (**a**) Distance distributions calculated for p75ICD. The different curves were calculated for the tags described in the figure. The *dotted-dashed curve* was calculated by assuming complete immobilization of one of the Gd^{3+} ions by coordination to the tag (attached to C416) and D397. *Lower panel*: Distance distributions calculated for τ_C14 for the tags described in the figure. (**b**) Cartoon of the NMR structure of p75ICD tagged with two 4MMDPA-Gd^{3+} complexes. The conformer chosen shows the Gd^{3+} ion coordinated to the tag as well as to D397. The Gd^{3+}–Gd^{3+} distance is indicated for a random conformer of the 4MMDPA tag attached to C379. (**c**) Cartoon of the NMR structure of τ_C14 tagged with two 3MDPA-Gd^{3+} complexes. The Gd^{3+}–Gd^{3+} distance is indicated for a randomly chosen conformer of the tags attached to C528 and C553. Adapted with permission from [68]. Copyright 2010 American Chemical Society

In order to better understand the features of the dipicolinic acid tags in the context of Gd^{3+} spin labeling for distance measurement, a model peptide, melittin, was labeled with 4MMDPA and investigated extensively [66]. Specifically, the effects of the solution molar ratio of Gd^{3+} and the labeled peptide, the temperature, and the maximum DEER evolution time, on the DEER modulation depth were studied. The optimum [Gd^{3+}]/[4MMDPA tag] ratio was found to be around 0.6–0.8 to avoid free Gd^{3+} that masks the DEER effect on the one hand, and the formation of peptide dimers on the other. The latter appears to be due to the formation of Gd^{3+}-tag_2 complexes because a single 4MMDPA tag provides only three coordination sites, while Gd^{3+} can coordinate up to nine ligands. In addition, the modulation depth was found to be not only determined by the spectral bandwidth of the pump pulse as compared to the EPR spectral width, but it is also sensitive to random flips of the pumped B spins due to spectral diffusion or fast electron spin relaxation that decrease the modulation depth. The sensitivity to the presence of free Gd^{3+} arises from the much narrower width of the central transition of the Gd^{3+} aquo complex as compared to Gd^{3+}-4MMDPA.

The Gd^{3+}–Gd^{3+} distance in {Gd^{3+}-4MMDPA mel-$C_{15}C_{27}$} of 3.4 nm was found to be 1.2 nm longer than the NO–NO distances in nitroxide-labeled mel-$C_{15}C_{27}$. This difference was attributed to the different orientations and conformations of the nitroxide and Gd^{3+} labels due to their different properties. This difference is similar to that observed for the proteins discussed above. This suggests that the two types of labels can provide complementary structural information.

The first "real" application of Gd^{3+} spin labeling for distance determination has been recently reported [71]. ERp29 is a carcinogenic chaperone ubiquitously expressed in the endoplasmic reticulum where it facilitates processing and transport of proteins [72, 73]. It forms a 51 kDa homodimer which is essential for the function. The 3-D structures of the N- and C-terminal domains were first determined individually for the rat protein by NMR spectroscopy [74] and subsequently for the human full-length protein by X-ray crystallography [75]. The amino acid sequences of the N-terminal domains of the rat and human proteins are identical except for residue 133 (serine in rat ERp29, threonine in human ERp29). However, different dimer interfaces were identified by NMR and X-ray crystallography. DEER measurements were carried out to determine the dimer interface of the rat protein in solution and resolve the above discrepancy [71]. The tag used was C1 (see Fig. 4c). Although larger than the 4MMDPA and 3MDPA tags, it has several advantages. It is based on a DOTA amide derivative with a 2-(pyridin-2-yldisulfanyl)ethyl amino pendant for spontaneous reaction with a cysteine thiol group under formation of a disulfide bond [76]. DOTA is a chelate with eight coordinating atoms, and therefore, it has a very large binding constant. It can be attached to the protein with the Gd^{3+} already coordinated, thus eliminating problems arising from free Gd^{3+} in solution. It has a smaller ZFS, and consequently, the central transition is narrow and the EPR signal is very intense. Finally, substituents of C1 are designed to induce steric hindrance and thus prevent a large mobility of the tag.

Two double mutants, C157S/S114C and C157S/G147C, were prepared. In the following, these are referred to as S114C and G147C, respectively. The S114C was produced as a perdeuterated protein, while G147C was produced without perdeuteration. The final monomer concentration was 100 μM with about 90% and 50% labeling for S114C and G147C, respectively. Figure 13 shows the DEER

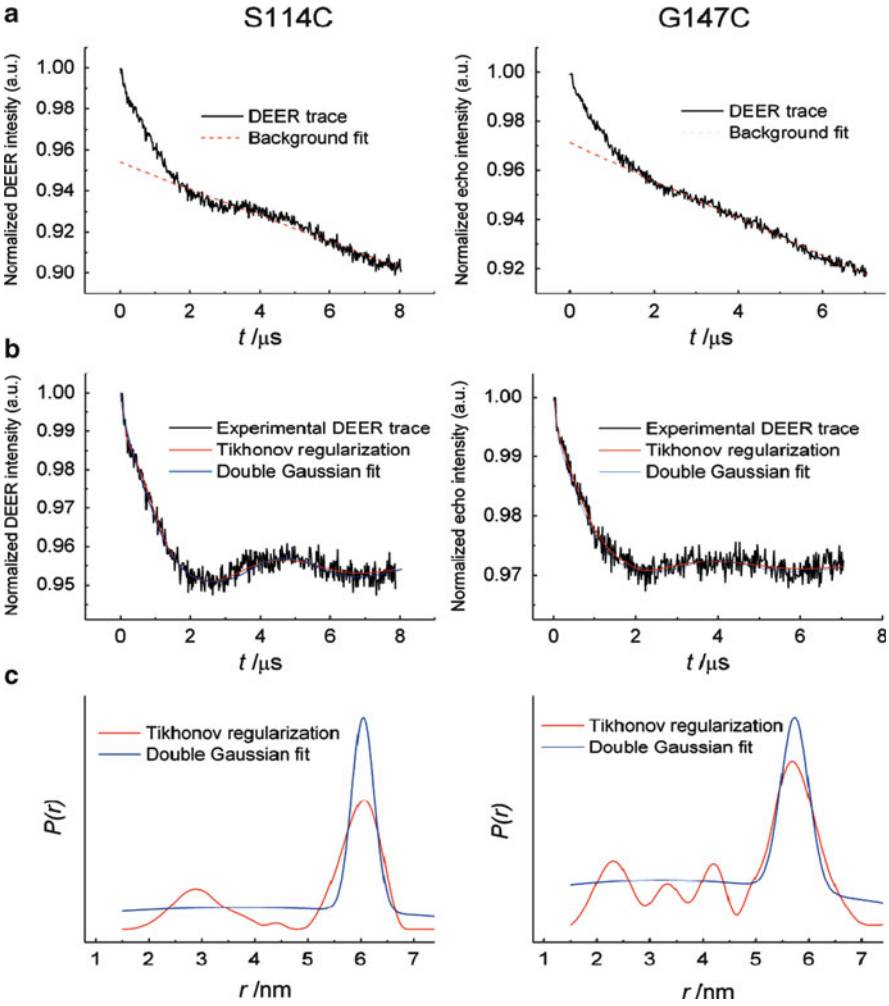

Fig. 13 Four-pulse DEER results obtained with about 3 μL of 100 μM frozen solutions of the ERp29 mutants S114C (*left panel*) and G147C (*right panel*) in 80% D_2O/20% glycerol-d_8 at 10 K. The spectra were recorded in about 12 h each. (**a**) Normalized DEER traces fitted with appropriate background decay (in *red*). (**b**) Same DEER traces after background removal along with the fits obtained by either Tikhonov regularization (*red*) or by fitting two weighted Gaussians (*blue*). (**c**) Distance distribution obtained by the two different fits shown in (**b**). The data were analyzed using the program DeerAnalysis [37]. Adapted with permission from [71]. Copyright 2011 American Chemical Society

results of both mutants. The data were recorded with a dipolar evolution time, t, reaching values as high as 7.0 and 8 μs. Both DEER traces clearly reveal dipolar modulations. Distance distribution is shown in Fig. 13c, exhibiting a maximum at 6.05 and 5.68 nm for the S114C and G147C mutants, respectively. Using the crystal structure of the human ERp29 dimer (PDB ID 2QC7) and the crystal structure of the symmetrical parent compound of the C1 tag (DOTAMPh-Gd complex, CSD accession code EQOZUF), a distance distribution was calculated taking into account all possible conformers of the C1 tag. The protein coordinates were kept fixed, and conformers with steric clashes between tag and protein were eliminated. The maxima of the distance distributions are located remarkably close to those obtained by the DEER experiments (6.05 and 5.8 nm), suggesting that the DEER measurements delivered the distance between the Gd^{3+} ions with high accuracy. Paramagnetic NMR measurements were carried out as well with paramagnetic (Tb^{3+}, Tm^{3+}) and diamagnetic (Y^{3+}) metal ions, and these experimental results also showed excellent agreement with the calculated distance distribution and the DEER data. This excellent agreement further supports the validity of the DEER data analysis using the standard expressions of two $S = 1/2$ spins [64] and of the DeerAnalysis software [37]. The close agreement of the DEER and NMR data with the crystal structure of human ERp29 unequivocally confirms that the dimer interface of the crystal structure prevails in solution.

3.3.3 Nucleic Acids

An efficient method for attaching Gd^{3+} chelates to the ends of a DNA molecule has been reported [77]. Two labels, Gd-595 and Gd-538 (Fig. 4d), were attached using click chemistry to a modified base at the 5′ end of the oligonucleotides. In order to maintain the shortest possible linker between the Gd^{3+} chelate and the attachment point to the oligonucleotide backbone, 5′-I-dT was converted to an azido functional group after oligonucleotide elongation [77]. Two singly labeled complementary chains were prepared, and then, a double-strand DNA was formed. This approach is similar to that used for nitroxide spin labeling of DNA which has been used as a ruler for distance measurements [78, 79]. The motivation was to estimate the high end of the range of distances that can be probed by Gd^{3+} spin labels. The Gd- 595 tag is more symmetric than Gd-538, and therefore, it has a lower D-value (~20 and ~40 mT, respectively) [80]. This leads to a better S/N for Gd-595, which unfortunately has the longer tether.

The Ka-band DEER results obtained from the Gd-595 tag are shown in Fig. 14a, b. The DEER trace displayed is after the removal of the background decay, which was determined by comparison of the DEER traces of two samples with different concentrations [80]. Data acquired up to 6 μs reveal a clear modulation period and the distance distributions peaks at 5.7 nm which is in very good agreement with molecular dynamics (MD) simulations. The distance obtained for Gd-538

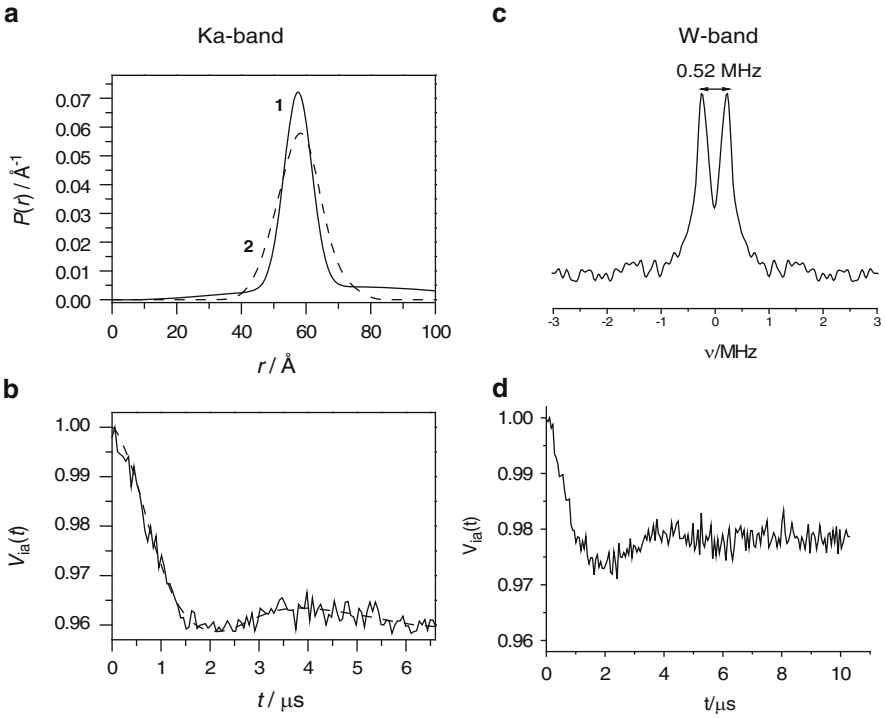

Fig. 14 (**a**) Trace 1, distance distribution function *P(r)* obtained from $V_{ia}(t)$ of the double-stranded Gd595-DNA (presented in Fig. 4b) using "the two-Gaussian fit option" in the DeerAnalysis software package. *P(r)* is the sum of two weighted Gaussians, with (x_o, δ) = (57.3 Å, 6 Å) and (73 Å, 50 Å), where x_o and δ are the center and width of the Gaussians. Trace 2, distance distribution function obtained by MD simulations. (**b**) Experimental DEER traces after background removal (solid) of Gd595-DNA and the calculated fitted data obtained with the distribution function shown by trace 1 in (**a**). Experimental conditions: Ka-band, 10 K, t_p = 15, t_o = 20, 20, 20 ns, 20 µM dimer concentration, 20 µl sample volume, $\Delta\nu$ = 100–120 MHz, accumulation time 14 h [80]. (**d**) DEER data of the double-stranded Gd595-DNA measured at W-band at 10 K after background removal and (**c**) the corresponding FT spectrum. The splitting of 0.52 MHz yields a distance of 5.8 nm. Experimental parameters: t_p =15 ns, t_o = 25, 50, 50 ns, $\Delta\nu$ = 120 MHz, accumulation time ~16 h, sample volume 2–3 µl

was 5.2 nm. Here, the depth is lower, and the accumulation time needed was longer because of the broader central peak. Sample concentrations were very low, 40–80 µM Gd^{3+}, and the sample volume was about 20 µl [80]. W-band measurements were carried out on these samples as well. Due to the narrower central transition at W-band, DEER traces of both Gd-538 and Gd-595 could be collected up to 11 µs, and a good S/N was obtained within an accumulation time similar to that of the Ka-band measurements. The results for Gd-595 are shown in Fig. 14c, d.

3.4 DEER Analysis in High-Spin Systems

The spin Hamiltonian of two Gd^{3+} ions coupled by a dipolar interaction is

$$\mathcal{H} = \sum_{\mathrm{i=A,B}} \left[g\beta_e \vec{B}\hat{S}_{z,i} + \hbar \hat{S}_i \cdot \boldsymbol{D}_i \cdot \hat{S}_i \right] + \mathcal{H}_{\mathrm{dip}} \tag{24}$$

$\mathcal{H}_{\mathrm{dip}}$ is given in (6). The effect of the ZFS term is to tilt the quantization axis of the electron spin away from B_0. This should, in principle, modify the dipolar splitting and the phase acquired in the DEER experiment. Similar to the $S = 1/2$ case, only the secular terms of the dipolar interaction are considered. A second-order perturbation derivation concentrating on the effect of the ZFS on the dipolar splitting has been reported, and general expressions were given [67].

In the context of ENDOR and ESEEM (electron spin echo envelope modulation), where the nuclear frequencies are of interest, the ZFS effect has been taken into account by the introduction of effective projection operators using perturbation theory for a small ZFS, $\hbar D/g\beta_e B_0 \ll 1$ [81, 82]. It was shown that the corrections to the effective projection operator $<\hat{S}_{zi}>$ are proportional to $(\hbar D/g\beta_e B_0)^2$ and are, therefore, negligible for Gd^{3+} at both Ka- and W-bands. The corrections to $<\hat{S}_{xi}>$ and $<\hat{S}_{yi}>$ are more significant because they are proportional to $\hbar D/g\beta_e B_0$. Nonetheless, second-order perturbation theory shows that the shift of the respective energy levels due to terms involving $<\hat{S}_{x,y}>$ does not result in a correction to ω_{dd} [64]. Exact calculation show that such a contribution amounts to only 1–2% of the nominal value of ω_{dd}. For $D \leq 1{,}200$ MHz, which applies to most Gd^{3+} complexes [62], the apparent DEER modulation frequency can deviate from ω_{dd} by no more than 3–5% if the measurements are performed at Ka-band or higher. This is confirmed by the experimental results reported so far (see Sects. 3.3–3.4).

Naturally, the subspectrum of the central transition is the most attractive for placing the pump and observes pulses. In this case, the two spins can be regarded as effective $S = 1/2$ systems, and the excellent and convenient DeerAnalysis software [37] can be used for data analysis. This was done for the bis-Gd rigid model [64]. There, the maximum of the distance distribution gave a distance very close to that obtained by crystal structure, whereas the width of the distance distribution was considerably larger than expected. The source of the fast damping of the dipolar modulations is unclear and could be a consequence of the high-spin system properties that have not been taken into account. One possibility is the contributions of the pseudosecular terms of the dipolar interaction that are usually neglected for $S = 1/2$ systems but may have effectively larger contributions for $S = 7/2$ and should not be ignored [67].

There are cases where the contributions of the broad background at both the observer and pump frequencies are not negligible. This depends on the magnitude of D, the temperature, and the spectrometer frequency. Moreover, often, the central transition is too narrow to accommodate both pump and observer pulses, and the frequency of the observer pulse has to be placed on the broad signal of the other

EPR transitions. There have been several reports of such experimental conditions [71, 80], yet the data were treated using the expressions pertinent to spin $S = 1/2$ systems. The distances obtained matched well-distances predicted by MD simulations [80] and NMR and crystal structure data [64, 71] justifying this simplification. This approach is valid as long as the pump pulse causes spin flips in B corresponding only to single-quantum transitions. Such a flip will change the local field at the A spin by an amount that is the same as that of a flip of a spin with $M_S = \pm 1/2$. Nevertheless, the theoretical justification for this should be developed and established. This can be done using the general expression for the dipolar evolution frequency corresponding to any pair of M_S, M_S' spins [67].

3.5 Modulation Depth and General Sensitivity Considerations

The total sensitivity of the DEER experiment depends on both λ and the echo intensity V_0 at time $t = 0$ according to [5, 80]

$$S(\text{DEER}) = \lambda(T, \nu_0, D)V_0(T, \nu_0, D). \tag{25}$$

In (25), ν_0 corresponds to the spectrometer frequency, and T is the temperature. V_0 naturally depends on many instrumental parameters that are often beyond the control of the user, the length and frequency of the observer pulses, the EPR lineshape, the temperature and the relaxation times, T_1 and T_M. λ depends on the pump-pulse length and frequency and the EPR lineshape. Because the lineshape is temperature and spectrometer frequency dependent, these parameters affect both λ and V_0 of HFHS. A sensitivity analysis of DEER using nitroxide labels has been reviewed in detailed [5], and some of the parameters discussed apply to Gd^{3+} as well. Next, we shall focus only on the parameters that are unique for Gd^{3+}. These are the dependence of the spectrum lineshape on temperature due to the multitude of M_S energy levels and the strong thermal polarization associated with them, on the spectrometer frequency and the ZFS parameter D. While at a particular frequency the low temperature spectra of different nitroxides are highly similar and variations are subtle, for Gd^{3+}, different tags have different D values, and it is important to understand the range of D values for which reasonable sensitivity can be obtained at a particular spectrometer frequency.

Next, we limit ourselves to the case where the pump pulse is placed at the maximum signal, namely, the maximum of the central transition. We recall that λ represents the probability that spin B is flipped by the action of the pump pulse, and in (13), $g(\Delta\omega)$ represents the number of spins at a particular resonance frequency, $\Delta\omega$. While this is valid for an $S = 1/2$ system, this is not the case for HFHS systems, where the lineshape is a superposition of several transitions varying in their transition probabilities and population differences. Therefore, the echo intensity at a particular position within the EPR lineshape cannot be taken as simply proportional to the number of spins that resonate at this particular

field/frequency position. Here, different proportionality constants for each EPR transition should be taken into account. Accordingly, the general expression for λ is

$$\lambda(T, v_0, D) \propto \sum_{i=1}^{2S} \int \frac{\omega_{1,i}^2}{\Omega_i^2} \sin^2\left[\frac{\Omega_i}{2} t_p\right] (P(M_S) + (P(M_S^{'}))g_i(\Delta\omega)\mathrm{d}(\Delta\omega). \tag{26}$$

In (26), $\omega_{1,i}$ is the nutation frequency of each transition, where $\omega_{1,i} = \left(TP_{M_s \to M_s'}\right)^{1/2} \gamma B_1$. B_1 is the amplitude of the mw field, and $\mathrm{TP}_{M_s \to M_s'}$ is the transition probability (see (23)). $g_i(\Delta\omega)$ is the normalized lineshape of the individual transitions, and $P(M_s)$ the population of level M_s. Equation (26) shows that the calculation of the modulation depth from the full-EPR lineshape is complicated as it requires the deconvolution of the spectrum to its individual transitions.

This can be simplified by considering only the central transition. If we neglect contributions from other transitions at the pump position, taking into account only the lineshape of the $|-1/2> \to |1/2>$ subspectrum, using (13), one can obtain $\lambda_{\mathrm{central}}$ and then scale it down by the relative populations of the $M_S = \pm 1/2$ levels such that [64]

$$\lambda(T, v_0, D) = \lambda_{\mathrm{central}}(T, v_0, D)\left[P\left(-\frac{1}{2}, T\right) + P\left(\frac{1}{2}, T\right)\right]. \tag{27}$$

The width of the central transition is proportional to D^2/v_0, and therefore, $\lambda_{\mathrm{central}} \propto [D^2/v_0]^{-1}$. The temperature dependence enters through the populations of the $M_S = \pm 1/2$, $P(-1/2) + P(1/2)$. The latter increases with temperature until it reaches its maximal value of 0.25.

Table 1 summarizes the λ values for various samples calculated using (27) and the λ_{exp} values determined from the asymptotic value of $V_{\mathrm{intra}}(t)$ according to (12). It shows that λ_{exp} is considerably smaller than that obtained for nitroxides at X-band, which can reach values as high as 0.4. This is because the spectrum is much broader; more than 75% of the spins contribute to the broad background. Furthermore, for Gd^{3+} λ_{exp} is usually smaller than the theoretical λ. It clearly shows that it depends on the width of the central transition, and therefore, for the same sample and pump-pulse length, λ should be larger at W-band as compared to Q-band as long as one works at a temperature where the central transition has a significant intensity. At W-band, this is reached at 9 K, and at Q-band, at 3 K (see Fig. 6). This statement is correct as long as spin dynamics effects such as spectral diffusion are negligible.

Next, we consider the S/N of V_0, namely, the echo intensity. Assuming that the frequency of the observer pulses is within the central transition and taking into account the effect of T_1 and the phase memory time, T_M, along with the Boltzmann distribution [5, 80], we obtain

$$S/N(V_o, \mathrm{central}) \propto \frac{1}{\sqrt{T_1(T)}} \exp(-2t_{\max}/T_M(T)) g_{-1/2 \to 1/2}(\omega_{\mathrm{obs}})[P(\tfrac{-1}{2}, T) - P(\tfrac{1}{2}, T)]). \tag{28}$$

Table 1 Summary of DEER distance measurements on Gd^{3+}–Gd^{3+} pairs

Gd tag	Frequency band	T (K)	Linewidth[a] (mT)	D (mT)	Distance[b] (nm)	λ (%)	λ_{exp} (%)	Pump pulse (ns)	Ref
bis-Gd model	W	10	3.6	37	2.05	5.6	2.5	16	[64]
	W	25	3.6			8.3	5	16	
	K	13	10			4.3	2	12	
4MMDPA melittin	W	10	13.9		3.4	2.8	2.2	12.5	[66]
		25				3.5	1.7	or 15	
Gd-595 model	W	25	1.3	~20	2.6	8.5	1.1	25	[67]
	Ka	15	3.0		2.0	5.5	2.2	12	
	Ka	15			15	12		8	(Raitsimring, unpublished results)
Gd-595 DNA	Ka	10	3.0	20	5.73	7.5–8	4.2	15	[80]
	W	10					4.5	15	
Gd-538 DNA	Ka	10	12.0	40	5.43		1.7	15	[80]
	W	10	4.0				1.7	15	
DOTA ERp29									[71]
S114C	W	10	1.1		6		4.5	15	
G147F	W	10	1.1		5.7		3.0	15	

[a]Width at half-height of central transition
[b]Max of distance distribution

Table 2 Summary of T_1 and T_M of Gd^{3+} chelates at low temperatures

Sample	Frequency	Temperature (K)	T_1 (μs)	T_M (μs)	Gd^{3+} conc (μM)	Ref
Mellitin-4MMDPA	W	10	100 (22)[a]	3.6	200	[66]
		25	91 (12)	2.6	200	
Gd-terpyridine	Q	5	130	2	600	[83]
		10	20	3	600	
Aquo complex	W	10	100		200	

[a]The data were fitted to two exponentials

In (28), the T_1 dependence reflects the efficiency of signal averaging, t_{max} is the maximum time evolution of the dipolar interaction in the four-pulse sequence, and $g_{-1/2\rightarrow 1/2}(\omega_{obs})$ stands for the lineshape of the central transition and its intensity at the observer frequency, ω_{obs}. The latter corresponds to the off-resonance frequency of the observer pulses. Here, the maximum intensity of $g_{-1/2\rightarrow 1/2}$ is proportional to ν_0/D^2. The last term in (28) corresponds to the population difference. While for Gd^{3+}, λ is inferior to nitroxides at X-band, $V_{0,central}$ is significantly larger because T_1 is considerably shorter at both Q- and W-band (see Table 2), and a large polarization can be obtained at reasonable temperatures (see Fig. 6). From our limited experience, T_M at W-band is longest around 6–10 K (Table 2), although it may be even longer at lower temperatures due to spin bath polarization [84]. We have not checked temperatures lower than 6 K.

Equations (26)–(28) show that in terms of S/N, the lower is D the better. However, when the central line becomes too narrow, as occurs for DOTA derivatives at W-band (see Table 1), then the observer pulse has to be placed outside the central transition, on the broad background of the other transitions. This is configuration is needed also when short distances are of interest and a large $\Delta\nu$ is required. In this case, V_0 is determined by the broad signal of all transitions other than the central one according to

$$S/N(V_{0,other}) \propto \frac{1}{\sqrt{T_1(T)}} \exp(-2t_{max}/T_M(T)\overline{g_{M_s\rightarrow M_s'}(\omega_{obs})[(P(M_s,T) - PM_s',T)]}. \tag{29}$$

In (29), the bar represents a weighted average of all transitions taking into account their lineshape and relative intensity at the position of the observer pulses. Detailed calculations comparing the DEER sensitivity as a function of the width of the central transition and temperature have not been reported as yet but are necessary for optimization of the DEER experiment. Furthermore, systematic measurements of T_1 and T_M as a function of temperature and field are also required. In Table 2, we present the relaxation times reported to date.

3.6 HFHS Metal Ion- Nitroxide Systems

Distance measurements between a nitroxide and a Gd^{3+} spin label may be also a useful approach for a particular set of problems (see Sect. 2.5), for example, when the

interaction between different biomolecules is of interest. Labeling a single molecule with two types of labels is synthetically demanding, and using the site-directed spin labeling approach will lead to a distribution of labeled species with only half of the molecules being hetero-labeled, and this reduces sensitivity. Therefore, it is not an attractive general approach. This is not the case for biomolecule complexes involving two types of molecules where each molecule is labeled with a different label. Thus Gd^{3+} labels that are rather large could be used to label surface sites in one protein, while inner sites in the other protein could be labeled with a nitroxide. In such a case, some of the advantages of using Gd^{3+} labels would still be preserved.

DEER distance measurements at X- and Q-band on a Gd^{3+} – nitroxide rigid model have been recently reported [83]. The S/N at X-band was very poor compared to Q-band measurements, as expected considering the frequency dependence of the central transition. Moreover, the ZFS approximated at 40–50 mT is rather large and may affect the dipolar modulation at X-band. The DEER traces are shown in Fig. 15. Clear modulations are observed, and data analysis yielded a peak at 2.45 nm and an artifact signal at 3 nm, the source of which is not clear. The measurement temperature was 10 K, and the best results were obtained with short π and $\pi/2$ pulses of 12 ns for both pump and observer pulses with $\Delta\nu = 80$ MHz. Under these conditions, the modulation depth λ_{exp} was about 0.2. Here, the observer frequency was set to the Gd^{3+} signal in order to take advantage of its short

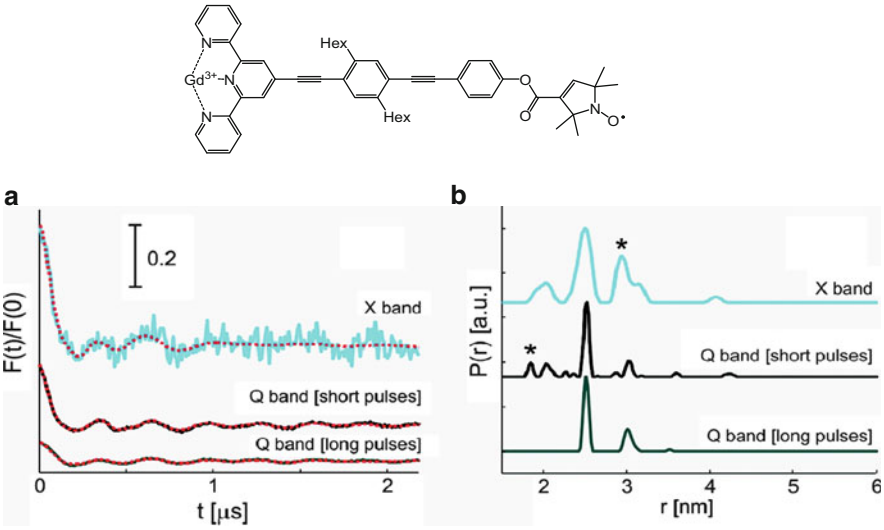

Fig. 15 *Top*: the Gd^{3+} – nitroxide model compound. (**a**) DEER data (after background removal) of Gd^{3+} – nitroxide spin pairs (X-band, *cyan*; Q-band [short pulses], *black*; Q-band [long pulses], *green*) performed at 10 K (repetition time = 357 µs) of a sample with a Gd^{3+} concentration of 600 µM and best fits as calculated by DeerAnalysis 2009 (*red dotted*). (**b**) The corresponding distance distributions $P(r)$ with artifacts due to admixing ^2H nuclear modulation marked with (*asterisk*). Spectra and distributions are shifted vertically for better visualization. Adapted with permission from [83]. Copyright 2011 American Chemical Society

T_1 that allows for fast signal averaging, and the pump pulse was set to the maximum of the nitroxide signal to obtain maximum λ. This indeed maximizes S(DEER) according to (25). As this is a preliminary report, the issue of orientation selection has not been explored, although it is clear that it will be reduced compared to two nitroxides. Moreover, at Q-band, the problem is less severe than at W-band. This work, just as the earlier DEER results on a pair of Gd^{3+}, highlights the need to understand the spin dynamics of Gd^{3+} before such measurements can become routine.

4 Future Outlook

In this chapter, the use of paramagnetic metal centers for nanoscale distance measurements has been reviewed. Several types of such centers were described, intrinsic metal centers, paramagnetic metal ions substituting for diamagnetic ones, and chelated metal ions that serve as general purpose spin labels, just like nitroxide spin labels. The spectral properties of metal centers with $S = 1/2$, which are dominated by the g-anisotropy already at X-band frequencies, prevent their use as general purpose spin labels. They are usually inferior to nitroxide spin labels in terms of sensitivity and ease of data analysis due to the presence of complicating orientation selection issues. They are of course very useful for probing specific metal-binding sites. The situation is different for high-spin metal ions with a half-filled valence shell like Gd^{3+}. Its spectral properties at spectrometer frequencies higher than *ca*. 30 GHz make it a highly attractive general purpose spin label that can be attached to biomolecules via chelating tags. So far, DEER measurements were carried out at both Ka- and W-band frequencies, showing that distances of up to 6 nm can be accessed routinely, and the results indicate that this can be extended to 8 nm. It has also been shown that the data analysis can be carried out with the existing sophisticated DeerAnalysis software, and distance distributions can be readily obtained. The sensitivity of Gd^{3+} labels is very high, particularly at W-band, where the sample amount required is 2–3 μl of a ~50 μM solution of a doubly labeled biomolecule.

On the basis of the results obtained so far, we can safely state that Gd^{3+} spin labels for distance measurements have moved from infancy to childhood. More work in two main directions is needed to achieve complete maturation. One is the development of the ultimate tag that would provide the highest S/N (small ZFS) has a long phase memory time, and has a limited size and a restricted mobility. From the body of presently reported results, it seems that the DOTA-based tags provide the best results. In the few examples that have been published recently, the Gd^{3+} tags were attached to the external surface of the protein; it is, however, not clear whether such tags can be used to label internal sites in the proteins. In the direction of tag development, efforts should be joined with those made for tag developments for paramagnetic NMR applications, seeking for multifunctional tags for both NMR and EPR applications [71].

The second direction that needs considerable work is to develop our understanding of the spin physics of Gd^{3+}. What determines the phase memory time and the spin lattice relaxation? How do they depend on spectrometer frequency and temperature? We have already seen that the modulation depth is highly susceptible to spectral diffusion, and short T_1's can also be detrimental. It is not clear if there is yet another factor, in addition to the distance distribution that causes damping of the dipolar modulations in the DEER traces. It has been suggested that one has to consider the pseudosecular terms of the dipolar interaction that are usually neglected. This has to be verified. The potential of measurements at frequencies higher than W-band has not been explored at all, and these may reveal further improvements. The potential of hetero Gd^{3+} and nitroxides spin labeling has not been investigated, and there is plenty of room for developments in this direction.

To summarize, the emerging field of Gd^{3+} spin labeling has considerable potential in providing sparse structural information on biomolecules, and their complexes and hopefully more groups will become involved in its development and help bring the approach to maturation.

Acknowledgments I thank Arnold Raitsimring and Gottfried Otting for their continuous, wonderful collaboration on the Gd^{3+} spin labeling endeavor and their inspiration. I thank Arnold Raitsimring for making unpublished results available for presentation in the chapter. I also thank my former and current group members who carried out some of the work presented here, Alexey Potapov, Michal Gordon-Grossman, Ilia Kaminer, and Debamalya Banerjee. I am in debt to David Milstein, Chidambaram Gunanathan, Hirosama Yagi, Tom Mead, and Ying Song for the synthesis of the bis-Gd^{3+} models, the labeled proteins, and DNA. I greatly appreciate the efforts of Yaacov Lipkin and Yehoshua Gorodetski in building our high-power W-band microwave bridge, and Boris Epel for his constant support of the software controlling the spectrometer. This research was supported by the binational USA–Israel Science Foundation, in part by the ISF-VATAT Converging technologies program and by the Minerva Foundation, and is made in part possible by the historic generosity of the Harold Perlman Family. D.G holds the Erich Klieger Professorial chair in Chemical Physics.

References

1. Stone TJ, Buckman T, Nordio PL, McConnel HM (1965) Proc Natl Acad Sci USA 54:1010–1017
2. Hubbell WL, Gross A, Langen R, Lietzow MA (1998) Curr Opin Struct Biol 8:649–656
3. Milov AD, Ponomarev AB, Tsvetkov YD (1984) Chem Phys Lett 110:67–72
4. Borbat PP, Freed JH (2007) Two-component signaling systems, Part B. Methods Enzymol 423:52–116
5. Jeschke G, Polyhach Y (2007) Phys Chem Chem Phys 9:1895–1910
6. Schiemann O, Prisner TF (2007) Q Rev Biophys 40:1–53
7. Hubbell WL, Altenbach C (1994) Curr Opin Struct Biol 4:566–573
8. Fleissner MR, Brustad EM, Kalai T, Altenbach C, Cascio D, Peters FB, Hideg K, Peuker S, Schultz PG, Hubbell WL (2009) Proc Natl Acad Sci USA 106:21637–21642
9. Zhang XJ, Cekan P, Sigurdsson ST, Qin PZ (2009) in Methods in Enzymology In: Herschlag D (ed) Biophysical, chemical, and functional probes of RNA structure, interactions and folding, Part B. 469:303–328

10. Reed GH (1985) Biochem Soc Trans 13:567–571
11. Hunsicker-Wang L, Vogt M, DeRose VJ (2009) Biophysical, chemical, and functional probes of RNA structure, interactions and folding, Part A, vol 468. Elsevier Academic, San-Diego, pp 335–367
12. He MM, Voss J, Hubbell WL, Kaback HR (1995) Biochemistry 34:15667–15670
13. Berliner LJ, Eaton SS, Eaton GR (2000) Distance measurements in biological systems by EPR, vol 19. Kluwer Academic, New York
14. Banham JE, Baker CM, Ceola S, Day IJ, Grant GH, Groenen EJJ, Rodgers CT, Jeschke G, Timmel CR (2008) J Magn Reson 191:202–218
15. Jager H, Koch A, Maus V, Spiess HW, Jeschke G (2008) J Magn Reson 194:254–263
16. Denysenkov VP, Biglino D, Lubitz W, Prisner TF, Bennati M (2008) Angew Chem Int Ed 47:1224–1227
17. Denysenkov VP, Prisner TF, Stubbe J, Bennati M (2006) Proc Natl Acad Sci USA 103:13386–13390
18. Polyhach Y, Godt A, Bauer C, Jeschke G (2007) J Magn Reson 185:118–129
19. Goldfarb D, Lipkin Y, Potapov A, Gorodetsky Y, Epel B, Raitsimring AM, Radoul M, Kaminker I (2008) J Magn Reson 194:8–15
20. Cruickshank PAS, Bolton DR, Robertson DA, Hunter RI, Wylde RJ, Smith GM (2009) Rev Sci Instrum 80:103102
21. Ghimire H, McCarrick RM, Budil DE, Lorigan GA (2009) Biochemistry 48:5782–5784
22. Ward R, Bowman A, Sozudogru E, El-Mkami H, Owen-Hughes T, Norman DG (2010) J Magn Reson 207:164–167
23. Gajula P, Milikisyants S, Steinhoff HJ, Huber M (2007) Appl Magn Reson 31:99–104
24. Larsen RG, Singel DJ (1993) J Chem Phys 98:5134–5146
25. Yang Z, Becker J, Saxena S (2007) J Magn Reson 188:337–343
26. Bode BE, Plackmeyer J, Prisner TF, Schiemann O (2008) J Phys Chem A 112:5064–5073
27. Lovett JE, Bowen AM, Timmel CR, Jones MW, Dilworth JR, Caprotti D, Bell SG, Wong LL, Harmer J (2009) Phys Chem Chem Phys 11:6840–6848
28. Endeward B, Butterwick JA, MacKinnon R, Prisner TF (2009) J Am Chem Soc 131:15246–15250
29. Schiemann O, Cekan P, Margraf D, Prisner TF, Sigurdsson ST (2009) Angew Chem Int Ed 48:3292–3295
30. Yang ZY, Kise D, Saxena S (2010) J Phys Chem B 114:6165–6174
31. Stoll S, Schweiger A (2006) J Magn Reson 178:42–55
32. Riplinger C, Kao JPY, Rosen GM, Kathirvelu V, Eaton GR, Eaton SS, Kutateladze A, Neese F (2009) J Am Chem Soc 131:10092–10106
33. Kay CWM, El Mkami H, Cammack R, Evans RW (2007) J Am Chem Soc 129:4868–4869
34. Pannier M, Veit S, Godt A, Jeschke G, Spiess HW (2000) J Magn Reson 142:331–340
35. Milov AD, Maryasov AG, Tsvetkov YD (1998) Appl Magn Reson 15:107–143
36. Salikhov KM, Dzuba SA, Raitsimring AM (1981) J Magn Reson 42:255–276
37. Jeschke G, Chechik V, Ionita P, Godt A, Zimmermann H, Banham J, Timmel CR, Hilger D, Jung H (2006) Appl Magn Reson 30:473–498
38. Elsasser C, Brecht M, Bittl R (2002) J Am Chem Soc 124:12606–12611
39. Borbat PP, Freed JH (1999) Chem Phys Lett 313:145–154
40. Borbat PP, McHaourab HS, Freed JH (2002) J Am Chem Soc 124:5304–5314
41. Kulik LV, Dzuba SA, Grigoryev IA, Tsvetkov YD (2001) Chem Phys Lett 343:315–324
42. Kulik LV, Paschenko SV, Dzuba SA (2002) J Magn Reson 159:237–241
43. Milikisyants S, Scarpelli F, Finiguerra MG, Ubbink M, Huber M (2009) J Magn Reson 201:48–56
44. van Amsterdam IMC, Ubbink M, Canters GW, Huber M (2003) Angew Chem Int Ed 42:62–64
45. Fittipaldi M, Warmerdam GCM, de Waal EC, Canters GW, Cavazzini D, Rossi GL, Huber M, Groenen EJJ (2006) Chemphyschem 7:1286–1293
46. Becker JS, Saxena S (2005) Chem Phys Lett 414:248–252

47. Elsaesser C, Brecht M, Bittl R (2005) Biochem Soc Trans 33:15–19
48. Voss J, Hubbell WL, Kaback HR (1995) Proc Natl Acad Sci USA 92:12300–12303
49. Leigh JS (1970) J Chem Phys 52:2608–2612
50. Narr E, Godt A, Jeschke G (2002) Angew Chem Int Ed 41:3907–3910
51. Bode BE, Plackmeyer J, Bolte M, Prisner TF, Schiemann O (2009) J Organomet Chem 694:1172–1179
52. Hara H, Kawamori A, Astashkin AV, Ono T (1996) Biochim Biophys Acta 1276:140–146
53. Kuroiwa S, Tonaka M, Kawamori A, Akabori K (2000) Biochim Biophys Acta 1460: 330–337
54. Astashkin AV, Elmore BO, Fan WH, Guillemette JG, Feng CJ (2010) J Am Chem Soc 132:12059–12067
55. Voss J, Hubbell WL, Kaback HR (1996) FASEB J 10:827
56. Voss J, Wu JH, Hubbell WL, Jacques V, Meares CF, Kaback HR (2001) Biochemistry 40:3184–3188
57. Otting G (2008) J Biomol NMR 42:1–9
58. Su X-C, Otting G (2010) J Biomol NMR 46:101–112
59. Haberz P, Rodriguez-Castaneda F, Junker J, Becker S, Leonov A, Griesinger C (2006) Org Lett 8:1275–1278
60. Iwahara J, Anderson DE, Murphy EC, Clore GM (2003) J Am Chem Soc 125:6634–6635
61. Meirovitch E, Poupko R (1978) J Phys Chem 82:1920–1925
62. Raitsimring AM, Astashkin AV, Poluektov OG, Caravan P (2005) Appl Magn Reson 28:281–295
63. Manikandan P, Carmieli R, Shane T, Kalb AJ, Goldfarb D (2000) J Am Chem Soc 122:3488–3494
64. Raitsimring AM, Gunanathan C, Potapov A, Efremenko I, Martin JML, Milstein D, Goldfarb D (2007) J Am Chem Soc 129:14138–14140
65. Gunanathan C, Diskin-Posner Y, Milstein D (2010) Cryst Growth Des 10:4235–4239
66. Gordon-Grossman M, Kaminker I, Gofman Y, Shai Y, Goldfarb D (2011) Phys Chem Chem Phys 13:10771–10780
67. Potapov A, Song Y, Meade TJ, Goldfarb D, Astashkin AV, Raitsimring A (2010) J Magn Reson 205:38–49
68. Potapov A, Yagi H, Huber T, Jergic S, Dixon NE, Otting G, Goldfarb D (2010) J Am Chem Soc 132:9040–9048
69. Liepinsh E, Ilag LL, Otting G, Ibanez F (1997) EMBO J 16:4999–5005
70. Su XC, Jergic S, Keniry MA, Dixon NE, Otting G (2007) Nucleic Acids Res 35: 2825–2832
71. Yagi H, Banerjee D, Graham B, Huber T, Goldfarb D, Otting G (2011) J Am Chem Soc 133:10418–10421
72. Rainey-Barger EK, Mkrtchian S, Tsai B (2009) J Virol 83:1483–1491
73. Zhang D, Richardson DR (2011) Int J Biochem Cell Biol 43:33–36
74. Liepinsh E, Baryshev M, Sharipo A, Ingelman-Sundberg M, Otting G, Mkrtchian S (2001) Structure 9:457–471
75. Barak NN, Neumann P, Sevvana M, Schutkowski M, Naumann K, Malesevic M, Reichardt H, Fischer G, Stubbs MT, Ferrari DM (2009) J Mol Biol 385:1630–1642
76. Graham B, Loh CT, Swarbrick JD, Ung P, Shin J, Yagi H, Jia X, Chhabra S, Pintacuda G, Huber T, Otting G (2011) Bioconj Chem 22:2118–2125
77. Song Y, Kohlmeir EK, Meade TJ (2008) J Am Chem Soc 130:6662–6663
78. Cai Q, Kusnetzow AK, Hideg K, Price EA, Haworth IS, Qin PZ (2007) Biophys J 93:2100–2117
79. Cai Q, Kusnetzow AK, Hubbell WL, Haworth IS, Gacho GPC, Van Eps N, Hideg K, Chambers EJ, Qin PZ (2006) Nucleic Acids Res 34:4722–4730
80. Song Y, Meade TJ, Astashkin AV, Klein EL, Enemark JH, Raitsimring A (2011) J Magn Reson 210:59–68

81. Vardi R, Bernardo M, Thomann H, Strohmaier KG, Vaughan DEW, Goldfarb D (1997) J Magn Reson 126:229–241
82. Astashkin AV, Raitsimring AM (2002) J Chem Phys 117:6121–6132
83. Lueders P, Jeschke G, Yulikov M (2011) J Phys Chem Lett 2:604–609
84. Takahashi S, Hanson R, van Tol J, Sherwin MS, Awschalom DD (2008) Phys Rev Lett 101:047601

Struct Bond (2014) 152: 205–248
DOI: 10.1007/430_2012_88

Published online: 19 April 2013

Structural Information from Spin-Labelled Membrane-Bound Proteins

Johann P. Klare and Heinz-Jürgen Steinhoff

Abstract Site-directed spin labelling (SDSL) in combination with electron paramagnetic resonance (EPR) spectroscopy is a powerful tool for the investigation of the structure and conformational dynamics of biomolecules including membrane proteins under native-like conditions. EPR spectroscopy of the spin-labelled molecules provides information about the spin label side chain mobility, its solvent accessibility, the polarity of its immediate environment and intra- or intermolecular distances to another paramagnetic centre or spin label. This chapter provides an overview of the basics as well as recent progress in SDSL and related EPR techniques. Continuous wave EPR spectra analyses and pulse EPR techniques are reviewed with special emphasis on applications to the membrane-embedded sensory rhodopsin–transducer complex mediating the photophobic response of the halophilic archaeum *Natronomonas pharaonis*, the maltose ABC importer $MalFGK_2$ and the mechanosensitive channel MscS.

Keywords Accessibility · Distance measurements · EPR · Membrane proteins · Mobility · Polarity · Saturation recovery · Site-directed spin labelling

Contents

J.P. Klare and H.-J. Steinhoff (✉)
Physics Department, University of Osnabrück, Barbarastr. 7, 49076 Osnabrück, Germany
e-mail: jklare@uni-osnabrueck.de; hsteinho@uni-osnabrueck.de

Abbreviations

CrOx	Chromium oxalate
cw	Continuous wave
DEER	Double electron–electron resonance
DPPH	Diphenylpikrylhydrazine
DQC	Double quantum coherence
EPR	Electron paramagnetic resonance
HtrII	Halobacterial transducer II
MD	Molecular dynamics
MOMD	Microscopic ordering with macroscopic disordering model
NiEDDA	Ni(II)-ethylenediaminediacetate
PDB	Protein data bank
PELDOR	Pulsed electron double resonance
SDSL	Site-directed spin labelling
SR-EPR	Saturation recovery EPR
SRII	Sensory rhodopsin II
SRLS	Slowly relaxing local structure
T4L	T4 lysozyme

1 Introduction

Site-directed spin labelling (SDSL) [1, 2] in combination with electron paramagnetic resonance (EPR) spectroscopy has emerged as a powerful tool to investigate the structure and the conformational dynamics of biomolecules, especially membrane proteins, under conditions close to the physiological, i.e. functional, state of the system under exploration. The technique is applicable to soluble molecules and, what will be in the focus of this review, membrane-bound proteins either solubilized in detergent or embedded in a lipid bilayer in liposomes or nanodiscs. The size and the complexity of the system under investigation is almost arbitrary (for reviews, see, e.g., [3–7]).

In SDSL a spin label side chain is site-specifically introduced into a protein or nucleic acid. The most common technique for proteins is still the introduction of a cysteine residue at the desired site and the reaction with a sulfhydryl-specific paramagnetic nitroxide reagent. Nevertheless, in the past years a wider range of coupling schemes have been established, including, for example, the highly specific introduction of the spin label side chain via "click chemistry". A detailed review about currently available labelling techniques can be found in volume 1 of this series [121].

The continuous wave (cw) EPR spectra of nitroxide-labelled molecules provide information about the mobility of the nitroxide side chain, its solvent accessibility, and the polarity and proticity of its immediate environment. Furthermore, if a second nitroxide is introduced into the same molecule or a complex is formed with a second spin-labelled moiety, the distance between the two labels can be determined. Thus, EPR studies on a series of spin-labelled variants of the system under investigation ("nitroxide scanning") can provide information about the topology of the system, enabling the identification of secondary structure elements, the tertiary and quarternary structure of a protein or complexes thereof, and, being of specific interest in this chapter, the localization of a side chain, a secondary structure element or a protein domain with respect to a lipid membrane–water interface. Furthermore, beyond the possibility to investigate static structures, EPR can provide valuable information about the dynamics of biomolecules. Protein conformational equilibria and conformational changes, occurring, for example, during the functional cycle of a signalling protein or an enzyme, can be studied on a wide timescale ranging from picoseconds to seconds.

This chapter is organized as follows. First, the main experimental techniques to obtain information about spin-labelled proteins are introduced including the relevant theoretical background for the respective technique in Sects. 2–5. Each method is exemplified with an example from the recent literature. Therein, special emphasis is given to recently developed techniques and methods being specifically relevant to investigations of membrane proteins. In the last section of this chapter (Sect. 6) selected examples for the application of SDSL EPR on membrane proteins and membrane protein complexes are given, namely, the sensory rhodopsin–transducer complex *Np*SRII/*Np*HtrII mediating the photophobic response of the halophilic archaeum *Natronomonas pharaonis*, the maltose ABC importer $MalFGK_2$, and the mechanosensitive channel of small conductance (MscS).

2 Spin Label Side Chain Mobility

The shape of a room temperature cw EPR spectrum reflects the reorientational motion of the nitroxide side chain due to partial averaging of the anisotropic components of the g- and hyperfine tensors. How this effect influences the spectral shape has been reviewed in detail [8–10], and the relationship between the

dynamics of the spin label side chain and protein structure has been extensively studied for T4 lysozyme (T4L) [11–15].

2.1 Theoretical Background

The motion of a nitroxide spin label side chain is characterized by three mechanisms (summarized from [3]):

1. The rotational diffusion of the entire protein
2. The rotational isomerization about the bonds linking the nitroxide to the backbone
3. The segmental motion of the protein backbone with respect to the average protein structure

The rotational correlation time for the rotational diffusion of the entire protein or, more generally, the system under investigation can be calculated using the Stokes–Einstein equation:

$$\tau_R = \frac{\eta V}{k_B T} = \frac{\eta}{k_B T} \cdot \frac{\bar{V} M}{N_A}, \tag{1}$$

where η is the viscosity of the solution, V the volume of the molecule/complex, k_B the Boltzmann constant and T the absolute temperature. The volume of a protein, protein complex or nucleic acid is often unknown but can be also expressed as the product of the partial specific volume $\bar{V}$ and the molecular mass M, divided by Avogadro's number, N_A. For most proteins at room temperature (293 K) in pure water, $\bar{V} \cong 0.73\,g^{-1}\,cm^3$ [16]. Especially for membrane-bound proteins or soluble systems with a molecular weight above ~200 kDa, the rotational correlation time for the overall tumbling of the system is beyond the sensitive time window of the EPR timescale ($> \sim$60 ns). For smaller biomolecules, the viscosity of the aqueous solution can be increased by addition of sucrose (usually 30% w/v), thus minimizing the spectral effects due to the overall tumbling of the molecule [15, 17].

The effective correlation time due to the reorientation of the spin label side chain (Fig. 1b) is a complex function of the spin label molecular structure and the primary, secondary, tertiary and eventually quaternary structure of the protein/system under investigation and can be assessed using motional models or molecular dynamics simulations (see Sect. 2.2). The third motional mechanism mentioned above may be quantified by effective correlation times due to the backbone motion and is related to the backbone flexibility, thus to the secondary structure of the protein or nucleic acid (see also Sect. 2.2.).

In a semi-empirical approach, the term "mobility" is used to characterize the effects on the EPR spectral features due to the motional rate, amplitude and anisotropy of the overall reorientational motion of the nitroxide spin label side chain. Spin-labelled sites exposed to bulk water exhibit weak interactions with the

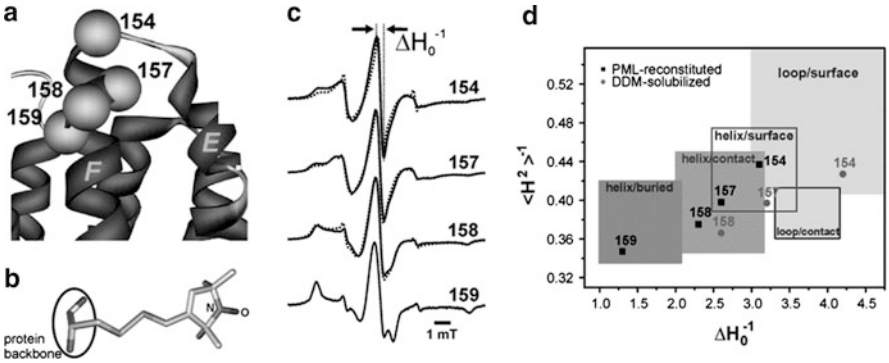

Fig. 1 Mobility analysis of spin-labelled proteins. (**a**) Crystal structure of *Np*SRII [18] showing the C_α atoms of spin-labelled sites as spheres. (**b**) Structure of the MTS spin label side chain. (**c**) X band EPR spectra of spin-labelled *Np*SRII solubilized in detergent (*dotted lines*) or reconstituted in purple membrane lipids (*solid lines*). (**d**) Two-dimensional mobility plot of the inverse of the second moment versus the inverse of the central linewidth (solubilized: *grey circles*, reconstituted: *black squares*), determined from the spectra in **b**. Topological regions of the protein according to Isas et al. [19] and Mchaourab et al. [15] are indicated by boxes

rest of the protein as found for helix surface sites or loop regions and consequently display a high degree of mobility characterized by a small apparent hyperfine splitting and narrow line widths (Fig. 1a, c; position 154). In contrast, if the side chain's motion is restricted due to strong interaction with neighbouring side chains or backbone atoms as found for tertiary contact or buried sites (Fig. 1, position 159), the apparent hyperfine splitting and line width are increased (Fig. 1c). In general, this motion is anisotropic due to the interaction of the nitroxide with neighbouring protein atoms. This has been shown by molecular dynamics simulations [20, 21]. In addition, a distribution of motional states can be concluded from those spectra which exhibit more than one component. This aspect will be treated in more detail in Sect. 2.3.

Although the relation between nitroxide dynamics and the spectral line shape appears to be quite complex, two parameters have been found to be correlated with the structure of the binding site environment and can therefore be used as simple semi-empirical mobility parameters [4, 15]: the inverse of the line width of the central line ($m_I = 0$), $(\Delta H^0)^{-1}$ and the inverse of the spectral breadth or second moment, $\langle H^2 \rangle^{-1}$, with

$$\langle H^2 \rangle = \frac{\int (B - \langle H \rangle)^2 S(B) \mathrm{d}B}{\int S(B) \mathrm{d}B} \tag{2}$$

and the first moment $\langle H \rangle$ is given by

$$\langle H \rangle = \frac{\int B\, S(B) \mathrm{d}B}{\int S(B) \mathrm{d}B}, \tag{3}$$

where B is the magnetic field and $S(B)$ is the absorption spectrum of the spin-labelled protein. In general, the values of $(\Delta H^0)^{-1}$ and $\langle H^2 \rangle^{-1}$ increase with increasing mobility of the spin label side chain. Nevertheless, in the case of multi-component spectra (see Sect. 2.3) it has to be kept in mind that $(\Delta H_0)^{-1}$ will be dominated by the most mobile component, whereas $\langle H^2 \rangle^{-1}$ will be biased towards the least mobile component.

For proteins, the plot of ΔH_0^{-1} or $\langle H^2 \rangle^{-1}$ versus the residue number reveals secondary structure elements through the periodic variation of the mobility. The assignment of α-helices, β-strands or random structures from the data is straightforward. Furthermore, a general classification of regions accommodating buried, surface-exposed, or loop residues can be obtained from the correlation between the two parameters as shown in Fig. 1d. With this simple approach, side chains from different topographical regions of a protein can be classified using as a basis the X-ray structure results from T4L and annexin 12 [4, 15, 19].

2.2 EPR Spectra Simulation

For a more quantitative interpretation of the experimental data in terms of dynamics and local structure, simulations of the EPR spectra are invaluable. Based on the dynamic models developed by Freed and co-workers [22–24], excellent agreement of simulations with the corresponding experimental spectra can be obtained. Furthermore, simulations of EPR spectra can be performed with molecular dynamics (MD) simulations [20, 21, 25–30]. They provide a direct link between the molecular structure and the EPR spectral line shape, thus allowing verification, refinement or prediction of structural models.

The applicability of MD simulation-based EPR spectra calculation is exemplified with the identification of a spin-labelled cysteine side chain in the photosynthetic reaction centre from *Rhodobacter sphaeroides* R26 [31]. EPR experiments revealed that only one of the five native cysteine residues present in the complex is accessible for spin labelling, either C156 or C234, both located on subunit H of the reaction centre (Fig. 2a). EPR spectra have been calculated from MD simulation trajectories for both candidate positions. Comparison of the simulated spectra with an experimental one revealed that only the spin label side chain at position 156 shows a spectrum which is in agreement with the experiment (see Fig. 2b).

2.3 Multi-frequency EPR

As mentioned at the beginning of the chapter, the motion of a nitroxide spin label side chain is characterized by three correlation times that can differ in their timescales. Therefore, if the dynamic behaviour of a nitroxide bound to a

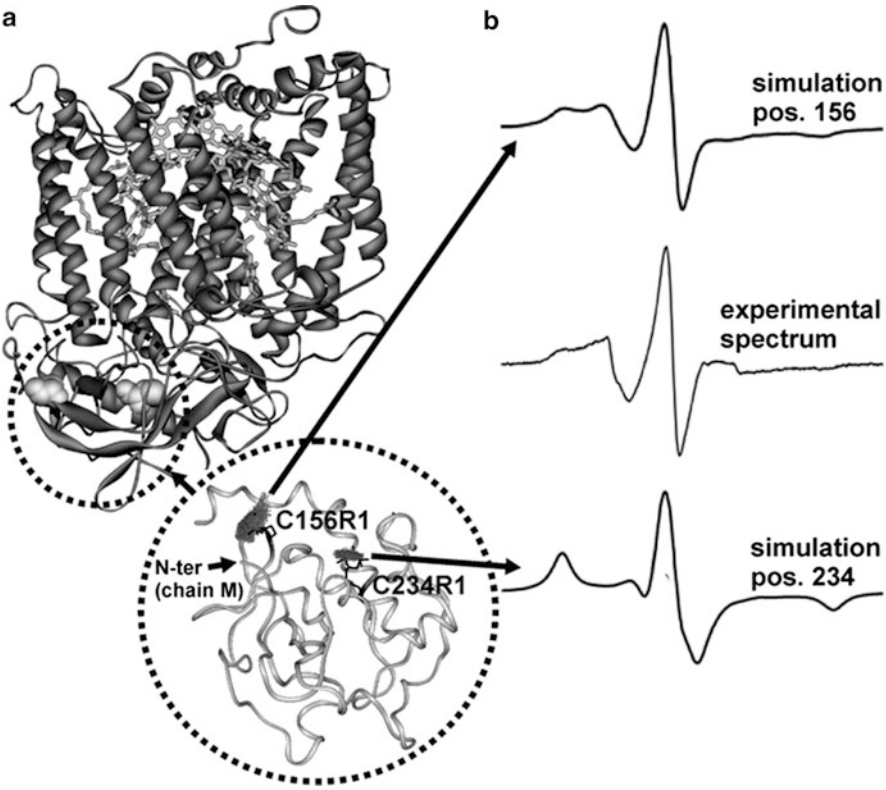

Fig. 2 EPR spectra calculations based on MD simulations exemplified on two spin-labelled positions in the photosynthetic reaction centre from *R. sphaeroides*. (**a**) Structure of the reaction centre [protein data bank (PDB): 1AIJ] showing the two "candidate" cysteines for labelling. The conformational space sampled by the spin label nitroxide group is depicted as a small grey "cloud". (**b**) Experimental (*middle*) and calculated EPR spectra for positions 156 (*top*) and 234 (*bottom*). Only the simulated EPR spectrum for a spin label at position 156 is in satisfactory agreement with the experimental one [31]

biomolecule has to be analysed in detail, an appropriate model should include all different motional mechanisms that contribute to the nitroxide dynamics. In terms of reorientational rates, the experiment(s) should be sensitive to motions in the range from 10^6 to 10^{12} s^{-1}. EPR spectra at different microwave frequencies are sensitive to motions on different timescales. EPR at lower frequencies is sensitive to slow motions whereas faster motions lead to a complete averaging of the anisotropic components of the g- and A-tensors. On the other hand, high-frequency EPR can resolve such fast motions, but slower motions are "frozen" at the high-frequency timescale. More precisely, EPR at frequencies from 9 to 35 GHz is sensitive to motions in the range of 10^6 to 10^{10} s^{-1} [32], whereas, for example, EPR at 250 GHz is sensitive to reorientational rates in the 10^{12} s^{-1} range [33]. Consequently, combining EPR at different microwave frequencies (multi-frequency EPR) allows separation of various motional modes in a spin-labelled protein according to their different

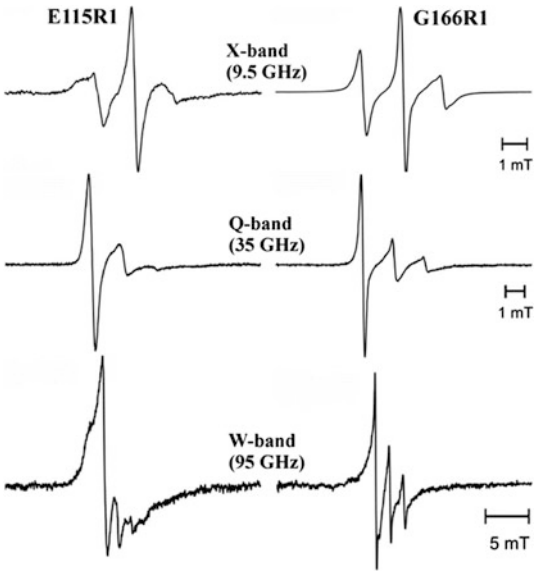

Fig. 3 Comparison of room temperature X-, Q- and W-band EPR spectra of the colicin A pore-forming domain labelled at positions 115 (*left*) and 166 (*right*) [34]

timescales. Furthermore, high-frequency EPR provides a significantly larger ***g***-tensor resolution due to the fact that the Zeeman splitting is proportional to the resonance frequency, whereas the ***A*** tensor components can be more precisely measured at low microwave frequencies (Fig. 3; see also Sect. 4.2).

Due to instrumental limitations (EPR spectrometers working at frequencies >95 GHz are usually homebuilt machines; just recently a 263 GHz spectrometer became available, the Bruker ELEXSYS E780, Bruker BioSpin, Rheinstetten, Germany) only a limited number of multi-frequency studies addressing spin label dynamics have been carried out so far. Most of the work has been done using spin-labelled T4L as a model system. Two studies combined EPR at 9 GHz and 250 GHz [35, 36]. Recently, this investigation was extended, using EPR spectra recorded at 9, 95, 170, and 240 GHz [37]. Combined with an appropriate model as, for example, the slowly relaxing local structure (SRLS) model developed by Freed [38, 39] that accounts for the internal motions as well as for the overall tumbling of the protein, such multi-frequency studies allow to separate effects of fast internal motions from slow overall motions and thereby more comprehensively characterize the complex dynamics of the system compared to single-frequency studies.

Further applications of high-field EPR will be reviewed in Sect. 4.

2.4 Multi-component Spectra

Proteins are inherently dynamic structures that often exhibit a number of conformational substates which play an important role in their function [40–42]. A given state of a protein consists of a limited number of such substates with lifetimes in the

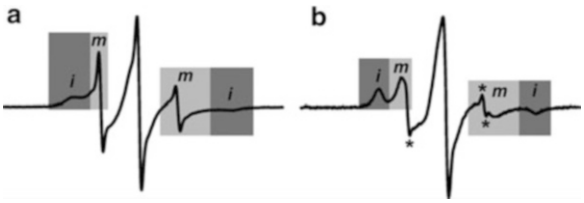

Fig. 4 Experimental multi-component cw EPR spectra. The *shaded areas* indicate regions, where the spectral intensities corresponding to relatively mobile (*m*, *light grey*) and immobile (*i*, *dark grey*) components in most cases appear nicely separated (in contrast to the centre resonance line, where components with different mobilities superimpose and can often not be separated). The spectrum in (**b**) has additional (minor) contributions of unbound spin label (*)

μs to ms time range that might, for example, correspond to open and closed states of ligand-binding pockets or specific conformations in the catalytic cycle of an enzyme. If different substates are characterized by different spin label side chain mobilities, they can be recognized in room temperature cw EPR spectra, since the lifetime of the substates is in the slow exchange limit for EPR (>100 ns). Such spectra are called "multi-component" spectra (Fig. 4).

"Multi-component" spectra can also arise from a spin label side chain existing in different rotameric states that also exhibit slow exchange on the EPR timescale, as has been established by X-ray crystallography, mutagenesis and EPR studies [43–45]. Consequently, techniques are required that allow to discriminate between protein conformational equilibria relevant to function, and spin label rotameric equilibria, as the origin of multi-component spectra.

In the past years, Hubbell and co-workers established three experimental techniques to analyse conformational equilibria in proteins and to dissect them from spin label rotameric exchange: they applied osmolyte perturbation [46], saturation recovery [47] and high-pressure EPR [48]. These techniques will be described in the following sections.

2.4.1 Osmolyte Perturbation

The first EPR-based approach to distinguish between rotameric exchange and conformational exchange was published in 2009 [46]. In this approach, the response of the spin-labelled protein to solvent perturbation by osmolytes is measured. Osmolytes are small organic molecules that either stabilize (protecting osmolytes, e.g. carbohydrates, free amino acids or methylamines [49]) or destabilize (denaturing osmolytes, e.g. urea or guanidine hydrochloride) the native fold of proteins. Protecting osmolytes are excluded from the surface of the protein (preferential hydration). This effect raises the chemical potential of the protein in relation to the solvent-exposed area [50], which is usually larger for the unfolded state of

the same protein. Consequently, the native (folded) state of the protein is stabilized, and furthermore, conformational fluctuations in the protein are reduced [51, 52]. Contrarily, denaturing osmolytes accumulate at the protein surface and have the opposite effect [53].

In most cases different conformational substates of a protein can be expected to have different solvent-exposed areas. Even if these differences are much smaller than for the folded–unfolded transition, osmolytes should be able to shift the equilibrium between conformational substates and should therefore have measurable effects on multi-component EPR spectra arising from the presence of such substates. On the other hand, different rotameric states of the spin label side chain are expected to have negligible influence on the solvent accessible area of the protein. Thus, no significant influence of the osmolyte on multi-component spectra arising from rotameric exchange should be observable.

Hubbell and co-workers showed the expected osmolyte dependencies of multi-component EPR spectra for spin-labelled T4L, rat intestinal fatty acid-binding protein, myoglobin and the photoreceptor rhodopsin [46]. In this study, sucrose was used as a protecting osmolyte [54]. To be able to distinguish between osmolyte and viscosity effects on the EPR spectral shapes, solutions of Ficoll 70 with viscosities equal to those of the sucrose solutions were used to obtain the "reference" spectra in the absence of osmolytes. Ficoll was chosen as a reference medium as solutions thereof are highly viscous but exhibit low osmolarity. Furthermore, Ficoll is known to be inert with respect to protein interactions. An example from this study, a comparison of the effects of sucrose on multi-component EPR spectra of spin-labelled apo-myoglobin (apo-Myb), is shown in Fig. 5.

It is obvious that the EPR spectra of apo-Myb spin-labelled in ordered regions (Fig. 5b) are insensitive to osmolyte perturbation, indicating that rotameric exchange is responsible for the presence of multi-component spectra for these sites. In contrast, the EPR spectra recorded for spin-labelled positions on helix F (Fig. 5c) exhibit a significant effect on the relative populations of the immobilized (*i*) and mobile (*m*) states of the spin label side chains, and in all cases the osmolyte shifts the populations towards the immobilized state. Thus, the equilibrium between two conformational states for helix F is reflected in the osmolyte-dependency of the EPR spectra, whereas the absence of the osmolyte-dependency for spin-labelled sites in the ordered regions suggests, as expected, the multi-component nature of the spectra to arise from rotameric exchange.

This method offers an easy-to-use tool to identify regions of proteins that are putatively involved in conformational transitions, for example, binding pockets which fluctuate between an open and closed conformation already in the absence of ligands, domains moving to facilitate substrate translocation in transport proteins, or secondary structure elements involved in signalling. Therein, osmolyte perturbation appears to be suited for high-molecular-weight and membrane-bound/associated proteins.

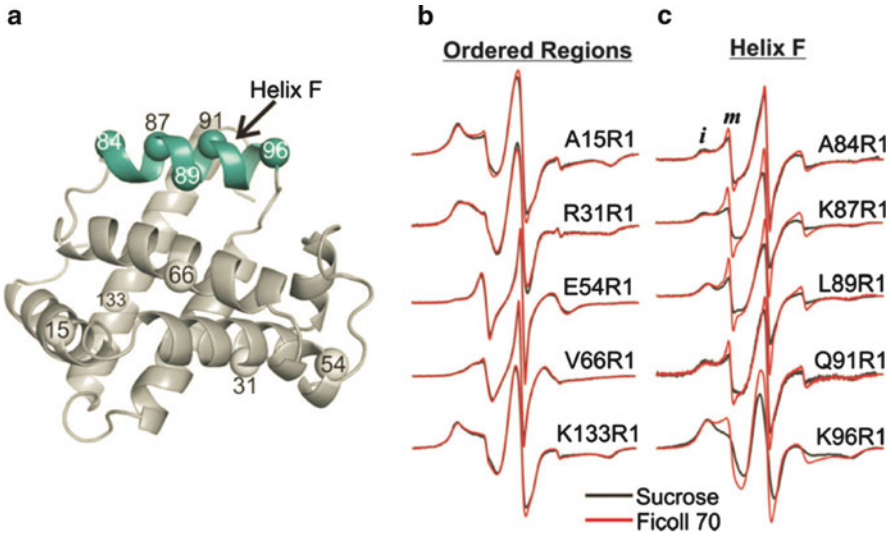

Fig. 5 Effect of osmolyte perturbation on EPR spectra of spin-labelled sites in apo-Myb. (**a**) Ribbon diagram of holo-myoglobin (PDB 2MBW). Labelled sites are indicated by spheres. Helix F, being in conformational exchange in the apo-form, is shown in *green*. (**b**) EPR spectra of apo-Myb labelled at sites in ordered regions in 30% w/w sucrose (*black spectra*) and 25% *w/w* Ficoll 70 (*red spectra*). (**c**) EPR spectra of apo-Myb labelled at sites in helix F in 30% *w/w* sucrose and 25% *w/w* Ficoll 70 (*black* and *red spectra*, respectively). The letters *i* and *m* indicate spectral components corresponding to relatively immobile and mobile states of the spin label, respectively [46] (Copyright 2009 Wiley. Used with permission from Carlos J. López, Mark R. Fleissner, Zhefeng Guo, Ana K. Kusnetzow and Wayne L. Hubbell, Osmolyte perturbation reveals conformational equilibria in spin-labelled proteins, Protein Science and WileyBlackwell)

2.4.2 Saturation Recovery

Protein conformational exchange, taking place on the μs timescale or slower, does not influence EPR spectral line shapes. Nevertheless, if this exchange is on the 1–100 μs timescale, it can influence the nitroxide spin–lattice relaxation rate $W = (2T_1)^{-1}$, where T_1 is the spin–lattice relaxation time. Consequently, determination of T_1 can provide means to investigate protein conformational exchange kinetics [47]. The spin–lattice relaxation time T_1 at physiological temperatures can be measured by saturation recovery EPR (SR, SR-EPR), developed by Hyde and co-workers [55, 56]. SR-EPR can also be used to determine accessibilities of nitroxide spin labels towards paramagnetic exchange reagents (see Sect. 3.3).

In SR-EPR the recovery of the z-magnetization after a saturating microwave pulse is monitored as a function of time. Consequently, in a two-component system arising from conformational exchange between states where the spin label side chain experiences different environments leading to different T_1 values, relaxation to equilibrium (recovery of the z-magnetization) should be bi-exponential, and the relaxation rate constants are functions of the distinct T_1 values, the exchange rates

and the equilibrium constant. A detailed derivation of the expression for such SR-EPR signals, $i(t)$, is given in Bridges et al. [47]. Experimental SR-EPR data are fit to the equation [47]:

$$i(t) = A_\alpha e^{-W_\alpha t} + A_\beta e^{-W_\beta t} + i_0, \tag{4}$$

where A_α and A_β are the exponential amplitudes for the two conformational states α and β, respectively, W_α and W_β are the corresponding relaxation rates and i_0 is the baseline offset of the experimental data.

Further information about the timescale of the exchange process under investigation can be revealed from SR experiments in the presence of fast relaxing paramagnetic reagents, such as molecular oxygen or Ni(II)-ethylenediaminediacetate (NiEDDA). Such reagents increase the relaxation rate(s) of the nitroxide depending on the collision rate between the nitroxide and the reagent (see also Sect. 3). For the fast and slow exchange limits, expected for fast rotameric exchange and protein conformational exchange, respectively, the relaxation rates are linear functions of the reagent concentration. A nonlinear dependency of the relaxation rates on the concentration of the relaxing reagent can be observed, if the exchange process takes place on an intermediate (μs) timescale [47].

In Fig. 6 examples are given for spin-labelled sites on T4L exhibiting fast exchange between spin label side chain rotamers (44R1) and slow conformational exchange (46R1) [47]. For T4L-44R1, the EPR spectrum (Fig. 6b) shows the presence of two spectral components, one being relatively mobile (α) and the other one immobilized (β). Figure 6c shows the saturation recovery curve from T4L to 44R1. The experimental data can be satisfactorily fitted with a single exponential as can be deduced from the tenfold magnified residual of the fit. The inset in Fig. 6c shows the linear dependence of the spin–lattice relaxation rate W on the concentration of molecular oxygen, indicating that the rotameric exchange process for 44R1 is indeed in the fast exchange limit.

For T4L–46R1, a variant that is destabilized relative to the wild-type protein, the EPR spectrum (Fig. 6e) also shows the presence of two components α and β, being relatively mobile and immobile, respectively. The best fit of this spectrum to a two-component model (dashed trace) reveals effective reorientational correlation times of 8.4 ns and 1.1 ns for the two states. The saturation recovery data for this variant (Fig. 6f) cannot be satisfactorily fitted with a single exponential as can be clearly seen from the tenfold magnified residual of the fit. Contrarily to T4L–44R1, the best fit is obtained with two exponential functions with individual relaxation times of 4.8 and 2.3 μs. The inset in Fig. 6f shows the linear dependence of the spin–lattice relaxation rates for the two components, W_α and W_β, on NiEDDA concentration, indicating that 46R1 is in the slow-exchange limit. This is consistent with the assumption that 46R1 monitors exchange between two local conformations of the helix it is attached to.

2.4.3 High-Pressure EPR

High-pressure effects on protein conformational equilibria were first demonstrated and investigated by NMR spectroscopy, for example on prion proteins [57, 58], but had previously already been recognized at the beginning of the last century [59]. In the 1980s, it was established that this pressure-dependency is based on differences in the partial volumes and the compressibilities of the states of the protein being in equilibrium [60]. For a pressure-dependent equilibrium of two conformational states, the equilibrium constant at a given pressure P, $K(P)$, relative to $K(0)$ at atmospheric pressure (1 bar) is given to second order in P by [48]:

$$\ln\frac{K(P)}{K(0)} = -\frac{\Delta\bar{V}^0}{RT}(P) + \frac{\Delta(-(\delta\bar{V}/\delta P))}{2RT}(P)^2, \tag{5}$$

where $\Delta\bar{V}^0$ and $\Delta(-(\delta\bar{V}/\delta P))$ are the differences in partial volume and partial molar isothermal compressibility of the two states, respectively, at reference pressure (1 bar) and temperature (294 K). Consequently, changing the pressure can shift the equilibria between different conformational states in an elegant way. This is especially of advantage if a conformational state of low occupancy under physiological conditions can be populated by increasing the pressure, making this state and the corresponding equilibrium accessible for EPR spectroscopy. In a very recent initial study by McCoy and Hubbell, the effect of pressure was investigated using spin-labelled T4L and mutants thereof [48]. Their results show (i) changes in the internal dynamics of the spin label side chain due to changes in the volume of the solvent cage around the "kinetic unit" in the transition state necessary for a rotational diffusive step. Depending on the point of spin label attachment, the "kinetic unit" can be the spin label side chain, a part of it, if isomerization around specific bonds of the spin label linker is inhibited by the surrounding, or parts of the protein backbone if the label is attached to a dynamic loop region. In all cases, a plot of $\ln(\tau/\tau_0)$ versus P, where τ is the reorientational correlation time at a given pressure and τ_0 is the correlation time at ambient pressure (1 bar), is linear; (ii) a linear behaviour of $\ln K(P)$ for rotameric equilibria of the spin label side chain and (iii) a nonlinear behaviour of $\ln K(P)$ for protein conformational equilibria.

For spin-labelled sites belonging to type (i), the activation volume $\Delta V^{\ddagger}$ can be determined, according to activated state theories, by analysis of the pressure-dependency of τ given by:

$$\ln\frac{\tau}{\tau_0} = \frac{\Delta V^{\ddagger}}{RT}P, \tag{6}$$

where τ and τ_0 are the rotational correlation times at gauge pressures P and $P = 0$, respectively, and $\Delta V^{\ddagger}$ is the activation volume.

Examples for pressure-dependent equilibria of type (i) and (ii) are given in Fig. 7 [48]. For a spin label attached to position 44 of T4L two rotamers about the S–C bond χ_4 coexist as reflected by the presence of two components with different

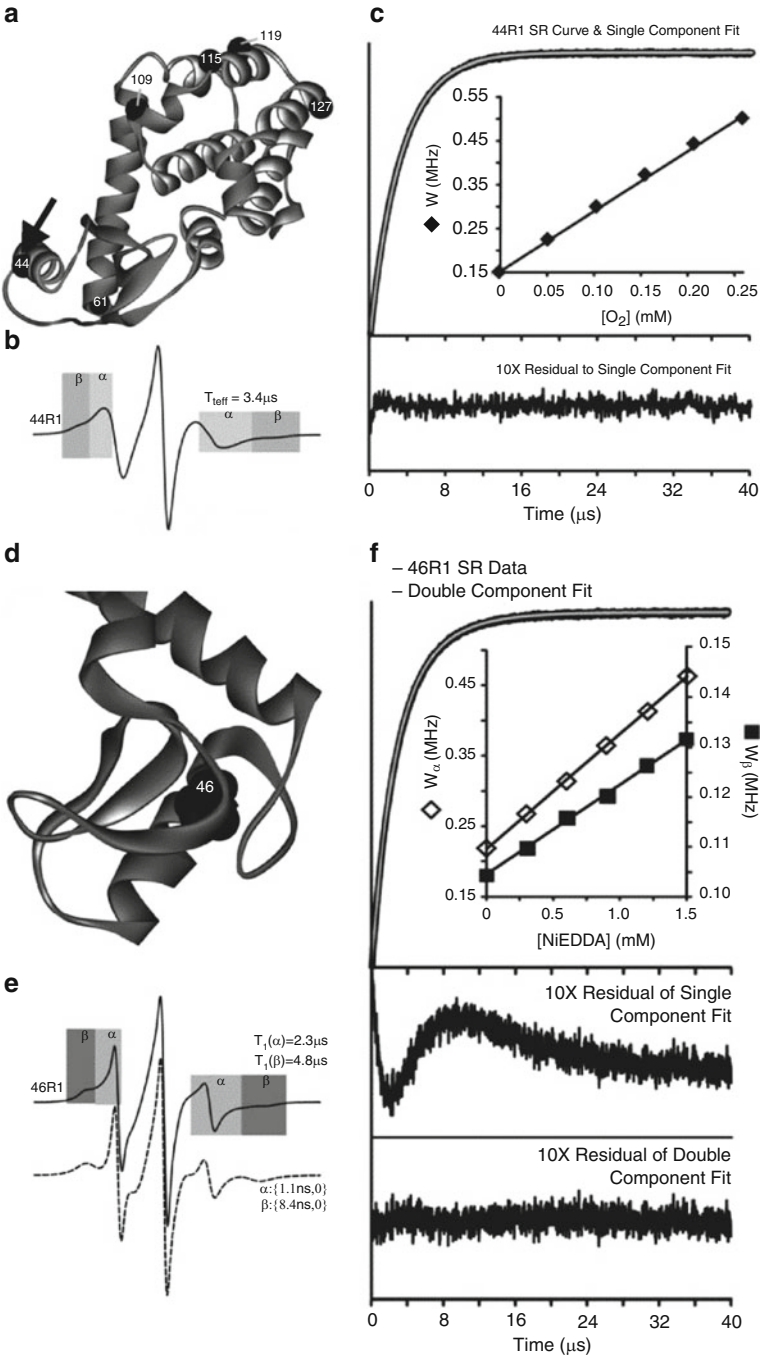

Fig. 6 Characterization of rotameric and conformational equilibria by SR-EPR, exemplified by two spin label sites (44: (**a**)–(**c**) and 46: (**d**)–(**f**)) on T4L [47]. (**a**) Ribbon model showing the location of position 44 (*arrow*). (**b**) EPR spectrum of 44R1. The *shaded areas* indicate regions,

mobilities in the cw EPR spectrum (Fig. 7b). Therefore, this position should exhibit a pressure dependence according to type (ii). The rotamer responsible for the immobile component (*i*) exhibits an interaction of the nitroxide ring with the neighbouring residue Glu45, whereas the other rotamer is not subject to significant secondary or tertiary interactions, giving rise to the mobile component (*m*) in the cw EPR spectrum (Fig. 7b). Clearly, increasing the pressure shifts the relative populations of the two states. The apparent equilibrium constants, $K(P) = [i]/[m]$ were determined from fits of the spectra and a plot of $\ln[K(P)/K(0)]$ versus pressure reveals a linear dependence. A fit according to Eq. 5 yields the differences of the partial volume, $\Delta\bar{V}^0 = (-9.4 \pm 2.2)\,\mathrm{ml\,mol^{-1}}$, and a partial molar isothermal compressibility, $\Delta(-(\delta\bar{V}/\delta P)) = 0$. Obviously, high pressure favours the interaction of the spin label side chain with Glu45 due to a smaller volume of this state. Nevertheless, the compressibility of the protein does not differ significantly between the two states.

The type (iii) behaviour is exemplified with position 118 on T4L, shown in Fig. 7c–e. A spin label attached at this position is partially buried in a hydrophobic pocket, but also has a destabilizing effect on a neighbouring short helix which appears unfolded in the crystal structure (Fig. 7c). The partially buried location of the label is clearly reflected in the EPR spectra (Fig. 7d, top). Increasing the pressure produces only small spectral changes that have mainly been attributed to the increase in viscosity under pressure. If the protein is unfolded in 8 M urea, the resulting EPR spectrum (Fig. 7d, bottom) is characteristic of a disordered polypeptide. At high pressure, the reorientational correlation time of the label side chain is increased. The authors used the equilibrium between the folded and the unfolded state of this mutant at 2 M urea (Fig. 7e) to generate a system of type (iii). The EPR spectrum of T4L–118R1 in 2 M urea at atmospheric pressure reveals this equilibrium through the presence of a mobile (*m*) and an immobile (*i*) component. The pressure dependence of the EPR spectra reveals a strong nonlinear behaviour of $\ln[K(P)/K(0)]$ versus pressure.

Fitting the parameters of Eq. 5 gave $\Delta\bar{V}^0 = (-51.0 \pm 1.7)\mathrm{ml\,mol^{-1}}$ and $\Delta(-(\delta\bar{V}/\delta P)) = (-0.017 \pm 0.001)\,\mathrm{ml\,mol^{-1}bar^{-1}}$. The linear increase of $\ln[K(P)/K(0)]$ with pressure up to ~1 kbar reveals the shift of the equilibrium towards

Fig. 6 (continued) where spectral intensity corresponds to relatively mobile (α, *light grey*) and immobile (β, *darker grey*) states. (**c**) SR curve for 44R1 and single-exponential fit, together with the 10× magnified residual of the fit. The *inset* shows the dependence of the spin–lattice relaxation rate *W* on oxygen concentration. (**d**) Ribbon model showing the location of position 46. (**e**) EPR spectrum of 46R1 (*black trace*) and the corresponding two-component MOMD fit (*dashed trace*). Rotational correlation times and order parameters determined from the fit are given. Shaded regions are the same as described for (**b**). (**f**) SR curve for 46R1 with the double-exponential fit, and the 10× magnified residuals to a single- and the double-exponential fit. The inset shows the dependence of the relaxation rates for the two components, W_α and W_β, on NiEDDA concentration [47] (Copyright 2009 Springer. Used with permission from Michael D. Bridges, Kálmán Hideg and Wayne L. Hubbell, Resolving conformational and rotameric exchange in spin-labelled proteins using saturation recovery EPR, Applied Magnetic Resonance and Springer)

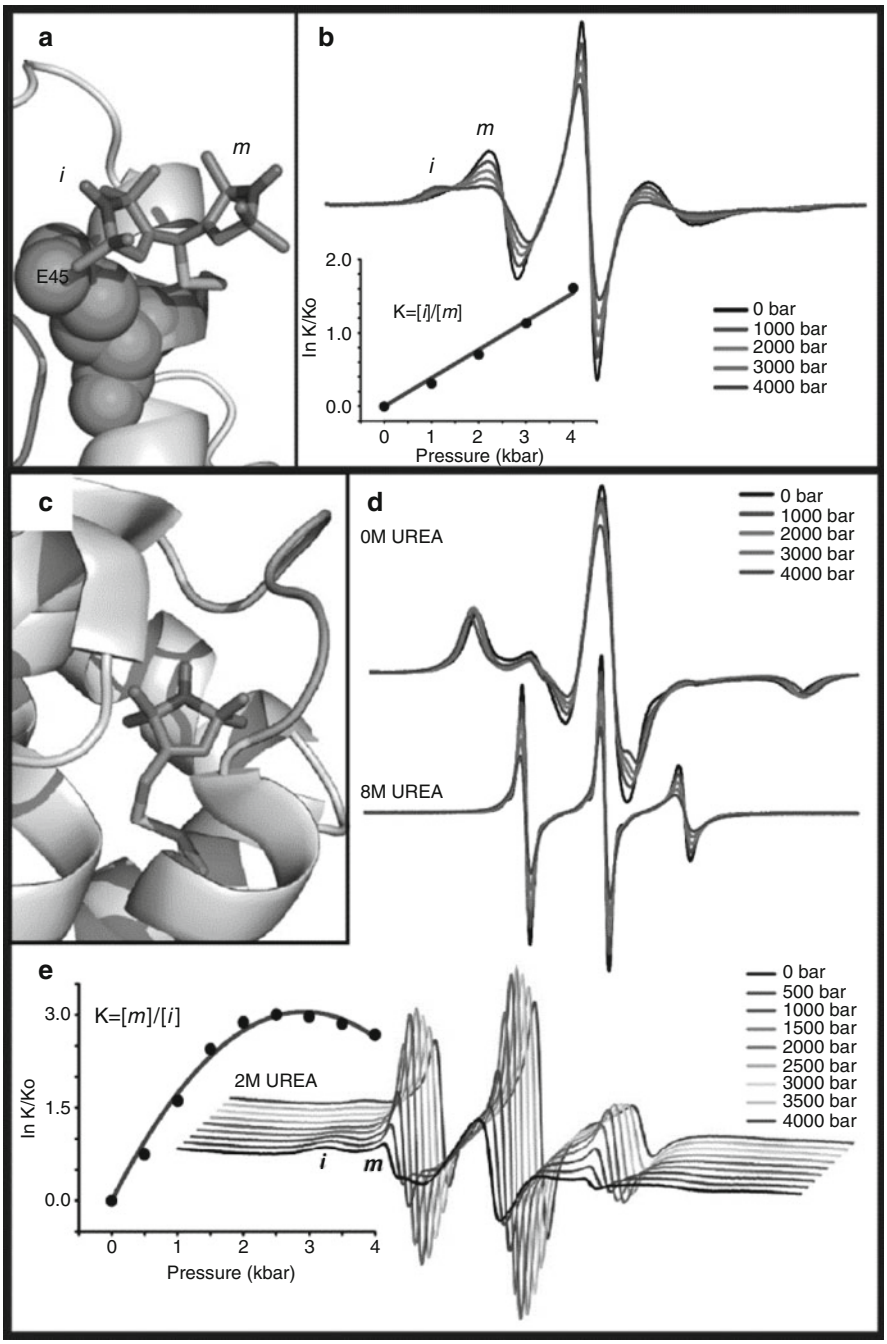

Fig. 7 Dissection of rotameric and conformational equilibria by high-pressure EPR, exemplified on two sites on T4L. (**a**) Model of the spin label side chain 44R1 based on the crystal structure (PDB: 2QE9). The two rotamers are indicated. (**b**) Pressure dependence of the EPR spectra.

the more disordered (unfolded) state in accordance with the volume theorem [57]. At pressures exceeding 1 kbar, the strongly convex curvature of the plot reveals a decrease in compressibility with increasing pressure. This is in accordance with theoretical considerations for equilibria between folded and unfolded states of proteins, although the magnitude and the sign of the observed changes in the compressibility for partial and completely unfolded proteins are still a matter of debate [61].

3 Solvent Accessibility of Protein-Bound Nitroxides

Supplementing the motional analysis, the accessibility of the spin label side chain towards paramagnetic probes, which selectively partition in different environments of the system under investigation, can be used to define the location of a nitroxide group with respect to the protein–water–membrane boundaries. Two experimental techniques can be used to determine the nitroxide's accessibility towards the paramagnetic probes: Cw power saturation, described in Sect. 3.2 (summarized from [3]) and saturation recovery as described in Sect. 3.3.

3.1 Theoretical Background

The accessibility of a nitroxide spin label side chain is defined through its Heisenberg exchange frequency, W_{ex}, with a paramagnetic exchange reagent diffusing in its environment. Water-soluble metal ion complexes, for example NiEDDA or chromium oxalate (CrOx), quantify the accessibility from the bulk water phase, whereas molecular oxygen or hydrophobic organic radicals, which preferentially partition in the hydrophobic part of the lipid bilayer, define the accessibility from the lipid phase. It has been shown that the concentration gradients of NiEDDA and molecular oxygen along the membrane normal can be

Fig. 7 (continued) The *inset* shows the plot of the equilibrium constants determined from fits to the spectra versus pressure. The *solid line* is a fit to Eq. 5. (**c**) Model of the spin label side chain 118R1 based on the crystal structure (PDB: 2NTH). (**d**) Pressure dependence of EPR spectra in buffer (*top*) and in the presence of 8M urea (*bottom*). (**e**) Pressure dependence of EPR spectra in the presence of 2 M urea. The equilibrium constants determined from fits to the spectra (*right*) is plotted versus pressure (*left*). The solid line is a fit to Eq. 5 [48] (Copyright 2010 the National Academy of Sciences. Used with permission from John McCoy and Wayne L. Hubbell, High-pressure EPR reveals conformational equilibria and volumetric properties of spin-labelled proteins, Proceedings of the National Academy of Sciences and the National Academy of Sciences)

used to characterize the immersion depth of the spin label side chain with respect to the membrane/water interface [62, 63].

The Heisenberg exchange mechanism alters the relaxation properties of the spin label that are characterized by the spin–lattice relaxation time T_{1e} and the spin–spin relaxation time T_{2e}. If the longitudinal relaxation time of the reagent is smaller than the encounter complex lifetime ($T_{1R} < \tau_c$), Heisenberg exchange leads to equal changes in T_{1e} and T_{2e}:

$$W_{ex} = \Delta\left(\frac{1}{T_{1e}}\right) = \Delta\left(\frac{1}{T_{2e}}\right) = k_{ex} C_R, \tag{7}$$

where W_{ex} is the Heisenberg exchange frequency, k_{ex} is the exchange constant and C_R is the concentration of the paramagnetic exchange reagent. If Heisenberg exchange is diffusion controlled, i.e. being in the strong exchange limit, the exchange constant k_{ex} [L mol^{-1} s^{-1}] can be written as [64]:

$$k_{ex} = P_{max} f\, k_D = P_{max} f \left(4\pi N_A (D_N + D_R) r_C \cdot 10^3\right), \tag{8}$$

where P_{max} is the maximum exchange efficiency (in the strong exchange limit and for $T_{1R} < \tau_c$, $P_{max} = 1$), f is a dimensionless steric factor, k_D is the diffusion-controlled rate constant [L mol^{-1} s^{-1}], N_A is the Avogadro number, D is the diffusion constant for the nitroxide (N) and the reagent (R) [m^2 s^{-1}], and r_C is the collision radius (the sum of the effective radii of the nitroxide and the reagent, [m]).

For protein-bound spin labels, D_N becomes the diffusion constant of the protein. Consequently, D_N is significantly smaller than D_R and can therefore be neglected in the equation. The effective collision frequency of the nitroxide towards the paramagnetic reagent can be reduced by the influence of the local protein environment and interactions of the spin label side chain with neighbouring residues. These effects are considered in the equation

$$W_{ex} = \rho f\, 4\pi N_A D_N r_C\, 10^3 C_R, \tag{9}$$

where ρ is a proportionality factor reflecting these effects [64] with the concentration of the exchange reagent, C_R, expressed in mol L^{-1}.

3.2 Cw Power Saturation

Most commonly, Heisenberg exchange rates for nitroxide side chains in proteins are measured using cw power saturation. Here, the EPR signal amplitude is monitored as a function of the incident microwave power in the absence and presence of the paramagnetic quencher. From the saturation behaviour of the nitroxide, an accessibility parameter, Π, can be extracted that is proportional to

W_{ex} [1, 64, 65]. In the following it is described how Π is obtained from a power saturation experiment.

The amplitude of the first derivative, Y', of a Lorentzian absorption line is given by [66]

$$Y' \propto \frac{H_1}{\left(1 + H_1^2 \gamma^2 T_{1e} T_{2e}\right)^{3/2}} = \frac{\Lambda \sqrt{P}}{\left(1 + \Lambda^2 P \gamma^2 T_{1e} T_{2e}\right)^{3/2}}. \tag{10}$$

H_1 is the microwave magnetic field, which is proportional to the square root of the incident microwave power P, and Λ describes the properties of the microwave resonator, i.e. an instrumental calibration for the conversion of incident microwave power to microwave magnetic field H_1 ($H_1 = \Lambda \cdot \sqrt{P}$). γ is the gyromagnetic ratio of the electron and T_{1e} and T_{2e} are the spin–lattice and spin–spin relaxation times, respectively. Equation 10 reveals that Y' is proportional to the square root of P for low microwave power, whereas for higher microwave power Y' becomes proportional to $1/P$. A parameter related to the relaxation quantity $T_{1e}T_{2e}$ that can easily be obtained from a power saturation experiment is $P_{1/2}$, which is the microwave power at which Y' reaches half of the theoretical value reachable in the absence of saturation:

$$Y'(P_{1/2}) = \frac{\Lambda \sqrt{P_{1/2}}}{2}. \tag{11}$$

If $P_{1/2}$ for a homogeneously broadened line is expressed as:

$$P_{1/2} = \frac{\left(2^{2/3} - 1\right)}{\Lambda^2 \gamma^2 T_{1e} T_{2e}}, \tag{12}$$

Eq. 10 can be rewritten accordingly as:

$$Y' \propto \frac{\Lambda \sqrt{P}}{\left(1 + \left(2^{1/\varepsilon} - 1\right) P/P_{1/2}\right)^{\varepsilon}}, \tag{13}$$

with $\varepsilon = 3/2$. For the inhomogeneously broadened line an analogous expression can be obtained with $\varepsilon = 1/2$. Experimentally, the EPR signal amplitude Y' is monitored as a function of the incident microwave power P, and a plot of Y' vs. $\sqrt{P}$ (Fig. 8) can be fitted using the equation:

$$Y' = \frac{I \sqrt{P}}{\left(1 + \left(2^{1/\varepsilon} - 1\right) P/P_{1/2}\right)^{\varepsilon}}, \tag{14}$$

with a scaling factor I including the instrumental calibration factor Λ, the measure ε for the homogeneity of saturation of the resonance line, and the microwave power $P_{1/2}$, where the first derivative signal amplitude is reduced to half of its unsaturated value, as adjustable parameters.

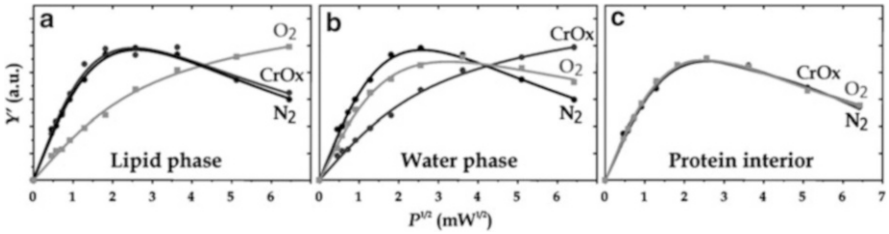

Fig. 8 Saturation curves (plot of the peak-to-peak amplitude of the central EPR line, Y', vs. $\sqrt{P}$) for (**a**) a nitroxide located in the hydrophobic region of a lipid bilayer, (**b**) a water-accessible nitroxide, and (**c**) for a nitroxide deeply buried in the interior of a protein, therefore not being accessible for either of the exchange reagents used

Collision of paramagnetic exchange reagents with the nitroxide group leads to a decrease in the relaxation times of the nitroxide, and hence to an increase of $P_{1/2}$. Thus, determination of the $P_{1/2}$ values in the presence of paramagnetic reagents and in a nitrogen-atmosphere as a reference provides means to estimate the Heisenberg exchange frequency W_{ex} based on the following equation:

$$\Delta P_{1/2} = P^{R}_{1/2} - P^{0}_{1/2} \propto \frac{1}{T^{R}_{1e}\,T^{R}_{2e}} - \frac{1}{T^{0}_{1e}\,T^{0}_{2e}} \propto \frac{W_{\mathrm{ex}}}{T^{0}_{2e}}, \tag{15}$$

where the indices R and 0 indicate the parameters in the presence and in the absence of a relaxing agent, respectively. In the above equation the approximation $T^{\mathrm{R}}_{2e} \cong T^{0}_{2e}$ has been made based on the assumption that $T_{2e} \ll \tau_{\mathrm{c}}$ and consequently the spin–spin relaxation time is not affected by the presence of the paramagnetic exchange reagent. As is obvious from Eq. 15, the $P_{1/2}$ values reflect the relative collision frequencies and therefore the accessibility of the nitroxide towards the exchange reagent [1, 62, 67], but still also depend on T_{2e}. To eliminate this dependency, the $P_{1/2}$ values are divided by the spectra line widths ΔH_0 as a measure for T^{-1}_{2e}. Consequently, one obtains [65]:

$$\Delta P'_{1/2} = \frac{\Delta P_{1/2}}{\Delta H_0} \propto W_{\mathrm{ex}}. \tag{16}$$

The approximation made for Eq. 15 directly implies that the EPR line width remains unchanged upon the addition of the exchange reagent. Nevertheless, for nitroxides of high mobility and high reagent concentrations (CrOx $>$ 25 mM or NiEDDA $>$ 10 mM) this approximation may not be valid $\left(T^{\mathrm{R}}_{2e} \neq T^{0}_{2e}\right)$. This problem can be overcome either by decreasing the reagent concentration or by eliminating the T_{2e} dependency of $\Delta P_{1/2}$ through separate division of $P^{\mathrm{R}}_{1/2}$ and $P^{0}_{1/2}$ by the respective line widths:

$$\Delta P'_{1/2} = \frac{P^{\mathrm{R}}_{1/2}}{\Delta H^{\mathrm{R}}_{0}} - \frac{P^{0}_{1/2}}{\Delta H^{0}_{0}}. \tag{17}$$

Furthermore, to account for instrumental variability (for example resonator properties that influence saturation behaviour), normalization of $\Delta P'_{1/2}$ with a reference sample, for example 2,2-diphenyl-1-picrylhydrazyl (DPPH) powder diluted in KCl, is performed to yield the dimensionless accessibility parameter Π:

$$\Pi = \Delta P'_{1/2} \frac{\Delta H_0(\mathrm{DPPH})}{P_{1/2}(\mathrm{DPPH})} \propto W_{\mathrm{ex}}. \tag{18}$$

Alternatively, the Π values can be divided by a resonator-specific proportionality factor α [MHz^{-1}] to obtain directly W_{ex} rates (see [64]):

$$\Pi = \alpha W_{\mathrm{ex}}. \tag{19}$$

In practice, the use of air (21% O_2) and 10 mM NiEDDA as exchange reagents to monitor the accessibility of a nitroxide side chain towards lipid and bulk water phases, respectively, fulfils the $T_{2e}^{\mathrm{R}} \cong T_{2e}^{0}$ criterion. The neutral NiEDDA has advantages over the negatively charged CrOx as Coulomb interactions might influence the accessibility depending on the charge distribution in the immediate environment of the nitroxide. Furthermore, in the case of CrOx, Π might become dependent on the ionic strength of the buffer solution [68].

Experimentally, the sample is loaded into gas-permeable TPX capillaries with sample volumes of 10 µl or less, and placed into a loop-gap resonator, which provides a homogeneous and sufficiently large H_1 microwave field. For the "reference" measurement in the absence of exchange reagents the sample is deoxygenated by fluxing nitrogen gas around the capillary (20–30 min) and the EPR experiment is performed in the presence of N_2. To determine the accessibility towards oxygen, the nitrogen is replaced by air or 100% O_2. Samples containing soluble exchange reagents (CrOx or NiEDDA) are measured again in the presence of N_2. For all experiments, the peak-to-peak amplitude of the central EPR line is monitored as a function of the incident microwave power that is usually varied in the range from 0.1 to 50 mW and plotted vs. $\sqrt{P}$ (Fig. 8). From such saturation curves, $P_{1/2}$ values can be extracted by fitting of Eq. 14.

In Fig. 9, the accessibility analysis performed on a 24 amino acid long segment of the halobacterial transducer *Np*HtrII in complex with its cognate photoreceptor *Np*SRII (see Sect. 6.1 for a more detailed description of this system) is shown as an example [69]. Figure 9a shows the crystal structure of the transmembrane region of the complex [70] embedded in a lipid bilayer. The segment investigated in this study starts at position 78 in the transmembrane region and extents to position 101 in the cytoplasm. Power saturation experiments have been performed with air (21% O_2) and 50 mM CrOx, respectively. The Π values calculated from these experiments are shown in panel b as a function of the residue number. The low Π values for both oxygen and CrOx in the region 78–86 indicate its location in a densely packed protein–protein interface.

Furthermore, the clear periodicity of 3.6 residues (see inset in panel b, gray) corroborates the assumption that this region is α-helical. For positions 87–94 a gradual increase in the Π_{CrOx} values is observed, providing strong evidence that this

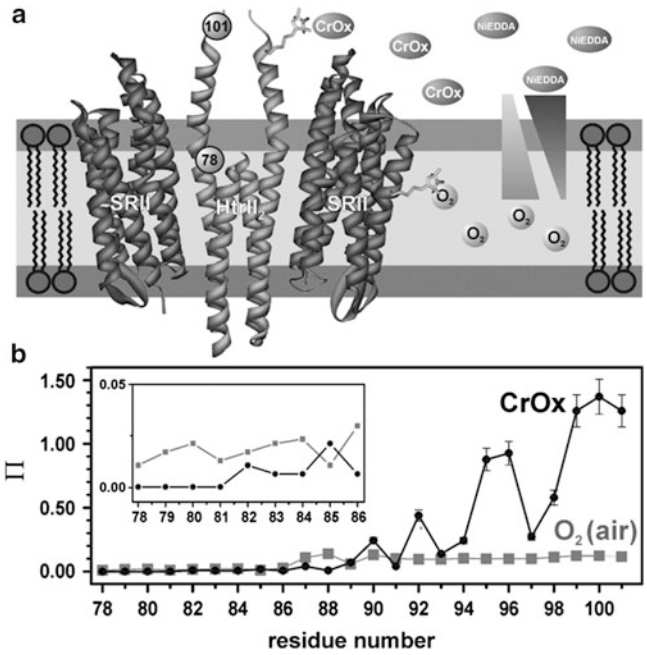

Fig. 9 Determination of solvent accessibilities by power saturation exemplified with the *Np*SRII/*Np*HtrII complex reconstituted in a lipid bilayer. (Data taken from [69]). (**a**) Ribbon representation of the complex in a lipid bilayer (*light grey*: hydrophobic region, *medium grey*: headgroup region). The gradients of concentration for water-soluble reagents (CrOx and NiEDDA) and lipid-soluble reagents (O_2) are indicated by shaded triangles. The first (78) and last residue (101) of the region investigated by power saturation are indicated by numbered spheres. The corresponding data is shown in panel **b**. (**b**) Accessibility parameters Π_{CrOx} (*black circles*) and Π_{Oxygen} (*grey squares*) vs. residue number. Π_{CrOx} values have been obtained with 50 mM CrOx, Π_{Oxygen} values with air (21% O_2). The *inset* depicts the region from residues 78–86 to show the periodicity of 3.6 for Π_{Oxygen} corresponding to the α-helical secondary structure

region is protruding out of the protein–protein interface into the cytoplasm. Accordingly, the Π_{Oxygen} values also increase. For positions 92–101 Π_{CrOx} values typical for water exposed residues are obtained, and also here a periodical pattern is observed, indicating an α-helical secondary structure also for this region.

3.3 Saturation Recovery

SR-EPR allows measuring the spin–lattice relaxation time, T_{1e}, (see Sect. 2.4.2), and therefore the Heisenberg exchange frequency, W_{ex}, can be determined directly from the saturation recovery curves obtained in the absence and in the presence of exchange reagents [1, 56, 67, 68, 71]. The major advantages of SR-EPR compared to

cw power saturation (Sect. 3.2) are that no assumptions regarding the magnitude of the spin–spin relaxation time T_{2e} or the homogeneous nature of the resonance line are necessary, and that spin label side chain accessibilities towards the exchange reagents are expressed in an instrument-independent way without the need for calibration of $\Delta P'_{1/2}$ values with reference samples. Moreover, in cases where multiple spin populations are present (see also Sect. 2.3), the corresponding T_{1e} values and accessibilities can be determined by SR-EPR. In contrast, cw power saturation can only provide an average accessibility for all components present in the cw EPR spectrum, and moreover, this average value will be biased towards the most mobile component as it dominates the amplitude of the resonance lines.

The amplitude f of the SR-EPR signal observed on the central resonance line of a nitroxide spectrum comprising a single component in the presence of an exchange reagent can be expressed as [72]:

$$\begin{aligned} f = {} & A_1 \mathrm{e}^{-(2W_\mathrm{e}-2W_\mathrm{ex})\,t} + A_2 \mathrm{e}^{-(2W_\mathrm{e}+2W_\mathrm{ex}+3W_\mathrm{n})\,t} \\ & + A_3 \mathrm{e}^{-(2W_\mathrm{e}+2W_\mathrm{ex}+2W_\mathrm{R})\,t} + A_4 \mathrm{e}^{-(2W_\mathrm{e}+2W_\mathrm{ex}+3W_\mathrm{n}+2W_\mathrm{R})\,t} + \mathrm{H.O.T.}, \end{aligned} \tag{20}$$

where W_e is the electron spin–lattice relaxation rate, W_n is the ^{14}N nuclear spin–lattice relaxation rate, W_R is the rotational diffusion rate of the nitroxide and *H.O.T.* are higher order terms [71, 73]. The relaxation rates in this equation are derived from the corresponding relaxation times according to $2W_\mathrm{e} = T_\mathrm{1e}^{-1}$, $2W_\mathrm{n} = T_\mathrm{1n}^{-1}$ and $2W_\mathrm{R} = \tau_\mathrm{R}^{-1}$. τ_R is the rotational correlation time of the nitroxide. The decay rate given by the first term of Eq. 20 represents the sum of the electron relaxation rate and the exchange rate. The rate for the other components is further increased by contributions from nuclear relaxation and rotational correlation rates, but these contributions can be neglected in SR-EPR. The reorientational correlation times for protein-bound nitroxides are of the order of several 100 ps to usually not more than 10–20 ns. For correlation times in this range, W_n is of the order of 10^7 s^{-1} [74]. Therefore, contributions from both, nuclear relaxation and reorientation, to saturation recovery effectively decay within the spectrometer dead time. The dead time is usually in the range of 50–100 ns, and W_e and W_ex, both being in the order of 10^5 s^{-1}, are the only rates reflected in the recorded recovery curve. Consequently, single exponentials reflecting the first term of Eq. 20 should appropriately describe saturation recovery curves of spin label side chains exhibiting cw EPR spectra consisting of only a single spectral component.

Figure 10 shows saturation recovery curves for T4L labelled at positions 131 and 133 [72]. It is obvious that the presence of exchange reagents influences the spin–lattice relaxation time T_{1e}. Qualitatively, residue 131 exhibits similar accessibility for oxygen and NiEDDA, whereas residue 133 is accessible to oxygen to a much lesser extent compared to residue 131, and not accessible for NiEDDA. With T4L being a soluble protein, one can deduce from the SR data that residue 131 is surface exposed, whereas residue 133 is partially buried in the interior of the protein, rendering it slightly accessible for the relatively small O_2 molecules but not accessible for the larger Ni complex.

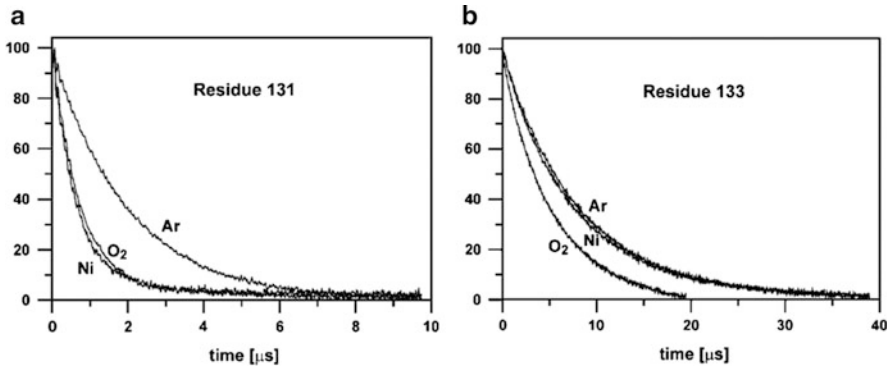

Fig. 10 Nitroxide accessibility determined by saturation recovery EPR. Saturation curves for T4L labelled at positions 131 (**a**) and 133 (**b**). Experiments have been performed under argon atmosphere (Ar), in the presence of oxygen in equilibrium with air (O_2) , and in the presence of 3 mM NiEDDA (Ni) [72] (Copyright 2005 Elsevier. Used with permission from Janusz Pyka, Jan Ilnicki, Christian Altenbach, Wayne L. Hubbell and Wojciech Fronciaz, Accessibility and dynamics of nitroxide side chains in T4 lysozyme measured by saturation recovery EPR, Biophysical Journal and Elsevier)

Furthermore, the T_1-relaxation enhancement induced by molecular oxygen diffusing in the hydrophobic core of lipid bilayers can be used to determine transmembrane profiles that reveal the immersion depth of the position under investigation in the lipid bilayer. Figure 11 shows an example from a recent study on spin-labelled DOXYL-lipids and spin-labelled peptides [75].

Moreover, saturation recovery can be used to distinguish between rotamer exchange for the spin label side chain (~0.1–1 μs range) and conformational exchange of the protein, which is at least one order of magnitude slower [47] (Sect. 2.4.2).

4 Polarity and Proticity of the Nitroxide Micro-environment

The polarity and the proticity (the propensity to form hydrogen bonds) in the immediate environment of a spin label side chain can provide information about the structural and topological details of a protein enhancing the understanding of specific biological processes on the molecular level. For example, scanning the polarity and proticity of the spin label micro-environment in ion channels can allow monitoring of the water density and its variation upon conformational changes and may enable identification of the hydrophobic barriers along such channels in transmembrane proteins.

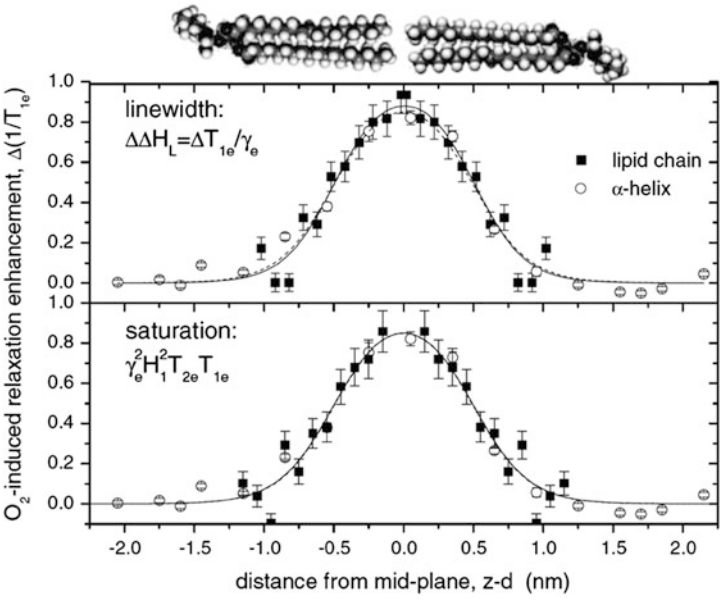

Fig. 11 Transmembrane profiles of T_1-relaxation enhancement induced by molecular oxygen (with respect to samples measured in the absence of oxygen or other relaxing agents) for spin-labelled lipids mixed with PC lipids (*solid squares*) and spin-labelled model peptides (*open circles* with *inserted error bars*). *Upper panel*: Relaxation enhancements for spin-labelled lipids determined from the linewidth of the central resonance line, and peptide relaxation enhancements determined by saturation recovery EPR. *Bottom panel*: Lipid relaxation enhancements from power saturation measurements compared to peptide relaxation enhancements from saturation recovery EPR [75] (Copyright 2009 Springer. Used with permission from Derek Marsh, Spin-label EPR for determining polarity and proticity in biomolecular assemblies: Transmembrane proteins, Applied Magnetic Resonance and Springer)

4.1 Theoretical Background

The polarity and proticity of the nitroxide spin label micro-environment can be determined from EPR spectra by means of the hyperfine component A_{zz} and the $\boldsymbol{g}$ tensor component g_{xx}.

In general, a polar environment shifts the tensor component A_{zz} to higher values, whereas the tensor component g_{xx} is decreased. Theoretically, both tensor components should exhibit a linear dependency on the spin density in the π-orbital of the oxygen atom of the nitroxide group, ρ_π^{O}. The hyperfine tensor component A_{zz} is given by ([122]):

$$A_{zz} = Q_\pi^{\mathrm{N}} \rho_\pi^{\mathrm{N}}. \tag{21}$$

The linear dependency of A_{zz} from ρ_π^{O} arises from the sum condition

$$\rho_\pi^{\mathrm{O}} + \rho_\pi^{\mathrm{N}} \cong 1, \tag{22}$$

following from the fact that to a good approximation the spin density is fully confined to the nitroxide group.

Also the g tensor component g_{xx} is directly proportional to ρ_π^{O} but exhibits an additional dependency on the specific properties of the lone-pair orbitals on the oxygen atom of the nitroxide group, originating from an approximate expression for g_{xx} of organic π-radicals [76]:

$$g_{xx} \cong g_{\mathrm{e}} + \frac{2\,\zeta(O)\,\rho_\pi^{\mathrm{O}}\,c_{ny}^2}{\Delta E_{n\pi*}}, \tag{23}$$

where $g_{\mathrm{e}} = 2.0023$ is the g value of the free electron, ζ(O) is the oxygen spin–orbit coupling parameter, ρ_π^{O} is the π spin density in the $2p_z$ atomic orbital of the oxygen, c_{ny} is the LCAO coefficient of the $2p_y$ atomic orbital which contributes to the oxygen lone-pair molecular orbital, and $\Delta E_{n\pi*} = E_{\pi*} - E_n$ is the excitation energy for the $n \rightarrow \pi^*$ transition.

The dependency of ρ_π^{O} on the polarity of the immediate environment of the nitroxide arises from the variation of ρ_π^{N}, which in turn is caused by the interaction of the permanent electric dipole induced by the charge displacement in the NO π bond with the intermolecular fields in the vicinity of this bond. These fields can be described by an average local field E_{local}, where $E_{\mathrm{local},x}$ is the field component along the NO bond [122, 123]:

$$\Delta\rho_\pi^{\mathrm{N}} = C_1\,E_{\mathrm{local},x} \quad (C_1 > 0). \tag{24}$$

Furthermore, it is known that the lone-pair orbital energy E_{n} is sensitive to the polarity of the environment, and particularly to hydrogen bonding of the lone-pairs to water and/or polar amino acid side chains in its vicinity. In addition, hydrogen bonding can affect the electron population of the lone-pair orbitals, c_{ny}^2.

Consequently, changes in $\delta\Delta g_{xx} = \delta(g_{xx} - g_{\mathrm{e}})$ caused by the local environment of the nitroxide have to be described by three contributions:

$$\frac{\delta\Delta g_{xx}}{\Delta g_{xx}} \cong -\frac{\rho_\pi^{\mathrm{N}}}{\rho_\pi^{\mathrm{O}}}\frac{\delta A_{zz}}{A_{zz}} - \frac{\delta\Delta E_{n\pi*}}{\Delta E_{n\pi*}} + \frac{\delta c_{ny}^2}{c_{ny}^2}. \tag{25}$$

The first term of the above equation correctly predicts the negative slope observed in g_{xx} versus A_{zz} plots [77–79, 122], while the last two terms account for additional vertical displacement in the plots depending on the proticity of the nitroxide micro-environment.

4.2 Polarity and Proticity Investigated by High-Field EPR

The hyperfine tensor component A_{zz} can be obtained by analysis of EPR spectra recorded at X-band (9.5 GHz/0.34 T) frequencies and temperatures below 200 K. At these temperatures the reorientational motion of a spin label side chain is slowed down such that the corresponding correlation time exceeds 100 ns [80], and the nitroxide may be considered as immobilized on the EPR timescale. Small amplitude librational motions are still present, but can be usually neglected as the measured A_{zz} values deviate by less than 2% from their rigid limit values due to partial motional averaging [80]. Higher precision of the determined tensor values can be obtained by further decreasing the temperature.

Increasing the microwave frequencies from X-band to higher bands provides the spectral resolution necessary to resolve the anisotropy of the g tensor and to determine g_{xx}. For nitroxide spin labels, the g anisotropy is already well resolved at W-band (95 GHz/3.4 T). As an example, Fig. 12 shows the polarity analysis for a set of spin-labelled *Np*HtrII mutants (positions 88–94) in the *Np*SRII/*Np*HtrII complex reconstituted in purple membrane lipids [81]. The variation of g_{xx} and A_{zz} along this sequence is nicely resolved and reflects the different water densities on both sides of this helix. Furthermore this plot reveals the relation between the average g_{xx} and A_{zz} values.

From the low-temperature W-band EPR spectrum of *Np*SRII-V17R1 shown in Fig. 12c the presence of different spectral components characterized by different g_{xx} values is obvious. Such a composite nature of g_{xx} in high-field EPR spectra was already recognized earlier, for example for spin-labelled lipids [83] and for spin-labelled azurin proteins [84]. In both cases, it was suggested that two nitroxide populations characterized by the presence or absence of a hydrogen bond to the nitroxide group account for these observations. Indeed, utilizing pulsed ENDOR at 130 GHz, the presence of a hydrogen bond to the nitroxide group of 5-doxyl stearic acid causing a reduction in g_{xx} was confirmed, and it was possible to determine the geometry of this hydrogen bond [83].

The origin of this heterogeneity in the g_{xx} region was analysed in further detail, employing multi-frequency EPR at 95, 275, and 360 GHz [85]. These experiments revealed the existence of three different spectral components. Figure 13 shows the low-temperature high-field EPR spectra for *Np*SRII-V17R1 determined at 95 and 275 GHz (Fig. 13a), and for *Np*SRII/*Np*HtrII-L93R1 determined at 95 GHz and 360 GHz (Fig. 13b).

In both cases, the three components already visible at 95 GHz are nicely resolved at 275 or 360 GHz. In Fig. 13c the three g_{xx} values obtained from the spectral fits (g_{xx}^i, $i = 0, 1, 2$) are plotted versus the average hyperfine tensor component $\bar{A}_{zz}$. The g_{xx}^i values fall into three distinct regions of the plot, showing a clear correlation with the $\bar{A}_{zz}$ values. The spectral components are separated by $\Delta g \sim 4 \times 10^{-4}$,

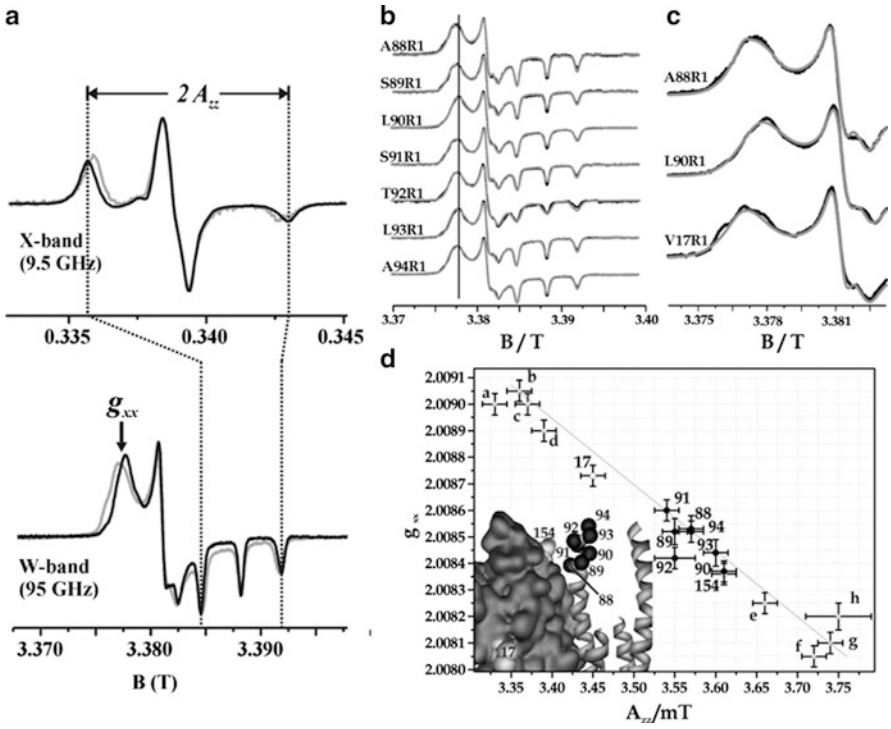

Fig. 12 W-band polarity analysis for a set of spin-labelled *Np*HtrII mutants (positions 88–94) in the *Np*SRII/*Np*HtrII complex reconstituted in purple membrane lipids. (Data taken from [81]). (**a**) Determination of A_{zz} and g_{xx} from X- and W-band low-temperature (175 K) spectra. (**b**) W-band EPR (175 K) spectra (*black traces*) and calculated line shapes (*grey traces*) (DIPFIT) [82]. The *vertical line* marks the g_{xx} position of L90R1. (**c**) Comparison of the low-field region of the spectra (*black*) for positions A88R1 and L90R1 in *Np*HtrII, and residue V17R1 in *Np*SRII located in the centre of the lipid bilayer. Corresponding calculated spectra using an average g_{xx} are shown in *grey*. (**d**) Plot of g_{xx} vs. A_{zz} for the analysed spin label positions (*Np*HtrII: 88–94, *Np*SRII: 17 & 154). For comparison, several points derived from the literature are shown representing the apolar/aprotic and the polar/protic extremes of g_{xx} vs. A_{zz}: (*a*) MTSSL in toluene/polystyrene 9:1 mixture (Q-band); (*b*) MTSSL in toluene/polystyrene 9:1 mixture (W-band); (*c*) MTSSL in ethyl acetate (W-band, $T = 140$ K); (*d*) MTSSL-β-mercaptoethanol in ethyl acetate (W-band); (*e*) MTSSL in water/ethanol 1:1 mixture (W-band); (*f*) MTSSL in water/ethanol 1:1 mixture (Q-band); (*g*) MTSSL in water with 10% glycerol (v/v) (W-band, T=175 K); (*h*) MTSSL-β-mercaptoethanol in water with 10% glycerol (v/v) (W-band). For corresponding references see Brutlach et al. [81]. The *inset* shows the localization of the respective spin-labelled *Np*HtrII and *Np*SRII variants in a structural model of the complex

corresponding to the theoretical value expected for the addition of one hydrogen bond to the nitroxide group. Consequently, the authors of this study suggested the three spectral components to correspond to nitroxide populations exhibiting 0, 1, or 2 hydrogen bonds (with the largest g^i_{xx} corresponding to 2 hydrogen bonds).

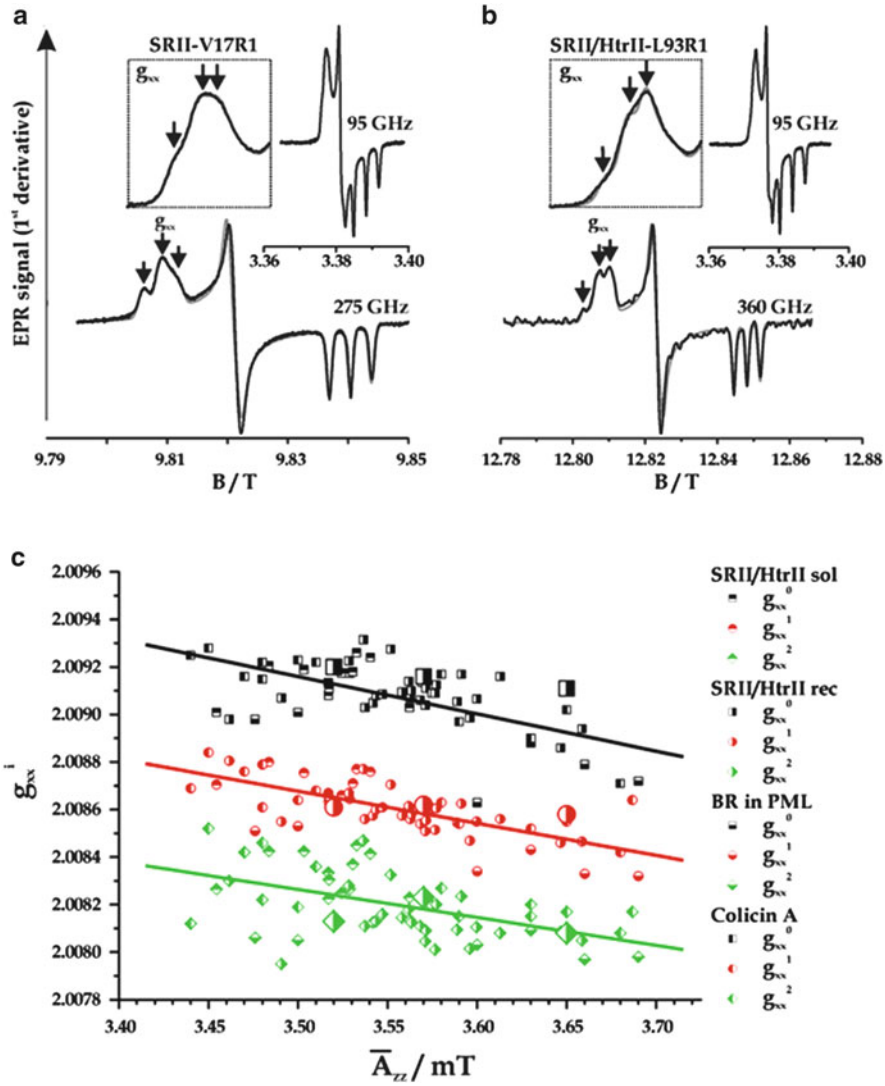

Fig. 13 Polarity/proticity analysis performed at 95, 275 and 360 GHz to resolve the g_{xx} heterogeneity. (Data taken from [85]). (**a**) Spectra of *Np*SRII-V17R1 recorded at 95 GHz/170 K (*upper panel*) and 275 GHz/70 K (*bottom panel*). (**b**) Spectra of NpSRII/NpHtrII-L93R1 recorded at 95 GHz/175 K (*upper panel*), and 360 GHz/160 K (*bottom panel*). *Black lines* are the experimental data, and *grey lines* are the corresponding simulated spectra. *Insets* in the *upper panels* show the enlarged g_{xx} region of the 95 GHz spectra and the corresponding fits. (**c**) Plot of g_{xx} versus $\bar{A}_{zz}$ obtained by fitting of the EPR spectra recorded at 95 (small symbols), 275 and 360 GHz (large symbols) of a series of different spin-labelled proteins (see legend). The three spectral components characterized by their respective g_{xx} values (indices 0, 1 and 2) are shown as *black*, *red* and *green* symbols

5 Inter-nitroxide Distance Measurements

If two spin label side chains are introduced into a biomolecule or two singly spin-labelled molecules are in a stable macromolecular complex, the distance between the two labels can be determined through quantification of their spin–spin interaction, thus providing valuable structural information.

The spin–spin interaction is composed of contributions from the static dipolar interaction, modulation of the dipolar interaction by the residual motion of the spin label side chains, and exchange interaction. The theoretical background of dipolar coupling between electrons can be found in [86]. The static dipolar interaction in an unordered, immobilized sample leads to detectable broadening of rigid-limit (low-temperature) cw EPR spectra if the interspin distance is <2 nm (see Fig. 14a). Quantification of the interspin distance in this case can be carried out by a detailed lineshape analysis using spectra convolution or deconvolution techniques for spectra measured below 200 K [82, 87, 88] or in solutions of high viscosity [89]. Software packages are available for interspin distance determination from cw EPR spectra, e.g. the program DIPFIT [82, 87], that considers a Gaussian distance distribution and variable contributions of singly labelled species, or the software "Short Distances" by C. Altenbach [90] that considers multiple Gaussian distributions also and arbitrary distributions applying Tikhonov regularization procedures. Figure 14c shows two examples, where interspin distances have been determined from cw EPR spectra recorded at 160 K or by DEER spectra recorded at 50 K. Numerous examples from the literature underline the applicability of cw EPR for short-range distance determinations [88, 89, 91–96].

Besides the use of spectra convolution and deconvolution techniques, interspin distances can often be determined also from empirical or semi-empirical parameters. As long as exchange interaction due to partial overlap of the nitroxide π-orbitals can be neglected spectral amplitude ratios [126] or differences of the spectral second moments of singly and doubly spin-labelled samples can be used for distance quantification. In the latter case the interspin distance is given by

$$r = 2.32 \cdot \left\langle \Delta H^2 \cdot 10^8 \right\rangle^{-\frac{1}{6}} \text{nm}, \tag{26}$$

with ΔH^2 being the difference of the second moments between and doubly spin-labelled samples (see Eqs. 2 and 3) given in T^{-1}. The upper distance limit for the use of this method is 1.5–1.7 nm and the reliability of the distance calculated strongly depends on the quality of the spectra, especially of the baseline. In the distance range <0.8 nm partial overlapping of the nitroxide π-orbitals leads to exchange interactions that can no longer be neglected in the cw EPR spectra, rendering interspin distance quantification in this distance range difficult [97, 98]. In such cases accurate distance measurements can be carried out by determination of the amplitude of the half-field resonances [99] that are not affected by exchange interactions. In the presence of dipolar interaction the probability of these "forbidden" transitions is strongly increased and the amplitude of this resonance is proportional to r^{-6}. The use of the

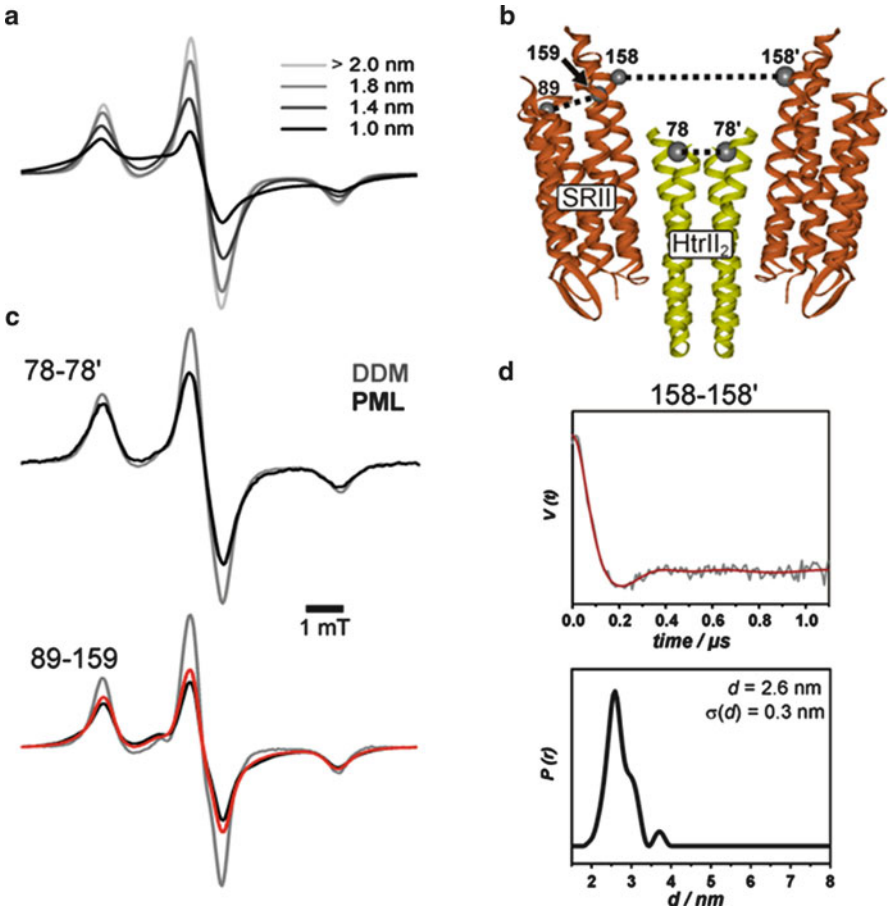

Fig. 14 Interspin distance measurements. (**a**) Simulated powder spectra (normalized to constant spin number) for different interspin distances (DIPFIT) [82]. Simulation parameters: $g_{xx} = 2.0086$, $g_{yy} = 2.0066$, $g_{zz} = 2.0026$, $A_{xx} = 0.52$ mT, $A_{yy} = 0.45$ mT, and $A_{zz} = 3.5$ mT. The spectra were convoluted with a field-independent lineshape function composed of a superposition of 44% Lorentzian and 56% Gaussian of 0.33 and 0.39 mT width, respectively, and a fraction of a singly spin-labelled component of 30%. (**b**) X-ray structure of the 2:2 SRII-HtrII complex (PDB 1H2S). C_β atoms of the labelled positions are shown as spheres. (**c**) (*top*) Cw EPR (160 K) of HtrII157-V78R1 solubilized in DDM (*grey*) or reconstituted in PML (*black*) in the absence of SRII. The interspin distance obtained in the reconstituted sample is 1.3 ($\pm$ 0.2) nm (singly labelled fraction = 57%; data from [124]. (*bottom*) Cw EPR (160K) of SRII-L89R1/L159R1 in the receptor ground state (*black*) and in the trapped signalling state (*red*). Comparison with the sum of the spectra of the corresponding singly labelled samples (*grey*) reveals line broadening due to spin–spin interaction. (Data from [3] (**d**) (*upper panel*) DEER time domain data after background correction for SRII-S158R1. (*bottom panel*) Distance distribution obtained by Tikhonov regularization using DeerAnalysis 2008 [125] revealing a mean distance of 2.6 nm

half-field transitions allows accurate distance determination (error < 0.05 nm) for distances below 1 nm [100].

Advances in pulse EPR expanded the accessible distance range up to 8 nm [86, 101, 102], and, utilizing fully perdeuterated systems (including perdeuterated solvents and biomolecules), in favourable cases even up to 10 nm or more [103]. Nowadays, two major protocols are successfully applied, 4-pulse double electron–electron resonance (DEER) or pulsed electron double resonance (PELDOR), and double quantum coherence (DQC) [86, 104]. Combining cw and pulse EPR techniques, and taking into account borderline effects in the region of 1.6–1.9 nm [105], provides means to determine interspin distances in the range of 1–8 nm, thereby covering the most important distance regime necessary for structural investigations on proteins, nucleic acids or complexes thereof. Figure 14d shows an example of interspin distance measurements by DEER spectroscopy, where the distance between SRII-S158R1 in the 2:2 complex (see Fig. 14b) has been determined. A detailed review about distance measurements by pulse EPR as well as a chapter about the interpretation of dipolar EPR data in terms of protein structure can be found in volume 1 of this series [86, 106].

6 Application to Membrane Proteins

In the following, examples are given where SDSL EPR has been applied for the investigation of membrane proteins, addressing structural as well as the dynamic properties of the systems under investigation.

6.1 The Photoreceptor/Transducer Complex SRII/HtrII

In haloarchaea like *Natronomonas pharaonis* phototaxis is mediated by transducer proteins (Htrs) that share structural and functional similarities with a variety of chemoreceptors reactive to attractant and repellent stimuli [107, 108]. Cognate sensor proteins, sensory rhodopsins (SRs), which belong to the seven-transmembrane helices protein family, are responsible for recognition of the external stimulus. SDSL and EPR spectroscopy on the sensory rhodopsin II/transducer (*Np*SRII/*Np*HtrII) complex from *Natronomonas pharaonis* have yielded insights into the structure of the complex, the mechanisms of signal perception and signal transduction across the membrane and of the subsequent information transfer within the transducer protein towards the components of the intracellular signalling pathway [109]. Some examples have already been given in Sects. 2–5 of this chapter, i.e. a mobility analysis of the C-terminal end of helix F in *Np*SRII (Sect. 2.1), an accessibility analysis of the membrane-adjacent region of *N*pHtrII, revealing an α-helical structure in this region (Sect. 3.2), and a polarity/proticity study of a part of the same region in *Np*HtrII (Sect. 4.2).

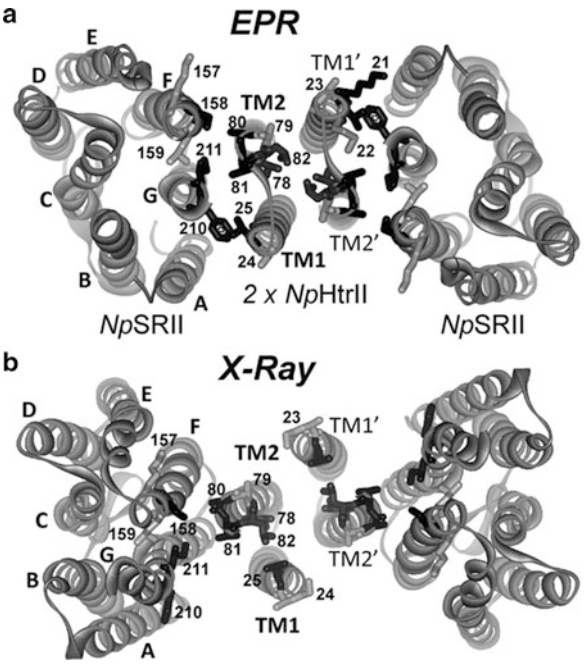

Fig. 15 Membrane topology of the *Np*SRII/*Np*HtrII complex revealed by EPR spectroscopy. (**a**) EPR-based model of the transmembrane region of the complex viewed from the cytoplasmic side [110]. Side chains mutated to cysteines and subsequently spin labelled are shown in stick representation. (**b**) Crystal structure of the complex (PDB: 1H2S)

6.1.1 A Model of the Membrane-Embedded Part of the Complex Based on Interspin Distance Constraints

Based on the mobility analyses of singly spin-labelled variants and interspin distances determined for 26 different pairs of spin label side chains introduced into the cytoplasmic portions of *Np*SRII and *Np*HtrII, the arrangement of the transmembrane domains of this complex was modelled (Fig. 15a) [110].

Direct comparison of the EPR model with the crystal structure obtained later ([70], see Fig. 15b) emphasizes the consistency of the EPR model with that of the X-ray structure, especially, if the general topology, the location, and the relative orientation of the transmembrane helices are considered. Notably, most of the side chain orientations within the complex coincide quite well in the two models, although in the EPR model the bacteriorhodopsin structure had to be used as a template for *Np*SRII, since the *Np*SRII structure was not known.

6.1.2 Dynamics of the HAMP Domain

A detailed SDSL EPR study on the first *Np*HtrII HAMP domain investigating the structural and dynamic features revealed that this domain is engaged in a

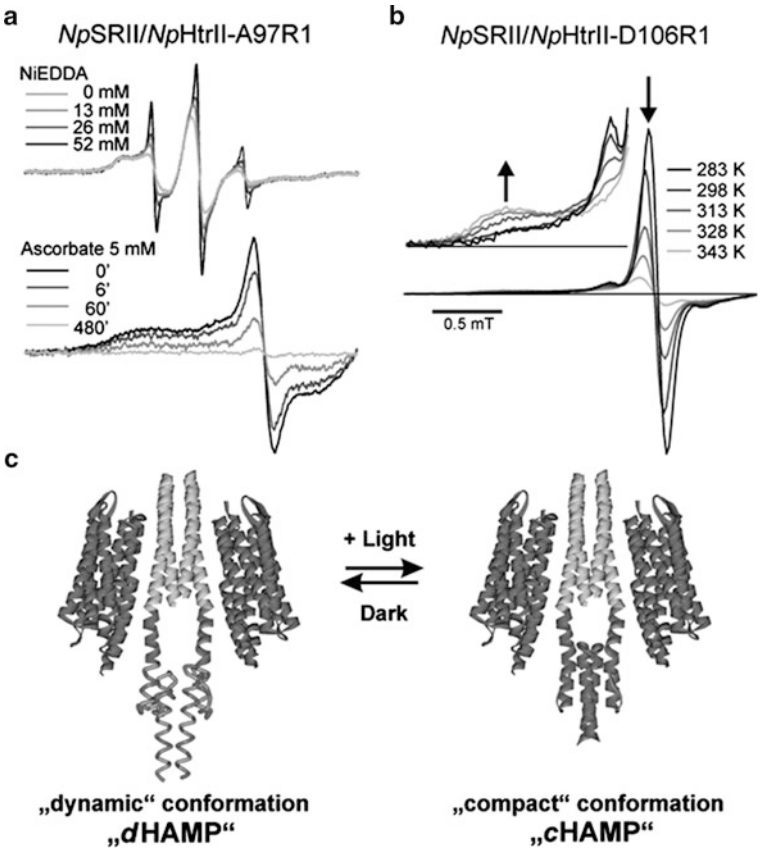

Fig. 16 Dynamics of the first *Np*HtrII HAMP domain. (**a**) Effects of reversible and irreversible quenching on the two spectral components of *Np*SRII/*Np*HtrII$_{157}$-A97R1. *Upper panel*: Effects of increasing NiEDDA concentrations. *Bottom panel*: Time evolution of ascorbate-induced spectral changes. (**b**) Temperature-dependent spectral changes of the low-field line for *Np*SRII/*Np*HtrII$_{157}$-D106R1. *Arrows* indicate the direction of the spectral changes upon a decrease in temperature: The equilibrium is shifted towards the compact conformation. (**c**) Models of the dynamic and compact HAMP conformations. The compact conformation has been modelled according to the NMR structure of the HAMP domain of Af1503 from *Archaeoglobus fulgidus* [112]. Light activation of *Np*SRII shifts the equilibrium towards the compact state [111]

"two-state" equilibrium between a highly dynamic (dHAMP) and a compact (cHAMP) conformation [111] (Fig. 16). The structural properties of the cHAMP conformation as deduced from spin label side chain mobility, accessibility and intra-transducer-dimer distance data have been found to be in line with a four-helical bundle model of the HAMP domain from *Archaeoglobus fulgidus* obtained by NMR.

To investigate the origin of the observed two spectral components in terms of the two-state equilibrium, titration experiments with NiEDDA and ascorbate (Fig. 16a) were performed. NiEDDA reversibly decreases the nitroxide relaxation times due to

exchange interaction with the spin label. In contrast, ascorbate reduces the nitroxide irreversibly. In both cases the reaction only takes place for nitroxides accessible from the water phase. The addition of 52 mM NiEDDA leads to complete suppression of the more mobile component corresponding to the dHAMP conformation. In contrast, ascorbate leads to an overall decrease of the spectral intensity, leaving the ratio between the two spectral components constant. These results have proven the existence of an equilibrium between the c- and dHAMP conformations with interconversion rates smaller than the magnetic relaxation rates. Furthermore, the temperature dependence of the spectra was analysed (Fig. 16b). Decreasing the temperature resulted in a shift of the equilibrium towards the cHAMP conformation. From the fitting of simulated spectra to the experimental ones it was possible to determine the fractions of the two components in each spectrum and the data could be used to calculate the free Gibbs energy and the equilibrium constant for the transition between the two conformations [111]. The agreement of the equilibrium constants determined for numerous positions in different segments of the HAMP domain further corroborated the hypothesis of a two-state equilibrium between the two, cHAMP and dHAMP, conformations (Fig. 16c). Time-resolved detection of changes in the spin label mobility showed that light activation of *Np*SRII shifts the equilibrium towards the compact cHAMP state [109].

6.2 The Maltose ABC Importer $MalFGK_2$

ABC transporters are a class of ubiquitous membrane proteins which use the energy of ATP hydrolysis to transport solutes across membranes [113]. ABC transporters are modular protein complexes comprising of two nucleotide-binding domains (NBDs) and two transmembrane domains (Fig. 17a). In prokaryotic variants of this complex an additional periplasmic substrate-binding protein is required for function. The present structural models of ABC transporters suggest a functional mechanism in which translocation of the substrate is achieved by alternating access of the translocation pore to the extra- and intracellular space, driven by ATP hydrolysis in the NBDs [115]. By far the best characterized representative of this protein class is the enterobacterial maltose transporter $MalFGK_2$. For this system crystal structures are available not only for different conformations of the isolated NBD dimer $MalK_2$ [116] but also for the complete $MalFGK_2$ unit with the bound maltose-binding protein MalE [117]. Nevertheless, the mechanistic details of how ATP hydrolysis is coupled to substrate translocation, and the function of MalE in the catalytic cycle, was still obscure.

Grote et al. addressed these questions in two studies using cw and pulse EPR spectroscopy [114, 118]. They performed an analysis of conformational changes of the NBD subunits, $MalK_2$, during the transport cycle. Their data support a slightly modified "tweezers-like" model of closure and reopening of the NBDs during the catalytic cycle. They furthermore show that this motion only occurs with MalE bound to the complex. [118]. Distance measurements between pairs of spin labels

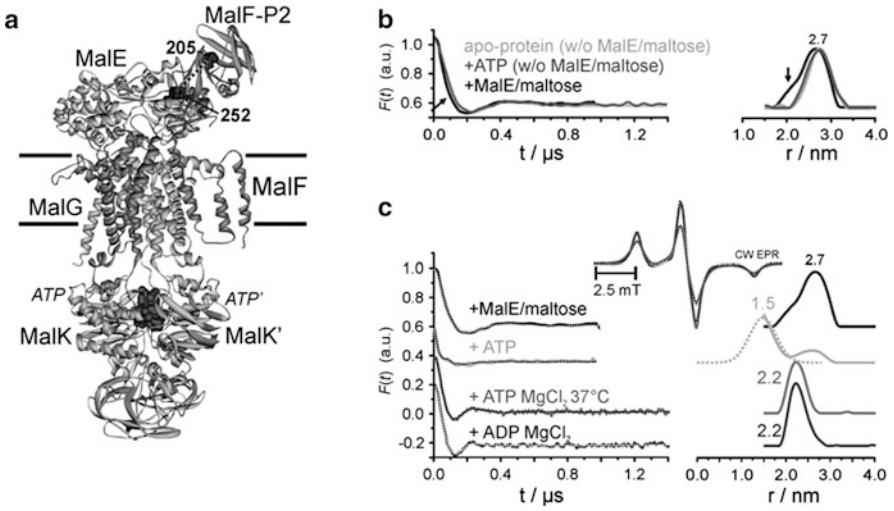

Fig. 17 Conformational changes in $MalFGK_2$ during the ATPase cycle monitored by measurements of interspin distances. (Data taken from [114]). (**a**) $MalFGK_2$-E crystal structure (PDB: 2R6G). Residues 205 and 252 that were exchanged by cysteines and spin labelled are indicated. (**b**) Effects of ATP and MalE/maltose on the MalF-P2 conformation. *Left panel*: background corrected DEER data. *Right panel*: corresponding distance distributions. The *arrows* in both panels indicate changes induced by MalE/maltose. (**c**) Effects of different nucleotides on the MalF-P2 conformation in the presence of MalE/maltose. In addition to the DEER experiments, low-temperature cw EPR spectra were recorded to determine the distance in the presence of ATP, see top spectra; *dark grey*, ADP bound state, no broadening; *light grey*, ATP bound state. Simulations (*dotted lines*) revealed a Gaussian distance distribution centred at 1.5 nm in the presence of ATP, which is superimposed to the DEER-derived distribution in the *right panel* (*dotted distance distribution*)

introduced into the periplasmic segment MalF-P2 at positions 205 and 252 (Fig. 17b, c) revealed transmembrane communication between the NBDs and the periplasmic domain of the protein. Three conformations of MalF-P2 could be discriminated, corresponding to defined steps in the ATPase cycle of $MalK_2$ [114]. Figure 17c shows the 205R1-252R1 inter-nitroxide distance changes observed by cw and DEER EPR spectroscopy in the presence of MalE/maltose and different nucleotides. The distance of 2.7 nm (obtained by DEER spectroscopy) observed for the nucleotide-free state decreases to 1.5 nm (measured by low temperature cw EPR) upon ATP binding (ATP hydrolysis was inhibited by EDTA) and increases again to 2.2 nm upon ATP hydrolysis. The identical distance distributions for the ATP and ADP forms in the presence of $MgCl_2$ prove that the latter conformational change is indeed a consequence of ATP hydrolysis. Based on their findings, the authors suggest a dynamic model for the coupling of substrate translocation and ATP hydrolysis. According to this model, binding of MalE/maltose and ATP modulate the equilibrium between different conformers of the transporter.

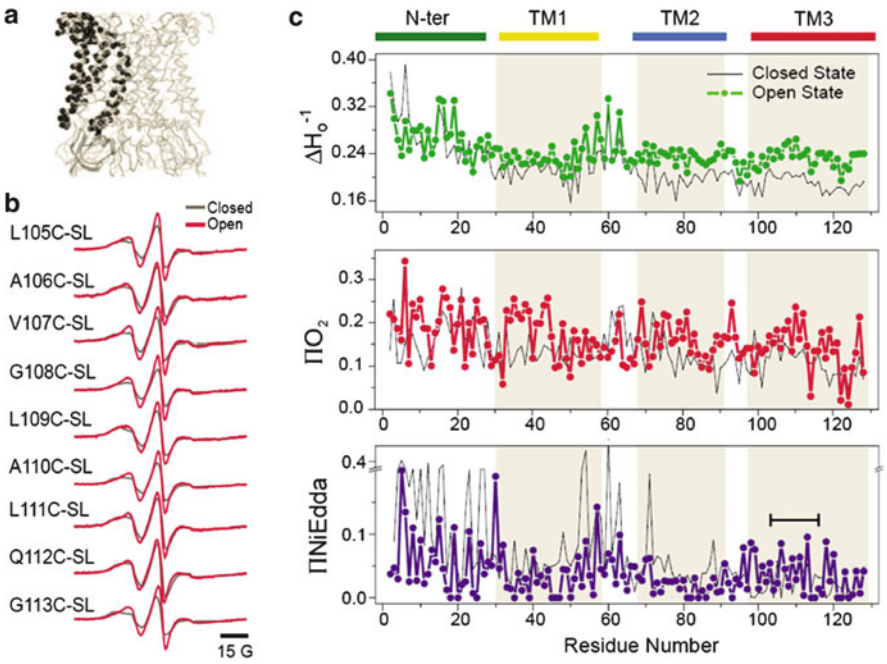

Fig. 18 Structural alteration upon MscS channel opening. (**a**) Crystal structure of the MscS pentamer, showing the sites subjected to SDSL as *black spheres* on one of the protomers. (**b**) Selected room temperature X-band EPR for residues on TM3 in the closed (*grey*) and open channel conformation (*red*). (**c**) Profiles for mobility (*upper panel*, inverse of centre linewidth) and accessibilities towards molecular oxygen (*middle panel*) and NiEDDA (*bottom panel*) for the closed state (*black*) and the open state (*green*, *red* and *blue*, respectively). Secondary structure elements are indicated at the top [120] (Copyright 2008 The American Association for the Advancement of Science. Used with permission from Valeria Vásquez, Marcos Sotomayor, Julio Cordeo-Morales, Klaus Schulten and Eduardo Perozo, A structural mechanism for MscS gating in lipid bilayers, Science and The American Association for the Advancement of Science)

6.3 *The Mechanosensitive Channel of Small Conductance*

In the past years, the MscS was subjected to extensive investigations using SDSL EPR spectroscopy [119] [120]. MscS plays a central role in the response of prokaryotes to osmotic stress and forms pentamers in lipid bilayers. Although crystal structures of MscS and its relative MscL (mechanosensitive channel of large conductance) have been determined, lack of structural information for the N-terminus and for the open channel conformation impeded establishing a mechanism for gating of MscS in lipid bilayers. Perozo and co-workers performed several studies on the three-dimensional architecture and the structural mechanism of MscS gating [119] [120]. As an example, Fig. 18 depicts mobility and accessibility data for the region from MscS's N-terminus up to the third transmembrane segment (TM3). It is obvious that channel opening leads to significant changes in the

parameters monitored, i.e. a systematic increase in the spin label side chain mobilities for transmembrane segments TM2 and TM3, as well as changes in the accessibilities towards oxygen (= accessibility from the lipid phase) for the whole sequence under investigation and towards NiEDDA (= accessibility from the bulk water phase) especially for the N-terminal region and the TM1-TM2 hairpin. For this study, the open conformation of MscS was trapped by modification of the pressure profile across the lipid bilayer through asymmetric incorporation of lysophospholipids.

Detailed computational analyses of the data allowed the authors to suggest a structural mechanism for MscS gating. According to this model, transition from the closed to the open channel state is characterized by a downward tilt of the TM1-TM2 hairpin and an expansion, tilt and rotation of TM3.

7 Summary and Outlook

SDSL in combination with EPR spectroscopy has become a powerful tool for the investigation of the structural and dynamical properties of biomolecules under native-like conditions, in particular of membrane proteins where other structural methods often fail. The methodology can provide information about the spin label side chain mobility, solvent accessibility, the polarity of its immediate environment and intra- or intermolecular distances between two labels. In the past years several new techniques, e.g. osmolyte perturbation and high-pressure EPR have been developed, thereby further extending the possible use of SDSL EPR for investigations of membrane proteins. Future developments, for example the design of spin labels for in vivo applications will further enhance the possible use of this technique in membrane protein research.

Acknowledgements Part of this work was supported by the Deutsche Forschungsgemeinschaft (SFB 944/P10).

References

1. Altenbach C, Flitsch SL, Khorana HG, Hubbell WL (1989) Structural studies on transmembrane proteins, 2: spin labeling of bacteriorhodopsin mutants at unique cysteines. Biochemistry 28:7806–7812
2. Altenbach C, Marti T, Khorana HG, Hubbell WL (1990) Transmembrane protein structure: spin labeling of bacteriorhodopsin mutants. Science 248:1088–1092
3. Bordignon E, Steinhoff HJ (2007) Membrane protein structure and dynamics studied by site-directed spin labeling ESR. In: Hemminga MA, Berliner LJ (eds) ESR spectroscopy in membrane biophysics. Springer, New York, pp 129–164
4. Hubbell WL, Mchaourab HS, Altenbach C, Lietzow MA (1996) Watching proteins move using site-directed spin labeling. Structure 4:779–783

5. Hubbell WL, Gross A, Langen R, Lietzow MA (1998) Recent advances in site-directed spin labeling of proteins. Curr Opin Struct Biol 8:649–656
6. Klare JP, Steinhoff HJ (2009) Spin labeling EPR. Photosynth Res 102:377–390
7. Klug CS, Feix JB (2008) Methods and applications of site-directed spin labeling EPR spectroscopy. In: Correia JJ, Detrich HW (eds) Methods in cell biology. Biophysical tools for biologists, volume one: in vitro techniques. Academic, New York, pp 617–658
8. Berliner LJ (ed) (1976) Spin labeling: theory and applications. Academic, New York
9. Berliner LJ (ed) (1979) Spin labeling II: theory and applications. Academic, New York
10. Berliner LJ, Reuben J (eds) (1989) Spin labeling theory and applications, Biological magnetic resonance, vol 8. Plenum Press, New York
11. Columbus L, Kalai T, Jekö J, Hideg K, Hubbell WL (2001) Molecular motion of spin labeled side chains in α-helices: analysis by variation of side chain structure. Biochemistry 40:3828–3846
12. Columbus L, Hubbell WL (2002) A new spin on protein dynamics. Trends Biochem Sci 27:288–295
13. Fleissner MR, Cascio D, Hubbell WL (2009) Structural origin of weakly ordered nitroxide motion in spin-labeled proteins. Protein Sci 18:893–908
14. Fleissner MR, Bridges MD, Brooks EK, Cascio D, Kalai T, Hideg K, Hubbell WL (2011) Structure and dynamics of a conformationally constrained nitroxide side chain and applications in EPR spectroscopy. Proc Natl Acad Sci USA 108:16241–16246
15. Mchaourab HS, Lietzow MA, Hideg K, Hubbell WL (1996) Motion of spin-labeled side chains in T4 lysozyme. Correlation with protein structure and dynamics. Biochemistry 35:7692–7704
16. Voet D, Voet JG (2004) Biochemistry, 3rd edn. Wiley, New York
17. Qin PZ, Hideg K, Feigon J, Hubbell WL (2003) Monitoring RNA base structure and dynamics using site-directed spin labeling. Biochemistry 42:6772–6783
18. Luecke H, Schobert B, Lanyi JK, Spudich EN, Spudich JL (2001) Crystal structure of sensory rhodopsin II at 2.4 Å: insights into color tuning and transducer interaction. Science 293:1499–1503
19. Isas JM, Langen R, Haigler HT, Hubbell WL (2002) Structure and dynamics of a helical hairpin and loop region in annexin 12: a site-directed spin labeling study. Biochemistry 41:1464–1473
20. Steinhoff HJ, Hubbell WL (1996) Calculation of electron paramagnetic resonance spectra from Brownian dynamics trajectories: application to nitroxide side chains in proteins. Biophys J 71:2201–2212
21. Beier C, Steinhoff HJ (2006) A structure-based simulation approach for electron paramagnetic resonance spectra using molecular and stochastic dynamics simulations. Biophys J 91:2647–2664
22. Barnes JP, Liang Z, Mchaourab HS, Freed JH, Hubbell WL (1999) A multifrequency electron spin resonance study of T4 lysozyme dynamics. Biophys J 76:3298–3306
23. Borbat PP, Costa-Filho AJ, Earle KA, Moscicki JK, Freed JH (2001) Electron spin resonance in studies of membranes and proteins. Science 291:266–269
24. Freed JH (1976) Theory of slow tumbling ESR spectra for nitroxides. In: Berliner LJ (ed) Spin labeling: theory and applications. Academic, New York, pp 53–132
25. Budil DE, Sale KL, Khairy K, Fajer PG (2006) Calculating slow-motional electron paramagnetic resonance spectra from molecular dynamics using a diffusion operator approach. J Phys Chem A 110:3703–3713
26. DeSensi SC, Rangel DP, Beth AH, Lybrand TP, Hustedt EJ (2008) Simulation of nitroxide electron paramagnetic resonance spectra from Brownian trajectories and molecular dynamics simulations. Biophys J 94:3798–3809
27. Oganesyan VS (2007) A novel approach to the simulation of nitroxide spin label EPR sdpectra from a single truncated dynamical trajectory. J Magn Reson 188:196–205

28. Sezer D, Freed JH, Roux B (2008) Parametrization, molecular dynamics simulation, and calculation of electron spin resonance spectra of a nitroxide spin label on a polyalanine α-helix. J Phys Chem B 112:5755–5767
29. Sezer D, Freed JH, Roux B (2008) Simulating electron spin resonance spectra of nitroxide spin labels from molecular dynamics and stochastic trajectories. J Chem Phys 128:165106–165116
30. Steinhoff HJ, Müller M, Beier C, Pfeiffer M (2000) Molecular dynamics simulation and EPR spectroscopy of nitroxide side chains in bacteriorhodopsin. J Mol Liquids 84:17–27
31. Gajula P, Borovykh IV, Beier C, Shkuropatova T, Gast P, Steinhoff HJ (2007) Spin-labeled photosynthetic reaction centers from *Rhodobacter sphaeroides* studied by electron paramagnetic resonance spectroscopy and molecular dynamics simulation. Appl Magn Reson 31: 167–178
32. Dalton L (ed) (1985) EPR and advanced EPR studies of biological systems. CRC, Boca Raton
33. Budil DE, Earle KA, Freed JH (1993) Full determination of the rotational diffusion tensor by electron paramagnetic resonance at 250 GHz. J Phys Chem 97:1294–1303
34. Urban L (2012) PhD thesis, University of Osnabrück
35. Liang Z, Freed JH (1999) An assessment of the applicability of multifrequency ESR to study the complex dynamics of biomolecules. J Phys Chem B 103:6384–6396
36. Liang Z, Lou Y, Freed JH, Columbus L, Hubbell WL (2004) A multifrequency electron spin resonance study of T4 lysozyme dynamics using the slowly relaxing local structure model. J Phys Chem B 108:17649–17659
37. Zhang Z, Fleissner MR, Tipikin DS, Liang Z, Moscicki JK, Earle KA, Hubbell WL, Freed JH (2010) Multifrequency electron spin resonance study of the dynamics of spin labeled T4 lysozyme. J Phys Chem B 114:5503–5521
38. Polnaszek CF, Freed JH (1975) Electron spin resonance studies of anisotropic ordering, spin relaxation, and slow tumbling in liquid crystalline solvents. J Phys Chem 79:2283–2306
39. Freed JH (1977) Stochastic-molecular theory of spin–relaxation for liquid crystals. J Chem Phys 66:4183–4199
40. Cooper A (1976) Thermodynamic fluctuations in protein molecules. Proc Natl Acad Sci USA 73:2740–2741
41. Frauenfelder H, Parak FG, Young RD (1988) Conformational substates in proteins. Annu Rev Biophys Biophys Chem 17:451–479
42. Frauenfelder H, Sligar SG, Wolynes PG (1991) The energy landscapes and motions of proteins. Science 254:1598–1603
43. Guo ZF, Cascio D, Hideg K, Kalai T, Hubbell WL (2007) Structural determinants of nitroxide motion in spin-labeled proteins: tertiary contact and solvent-inaccessible sites in helix G of T4 lysozyme. Protein Sci 16:1069–1086
44. Guo ZF, Cascio D, Hideg K, Hubbell WL (2008) Structural determinants of nitroxide motion in spin-labeled proteins: solvent-exposed sites in helix B of T4 lysozyme. Protein Sci 17:228–239
45. Langen R, Oh KJ, Cascio D, Hubbell WL (2000) Crystal structures of spin labeled T4 lysozyme mutants: implications for the interpretation of EPR spectra in terms of structure. Biochemistry 39:8396–8405
46. Lopez CJ, Fleissner MR, Guo Z, Kusnetzow AN, Hubbell WL (2009) Osmolyte perturbation reveals conformational equilibria in spin-labeled proteins. Protein Sci 18:1637–1652
47. Bridges MD, Hideg K, Hubbell WL (2010) Resolving conformational and rotameric exchange in spin-labeled proteins using saturation recovery EPR. Appl Magn Reson 37:363–390
48. McCoy J, Hubbell WL (2011) High-pressure EPR reveals conformational equilibria and volumetric properties of spin-labeled proteins. Proc Natl Acad Sci USA 108:1331–1336
49. Yancey PH (2005) Organic osmolytes as compatible, metabolic and counteracting cytoprotectants in high osmolarity and other stresses. J Exp Biol 208:2819–2830

50. Arakawa T, Timasheff SN (1985) The stabilization of proteins by osmolytes. Biophys J 47:411–414
51. Kendrick BS, Chang BS, Arakawa T, Peterson B, Randolph TW, Manning MC, Carpenter JF (1997) Preferential exclusion of sucrose from recombinant interleukin-1 receptor antagonist: role in restricted conformational mobility and compaction of native state. Proc Natl Acad Sci USA 94:11917–11922
52. Cioni P, Bramanti E, Strambini GB (2005) Effects of sucrose on the internal dynamics of azurin. Biophys J 88:4213–4222
53. Timasheff S, Xie G (2003) Preferential interactions of urea with lysozyme and their linkage to protein denaturation. Biophys Chem 105:421–448
54. Lee JC, Timasheff SN (1981) The stabilization of proteins by sucrose. J Biol Chem 256: 7193–7201
55. Huisjen M, Hyde JS (1974) A pulsed EPR spectrometer. Rev Sci Instrum 45:669–675
56. Percival PW, Hyde JS (1975) Pulsed EPR spectrometer, 2. Rev Sci Instrum 46:1522–1529
57. Li H, Akasaka K (2006) Conformational fluctuations of proteins revealed by variable pressure NMR. Biochim Biophys Acta 1764:331–345
58. Akasaka K (2006) Probing conformational fluctuations of proteins by pressure perturbation. Chem Rev 106:1814–1835
59. Bridgman PW (1914) The coagulation of albumen by pressure. J Biol Chem 19:511–512
60. Kauzmann W (1987) Thermodynamics of unfolding. Nature 325:763–764
61. Royer CA (2002) Revisiting volume changes in pressure-induced protein folding. Biochim Biophys Acta 1595:201–209
62. Altenbach C, Greenhalgh DA, Khorana HG, Hubbell WL (1994) A collision gradient method to determine the immersion depth of nitroxides in lipid bilayers: application to spin-labeled mutants of bacteriorhodopsin. Proc Natl Acad Sci USA 91:1667–1671
63. Marsh D, Dzikovski BG, Livshits VA (2006) Oxygen profiles in membranes. Biophys J 90: L49–L51
64. Altenbach C, Froncisz W, Hemker R, Mchaourab HS, Hubbell WL (2005) Accessibility of nitroxide side chains: absolute Heisenberg exchange rates from power saturation EPR. Biophys J 89:2103–2112
65. Farahbakhsh ZZ, Altenbach C, Hubbell WL (1992) Spin labeled cysteines as sensors for protein lipid interaction and conformation in rhodopsin. Photochem Photobiol 56:1019–1033
66. Poole CP (1983) Electron spin resonance. Wiley, New York
67. Altenbach C, Froncisz W, Hyde JS, Hubbell WL (1989) Conformation of spin-labeled melittin at membrane surfaces investigated by pulse saturation recovery and continuous wave power saturation electron-paramagnetic resonance. Biophys J 56:1183–1191
68. Nielsen RD, Canaan S, Gladden JA, Gelb MH, Mailer C, Robinson BH (2004) Comparing continuous wave progressive power saturation EPR and time domain saturation recovery EPR over the entire motional range of nitroxides psin labels. J Magn Reson 169:129–163
69. Bordignon E, Klare JP, Döbber MA, Wegener AA, Martell S, Engelhard M, Steinhoff HJ (2005) Structural analysis of a HAMP domain: the linker region of the phototransducer in complex with sensory rhodopsin II. J Biol Chem 280:38767–38775
70. Gordeliy VI, Labahn J, Moukhametzianov R, Efremov R, Granzin J, Schlesinger R, Büldt G, Savopol T, Scheidig AJ, Klare JP, Engelhard M (2002) Molecular basis of transmembrane signalling by sensory rhodopsin II-transducer complex. Nature 419:484–487
71. Yin JJ, Pasenkiewicz-Gierula M, Hyde JS (1987) Lateral diffusion of lipids in membranes by pulse saturation recovery electron-spin-resonance. Proc Natl Acad Sci USA 84:964–968
72. Pyka J, Ilnicki J, Altenbach C, Hubbell WL, Froncisz W (2005) Accessibility and dynamics of nitroxide side chains in T4 lysozyme measured by saturation recovery EPR. Biophys J 89:2059–2068
73. Haas DA, Sugano T, Mailer C, Robinson BH (1993) Motion in nitroxide spin labels: direct measurement of rotational correlation times by pulsed electron double resonance. J Phys Chem 97:2914–2921

74. Robinson BH, Haas DA, Mailer C (1994) Molecular dynamics in liquids: spin-lattice relaxation of nitroxide spin labels. Science 263:490–493
75. Marsh D (2010) Spin-label EPR for determining polarity and proticity in biomolecular assemblies: transmembrane profiles. Appl Magn Reson 37:435–454
76. Stone AJ (1963) Gauge invariance of the g tensor. Proc R Soc Lond A 271:424–434
77. Möbius K, Savitsky A, Wegener C, Plato M, Fuchs M, Schnegg A, Dubinskii AA, Grishin YA, Grigor'ev IA, Kühn M, Duché D, Zimmermann H, Steinhoff HJ (2005) Combining high-field EPR with site-directed spin labeling reveals unique information on proteins in action. Magn Reson Chem 43:S4–S19
78. Steinhoff HJ, Savitsky A, Wegener C, Pfeiffer N, Plato M, Möbius K (2000) High-field EPR studies of the structure and conformational changes of site-directed spin labeled bacteriorhodopsin. Biochim Biophys Acta 1457:253–262
79. Wegener C, Savitsky A, Pfeiffer M, Möbius K, Steinhoff HJ (2001) High-Field EPR-detected shifts of magnetic tensor components of spin label side chains reveal protein conformational changes: the proton entrance channel of bacteriorhodopsin. Appl Magn Reson 21:441–452
80. Steinhoff HJ, Lieutnant K, Schlitter J (1989) Residual motion of hemoglobin-bound spin labels as a probe for protein dynamics. Z Naturforsch C 44:280–288
81. Brutlach H, Bordignon E, Urban L, Klare JP, Reyher HJ, Engelhard M, Steinhoff HJ (2006) High-field EPR and site-directed spin labeling reveal a periodical polarity profile: the sequence 88 to 94 of the phototransducer, *Np*HtrII, in complex with sensory rhodopsin, *Np*SRII. Appl Magn Reson 30:359–372
82. Steinhoff HJ, Radzwill N, Thevis W, Lenz V, Brandenburg D, Antson A, Dodson GG, Wollmer A (1997) Determination of interspin distances between spin labels attached to insulin: comparison of electron paramagnetic resonance data with the X- ray structure. Biophys J 73:3287–3298
83. Smirnova TI, Smirnov AI, Paschenko SV, Poluektov OG (2007) Geometry of hydrogen bonds formed by lipid bilayer nitroxide probes: a high-frequency pulsed ENDOR/EPR study. J Am Chem Soc 129:3476–3477
84. Finiguerra MG, Blok H, Ubbink M, Huber M (2006) High-field (275 GHz) spin-label EPR for high-resolution polarity determination in proteins. J Magn Reson 180:197–202
85. Bordignon E, Brutlach H, Urban L, Hideg K, Savitsky A, Schnegg A, Gast P, Engelhard M, Groenen EJJ, Möbius K, Steinhoff HJ (2010) Heterogeneity in the nitroxide microenvironment: polarity and proticity effects in spin-labeled proteins studied by multifrequency EPR. Appl Magn Reson 37:391–403
86. Borbat PP, Freed JH (2012) Pulse dipolar ESR: distance measurements. Struct Bond. doi:10.1007/430_2012_82
87. Steinhoff HJ, Dombrowsky O, Karim C, Schneiderhahn C (1991) Two-dimensional diffusion of small molecules on protein surfaces: an EPR study of the restricted translational diffusion of protein-bound spin labels. Eur Biophys Lett 20:293–303
88. Rabenstein MD, Shin YK (1995) Determination of the distance between 2 spin labels attached to a macromolecule. Proc Natl Acad Sci USA 92:8239–8243
89. Altenbach CA, Oh KJ, Trabanino RJ, Hideg K, Hubbell WL (2001) Estimation of inter-residue distances in spin labeled proteins at physiological temperatures: Experimental strategies and practical limitations. Biochemistry 40:15471–15482
90. Altenbach C, Hubbell WL (2008) Improved distance determination from dipolar broadening of EPR spectra, Biophys J 94, Supplement I, 826–832
91. Hustedt EJ, Smirnov AI, Laub CF, Cobb CE, Beth AH (1997) Molecular distances from dipolar coupled spin-labels: the global analysis of multifrequency continuous wave electron paramagnetic resonance data. Biophys J 72:1861–1877
92. McNulty JC, Silapie JL, Carnevali M, Farrar CT, Griffin RG, Formaggio F, Crisma M, Toniolo C, Millhauser GL (2001) Electron spin resonance of TOAC labeled peptides: folding transitions and high frequency spectroscopy. Biopolymers 55:479–485

93. Hanson P, Millhauser G, Formaggio F, Crisma M, Toniolo C (1996) ESR characterization of hexameric, helical peptides using double TOAC spin labeling. J Am Chem Soc 118:7618–7625
94. Hanson P, Anderson DJ, Martinez G, Millhauser G, Formaggio F, Crisma M, Toniolo C, Vita C (1998) Electron spin resonance and structural analysis of water soluble, alanine-rich peptides incorporating TOAC. Mol Phys 95:957–966
95. Rabenstein MD, Shin YK (1996) HIV-1 gp41 tertiary structure studied by EPR spectroscopy. Biochemistry 35:13922–13928
96. Xiao W, Poirier MA, Bennett MK, Shin YK (2001) The neuronal t-SNARE complex is a parallel four-helix bundle. Nat Struct Biol 8:308–311
97. Closs GL, Forbes MDE, Piotrowiak P (1992) Spin and reaction dynamics in flexible polymethylene biradicals as studied by EPR, NMR, and optical spectroscopy and magnetic field effects: measurements and mechanisms of scalar electron-spin spin coupling. J Am Chem Soc 114:3285–3294
98. Fiori WR, Millhauser GL (1995) Exploring the peptide 3(10)-helix-reversible-arrow-alpha-helix equilibrium with double-label electron-spin-resonance. Biopolymers 37:243–250
99. Eaton SS, More KM, Sawant BM, Eaton GR (1983) Use of the EPR half-field transition to determine the interspin distance and the orientation of the interspin vector in systems with two unpaired electrons. J Am Chem Soc 105:6560–6567
100. Persson M, Harbridge JR, Hammarstrom P, Mitri R, Martensson LG, Carlsson U, Eaton GR, Eaton SS (2001) Comparison of electron paramagnetic resonance methods to determine distances between spin labels on human carbonic anhydrase II. Biophys J 80:2886–2897
101. Borbat PP, Freed JH (1999) Multiple-quantum ESR and distance measurements. Chem Phys Lett 313:145–154
102. Pannier M, Veit S, Godt A, Jeschke G, Spiess HW (2000) Dead-time free measurement of dipole-dipole interactions between electron spins. J Magn Reson 142:331–340
103. Ward R, Bowman A, Sozudogru E, El-Mkami H, Owen-Hughes T, Norman DG (2010) EPR distance measurements in deuterated proteins. J Magn Reson 207:164–167
104. Schiemann O, Prisner TF (2007) Long-range distance determinations in biomacromolecules by EPR spectroscopy. Q Rev Biophys 40:1–53
105. Banham JE, Baker CM, Ceola S, Day IJ, Grant GH, Groenen EJJ, Rodgers CT, Jeschke G, Timmel CR (2008) Distance measurements in the borderline region of applicability of CW EPR and DEER: a model study on a homologous series of spin-labelled peptides. J Magn Reson 191:202–218
106. Jeschke G (2012) Interpretation of dipolar EPR data in terms of protein structure. Struct Bond. doi:10.1007/430_2011_61
107. Klare JP, Gordeliy VI, Labahn J, Büldt G, Steinhoff HJ, Engelhard M (2004) The archaeal sensory rhodopsin II/transducer complex: a model for transmembrane signal transfer. FEBS Lett 564:219–224
108. Klare JP, Chizhov I, Engelhard M (2007) Microbial rhodopsins: scaffolds for ion pumps, channels, and sensors. Results Probl Cell Differ 45:73–122
109. Klare JP, Bordignon E, Engelhard M, Steinhoff HJ (2011) Transmembrane signal transduction in archaeal phototaxis: the sensory rhodopsin II-transducer complex studied by electron paramagnetic resonance spectroscopy. Eur J Cell Biol 90:731–739
110. Wegener AA, Klare JP, Engelhard M, Steinhoff HJ (2001) Structural insights into the early steps of receptor-transducer signal transfer in archaeal phototaxis. EMBO J 20:5312–5319
111. Döbber M, Bordignon E, Klare JP, Holterhues J, Martell S, Mennes N, Li L, Engelhard M, Steinhoff HJ (2008) Salt-driven equilibrium between two confromations in the HAMP domain from Natronomonas pharaonis: the language of signal transfer? J Biol Chem 283:28691–28701
112. Hulko M, Berndt F, Gruber M, Linder J, Truffault V, Schulz A, Martin J, Schultz JE, Lupas AN, Coles M (2006) The HAMP domain structure implies helix rotation in transmembrane signaling. Cell 126:929–940

113. Holland IB, Cole SPC, Kuchler K, Higgins CF (2002) ABC proteins: from bacteria to man. Academic, New York
114. Grote M, Polyhach Y, Jeschke G, Steinhoff HJ, Schneider E, Bordignon E (2009) Transmembrane signaling in the maltose ABC transporter MALFGK2-E: the periplasmic MalF-P2 loop communicates substrate availability to the ATP-bound MalK dimer. J Biol Chem 284:17521–17526
115. Oldham ML, Davidson AL, Chen J (2008) Structural insights into ABC transporter mechanism. Curr Opin Struct Biol 18:726–733
116. Lu G, Westbrooks JM, Davidson AL, Chen J (2005) ATP hydrolysis is required to reset the ATP-binding cassette dimer into the resting-state conformation. Proc Natl Acad Sci USA 102:17969–17974
117. Oldham ML, Khare D, Quiocho FA, Davidson AL, Chen J (2007) Crystal structure of a catalytic intermediate of the maltose transporter. Nature 450:515–521
118. Grote M, Bordignon E, Polyhach Y, Jeschke G, Steinhoff HJ, Schneider E (2008) A comparative EPR study of the nucleotide-binding domains' catalytic cycle in the assembled maltose ABC-importer. Biophys J 95:2924–2938
119. Vasquez V, Sotomayor M, Marien-Cortez D, Roux B, Schulten K, Perozo E (2008) Three-dimensional architecture of membrane-embedded MscS in the closed conformation. J Mol Biol 378:55–70
120. Vasquez V, Sotomayor M, Cordero-Morales J, Schulten K, Perozo E (2008) A structural mechanism for MscS gating in lipid bilayers. Science 321:1210–1214
121. Shelke SA, Sigurdsson STh (2011) Site-directed nitroxide spin labeling of biopolymers. Struct Bond. doi:10.1007/430_2011_62 (in the first volume of this series)
122. Plato M, Steinhoff H-J, Wegener C, Törring JT, Savitsky A, Möbius K (2002) Molecular orbital study of polarity and hydrogen bonding effects on the g and hyperfine tensors of site directed NO spin labelled bacteriorhodopsin. Mol Phys 100:3711–3721
123. Griffith OH, Dehlinger PJ, Van SP (1974) Shape of the hydrophobic barrier of phospholipid bilayers (evidence for water penetration in biological membranes). J Membrane Biol 15:159–192
124. Klare JP, Bordignon E, Döbber MA, Fitter J, Kriegsmann J, Chizhov I, Steinhoff H-J, Engelhard M (2006) Effects of solubilization on the structure and function of the sensory Rhodopsin II/Transducer Complex. J Mol Biol 356:1207–1221
125. Jeschke G, Chechik V, Ionita P, Godt A, Zimmermann H, Banham JE, Timmel CR, Hilger D, Jung H (2006) DeerAnalysis2006 - a comprehensive software package for analyzing pulsed ELDOR data. Appl Magn Reson 30:473–498
126. Likhtenshtein GI (1976) Spin labeling methods in molecular biology. Wiley, New York

Struct Bond (2014) 152: 249–282
DOI: 10.1007/430_2012_76

Published online: 27 March 2012

Structural Information from Oligonucleotides

Richard Ward and Olav Schiemann

Abstract The important role of DNA in biology has been known for a long time, but during the last decade it has become apparent that also RNA has many more functions than previously believed, ranging from gene regulation to catalysis of the polypeptide bond formation in the ribosomes. Thus, biophysical methods are needed that will allow the unravelling of their structures and conformational changes as well as dynamics and complex formations. Advances in site-directed spin labelling (SDSL) of oligonucleotides and electron paramagnetic resonance (EPR) spectroscopic methods like pulsed electron–electron double resonance (PELDOR or synonymously know as DEER) offer a means to achieve this and have been applied to various oligonucleotide systems. This chapter will give an overview of recent developments and applications in this field.

Keywords DEER · DNA · EPR · PELDOR · RNA

Contents

R. Ward (✉)
Biomedical Sciences Research Complex, Centre of Magnetic Resonance, University of St Andrews, St Andrews, Fife KY16 9ST, UK
e-mail: rw60@st-andrews.ac.uk

O. Schiemann (✉)
Institute of Physical and Theoretical Chemistry, University of Bonn, Wegelerstr. 12, 53115 Bonn
e-mail: schiemann@pc.uni-bonn.de

Abbreviations

CD	Circular dichroism
CW	Continuous wave
DEER	Double electron–electron resonance
DMT	Dimethoxytrityl
EPR	Electron paramagnetic resonance
FRET	Förster resonance energy transfer
NMR	Nuclear magnetic resonance
PELDOR	Pulsed electron–electron double resonance
TBDMS	*tert*-Butyldimethylsilyl

1 Introduction

The role of DNA as keeper of the genetic information as well as its tertiary structure, the double helix, has long been known. The double helix can adopt A-, B- or Z-forms and the chromosomal DNAs have at their ends single-stranded overhangs, the telomeres. It can form triple helices, quadruplexes and junctions. Beyond the tertiary structure it forms complex higher order structures and winds around proteins, e.g. the histones, forming the macroscopic chromosomes. Irradiation or chemicals can damage DNA leading to local structural changes such as bends, kinks or lesions. During damage repair or processing, DNA binds to proteins, unwinds and forms bubbles and forks. In addition to DNA and only during the last 10 years, RNA and its structural diversity have gained major attention, in particular through the finding of RNAi as a natural antiviral mechanism of cells, the discovery that it is RNA that facilitates the peptide bond formation in the ribosomes and the discovery of riboswitches, a class of RNAs in bacteria, specialized in translational regulation. Furthermore, the folding of RNA and its conformational changes, induced by interactions with proteins, metal ions or small molecules, are essential for its biological function.

Thus, understanding the hierarchy of oligonucleotide structure formation and associated dynamics, their interactions with proteins and how structures can be induced or inhibited opens up a way to rationally approach nucleic acids as a three-dimensional target. Electron paramagnetic resonance (EPR) has already proved its suitability in characterizing the structural environment of paramagnetic centres, as well as the global arrangement of domains in proteins and protein complexes. Yet, EPR-based studies on the local structure of, e.g. metal ion-binding sites or of

tertiary structure elements in oligonucleotides and their complexes with proteins have only recently started to appear, even though EPR offers several advantages compared with, e.g. NMR or FRET:

- The large magnetic dipole moment of the electron enables long-range distance measurements of up to 8 nm.
- Dipolar and exchange coupling mechanisms and orientation correlation effects can be easily differentiated.
- EPR has no size restriction with respect to the biomolecule.
- It is rather sensitive, requiring usually only 5–10 nmol of material.
- It is tolerant of a great range of buffer conditions and allows measurements within membranes.

2 Spin Labelling of Oligonucleotides

In order to study the structure, folding and dynamics of oligonucleotides with EPR, they have to contain unpaired electrons. Since nucleic acids usually do not contain such paramagnetic centres, they have to be artificially incorporated. One strategy can be to replace diamagnetic metal ions with paramagnetic ones, e.g. the exchange of Mg^{2+} by Mn^{2+} in the case of the hammerhead ribozymes (HHRz) [1–4] or the incorporation of artificial metal ion-binding sites [5]. More commonly, organic radicals are used that are covalently and site specifically attached [6]. This technique is called site-directed spin labelling (SDSL), and the organic radicals mainly used are based on nitroxides (Fig. 1).

Nitroxides are thermodynamically stable and kinetically protected by four bulky methyl groups meaning that they are stable for long times and that the N–O group usually does not undergo reactions with the biomolecule. The electron spin density resides to over 90% within the N–O group making them very good candidates for EPR-based long-range distance measurements because of the validity of the point dipole model. In addition, the three line continuous wave (CW) EPR spectrum is sensitive to dynamics, local pH values and solvent viscosity, and a careful analysis of such spectra thus reports on these properties.

Generally, SDSL of nucleic acids is based on incorporation of modified nucleotides into the oligonucleotide where the modification can be at the base, the sugar or the phosphate moiety. The modification may already be a spin label or a functional group that reacts with a correspondingly functionalized nitroxide. In the latter case, the nitroxide/nucleotide coupling reaction can be performed either during or after the synthesis of the DNA or RNA strand. Having successfully labelled the nucleic acid, it is important to check that the spin label does not induce perturbations of the structure or function of the oligonucleotide. Usually, this is done by means of UV–vis-based thermal denaturation, circular dichroism (CD) or biochemical assays. Which label one chooses will strongly depend on the need to

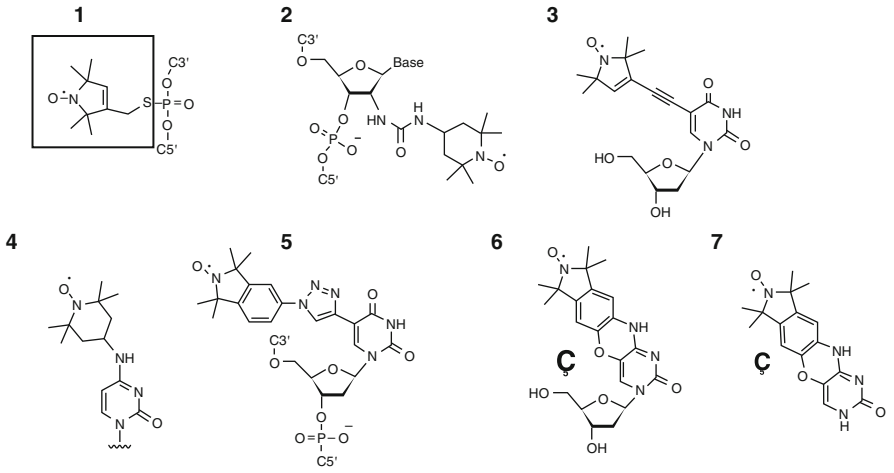

Fig. 1 Examples of nitroxide spin labels used for spin labelling of nucleic acids. (*1*) Thiol-reactive nitroxide, 3-iodomethyl-(1-oxy-2,2,5,5-tetramethylpyrroline), reacted with a phosphorothioate modification, the boxed fragment is referred to as R5. (*2*) Isocyanate tetramethylpiperidyl-*N*-oxy reacted to 2′-amino-uridine. (*3*) 2,2,5,5-Tetramethylpyrroline-1-oxyl-3-acetylene reacted with 5-iodo-uridine. (*4*) 4-Amino tetramethylpiperidyl-*N*-oxy reacted to correspondingly modified cytidine. (*5*) Azidoisoindoline-*N*-oxy reacted to alkyne-modified uridine. (*6*) **Ç** spin label. (*7*) Analogue of the **Ç** spin label that binds non-covalently to nucleic acids

minimize structural and dynamical alterations and the questions to be answered. For details see, for example [7].

3 Dipolar Coupling

Structural information on the nanometre scale can be obtained by measuring the distance between multiple pairs of spin labels. With EPR spectroscopy, nanometre distances are measured via the dipolar coupling between unpaired electrons [8].

Classically, the interaction energy of the magnetic dipole–dipole coupling between two unpaired electron spins can be described as:

$$E = \frac{\vec{\mu}_A \cdot \vec{\mu}_B}{R^3} - \frac{3(\vec{\mu}_A \cdot \vec{R})(\mu_B \cdot \vec{R})}{R^5} \tag{1}$$

where R and $\vec{R}$ are the distance and distance vector between the spins A and B, while $\vec{\mu}_A$ and $\vec{\mu}_B$ are the dipole moments of spins A and B. Under suitable approximations (high-field and point dipole approximation), (1) can be converted into (2) [9]:

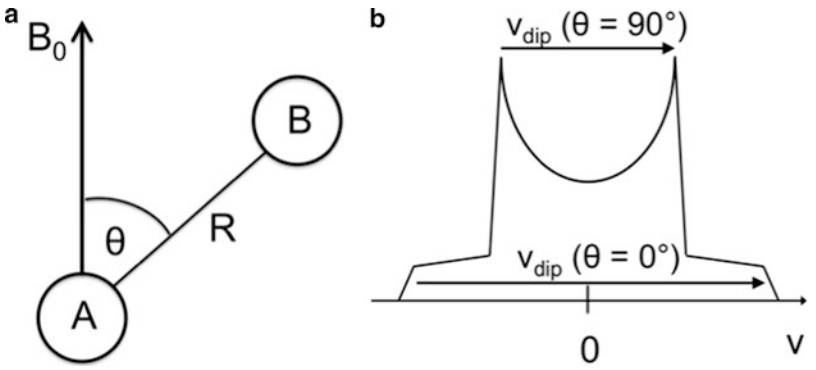

Fig. 2 (**a**) Schematic of the interacting spin pair A–B in a magnetic field B_0. (**b**) Pake pattern of a powder sample with $v_{dip}(\theta = 0°) = 2v_{dip}(\theta = 90°)$

Table 1 Distances converted to dipolar coupling frequencies for nitroxides

Distance (nm)	Dipolar coupling in MHz (Gauss)
1	52 (18)
2	6.5 (2.3)
3.7	1 (0.35)
8	0.1 (0.036)

$$v_{dip} = \frac{D_{dip}}{R^3}(1 - 3\cos^2\theta) \tag{2}$$

where v_{dip} is the dipolar coupling frequency in MHz, D_{dip} is the splitting constant which amounts to 52.16 MHz nm^3, R is the distance between the two spins in nm and θ is the angle between the distance vector and the external magnetic field, see Fig. 2a. Rearranging (2) and assuming nitroxides ($g = 2$) as the spin centres lead to:

$$R = \sqrt[3]{\frac{52.16}{v_{dip}(\theta = 90°)}} \tag{3}$$

Thus, (3) allows one to convert the measured dipolar coupling into the corresponding distance in nanometres if v_{dip} is in MHz. For examples, see Table 1.

For a single spin pair fixed relative to the magnetic field B_0, the dipole–dipole interaction leads to a splitting of the resonance line of each spin centre into a doublet centred about the resonance frequencies of the respective spin centre. The magnitude of the splitting depends on the distance R and the angle θ. If the single spin pair is oriented in such a way that $\theta = 0°$, the doublets will be split by $2D_{dip}/R^3$, at $\theta = 54.7°$, the two lines will coalesce and the dipolar frequency would be zero, and at $\theta = 90°$, the doublet will be split by D_{dip}/R^3. For a frozen solution or a powder sample, all orientations of θ are present and the resulting spectrum is the so-called Pake pattern (Fig. 2b). If the spin pair tumbles fast on the

EPR time scale (here the dipole coupling frequency) as in liquid solutions, the dipolar coupling is averaged to zero. Hence, measurements of the dipolar coupling are done under solid-state conditions. If the distance between the two spins is very small (<1.5 nm), one might have to take into account the exchange coupling constant, especially in the case of conjugated bond systems [10].

4 EPR Methods to Measure the Dipolar Coupling

EPR spectroscopy offers a variety of methods to measure the dipolar coupling between two unpaired electrons. CW methods are usually restricted to rather short distances, whereas pulsed EPR experiments have been shown to reliably measure distances of up to 8 nm.

4.1 CW EPR Experiments

Precise interspin distances can be obtained from CW EPR spectra if the dipolar splitting is larger than the inhomogeneous linewidth of the radical centres. For nitroxides in frozen solution, this linewidth is roughly 6–8 Gauss. Thus, the CW EPR lineshape will only be broadened significantly at distances shorter than 2.5 nm [11]. The dipolar coupling can be extracted from such CW EPR spectra by simulation or deconvolution techniques taking the lineshape of the singly spin labelled biomolecule into account [7].

4.2 Pulsed EPR Experiments

Figure 3 gives an overview of a selection of pulsed EPR sequences used to measure distances [9]. In a simple two-pulse electron spin echo envelope modulation (ESEEM) experiment, the dipolar coupling frequency can be observed as an oscillation of the Hahn-echo intensity. However, hyperfine couplings to nearby nuclei usually obscure the dipolar frequency. More advanced but still single frequency pulse sequences that suppress the hyperfine coupling contribution are "2 + 1", SIFTER, double-quantum coherence (DQC) EPR and relaxation-induced dipolar modulation enhancement (RIDME). Of these "2 + 1" has still rather strong hyperfine coupling contributions and RIDME relies on one of the spin centres having a much faster T_1 relaxation time than the other. SIFTER is based on the solid echo sequence known from NMR but has not been used often. DQC-EPR is based on a double-quantum filter and is an elegant way to select the dipolar coupling; however, it requires very strong and short mw pulses and for radicals with large spectral width such as nitroxides, it is technically rather demanding.

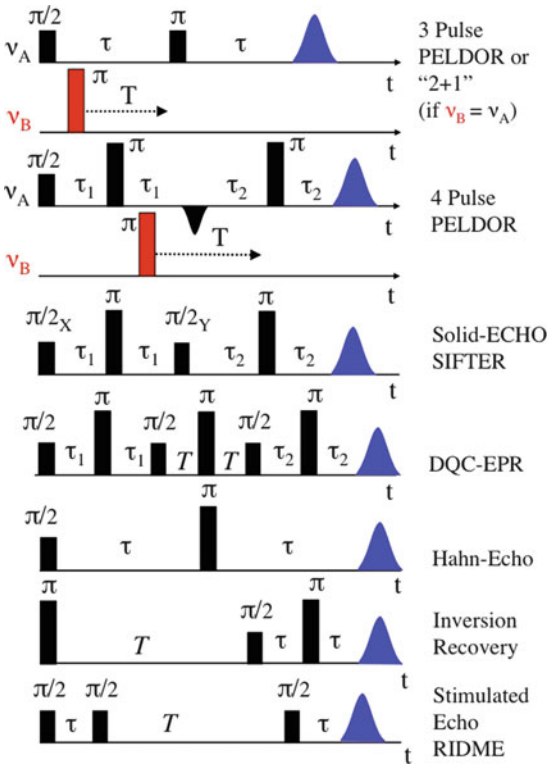

Fig. 3 Selected pulse sequences that have been used to determine the dipolar coupling frequency

Light-induced radical pairs provide additional means of measuring the dipolar coupling, for example via the out-of-phase echo.

An alternative strategy for removing unwanted hyperfine interactions is used in pulsed electron–electron double resonance (PELDOR or DEER). Here, two different microwave frequencies generated from two non-phase correlated microwave sources are used. Initially, a three-pulse experiment was established which was later on extended to the dead-time free four pulse PELDOR experiment, which allows a more accurate measurement of the dipolar coupling to be made.

All the experiments above extract the dipolar coupling from oscillations in the corresponding time traces. Another possibility is to analyse changes in transverse or longitudinal relaxation times, for example via two-pulse ESEEM or inversion recovery experiments, respectively. If a single paramagnetic centre relaxes with relaxation times T_1 and T_2, then the change in these relaxation times in the presence of a second paramagnetic centre can be used to calculate the dipolar coupling and thus the distance between the spin centres. These calculations require knowledge of the relaxation times in the non-dipolar-coupled system under identical conditions. An advantage of these relaxation-based measurements is that they can be performed in the liquid state [12]. For the following examples, the focus is on PELDOR.

5 Applications of EPR to Oligonucleotides

EPR spectroscopic studies on RNA or DNA date back to the 1970s. They were aimed at the identification of global or sequence dependent dynamics of oligonucleotides and used the dependence of CW EPR spectra on mobilities [13–18]. Only recently, several groups started to use EPR-based distance measurements between nitroxides to identify structure elements in RNA/DNA. Examples of these are discussed in the following.

5.1 DNA

5.1.1 Model DNA Structures

A number of studies have been carried out on duplex DNAs in order to demonstrate the potential of different SDSL chemistries and to establish the range, accuracy and robustness of distance determination using PELDOR.

The first such study [19] incorporated an iodo-deoxyuridine at the desired site and then used a metal cross-coupling reaction to attach a spin label, called TPA, to the DNA during the chemical synthesis (Fig. 1, number 3). DNA duplexes of between 12 and 18 base pairs (bp) in length were prepared, and distances from 19.2 to 52.5 Å were measured. The distances were obtained directly from the Pake pattern, i.e. the Fourier transformed time trace data, by measuring the dipolar coupling frequency at $\theta = 90°$. It was found that an all-atom molecular dynamics treatment with water explicitly included and assuming a B-form double helix DNA structure yielded excellent agreement with the experimental data.

Another approach was to chemically synthesize DNA strands containing a phosphorothiolate at the required labelling position [20]. These DNA molecules were then derivatized with iodomethylnitroxide (Fig. 1, label 1). The main advantage of this method is that it is sequence independent; however, a drawback of this approach is that further purification is required to resolve the Rp and Sp stereoisomers. The PELDOR data were then analysed within the DeerAnalysis2004 package [21] to obtain a set of distance distributions. The average distances measured ranged from 21.2 to 38.8 Å on the set of doubly labelled dodecamer DNA duplexes, and showed good agreement with structural models based on either NMR data or a generic B-form DNA (Fig. 4). However, the experimental and modelled distance distribution widths differed in most cases suggesting that refinement of the modelling approach was required.

Ward et al. [22] prepared 27-mer DNA strands containing a 2′-amino-uridine at the appropriate labelling site, which could then be functionalized using an isocyanate nitroxide label (Fig. 1, number 2). DeerAnalysis2006 was used to extract the distance distributions from the PELDOR data. The most probable distances measured ranged from 28 to 68 Å. It was found that these distances were consistent

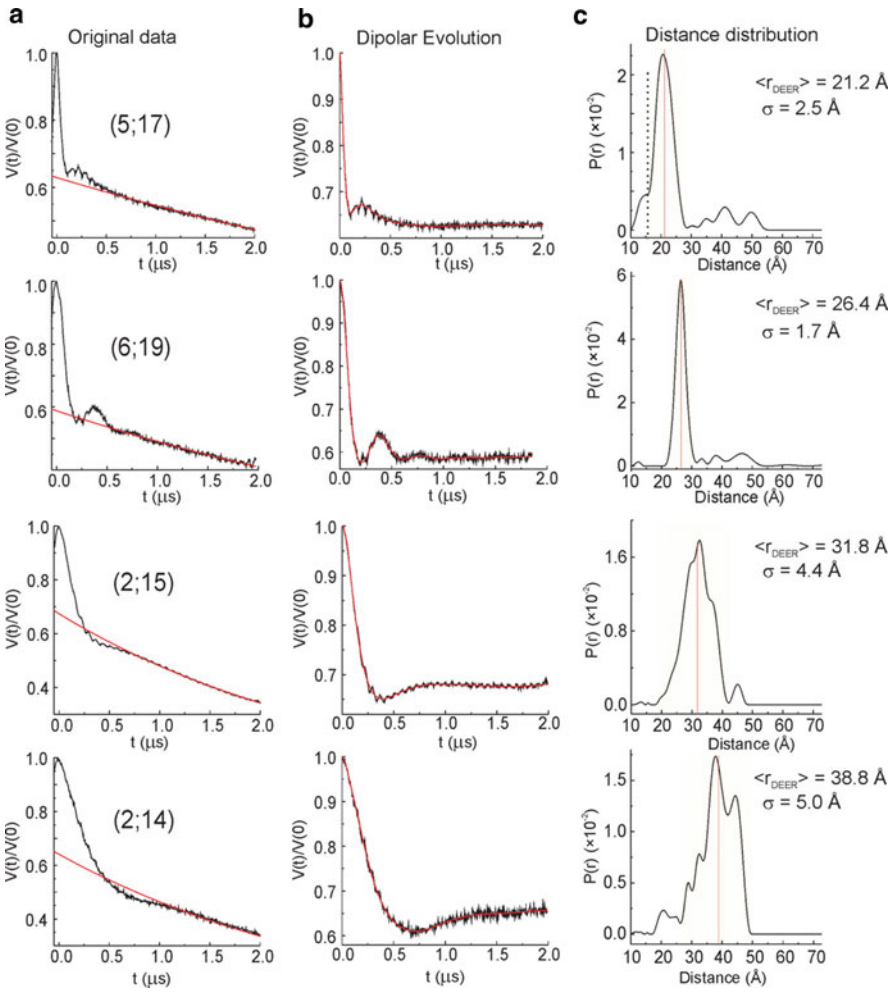

Fig. 4 DEER data for double R5 labelled duplexes, with the positions of R5 shown in the parenthesis. (**a**) Original echo decay data. The *red traces* are the background echo decay computed using a homogeneous 3D spin distribution. (**b**) Dipolar evolution functions. (**c**) Distance distributions $P(r)$ computed using Tikhonov regularization. The *dotted line* in the (5;17) dataset marks the lower limit of distances that are detectable by DEER with the reported experimental setup. Adapted with permission from [20]

with a predominantly B-form DNA but with a local distortion at the labelling site, since modelling the EPR distances led to the spin position being extremely close to the phosphodiester backbone. It was also shown that binary mixtures of DNAs could be deconvolved using PELDOR (Fig. 5). However, although the main distances from the binary mixture were consistent with the distances measured for the single DNA duplexes, the appropriate ratios of the components was not obtained, which was either to do with inaccuracies of pipetting viscous liquids or an

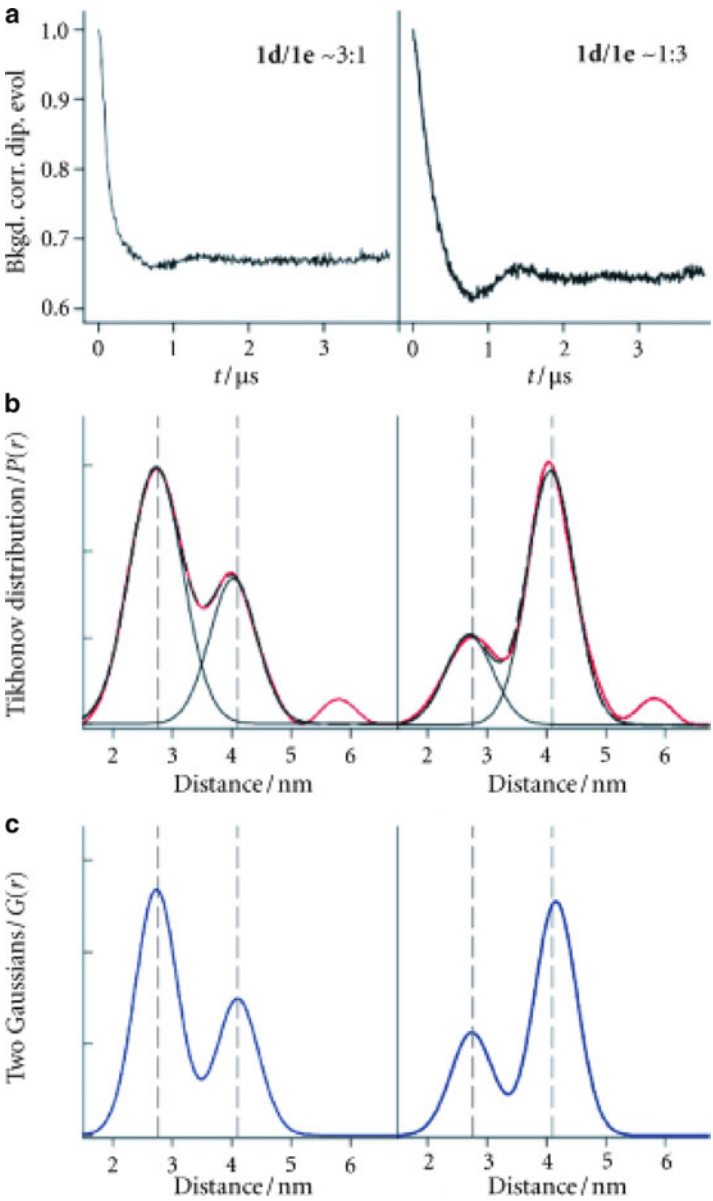

Fig. 5 DEER data obtained for different mixtures of two doubly spin labelled DNA duplexes called 1d and 1e. (**a**) Background-corrected dipolar evolution data with derived distance-distribution fits. (**b**) Tikhonov regularization distance distribution curves (*red*), these distance distributions have been fitted with two Gaussians by using non-linear least-squares (*black dashed*), and the deconstructed Gaussians shown (*black solid*). (**c**) Two Gaussian fits made directly to the dipolar evolution data (*blue*). The peak values of the Tikhonov regularization distributions obtained for the single constructs are plotted (*grey dashed*). DNA duplexes 1d and 1e have spin labels separated by 9 or 12 bp, respectively. Adapted with permission from [22]

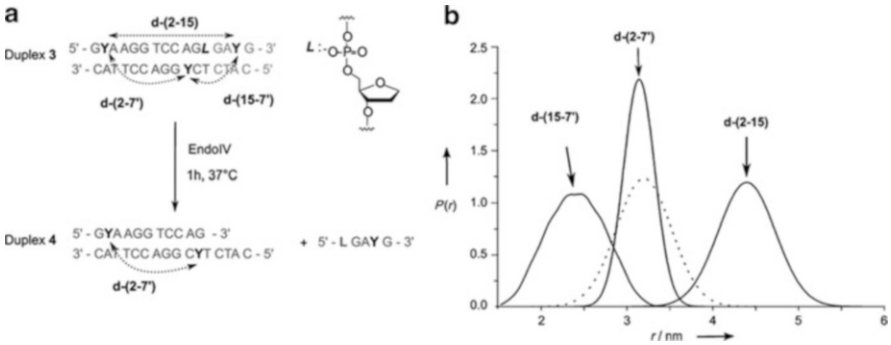

Fig. 6 (**a**) Tri-labelled DNA duplex 3 before and after its cleavage by the EndoIV abasic site repair enzyme. Spin label at site Y and abasic lesion at site Y. (**b**) Distance distributions obtained for the tri-labelled DNA duplex before (*solid black line*, triangular model) and after (*black dots*, pair model) treatment with EndoIV. Adapted with permission from [26]

inherent limitation of the PELDOR technique. Attempts to investigate more complicated mixtures resulted in oscillation-free time trace data that resulted in broad distance distributions that could not be unambiguously interpreted.

Several studies have used the Huisgen–Sharpless–Meldal alkyne–azide cycloaddition reaction, also known as the "click" reaction [23] for spin labelling oligonucleotides. Flaender et al. [24] introduced either one or two 2′-*O*-propargyl-uridine nucleosides into a 20 mer DNA strand during chemical synthesis. Post synthesis and purification, an azido-TEMPO spin label was efficiently coupled to these alkyne bearing positions. The main distance of 32.7 Å was found to be consistent for a B-form DNA duplex, i.e. assuming 3.3 Å for each base pair separation. However, the distance distribution width was quite broad, 13.7 Å full width at half height, suggesting that the label was quite mobile at this position. Another group applied the same chemistry but attached the TEMPO spin label to the nucleobases adenine and thymine instead of the sugar [25]. It was found that attachment to the nucleobase site gave rise to a much narrower distance distribution, suggesting that the spin label is more restricted and thus could be used for orientation-selective studies. This synthetic approach has also been used to prepare a DNA duplex that contained three spin labels (Fig. 6), two on one strand and one on the complementary strand, and an abasic site [26]. The spin labels were attached to the nucleobase thymine. This study showed that the PELDOR data were of sufficient quality that the three distances could be deconvolved using DeerAnalysis2008. In addition, it was shown that the abasic site was still recognized and cut by an endonuclease, despite the presence of the spin labels, yielding a duplex that contained only two spins, from which only a single distance was measured.

Recently, the view of the DNA duplex as an elastic rod has been challenged by two different techniques – rotor bead tracking [27] and small angle X-ray scattering interference [28]. In order to provide further experimental evidence for a particular

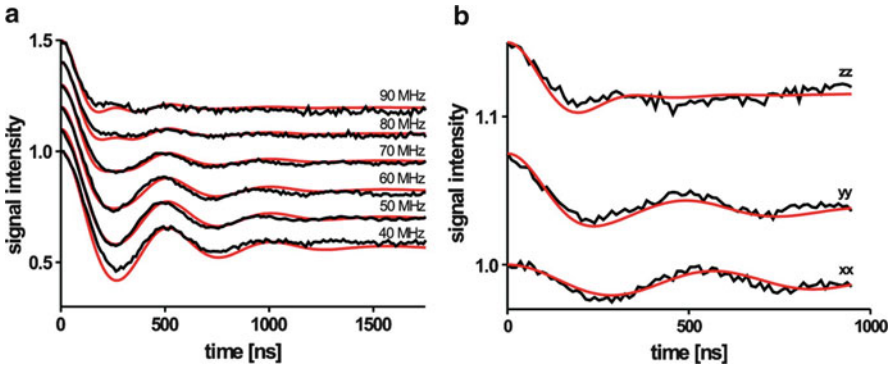

Fig. 7 (**a**) Experimental (*black*) and simulated (*red*) X-band PELDOR time traces for different offsets $\Delta\nu$ (in MHz) between probe and pump pulse frequency for one of the DNAs. (**b**) G-band PELDOR time traces at the three magnetic field positions corresponding to the principal g-tensor components. In these experiments, the difference between pump and probe frequency was kept constant at $\Delta\nu = 70$ MHz. Adapted with permission from [29]. Copyright (2011) American Chemical Society

model of DNA stretching, Marko et al. [29] incorporated the very rigid **Ç** spin label [30] (Fig. 1, number 6) into 12 DNA duplexes and carried out PELDOR experiments at both X-band and G-band (180 GHz). By simulating the time trace data at both frequencies, they were able to obtain both the distance distributions and angles between the two labels (Fig. 7). The data also suggested a correlated stretch-twist breathing model in which the helix pitch of the DNA is not changed, but the radius is. Intuitively it does not seem plausible to be able to measure the dynamics of the DNA using an experimental technique that is carried out at 50 K. However, the DNA sample freezes at about 243 K (−30°C), and so all of the conformational states present at that temperature will be measured in the PELDOR experiment. Also, dynamic information could only be obtained because they used a very rigid label, i.e. the movements of the labels were highly correlated with those of the DNA.

All these model studies have provided convincing evidence that the spin labelling chemistries do not adversely affect the DNA to which they are attached, i.e. DNA duplex melting, CD, enzymatic recognition and the distance measurements themselves. They have shown that the PELDOR experiments can accurately measure distances of up to 68 Å, but also deconvolute sufficiently disparate distances from a multi-spin system and provide information on angles and dynamics.

5.1.2 Monitoring DNA Conformational Changes

A study by Sicoli et al. [31] (Fig. 8) used PELDOR to investigate the transition of B-form duplex DNA to A-form [32]. This transition is biologically relevant because it

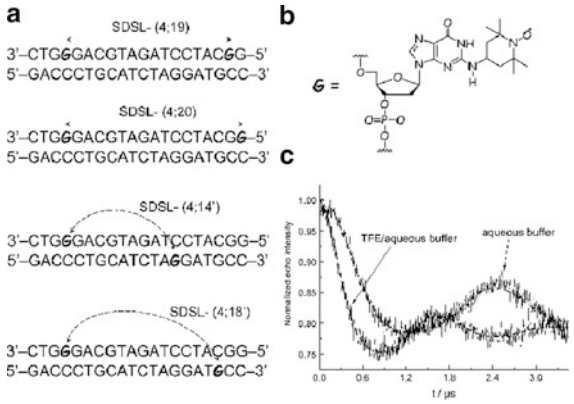

Fig. 8 (**a**) Double spin labelled DNA duplex sequences. Spin label at *bold* G position. (**b**) Derivatized guanine as TEMPO-type spin probe (TEMPO-G). (**c**) Normalized PELDOR time trace for the double SDSL (4;18′) duplex in aqueous buffer (100%, 100 μm) and in TFE/aqueous buffer (85:15, 10 μm). Adapted with permission from [31]

occurs in double-stranded RNA or can be brought about by spore proteins or organic solvents. DNA strands were synthesized containing a nucleoside bearing the base 2-fluorohypoxanthine, which can be converted to a guanine analogue that is spin labelled at the 2 position by the addition of 4-amino TEMPO after chemical synthesis of the DNA. Upon addition of at least 75% (v/v) trifluoroethanol, there was a shift of 8 Å to a shorter distance, which was consistent with the modelled transition from B- to A-form.

Singh et al. [33] were able to monitor the different conformations a human telomeric quadruplex adopted under different salt conditions (Fig. 9). A single DNA strand was spin labelled at two different sites by attaching the label to the 5 position of a thymine base. This was achieved in a similar manner to how Schiemann et al. [19] attached TPA, except that a six-membered ring analogue, called TEMPA, was used instead. The PELDOR data showed that in the presence of sodium ions a single species was present that was consistent with the antiparallel basket form. However, in the presence of potassium ions a mixture of species was present that suggested a mixture of antiparallel basket and propeller forms. In addition, the hybrid 3 + 1 form cannot be ruled out from also being present since the distance distributions obtained are rather broad and also cover the appropriate distance for this form. The authors do not comment on the rather shallow modulation depth, which may suggest that they do not have 100% spin labelling efficiency.

Four-way DNA junctions are critical intermediates in genetic recombination and are specifically cut by resolvase enzymes to regenerate DNA duplexes and thus maintain genomic integrity. Freeman et al. [34] prepared a spin labelled four-way DNA junction and monitored its interaction with an inactivated resolvase (endonuclease I) using PELDOR (Fig. 10). They used the isocyanate labelling chemistry to attach a spin label to a site specifically inserted 2′-amino-uridine. It was found that

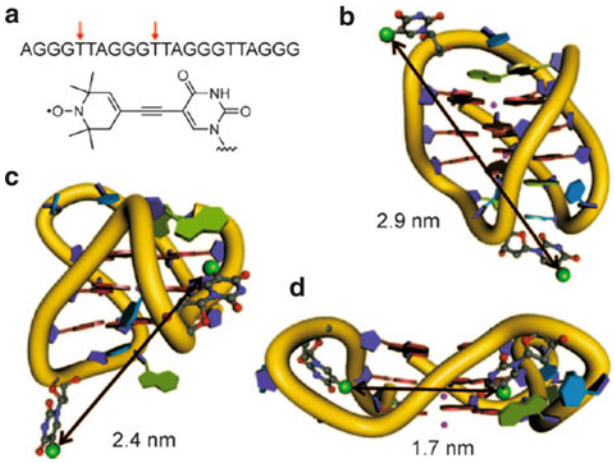

Fig. 9 (**a**) Human telomeric quadruplexes sequence where *red arrows* indicate sites of 5-TEMPA-modified deoxyuridine. (**b**) NMR spectroscopy structure of the antiparallel basket quadruplex in Na^+ ion containing solution (PDB: 143D). (**c**) NMR spectroscopic structure of a hybrid 3 + 1 quadruplex of a slightly modified sequence in K^+ ions (PDB: 2GKU). (**d**) Crystal structure of the parallel propeller form in the presence of K^+ ions (PDB: 1KF1). *Black arrows* indicate distances measured between C5 methyl carbon atoms of deoxythymidine residues. Reproduced with permission from [33]

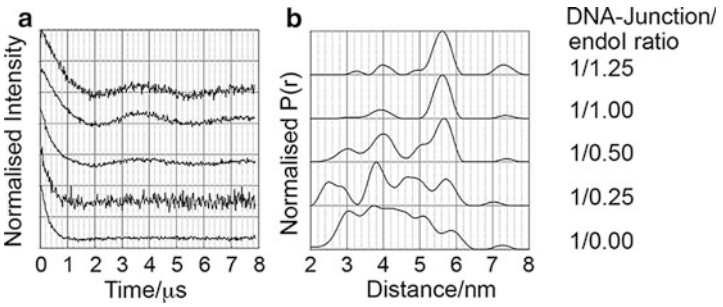

Fig. 10 EPR data for spin labelled four-way DNA junction as a function of endonuclease I concentration. (**a**) Background-corrected PELDOR data. (**b**) Tikhonov-derived distance distribution. Adapted with permission from [34]. Copyright (2011) American Chemical Society

the four-way junction alone gave an extremely broad distance distribution suggesting the presence of multiple different conformers. However, upon titration with endonuclease I a predominant and narrow distribution of distances resulted indicating that the junction was bound to the protein in a single conformer.

5.1.3 DNA Damage Examples

There are various agents that damage DNA, e.g. reactive oxygen species (products of metabolism), UV light, gamma radiation, plant toxins, mutagenic chemicals, etc. This damage can have various results, such as oxidation, alkylation or hydrolysis of the nucleobases, e.g. the formation of 8-oxo guanine, 6-*O*-methylguanine or an abasic site, respectively. These modifications will have effects on DNA replication and protein translation and thus, if not corrected, will lead to various diseases including cancer. It is therefore fundamentally important to understand these structural changes so that solutions can be found to rectify them.

Bowman et al. [35] used PELDOR to estimate the spatial distribution of radicals in tracks of heavy atom irradiated DNA.

One study involved investigating the effect on DNA duplex structure when one strand contained certain types of lesions [36]. The undamaged strand contained two spin labelled guanosine nucleotides, which was achieved by using the same chemistry that this group had used previously [31]. The damaged strand contained the following types of lesions, 8-oxoguanosine, a nick, a gap, a bulge, an abasic site or an anucleosidic site (see Fig. 11). For clarity, the nicked strand did not have a phosphate group present at the nick site and thus was made from two separate 7 and 13 mer complementary strands. Similarly, the strand with a gap was made of a 7 and 12 mer strand. By measuring the distance distributions for each of these duplexes and comparing with an undamaged duplex it was possible to deduce structural changes. The types of changes were divided into two groups. The first group, which included the nick, gap or bulge, showed a moderate broadening of the distance distribution (up to 0.5 Å for the gap) and a small increase in the most probable distance (up to 0.6 Å for the nick). The second group, which consisted of the abasic or anucleosidic site modifications, gave rise to a more significant broadening (up to 2.44 Å for the propyl linker modification) and an asymmetry of the distance distribution and a reasonable shortening of the distance (up to −3.5 Å for the THF sugar analogue modification). This study showed that changes to the distance distribution widths could be unambiguously detected and related to structural changes. These results owe a lot to the choice of labelling chemistry, which yields very narrow distance distributions.

5.1.4 In Vivo PELDOR Experiments with DNA

Recently, two very exciting papers have demonstrated that it is possible to perform PELDOR experiments within *Xenopus laevis* oocytes cells [37,38]. This paves the way for being able to monitor the structural changes of nucleic acids within the actual cellular milieu. It appears that Krstić et al. were able to achieve better results than Azarkh et al. because they used a five-membered ring nitroxide, which had a longer lifetime in the reducing conditions of the cell, and a longer and more stable DNA duplex, theirs was 12 bp instead of 7.

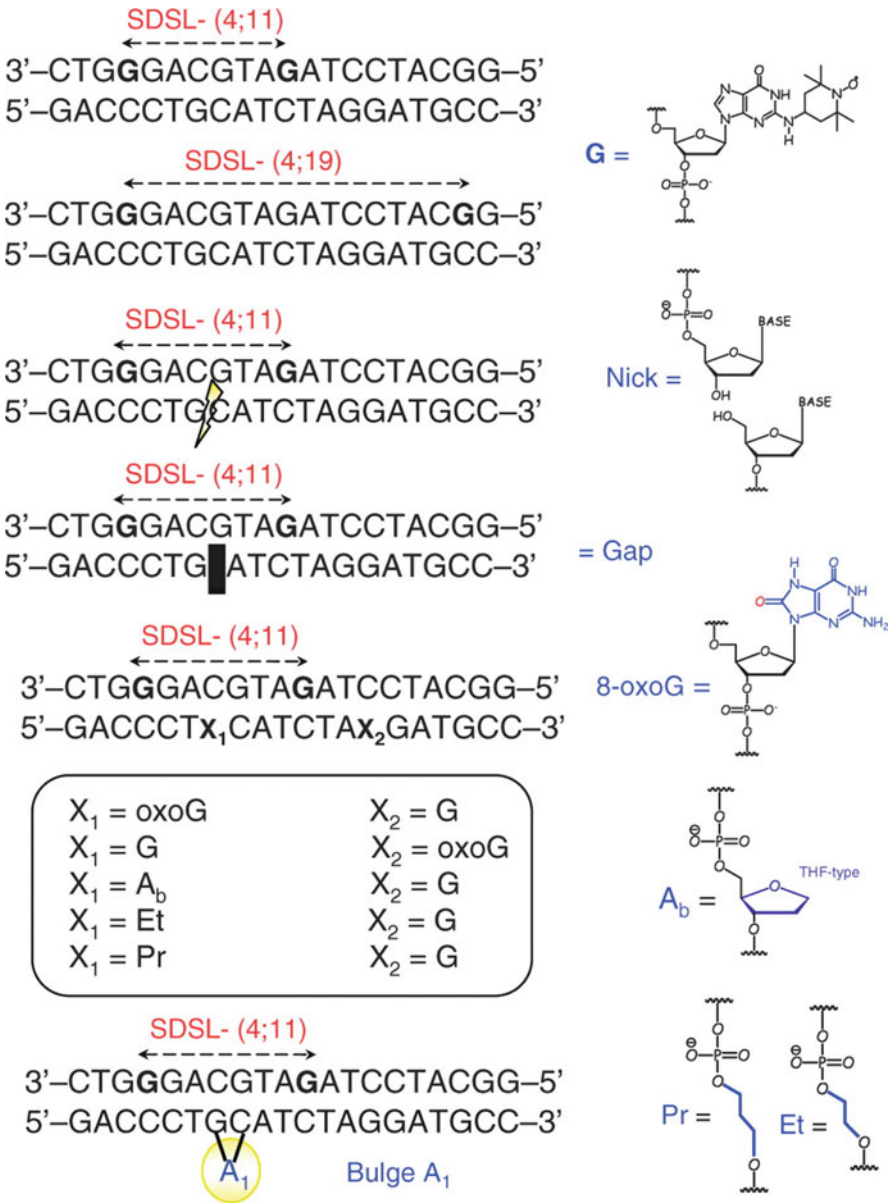

Fig. 11 Double spin labelled DNA strands with lesions in the complementary strand; the *bold* G position indicates the site of the spin label. The *right hand column* shows the spin label attachment site and the various types of lesions: nick, gap, 8-oxoG, bulge A1, abasic site and anucleosidic sites. Adapted from [36] with permission from Oxford University Press

5.2 RNA

5.2.1 CW EPR Examples

In 1999, the first report of using CW EPR to measure a distance between a strand of RNA and a peptide that were both singly nitroxide spin labelled was made [39]. The proof of principle investigation was carried out on the HIV Rev response element (RRE)–Rev system. The RRE, a nucleotide sequence found at the 5′ end of HIV RNA, binds to the HIV Rev protein to signal the export of the unspliced viral RNA from the nucleus. This was a good test system since the NMR structure of an HIV RRE–Rev peptide complex had recently been solved and could be used to validate the CW EPR distances determined. Macosko et al. incorporated a guanosine monophosphorothioate, which they synthetically prepared, at the 5′ end of the RRE RNA by using T7 RNA polymerase in vitro transcription, see Fig. 12. The sulphur of the phosphorothioate was then functionalized with *S*-(1-oxy-2,2,5,5-tetramethylpyrroline-3-methyl) methanethiosulphonate (typically used in protein spin labelling and abbreviated to MTSSL). The Rev peptide was chemically synthesized with a single cysteine and then postsynthetically reacted with MTSSL to generate the singly spin labelled peptide. The nucleotide sequences of the three RRE constructs were altered so as to shift the 5′ end of the RNA with respect to the binding site for the Rev peptide such that RRE1 and RRE2 would be within 25 Å but RRE3 should be at least 40 Å away and therefore not measurable by CW EPR. Consistent with this, the low temperature (133 K) CW EPR carried out showed spectral line broadening for the Rev peptide bound to RRE1/RRE2 but not when bound to RRE3, compared to the singly labelled spectra of the Rev peptide or the RRE1 RNA construct.

A more recent report used a series of spin labelled RNA duplexes, with different interspin distances, to act as a distance ruler to calibrate the line broadening effects seen in their CW EPR spectra [40]. By incorporating a 2′-amino-uridine into each RNA strand, it was then possible to attach a commercially available proxyl spin label at this position via an amide bond, resulting in a short and semi-rigid linker between the sugar and the unpaired electron in the nitroxide group, see Fig. 13. Unfortunately the yield of this reaction was quite low (50%) for these ten nucleotide long pieces of RNA and dropped even lower (20%) for a 35 nucleotide long piece of RNA. The effect of the spin label on the structure of the RNA duplex was investigated by UV-melting studies and was found to give rise to a 10°C change, with respect to the unmodified RNA, per spin label, which is quite a large change. The interspin distances were extracted from the low temperature (183 K) CW EPR line shapes by Fourier deconvolution. In order to apply this technique, it was also necessary to prepare singly labelled RNA duplexes and record their CW EPR line shapes as well, see Fig. 14. The distances obtained (9–22 Å) compared very favourably to the average distances determined from a molecular dynamics experiment on an A-form piece of RNA with the nitroxide spin labels attached, where distances were measured between the two nitroxide nitrogen atoms. Having

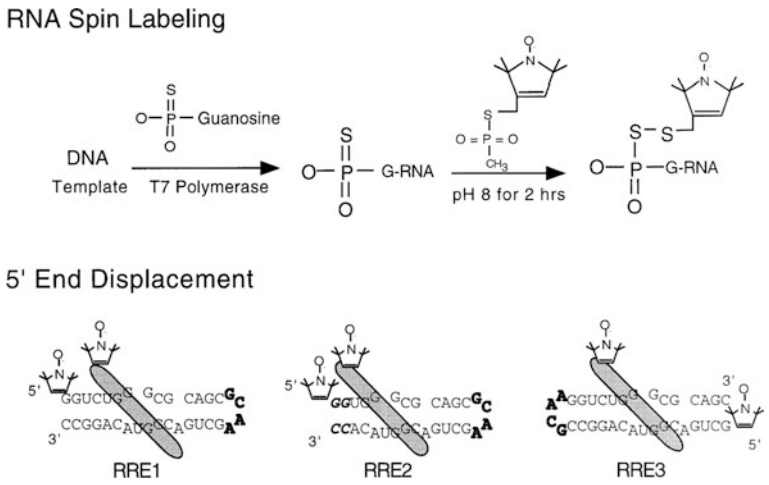

Fig. 12 A schematic of the RNA spin labelling strategy. RNA is transcribed by T7 RNA polymerase in the presence of guanosine 5′ phosphorothioate, then spin labelled with *S*-(1-oxy-2,2,5,5-tetramethylpyrroline-3-methyl) methanethiosulphonate spin label. Below this is the sequence and secondary structure of the three RRE constructs, showing the spin label at the 5′ end. *Diagonal grey rods* represent the bound Rev with attached spin label. Adapted with permission from [39]

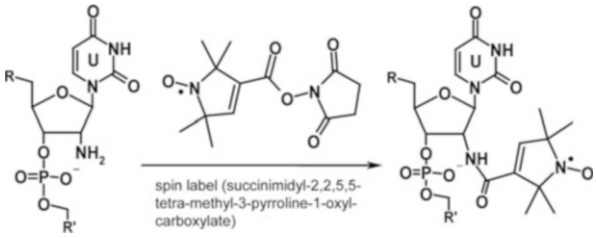

Fig. 13 Spin labelling reaction to form 2′-amide linked proxyl spin label. Reprinted from [40] with permission from Elsevier

validated their approach, Kim et al. went on to investigate a biologically relevant HIV-1 transactivating responsive region (TAR) RNA structure, which is required for the activation of HIV gene expression. The TAR RNA was spin labelled at two sites that were close to a three base bulge, which had been predicted to undergo structural changes upon binding of either the HIV Tat protein or metal ions, e.g. magnesium or calcium. The low temperature CW EPR spectra of the TAR RNA alone were measured and yielded a distance of approximately 12 Å. Upon the addition of both calcium and magnesium ions, this distance increased to 14 Å. This change in distance was rationalized in terms of a conformational change, possibly resulting from the two helices in the RNA structure becoming coaxially stacked.

It is worth mentioning that another group also used 2′-amino-uridine to site specifically label sugar groups within TAR RNA but they used a 4-isocyanate TEMPO spin label instead, which can be synthesized in one step from a

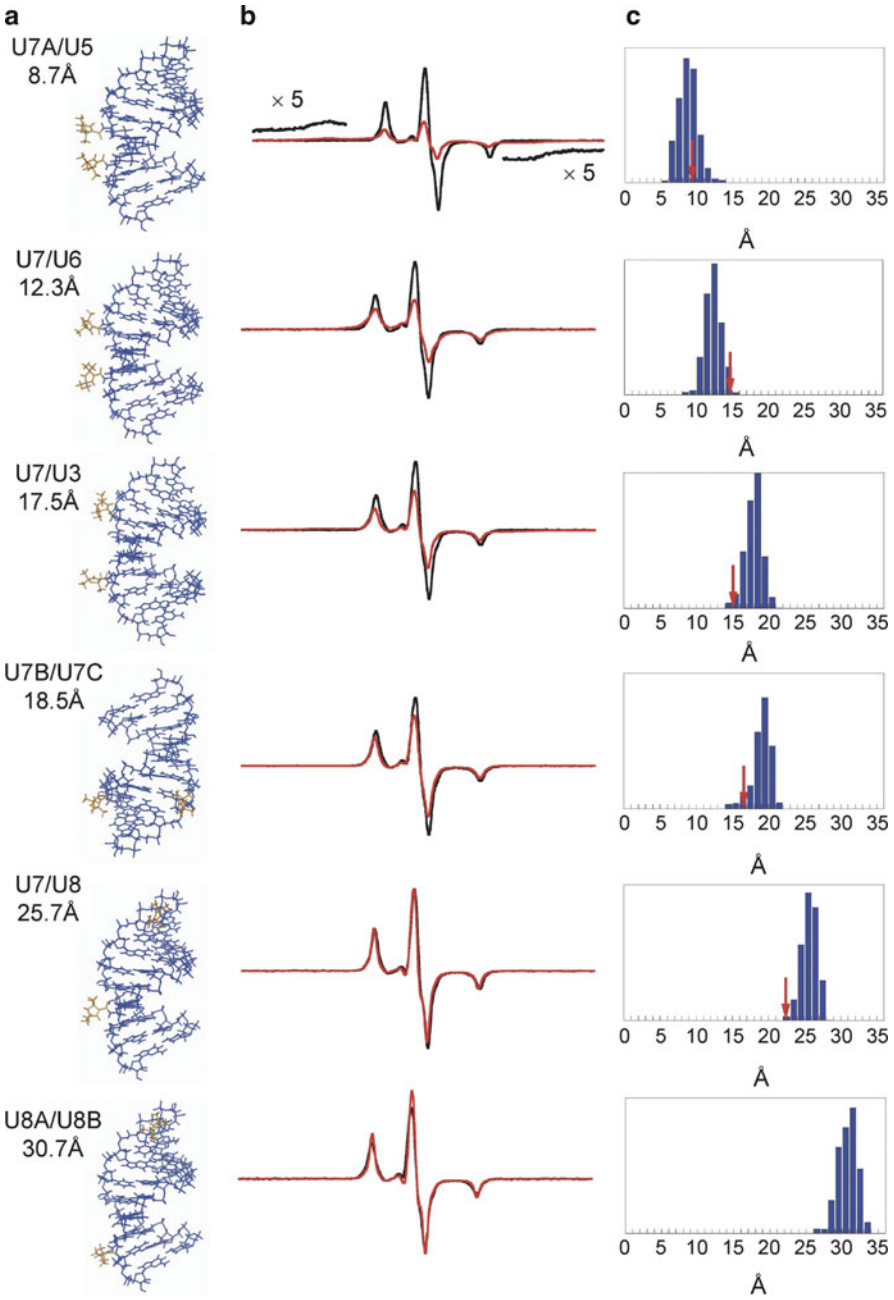

Fig. 14 CW EPR spectra and predicted interspin distances for spin labelled RNA duplexes. (**a**) The structures of spin labelled A-form RNA 10-mers simulated. (**b**) EPR spectra of the doubly labelled 10-mers (*red*) and the summed spectra of two singly labelled duplexes (*black*). (**c**) Distributions of the interspin distances for all duplexes predicted from molecular dynamics

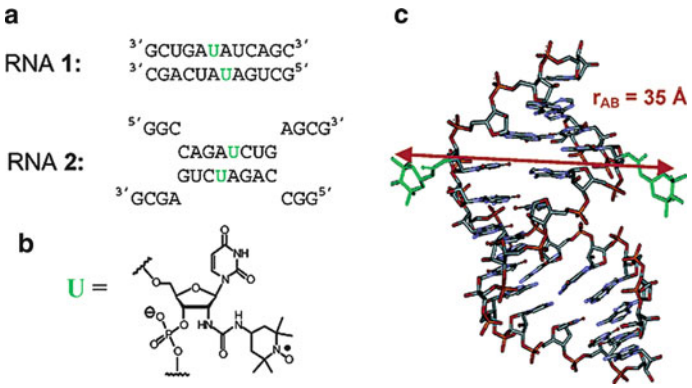

Fig. 15 (**a**) Sequence of RNA **1** and **2**. A *green* U marks the position of the spin label. (**b**) The structure of the spin labelled U. (**c**) Crystal structure of an A-form RNA. The *red arrow* is the O–O distance r_{AB} between the nitroxides. Reproduced with permission from [42]. Copyright (2003) American Chemical Society

commercially available starting material, and report significantly better yields of greater than 90%. However, this study was concerned with investigating the local dynamics of the RNA at different positions in the absence and presence of two Tat-derived peptides [41].

5.2.2 Pulsed EPR Examples

Pulsed EPR experiments are particularly powerful as they pick out just the distance-dependent dipolar coupling separating it from other interactions affecting the spin system such as those defined by the *g*-values and the hyperfine couplings.

Model RNA Structures

Schiemann et al. [42] presented the first PELDOR data on a duplex piece of RNA in frozen aqueous solution. They chemically synthesized two 12 nucleotide long pieces of RNA with a 2′-amino-uridine at the centre of each sequence. The 2′-amino group was then modified by reaction with 4-isocyanate TEMPO, yielding a urea linker between the sugar of the RNA and the carbon ring that contains the nitroxide radical, see Fig. 15. They used the three-pulse ELDOR experiment and

Fig. 14 (continued) calculations (*blue*) and the averaged interspin distances obtained from Fourier deconvolution analysis of EPR spectra (*red arrow*). Note that for the longest distance separation, *bottom panel*, there is no *red arrow* because there is no difference between the spectra for single and double spin labelled duplexes. Reprinted from [40] with permission from Elsevier

were able to extract a distance of 35 Å by examining the Fourier transformation of the background-corrected data. This distance was in excellent agreement with the O–O distance measured from a computer model of this duplex RNA with the spin labels attached. This group carried out their PELDOR experiments in a cryoprotectant-free solution in order to provide a more biologically relevant environment. However, this resulted in very short electron spin phase memory times, which significantly shortened the time over which data could be collected for the ELDOR experiment. Subsequently the authors improved the aqueous solution conditions by adding the cryoprotectant ethylene glycol for further measurements without observable change of the structure [19].

Using a refinement to the DQC pulse sequence in combination with a home-built K-band spectrometer, allowing for short pulses, Borbat et al. [43] were able to measure a very long distance of approximately 70 ± 5 Å on a 26 bp duplex RNA. The measured distance, extracted from the Fourier transformed data, compared favourably to the 65 Å that was anticipated from a model generated from the high-resolution crystal structure (PDB 1QC0) of an A-form piece of RNA. The RNA used for the study was chemically synthesized with a 4-thiouracil incorporated at the 5′ end of each strand, see Fig. 16. A commercially available iodoacetamide proxyl spin label was then reacted to generate the spin labelled RNA strands. This work demonstrated that by using the double-quantum filtered refocused electron spin echo pulse sequence, it is possible to suppress the effects of nuclear spin diffusion and thus increase the electron spin phase memory time, thus permitting one of the longest distance measurements ever made.

One of the limitations to structural studies on RNA by EPR was the limited number of attachment sites that were available, i.e. the 2′ position on the sugar, the phosphate backbone and the 4 position on uridine. Piton et al. [44] were able to expand this range of sites by synthetically preparing phosphoramidites, the building blocks of nucleic acids in chemical synthesis, that had a site on either uridine, cytidine or adenosine that made it possible to covalently attach an alkyne functionalized proxyl spin label, called 2,2,5,5-tetramethylpyrrolin-1-yloxyl-3-acetylene (TPA), via a palladium-catalyzed cross-coupling reaction, see Fig. 17. The spin label was also synthesized, but only small amounts were required for the coupling reaction. During their investigation, they found that BzH and ACE protection chemistries, structures shown in Fig. 17, which had recently been developed for RNA synthesis, were significantly better than the existing dimethoxytrityl (DMT) and *tert*-butyldimethylsilyl (TBDMS) ether protection methodology. This was because far less reduced nitroxide was found in the end product, the details of which are covered within the paper. The impact of the spin label on the structure of the resultant duplex RNAs was accessed by CD and UV-melting curves, both of which suggested that the spin labels only minimally perturb the A-form RNA structure.

All the RNA duplexes showed clear oscillations in the PELDOR time traces, indicative of well-defined distance distributions, as would be expected from an RNA molecule that behaves like a semi-rigid rod to which a rigid spin label has been attached. The distances were extracted by using Tikhonov regularization to

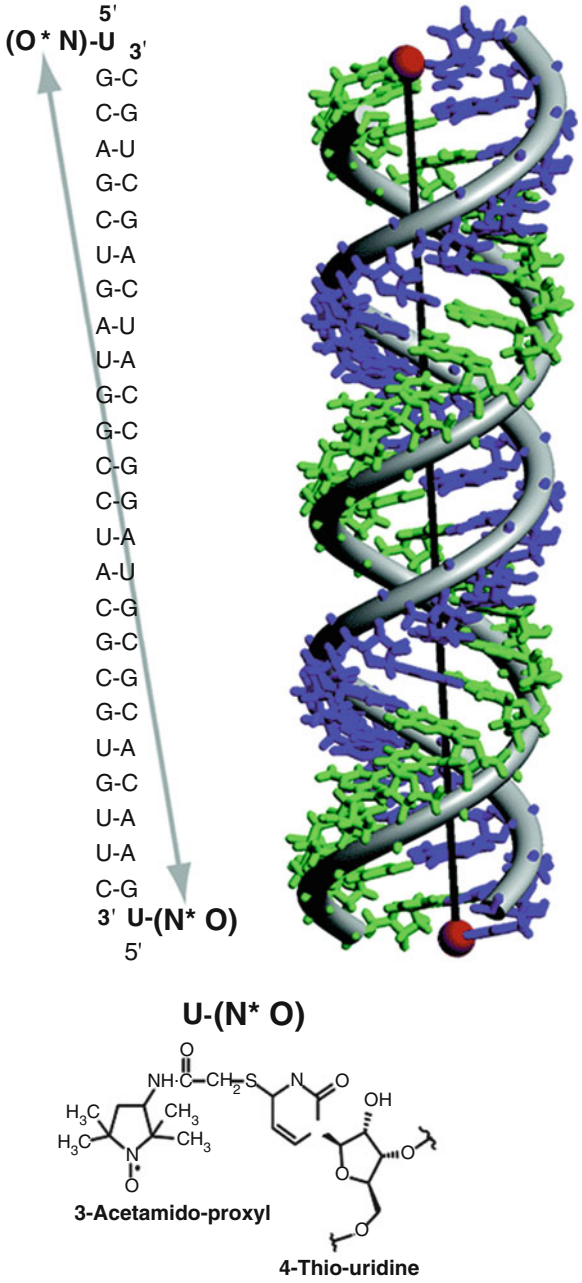

Fig. 16 A-form RNA sequence (26 bp) with the nitroxide label that is attached to the 4-thiouridine residue at the 5′ end. High-resolution X-ray crystal structure of an A-form duplex (PDB ID 1QC0) is also shown with spin labels attached as *red spheres*. Reproduced with permission from [43]. Copyright (2004) American Chemical Society

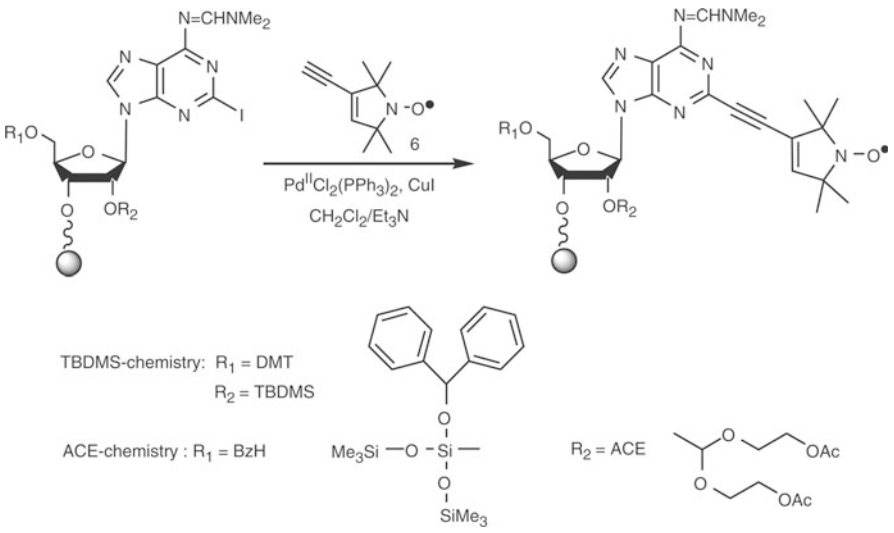

Fig. 17 Sonogashira cross-coupling reaction during the solid-phase synthesis (e.g. 2-iodoadenosine) of RNA. Reproduced from [44] with permission from Oxford University Press

find an appropriate fit to the background-corrected time trace PELDOR data [21]. These distances agreed well with molecular dynamics simulations on an A-form RNA structure with the spin labels attached. The results also allowed discrimination between A-form RNA and B-form DNA. This spin labelling chemistry has also been used to investigate RNA–DNA hybrids, which are critical intermediates in gene regulation [45]. The PELDOR data yields distances that suggest that the DNA (dA)–RNA(rU) adopts an overall B-form structure, whereas the DNA(dT)–RNA (rA) adopts a more A-form structure, when compared with distances generated for an all DNA (B-form) or RNA structure (A-form). This was in excellent agreement with the cleavage rates of the DNA/RNA hybrids with RNase H1, which recognizes an A-form structure, where the DNA(dT)/RNA(rA) was cleaved faster than the DNA(dA)/RNA(rU) hybrid.

Another group used the same approach that they had used with DNA [20] to incorporate a phosphorothioate group, during solid-phase RNA synthesis, into RNA strands, which could then be reacted with an iodomethyl proxyl spin label to form what they describe as an R5 label [46], see Fig. 18. This is quite a cost-effective method for the synthesis of spin labelled RNA since all the reagents are commercially available and relatively cheap. One issue with this approach is that if the 2′ hydroxyl group adjacent to the labelled phosphorothioate is not removed, then strand scission can occur upon covalent attachment of the spin label. Since the removal of a 2′ hydroxyl group may affect the folding of a more complicated piece of RNA, greater thought may be required to use this labelling strategy in comparison to some of the other methods. In total, six spin labelled RNA duplexes, where each strand contained a single label, were prepared for PELDOR, but before this

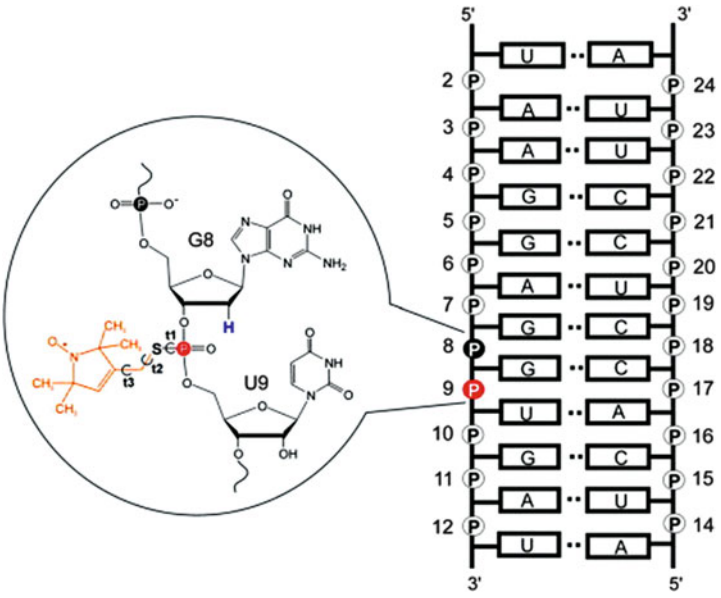

Fig. 18 RNA duplex sequence showing spin labelling at phosphate position 9, shown as a *red sphere*. *Inset* shows the detailed chemical structure of the R5 spin label (*orange*) attached at position 9. Notice the deoxyribose substitution at nucleotide 8, which replaces the 2′-OH group adjacent to the labelled phosphorothioate with a 2′-H (*blue*). Reproduced from [46] with permission from Elsevier

their secondary structure was checked by CD, which showed a typical A-form spectrum, and UV-melting temperature studies, which showed at most a 10°C change, with respect to the unlabelled RNA duplex. The majority of the PELDOR time trace data showed oscillations, although not always as pronounced as seen in [44]. The distance distributions obtained were multicomponent, which may in part be because the label can attach to form two diastereoisomers. Additionally, however, the A-form RNA has a narrower and deeper major groove thus making it more difficult to accommodate the spin label, which may lead to greater local structural heterogeneity in the RNA. Despite these observations, the distances obtained from the PELDOR data agreed well with those obtained from a label conformer search algorithm applied to an in silico spin labelled RNA X-ray structure that was static (PDB code 1SDR).

An alternative method for the incorporation of spin labels into RNA is based on the use of commercially available convertible nucleosides, which are nucleobases that contain a base labile functional group, during the solid-phase RNA synthesis [47]. Once the RNA had been synthesized, 4-amino TEMPO was used to displace the base labile functional group. In this way RNA strands with a TEMPO spin label attached to either cytosine, adenosine or guanosine could be prepared. Being able to spin label three out of the four bases clearly provides a great deal of flexibility in the choice of RNA labelling site. Sicoli et al. then prepared a number of different spin

labelled RNA structures. They started with four RNA duplexes where one strand was double spin labelled and the other was unlabelled. CD was used to verify the A-form structure of these duplexes. The UV-melting experiments showed a destabilization of 5–6°C per TEMPO label added, which may suggest a local perturbation of the RNA structure. The PELDOR data showed clear oscillations for all of the duplexes. This gave rise to narrow distance distributions that were in good qualitative agreement with the values expected for a perfect A-form structure. Next an RNA G-quadruplex was examined whose structure had recently been solved by NMR. UV-melting experiments were used to verify that the spin labels had not prevented the RNA from forming a quadruplex structure. Once again the PELDOR data showed a clear oscillation, yielding a well-defined distance distribution for the G-quadruplex. The distance of 37 Å agreed well with the 36.5 Å measured between attachment sites on the NMR structure. Finally, a single RNA strand, which was double spin labelled, was synthesized that would form a very stable hairpin structure. In the hairpin state, the spin labels were only 6 bp apart, which corresponded to a distance of 18 Å. Upon addition of a complementary RNA strand, which was not labelled, a duplex conformation would be preferred where the spin labels were 11 bp apart, which corresponded to a distance of 31 Å. By titrating in the complementary strand until there was an excess of it, with respect to the double spin labelled strand, all of the RNA could be converted to a duplex structure and this could be observed in the distance distributions obtained by PELDOR, see Fig. 19.

Complex RNAs

Having established a range of RNA spin labelling strategies and demonstrated that the PELDOR experiments yield accurate distance information, the next step was to investigate the structures and conformational changes of functional RNAs. Thus far a ribozyme has been investigated in vitro, while a riboswitch has been monitored in vivo as well as in vitro, these examples are discussed below.

The HHRz is a small self-cleaving RNA motif that is induced to fold, and therefore becomes catalytically active upon the addition of magnesium ions. A loop–loop interaction between stem I and stem II, which is distant from the active site of HHRz, has also been shown to dramatically increase the rate of catalysis. In order to investigate the folding of HHRz and the importance of the loop–loop interaction, two RNA strands were prepared, an enzyme strand and a substrate strand, and labelled next to each loop, see Fig. 20 [48]. The spin labelling chemistry used was the incorporation of either 2′-amino-uridine or cytosine into the synthesized RNA strand followed by reaction with 4-isocyanato TEMPO. The effects of the TEMPO on the ribozyme structure appeared to be negligible since the catalytic rates of the spin labelled ribozyme were shown to be the same as the unlabelled form. For the PELDOR experiments, the spin labelled substrate strand was also protected from cleavage by the incorporation of a 2′-OMe, in an attempt to lock the enzyme in its catalytically active form. In addition, two spin labelled

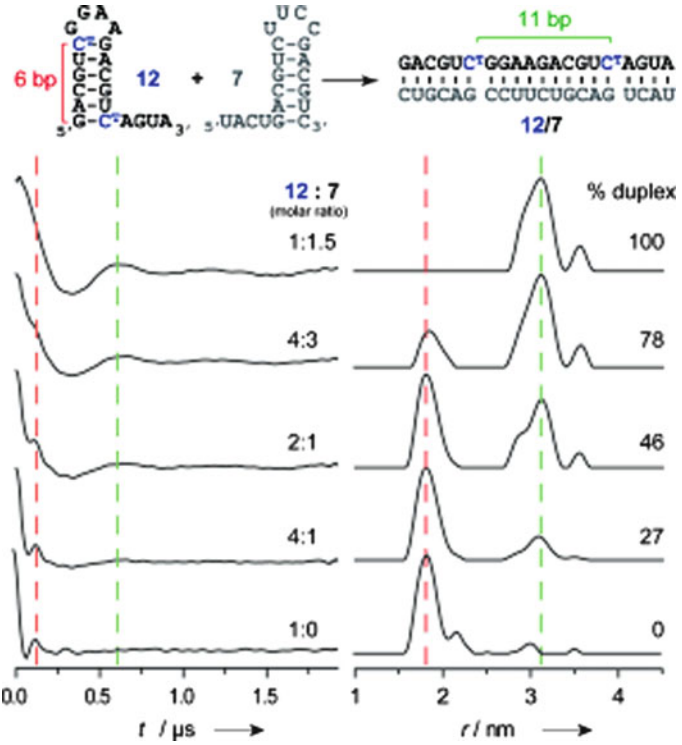

Fig. 19 PELDOR titration experiment using double spin labelled RNA construct 12 and non-spin labelled RNA construct 7. Spin label position marked with a *blue* C. Individually both RNA constructs fold into hairpin conformations but form an extended duplex when mixed. Stepwise addition of hairpin 7 to hairpin 12 generates 25%, 50%, 75%, and 100% duplex in the mixture (duplex content increases from *bottom* to *top*), which is approximately matched by the amount of duplex seen in the distance distribution. Note that the percentage duplex, shown on the *right hand side*, has been calculated from the relative areas under the distance distributions for the hairpin structure (maximum indicated by *red line*) and the duplex structure (maximum indicated by g*reen line*). Adapted with permission from [47]. Copyright 2010 Wiley-VCH Verlag GmbH & Co. KGaA, Weinheim

enzyme strands were prepared, one with a "wild-type" structure and the other with a modified "U-loop", which does not form the loop–loop interaction.

PELDOR experiments were then carried out with different magnesium concentrations present in solution, between 0 and 50 mM. The PELDOR distance distribution data for the "wild-type" enzyme in complex with the substrate strand showed no clear distance until 10 mM magnesium was added, and the intensity of this peak increased upon addition of further magnesium. The extracted distance of 24 Å agreed well with the 25 Å determined from the model structure. As anticipated, the PELDOR data for the "U-loop" enzyme showed no clear distance peak at 10 mM magnesium concentration suggesting that the two loops do not interact to form a well-defined structure. This result was consistent with the very

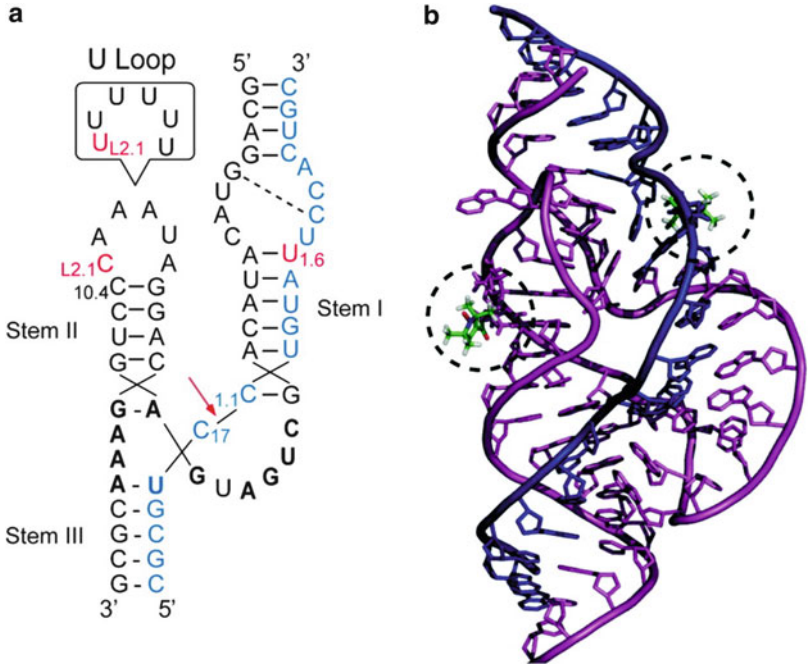

Fig. 20 Hammerhead ribozyme (HHRz) structure. (**a**) Secondary structure of the extended HHRz from *Schistosoma mansoni*. The enzyme sequence is written in *black*, substrate in *blue*, and spin labelling sites in *red*. The ribozyme cleavage site is marked with a *red arrow*, and the base-pairing in loop I is indicated with a *dashed line*. The U-loop substitutions are indicated. (**b**) Model of spin labelled extended HHRz created from the crystal structure (PDB ID 2GOZ). The substrate is shown in *dark blue*, and the enzyme is in *magenta*. The spin labels are shown in *green* with *dashed circles*. Adapted with permission from [48]. Copyright (2010) American Chemical Society

low catalytic rate observed for this mutant enzyme compared to the wild type. This clearly demonstrates that PELDOR is capable of monitoring the folding event that generates the catalytically active ribozyme.

Riboswitches are regulatory RNA structures that can switch gene expression on or off by undergoing a conformational change upon binding to their specific target molecule. Since most natural riboswitches are known to occur in bacteria, it is thought that these may be potential drug targets in the future. Due to their utility as genetic switches, artificially engineered riboswitches have also been generated that are called aptamers. These RNA molecules have been identified by applying both in vitro selection, which results in aptamers that bind to a predefined ligand with high affinity, and in vivo screening, which results in RNAs with the required functionality within cells. The tetracycline (Tc)-binding aptamer [49] and the neomycin-responsive aptamer [50] have both been investigated by SDSL and PELDOR spectroscopy.

Wunnicke et al. [49] prepared the Tc aptamer by solid-phase RNA synthesis. At the positions chosen for labelling, either a 4-thiouridine or a 2′-amino-uridine

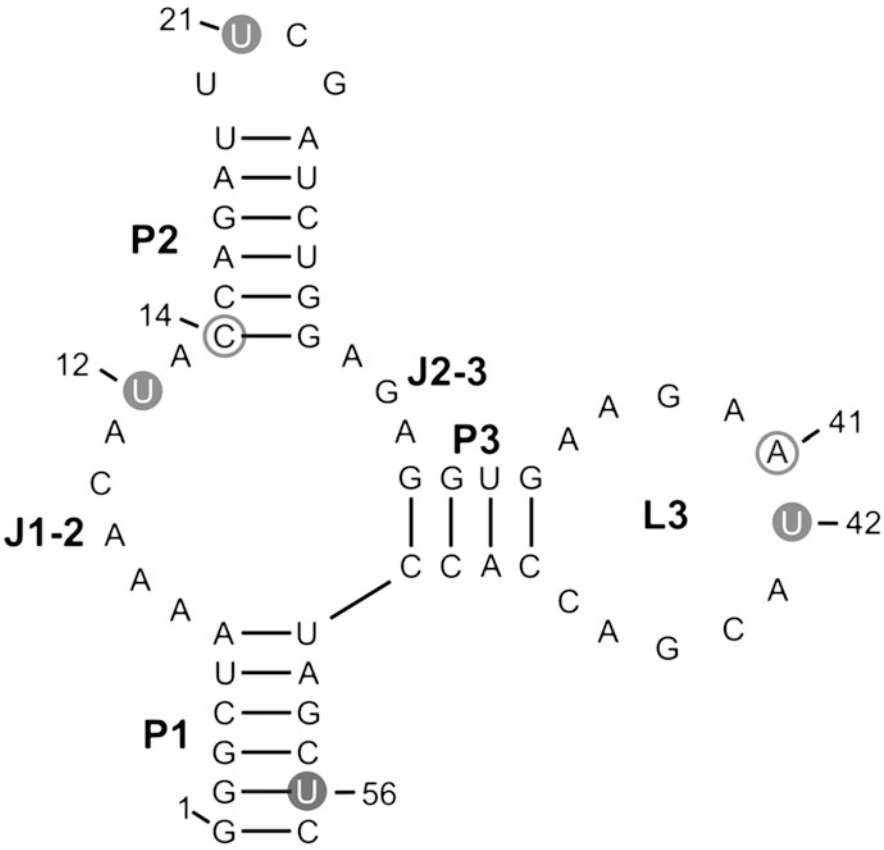

Fig. 21 Secondary structure predicted for the tetracycline (Tc) aptamer. Thiouridines (U) spin labelled with MTSSL are marked by *full grey circles*. Adapted with permission from [49]

was incorporated, see Fig. 21. After RNA synthesis the 4-thiouridine was chemically modified with MTSSL, and the 2′-amino-uridine was labelled with 4-isocyanato-TEMPO. The effects of the spin label modification on the Tc aptamer were checked by determining the binding constant between the RNA and Tc. Both types of spin labelled Tc aptamers still bound Tc, but neither as well as the unlabelled control sample. Interestingly, the 2′-amino-uridine-modified RNA seemed to have the least impact on Tc binding. PELDOR data were collected on four double spin labelled aptamer samples in the absence and presence of Tc. The inferred changes in the distance distributions, determined using DeerAnalysis2006 [21], suggested that the aptamer exists in a thermodynamic equilibrium between two conformations in the absence of Tc, and that one conformer is then preferred upon Tc binding. Modelling of these distance data using the X-ray structure of the Tc aptamer (PDB code 3EGZ) suggested that a subtle repositioning of the loop in region J1–2 occurs.

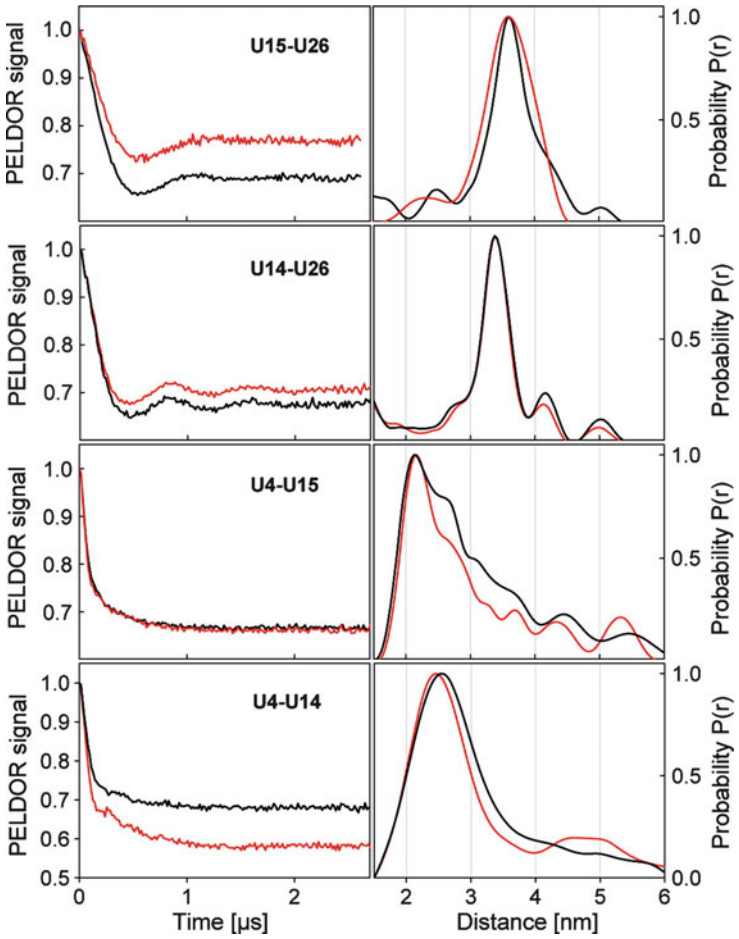

Fig. 22 *Left column*: background-corrected PELDOR time traces of double-labelled neomycin-responsive aptamer samples with neomycin in a ratio 1:1 (*red*) and without neomycin (*black*). *Right column*: Tikhonov regularization-derived distance distributions. Adapted with permission from [50]. Copyright (2010) American Chemical Society

Krstić et al. [50] used the rigid spin label TPA, and its associated chemistry, to study the neomycin-responsive aptamer. Interestingly, their PELDOR data showed no significant differences between the aptamer alone and when in complex with neomycin, see Fig. 22, despite having evidence from UV-melting and room temperature CW EPR experiments that neomycin was bound to the aptamer. These data led the authors to speculate that the RNA aptamer exists in an ensemble of conformations, and that neomycin binds by RNA conformational selection rather than by an induced fit.

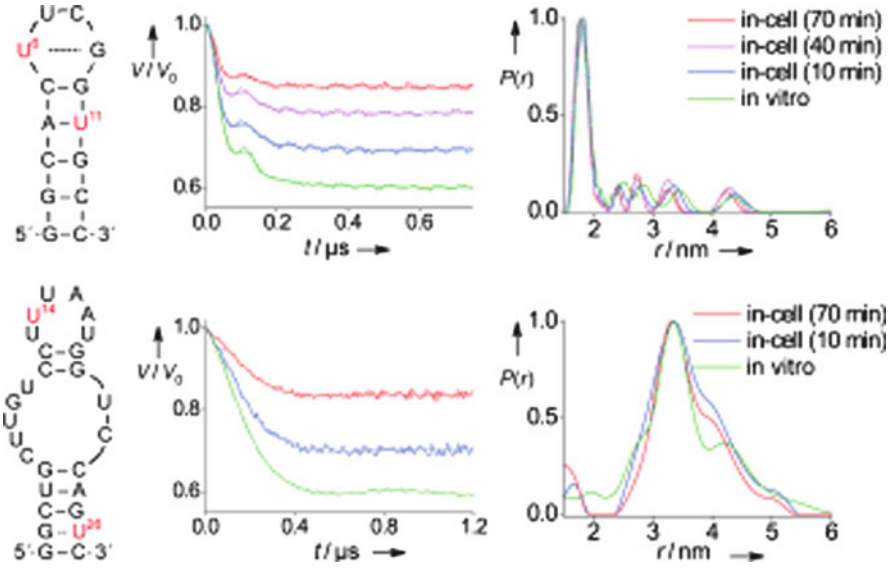

Fig. 23 *Left column*: secondary structures of RNA constructs (with spin labelled nucleotides in *red*); *Middle column*: baseline-corrected PELDOR time traces; *Right column*: distance distribution functions. Data for the double-labelled 14-mer cUUCGg tetraloop hairpin RNA (*upper panel*) and the 27-mer neomycin-sensing riboswitch (*lower panel*). The in-cell data after different incubation times are compared with in vitro data. Adapted with permission from [38]

Most recently, the same group successfully demonstrated that spin labelled RNAs can be introduce
d into *X. laevis* oocytes and still be measured using PELDOR spectroscopy [38]. In addition to this amazing technical feat, the results suggest that the structure of the neomycin-responsive aptamer within the cells is the same as observed in an in vitro sample, see Fig. 23.

6 Summary

Oligonucleotides are important biological molecules and more detailed studies are required to understand the way in which their structure is recognized and altered by other nucleic acids, proteins, small molecules, and metal ions. It is now possible to site specifically label all components of the nucleic acid, i.e. phosphate, sugar and bases, and EPR methods for reliable measurements of nanometre distances are available. The future challenge to EPR investigation of RNA structure will be to develop new approaches [51] for investigating much larger pieces of RNA, which presently cannot be chemically synthesized. This will take a synergistic effort from molecular biologists, chemists and EPR spectroscopists.

Acknowledgements The BBSRC (BB/H017917/1) and the Wellcome Trust (13973) are acknowledged for funding and the Research Councils of the UK are thanked for an RCUK fellowship.

References

1. Hunsicker-Wang L, Vogt M, Derose VJ (2009) EPR methods to study specific metal-ion binding sites in RNA. Methods Enzymol 468:335–367
2. Schiemann O, Fritscher J, Kisseleva N, Sigurdsson ST, Prisner TF (2003) Structural investigation of a high-affinity MnII binding site in the hammerhead ribozyme by EPR spectroscopy and DFT calculations. Effects of neomycin B on metal-ion binding. Chembiochem 4 (10):1057–1065
3. Kisseleva N, Khvorova A, Westhof E, Schiemann O (2005) Binding of manganese(II) to a tertiary stabilized hammerhead ribozyme as studied by electron paramagnetic resonance spectroscopy. RNA 11(1):1–6
4. Kisseleva N, Kraut S, Jäschke A, Schiemann O (2007) Characterizing multiple metal ion binding sites within a ribozyme by cadmium-induced EPR silencing. HFSP J 1(2):127–136
5. Clever GH, Reitmeier SJ, Carell T, Schiemann O (2010) Antiferromagnetic coupling of stacked Cu(II)-salen complexes in DNA. Angew Chem Int Ed Engl 49(29):4927–4929
6. Berliner LJ (2010) From spin-labeled proteins to in vivo EPR applications. Eur Biophys J 39(4):579–588
7. Zhang X, Cekan P, Sigurdsson ST, Qin PZ (2009) Studying RNA using site-directed spin-labeling and continuous-wave electron paramagnetic resonance spectroscopy. Methods Enzymol 469:303–328
8. Berliner LJ, Eaton SS, Eaton GR (eds) (2000) Distance measurements in biological systems by EPR. In: Biological magnetic resonance, vol 19. Kluwer Academic/Plenum, New York
9. Schiemann O, Prisner TF (2007) Long-range distance determinations in biomacromolecules by EPR spectroscopy. Q Rev Biophys 40(1):1–53
10. Margraf D, Cekan P, Prisner TF, Sigurdsson ST, Schiemann O (2009) Ferro- and antiferromagnetic exchange coupling constants in PELDOR spectra. Phys Chem Chem Phys 11 (31):6708–6714
11. Rabenstein MD, Shin YK (1995) Determination of the distance between two spin labels attached to a macromolecule. Proc Natl Acad Sci USA 92:8239–8243
12. Marsh D, Horvath LI (1989) Spin label studies of the structure and dynamics of lipids and proteins in membranes. In: Hoff AJ (ed) Advanced EPR. Applications in biology and biochemistry. Elsevier, Amsterdam, pp 707–752
13. Robinson BH, Drobny GP (1995) Site-specific dynamics in DNA: theory and experiment. Methods Enzymol 261:451–509
14. Robinson BH, Mailer C, Drobny G (1997) Site-specific dynamics in DNA: experiments. Annu Rev Biophys Biomol Struct 26:629–658
15. Keyes RS, Bobst AM (1998) Spin-labeled nucleic acids. In: Berliner LJ (ed) Spin labeling. The next millennium, vol 14. Plenum, New York, pp 283–338
16. Liang ZL, Freed JH, Keyes RS, Bobst AM (2000) An electron spin resonance study of DNA dynamics using the slowly relaxing local structure model. J Phys Chem B 104:5372–5381
17. Qin PZ, Butcher SE, Feigon J, Hubbell WL (2001) Quantitative analysis of the isolated GAAA tetraloop/receptor interaction in solution: a site-directed spin labeling study. Biochemistry 40:6929–6936
18. Qin PZ, Dieckmann T (2004) Application of NMR and EPR methods to the study of RNA. Curr Opin Struct Biol 14:350–359
19. Schiemann O, Piton N, Mu Y, Stock G, Engels JW, Prisner TF (2004) A PELDOR-based nanometer distance ruler for oligonucleotides. J Am Chem Soc 126(18):5722–5729

20. Cai Q, Kusnetzow AK, Hubbell WL, Haworth IS, Gacho GP, Van Eps N, Hideg K, Chambers EJ, Qin PZ (2006) Site-directed spin labeling measurements of nanometer distances in nucleic acids using a sequence-independent nitroxide probe. Nucleic Acids Res 34(17):4722–4730
21. Jeschke G, Chechik V, Ionita P, Godt A, Zimmermann H, Banham J, Timmel CR, Hilger D, Jung H (2006) DeerAnalysis2006 – a comprehensive software package for analyzing pulsed ELDOR data. Appl Magn Reson 30:473–498
22. Ward R, Keeble DJ, El-Mkami H, Norman DG (2007) Distance determination in heterogeneous DNA model systems by pulsed EPR. Chembiochem 8(16):1957–1964
23. Kolb HC, Finn MG, Sharpless KB (2001) Click chemistry: diverse chemical function from a few good reactions. Angew Chem Int Ed Engl 40(11):2004–2021
24. Flaender M, Sicoli G, Fontecave T, Mathis G, Saint-Pierre C, Boulard Y, Gambarelli S, Gasparutto D (2008) Site-specific insertion of nitroxide-spin labels into DNA probes by click chemistry for structural analyses by ELDOR spectroscopy. Nucleic Acids Symp Ser (Oxf) 52:147–148
25. Ding P, Wunnicke D, Steinhoff HJ, Seela F (2010) Site-directed spin-labeling of DNA by the azide-alkyne 'click' reaction: nanometer distance measurements on 7-deaza-2′-deoxyadenosine and 2′-deoxyuridine nitroxide conjugates spatially separated or linked to a 'dA-dT' base pair. Chemistry 16(48):14385–14396
26. Flaender M, Sicoli G, Aci-Seche S, Reignier T, Maurel V, Saint-Pierre C, Boulard Y, Gambarelli S, Gasparutto D (2011) A triple spin-labeling strategy coupled with deer analysis to detect DNA modifications and enzymatic repair. Chembiochem 12:2560–2563
27. Gore J, Bryant Z, Nöllmann M, Le MU, Cozzarelli NR, Bustamante C (2006) DNA overwinds when stretched. Nature 442(7104):836–839
28. Mathew-Fenn RS, Das R, Harbury PA (2008) Remeasuring the double helix. Science 322 (5900):446–449
29. Marko A, Denysenkov V, Margraf D, Cekan P, Schiemann O, Sigurdsson ST, Prisner TF (2011) Conformational flexibility of DNA. J Am Chem Soc 133(34):13375–13379
30. Schiemann O, Cekan P, Margraf D, Prisner TF, Sigurdsson ST (2009) Relative orientation of rigid nitroxides by PELDOR: beyond distance measurements in nucleic acids. Angew Chem Int Ed Engl 48:3292–3295
31. Sicoli G, Mathis G, Delalande O, Boulard Y, Gasparutto D, Gambarelli S (2008) Double electron–electron resonance (DEER): a convenient method to probe DNA conformational changes. Angew Chem Int Ed Engl 47(4):735–737
32. Saenger W (1984) Principles of nucleic acid structure. Springer, New York
33. Singh V, Azarkh M, Exner TE, Hartig JS, Drescher M (2009) Human telomeric quadruplex conformations studied by pulsed EPR. Angew Chem Int Ed Engl 48(51):9728–9730
34. Freeman AD, Ward R, El Mkami H, Lilley DM, Norman DG (2011) Analysis of conformational changes in the DNA junction-resolving enzyme T7 endonuclease I on binding a four-way junction using EPR. Biochemistry 50(46):9963–9972
35. Bowman MK, Becker D, Sevilla MD, Zimbrick JD (2005) Track structure in DNA irradiated with heavy ions. Radiat Res 163(4):447–454
36. Sicoli G, Mathis G, Aci-Sèche S, Saint-Pierre C, Boulard Y, Gasparutto D, Gambarelli S (2009) Lesion-induced DNA weak structural changes detected by pulsed EPR spectroscopy combined with site-directed spin labelling. Nucleic Acids Res 37(10):3165–3176
37. Azarkh M, Okle O, Singh V, Seemann IT, Hartig JS, Dietrich DR, Drescher M (2011) Long-range distance determination in a DNA model system inside *Xenopus laevis* oocytes by in-cell spin-label EPR. Chembiochem 12(13):1992–1995
38. Krstić I, Hänsel R, Romainczyk O, Engels JW, Dötsch V, Prisner TF (2011) Long-range distance measurements on nucleic acids in cells by pulsed EPR spectroscopy. Angew Chem Int Ed Engl 50(22):5070–5074
39. Macosko JC, Pio MS, Tinoco I, Shin Y-K (1999) A novel 5′ displacement spin-labeling technique for electron paramagnetic resonance spectroscopy of RNA. RNA 5:1158–1166

40. Kim N-K, Murali A, DeRose VJ (2004) A distance ruler for RNA using EPR and site-directed spin labeling. Chem Biol 11:939–948
41. Edwards TE, Okonogi TM, Sigurdsson ST (2002) Investigation of RNA-protein and RNA-metal ion interactions by electron paramagnetic resonance spectroscopy. The HIV TAR-Tat motif. Chem Biol 9(6):699–706
42. Schiemann O, Weber A, Edwards TE, Prisner TF, Sigurdsson ST (2003) Nanometer distance measurements on RNA using PELDOR. J Am Chem Soc 125(12):3434–3435
43. Borbat PP, Davis JH, Butcher SE, Freed JH (2004) Measurement of large distances in biomolecules using double-quantum filtered refocused electron spin-echoes. J Am Chem Soc 126(25):7746–7747
44. Piton N, Mu Y, Stock G, Prisner TF, Schiemann O, Engels JW (2007) Base-specific spin-labeling of RNA for structure determination. Nucleic Acids Res 35(9):3128–3143
45. Romainczyk O, Endeward B, Prisner TF, Engels JW (2011) The RNA-DNA hybrid structure determined by EPR, CD and RNase H1. Mol Biosyst 7(4):1050–1052
46. Cai Q, Kusnetzow AK, Hideg K, Price EA, Haworth IS, Qin PZ (2007) Nanometer distance measurements in RNA using site-directed spin labeling. Biophys J 93(6):2110–2117
47. Sicoli G, Wachowius F, Bennati M, Höbartner C (2010) Probing secondary structures of spin-labeled RNA by pulsed EPR spectroscopy. Angew Chem Int Ed Engl 49(36):6443–6447
48. Kim NK, Bowman MK, DeRose VJ (2010) Precise mapping of RNA tertiary structure via nanometer distance measurements with double electron-electron resonance spectroscopy. J Am Chem Soc 132(26):8882–8884
49. Wunnicke D, Strohbach D, Weigand JE, Appel B, Feresin E, Suess B, Müller S, Steinhoff HJ (2011) Ligand-induced conformational capture of a synthetic tetracycline riboswitch revealed by pulse EPR. RNA 17(1):182–188
50. Krstić I, Frolow O, Sezer D, Endeward B, Weigand JE, Suess B, Engels JW, Prisner TF (2010) PELDOR spectroscopy reveals preorganization of the neomycin-responsive riboswitch tertiary structure. J Am Chem Soc 132(5):1454–1455
51. Reginsson GW, Hunter RI, Cruickshank PAS, Bolton DR, Sigurdsson ST, Smith GM, Schiemann O (2011) W-Band PELDOR with 1kW Microwave Power: Molecular Geometry, Flexibility and Exchange Coupling. J Mag Res, doi: 10.1016/j.jmr.2012.01.019

Struct Bond (2014) 152: 283–328
DOI: 10.1007/430_2013_115

Published online: 24 August 2013

Orientation-Selective DEER Using Rigid Spin Labels, Cofactors, Metals, and Clusters

Alice M. Bowen, Claudia E. Tait, Christiane R. Timmel, and Jeffrey R. Harmer

Abstract The dipolar interaction between two paramagnetic centres depends upon their spin–spin distance and relative orientation. Generally most experiments are carried out under conditions where the DEER signal only reports on the spin–spin distances and, for this type of data, sophisticated analysis methods for obtaining distance distributions have been developed. Recently there have been an increasing number of studies on systems where the DEER signals depend upon both distance and spin pair orientation. These investigations have relied on the use of rigid spin labels (those with a well-defined spatial position) and/or spectrometers operating at Q-band frequencies and above capable of performing DEER experiments with high resolution and sensitivity. In this article we discuss in detail orientation-selective DEER experiments for which the modulation depth and the dipolar frequencies depend on the relative orientation of the two paramagnetic centres and the distance. Analysis of the data in the presence of distance and orientation distributions is discussed, and representative examples from the literature are given for systems containing spin labels, organic cofactors, metals, and metal clusters.

Keywords Distance measurement · DEER · EPR · ESR · Metal · Metal cluster · Orientation selection · PELDOR · Spin label · Structural information

A.M. Bowen, C.E. Tait, and C.R. Timmel (✉)
Department of Chemistry, Centre for Advanced Electron Spin Resonance, University of Oxford, South Parks Road, Oxford OX1 3QR, UK
e-mail: christiane.timmel@chem.ox.ac.uk

J.R. Harmer (✉)
Department of Chemistry, Centre for Advanced Electron Spin Resonance, University of Oxford, South Parks Road, Oxford OX1 3QR, UK

Centre for Advanced Imaging, University of Queensland, St Lucia, QLD 4072, Australia
e-mail: jeffrey.harmer@cai.uq.edu.au

Contents

Abbreviations

DEER	Double electron—electron resonance
DQC	Double–quantum coherence
ENDOR	Pulsed electron—nuclear double resonance
EPR	Electron paramagnetic resonance
f.w.h.m	Full width half maximum
Fe-S	Iron-Sulphur
HYSCORE	Hyperfine sublevel correlation
MTSL	1-Oxyl-2,2,5,5-tetramethylpyrrolinyl-3-methyl)-methanethiosulphonate
mw	Microwave
os-DEER	Observer-selective DEER
PELDOR	Pulsed electron—electron double resonance
RIDME	Relaxation-induced dipole modulation enhancement
TWTA	Travelling wave tube amplifier
ZFS	Zero-field splitting

1 Introduction

Distance and orientation information between two paramagnetic centres can be obtained from their dipolar spectra measured using double electron—electron resonance (DEER) spectroscopy or synonymously pulsed electron—electron double resonance (PELDOR). This technique is applicable to spins (paramagnetic centres)

separated by ca. 15–80 Å, and recently it was shown that distance measurements of ca. 120 Å using fully deuterated samples should be possible [1, 2].

The electronic spin–spin interaction can be separated from the other magnetic interactions (e.g. the hyperfine interactions) by DEER spectroscopy [3] to provide information on the distance between the spin centres and the orientation of the spin—spin vector relative to the g-matrix reference frames (or more generally the spin Hamiltonian). The first DEER pulse sequence consisting of three microwave (mw) pulses was established by Milov et al. [4, 5], and later a four–pulse DEER sequence with the advantage of zero dead time was introduced [6, 7]. Other EPR techniques for measuring electron–electron couplings include the "2+1" sequence [8], double-quantum coherence (DQC) EPR which notably also enables shorter distances to be measured [9] and relaxation-induced dipolar modulation enhancement (RIDME) [10–13]. Under suitable conditions and for distances less than ca. 20 Å for $S = 1/2$ spin systems (but longer for e.g. Gd^{3+}, $S = 7/2$), the dipolar interaction can be estimated by continuous wave (CW) EPR [2]. Usually DEER measurements are made between two spin centres (e.g. organic radicals such as nitroxides) in such a way that all orientations of the spin—spin vectors relative to the spectrometer field vector $\mathbf{B}_0$ contribute and a complete powder-averaged dipolar spectrum results (referred to as a Pake pattern). If the spin centres are separated by one clearly defined distance, then the latter can be determined from the positions of the turning points in the dipolar spectrum. For the usual case where there is a distribution of distances, sophisticated model-free analysis methods exist based on Tikhonov regularisation [14–16]. If the mw pulses of the DEER experiment excite resonances from a limited range of spin—spin vectors with respect to $\mathbf{B}_0$, then a limited angular range of the dipolar interaction is measured and the analysis must consider explicitly this reduced orientation set. If individual DEER traces can be recorded such that sufficient orientations are sampled, then a full analysis of all the traces will deliver not only distance information but also orientations of the spin—spin vector relative to the g-matrix reference frames of the radicals. This type of data requires a model considering both the relative orientation of the radicals and the inter-spin distance.

Such orientation information is potentially very valuable for a 3D structure determination if the radical orientations relative to, e.g. a protein, are known. If a pair of radicals have a fixed orientation with respect to RNA/DNA molecules, for example, then very subtle translation and rotation of the motifs can be quantified [17]. Paramagnetic cofactors and spin labels for nucleic acids often fall into this category, whereas the MTSL spin label commonly used for protein DEER studies is generally too flexible and orientation information (particularly at X-band) is not accessible. However, in some protein systems, MTSL spin labels have been shown to exhibit very tight rotamer distributions and thus narrow distance distributions, as discussed later in this review. As compared to flexible labels, the use of rigid labels also significantly reduces the number of spin-labelled mutants required for a structural analysis of a protein or protein complex. The restriction of spin label flexibility (especially for DEER work in proteins) is currently an active area of research; recent developments include the synthesis of a nitroxide ($NO^{\bullet}$) spin label (3,4-bis-(methanethiosulfonylmethyl)-2,2,5,5-tetramethyl-2,5-dihydro-1H-

pyrrol-1-yloxy radical) that forms two covalent links with cysteine residues 3 to 4 residues apart in helices or β-strands [18]. However, the use of rigid spin labels may have disadvantages by restricting structural and conformational dynamics. Part of the success of flexible labels, like MTSL, can be attributed to their ability to adapt to the environment around the labelling site. This is much preferable to forcing the label site to adapt to a (rigid) label's position, thus potentially leading to misfolding of proteins and other distorting effects.

This review is organised as follows: Sect. 2 describes the DEER sequence and presents the most important features pertinent to orientation-selective DEER measurements; Sect. 3 introduces the properties and mathematical fundamentals of the dipolar interaction; Sect. 4 presents the nuts-and-bolts of orientation-selective DEER time-trace calculations and discusses fitting DEER traces to data with distributions of orientations and distances; Sect. 5 covers a selection of applications with organic radicals, metals, and clusters; and Sect. 6 summarises the main applications and future directions. Appendix I lists the dipolar interaction and Hamiltonian explicitly as vectors and matrices, Appendix II outlines a density matrix approach to the calculation of a 4-pulse DEER time trace, and Appendix III presents the corresponding implementation in MATLAB code.

2 Measurement Techniques

2.1 DEER Sequence

The DEER pulse sequence is designed to separate the electron-electron dipolar interaction from other interactions of a paramagnetic centre with its environment, such as the electron Zeeman and hyperfine interactions. Two distinct pulse sequences are routinely used (Fig. 1): a three–pulse version established first by Milov et al. [5] and a four–pulse version introduced later with the advantage of zero dead time [6, 7]. Both sequences employ two microwave (mw) frequencies to measure the dipolar coupling. In the three–pulse sequence, pulses at frequency ν_{det} applied to the detection spins produce a primary echo at time 2τ. The π-pulse at frequency ν_{pump} inverts the pump spins changing the local magnetic field experienced by the detection spins. A DEER trace is recorded by monitoring the detection spin-echo height with a fixed τ value while the pump pulse is moved within the first τ-evolution period. Because the π-pulse applied to the pump spin changes the local magnetic field at the detection spin, the primary echo is refocused with time-dependent phases and is consequently modulated by the dipolar coupling frequency. The accelerated and de-accelerated detection spins experience phase shifts of $\omega_{\mathrm{AB}}t$ and $-\omega_{\mathrm{AB}}t$, respectively, and the sum of the magnetisation of these two sub-ensembles oscillates as $\exp(i\omega_{\mathrm{AB}}t) + \exp(-i\omega_{\mathrm{AB}}t) = \cos(\omega_{\mathrm{AB}}t)$. Time t is defined in Fig. 1 and ω_{AB} is the dipolar frequency between spins A and B. In three–pulse DEER typically the first ca. 40 ns of the time trace are obscured due to overlap of the detection-spin and pump-spin pulses at time $t = 0$ (t_0). This

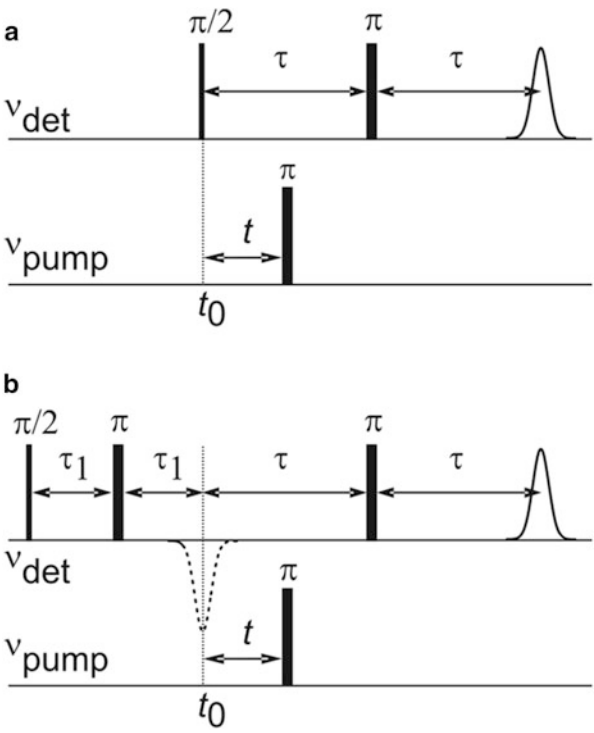

Fig. 1 (**a**) Three-pulse DEER. The subsequence of mw pulses at frequency ν_{det} is applied to the detection spins, and a π-pulse at frequency ν_{pump} is applied to the pump spins and moved within the first τ evolution period. (**b**) Four-pulse DEER. The refocused echo from the detection spins at time $2\tau_1 + 2\tau$ is observed as a function of time (t), where $t_0 = 2\tau_1$ is outside the observation dead time

shortcoming is overcome with four–pulse DEER by insertion of an additional refocusing pulse in the detection-spin subsequence at the cost of prolonging the overall experiment and the consequent loss of some sensitivity.

A variant of DEER, os-DEER, has also been introduced which enables highly selective observer mw pulses to be used which may improve orientation selection in cases where hard mw pulses with a large excitation bandwidth may be a limiting factor [19].

Recently sequences to suppress nuclear spin diffusion have been described which allow the length of the measured dipolar trace to be extended (to a level similar to that which would be possible by fully deuterating the sample). A 5-pulse sequence with suppression of nuclear spin diffusion is discussed by Borbat and Freed [20, 21].

2.2 Experimental Considerations

2.2.1 Suitable Paramagnetic Centres

The two main criteria to obtain orientation-selective data are (1) a pair of radicals with a fixed relative orientation and (2) selectivity of the mw pump or detection

pulses so that only a range of spin–spin orientations (vectors) with respect to the spectrometer field vector $\mathbf{B}_0$ are excited. The latter criterion is more easily fulfilled as the spectrometer frequency is increased, and with typically encountered organic radicals, good selectivity is usually obtained at W-band and above, although some orientation information can be obtained at X-band depending upon the distribution of relative orientations between pairs of radicals. If metal paramagnetic centres are used then, generally, the spectrum anisotropy provided by the g-matrix (and hyperfine coupling) is typically already sufficient at X-band to achieve good pulse orientation selectivity. Very often, however, metal EPR spectra are too broad and thus very difficult to study by DEER; for example, high-spin and low-spin Fe^{3+} complexes typically fall into this category.

To make a full orientationally selective DEER characterisation, it is very advantageous to be able to probe all conceivable biradical orientations; the full range is certainly accessible if a measurement can be made with the pump and detection pulses separated by the total width of the field-swept EPR spectra. For example, with Cu(II) centres $g_{\|}$ and $g_{\perp}$ can be ca. 500 MHz or more apart at X-band, and thus a very broadband (and intrinsically less sensitive) resonator needs to be used. The commonly used Bruker X-band 3 mm split-ring resonator when fully over-coupled combined with a 1 kW TWTA allows a pulse separation of up to ca. 400 MHz while still achieving detection/pump pulses of lengths $t_{\pi} = 32$ ns/$t_{\pi} = 20$ ns, respectively. A Bruker 2 mm split-ring resonator permits separations of up to ca. 600 MHz, still with $t_{\pi} = 32$ ns/$t_{\pi} = 20$ ns. This just about allows orientation-selective measurements to probe all conceivable biradical orientations with most Cu^{2+} paramagnetic centres. However, many other metal centres exhibiting much broader EPR spectra (e.g. many high- and low-spin Fe^{3+} complexes, some Fe–S clusters) remain out of reach or only a limited number of orientations can be probed. The achievable pulse separation can also become an issue for organic radicals at high fields as their EPR spectra broaden.

Besides designing broader bandwidth resonators (e.g. loop-gap resonators), several alternative options exist. A dual-mode resonator can be employed, such as the one reported by Tkach et al. [22–24] operating at W-band (at/near 94 GHz) capable of a variable separation of "pump" and "detection" frequencies up to $\Delta\nu = 350$ MHz. Another, technically very challenging, alternative is to jump the spectrometer field while the pump pulse is applied [25]. Such an approach for DEER was reported in [25, 26].

2.2.2 Acquisition Schemes

All orientation-selective pulse EPR experiments (e.g. DEER, ENDOR) lend themselves to a parallel acquisition scheme which aims to make best use of the spectrometer measurement time [27]. Typically experiments are performed consecutively at different magnetic field positions within the inhomogeneously broadened EPR spectrum, namely a particular field position is chosen, data are accumulated until the signal-to-noise ratio is satisfactory, and then the next field position is

chosen and data are accumulated. In a parallel acquisition scheme, e.g. DEER, several measurements are performed within the waiting (repetition) time between consecutive pulse sequences during which spin—lattice relaxation takes place. This is achieved by rapidly changing the main magnetic field, B_0, to different values within the EPR spectrum, performing the same experiment on the otherwise idle spins. This method is useful for all types of orientation-selective pulse EPR experiments.

3 The Dipolar Interaction

The DEER technique is based on measurement of the dipolar interaction $\mathbf{D}_{\mathrm{AB}}$ between the magnetic moments of two electron spins A and B separated by distance r_{AB}:

$$\mathbf{D}_{\mathrm{AB}} = \frac{\mu_0 {\beta_e}^2}{4\pi\hbar} \frac{\mathbf{g}_{\mathrm{A}}\mathbf{g}_{\mathrm{B}}^{\mathrm{T}} - 3(\mathbf{g}_{\mathrm{A}}\mathbf{n}_{\mathrm{AB}}^{\mathrm{T}})(\mathbf{g}_{\mathrm{B}}\mathbf{n}_{\mathrm{AB}}^{\mathrm{T}})^{\mathrm{T}}}{r_{\mathrm{AB}}^3}. \tag{1}$$

Here $\mathbf{D}_{\mathrm{AB}}$ is in radians and $\mathbf{g}_{\mathrm{A}}$ and $\mathbf{g}_{\mathrm{B}}$ are 3×3 g-matrices describing the electron Zeeman interactions of each spin, r_{AB} is the inter-spin distance, $\mathbf{n}_{\mathrm{AB}}$ is the unit row vector parallel to the A−B direction, and T represents a transpose. In this article scalar quantities are given in italics, vectors and matrices in bold, and operators with a carat (^) above the symbol. Appendix I shows (1) explicitly in matrix form. The corresponding Hamiltonian is

$$\hat{H}_{\mathrm{dd}}^{\mathrm{AB}} = \hat{\mathbf{S}}_{\mathrm{A}}\mathbf{D}_{\mathrm{AB}}\hat{\mathbf{S}}_{\mathrm{B}}^{\mathrm{T}}, \tag{2}$$

where $\hat{\mathbf{S}}_i = [\hat{S}_x^i \quad \hat{S}_y^i \quad \hat{S}_z^i]$ is a vector of spin operators. Including the electron Zeeman interactions of the two spins in addition to the dipolar interaction gives

$$\begin{aligned}\hat{H} &= \hat{H}_{\mathrm{eZ}}^{\mathrm{A}} + \hat{H}_{\mathrm{eZ}}^{\mathrm{B}} + \hat{H}_{\mathrm{dd}}^{\mathrm{AB}} \\ &= \frac{\beta_e}{\hbar}\mathbf{B}_0\mathbf{g}_{\mathrm{A}}\hat{\mathbf{S}}_{\mathrm{A}}^{\mathrm{T}} + \frac{\beta_e}{\hbar}\mathbf{B}_0\mathbf{g}_{\mathrm{B}}\hat{\mathbf{S}}_{\mathrm{B}}^{\mathrm{T}} + \hat{\mathbf{S}}_{\mathrm{A}}\mathbf{D}_{\mathrm{AB}}\hat{\mathbf{S}}_{\mathrm{B}}^{\mathrm{T}},\end{aligned} \tag{3}$$

where $\mathbf{B}_0 = [B_x\, B_y\, B_z]$ is the magnetic field row vector. Provided the g-anisotropy is small, the dipolar interaction can be recast in terms of the effective g-values g_{A} and g_{B} along $\mathbf{B}_0 = \mathbf{B}_0(\Theta, \Phi)$ (see Fig. 4):

$$D_{\mathrm{AB}} = \frac{\mu_0 {\beta_e}^2}{4\pi\hbar} g_{\mathrm{A}}(\Theta,\Phi) g_{\mathrm{B}}(\Theta,\Phi) \frac{1 - 3\cos^2\theta}{r_{\mathrm{AB}}^3}, \tag{4}$$

in which $g_k^2(\Theta,\Phi) = \mathbf{n}_{B_0}\mathbf{g}_k\mathbf{g}_k^T\mathbf{n}_{B_0}^T$ (k = A or B) and $\mathbf{n}_{B_0}$ is the unit row vector along $\mathbf{B}_0$. Using this form of the dipolar interaction, the corresponding Hamiltonian (2) can be conveniently written in terms of the dipolar alphabet:

$$\hat{H}_{dd} = \frac{\mu_0 {\beta_e}^2}{4\pi\hbar}\frac{g_A g_B}{r_{AB}^3}(a+b+c+d+e+f), \tag{5}$$

where

$$\begin{aligned}
a &= \hat{S}_z^A\hat{S}_z^B(1-3\cos^2\theta)\\
b &= -\tfrac{1}{4}(\hat{S}_+^A\hat{S}_-^B + \hat{S}_-^A\hat{S}_+^B)(1-3\cos^2\theta)\\
c &= -\tfrac{3}{2}(\hat{S}_+^A\hat{S}_z^B + \hat{S}_z^A\hat{S}_+^B)\sin\theta\cos\theta e^{-i\phi}\\
d &= -\tfrac{3}{2}(\hat{S}_-^A\hat{S}_z^B + \hat{S}_z^A\hat{S}_-^B)\sin\theta\cos\theta e^{+i\phi}\\
e &= -\tfrac{3}{4}\hat{S}_+^A\hat{S}_+^B\sin^2\theta e^{-2i\phi}\\
f &= -\tfrac{3}{4}\hat{S}_-^A\hat{S}_-^B\sin^2\theta e^{+2i\phi},
\end{aligned} \tag{6}$$

where $\hat{S}_+/\hat{S}_-$ are the raising and lowering operators. In the high-field approximation, implying that $\hat{H}_{eZ}^A, \hat{H}_{eZ}^B >> \hat{H}_{dd}$, the non-secular terms c-f can be neglected and only the secular (a) and pseudosecular (b) terms in (6) need to be retained:

$$\begin{aligned}
\hat{H}_{dd} &= \frac{\mu_0 {\beta_e}^2}{4\pi\hbar}\frac{g_A g_B}{r_{AB}^3}(a+b)\\
&= \frac{\mu_0 {\beta_e}^2}{4\pi\hbar}\frac{g_A g_B}{r_{AB}^3}(1-3\cos^2\theta)(\hat{S}_z^A\hat{S}_z^B - \tfrac{1}{4}(\hat{S}_+^A\hat{S}_-^B + \hat{S}_-^A\hat{S}_+^B)).
\end{aligned} \tag{7}$$

Dipolar splittings calculated from (7) depend upon the difference in the resonance frequency of the two electron spins, $\Delta\omega = \omega_A - \omega_B$, compared to the dipolar splitting constant defined in (8):

$$\omega_{dd} = \frac{\mu_0 {\beta_e}^2}{4\pi\hbar}\frac{g_A g_B}{r_{AB}^3}. \tag{8}$$

In special cases where $\Delta\omega << \omega_{dd}$, the pseudosecular term b in (7) must be retained and the dipolar splitting constant becomes

$$\omega_{dd}^{pseudo} = \frac{3}{2}\frac{\mu_0 {\beta_e}^2}{4\pi\hbar}\frac{g_A g_B}{r_{AB}^3} = \frac{3}{2}\omega_{dd}. \tag{9}$$

This situation is typically not encountered in DEER spectroscopy since the detection and pump pulses are separated by ca. 65 MHz, which is much larger than the size of the dipolar coupling between two spins if $r_{AB} > 15$ Å (giving

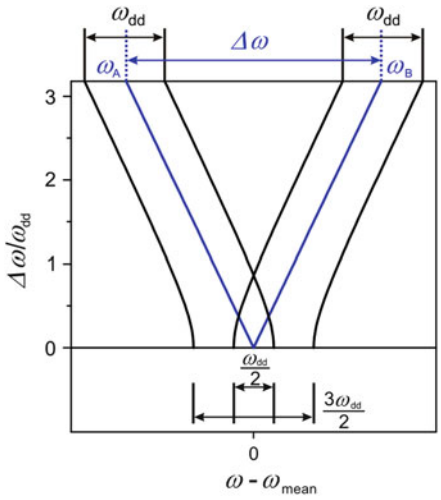

Fig. 2 Energy level diagram obtained from (3) in the high-field regime (or with $\hat{H}_{dd}$ defined according to (7)). The four energy levels of the two spin system (*black lines*) are plotted as a function of $\Delta\omega/\omega_{dd}$ for a constant $\omega_{dd} = 2$ MHz; note $\Delta\omega = \omega_A - \omega_B$. The blue lines show the two electron Zeeman energies ω_A and ω_B for each electron spin in the absence of the dipolar splitting. Note the *x*-axis is plotted around the mean electron Zeeman energy, $\omega_{mean} = (\omega_A + \omega_B)/2$, which is much greater than the dipolar splitting (high-field regime). DEER experiments are typically set-up so that $\Delta\omega >> \omega_{dd}$

$\omega_{dd} = 15.5$ MHz). In the typical case, $\Delta\omega >> \omega_{dd}$, the pseudosecular term b in (7) can be dropped, giving

$$\hat{H}_{dd} = \omega_{dd}(1 - 3\cos^2\theta)\hat{S}_Z^A\hat{S}_Z^B, \tag{10}$$

with the dipolar frequency calculated as

$$\omega_{AB} = \frac{\mu_0\beta_e^{\,2}}{4\pi\hbar}\frac{g_A g_B}{r_{AB}^3}(1 - 3\cos^2\theta) = \omega_{dd}(1 - 3\cos^2\theta). \tag{11}$$

The energy levels for the two coupled spins calculated with (3) are shown in Fig. 2, where they are plotted against the ratio $(\Delta\omega/\omega_{dd})$. An expanded discussion is given in [20].

Commonly DEER data are analysed under the assumption that the Heisenberg exchange coupling is negligible ($\mathbf{J}_{AB} \rightarrow 0$) as most systems suitable for DEER studies involve localised spins separated by $r_{AB} > 15$ Å. However, if J_{AB} is significant it is possible under suitable conditions to separate the exchange and dipole contribution using DEER data [28–30]. The Heisenberg exchange interaction is given by

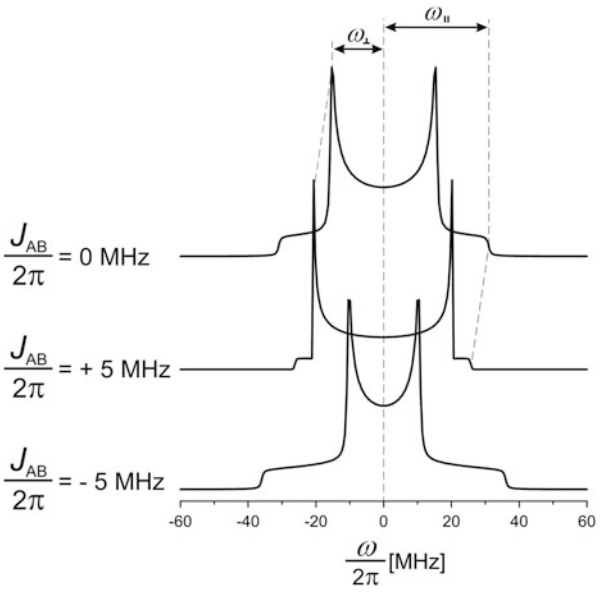

Fig. 3 Pake patterns simulated for a spin system with $r_{AB} = 15$ Å ($\omega_{dd}/2\pi = 15.5$ MHz) and three different values of the exchange coupling constant $J_{AB}/2\pi = 0, 5, -5$ MHz. The turning points $\omega_{\perp}$ and $\omega_{\parallel}$ can be used to calculate $\omega_{dd} = (\omega_{\parallel} - \omega_{\perp})/3$ and $J_{AB} = (2\omega_{\perp} + \omega_{\parallel})/3$. Note that for $J_{AB} = 0$ $|\omega_{\parallel}| = 2|\omega_{\perp}|$. The *dashed lines* show how the $\omega_{\parallel}$ and $\omega_{\perp}$ turning points move when $J_{AB}/2\pi = +5$ MHz is added to the dipolar interaction

$$\hat{H}_{\text{exchange}} = \hat{\mathbf{S}}_A \mathbf{J}_{AB} \hat{\mathbf{S}}_B^T \cong J_{AB} \hat{\mathbf{S}}_A \hat{\mathbf{S}}_B^T, \tag{12}$$

where $\mathbf{J}_{AB}$ is the exchange matrix and J_{AB} is the isotropic value. In the isotropic exchange case the DEER frequencies are given by

$$\omega_{AB} = \frac{\mu_0 \beta_e{}^2}{4\pi\hbar} \frac{g_A g_B}{r_{AB}^3} (1 - 3\cos^2\theta) + J_{AB} = \omega_{dd}(1 - 3\cos^2\theta) + J_{AB}. \tag{13}$$

If the two turning points in the Pake spectrum (powder spectrum) can be measured, then ω_{dd} and J_{AB} contributions can be separated. Figure 3 shows dipolar spectra for $\omega_{dd}/2\pi = 15.5$ MHz and $J_{AB}/2\pi = 0, 5, -5$ MHz.

4 Calculation of the Orientation-Selective Form Factor

4.1 Calculation of the DEER Trace

Experimental data and a theoretical description of orientation-selective DEER time traces were first presented by Larsen and Singel [31]. Subsequently there have been a number of implementations of the theory presented in the literature; see, for example, [13, 32–36]. In the following we describe the salient points of the calculation. The general form of the normalised dipolar evolution function for a DEER experiment is given by [37]

$$D(t) = \frac{\left(\sum_{d=1}^{N} f_d \prod_{p=1, p\neq d}^{N} \left[1 - \lambda_p (1 - \cos(\omega_{pd} t))\right] \right)}{\sum_{d=1}^{N} f_d}, \tag{14}$$

where indices d (detection spins) and p (pump spins) run over all spins in the sample, so that both inter- and intra-molecular contributions are included. The intensity of the detection spins f_d (e.g. the experimentally recorded echo intensity) and modulation depths λ_p have a complicated dependence upon the spin Hamiltonians of the paramagnetic centres and their orientations to the spectrometer magnetic field $\mathbf{B}_0(\Theta, \Phi)$ and the frequencies, lengths, and strengths of the detection and pump pulses. Equation (14) can be separated into a background factor $B(t)$ due to interaction of detection spins with all other nano-objects and a form factor $F(t)$ due to interactions within the same nano-object (a nano-object with two or more radicals could be, for example, a protein, a protein complex, or an oligomer) [37]

$$D(t) = B(t)F(t). \tag{15}$$

Within the framework of this theory, the decay of $B(t)$ is due to the background distribution of paramagnetic centres. The structural information is contained in the form factor $F(t)$, which for a pair of interacting spins A and B with a single conformation gives from (14):

$$F(t) = \frac{\sum_{i\in\Theta,\Phi} f_{\mathrm{A}}^{i} \left[1 - \lambda_{\mathrm{B}}^{i}(1 - \cos(\omega_{\mathrm{AB}}^{i} t))\right] + f_{\mathrm{B}}^{i} \left[1 - \lambda_{\mathrm{A}}^{i}(1 - \cos(\omega_{\mathrm{AB}}^{i} t))\right]}{\sum_{i\in\Theta,\Phi} (f_{\mathrm{A}}^{i} + f_{\mathrm{B}}^{i})}. \tag{16}$$

The summation is over all i orientations of the field $\mathbf{B}_0^i(\Theta, \Phi)$ in the molecular frame (Fig. 4); f_{A}^i and f_{B}^i are the echo intensities from spins A and B, respectively, at the detection frequency ω_{det} of the DEER trace at time $t = 0$; and λ_{B} and λ_{A} are the corresponding modulation depth functions which depend upon the spin-flip probability resulting from the π-pump pulse at frequency ω_{pump}. For our purposes the form factor $F(t)$ for a pair of interacting spins A and B can be calculated under the following assumptions: (1) the bandwidth of the mw pulses is large compared to the dipolar coupling, (2) $\Delta\omega >> \omega_{\mathrm{dd}}$ so Eq. (10)/(11) applies, and (3) the frequency separation between the pump (ω_{pump}) and detection (ω_{det}) pulses is large enough that the pump pulse does not act on the detection spins, and conversely detection pulses do not act on the pump spins (but see Appendix II).

The coordinate system used here is defined in Fig. 4. Spin A can be arbitrarily chosen so that its axes $\mathbf{g}_x$, $\mathbf{g}_y$, and $\mathbf{g}_z$ are aligned along the molecular frame axes **x**, **y**, and **z**, respectively. The spatial position of spin B can be defined relative to spin A by the distance r_{AB} and the unit vector between the two spins $\mathbf{n}_{\mathrm{AB}}(\xi, \phi)$ which also corresponds to the direction of the unique principal axis of the dipole interaction.

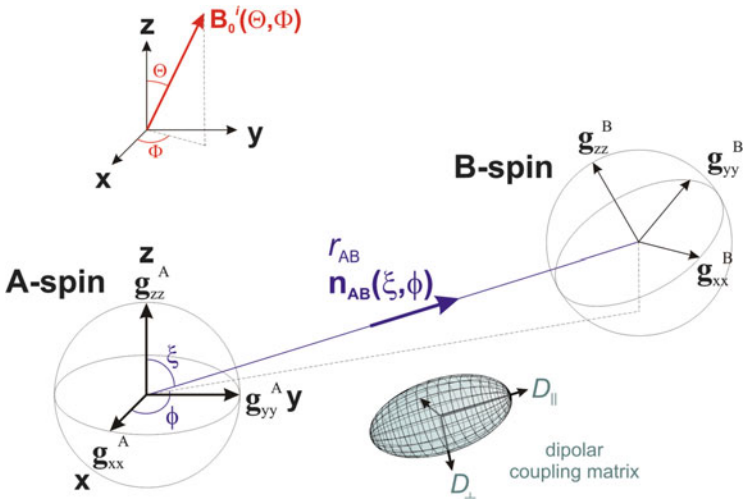

Fig. 4 The coordinate system for the description of a DEER signal for a single mutual orientation of two spins A and B. Spin A has its g-matrix axes coincident with the molecular frame; the g-matrix axes of the spin B are defined by the Euler angles (α, β, γ). The unique principal axis of the dipole tensor points between the two radicals and is axial in form (–1, –1, +2) when the spin densities of spins A and B are considered as points

If the spin density is modelled as a distribution, then a sum over all the pairs of spin densities between each paramagnetic centre needs to be carried out (see (24)). The orientation of spin B is defined by the rotation matrix $\mathbf{R}(\alpha, \beta, \gamma)$ with (α, β, γ) being the three Euler angles. The geometry of the biradical and its dipolar coupling are thus characterised by five angles: $\mathbf{n}_{AB}(\xi, \phi)$ and $\mathbf{R}(\alpha, \beta, \gamma)$.

Next, in a numerical calculation approach, a grid of i orientations for $\mathbf{B}_0^i(\Theta, \Phi)$ on a unit sphere, appropriate for the symmetry of the problem, is defined. At each of the i orientations of the spectrometer field $\mathbf{B}_0^i(\Theta, \Phi)$ in the molecular frame, the resonance frequencies and intensities of spin A (I_A^i) and spin B (I_B^i) are calculated; see (26) for a system example. These resonances can be calculated with the spin Hamiltonian used to simulate the field-swept EPR spectrum (e.g. for a nitroxide an electron Zeeman interaction (g-matrix), the resolved nitrogen hyperfine interaction ($\mathbf{A}(^{14}\mathrm{N})$), and a linewidth). Now consider the case where spin A is detected and spin B pumped. The contribution of the spin A resonances, I_A^i, to the detection-spin-echo intensity f_A^i can be quantified using the excitation profile for transverse magnetisation of the detection pulse sequence P_{det} at frequency ω_{det} as

$$f_A^i = \int_0^\infty I_A^i(\omega) P_{det}(\omega_{det} - \omega) d\omega. \tag{17}$$

A suitable approximate expression for P_{det} is [7, 38]

$$P_{\mathrm{det}}(\Delta\omega_{\mathrm{det}}) = \left(\frac{\omega_1}{\omega_{\mathrm{eff}}}\right)^5 \sin^5(\omega_{\mathrm{eff}} t_{\pi/2}), \tag{18}$$

with

$$\Delta\omega_{\mathrm{det}} = \omega_{\mathrm{det}} - \omega, \tag{19}$$

and

$$\omega_{\mathrm{eff}} = \sqrt{\Delta\omega_{\mathrm{det}}^2 + \omega_1^2}, \tag{20}$$

where ω_1 is the detection pulse B_1 field strength ($\omega_1/2\pi = 16.25$ MHz for $t_{\pi/2} = 16$ ns). Function $P_{\mathrm{det}}(\Delta\omega_{\mathrm{det}})$ is plotted in Fig. 5 as a function of the offset $\Delta\omega_{\mathrm{det}}$. The function $P_{\mathrm{det}}(\Delta\omega_{\mathrm{det}})$ approximates the transverse magnetisation created by the detection pulse sequence as a function of frequency offset from the pulse carrier frequency ω_{det}. At each offset $\Delta\omega_{\mathrm{det}}$ value, $P_{\mathrm{det}}(\Delta\omega_{\mathrm{det}})$ is multiplied by the A-spin signal intensity $I_{\mathrm{A}}^i(\omega)$ at this offset.

Next to be determined at the field orientation $\mathbf{B}_0^i(\Theta, \Phi)$ is the flip probability of spin B by the pump π-pulse at the carrier frequency ω_{pump}:

$$\lambda_{\mathrm{B}}^i = \int_0^\infty I_{\mathrm{B}}^i(\omega) P_{\mathrm{pump}}(\omega_{\mathrm{pump}} - \omega) d\omega, \tag{21}$$

with the pump pulse profile [31] (see Fig. 5)

$$P_{\mathrm{pump}}(\Delta\omega_{\mathrm{pump}}) = \left(\frac{\omega_1}{\omega_{\mathrm{eff}}}\right)^2 \sin^2(\omega_{\mathrm{eff}} t_{\pi/2}), \tag{22}$$

where analogous relationships of (19) and (20) define $\Delta\omega_{\mathrm{pump}}$ and ω_{eff} but refer to the pump pulse frequency ω_{pump} and strength ω_1, respectively. The total contribution of spin A to the DEER signal of the ith orientation $\mathbf{B}_0^i(\Theta, \Phi)$ is given by

$$F^i(t) = f_{\mathrm{A}}^i \left(1 - \lambda_{\mathrm{B}}^i (1 - \cos(\omega_{\mathrm{AB}}^i t))\right). \tag{23}$$

Including also B as detection spin and A as pump spin gives the two terms of (16). The dipolar frequency $\omega^i{}_{\mathrm{AB}}$ is given by (11). If the spin density on either or both paramagnetic centres is distributed over a number of nuclei, or the paramagnetic centre results from spin coupling (e.g. an iron–sulphur cluster; see Sect. 5), then a sum over the spin-density distribution of each paramagnetic centre is needed:

$$\omega_{\mathrm{AB}}^i = \frac{\mu_0 {\beta_e}^2}{4\pi\hbar} g_{\mathrm{A}}^i g_{\mathrm{B}}^i \sum_j \sum_k \rho_{\mathrm{A}}^j \rho_{\mathrm{B}}^k \frac{1 - 3\cos^2\theta^i_{\mathrm{A}j,\mathrm{B}k}}{r^3_{\mathrm{A}j,\mathrm{B}k}}, \tag{24}$$

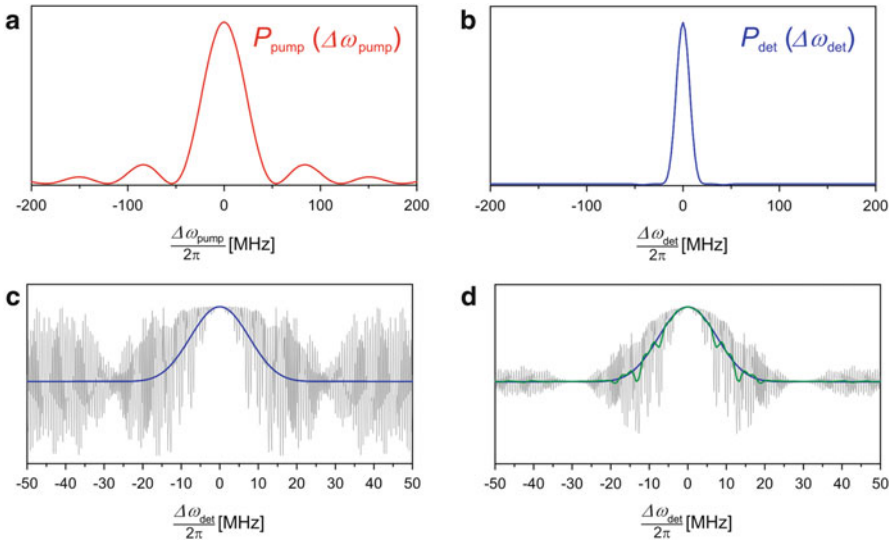

Fig. 5 Excitation profiles of (**a**) a $t_\pi = 16$ ns pump pulse and (**b**) 32 ns detection pulses calculated using (22) and (18), respectively. (**c**) Excitation profile obtained from a density matrix simulation for a refocused echo, $t_{\pi/2}$-τ_1-t_π-τ_1-τ-t_π-τ-*echo*, with rectangular pulses employing $t_{\pi/2} = t_\pi = 32$ ns, $\tau_1 = 200$ ns, and $\tau = 2000$ ns, with single-point signal acquisition at the echo maximum. No relaxation or resonator bandwidth is considered. (**d**) Simulation as in (**c**) but with an integration window of $\Delta t = 32$ ns symmetrically placed to the echo maximum, which provides a low-pass filter on the signal response. The *green line* in (**d**) shows the pulse profile convoluted by a Lorentzian function with a T_2 relaxation time of 2 μs (f.w.h.m) and an integration window of $\Delta t = 32$ ns. The *blue line* in (**c**) and (**d**) shows the profile in (**b**) for comparison

where ρ_A^j and ρ_B^k are the A- and B-spin densities at points in space. For spin $S = 1/2$ the normalisation condition is required:

$$\sum_j \rho_A^j = 1 \text{ and } \sum_k \rho_B^k = 1. \tag{25}$$

To model accurately the experimental DEER signal response, it is also essential to consider the resonator characteristics. Most important is the B_1 field inhomogeneity and pulse shapes experienced by the sample; see, for example, [33]. Inhomogeneity of the excitation mw B_1 field over the sample can be large if the resonator is filled with sample, and the resonator coupling condition and thus bandwidth will strongly influence the pulse shapes and corresponding excitation profiles. These effects can be quantified with a set of calibration pulse measurements on a small (point) sample moved within the resonator volume. Profiles P_{det} and P_{pump} can also be measured and the DEER trace calculated as a weighted integration over the B_1 field inhomogeneity.

4.2 Calculation Example for a Nitroxide Radical Pair

To demonstrate the approach we take a rigid nitroxide biradical as an example. Calculation of $F^i(t)$ (23) at a single orientation $\mathbf{B}_0^i(\Theta, \Phi)$ requires the quantities f_A^i (17) and λ_B^i (21), as shown graphically in Fig. 6. The resonance frequencies of the A-spin (with intensity $I^i{}_\mathrm{A}$ in (17)) and B-spin (with intensity $I^i{}_\mathrm{B}$ in (21)) for each orientation can be calculated by diagonalisation of a Hamiltonian containing an electron Zeeman and hyperfine interaction (or an appropriate analytical expression) [3]:

$$\hat{H}^i = \frac{\beta_e}{\hbar}\mathbf{B}_0^i\mathbf{g}_k\hat{\mathbf{S}}_k^\mathrm{T} + \hat{\mathbf{S}}_k\mathbf{A}_k\hat{\mathbf{I}}_k{}^\mathrm{T};\ k = \mathrm{A\ or\ B}. \tag{26}$$

$\mathbf{g}_k$ and $\mathbf{A}_k$ are the electron Zeeman and hyperfine matrices in the chosen molecular frame. Matrices $\mathbf{g}_k$ and $\mathbf{A}_k$ are obtainable from their eigenframes via the rotation matrix $\mathbf{R}(\alpha, \beta, \gamma)$ with the Euler angles defined in Fig. 4, for example, $\mathbf{g}_k = \mathbf{R}\mathbf{g}_k{}^\mathrm{eig}\mathbf{R}^\mathrm{T}$. A further rotation matrix for $\mathbf{A}_k$ would be needed if it were not collinear with $\mathbf{g}_k$. Figure 6 shows in the molecular frame the intensity f_A^i of the transverse magnetisation of the A-spins as a consequence of the detection pulse sequence at ω_det and the corresponding modulation depth fraction λ_B^i from the B-spins flipped by the pump pulse at frequency ω_pump. At orientations where these two patterns overlap, the A-spin is at least partially modulated by the dipolar coupling since the B-spin is at least partially flipped; any A-spin intensity not intersecting with the corresponding B-spin modulation depth function pattern λ_B contributes an unmodulated component to the form factor $F(t)$.

For nitroxide spins the pump pulse is generally placed at the maximum intensity of the EPR spectrum which excites all spin orientations with respect to the magnetic field, even if not uniformly (see Fig. 6c, sphere λ_B). The pulse selection can be appreciated by inspection of a road map of the energy levels of the nitroxide spin at X-band (Fig. 7). A strong mw pulse placed at ca. 349 mT will excite orientations from $m_\mathrm{I} = 0$; g_{zz}/A_{zz} ($\Theta = 0$) to $m_\mathrm{I} = -1,\ 0,\ 1$; g_{xx}/A_{xx} and g_{yy}/A_{yy} ($\Theta = 90°$, $\Phi = 0$, and 90°).

Naturally, the orientation selection resolution for the nitroxide spin improves as the microwave frequency increases. At W-band (ca. 94 GHz) the g-values of the nitroxide spin are well resolved and DEER measurements can be very sensitive to the position of the pump and detection pulses, as demonstrated in Fig. 8. Shown are simulations for nitroxide spin pairs of two different orientations with the pump pulse always on g_{yy} and three detection observer positions at g_{xx} (1), near g_{yy} (2), and g_{zz} (3).

If at all possible both the modulation depth and the dipolar frequency information that is encoded in a set of DEER traces from a given sample should be used in any structure determination. Provided that the orientation selection is governed by the electron Zeeman and hyperfine interaction (i.e. not the dipolar coupling), then the modulation depth also only depends upon these interactions, i.e. for a nitroxide pair only on the relative orientation of $\boldsymbol{g}$ and $\mathbf{A}(^{14}\mathrm{N})$ matrices, and not on their

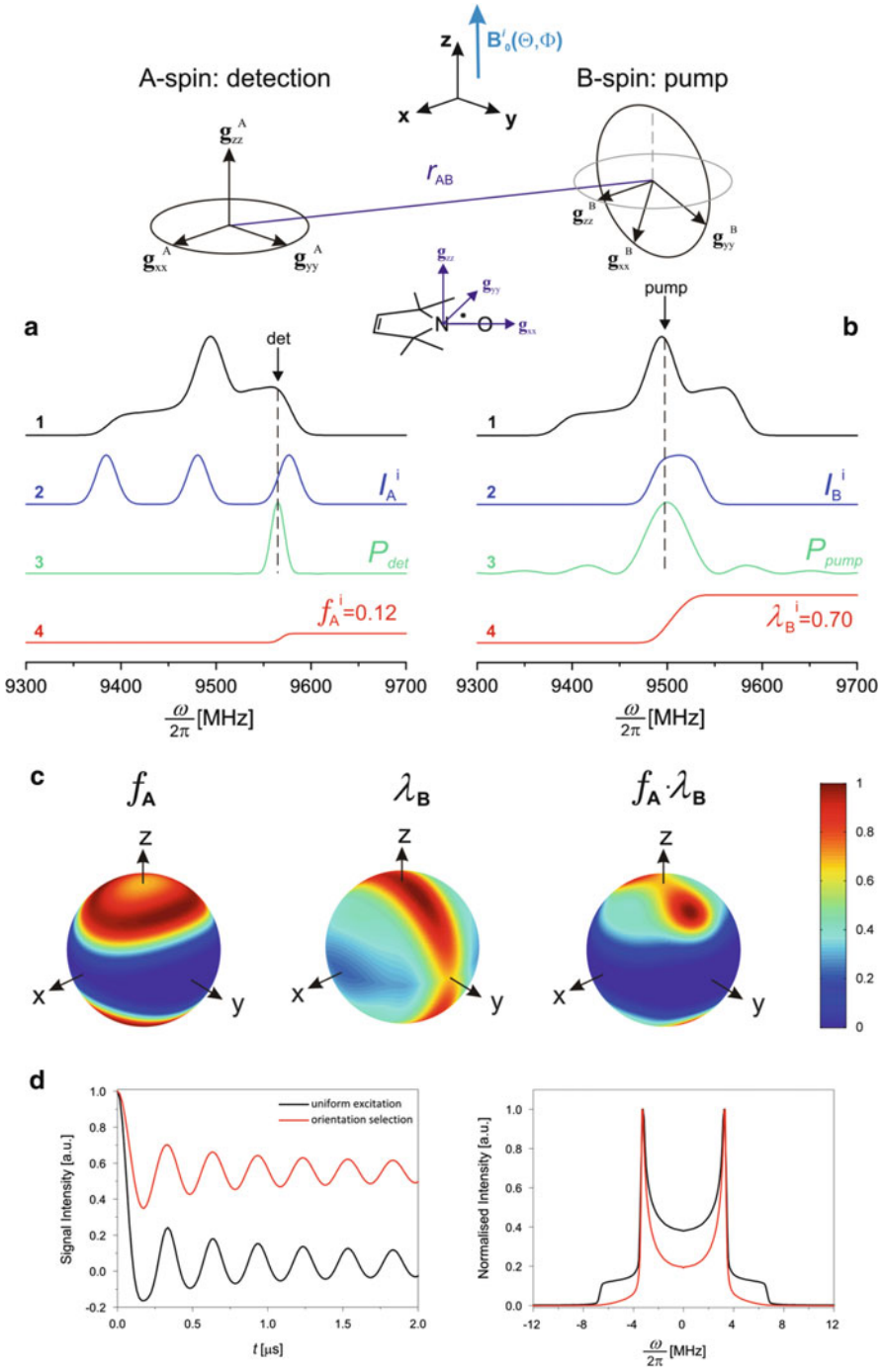

Fig. 6 Calculation of the orientation-dependent form factor $F(t)$ for two NO$^{\bullet}$ radicals at X-band with the relative g-matrix and A-matrix orientation shown at the top of the figure. (**a**.**1**) (*black line*) Detection pulse position in the NO$^{\bullet}$ EPR spectrum; (**a**.**2**) (*blue line*) A-spin resonances I^i_A for the $\mathbf{B}^i{}_0$ orientation indicated by the *blue line* shown in the molecular frame at the top of the figure;

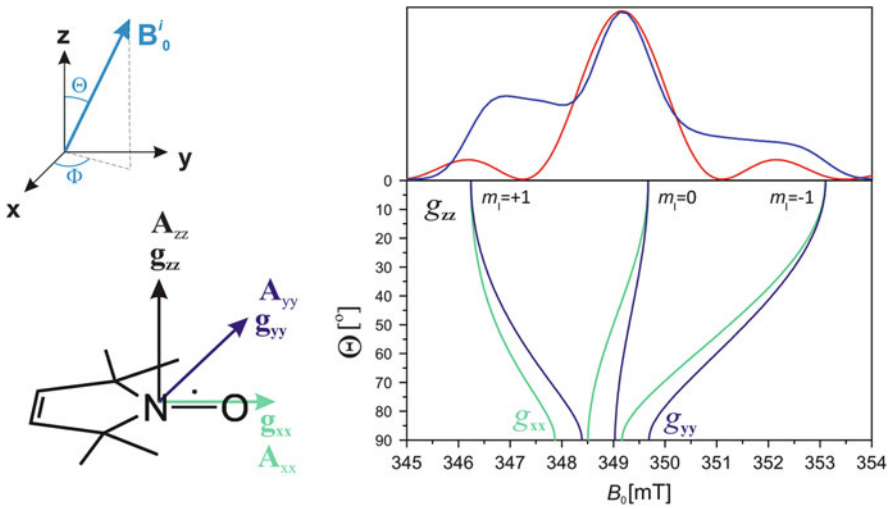

Fig. 7 Road map of the three energy levels ($m_I(^{14}N) = -1, 0, 1$) from g_{zz} ($\Theta = 0°$) to g_{xx} and g_{yy}. ($\Theta = 90°$, $\Phi = 0$, and 90°) of the nitroxide spin at X-band frequencies. The nitroxide spectrum (*blue*) and the excitation profile for a 16 ns pump pulse (*red*) are shown above. The $t_\pi = 16$ ns pulse (bandwidth *f.w.h.m.* = 2 mT) would excite all orientations of the molecule but not uniformly. Nitroxide parameters used are [g_{xx}, g_{yy}, g_{zz}] = 2.0090, 2.0060, 2.0024 and [A_{xx}, A_{yy}, A_{zz}] = 18, 18, 96 MHz. The g- and A-matrix orientations for a nitroxide are shown on the left, along with the definition of the field orientation $\mathbf{B}_0(\Theta, \Phi)$

relative spatial positions. This is demonstrated in Fig. 9a where the relative orientation of the $\boldsymbol{g}$ and $\mathbf{A}(^{14}N)$ matrices between the two radicals is kept constant while the spatial orientation of the two spin centres is changed as a function of κ_1 (see the figure for a definition of κ_1); the modulation depth is constant (Fig. 9a.2) while the frequency response changes (Fig. 9a.3) with angle κ_1. In Fig. 9b the relative orientation between $\mathbf{g}^A/\mathbf{A}(^{14}N)^A$ and $\mathbf{g}^B/\mathbf{A}(^{14}N)^B$ of the two spins, defined by κ_2, is varied. The modulation depth changes (Fig. 9b.2) with κ_2 as the orientation selection changes, and the set of contributing dipolar frequencies is constant as κ_2 is varied since the dipolar angle θ (11) is fixed (at least if the two radicals are

Fig. 6 (continued) (**a.3**) (*green line*) pulse profile P_{det} for $t_\pi = 32$ ns; and (**a.4**) (*red line*) cumulative integration of $I^i_A P_{det}$ to give $f^i_A = 0.12$ (17), the contribution of the A-spin to the detection echo for orientation $\mathbf{B}^i_0$. (**b.1**) (*black line*) Pump pulse position in the NO• EPR spectrum, (**b.2**) (*blue line*) B-spin resonances I^i_B for the orientation $\mathbf{B}^i_0$, (**b.3**) (*green line*) pulse profile P_{pump} for $t_\pi = 16$ ns, and (**b.4**) (*red line*) cumulative integration of $I^i_B P_{pump}$ to give the modulation depth fraction $\lambda^i_B = 0.70$ (21). (**c**) Contributions for all orientations $\mathbf{B}^i_0$ of the A-spins to the detection echo f_A, the modulation depth function λ_B, and the product $f_A\lambda_B$ showing the orientations giving the largest contributions to the modulations in the DEER trace. *Red* represents high intensity and blue is zero intensity; contributions to f_A and λ_B are shown on the same scale. (**d**) DEER traces and their dipolar spectra simulated without orientation selection (*black*) and with orientation selection (*red*) for the NO•–NO• system shown above

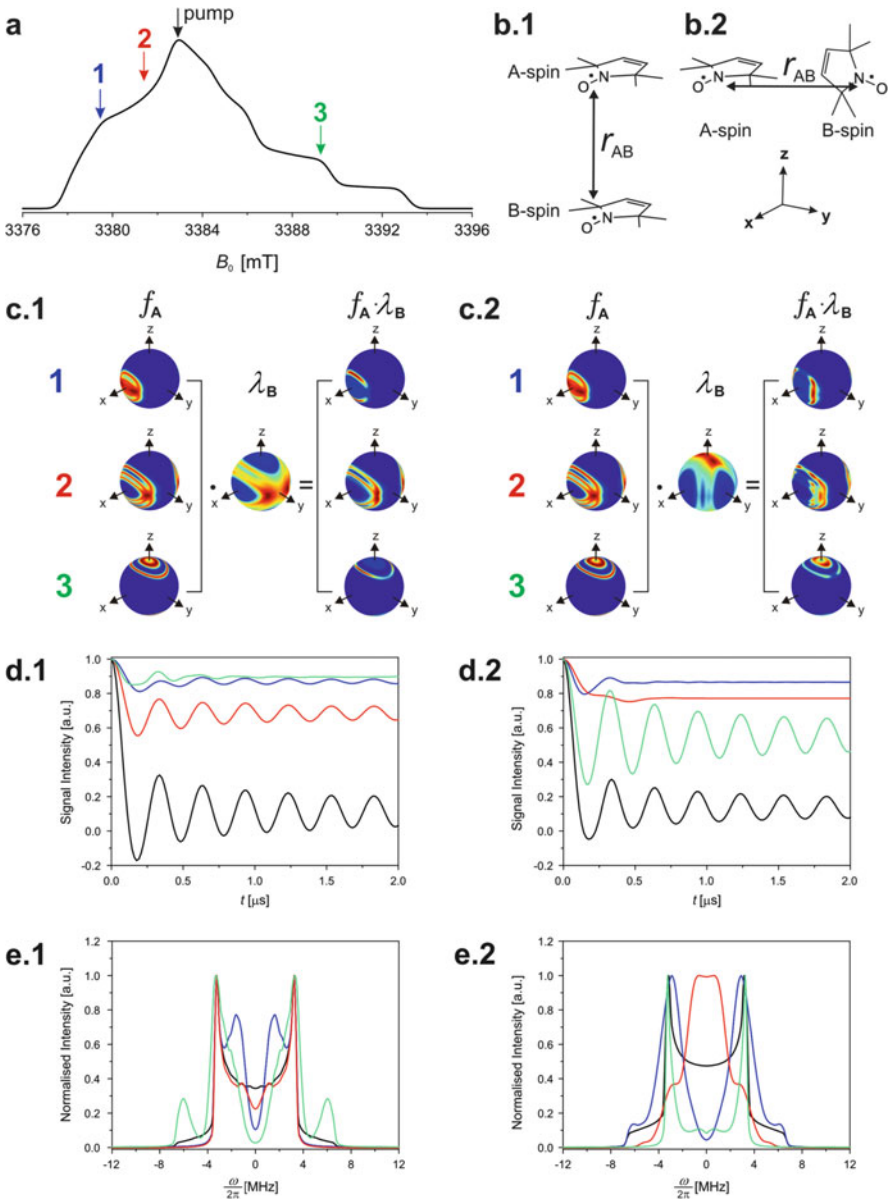

Fig. 8 Orientation-selective DEER simulations at W-band. (**a**) Nitroxide EPR spectrum, indicated are the detection mw pulse positions (arrows 1, 2, 3) as well as the pump position for orientation selection calculations. (**b**.**1**/**b**.**2**) Relative orientations of the nitroxide radicals in the molecular frame for two cases. (**c**.**1**/**c**.**2**) Orientations selected by detection ($t_\pi = 32$ ns) and pump ($t_\pi = 16$ ns) mw pulses for the biradicals (**b**.**1**) and (**b**.**2**), respectively. The intensity with which an orientation is excited is coded by colour: *red* (intensely excited) to *blue* (not excited). (**d**.**1**/**d**.**2**) DEER time traces for the pump and detection pulse combinations given in (**c**) and for comparison the time trace without orientation selection (*black line*). (**e**.**1**/**e**.**2**) Corresponding orientation-selective dipolar spectra and the Pake pattern without orientation selection (*black line*). The maximum intensity has been normalised to 1 to allow comparison of the frequency profiles (modulation depth information is retained in (**d**))

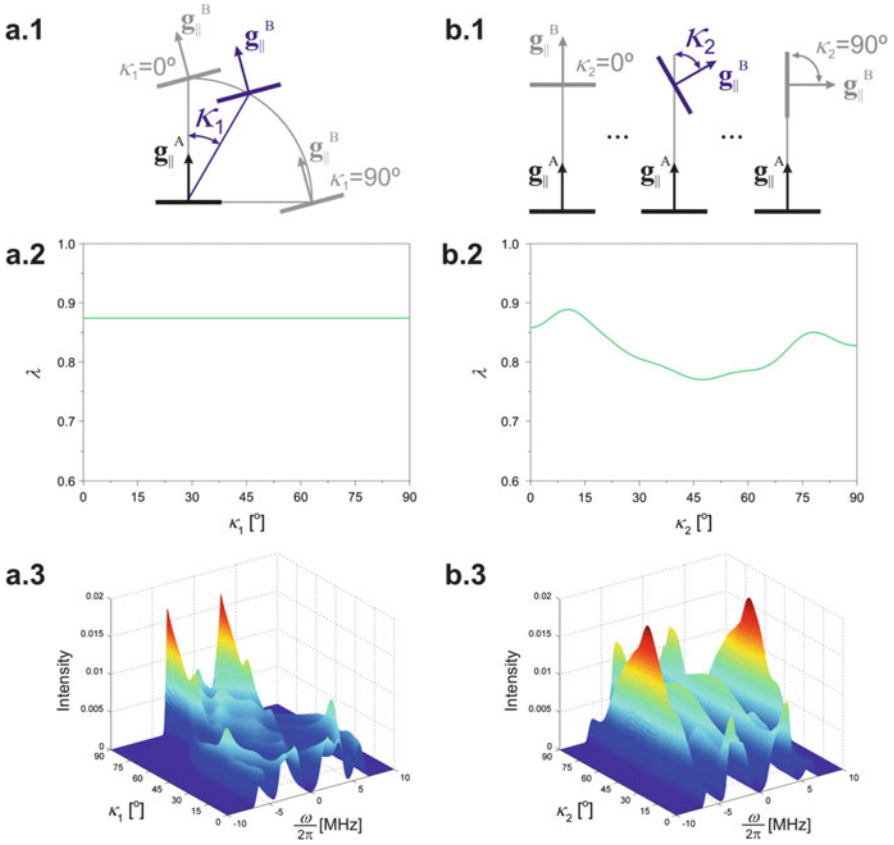

Fig. 9 Dependence of the dipolar frequencies and modulation depth on the relative spatial orientation and spin Hamiltonian orientation between the radicals, demonstrated for two nitroxide radicals. The $t_\pi = 16$ ns pump pulse is positioned at the intensity maximum in the EPR spectrum and the $t_\pi = 32$ ns detection pulse is offset by 65 MHz. (**a**.**1**) The relative orientations of matrices **g** and **A**(^{14}N) between the radicals are kept constant, while their spatial orientation is varied from $\kappa_1 = 0$–$90°$. The modulation depth is constant (**a**.**2**), but the set of selected θ values (11) changes and thus the dipolar frequencies change (**a**.**3**). (**b**.**1**) The relative orientations of matrices **g** and **A**(^{14}N) between the two spin centres are varied from $\kappa_2 = 0$–$90°$, while their spatial orientation is fixed. In this case the set of θ values (11) is constant but the intensity of the dipolar frequencies changes (**b**.**3**) within this set as the orientation selection of the detection and pump pulse depends upon the relative orientations of matrices **g** and **A**(^{14}N). This also changes the modulation depth (**b**.**2**) which in general depends upon the relative g-matrix and nitrogen hyperfine matrix orientations between the spin pair

considered as points). However, their intensity in the dipolar spectrum changes with the orientations excited by the detection and pump pulses.

Practically, the frequency response is a robust experimental parameter and easy to calculate. The determination of the modulation depth needs great care if accurate values are required as it depends strongly upon B_1 inhomogeneity and resonator

bandwidth, the latter being a function of the user controlled resonator coupling which may vary from sample to sample. With due care these parameters can be accurately quantified. Perhaps a more serious issue in determining absolute modulation depths is the spin labelling efficiency which is often not 100% and may be difficult to quantify sufficiently accurately.

If the orientation-selective experiments for a given sample are recorded with a fixed pump and detection frequency and only the magnetic field is varied, then the experimental conditions determining modulation depths remain exactly the same. Relative modulation depths are then reliable, i.e. the dependence of modulation depth on magnetic field can be fitted with one additional parameter, a scaling factor that is the same for all measurements [32]. This restriction, however, limits the information obtained which reduces the accuracy and reliability of the analysis (e.g. for nitroxides there may be no data from pump and detection positions corresponding to field positions given by the g-values g_{xx} and g_{zz}).

Figure 9a, b shows two possible orientations of a pair of spin centres and thus a portion of the possible frequency/modulation depth space. If experimental DEER data need to be fitted to an unknown structure, then clearly there are many local minima where a search algorithm could converge to (get stuck in). For this reason most investigations have generated a set of simulated DEER traces covering all possible orientations of the radicals for a given experimental parameter set and structural problem and determined the global minimum by fitting data to every orientation in this frequency/modulation depth space.

4.3 Symmetry Constraints on the Biradical Orientations

Due to the inversion symmetry of the magnetic tensors (spin Hamiltonian interactions), there are a number of relative orientations of the biradicals which produce identical DEER time traces. For instance, for a rhombic spin A and spin B system, identical solutions are obtained at orientations related by $\pm n\pi$; $\mathbf{R}(\alpha \pm n\pi, \beta \pm n\pi, \gamma \pm n\pi)$ and $\mathbf{n}_{AB}(\xi \pm n\pi, \phi \pm n\pi)$, where n is an integer (angles are defined in Fig. 4). These considerations are summarised in Table 1 for the combinations of isotropic, axial, and rhombic spin systems. These symmetry restrictions are only valid if each spin is considered as a point in space, a good approximation in most circumstances. If a paramagnetic centre needs to be described by a spin-density distribution, such as the iron–sulphur clusters described in Sect. 5, then the inversion symmetry is no longer (strictly) valid and it may be possible to discriminate between radicals A and B at the positions, e.g. A/B: 0/–x or A/B: 0/+x. As pointed out in [39], the symmetry imposed by the $(1–3\cos^2\theta)$ dependence of the dipolar coupling also causes identical solutions to occur for different θ values, e.g. $\theta = 45°$ or 135° giving $(1–3\cos^2\theta) = –0.5$, and the insensitivity of the DEER experiment to sign changes of ω_{AB} (see Fig. 10b). This introduces several identical solutions for different relative orientations of the two radicals that can only be resolved with additional information, e.g. from molecular modelling.

Table 1 Range of the Euler angles (α,β,γ) and polar angles (ξ,ϕ) required to simulate DEER traces for all possible orientations of two radicals in the cases of isotropic, axial, and rhombic spin Hamiltonians describing the EPR spectra of spins A and B

Spin A	Spin B	α	β	γ	ξ	ϕ
Axial	Isotropic	n.a.	n.a.	n.a.	0-π/2	n.a
Axial	Axial	0-π	0-π/2	n.a.	0-π/2	n.a.
Rhombic	Isotropic	n.a	n.a.	n.a.	0-π/2	0-π/2
Rhombic	Axial	0-π	0-π/2	n.a.	0-π/2	0-π
Rhombic	Rhombic	0-π	0-π/2	0-π	0-π/2	0-π

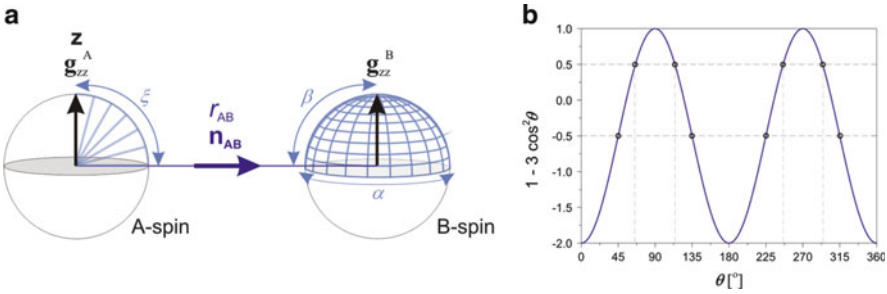

Fig. 10 (**a**) Definition of the parameters defining the DEER simulation space of two axial paramagnetic centres. In this case the relative orientation of the two paramagnetic centres A and B is defined by three angles: ξ is the angle between the A-spin g_{zz}-axis and the spin—spin vector $\mathbf{n_{AB}}$ and α and β are the Euler angles defining the orientation of the g-matrix of spin B with respect to that of spin A. The three angles are varied in the ranges given in row 2 of Table 1 and shown in blue in the figure. (**b**) Angular dependence of the dipolar interaction, showing, for example, that eight θ values give $(1–3\cos^2\theta) = |\pm 0.5|$ in the range $\theta = 0°$ to 360°. Note that the DEER signal oscillation $\cos(\omega_{AB}t)$, an even function, is independent of the sign of ω_{AB}

4.4 Analysis in the Presence of Distance and Angular Distributions

As shown above, the DEER signal depends in a complicated way on the experimental parameters and the structure of the two radicals being investigated. Once the experimental data has been collected, the problem is to infer both the distance and relative orientation between the two radicals. In the case of unselective DEER data, the time trace does not depend upon the relative orientation between the two radical centres, and a model-free analysis using Tikhonov regularisation provides a distance distribution. This can be expressed as

$$f(t) = 1 + \int_0^1 \frac{1}{N}\left(\sum_{n=1}^{N}\cos(\omega_{dd}(1-3z^2)t) - 1\right)dz = 1 + \int_0^1 k(z,t)dz, \qquad (27)$$

with $z = \cos(\theta)$ where θ is the angle between $\mathbf{B}_0$ and the inter-spin vector, $k(z, t)$ is known as the kernel function, and here $f(t)$ is a reduced form factor (only the

modulated part). Index n runs over all pairs of spins. Equation (27) can be inverted and hence from $f(t)$ the distance distribution $P(r)$ can be computed. In the case of orientation selection, the problem is considerably more complicated and no general solution is known. Following on from (27), the normalised DEER signal is now a function of both distance and orientation:

$$F(t, \nu') = 1 + \int_0^1 \lambda(z, \nu') k(z, t) dz, \tag{28}$$

where ν' is a set of quantities defining the orientation selection (see (29) and Fig. 4). As described in Sect. 4.2 and shown in Fig. 9 the modulation depth in the general case depends upon the relative orientation of the biradical (defined by Euler angles α, β, γ) and the detection and pump pulses (excitation profiles and frequencies):

$$\lambda(z, \nu') = \frac{1}{f^{\text{total}}} \sum_{n=1}^{N} \lambda(z, \alpha^n, \beta^n, \gamma^n, P_{\text{det}}, \omega_{\text{det}}, P_{\text{pump}}, \omega_{\text{pump}}). \tag{29}$$

Term f^{total} normalises the intensities. Furthermore the z dependence in (29) indicates the calculation requires a weighted integration over the orientations ranging from $\theta = 0°$ to $90°$ ($z = \cos\theta$ depends upon ξ, ϕ and the $\mathbf{B}^i_0$ direction). Marko et al. [35, 36] have investigated the problem of inferring experimental orientation distributions without a chemical model under the assumption that the distance distribution is uncorrelated to the orientation distribution:

$$\langle \lambda(z, \nu') k(z, t) \rangle \approx \langle \lambda(z, \nu') \rangle \langle k(z, t) \rangle. \tag{30}$$

The brackets $<\cdots>$ in (30) signify a conformational average. In their first paper [35] a general solution approach involved first determining the distance distribution $k(z, t)$. This is, in principle, possible by either averaging all the orientation-selective DEER traces into a single orientation free trace or measuring an orientation free trace with hard non-selective mw pulses. Given the distance distribution $k(z, t)$, (28) yields the modulation depth function $\lambda(\theta)$, dependent only upon angle θ (or equivalently $z = \cos\theta$). The orientation between the radicals is then calculated and adjusted to best fit the function $\lambda(\theta)$; however no method for calculating the radical orientations directly from $\lambda(\theta)$ yet exists.

In a second paper Marko et al. [36] presented a solution for calculating the spatial orientations between two radicals for the special case where the two spin labels are parallel, as can be the case for spin-labelled DNA samples (Fig. 11). The method requires knowledge of the distance distribution so that (28) can be inverted to yield $\lambda(\theta)$, the modulation depth function, which can be determined for each DEER trace with offset $\Delta\omega = \omega_{\text{det}} - \omega_{\text{pump}}$. A plot of the experimental values of $\lambda(\theta = 0, \Delta\omega)$ versus $\Delta\omega$ is then dependent upon the angles β (Fig. 11b), allowing a β-value to be determined (note radians to Hertz: $\omega/2\pi = \nu$).

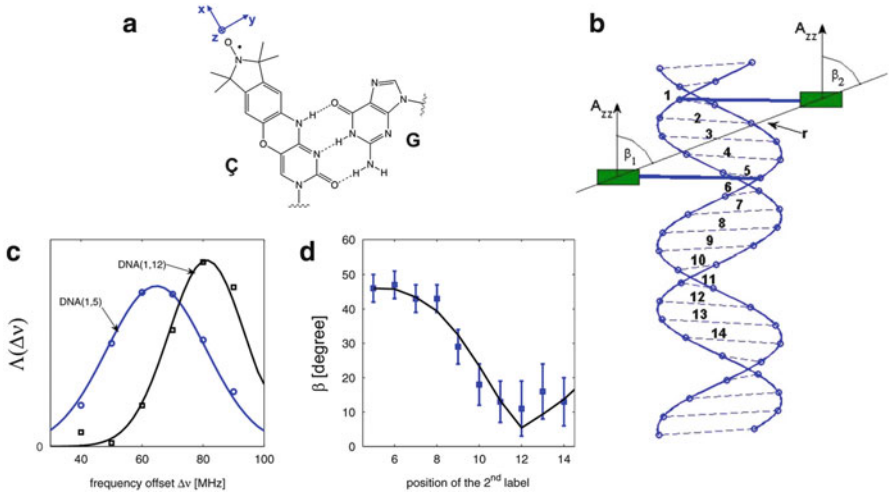

Fig. 11 (**a**) Chemical structure of the rigid spin label Ç, a cytidine analogue, base paired with guanine. (**b**) Spin labels attached to a doubly labelled DNA molecule at positions (1,5). If the angle $\beta_1 \approx \beta_2$, then analysis of orientation-selective DEER traces gives a fitting free evaluation for angle β. (**c**) Estimated values of the orientation intensity function $\Lambda(\Delta\nu) \propto \lambda(\theta = 0, \Delta\nu)$ for DNA with spin labels at position (1,5), *circles*, and (1,12), *rectangles*. Both estimations are fitted with Gaussian curves. (**d**) Estimated values of the angle β between spin label normals and inter-spin vector r versus the position of the second spin label compared to the values of these angles obtained from the DNA structure (*solid line*) [Reprinted with permission from [36]. Copyright 2010 by the American Physical Society. (http://link.aps.org/abstract/PRE/v81/e021911)]

Marko and Prisner [40] presented the development of a model-free analysis of orientation-selective X-band DEER data collected on nitroxide biradicals. Their fitting algorithm reconstructs experimental data by searching for an optimal combination of pre-simulated DEER time traces with all relative orientations and with inter-spin distances in the experimentally accessible range. Excellent fits to experimental DEER data on model nitroxide molecules were obtained that were in agreement with the known distances and relative radical orientations. However, as pointed out in the paper the solutions were not unique and application of the algorithm to unknown systems to determine a unique solution would require additional information to restrict the conformational space.

It has been suggested that the inversion of DEER data describing a general distribution of orientations and distances is not tractable [39]. Given this, at present, the best generic analysis method is probably via a structural model which defines the orientations of the radicals. From this orientation selectivity DEER traces can be readily simulated and compared to the experimental data. The structural model can then be refined under suitable structural constraints to minimise the difference between the simulated and experimental DEER traces. Many of the possible equivalent solutions could be anticipated to be rejected as they may give an unrealistic solution, such as two biomolecules overlapping.

5 Examples

5.1 Spin Labels: Nitroxide Radicals

Spin labels typically used in proteins are inherently flexible and orientation selection can often be neglected, even at frequencies as high as W-band [41]. However, if the biradical and/or the spin labels are sufficiently rigid, then orientation selection can be observed even at X-band frequencies. Orientation effects are clearly demonstrated in the paper by Margraf et al. [33] where X-band DEER measurements were made on a model nitroxide biradical molecule with restricted relative $NO^{\bullet}$ orientations (Fig. 12). DEER time traces were recorded with the pump frequency set at the centre of the nitroxide spectrum to achieve maximum pumping efficiency by exciting all orientations, and the detection sequence stepped between an offset of +40 and +80 MHz. The modulation frequencies and depths changed as a function of offset as a consequence of the orientation selection. Figure 12b shows these DEER traces, which could be simulated with a model where the relative orientations of the two nitroxides are constrained by two cones and a single bending motion of the bridge as depicted in Fig. 12a. Further examples on model molecules can be found in [35, 42].

The higher frequency of Ka- or Q-band offers increased orientation selectivity, and the benefit of much improved sensitivity over X-band, in particular if the spectrometer is equipped with a high power mw amplifier [43, 44]. Polyhach et al. [45] reported on the performance of their Q-band spectrometer (nominally 150 W TWTA and a home-built resonator facilitating the measurement of 3 mm sample tubes commonly used at X-band) for DEER measurements on nitroxides. This set-up enables short π pulses of ca. 12 ns to be created for both pump and detection spins in conjunction with large 3 mm sample tubes. The result of applying "soft" and "hard" pulses is shown in Fig. 13 for a model biradical molecule (Fig. 13a). Plotted in Fig. 13c are the dipolar spectra obtained under broad excitation (black dashed line) with 12 ns lengths for all pump and detection pulses with a separation of 80 MHz (denoted: 12 ns/80 MHz/12 ns) and using soft pulses of 40 ns with a separation of 35 MHz (40 ns/35 MHz/40 ns). The pulse positions of the various experiments, relative to the EPR spectrum, are indicated in Fig. 13b. Strong orientation selection (Fig. 13c) is evident which could not be entirely removed using the strongest pulses achievable with their experimental apparatus (black dashed line).

Importantly for a protein doubly spin labelled with the usually flexible MTSL spin label, the experimental results showed that their hard-pulse set-up (12 ns/80 MHz/12 ns) removes the orientation selectivity and the data obtained depend only upon distance, whereas the soft-pulse set-up retained orientation selection effects. This scenario may have advantages as both types of data can be collected for analysis.

Strong angular correlations between nitroxide spin labels attached to the tetrameric ion channel KcsA R64C-SL were observed with X- and Q-band DEER

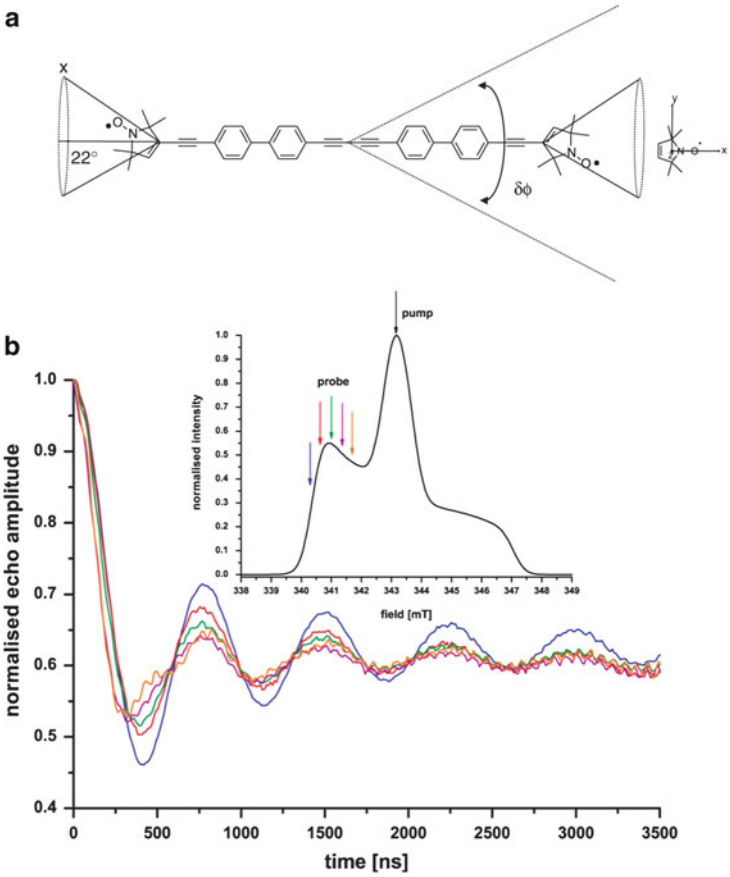

Fig. 12 (**a**) Structure of the biradical molecule used by Margraf et al. [33]. The geometric model used to create an ensemble of conformers and the molecular axis system are indicated. The nitroxide radicals are assumed to rotate freely around their acetylene bond (cone with angle 22°), and the mobility of the bridge is described by a single bending motion with a Gaussian distributed width δϕ. (**b**) Experimental DEER time traces for offset frequencies $\Delta\nu$ between +40 and +80 MHz. All time traces are normalised to 1 at $t = 0$, and the intermolecular decay is removed by division by a mono-exponential decay. *Inset*: field-swept EPR spectrum with the position of pump and detection (probe) frequencies indicated by arrows [Adapted from [33], reprinted by permission of Taylor & Francis Ltd.]

[46]. Experiments were performed with the pump pulse on the central peak of the EPR spectrum and with several detection frequency separations at X-band $\Delta\nu = +38$ to +80 MHz and at Q-band $\Delta\nu = +40$ to +70 MHz. These experimental parameters permitted the separation of orientation and distance information and enabled determination of the spin-label orientations. In this case the Q-band spectrometer had only 700 mW of mw power, allowing a 28 ns pump pulse but very weak detection pulses of length 92 ns.

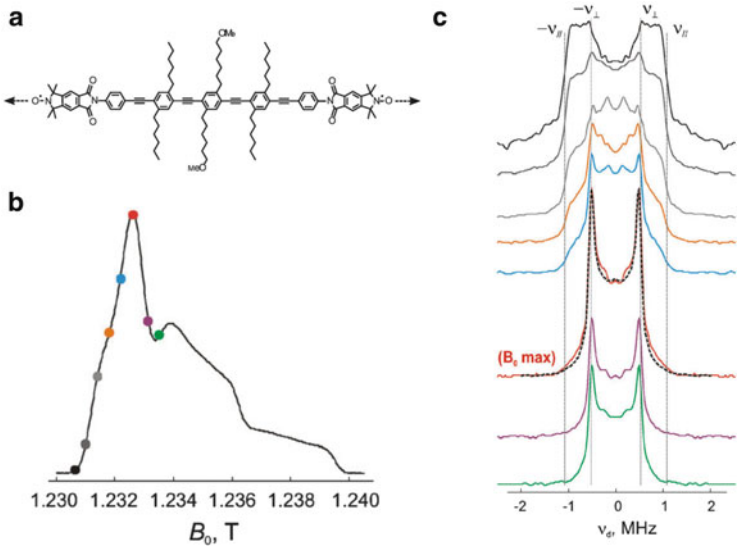

Fig. 13 Orientation-selective Q-band (34.1 GHz) DEER on the shape-persistent biradical molecule shown in (**a**). (**b**) The pump pulse positions (*coloured dots*) of the individual DEER traces plotted in (**c**) are depicted on the echo-detected EPR spectrum. (**c**) DEER versus B_0 pattern taken with the excitation scheme 40 ns/35 MHz/40 ns. The dipolar spectrum obtained under broadband excitation (12 ns/80 MHz/12 ns) and pumping on the maximum of the echo-detected EPR spectrum is shown for reference (*black dashed line*). Total collection time for the DEER versus B_0 pattern was about 2 days. The shape-persistent biradical was dissolved in perdeuterated *o*-terphenyl at 200 mM concentration [Adapted from [45] with permission of the PCCP Owner Societies]

A further example is discussed in a study on a doubly spin-labelled variant of the cytoskeletal protein vinculin tail [39] where X-band DEER measurements showed strong orientation selectivity.

At W-band and above, the selectivity of the mw pulses becomes strong as the *g*-values are resolved, as was shown in Fig. 8. However, at this frequency the microwave power of Bruker commercial spectrometers is currently very low, making DEER spectroscopy very restrictive [47]. A number of home-built instruments have, however, recently been reported that are suitable for DEER at W-band with organic radicals [13, 23, 48]. The W-band spectrometer built by Smith et al. is capable of using 3 mm o.d. quartz EPR tubes, achieving $\pi/2$ pulses of length between 4 and 10 ns over a bandwidth range compatible to that of the $NO^{\bullet}$ spectrum [49]. High sensitivity has been reported with measurements on ca. 1 μM samples (2 μM spins).

5.2 Organic Cofactors

Denysenkov et al. [50, 51] performed DEER measurements on class I ribonucleotide reductases (RNRs) for *Escherichia coli* which is composed of two subunits, R1 and R2. The R2 subunit contains the essential diferric cluster-tyrosyl radical ($Y^{\bullet}$) cofactor. DEER measurements at 180 GHz detected the dipolar interaction between the $Y^{\bullet}$ cofactors in each protomer of RNR R2, allowing distance (32.5 Å), and orientation information between the two radicals to be determined. Note that the long distance gives a small dipolar coupling constant of ca. 1.5 MHz permitting the use of relatively weak detection ($t_{\pi/2} = 30$ ns) and pump ($t_{\pi} \approx 80$ ns) pulses – to have an efficient experiment, the pulse bandwidths should be sufficient to excite both lines of the dipolar doublets of each spin.

A further example is the orientation selection measurements made between a spin label and organic cofactor in the reaction centre of a native cofactor and a spin label in the reaction centre of *Rhodobacter sphaeroides* [52].

ENDOR at Q-band (34 GHz) and orientation-selective DEER at W-band (95 GHz) have been used to investigate potential light-induced reductive structural changes associated with the formation of the $P^{\bullet+}Q_A^{\bullet-}$ state in the reaction centre from the photosynthetic bacterium *Rhodobacter sphaeroides* R-26 [53]. The measurements were recorded with the detection sequence on the narrow spectrum of $P^{\bullet+}$ and a range of pump pulse positions across the $Q_A^{\bullet-}$ radical EPR spectrum. Samples frozen in the dark and under illumination gave exactly the same DEER signals, providing evidence that no structural changes occur upon light-induced reduction.

5.3 Nucleic Acids

DEER measurements on nucleic acids are often carried out using rigid spin labels, which leads to significant orientation selection even at X-band. However, in several cases the orientation selectivity observed by comparing DEER traces recorded with a series of different frequency offsets has been shown to be weak, and orientation averaging [42] followed by data analysis using standard software has been successful at determining the distance between the spin labels [54–57]. This orientation-averaging approach is advantageous if only a distance is required since the data analysis is relatively simple.

To determine precisely relative orientations as well as distances, a rigid spin label, denoted as Ç, was introduced by Barhate et al. [58] (Fig. 11). Schiemann et al. have demonstrated that this spin label can be used to determine both distance and relative orientation of two spin-labelled nucleosides in DNA at X-band frequencies [59]. Marko et al. then developed an analytical method for the determination of the angle between the axis $\mathbf{g}_{zz}$ of the nitroxide spin label and the inter-spin vector, as discussed in Fig. 11 [36]. Orientation-selective DEER data recorded

at X- and G-band on a DNA duplex labelled with Ç have also been used to determine the dynamics of DNA strands [17] and to study changes in DNA structure and dynamics upon binding to the Lac repressor protein [56]. Wunnicke et al. also used orientation-selective DEER to study changes in the structure and dynamics of mispaired DNA duplexes [57]. Further details on spin labelling of nucleic acids and their structural characterisation can be found in the chapters of this book written by Shelke and Sigurdsson [60] and by Ward and Schiemann [61].

5.4 Metals

5.4.1 Copper

Copper centres in metalloproteins are another instance where orientation effects have to be considered in the analysis of experimental data. At X-band the Cu^{2+} EPR spectrum extends over ca. 2 GHz due to its g-anisotropy and the copper hyperfine coupling ($I = 3/2$ nucleus, ^{63}Cu and ^{65}Cu isotopes). The hard rectangular microwave pulses used in DEER typically excite only a small part of the spectrum, usually less than 50 MHz (Fig. 14).

In the first DEER studies on Cu^{2+}–nitroxide and Cu^{2+}–Cu^{2+} systems [63–66], excitation in the $g_{\perp}$ region of the copper spectrum led to negligible orientation selection and allowed a reasonable analysis of the data using Tikhonov regularisation considering that these computations usually employ complete Pake patterns at each distance (see (27)) which if fitted to experimental data comprising incomplete Pake patterns will cause distance distribution artefacts. These experimental data were later investigated by simulations [34]; excitation in the $g_{\perp}$ region always leads to the detection of the perpendicular dipolar splitting frequency in the Pake pattern, independently of the relative orientation of the two Cu^{2+} paramagnetic centres. This is a consequence of the orientation selection with nearly axial g-matrices so that $g_{\perp 1}$ and $g_{\perp 2}$ are not resolved and a plane of orientations is excited. Such data may then be exploited to determine the distance with a single DEER measurement yielding a dipolar spectrum with a distinct perpendicular dipolar splitting feature.

The feasibility of distance determinations between copper ions using DQC EPR instead of DEER has been shown by Becker and Saxena [66] on a model peptide with two Cu^{2+}-binding peptide sequences. These authors also demonstrated that the analysis of DQC data for copper ions is complicated by the presence of a series of ESEEM peaks, which have been assigned using a similar model containing just a single copper ion before attempting the distance analysis.

A series of papers on DEER of various copper-containing systems [34, 63, 64, 67, 68, 69] has clearly shown that in order to resolve orientation effects, high-quality experimental data is required due to the small modulation depths and only subtle changes with orientation. Yang et al. have studied the optimal conditions for data acquisition in the case of Cu^{2+}–nitroxide and Cu^{2+}–Cu^{2+} systems with regard

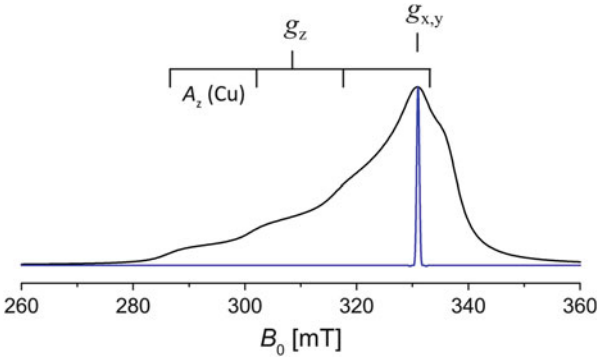

Fig. 14 Cu^{2+} X-band EPR spectrum simulated with an axial g-matrix ($g_\perp = 2.05$, $g_\parallel = 2.20$) and hyperfine interaction ($A_\perp = 10$, $A_\parallel = 450$ MHz) at $\nu_{mw} = 9.5$ GHz (*black*) using EasySpin [62] and the excitation profile of a refocused echo sequence (18) with $t_{\pi/2} = 32$ ns (*blue*)

to pulse lengths (16-48 ns), frequency offsets (up to 500 MHz), and magnetic field positions (from $g_\perp$ to $g_\parallel$) using a Bruker MD5 resonator [70].

Bode et al. studied at X-band the influence of orientation selection, spin-density distribution, conformational flexibility, and exchange coupling on DEER measurements of two structurally related nitroxide-labelled Cu(II) porphyrins [29, 69]. The conformational flexibility of the system was modelled considering a conical distribution of the nitroxide label with respect to the copper centre (see Fig. 15a) and, guided by DFT calculations, a spin-density distribution on the Cu^{2+} ion and ligating nitrogen nuclei. The comparison of the distance distribution obtained with this simulation approach to the distance distribution obtained using DeerAnalysis [16] showed that the latter approach (not surprisingly) fails in the presence of orientation selection [69]. Figure 15b plots the distribution functions of dipolar angles $P(\theta) = \lambda(\theta)\sin\theta$ versus angle θ for the system shown in Fig. 15a with orientation selection and for uncorrelated spin centres (as implemented in DeerAnalysis [16]). Further, the authors showed that through appropriate simulations, the contributions of dipolar through-space coupling and through-bond exchange coupling can be separated even in the presence of orientation selection effects.

Distance measurements between two Cu^{2+} ions in a covalently linked azurin dimer were reported by van Amsterdam et al. [64], a system that provides a single relative Cu^{2+}–Cu^{2+} orientation. Using pump and detection pulses in the $g_\perp$ region with a frequency offset of 75 MHz, they were able to conclude that the DEER measurement was affected by orientation selection and extracted a distance of 26 Å. Kay et al. were able to measure distances of 41.6 Å and 42.4 Å in dicupric human serum transferrin and lactoferrin using similar experimental parameters [65]; by performing DEER at the $g_\perp$ field position, the authors were able to minimise the effect of orientation selection and extracted the distance distribution using DeerAnalysis [16].

Yang et al. developed a thorough analysis method of orientation-selective Cu^{2+}–Cu^{2+} DEER data [67, 68] and used it for interpretation of experimental data recorded at five magnetic fields on a model peptide containing two Cu^{2+}-binding PHGGGW amino acid sequences (Fig. 16a). Only small differences could be

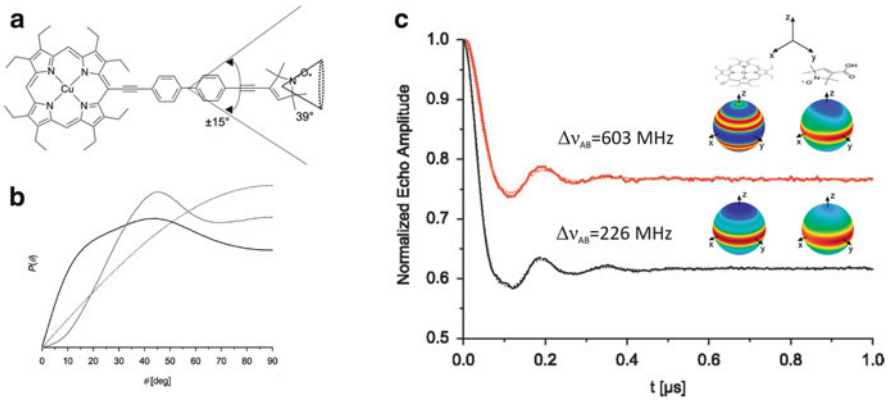

Fig. 15 (**a**) Geometric model of the nitroxide-labelled Cu^{2+} porphyrin studied in [29, 69] [Reprinted from [29], Copyright 2009, with permission from Elsevier]. (**b**) Calculated angular dependence of the DEER trace for the system shown in (**a**) for frequency offsets of 226 MHz (*black curve*) and 603 MHz (*grey curve*) compared to the $P(\theta) = \sin\theta$ distribution function distribution for uncorrelated spin centres (*dotted line*). $P(\theta) = \lambda(\theta)\sin\theta$ is the distribution function of dipolar angles. (**c**) Experimental (*solid lines*) and simulated (*dotted lines*) DEER data from reference [69] at two different frequency offsets. The pump frequency was resonant with the central transition of the nitroxide spectrum in both cases. The orientation selection on copper (*left*) and on the nitroxide (*right*) corresponding to each frequency offset is shown above the DEER trace (*red*, complete excitation; *dark blue*, no excitation); the orientation of the axes with respect to the molecular structure is also shown. For offset $\Delta\nu = 226$ MHz the pump pulse length was 12 ns, while it was 32 ns for $\Delta\nu = 603$ MHz [Adapted with permission from [69], Copyright 2008 American Chemical Society]

observed between the traces recorded by exciting in the $g_\perp$ region of the EPR spectrum (see Fig. 16b); however the DEER trace recorded by excitation in the $g_\parallel$ region is characterised by different modulation frequencies (Fig. 16b). Their DEER signal analysis was based on the theory of Maryasov et al. [71], and their structure model considers all relative orientations of the two copper centres confined within a sphere of radius ΔR to account for spin–spin flexibility (see Fig. 16a, c). In a subsequent paper the same approach was used to determine the distance distribution between two Cu^{2+} ions in the DNA-modifying enzyme *Eco*RI endonuclease [72].

Data analysis based on a structural model was used for the interpretation of DEER data recorded for three different magnetic fields and frequency offsets on a 3-phenyldiporphyrin dicopper model system by Lovett et al. [34] (Fig. 17a). A spin distribution over the Cu^{2+} ion and four coordinating pyrrole nitrogen nuclei of the porphyrin was used in the DEER trace calculations (see Fig. 17b). The dependence of the results on the model used as input for the orientationally selective DEER simulations was further investigated by Bowen [73] using a series of dicopper diporphyrin systems with phenyl-based linkers of varying length. Various conformers of these diporphyrin systems were generated by DFT and the distribution of the position of the second Cu^{2+} ion, relative to the first one, was found to form a "double-teardrop" shape rather than a stretched conical or spherical

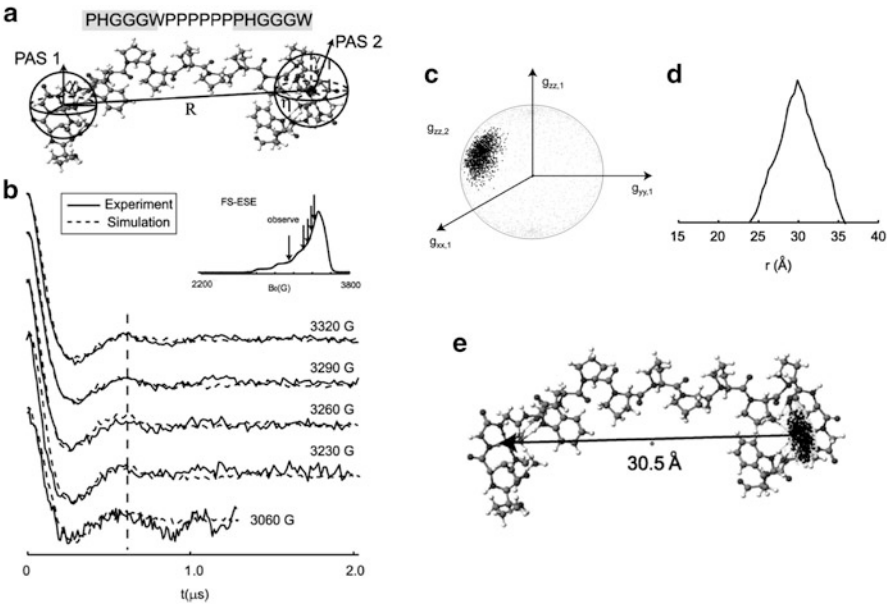

Fig. 16 (**a**) Peptide sequence and molecular structure of the model peptide from reference [68] with the definition of the parameters optimised in the fitting procedure; R, ΔR, and the orientation of the two Cu^{2+} centres. (**b**) DEER signal after baseline correction (*solid lines*) recorded for the peptide shown in (**a**), and corresponding simulations using the theoretical model developed in [68] (*dashed line*). The *inset* shows the observer positions used for recording the DEER traces; the pump frequency was always 92 MHz lower. (**c**) Orientations of the second Cu^{2+} g_{zz}-axis with respect to the first Cu^{2+} g-matrix axes shown by *black dots*. (**d**) Cu^{2+}–Cu^{2+} distance distribution function determined from the simulations in (**b**). (**e**) View of the proline-based model peptide obtained based on the relative orientation and flexibility determined from the analysis of the DEER data shown in (**b**) [Adapted with permission from [68], Copyright 2010 American Chemical Society]

distribution as was used previously for other systems [67–69]. Simulations based on this set of DFT-generated and other model structures emphasise the importance of the use of a model appropriate for a particular molecular system in terms of both the average position of the two centres and the distribution of one centre with respect to the other.

5.4.2 Multinuclear Metal Clusters

In a spin-coupled paramagnetic cluster, the magnetic moment is delocalised over the ions of the cluster. For example, in a reduced $[2Fe–2S]^+$ cluster the unpaired spins of the Fe^{2+} ion ($S = 2$) and Fe^{3+} ion ($S = 5/2$) couple anti-ferromagnetically to yield an $S = 1/2$ ground state. The assumptions that the ground state is well separated from the excited states and that the spins are localised on the Fe ions

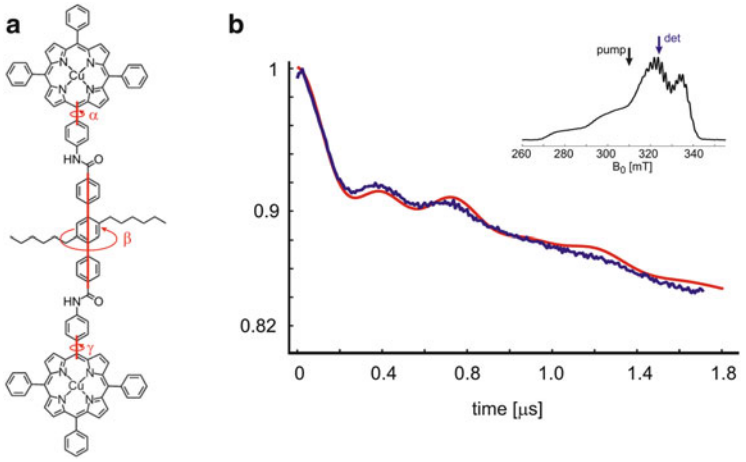

Fig. 17 (**a**) Chemical structure of the 3-phenyl-linked dicopper diporphyrin model system. (**b**) A simulated DEER trace (*red*) compared to the experimental trace (*blue*), with the detection and pump positions indicated in the inset. The DFT model uses relative orientations of the two copper ions obtained considering rotations around the dihedral bonds in the system and restricting the possible conformations to those accessible at the freezing point of the solvent [Figure adapted from [34] and [73]]

allow the spin projection factors of $k(Fe^{2+}) = -4/3$ and $k(Fe^{3+}) = +7/3$ to be calculated [74, 75]. The spin projection factors in essence describe the total magnetic moment via the k's located at the relevant nuclei and are used to calculate the dipolar coupling frequencies. For the case of a $[2Fe–2S]^+$ cluster coupled to a $NO^\bullet$ spin (considered as a point), (24) gives

$$\omega^{i}_{NO-[2Fe-2S]} = \frac{\mu_0 {\beta_e}^2}{4\pi\hbar} g^{i}_{NO} g^{i}_{[2Fe-2S]} \left(k_1 \frac{1-3\cos^2\theta^{i}_{NO,k_1}}{r^3_{NO,k_1}} + k_2 \frac{1-3\cos^2\theta^{i}_{NO,k_2}}{r^3_{NO,k_2}} \right), \quad (31)$$

where $k_1 = 7/3$ and $k_2 = -4/3$. This spin system was used by us to determine the docked structure of palustrisredoxin-B (PuxB) from *Rhodopseudomonas palustris* (CGA009) (containing a reduced $[2Fe–2S]^+$ ferredoxin) with the flavin-dependent palustrisredoxin reductase (PuR). The PuR was spin labelled using MTSL at a number of positions using site-directed mutagenesis [34]. The orientation selectivity is a result to the axial $[2Fe–2S]^+$ ferredoxin EPR spectrum ($g_{\|} = 2.0233$, $g_{\perp} = 1.9328$) which is ca. 15 mT (420 MHz) wide at X-band; five separate pump pulse positions were chosen across its EPR spectrum. The detection sequence position was placed on the $NO^\bullet$ echo maximum and thus was considered to be excited isotropically (all orientations). This symmetry corresponds to row 1 in Table 1 (if the asymmetry caused by the spin projection factors is ignored).

From a different point of view the electronic structure of a spin-coupled cluster can be investigated by measuring dipolar couplings to nearby magnetic nuclei, be

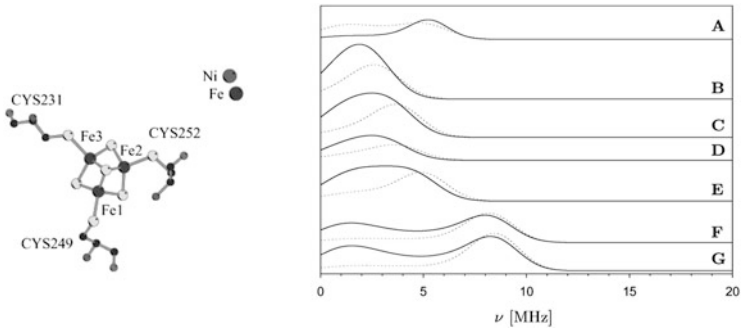

Fig. 18 *Left*: The [NiFe] and [3Fe–4S]$^{+}$ cofactors in the hydrogenase from *Desulfovibrio vulgaris* Miyazaki F. (PDB 1H2A). *Right:* Simulation of the hydrogenase DEER signals for different assignments of the spin projection factors to Fe1, Fe2, and Fe3: (*A*) $S = 1/2$ spin at the average Fe distance and (*B*) 2.28,−0.28, −1.00; (*C*) 2.28, −1.00, −0.28; (*D*) −1.00,−0.28,2.28; (*E*) −0.28, −1.00, 2.28; (*F*) −1.00,2.28,−0.28; and (*G*) −0.28,2.28,−1.00 [78]. Simulation F/G reproduces the main features of the experimental spectrum (not shown) [Adapted with permission from [78], Copyright 2002 American Chemical Society]

they nuclear or electron spins. ENDOR and HYSCORE spectroscopies have been used to measure the dipolar couplings between nearby ^{1}H nuclei and spin-coupled clusters; the nuclear–electron dipole interaction is obviously dependent upon the magnetic moments of the ^{1}H nucleus and the paramagnetic cluster [76, 77]. Characterisation of the cluster's electronic structure is also possible via DEER using a nearby unpaired spin as a probe [78, 79]. An example is the [3Fe–4S] cluster in *Desulfovibrio vulgaris* Miyazaki F. In the oxidised state of the enzyme, the paramagnetic centres are the [3Fe–4S]$^{+}$ cluster ($S = 1/2$, $k = 2.28$, –0.28, –1.00) and the [NiFe] active site ($S = 1/2$), the latter centre having the spin density largely located on the Ni ion. This arrangement is shown in Fig. 18a. The X-ray structure provided the distances between the three Fe ions and the Ni ion: r(Fe1) = 22.29 Å, r(Fe2) = 20.12 Å, and r(Fe3) = 21.72 Å. Assignment of the oxidation states of the Fe ions and thus the spin projection factors were unknown and were investigated by DEER [78]. The dipolar frequencies for the simulations were calculated using (24), where all possible permutations of the three spin projection factors were considered. These simulations are shown in Fig. 18b and demonstrate the great difference in the dipolar frequencies depending upon the assignment of the spin projection factors. Trace A shows the result if the Fe–S cluster is modelled as an $S = 1/2$ spin localised at the average Fe distance of 21.4 Å. The experimental trace (not shown) matched simulation F and G well, allowing $k = 2.28$ to be assigned to Fe2. A reasonable agreement to the experiment using only an $S = 1/2$ spin could also be calculated by reducing the average Fe to Ni distance by ca. 3 Å. This result allows an estimation of the error imposed on the electron–electron distance when the anisotropy of the Fe–S magnetic moment is ignored in the simulations.

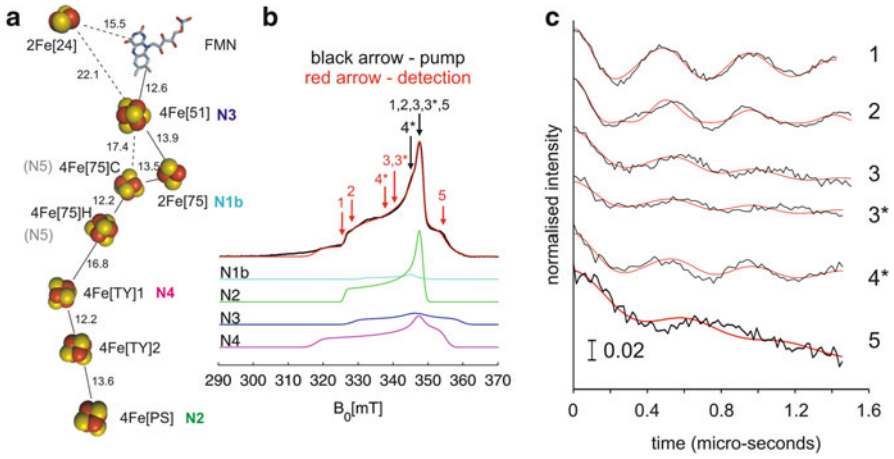

Fig. 19 (**a**) Fe–S clusters in the structure of the hydrophilic arm of *Thermus thermophilus* complex I (2FUG.pdb) conserved in *Bos taurus*, named according to their type (2Fe or 4Fe), subunit (named according to the standard nomenclature for *Bos taurus* 75 = 75 kDa, 51 = 51 kDa, 24 = 24 kDa, PS = PSST subunit, TY = TYKY subunit), and if necessary as C (all cys ligated) or H (one his ligand), or as cluster 1 or 2. Distances are centre to centre for the Fe–S clusters or the central ring of the isoalloxazine system. (**b**) X-band echo-detected EPR spectrum of complex I reduced to −0.4 V (or −0.3 V) recorded at 10 K and simulated with the four paramagnetic centres visible under these conditions: N1b, N2, N3, and N4. Experimental traces, *black*; summed simulations, *red* (N1b + N2 + N3 + N4). The markers correspond to the pump (*red*) and detection (*black*) pulse positions for the DEER traces in (**c**). Positions 3* and 4* refer to the −0.3 V sample; all others refer to the −0.4 V sample. (**c**) DEER data from *Bos taurus* complex I measured at 10 K. DEER traces (*black*) and best fit simulations (*red*) for the assignments shown in (**a**) (*coloured bold letters*). Intensity changes (indicating modulation depths) are denoted by the *scale bar* [Adapted from [80], Copyright 2010 National Academy of Sciences, USA]

DEER measurements have been made on the iron–sulphur (Fe–S) redox cofactors in *Thermus thermophilus* complex I [80], which form an unusually long electron transfer chain or "molecular wire" (Fig. 19a). The redox properties and corresponding field-swept EPR spectra of the paramagnetic clusters (Fig. 19b) were known, but there was no clear assignment of several of these EPR spectra to the structurally defined Fe–S positions in the electron transfer chain. Armed with the relative positions and orientations of the Fe–S clusters from crystal structure investigations, the DEER data (Fig. 19c) allow assignment of the EPR spectra (N1b/N2/N3/N4) to particular Fe–S clusters (Fig. 19a). The DEER simulations involved computing the time traces from all feasible permutations of EPR spectra assignments to particular Fe–S clusters. A definitive assignment was achieved by comparing these time-trace simulations to the experimental data. Combined with previous assignments for N1b, N2, and N3, a model of the physical properties of all the visible paramagnetic Fe–S clusters was established that revealed a fundamental picture of the electron transfer chain.

5.4.3 Gadolinium

Gd^{3+} complexes can be used as spin labels for high-field (Ka- to W-band) distance measurements, as demonstrated for rigid and flexible model systems [81, 82], for proteins [83–85] and for oligonucleotides [44]. The advantages of using Gd^{3+} ($S = 7/2$) spin labels are (1) the narrowing of the $|-1/2\rangle \rightarrow |1/2\rangle$ transition at higher magnetic fields, leading to an increased sensitivity at high fields; (2) the high transition probability of an $S = 7/2$ spin with respect to a $S = 1/2$ spin (nitroxide) which allows shorter pump pulses for equivalent B_1 excitation fields; (3) the short spin—lattice relaxation time that allows the use of shorter repetition times; and (4) the isotropic excitation resulting from a large distribution (inhomogeneity) in the zero-field splittings (ZFS) which typically suppresses orientation selection effects [81, 83, 84]. Since there is only a second-order contribution of the ZFS to the central transition, the system can be treated as an effective $S = 1/2$ spin and the DEER data can be analysed with standard software [84]. The DEER measurements are usually performed at ca. 25 K at a single magnetic field position, as orientation selection can be neglected; usually the pump pulse is set to the maximum of the central $|-1/2\rangle \rightarrow |1/2\rangle$ transition and the observer pulse is shifted by ca. 80 MHz [84]. Some possible disadvantages or complications are (1) contributions from other transitions (e.g. the pump/detection pulses could excite on the same spin the $|-1/2\rangle \rightarrow |1/2\rangle$ and $|1/2\rangle \rightarrow |3/2\rangle$ transitions, respectively) and (2) the validity of a treatment as an effective $S = 1/2$ system and neglect of pseudosecular terms of the dipolar interaction for an $S = 7/2$ spin system. In addition to Gd^{3+}–Gd^{3+} DEER, selective measurements of nitroxide–Gd^{3+} have also been shown to be possible [24, 86–88]. In the mixed case only the orientation selection for the nitroxide has to be considered, greatly simplifying the data analysis, since only two instead of five angles have to be considered (see also Table 1) [87]. The experimental aspects and analysis of Gd^{3+} DEER data are described in detail by Goldfarb [89] in this volume of Structure and Bonding.

5.4.4 Other Metal Centres

Three-pulse DEER at X-band was used to determine the distance between tyrosine D and the Mn cluster in the oxygen-evolving centre of photosystem II by Hara et al. [90]. A single measurement was performed by pumping on the tyrosine signal and detecting on the multi-line Mn^{2+} signal with a frequency offset of about 150 MHz. A distance of approximately 27 Å was determined [90]. A similar result was obtained when orientation selection was considered in the analysis.

Recently a new type of spin label based on Mn^{2+} was introduced for W-band DEER measurements by Banerjee et al. [91]. Similarly to Gd^{3+} ($S = 7/2$), Mn^{2+} ($S = 5/2$) is characterised by a high-field spectrum with narrow and intense central $|-1/2\rangle \rightarrow |1/2\rangle$ transitions and a short spin—lattice relaxation time. Its smaller coordination number allows, potentially, a greater variety of Mn^{2+} tags to

be developed and their application to a larger number of systems. Banerjee et al. performed measurements on the p75 neurotrophin receptor with two Mn^{2+}–EDTA (ethylenediaminetetraacetic acid) tags and showed the absence of orientation selection by comparing traces obtained at several magnetic fields within the central transition [91]. This allowed the data to be analysed by DeerAnalysis [16] and the resulting distance distribution was found to be in excellent agreement with modelling results. The authors, however, point out that for the present type of Mn^{2+} tag, DEER measurements using Gd^{3+} labels are still characterised by a higher sensitivity.

6 Conclusions and Future Prospects

Orientation-selective DEER data can provide useful 3D structural information. Orientation information is only available when there is a fixed orientation, or set of orientations, between the two radicals whose dipolar interaction is being probed. Naturally occurring organic cofactors, metal centres, and clusters in proteins are held in a fixed orientation with respect to the protein structure and are thus ideal spin probes if paramagnetic. Spin labels for nucleic acids also fall into this category. The spin label MTSL, most commonly used for proteins, has a flexible tether which under most circumstances renders the relative orientations of the two radicals essentially random, and only distance information is extractable from the DEER data.

With organic radicals, the orientation selection theoretically achievable strongly increases with spectrometer frequency as the resolution of the anisotropic electron Zeeman interaction is enhanced. However, even though the principal g-values of a nitroxide radical are not resolved at X-band, weak orientation selection effects may still be observed. This is a result of the ^{14}N hyperfine interaction which has a large and resolved $A_{\|}$ component, as compared to the two small $A_{\perp}$ values. At W-band and above, the principal g-values of a nitroxide radical are well resolved in field-swept EPR spectra and orientation-selective DEER data can be measured. However, this frequency and above is extremely challenging from a hardware point of view as ideally a broadband resonator is required along with strong mw pulses to excite enough of the spectrum to achieve good sensitivity (both echo intensity and modulation depth). Q- and Ka-bands are currently a very attractive choice due to the availability of reliable high-power TWT amplifiers and the ability to install this equipment on commercial (Bruker) spectrometers.

If metal centres or metal clusters are used as spin probes, in most circumstances X-band already provides good orientation resolution as a result of the large anisotropy of the g-matrix. In fact, many paramagnetic metal centres are presently not amenable to the DEER technique due to their very broad EPR spectra which cannot be suitably probed with the use of two frequencies and a single-mode resonator.

Possible solutions to this excitation bandwidth problem are bimodal resonators or the use of a single mw frequency with a field jump to reach the pump pulse observer position.

Analysis of orientation-selective DEER data on systems with broad orientation and distance distributions is very challenging. Due to the symmetry properties of both the spin Hamiltonian and dipolar interaction (which also gives the same $|\omega_{AB}|$ value for a number of θ values), there will be different orientations of the two radicals with respect to each other that produce identical DEER simulations. These solutions can only be distinguished with additional information, such as obtained from a chemical model. At present no general method exists for a model-free analysis as is the case for orientation-independent DEER data where Tikhonov regularisation is used. However, it is possible to simulate accurately DEER data from a given chemical model and adjust the model to obtain the desired 3D structural information.

Provided rigid spin labels are available, this approach offers the ability to measure accurately, for example, the heterogeneity of a protein structure in a molten globular state or subtle conformation changes in protein structure upon substrate recognition or ligand binding. Presently a big challenge to the versatility and applicability of DEER is the design of experimental conditions or additional measurements to determine precisely the exact orientation of the spin label relative to the attachment site (residue or structural unit).

Appendix I: Hamiltonians in Explicit Vector and Matrix Form

$$\begin{aligned}\mathbf{D}_{AB} &= \frac{\mu_0 {\beta_e}^2}{4\pi\hbar}\,\frac{\mathbf{g}_A\mathbf{g}_B^T - 3(\mathbf{g}_A\mathbf{n}_{AB}^T)(\mathbf{g}_B\mathbf{n}_{AB}^T)^T}{r_{AB}^3} \\ &= \frac{\mu_0 {\beta_e}^2}{4\pi\hbar}\,\frac{1}{r_{AB}^3}\left\{\begin{bmatrix} g_{xx}^A & g_{xy}^A & g_{xz}^A \\ & g_{yy}^A & g_{yz}^A \\ & & g_{zz}^A \end{bmatrix}\begin{bmatrix} g_{xx}^B & g_{xy}^B & g_{xz}^B \\ & g_{yy}^B & g_{yz}^B \\ & & g_{zz}^B \end{bmatrix}\right. \\ &\quad \left. -3\left(\begin{bmatrix} g_{xx}^A & g_{xy}^A & g_{xz}^A \\ & g_{yy}^A & g_{yz}^A \\ & & g_{zz}^A \end{bmatrix}\begin{bmatrix} n_x^{AB} \\ n_y^{AB} \\ n_z^{AB} \end{bmatrix}\right)\left(\begin{bmatrix} g_{xx}^B & g_{xy}^B & g_{xz}^B \\ & g_{yy}^B & g_{yz}^B \\ & & g_{zz}^B \end{bmatrix}\begin{bmatrix} n_x^{AB} \\ n_y^{AB} \\ n_z^{AB} \end{bmatrix}\right)^T\right\} \end{aligned} \quad (32)$$

$$\begin{aligned}\hat{H}_{\mathrm{dd}}^{\mathrm{AB}} &= \hat{\mathbf{S}}_{\mathrm{A}}\mathbf{D}_{\mathrm{AB}}\hat{\mathbf{S}}_{\mathrm{B}}^{\mathrm{T}} \\ &= \begin{bmatrix}\hat{S}_{\mathrm{x}}^{\mathrm{A}} & \hat{S}_{\mathrm{y}}^{\mathrm{A}} & \hat{S}_{\mathrm{z}}^{\mathrm{A}}\end{bmatrix}\begin{bmatrix}D_{\mathrm{xx}}^{\mathrm{AB}} & D_{\mathrm{xy}}^{\mathrm{AB}} & D_{\mathrm{xz}}^{\mathrm{AB}} \\ & D_{\mathrm{yy}}^{\mathrm{AB}} & D_{\mathrm{yz}}^{\mathrm{AB}} \\ & & D_{\mathrm{zz}}^{\mathrm{AB}}\end{bmatrix}\begin{bmatrix}\hat{S}_{\mathrm{x}}^{\mathrm{B}} \\ \hat{S}_{\mathrm{y}}^{\mathrm{B}} \\ \hat{S}_{\mathrm{z}}^{\mathrm{B}}\end{bmatrix},\end{aligned} \tag{33}$$

$$\begin{aligned}\hat{H} &= \hat{H}_{\mathrm{eZ}}^{\mathrm{A}} + \hat{H}_{\mathrm{eZ}}^{\mathrm{B}} + \hat{H}_{\mathrm{dd}}^{\mathrm{AB}} \\ &= \frac{\beta_e}{\hbar}\mathbf{B}_0\mathbf{g}_{\mathrm{A}}\hat{\mathbf{S}}_{\mathrm{A}}^{\mathrm{T}} + \frac{\beta_e}{\hbar}\mathbf{B}_0\mathbf{g}_{\mathrm{B}}\hat{\mathbf{S}}_{\mathrm{B}}^{\mathrm{T}} + \hat{\mathbf{S}}_{\mathrm{A}}\mathbf{D}_{\mathrm{AB}}\hat{\mathbf{S}}_{\mathrm{B}}^{\mathrm{T}},\end{aligned} \tag{34}$$

where

$$\hat{H}_{\mathrm{eZ}}^{k} = \frac{\beta_e}{\hbar}\begin{bmatrix}B_{0x} & B_{0y} & B_{0z}\end{bmatrix}\begin{bmatrix}g_{\mathrm{xx}}^{k} & g_{\mathrm{xy}}^{k} & g_{\mathrm{xz}}^{k} \\ & g_{\mathrm{yy}}^{k} & g_{\mathrm{yz}}^{k} \\ & & g_{\mathrm{zz}}^{k}\end{bmatrix}\begin{bmatrix}\hat{S}_{\mathrm{x}}^{k} \\ \hat{S}_{\mathrm{y}}^{k} \\ \hat{S}_{\mathrm{z}}^{k}\end{bmatrix}, \quad k = \mathrm{A}\text{ or }\mathrm{B}.$$

Appendix II: Density Matrix Simulations

If a fundamental description of the DEER time trace with respect to details of the mw pulses is required, then density matrix calculations can be employed. For 4-pulse DEER, this simulation involves an evolution Hamiltonian in a frame rotating with either the detection or pump pulse frequency:

$$\begin{aligned}\hat{H}^{\mathrm{rot}} &= \Omega_{\mathrm{A}}\hat{S}_{\mathrm{z}}^{\mathrm{A}} + \Omega_{\mathrm{B}}\hat{S}_{\mathrm{z}}^{\mathrm{B}} + \hat{\mathbf{S}}_{A}\mathbf{D}_{\mathrm{AB}}\hat{\mathbf{S}}_{\mathrm{B}}^{\mathrm{T}} \\ &\cong \Omega_{\mathrm{A}}\hat{S}_{\mathrm{z}}^{\mathrm{A}} + \Omega_{\mathrm{B}}\hat{S}_{\mathrm{z}}^{\mathrm{B}} + \omega_{\mathrm{dd}}(1 - 3\cos^2\theta)\hat{S}_{\mathrm{z}}^{\mathrm{A}}\hat{S}_{\mathrm{z}}^{\mathrm{B}},\end{aligned}$$

where $\Omega_{\mathrm{A}} = \omega_{\mathrm{A}} - \omega_{\mathrm{det}}$ and $\Omega_{\mathrm{B}} = \omega_{\mathrm{B}} - \omega_{\mathrm{det}}$ are the frequency offsets of the A- and B-spins from the detection pulse frequency, respectively. The offsets in the pump pulse frame are defined similarly. The mw pulse Hamiltonian, in the frame of rotation of either the detection pulse mw frequency or pump pulse mw frequency, is

$$\hat{H}_1 = \omega_1\hat{S}_{\mathrm{x}},$$

where ω_1 is the strength of the mw pulse, in radians. The density matrix $\rho(t)$ can then be propagated from the Boltzmann equilibrium $\rho(0) = \hat{S}_{\mathrm{z}}^{\mathrm{A}} + \hat{S}_{\mathrm{z}}^{\mathrm{B}}$ to the time of the echo,

$$\rho(\text{echo}) = U_{\text{ev4}}U_{\text{det}\,3}U_{\text{ev3}}U_{\text{coh}}U_{\text{p}}U_{\text{ev2}}U_{\text{det}\,2}U_{\text{ev1}}U_{\text{det}\,1}\rho(0) \times U^{\text{T}}_{\text{det}\,1}U^{\text{T}}_{\text{ev1}}U^{\text{T}}_{\text{det}\,2}U^{\text{T}}_{\text{ev2}}U^{\text{T}}_{\text{p}}U^{\text{T}}_{\text{coh}}U^{\text{T}}_{\text{ev3}}U^{\text{T}}_{\text{det}\,3}U^{\text{T}}_{\text{ev4}}.$$

The exponential operators U which propagate $\rho(t)$ are given by

$$\begin{aligned}
U_{\text{det}\,1} &= \exp(-i\hat{H}_{\text{det}}t_{\pi/2}) \\
U_{\text{ev1}} &= \exp(-i\hat{H}_0\tau_1) \\
U_{\text{det}\,2} &= \exp(-i\hat{H}_{\text{det}}t_{\pi}) \\
U_{\text{ev2}} &= \exp(-i\hat{H}_0 t) \\
U_{\text{p}} &= \exp(-i\hat{H}_{\text{pump}}t_{\pi}^{\text{pump}}) \\
U_{\text{coh}} &= \exp(-i\hat{H}_{\text{coherence}}t_{\pi}^{\text{pump}}) \\
U_{\text{ev3}} &= \exp(-i\hat{H}_0(\tau_1 + \tau + t_{\pi}^{\text{pump}} - t)) \\
U_{\text{det}\,3} &= \exp(-i\hat{H}_{\text{det}}t_{\pi}) \\
U_{\text{ev4}} &= \exp(-i\hat{H}_0\tau)
\end{aligned}$$

The propagator U_{coh} with $\hat{H}_{\text{coherence}} = (\omega_{\text{det}} - \omega_{\text{pump}})(\hat{S}^{\text{A}}_{\text{z}} + \hat{S}^{\text{B}}_{\text{z}})$ corrects for the relative phase accumulated in the pump pulse frame during the pump pulse to keep track consistently of the coherence evolution in the detection frame during the whole simulation. The components of the magnetisation M_x, M_y, and M_z are given by

$$M_i = \text{trace}(\rho\hat{S}_i), \text{ with } i = x, y, z.$$

Numerical implementation of the theory is straightforward on a computer. A useful example is given in [2] where a calculation to determine the lower distance limit of applicability of the DEER sequence due to the bandwidth of rectangular mw pulses was presented.

Appendix III: MATLAB Code for a 4-Pulse DEER Density Matrix Simulation

```
% Numerical density matrix simulation for the 4-pulse DEER experiment
% IMPORTANT MATLAB Variables
```

omega_a, omega_b	frequency offsets in rad/s of the A and B spins in the detection frame (varied independently throughout the spectrum)
omega_aP, omega_bP	frequency offsets in rad/s of the A and B spins in the pump frame
Delta	frequency difference between detection and pump spins in MHz
D	Dipolar frequency in rad/s
Theta	angle between the magnetic fi eld and the interspin vector (defined over a grid, for example by using the sphgrid function in EasySpin)
tp.det90/det180/pump180	pulse lengths of the pi/2 detection, the pi detection and the pi pump pulse (in microseconds)
W1.det90/det180/pump180	strength of the mw pulse; W1 = pulse flip angle / tp
tau1, tau	length of the interpulse delays in microseconds (see Figure 1)
tdeer	time axis of the DEER trace, tdeer = 0 when the pump pulse is centred on the primary echo of the first echo sequence

```
% Initial density matrix
P0 = Saz+Sbz;
% Spin Hamiltonians
% In the rotating frame of detection pulse
H0 = omega_a(k)*Saz+omega_b(l)*Sbz+D*(1-3*cos(theta)^2)*Saz*Sbz;
% In the rotating frame of pump pulse
H0P = omega_aP(k)*Saz+omega_bP(l)*Sbz+D*(1-3*cos(theta)^2)*Saz*Sbz;
% Propagators
% Microwave pulses
% Detection pulses
RxA90 = expm(-1i*(W1.det90*(Sax+Sbx) + H0)*tp.det90);
RxA180 = expm(-1i*(W1.det180*(Sax+Sbx) + H0)*tp.det180);
% Pump pulse
R=expm(-1i*phase*(Saz+Sbz)); % random phase of the pump pulse
RxB180 = expm(-1i*(W1.pump180*(R*(Sax+Sbx)*R') + H0P)*tp.pump180);
% Evolution during inter-pulse delays
% Evolution during tau1
Ev_tau1=expm(-1i*H0*tau1);
% Evolution before the pump pulse
Ev1=expm(-1i*H0*(tdeer(n)+(tau1+tp.det90/2-tp.pump180/2)));
% Evolution after the pump pulse
Ev2=expm(-1i*H0*(tau-tdeer(n)-tp.det90/2-tp.pump180/2));
% Operator accounting for the coherence evolution di fference between
the pump and detection rotating frame
Ev=expm(-1i*delta*(Saz+Sbz)*tp.pump180);
% Evolution operator for the echo integration
Ev_tau_d0(m)=expm(-1i*H0*(tau+d0(m)));
% Density matrix calculation
% Initial two-pulse sequence
P1=RxA180*Ev_tau1*RxA90*P0*RxA90'*Ev_tau1'*RxA180';
% Evolution before the pump pulse
P2 = Ev1*P1*Ev1';
% Pump pulse
P3 = Ev*RxB180*P2*RxB180'*Ev';
% Evolution after the pump pulse and last detection pulse
P4 = RxA180*Ev2*P3*Ev2'*RxA180';
% Final density matrix with integration over the final echo
P_signal=Ev_tau_d0(m)*P4*Ev_tau_d0(m)';
% Detection
% Magnetization of the A-spin
Ma(n)=[trace(P_signal*Sax) trace(P_signal*Say) trace(P_signal*Saz)];
% Magnetization of the B-spin
Mb(n)=[trace(P_signal*Sbx) trace(P_signal*Sby) trace(P_signal*Sbz)];
% Detection on both spins
Mab(n)=[trace(P_signal*(Sax+Sbx)) trace(P_signal*(Say+Sby))
        trace(P_signal*(Saz+Sbz))];
```

References

1. Ward R, Bowman A, Sozudogru E, El-Mkami H, Owen-Hughes T, Norman DG (2010) EPR distance measurements in deuterated proteins. J Magn Reson (San Diego, Calif: 1997) 207(1):164–167. doi:10.1016/j.jmr.2010.08.002
2. Banham JE, Baker CM, Ceola S, Day IJ, Grant GH, Groenen EJJ, Rodgers CT, Jeschke G, Timmel CR (2008) Distance measurements in the borderline region of applicability of CW EPR and DEER: a model study on a homologous series of spin-labelled peptides. J Magn Reson 191(2):202–218. doi:10.1016/j.jmr.2007.11.023
3. Schweiger A, Jeschke G (2001) Principles of pulse electron paramagnetic resonance. Oxford University Press, Inc., New York
4. Milov AD, Ponomarev AB, Tsvetkov YD (1984) Electron electron double resonance in electron-spin-echo – model biradical systems and the sensitized Photolysis of Decalin. Chem Phys Lett 110(1):67–72
5. Milov AD, Salikhov KM, Schirov MD (1981) Application of ENDOR in Electron-Spin Echo for Paramagnetic Center Space Distributions in Solids. Fiz Tverd Tela 23(4):975–982
6. Martin RE, Pannier M, Diederich F, Gramlich V, Hubrich M, Spiess HW (1998) Determination of end-to-end distances in a series of TEMPO diradicals of up to 2.8 nm length with a new four–pulse double electron electron resonance experiment. Angew Chem Int Edit 37:2834–2837
7. Pannier M, Veit S, Godt A, Jeschke G, Spiess HW (2000) Dead-time free measurement of dipole–dipole interactions between electron spins. J Magn Reson 142(2):331–340
8. Astashkin AV, Hara H, Kawamori A (1998) The pulsed electron—electron double resonance and "2+1" electron spin echo study of the oriented oxygen-evolving and Mn-depleted preparations of photosystem II. J Chem Phys 108(9):3805–3812
9. Saxena S, Freed JH (1997) Theory of double quantum two-dimensional electron spin resonance with application to distance measurements. J Chem Phys 107(5):1317–1340
10. Kulik LV, Paschenko SV, Dzuba SA (2002) 130 GHz ESEEM induced by electron–electron interaction in biradical. J Magn Reson 159(2):237–241. doi:10.1016/s1090-7807(02)00038-1
11. Milikisyants S, Scarpelli F, Finiguerra MG, Ubbink M, Huber M (2009) A pulsed EPR method to determine distances between paramagnetic centers with strong spectral anisotropy and radicals: the dead-time free RIDME sequence. J Magn Reson 201:48–56
12. Astashkin AV, Elmore BO, Fan W, Guillemette JG, Feng C (2010) Pulsed EPR determination of the distance between heme iron and FMN centers in a human inducible nitric oxide synthase. J Am Chem Soc 132:12059–12067
13. Savitsky A, Dubinskii AA, Zimmermann H, Lubitz W, Mobius K (2011) High-field dipolar electron paramagnetic resonance (EPR) spectroscopy of nitroxide biradicals for determining three-dimensional structures of biomacromolecules in disordered solids. J Phys Chem B 115(41):11950–11963. doi:10.1021/jp206841v
14. Jeschke G, Koch A, Jonas U, Godt A (2002) Direct conversion of EPR dipolar time evolution data to distance distributions. J Magn Reson 155:72–82
15. Chiang Y-W, Borbat PP, Freed JH (2005) The determination of pair distance distributions by pulsed ESR using Tikhonov regularization. J Magn Reson 172:279–295
16. Jeschke G, Chechik V, Ionita P, Godt A, Zimmermann H, Banham J, Timmel CR, Hilger D, Jung H (2006) DeerAnalysis2006 – a comprehensive software package for analyzing pulsed ELDOR data. Appl Magn Reson 30(3–4):473–498
17. Marko A, Denysenkov VP, Margraf D, Cekan P, Schiemann O, Sigurdsson ST, Prisner T (2011) Conformational flexibility of DNA. J Am Chem Soc 133:13375–13379
18. Fleissner MR, Bridges MD, Brooks EK, Cascio D, Kálai T, Hideg K, Hubbell WL (2011) Structure and dynamics of a conformationally constrained nitroxide side chain and applications in EPR spectroscopy. Proc Natl Acad Sci U S A 108:16241–16246
19. Milikisyants S, Groenen EJJ, Huber M (2008) Observer-selective double electron–electron-spin resonance, a pulse sequence to improve orientation selection. J Magn Reson 192:275–279

20. Borbat PP, Freed JH (2012) Pulse dipolar ESR: distance measurements. In: Timmel CR, Harmer JR (eds) Spin-labels and intrinsic paramagnetic centres in the biosciences: structural information from distance measurements. Struct Bond. Springer-Verlag, Berlin Heidelberg. doi:10.1007/430_2012_82
21. Borbat PP, Georgieva ER, Freed JH (2013) Improved sensitivity for long-distance measurements in biomolecules: five-pulse double electron electron resonance. J Phys Chem Lett 4:170–175. doi:10.1021/jz301788n
22. Tkach I, Sicoli G, Hobartner C, Bennati M (2011) A dual-mode microwave resonator for double electron–electron spin resonance spectroscopy at W-band microwave frequencies. J Magn Reson 209(2):341–346. doi:10.1016/j.jmr.2011.01.012
23. Tkach I, Pornsuwan S, Höbartner C, Wachowius F, Sigurdsson ST, Baranova TY, Diederichsen U, Sicoli G, Bennati M (2013) Orientation selection in distance measurements between nitroxide spin labels at 94 GHz EPR with variable dual frequency irradiation. Phys Chem Chem Phys 15:3433–3437
24. Kaminker I, Tkach I, Manukovsky N, Huber T, Yagi H, Otting G, Bennati M, Goldfarb D (2013) W-band orientation selective DEER measurements on a Gd^{3+}/nitroxide mixed-labeled protein dimer with a dual mode cavity. J Magn Reson 227:66–71
25. Dubinskii AA, Grishin YA, Savitsky AN, Möbius K (2002) Submicrosecond field-jump device for pulsed high-field ELDOR. Appl Magn Reson 22:369–386
26. Tsvetkov YD, Grishin YA (2009) Techniques for EPR spectroscopy of pulsed electron double resonance (PELDOR): a review. Instrum Exp Tech 52:615–636
27. Kaminker I, Florent M, Epel B, Goldfarb D (2011) Simultaneous acquisition of pulse EPR orientation selective spectra. J Magn Reson 208(1):95–102. doi:10.1016/j.jmr.2010.10.010
28. Weber A, Schiemann O, Bode B, Prisner TF (2002) PELDOR at S- and X-band frequencies and the separation of exchange coupling from dipolar coupling. J Magn Reson 157(2):277–285. doi:10.1006/jmre.2002.2596
29. Bode B, Plackmeyer J, Bolte M, Prisner T, Schiemann O (2009) PELDOR on an exchange coupled nitroxide copper(II) spin pair. J Organomet Chem 694:1172–1179
30. Margraf D, Cekan P, Prisner TF, Sigurdsson ST, Schiemann O (2009) Ferro- and antiferromagnetic exchange coupling constants in PELDOR spectra. Phys Chem Chem Phys 11(31):6708–6714. doi:10.1039/b905524j
31. Larsen RG, Singel DJ (1993) Double electron—electron resonance spin-echo modulation – spectroscopic measurement of electron-spin pair separations in orientationally disordered solids. J Chem Phys 98(7):5134–5146. doi:10.1063/1.464916
32. Polyhach Y, Godt A, Bauer C, Jeschke G (2007) Spin pair geometry revealed by high-field DEER in the presence of conformational distributions. J Magn Reson 185(1):118–129. doi:10.1016/j.jmr.2006.11.012
33. Margraf D, Bode BE, Marko A, Schiemann O, Prisner TF (2007) Conformational flexibility of nitroxide biradicals determined by X-band PELDOR experiments. Mol Phys 105(15–16):2153–2160. doi:10.1080/00268970701724982
34. Lovett JE, Bowen AM, Timmel CR, Jones MW, Dilworth JR, Caprotti D, Bell SG, Wong LL, Harmer J (2009) Structural information from orientationally selective DEER spectroscopy. Phys Chem Chem Phys 11(31):6840–6848. doi:10.1039/b907010a
35. Marko A, Margraf D, Yu H, Mu Y, Stock G, Prisner T (2009) Molecular orientation studies by pulsed electron—electron double resonance experiments. J Chem Phys 130(6). doi:06410210.1063/1.3073040
36. Marko A, Margraf D, Cekan P, Sigurdsson ST, Schiemann O, Prisner TF (2010) Analytical method to determine the orientation of rigid spin labels in DNA. Phys Rev E 81(2):9. doi:02191110.1103/PhysRevE.81.021911
37. Jeschke G (2011) Interpretation of Dipolar EPR Data in Terms of Protein Structure. In: Timmel CR, Harmer JR (eds) Spin-labels and intrinsic paramagnetic centres in the Biosciences: Structural information from distance measurements. Struct Bond. Springer-Verlag, Berlin Heidelberg. doi:10.1007/430_2011_61

38. Mims WB (1972) In: Geschwind S (ed) Electron paramagnetic resonance. Plenum, New York, pp 263–351
39. Abe C, Klose D, Dietrich F, Ziegler WH, Polyhach Y, Jeschke G, Steinhoff H-J (2012) Orientation selective DEER measurements on vinculin tail at X-band frequencies reveal spin label orientations. J Magn Reson 216:53–61. doi:10.1016/j.jmr.2011.12.024
40. Marko A, Prisner T (2013) An algorithm to analyze PELDOR data of rigid spin label pairs. Phys Chem Chem Phys 15:619–627
41. Song L, Larion M, Chamoun J, Bonora M, Fajer P (2010) Distance and dynamics determination by W-band DEER and W-band ST-EPR. Eur Biophys J 39:711–719
42. Godt A, Schulte M, Zimmermann H, Jeschke G (2006) How flexible are poly(para-phenyleneethynylene)s? Angew Chem Int Edit 45(45):7560–7564
43. Raitsimring A, Astashkin A, Enemark JH, Blank A, Twig Y, Song Y, Meade TJ (2011) Dielectric Resonator for Ka-band pulsed EPR measurements at cryogenic temperatures: probe head construction and applications. Appl Magn Reson 42(4):441–452. doi:10.1007/s00723-012-0313-1
44. Song Y, Meade TJ, Astashkin AV, Klein EL, Enemark JH, Raitsimring A (2011) Pulsed dipolar spectroscopy distance measurements in biomacromolecules labeled with Gd(III) markers. J Magn Reson 210(1):59–68. doi:10.1016/j.jmr.2011.02.010
45. Polyhach Y, Bordignon E, Tschaggelar R, Gandra S, Godt A, Jeschke G (2012) High sensitivity and versatility of the DEER experiment on nitroxide radical pairs at Q-band frequencies. Phys Chem Chem Phys 14:10762–10773
46. Endeward B, Butterwick JA, MacKinnon R, Prisner T (2009) Pulsed electron—electron double-resonance determination of spin-label distances and orientations on the tetrameric potassium ion channel KcsA. J Am Chem Soc 131:15246–15250
47. Sicoli G, Argirevic T, Stubbe J, Tkach I, Bennati M (2010) Effects in 94 GHz orientation-selected PELDOR on a rigid pair of radicals with non-collinear axes. Appl Magn Reson 37(1–4):539–548. doi:10.1007/s00723-009-0094-3
48. Goldfarb D, Lipkin Y, Potapov A, Gorodetsky Y, Epel B, Raitsimring AM, Radoul M, Kaminker I (2008) HYSCORE and DEER with an upgraded 95 GHz pulse EPR spectrometer. J Magn Reson 194(1):8–15. doi:10.1016/j.jmr.2008.05.019
49. Cruickshank PAS, Bolton DR, Robertson DA, Hunter RI, Wylde RJ, Smith GM (2009) A kilowatt pulsed 94 GHz electron paramagnetic resonance spectrometer with high concentration sensitivity, high instantaneous bandwidth, and low dead time. Rev Sci Inst 80:103101–103115
50. Denysenkov VP, Prisner TF, Stubbe J, Bennati M (2006) High-field pulsed electron—electron double resonance spectroscopy to determine the orientation of the tyrosyl radicals in ribonucleotide reductase. Proc Natl Acad Sci USA 103(36):13386–13390. doi:10.1073/pnas.0605851103
51. Denysenkov VP, Biglino D, Lubitz W, Prisner TF, Bennati M (2008) Structure of the tyrosyl biradical in mouse R2 ribonucleotide reductase from high-field PELDOR. Angew Chem Int Edit 47(7):1224–1227. doi:10.1002/anie.200703753
52. Gajula P, Milikisyants S, Steinhoff HJ, Huber M (2007) A short note on orientation selection in the DEER experiments on a native cofactor and a spin label in the reaction center of *Rhodobacter sphaeroides*. Appl Magn Reson 31(1–2):99–104
53. Flores M, Savitsky A, Paddock ML, Abresch EC, Dubinskii AA, Okamura MY, Lubitz W, Mobius K (2010) Electron–nuclear and electron–electron double resonance spectroscopies show that the primary quinone acceptor Q(A) in reaction centers from photosynthetic bacteria *Rhodobacter sphaeroides* remains in the same orientation upon light-induced reduction. J Phys Chem B 114(50):16894–16901. doi:10.1021/jp107051r
54. Sicoli G, Wachowius F, Bennati M, Hobartner C (2010) Probing secondary structures of spin-labeled RNA by pulsed EPR spectroscopy. Angew Chem Int Edit 49:6443–6447

55. Kuznetsov NA, Milov AD, Isaev NP, Vorobjev YN, Koval VV, Dzuba SA, Fedorova OS, Tsvetkov YD (2011) PELDOR analysis of enzyme-induced structural changes in damaged DNA duplexes. Mol Biosyst 7:2670–2680
56. Reginsson GW, Shelke SA, Rouillon C, White MF, Sigurdsson ST, Schiemann O (2012) Protein-induced changes in DNA structure and dynamics observed with noncovalent site-directed spin labeling and PELDOR. Nucl Acids Res 41(1):e11. doi:10.1093/nar/gks817
57. Wunnicke D, Ding P, Seela F, Steinhoff HJ (2012) Site-directed spin labeling of DNA reveals mismatch-induced nanometer distance changes between flanking nucleotides. J Phys Chem B 116(14):4118–4123. doi:10.1021/jp212421c
58. Barhate N, Cekan P, Massey AP, Sigurdsson ST (2007) A nucleoside that contains a rigid nitroxide spin label: a fluorophore in disguise. Angew Chem Int Edit 46:2655–2658
59. Schiemann O, Cekan P, Margraf D, Prisner TF, Sigurdsson ST (2009) Relative orientation of rigid nitroxides by PELDOR: beyond distance measurements in nucleic acids. Angew Chem Int Edit 48(18):3292–3295. doi:10.1002/anie.200805152
60. Shelke SA, Sigurdsson ST (2012) Site-directed nitroxide spin labeling of biopolymers. In: Timmel CR, Harmer J (eds) Spin-labels and intrinsic paramagnetic centres in the biosciences: structural information from distance measurements. Structure and Bonding. Springer, Berlin Heidelberg. doi:10.1007/430_2011_62
61. Ward R, Schiemann O (2012) Structural information from oligonucleotides. In: Timmel CR, Harmer J (eds) Spin-labels and intrinsic paramagnetic centres in the biosciences: structural information from distance measurements. Structure and bonding. Springer, Berlin Heidelberg. doi:10.1007/430_2012_76
62. Stoll S, Schweiger A (2006) EasySpin, a comprehensive software package for spectral simulation and analysis in EPR. J Magn Reson 178:42–55
63. Narr E, Godt A, Jeschke G (2002) Selective measurements of a nitroxide–nitroxide separation of 5 nm and a nitroxide–copper separation of 2.5 nm in a terpyridine-based copper(II) complex by pulse EPR spectroscopy. Angew Chem Int Edit 41(20):3907–3910. doi:10.1002/1521-3773(20021018)41:20<3907::aid-anie3907>3.0.co;2-t
64. van Amsterdam IMC, Ubbink M, Canters GW, Huber M (2003) Measurement of a Cu–Cu distance of 26 Angstrom by a pulsed EPR method. Angew Chem Int Ed 42(1):62–64
65. Kay CWM, El Mkami H, Cammack R, Evans RW (2007) Pulsed ELDOR determination of the intramolecular distance between the metal binding sites in dicupric human serum transferrin and lactoferrin. J Am Chem Soc 129:4868–4869. doi:10.1021/ja068966j
66. Becker J, Saxena S (2005) Double quantum coherence electron spin resonance on coupled Cu (II)–Cu(II) electron spins. Chem Phys Lett 414:248–252
67. Yang Z, Becker J, Saxena S (2007) On Cu(II)–Cu(II) distance measurements using pulsed electron electron double resonance. J Magn Reson 188(2):337–343. doi:10.1016/j.jmr.2007.08.006
68. Yang Z, Kise D, Saxena S (2010) An approach towards the measurement of nanometer range distances based on Cu^{2+} Ions and ESR. J Phys Chem B 114:6165–6174
69. Bode BE, Plackmeyer J, Prisner TF, Schiemann O (2008) PELDOR measurements on a nitroxide-labeled Cu(II) porphyrin: orientation selection, spin-density distribution, and conformational flexibility. J Phys Chem A 112(23):5064–5073. doi:10.1021/jp710504k
70. Yang Z, Ji M, Saxena S (2010) Practical aspects of copper ion-based double electron electron resonance distance measurements. Appl Magn Res 39:487–500
71. Maryasov AG, Tsvetkov YD, Raap J (1998) Weakly coupled radical pairs in solids: ELDOR in ESE structure studies. Appl Magn Reson 14:101–113
72. Yang Z, Kurpiewski MR, Ji M, Townsend JE, Mehta P, Jen-Jacobson L, Saxena S (2012) ESR spectroscopy identifies inhibitory Cu^{2+} sites in a DNA-modifying enzyme to reveal determinants of catalytic specificity. Proc Natl Acad Sci U S A 109:6366
73. Bowen AM (2012) Magnetic Resonance Studies of Proteins and Model Systems. University of Oxford, Oxford, (DPhil thesis)
74. Bencini A, Gatteschi D (1990) EPR of exchange coupled systems. Springer-Verlag, Berlin

75. Mouesca JM, Noodleman L, Case DA, Lamotte B (1995) Spin-densities and spin coupling in iron–sulfur clusters – a new analysis of hyperfine coupling-constants. Inorg Chem 34(17):4347–4359
76. Kappl R, Ebelshauser M, Hannemann F, Bernhardt R, Huttermann J (2006) Probing electronic and structural properties of the reduced [2Fe–2S] cluster by orientation-selective H-1 ENDOR spectroscopy: Adrenodoxin versus Rieske iron-sulfur protein. Appl Magn Reson 30(3–4):427–459
77. Abdalla JAB, Bowen AM, Bell SG, Wong LL, Timmel CR, Harmer J (2012) Characterisation of the paramagnetic $[2Fe–2S]^+$ centre in palustrisredoxin-B (PuxB) from *Rhodopseudomonas palustris* CGA009: g-matrix determination and spin coupling analysis. Phys Chem Chem Phys 14:6526–6537
78. Elsässer C, Brecht M, Bittl R (2002) Pulsed electron—electron double resonance on multinuclear metal clusters: assignment of spin projection factors based on the dipolar interaction. J Am Chem Soc 124(42):12606–12611. doi:10.1021/ja027348+
79. Elsässer C, Brecht M, Bittl R (2005) Treatment of spin-coupled metal-centres in pulsed electron—electron double-resonance experiments. Biochem Soc Trans 33:15–19
80. Roessler MM, King MS, Robinson AJ, Armstrong FA, Harmer J, Hirst J (2010) Direct assignment of EPR spectra to structurally defined iron–sulfur clusters in complex I by double electron—electron resonance. Proc Natl Acad Sci U S A 107(5):1930–1935. doi:10.1073/pnas.0908050107
81. Raitsimring A, Gunanathan C, Potapov A, Efremenko I, Martin JML, Milstein D, Goldfarb D (2007) Gd^{3+} complexes as potential spin labels for high field pulsed EPR distance measurements. J Am Chem Soc 129:14138–14139
82. Potapov A, Song Y, Meade TJ, Goldfarb D, Astashkin AV, Raitsimring A (2010) Distance measurements in model bis-Gd(III) complexes with flexible "bridge". Emulation of biological molecules having flexible structure with Gd(III) labels attached. J Magn Reson 205(1):38–49. doi:10.1016/j.jmr.2010.03.019
83. Potapov A, Yagi H, Huber T, Jergic S, Dixon NE, Otting G, Goldfarb D (2010) Nanometer-scale distance measurements in proteins using Gd^{3+} spin labeling. J Am Chem Soc 132(26):9040–9048. doi:10.1021/ja1015662
84. Gordon-Grossman M, Kaminker I, Gofman Y, Shai Y, Goldfarb D (2011) W-Band pulse EPR distance measurements in peptides using Gd^{3+}-dipicolinic acid derivatives as spin labels. Phys Chem Chem Phys 13(22):10771–10780. doi:10.1039/c1cp00011j
85. Yagi H, Banerjee D, Graham B, Huber T, Goldfarb D, Otting G (2011) Gadolinium tagging for high-precision measurements of 6 nm distances in protein assemblies by EPR. J Am Chem Soc 133:10418–10421
86. Lueders P, Jeschke G, Yulikov M (2011) Double electron—electron resonance measured between Gd^{3+} ions and nitroxide radicals. J Phys Chem Lett 2:604–609
87. Kaminker I, Yagi H, Huber T, Feintuch A, Otting G, Goldfarb D (2012) Spectroscopic selection of distance measurements in a protein dimer with mixed nitroxide and Gd^{3+} spin labels. Phys Chem Chem Phys 14(13):4355–4358. doi:10.1039/c2cp40219j
88. Yulikov M, Lueders P, Warsi MF, Chechik V, Jeschke G (2012) Distance measurements in Au nanoparticles functionalized with nitroxide radicals and Gd^{3+}-DTPA chelate complexes. Phys Chem Chem Phys 14:10732–10746
89. Goldfarb D (2012) Metal-based spin labeling for distance determination. In: Timmel CR, Harmer J (eds) Spin-labels and intrinsic paramagnetic centres in the biosciences: structural information from distance measurements. Structure and bonding. Springer-Verlag, Berlin Heidelberg. doi:10.1007/430_2011_63
90. Hara H, Kawamori A, Astashkin AV, Ono T (1996) The distances from tyrosine D to redox-active components on the donor side of Photosystem II determined by pulsed electron—electron double resonance. Biochim Biophys Acta Bioenerg 1276(2):140–146
91. Banerjee D, Yagi H, Huber T, Otting G, Goldfarb D (2012) Nanometer-range distance measurement in a protein using Mn^{2+} tags. J Physl Chem Lett 3(2):157–160. doi:10.1021/jz201521d

Index